

Elements of airplane performance

Elements of airplane performance

Ger J.J. Ruijgrok

Faculty of Aerospace Engineering
Delft University of Technology

VSSD

© VSSD
Second edition 2009

Published by VSSD
Leeghwaterstraat 42, 2628 CA Delft, The Netherlands
tel. +31 15 27 82124, telefax +31 15 27 87585, e-mail: hlf@vssd.nl
internet: <http://www.vssd.nl/hlf>
URL about this book: <http://www.vssd.nl/hlf/ae02.htm>

All rights reserved. No part of this publication may be reproduced, stored in a retrieval system, or transmitted, in any form or by any means, electronic, mechanical, photocopying, recording, or otherwise, without the prior written permission of the publisher.

Printed version 2nd edition
ISBN-13 978-90-6562-203-7
Electronic version 2nd edition
ISBN-13 978-90-6562-204-4

NUR 968

Key words: airplane performance

Preface

About the contents

This book presents a teaching text on airplane performance. This field has to do with the translational motion of flight vehicles, in which we study such questions as maximum flight speed, maximum rate of climb, range, and takeoff distances.

A number of books on the dynamics of flight have appeared in the last decades, aimed at a variety of subjects.

Concerning the treatment of the capability of airplanes to perform specific maneuvers and their operational tasks, most of the existing books are of limited scope. However, the technological developments and the growing importance for all airplane types to function economically have introduced the need for a comprehensive, modern book on the principles and practice of airplane performance prediction suited for use as a primary text in undergraduate engineering courses. The present book is intended to fulfill that need.

The book is a description of the regular courses on airplane performance as have been taught for many years by the author at the Faculty of Aerospace Engineering of Delft University of Technology (TUD), The Netherlands, and at the Faculty of Applied Sciences of the Brussels Free University (VUB), Belgium.

In the text, three fairly well-defined parts may be distinguished.

The first part comprises the chapters 1 to 7, which deal with some basic concepts of the airplane and its motion, the properties of the atmosphere, and the general equations of motion. Furthermore, these supporting chapters include the basics of the generation of aerodynamic forces and moments, the operating principles of the air data instruments and their application to flight, some fundamental aspects and operating characteristics of airplane propulsion systems, and the theory of the propeller. These subjects represent the required background knowledge necessary for the subsequent analysis of the performance of powered and unpowered airplanes.

The second part is formed by the chapters 8 to 13, where especially are discussed the classical methods of predicting the performance values of airplanes that pertain to a given point of time or a given point on the flight path (point performance). To illustrate the applications of the theory in practical problems, numerous worked examples, employing the SI-system of units and notation, are included in these chapters.

The last part of the main text (chapters 14 to 16) is devoted to giving an account

of the most common techniques used for estimating the performance items that are related to the course of the flight (integral performance).

In analyzing the performance in chapters 8 to 16, use is made of both analytical and graphical techniques.

In order to provide a clear understanding of the fundamental equations of motion, in Appendix A the essentials of Newtonian mechanics are described. In Appendix B are listed a number of conversion factors between English and metric units and between technical units and the equivalent Si units. In Appendix C is given a table of values for the International Standard Atmosphere up to an altitude of 32 km. Finally, in Appendix D, one-dimensional steady flow equations are reviewed of which the knowledge is a prerequisite for an appreciation of the aerodynamics and the many technical aspects of atmospheric flight.

References to the literature are indicated in the text and listed at the end of the book. In addition, a few more general references have been included.

My special thanks are due to the late Mr. Dirk M. van Paassen, who was a colleague in much of the preparation of the material presented, and without whose cooperation this book could not have been written.

Delft, The Netherlands

May 2007

G.J.J. Ruijgrok

In this second edition, apart from a few minor adjustments, all the material from the first edition has been retained and the errors found in the first edition have been rectified.

Delft, The Netherlands

August 2009

G.J.J. Ruijgrok

Contents

| | | |
|----------|---|-----------|
| 1 | BASIC CONCEPTS | 1 |
| 1.1 | Introduction | 1 |
| 1.2 | The airplane is regarded a rigid body | 1 |
| 1.3 | Application of Newton's law of motion with respect to an axis system attached to the Earth | 3 |
| 1.4 | Gravitation | 6 |
| 1.5 | The effect of curvature of the Earth | 8 |
| 1.6 | Coordinate systems | 9 |
| 1.7 | Angles and velocities describing the angular displacement of the airplane | 10 |
| 1.8 | The airplane | 16 |
| 1.9 | Flight types, airplane configuration and flight condition | 18 |
| 1.10 | Forces on the airplane | 19 |
| 1.11 | SI-system of units | 21 |
| 2 | THE ATMOSPHERE | 24 |
| 2.1 | Nature of the atmosphere | 24 |
| 2.2 | Variation of pressure with altitude | 27 |
| 2.3 | Standard atmospheres | 28 |
| 2.4 | Off-standard atmospheres | 33 |
| 2.5 | Humidity | 34 |
| 2.6 | Vertical motion in the atmosphere | 39 |
| 2.7 | Wind | 43 |
| 2.8 | Atmospheric fronts | 47 |
| 3 | EQUATIONS OF MOTION | 51 |
| 3.1 | Translational motion | 51 |
| 3.2 | Rotational motion | 52 |
| 3.3 | The most general steady motion | 55 |
| 3.4 | Special types of flight | 57 |
| 3.5 | Translational equation for variable mass | 61 |
| 4 | AERODYNAMIC BASIS | 63 |
| 4.1 | Aerodynamic coefficients | 63 |
| 4.2 | Airfoil and wing characteristics | 67 |

| | | |
|-----------|---|------------|
| 4.3 | The lift-drag polar | 73 |
| 4.4 | Parabolic lift-drag polar | 82 |
| 5 | AIR DATA INSTRUMENTS | 87 |
| 5.1 | Introduction | 87 |
| 5.2 | The altimeter | 87 |
| 5.3 | The vertical-speed indicator | 91 |
| 5.4 | The airspeed indicator | 92 |
| 5.5 | The machmeter | 97 |
| 5.6 | Ambient air temperature measurement | 98 |
| 6 | PROPULSION | 100 |
| 6.1 | Types of airplane propulsion systems | 100 |
| 6.2 | The piston engine | 104 |
| 6.3 | Definition of thrust for jet propulsion | 110 |
| 6.4 | Ideal turbojet cycle | 112 |
| 6.5 | Component efficiencies | 117 |
| 6.6 | Typical turbojet performance | 124 |
| 6.7 | The turboprop engine | 129 |
| 6.8 | The turbofan | 133 |
| 7 | PROPELLER PERFORMANCE | 140 |
| 7.1 | Propeller thrust and efficiency | 140 |
| 7.2 | Propeller geometry | 145 |
| 7.3 | Blade element theories | 148 |
| 7.4 | Propeller charts | 154 |
| 7.5 | Installed propeller performance | 159 |
| 8 | THE AIRPLANE IN SYMMETRIC FLIGHT | 161 |
| 8.1 | Fundamental equations | 161 |
| 8.2 | Integral and point performance | 166 |
| 8.3 | Air loads | 167 |
| 8.4 | Stalling speeds | 169 |
| 8.5 | Load factor envelopes | 171 |
| 9 | PERFORMANCE IN STEADY SYMMETRIC FLIGHT | 175 |
| 9.1 | Basic relations | 175 |
| 9.2 | Drag and power required | 177 |
| 9.3 | Thrust and power available | 184 |
| 9.4 | The performance diagram | 190 |
| 9.5 | Performance prediction using analytical expressions | 195 |
| 10 | EFFECT OF ALTITUDE | 200 |
| 10.1 | Effect of altitude on drag and power required | 200 |
| 10.2 | Rate of climb and climb angle | 201 |

| | | |
|-----------|--|------------|
| 10.3 | Stall, propulsion and buffet boundaries | 206 |
| 10.4 | Flight envelope | 211 |
| 11 | FLIGHT AND AIRPLANE CONDITION EFFECTS | 215 |
| 11.1 | Effect of weight | 215 |
| 11.2 | Effect of engine failure | 219 |
| 11.3 | Effect of changes of engine control setting | 224 |
| 11.4 | Effect of airplane configuration | 227 |
| 12 | TURNING PERFORMANCE | 231 |
| 12.1 | Governing equations | 231 |
| 12.2 | Equations for the performance in a coordinated turn | 233 |
| 12.3 | Calculation of turning performance | 239 |
| 12.4 | Analytic expressions for best turning performance | 242 |
| 12.5 | Climbing and descending turns | 245 |
| 13 | GLIDING FLIGHT | 249 |
| 13.1 | Symmetric flight | 249 |
| 13.2 | Effect of altitude | 254 |
| 13.3 | Effect of wind | 258 |
| 13.4 | Turning flight | 261 |
| 13.5 | Cross-country flight | 265 |
| 14 | SYMMETRIC CLIMB AND DESCENT | 269 |
| 14.1 | Quasi-steady symmetric flight | 269 |
| 14.2 | The unsteady quasi-rectilinear climb | 272 |
| 14.3 | Optimum climb | 275 |
| 14.4 | Effects of vertical wind gradients | 278 |
| 14.5 | Limitations on vertical velocity | 280 |
| 15 | CRUISE PERFORMANCE | 283 |
| 15.1 | Range and endurance | 283 |
| 15.2 | Approximate analytic expressions for range and endurance (propeller propulsion) | 286 |
| 15.3 | Approximate analytic expressions for range and endurance (jet propulsion) | 288 |
| 15.4 | Effect of wind on cruise performance | 293 |
| 15.5 | Weight breakdown | 295 |
| 15.6 | The economic performance of transport airplanes | 298 |
| 16 | AIRFIELD PERFORMANCE | 301 |
| 16.1 | The takeoff maneuver | 301 |
| 16.2 | Takeoff ground run | 303 |
| 16.3 | The airborne phase of the takeoff maneuver | 307 |
| 16.4 | Effect of wind on takeoff | 311 |

| | | |
|-------------------|--|------------|
| 16.5 | The landing maneuver | 312 |
| 16.6 | The airborne distance of the landing maneuver | 313 |
| 16.7 | The landing ground run | 316 |
| Appendices | | 321 |
| A | NEWTONIAN MECHANICS | 322 |
| A.1 | Newton's laws of motion | 322 |
| A.2 | Newton's first law | 322 |
| A.3 | Newton's second law of motion | 323 |
| A.4 | Effect of rotation | 324 |
| A.5 | Noninertial reference frames | 326 |
| A.6 | Systems of particles | 327 |
| A.7 | General bodies | 330 |
| A.8 | Rigid bodies | 332 |
| A.9 | Center of gravity | 333 |
| B | CONVERSION FACTORS | 334 |
| C | INTERNATIONAL STANDARD ATMOSPHERE | 335 |
| D | ONE-DIMENSIONAL STEADY FLOW EQUATIONS | 343 |
| D.1 | Continuity equation | 343 |
| D.2 | Bernoulli's equation | 344 |
| D.3 | The momentum equation | 345 |
| D.4 | The energy equation | 347 |
| D.5 | Isentropic relations | 349 |
| D.6 | The speed of sound | 350 |
| D.7 | Bernoulli's equation for compressible flow | 352 |
| D.8 | Isentropic flow of a perfect gas through a channel of varying cross-section | 353 |
| D.9 | Normal shock waves | 355 |
| D.10 | Oblique shock waves | 358 |
| References | | 362 |
| Index | | 366 |

Chapter 1

BASIC CONCEPTS

1.1 Introduction

This course book deals with performance prediction of aircraft. By performance we understand certain extremes of quantities that are related to the translational motion of the vehicle, such as: rate of climb, flight regime, takeoff and landing distance, range and endurance, turning rate, etc.

In this book the subject matter is limited to that class of aircraft known as airplanes. An airplane may be defined as a mechanically driven fixed-wing aircraft, heavier than air, which is supported by the reaction forces caused by the airflow against the surface of its body. Moreover, the attention is devoted to the examination of the performance of existing airplanes so that - in principle - pertinent airplane data are available. This means that the problem of designing an airplane that meets specified performance requirements, will not be discussed.

As a simplification, performance will be represented by the translational motion of the airplane as a response to the external forces acting on the center of mass of the airplane. The prerequisite for this treatment is the assumption that the airplane is regarded a rigid body.

Another important idealization may be the assumption of an airplane flying over an Earth that is considered to be nonrotating and flat. The different approximations will be discussed in some detail in subsequent sections of this chapter.

1.2 The airplane is regarded a rigid body

In this book we shall limit our analyses to rigid airplanes. In the case of rigidity, the motion of an airplane can be divided into a translational and a rotational motion.

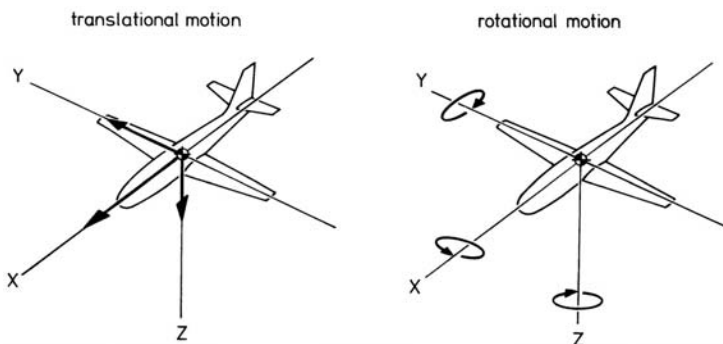


Figure 1.1 Division of airplane motion

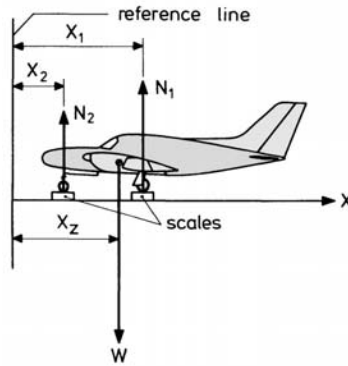


Figure 1.2 Determination of center of gravity

As illustrated by Figure 1.1, a rigid airplane has six degrees of freedom; the three components of the linear velocity and the three components of the angular velocity, acting along and about the X , Y and Z axes, respectively, where the origin of the axis system coincides with the center of mass of the airplane (see Appendix A).

The displacement of the airplane can be determined by treating the airplane as a point mass located at the center of mass, customarily referred to as the center of gravity (abbreviation: c.g.).

The rotation of the airplane depends on the moments about the center of gravity. The effects the moments have on the rotation of the airplane are studied in the field of aeronautics, called *stability and control*. The subjects stability and control concern the abilities to maintain and to change prescribed flight conditions, respectively.

Since throughout this book the emphasis is on the computation of airplane performance, we can limit our considerations to the effects that the application of the external forces and moments have on the displacement of the center of gravity of the airplane.

According to its definition, the center of gravity of an airplane is the point through which the resultant of the partial weights acts, independent of the attitude of the airplane.

The location of the center of gravity in longitudinal direction can be found by measuring the reaction forces N_1 and N_2 in the ground-based situation (Figure 1.2).

The sum of the loads at each wheel is equal to the weight of the airplane:

$$W = N_1 + N_2.$$

The sum of the moments of the loads at each wheel equals the weight multiplied by the distance between the center of gravity and the reference line:

$$N_1 X_1 + N_2 X_2 = W X_z.$$

From the latter equality we obtain

$$X_z = \frac{N_1 X_1 + N_2 X_2}{W}. \quad (1.1)$$

In order to determine the location of the center of gravity in vertical direction, weighing must be executed at inclined airplane positions.

To ensure save and convenient operation, every pilot has to be aware of the airplane weight, as well as the way this weight is distributed in the airplane, in order to make sure that allowable weight and approved center of gravity limits are not exceeded.

A typical light airplane loading graph and center of gravity moment envelope are sketched in Figures 1.3 and 1.4.

For a properly loaded airplane the actual weight and moment values must fall within the lines indicating forward and aft center of gravity.

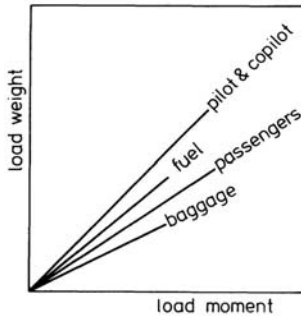


Figure 1.3 Loading graph

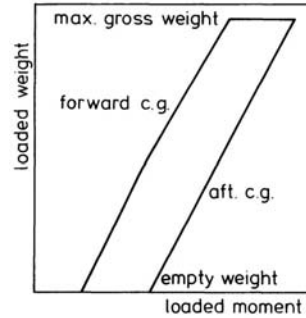


Figure 1.4 Center of gravity moment envelope

1.3 Application of Newton's law of motion with respect to an axis system attached to the Earth

The translational motion of a rigid body with constant mass is described by Newton's second law of motion :

$$F = Ma, \quad (1.2)$$

where F is the vector sum of all external forces acting on the body, M is its mass, and a is the absolute acceleration. Equation (1.2) must be written down with respect to an inertial frame of reference, that is to say, an axis system in a state of complete rest, or any coordinate system which translates with uniform velocity relative to the frame at rest.

According to the analysis in Appendix A, we can apply Equation (1.2) in a coordinate system attached to the Earth if two apparent forces are added to the force F ,

$$F - M\omega_e \times [\omega_e \times (R+h)] - M(2\omega_e \times V) = Ma_r, \quad (1.3)$$

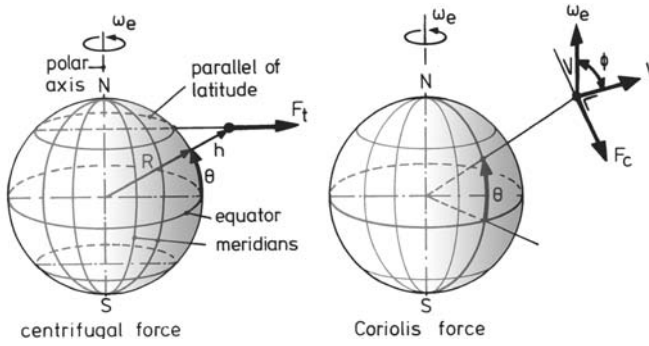


Figure 1.5 Forces due to the rotation of the Earth.

where ω_e is the Earth's angular velocity (about 7.29×10^{-5} radians per second), R is the Earth's radius vector, h is the height above the surface of the Earth, V is the velocity of the body with respect to the Earth, and a_r is the acceleration relative to the Earth.

The second term of the left-hand side of Equation (1.3) is a centrifugal force,

$$F_t = -M\omega_e \times [\omega_e \times (R+h)] = -Ma_t, \quad (1.4)$$

where a_t is a centripetal acceleration. The last term is a Coriolis force,

$$F_c = -M(2\omega_e \times V) = -Ma_c, \quad (1.5)$$

where a_c is the Coriolis acceleration.

In deriving Equation (1.3), the assumption is made that the Earth translates with a constant velocity along a straight line. This idealization of the Earth's translational motion may be correct since our performance analyses normally deal with small time intervals, that is, small with respect to the period of revolution of the Earth around the Sun.

By expressing the Equations (1.4) and (1.5) in trigonometric form, we obtain for the magnitude of the centrifugal force:

$$F_t = M\omega_e^2(R+h) \cos \theta, \quad (1.6)$$

and for the Coriolis force:

$$F_c = M2\omega_e V \sin \phi. \quad (1.7)$$

In the latter expressions the angle θ is latitude, positive in the Northern Hemisphere and negative in the Southern. The angle ϕ defines the direction of the velocity relative to the Polar axis. The forces and geometry used in Equations (1.6) and (1.7) are depicted in Figure 1.5. It is interesting to note that the radius to the North Pole is somewhat larger than the radius to the South Pole. This deviation from the sphere is indicated as the pear shape of the Earth.

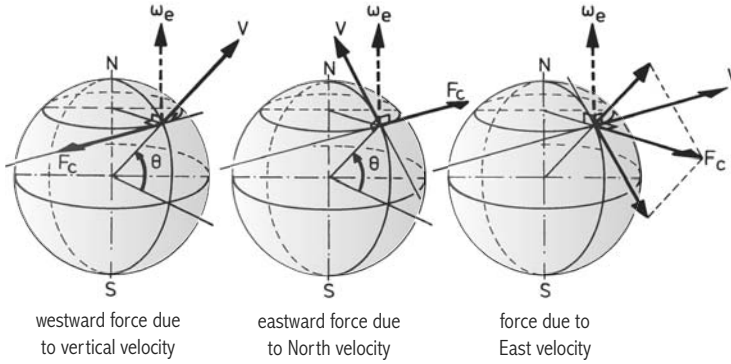


Figure 1.6 Coriolis forces

The centrifugal force is directed perpendicular to the Earth's Polar axis and points out from the Earth along a line intersecting the axis of rotation. At a position in the equator plane ($\theta = 0^\circ$) and near the Earth's surface we obtain for the magnitude of the centripetal acceleration, using the approximation that the Earth may be regarded a sphere with a radius $R_e = 6371$ km

$$a_t = \omega_e^2 R_e = (7.29 \times 10^{-5})^2 \times 6371 \times 10^3 = 0.034 \text{ m/s}^2.$$

Equation (1.7) shows that at a given velocity, the Coriolis acceleration, a_c , has its maximum value when the velocity is directed perpendicular to the polar axis ($\phi = 90^\circ$).

To illustrate the Coriolis force in more detail, the effect of a vertical velocity, a northward velocity, and an eastward velocity is considered successively in Figure 1.6, where the body is in a point on the Earth's surface. It follows from Equation (1.5) that a body moving vertically upward appears to an axis system referenced to the rotating Earth to be forced to the west by

$$F_c = M2\omega_e V \sin(90 - \theta).$$

When the body has a northward velocity, the Coriolis force becomes

$$F_c = M2\omega_e V \sin \theta.$$

In this case the body is subject to an eastward force.

Figure 1.6, finally, shows that a body with an eastward velocity appears to be forced outward from the Earth. It is seen from Equation (1.7) that now the Coriolis force is not dependent on latitude:

$$F_c = M2\omega_e V. \quad (1.8)$$

This force can be resolved into a component directed upward along the radius vector of the Earth, and a southward component.

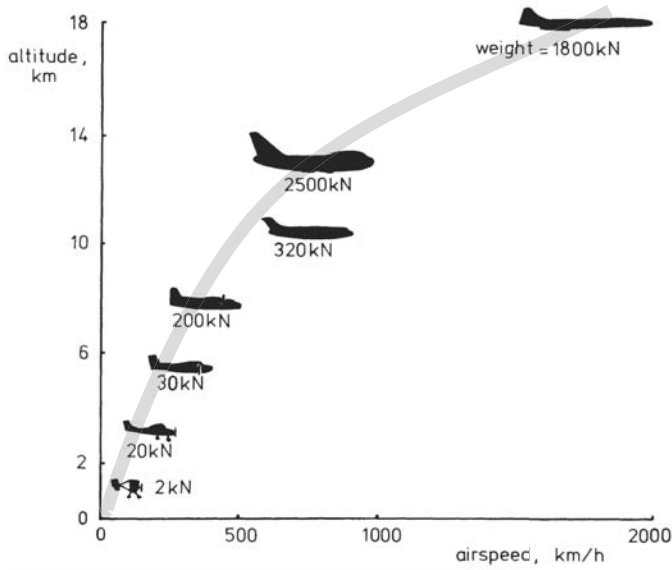


Figure 1.7 Typical flight velocities and altitudes.

In order to provide an idea of the degree of importance of the Coriolis acceleration, assume a body with a velocity of 2000 km/h to the east. Then,

$$a_c = 2\omega_e V = 2 \times 7.29 \times 10^{-5} \frac{2000}{3.6} = 0.081 \text{ m/s}^2.$$

Anticipating the discussion on gravitation in the following section, it can be noticed here that in comparison with the acceleration of gravity ($= 9.81 \text{ m/s}^2$ at the Earth's surface) the centripetal accelerations as well as the Coriolis accelerations are very small.

From the numerical examples given before it will also be clear that the effects of rotation of the Earth on the motion of a body may only become of interest in the study of high-altitude and high-velocity vehicles. This means that these effects are negligible for most airplane operations, which are executed at lower altitudes and at relatively low airspeeds. The latter conditions are evident from Figure 1.7, where are shown flight altitudes and airspeeds for typical airplane types.

Especially the layer below 20 km is an important region to aeronautics since most airplane operations are executed in this atmospheric shell.

1.4 Gravitation

Newton's law of gravitation states that any two particles attract one another with a force of magnitude :

$$F = \frac{\mu M_1 M_2}{R^2}, \quad (1.9)$$

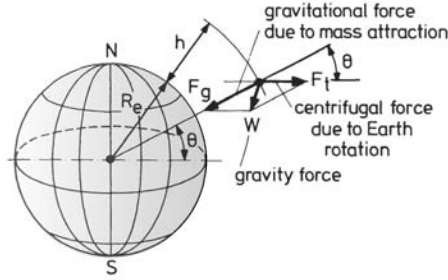


Figure 1.8 Components of gravity force

where M_1, M_2 are the masses of the particles, R is the distance between them and μ is a proportionality factor, known as the universal gravitational constant. The force F acts along the line joining the particles. Accordingly, if M is the mass of a particle outside the Earth, and M_e the mass of the Earth, the gravitational force F_g on the particle is given by (Figure 1.8)

$$F_g = \frac{\mu M_e M}{(R_e + h)^2}. \quad (1.10)$$

This equation says that the gravitational force due to the Earth is the same as if all mass M_e were concentrated at the center of the Earth. To derive Equation (1.10) the assumption must be made that the Earth can be considered a sphere (mean radius $R_e = 6371$ km), of which the density is a function of the distance to the center only.

As shown in Figure 1.8, the gravity force or weight W of a body is actually the vector sum of the gravitational force F_g and the centrifugal force F_t due to the rotation of the Earth about its Polar axis. Therefore, the gravity force does not point exactly to the center of the Earth.

The centrifugal force in Figure 1.8 results from the choice of an earthbound rotating frame of reference and is given by Equation (1.6), repeated below,

$$F_t = M\omega_e^2(R_e + h)\cos\theta. \quad (1.11)$$

The gravity force per unit mass is the acceleration of gravity, $g = W/M$.

The sea-level value of g may be given by, from Equations (1.10) and (1.11), and Figure 1.8,

$$g = \frac{\mu M_e}{R_e^2} - \omega_e^2 R_e \cos^2\theta. \quad (1.12)$$

At the Equator the centrifugal force is a maximum. There we get for the acceleration of gravity at the Earth's surface, using $\mu = 6.67 \times 10^{-11} \text{ m}^3\text{kg}^{-1}\text{s}^{-2}$, $M_e = 5.98 \times 10^{24} \text{ kg}$, $R_e = 6.371 \times 10^6 \text{ m}$, and $\omega_e = 7.29 \times 10^{-5} \text{ s}^{-1}$:

$$g = \frac{\mu M_e}{R_e^2} - \omega_e^2 R_e = 9.827 - 0.034 = 9.793 \text{ m/s}^2.$$

Because of the variation of the centrifugal force with latitude, the above value of g increases gradually to 9.827 m/s^2 at the Poles ($\theta = 90^\circ$).

At 45° geographic latitude the sea-level acceleration of gravity, denoted g_0 , becomes

$$g_0 = \frac{\mu M_e}{R_e^2} - \omega_e^2 R_e \cos^2 \theta = 9.827 - 0.034 \times 0.5 = 9.810 \text{ m/s}^2.$$

At this point, it is worthy to note that in particular for the International Standard Atmosphere (see Chapter 2) the acceleration of gravity g_0 is used and taken as 9.80665 m/s^2 .

In our applications, mostly, it is possible to ignore the effect of the centrifugal force when considering the variation of g with height. Then, it follows from Equation (1.10) that the acceleration of gravity varies inversely as the square of the distance from the center of the Earth

$$g = \frac{\mu M_e}{(R_e + h)^2}, \quad \text{and} \quad (1.13)$$

$$\frac{g}{g_0} = \frac{R_e^2}{(R_e + h)^2} = \left(1 + \frac{h}{R_e}\right)^{-2}. \quad (1.14)$$

Using the first two terms of the binomial expansion we get

$$\frac{g}{g_0} = 1 - 2\frac{h}{R_e}. \quad (1.15)$$

The latter expression may show that even at the maximum altitudes suitable for atmospheric flight ($h = 60 - 80 \text{ km}$), there is only a slight difference between g and g_0 . But certainly at the heights encountered during normal operations (less than 20 km) the actual value of g is very near to its standard sea-level value ($g/g_0 = 0.993$ at $h = 20 \text{ km}$).

1.5 The effect of curvature of the Earth

Considered is a body moving at constant speed in a circular orbit of radius $(R_e + h)$ around the Earth in a plane perpendicular to the Equator plane (Figure 1.9). If we neglect air forces, on the body act the weight W of the body in a direction approximately toward the center of the Earth and in the opposite direction an apparent force associated with the circular motion. The latter force is the familiar *centrifugal force*, C , which is given by (cf. Equation (1.4))

$$C = -M\dot{\theta} \times [\dot{\theta} \times (R_e + h)] = \frac{W}{g} \frac{V^2}{(R_e + h)}, \quad (1.16)$$

where θ is latitude and V is the velocity of the body.

The relative importance of the centrifugal force can be expressed by the ratio:

$$\frac{C}{W} = \frac{V^2}{(R_e + h)g}. \quad (1.17)$$

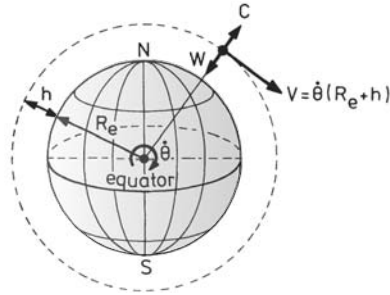


Figure 1.9 Flight around the Earth

The speed at which the centrifugal force equals the weight of the body is called the circular velocity V_c :

$$V_c = \sqrt{(R_e + h)g}. \quad (1.18)$$

At sea level ($h = 0$) we find from Equation (1.18), using $R_e = 6371 \times 10^3$ m and $g = g_0 = 9.80665$ m/s²: $V_{c_0} = 7904$ m/s = 28455 km/h.

Since Figure 1.7 indicates that our analyses mostly will concern airspeeds which are small with respect to the circular velocity, it follows from Equation (1.17) that we usually can ignore the effect of the centrifugal force ($C \ll W$) on the motion of the airplane so that the Earth can be regarded as ideally flat.

1.6 Coordinate systems

To describe the motion of an airplane four coordinate systems, employing right-handed, rectangular Cartesian axis systems, are used. The origin is denoted by "0" and the axes designated X, Y, Z . Displacements are positive in the positive senses of the axes and angles are positive in clockwise direction when looking along the appropriate axis in the positive direction. Velocities, angular velocities and accelerations also are positive in these directions.

- a. The Earth axis system or ground axis system (Figure 1.10). Earth axes are denoted by the subscript "g". The origin of this coordinate system is any point on the Earth's surface. The X_g - and Y_g -axes lie in the horizontal plane of the Earth. The X_g -axis points into an arbitrary direction. E.g., the X_g -axis is taken in the direction of flight. The Z_g -axis points vertically and positive downward.
- b. The moving Earth axis system or local horizon system (Figure 1.11). The axes are denoted by the subscript "e". The origin of the system is taken to be the center of gravity of the airplane. The X_e, Y_e and Z_e axes are parallel to the corresponding axes of the Earth axis system. Thus, the plane formed by the X_e - and Y_e -axes is always parallel to the surface of the Earth.

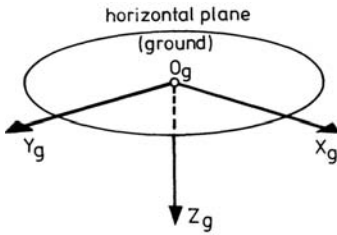


Figure 1.10 Earth axis system

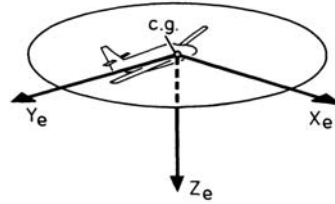


Figure 1.11 Moving Earth axis system

- c. The *body axis system* or airplane axis system (Figure 1.12). Body axes are denoted by the subscript “b”. The origin of the system is at the center of gravity of the airplane. The X_b -axis lies in the plane of symmetry of the airplane and points out of the nose of the airplane. The Z_b -axis is perpendicular to the X_b -axis, lies also in the plane of symmetry, and is directed downward for a normal flight attitude. The Y_b -axis is directed out of the right wing of the airplane. The body axes are fixed to the airplane and oriented by reference to some geometrical datum. The X_b -axis coincident with what is called the longitudinal axis of the airplane. The Y_b -axis usually is termed transverse or lateral axis and the Z_b -axis is named normal axis. The rotational components about X_b , Y_b and Z_b are called roll, pitch and yaw, respectively.
- d. The *air-path axis system* or flight-path axis system (Figure 1.13). Air-path axes are denoted by the subscript “a”. The origin is at the center of gravity of the airplane. The X_a -axis lies along the velocity vector. The Z_a -axis is taken in the plane of symmetry of the airplane, and is positive downward for a normal airplane attitude. Consequently, the Y_a -axis is positive to starboard.

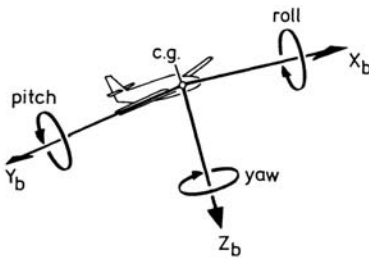


Figure 1.12 Body axis system

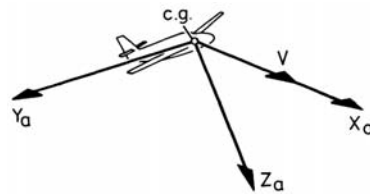


Figure 1.13 Air-path axis system

1.7 Angles and velocities describing the angular displacement of the airplane

In order to describe the attitude of the airplane with respect to the moving Earth axis system, a number of characteristic angles are used. These angles often are

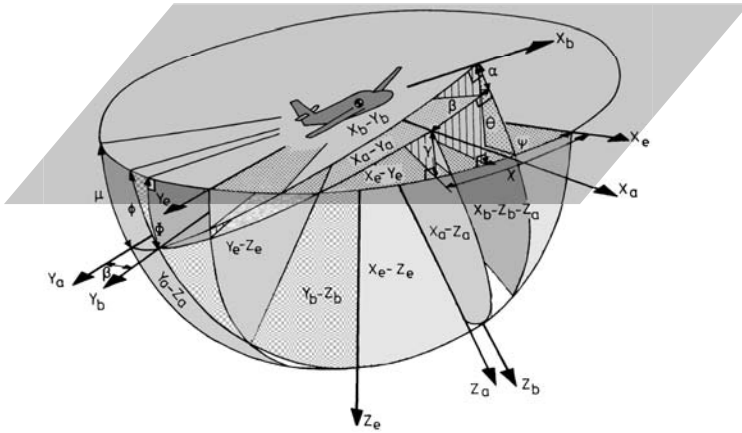


Figure 1.14 Eulerian angles

called Eulerian angles and are presented in Figure 1.14.

a. Eulerian angles defining the orientation of the airplane body axes. These angles are:

- Angle of yaw ψ ; the angle between the projection of the X_b -axis on the $X_e Y_e$ -plane (horizontal plane) and the X_e -axis.
- Angle of pitch θ ; the angle between the X_b -axis and its projection on the $X_e Y_e$ -plane.
- Angle of roll ϕ ; the angle between the Y_b -axis and the intersecting line of the $Y_b Z_b$ -plane with the $X_e Y_e$ -plane.

The Eulerian angles ψ , θ and ϕ are obtained by three defined successive rotations of the moving Earth axes. This procedure is illustrated in Figure 1.15. First, we rotate by ψ about Z_e , then by θ about Y' , and finally by ϕ about X_b . As shown in Figure 1.14, also may be used the angle of bank Φ , being the angle between the Y_b -axis and its projection on the $X_e Y_e$ -plane. The angle of bank can be written in terms of the angle of roll and the angle of pitch:

$$\sin \Phi = \sin \phi \sin(90 - \theta),$$

or

$$\sin \Phi = \sin \phi \cos \theta. \quad (1.19)$$

The relation (1.19) follows by applying a theorem from spherical trigonometry in the spherical triangle ABC in Figure 1.16.

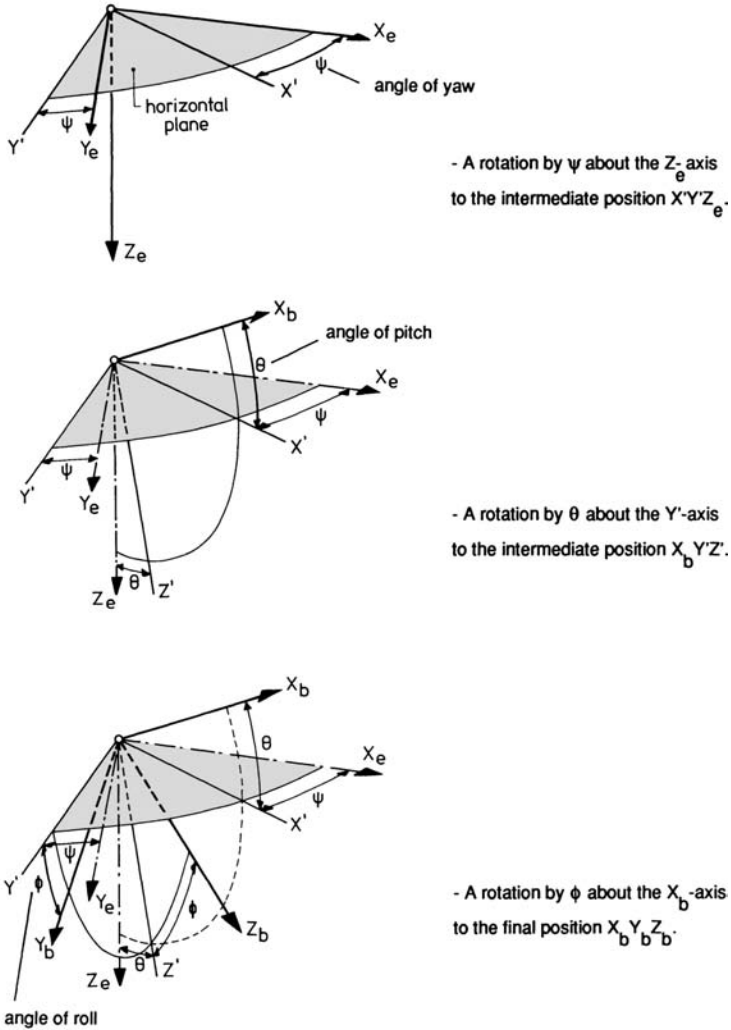


Figure 1.15 Orientation of body axes to moving Earth axes

b. Eulerian angles defining the orientation of the air-path axes. These angles are (Figure 1.14):

- Azimuth angle χ ; the angle between the projection of the X_a -axis on the X_eY_e -plane and the X_e -axis.
- Flight-path angle γ ; the angle between the X_a -axis and its projection on the X_eY_e -plane.
- Aerodynamic angle of roll μ ; the angle between the Y_a -axis and the intersecting line of the X_aY_a -plane with the X_eY_e -plane.

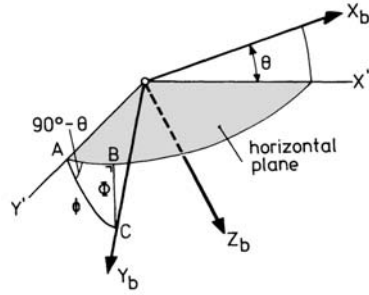


Figure 1.16 Relation between angle of roll, angle of pitch and angle of bank

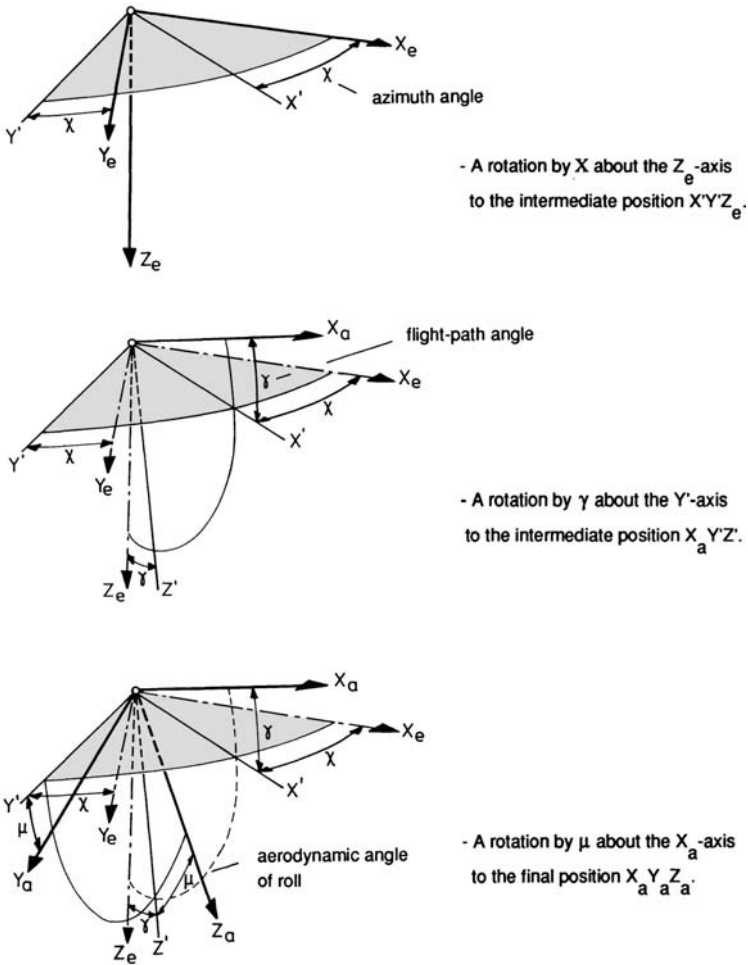


Figure 1.17 Orientation of air-path axes to moving Earth axes

The angles χ, γ and μ are also generated by three successive rotations of the moving Earth axes. The sequence of rotations is indicated in Figure 1.17. First, we

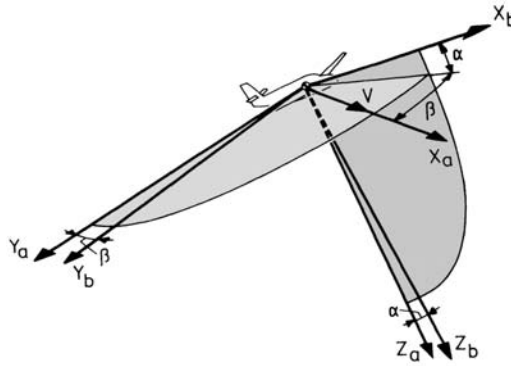


Figure 1.18 Orientation of air-path axes to body axes

rotate by χ about Z_e , then by γ about Y' , and finally by μ about X_a .

Of importance is also the relationship between the air-path axis system and body axis system. Both coordinate systems are shown in Figure 1.18. Since the Z_a -axis lies in the X_bZ_b -plane (plane of symmetry of the airplane), the orientation of the air-path axis system with respect to the body axis system is completely defined by the following two angles:

- Angle of attack α ; the angle between the projection of the X_a -axis on the plane of symmetry of the airplane and the X_b -axis.
- Angle of sideslip β ; the angle between the X_a -axis and its projection on the plane of symmetry of the airplane.

The angle of attack is positive when the velocity component along the Z_b -axis is positive. The angle of sideslip is positive when the velocity component along the Y_b -axis is positive.

At this point it is suited to define the components of the airspeed V along the X_b , Y_b and Z_b axes of the body axis system as u , v and w , respectively (Figure 1.19). The following relations are apparent:

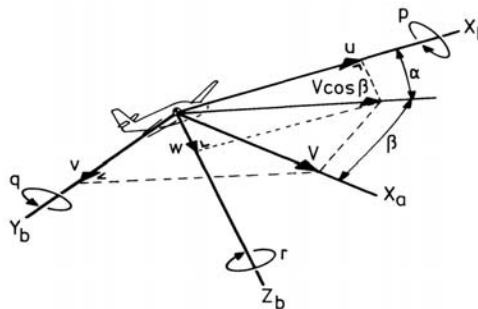


Figure 1.19 Components of airspeed

$$\left. \begin{aligned} V^2 &= u^2 + v^2 + w^2 \\ u &= V \cos \beta \cos \alpha \\ v &= V \sin \beta \\ w &= V \cos \beta \sin \alpha \end{aligned} \right\}. \quad (1.20)$$

Similarly, the resultant angular velocity Φ can be resolved into the components p , q and r along the X_b , Y_b and Z_b axes, respectively, where

$$\Phi^2 = p^2 + q^2 + r^2. \quad (1.21)$$

The angular velocity about the X_b -axis is the rolling velocity, positive if the right wing drops. The angular velocity about the Y_b -axis is the pitching velocity, positive if the nose of the airplane rises. The angular velocity about the Z_b -axis, finally, is the yawing velocity, positive if the nose of the airplane moves to the right (clockwise when observed from above).

In connection with the study of airplane motion, the relations between the angular velocities, p , q , r , about the body axes and the time rate of change of the Eulerian angles ψ , θ , ϕ , may be of importance.

According to the rotations defined in Figure 1.15, the vectors $\frac{d\psi}{dt}$, $\frac{d\theta}{dt}$, $\frac{d\phi}{dt}$ are directed along the Z_e , Y' and X_b axes, respectively.

Figure 1.20 shows these vectors. Resolving along the body axes leads to the following relationships between the two sets of angular velocities:

$$\left. \begin{aligned} p &= -\frac{d\psi}{dt} \sin \theta + \frac{d\phi}{dt} \\ q &= \frac{d\psi}{dt} \cos \theta \sin \phi + \frac{d\theta}{dt} \cos \phi \\ r &= \frac{d\psi}{dt} \cos \theta \cos \phi - \frac{d\theta}{dt} \sin \phi \end{aligned} \right\}, \quad (1.22)$$

and the inverse relationships:

$$\left. \begin{aligned} \frac{d\psi}{dt} &= \frac{1}{\cos \theta} (q \sin \phi + r \cos \phi) \\ \frac{d\theta}{dt} &= q \cos \phi - r \sin \phi \\ \frac{d\phi}{dt} &= p + \frac{d\psi}{dt} \sin \theta = p + (q \sin \phi + r \cos \phi) \tan \theta \end{aligned} \right\}. \quad (1.23)$$

In the presence of wind the velocity of the airplane with respect to the ground or ground speed V_g is the vector sum of the speed of the airplane relative to the air V and the wind velocity V_w (Figure 1.21):

$$\vec{V}_g = \vec{V} + \vec{V}_w. \quad (1.24)$$

Since the airplane is carried along by the wind, the projection of the velocity vector V on the ground is at a so-called drift angle with the actual flight track.

Figure 1.22 shows the components of the airspeed along the axes of the moving Earth axis system. From this figure we obtain:

$$\left. \begin{aligned} V_{X_e} &= V \cos \gamma \cos \chi \\ V_{Y_e} &= V \cos \gamma \sin \chi \\ V_{Z_e} &= V \sin \gamma \end{aligned} \right\}. \quad (1.25)$$

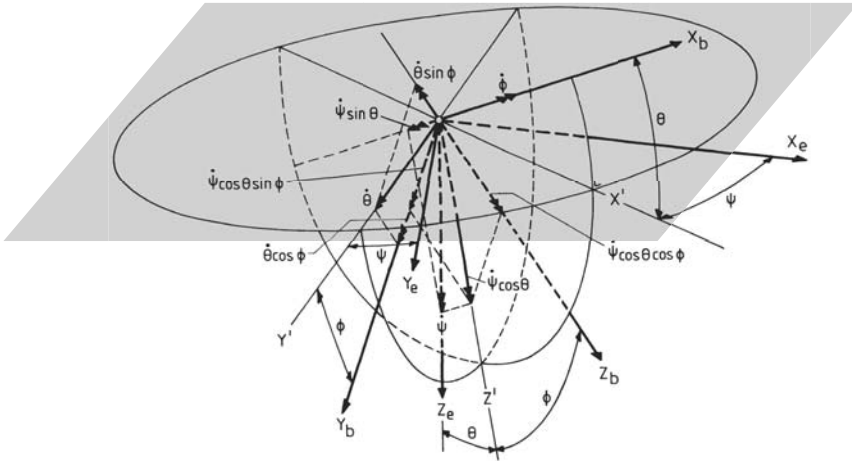


Figure 1.20 Angular velocities about the body axes

Note that a positive sign is given to the component of V in the direction of the negative Z_e -axis. Hence we find the components of the ground speed along the axes of the Earth axis system as:

$$\left. \begin{aligned} V_{X_g} &= V \cos \gamma \cos \chi + u_w \\ V_{Y_g} &= V \cos \gamma \sin \chi + v_w \\ V_{Z_g} &= V \sin \gamma + w_w \end{aligned} \right\} \quad (1.26)$$

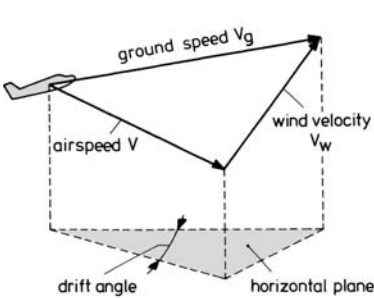


Figure 1.21 Ground speed

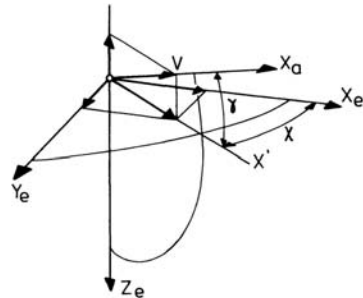


Figure 1.22 Components of airspeed

In Equation (1.26), wind data are given as u_w, v_w, w_w , being the respective components of the wind velocity in terms of the moving Earth axis system. The positive sense of w_w is taken in upward direction.

1.8 The airplane

Figure 1.23 shows in some detail the overall make-up of an airplane. Basic components are fuselage, wing, tail assembly, controls, landing gear, and engine (and propeller, in the case of propeller propulsion).

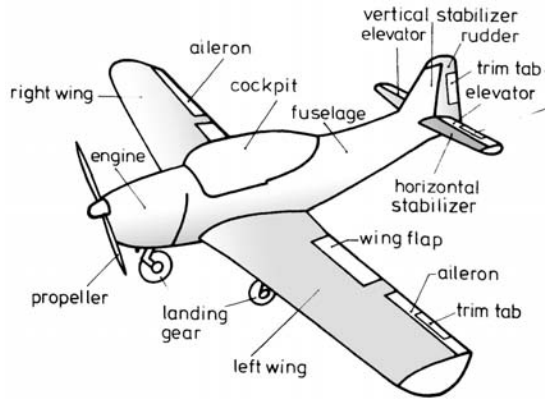


Figure 1.23 Basic airplane components

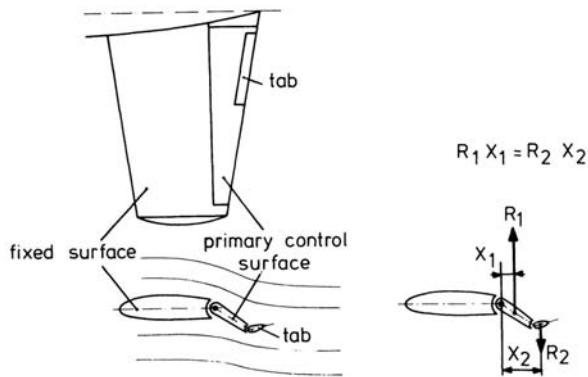


Figure 1.24 Balance and trim tab

The fuselage may be seen as the structural component to which the other main parts are connected. Further, it provides space for crew, passengers, cargo, airplane systems and instrumentation. Generally, the fuselage is streamlined to reduce its drag.

The wing is the principal component to generate the lift of the airplane by its motion with respect to the surrounding air. The wing may often be equipped with flaps. These adjustable parts are used to increase lift and drag at low airspeeds.

The tail assembly consists of the vertical and the horizontal stabilizer, which surfaces provide directional stability in yaw and stability in pitch, respectively.

Included in the tail assembly and the wing are the control surfaces. The usual position of the three primary controls is also illustrated in Figure 1.23. Yaw control is provided by the rudder, which is connected with the vertical stabilizer.

The elevators are attached to the horizontal stabilizer and control the pitch of the airplane. Roll control is provided by deflections of the ailerons which are located near the outer trailing edges of the wing.

Depending on the type of airplane, small auxiliary control surfaces may be in-

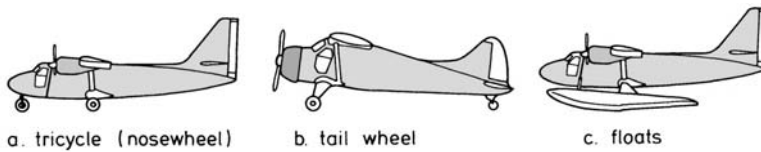


Figure 1.25 Landing gear types

stalled to the trailing edges of the elevators, rudder and ailerons. These movable surfaces are known as trim tabs and are adjusted by the pilot. As shown in Figure 1.24, the airflow over the trim tab creates a moment that holds the primary control surface in the desired position without any help from the pilot.

Tabs may also be used to assist the pilot in the movement of the primary controls; these are known as balance tabs.

The landing gear or undercarriage supports the airplane while it is in contact with the ground. Modern airplanes generally are equipped with a tricycle gear, consisting of nose wheel and main wheels. The landing gear may be retractable, except special forms which include skis for snow and floats for operations on water (Figure 1.25).

An important characteristic is the type of propulsion system. The main engine types are the piston engine (reciprocating engine), and the reaction engine such as turbojet, turboprop, and turbofan. Converting the power of a piston engine and a turboprop into a thrust is accomplished by the propeller(s).

1.9 Flight types, airplane configuration and flight condition

In Figure 1.26 are illustrated the typical flight phases encountered by an airplane during a trip over a given travel distance.

The takeoff consists of the takeoff run where the airplane is accelerated from standstill to the liftoff speed, followed by the climbout to a distance over, say, 10.7 m (35 ft) obstacle. After the takeoff the power of the engine(s) is reduced and the airplane climbs to cruise altitude at, approximately, constant velocity. The latter conditions hold as much with regard to the descent. Also cruise flight is executed in unaccelerated and straight flight.

An example of a curved flight path is the turn and particularly the so-called constant-altitude banked turn, where the airplane is inclined about the longitudinal axis. This type of turn is the usual manner in which the flight path heading is changed, e.g., in the holding maneuver. As depicted in Figure 1.26, during holding the airplane remains within a specified airspace whilst awaiting further clearance for the approach flight to the airport runway.

The final flight phase, naturally, is the landing, proceeding from the steady approach flight so as to clear the screen height at the beginning of the runway and to come to rest on the runway at the end of the ground run. Just like the takeoff, the landing is a case of unsteady airplane motion.

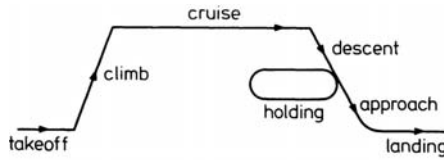


Figure 1.26 Typical flight phases

In the various flight phases, usually, the airplane is controlled in such a manner that the instantaneous motion satisfies certain conditions. This leads to well-defined flight types, such as:

- Gliding flight; flight in which the thrust is zero.
- Steady flight; flight in which the forces and moments acting on the airplane do not vary in time, neither in magnitude nor in direction.
- Nonsideslipping flight; flight in which the velocity vector is parallel to the plane of symmetry of the airplane (angle of sideslip is zero).
- Straight flight; flight in which the center of gravity of the airplane travels along a straight line.
- Symmetric flight; flight in which both the angle of sideslip is zero and the plane of symmetry of the airplane is perpendicular to the horizontal plane of the Earth.

At this point, it is useful to emphasize that symmetric flight, and in particular steady symmetric flight forms the basis of considerations on the performance of airplanes during most of their time of flying. In this connection, it may be clear that at best an airplane can perform a quasi-steady flight due to the consumption of engine fuel and/or the variation of atmospheric conditions.

The term *airplane configuration* or *airplane condition* indicates the description of the external shape of the airplane and any parameter affecting the motion of the airplane which is characterized by the fact that it remains constant during a certain period of time. Examples of airplane configuration elements are (Figure 1.27) landing gear position, flap angle, speedbrake and spoiler deflections, and number of operative engines.

The estimation of airplane performance may be treated by considering the airplane in a given configuration which is related to a particular flight phase, such as takeoff configuration, cruise configuration and landing configuration.

The term *flight condition* is the group of variables, which defines the motion of the airplane at each instant of the flight. A description of the flight condition will comprise airplane weight, altitude, atmospheric conditions, airspeed, power setting and control surface deflections.

1.10 Forces on the airplane

Practically, there are two different kinds of external forces that act on an airplane in flight, gravity forces and aerodynamic forces.

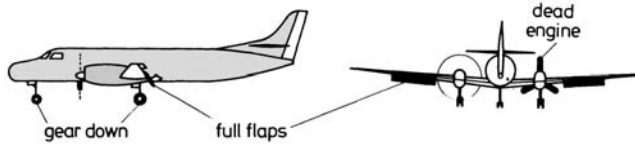


Figure 1.27 Example of airplane configuration

Gravity forces are related to the mass of a body and act from a distance. A common example is, of course, the weight of the airplane.

Aerodynamic forces are developed through application of Newton's third law of motion, which states that for every action there is an equal and opposite reaction (Appendix A). Therefore, essential to the generation of an aerodynamic force is the occurrence of relative motion between body and medium.

In this course book we shall use the symbol R to denote the aerodynamic force produced by the interaction between the air and the outer surface of the airplane. When resolved into components along the air-path axes, the vector force R delivers the lift, drag, and side force. The lift, designated by the symbol L , is the component along the negative Z_a -axis. The major portion of the lift arises from the airflow around the wing. The drag D and side force S are the components of the aerodynamic force R along the negative X_a -axis and Y_a -axis, respectively. A side force or cross force appears only when the airplane is in sideslipping flight. Figure 1.28 shows the aerodynamic force R in the case of symmetric flight. In this type of flight the motion is in the geometric plane of symmetry so that besides the X_b -axis, also the X_a -axis lies in the plane of symmetry of the airplane.

When studying rotational motion in symmetric flight it may be useful to employ the tangential force T and the normal force N being the components of R along the negative X_b -axis and Z_b -axis, respectively. As can be seen from Figure 1.28 the components L and D , and the components N and T are related by the expressions:

$$\left. \begin{aligned} L &= N \cos \alpha - T \sin \alpha \\ D &= N \sin \alpha + T \cos \alpha \\ N &= L \cos \alpha + D \sin \alpha \\ T &= -L \sin \alpha + D \cos \alpha \end{aligned} \right\}, \quad (1.27)$$

where α is the angle of attack.

Also the driving force of the propulsion system is an aerodynamic force. This force is called the thrust and also given the symbol T .

As indicated in Figure 1.29, the thrust acts in forward direction along a working line which makes a fixed angle η with the longitudinal axis of the airplane (X_b -axis). The type of flight considered in Figure 1.29 represents the case of steady symmetric flight. Maintaining this type of flight requires that the vector sum of the forces acting on the airplane is zero:

$$\vec{R} + \vec{T} + \vec{W} = 0. \quad (1.28)$$

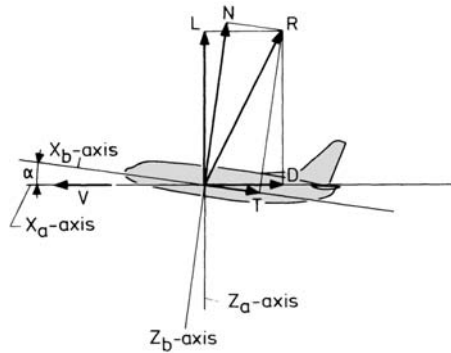


Figure 1.28 Aerodynamic force R and components

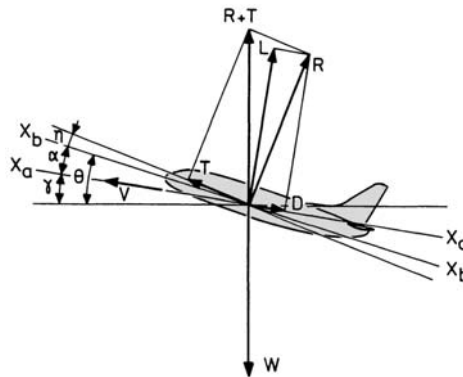


Figure 1.29 Forces in steady symmetric flight

The general definitions of the various angles used in Figure 1.29, i.e., the angle of attack α , the flightpath angle γ and the angle of pitch θ , have been given in Section 1.7.

1.11 SI-system of units

Throughout this book the International System of Units (Système International d'Unités) is used. This system has been adopted by many countries as the recommended system of units for weights and measures. According to the publications of the International Organization for Standardization (ISO) there are seven basic units, which are tabulated in Table 1.1.

Although the SI-unit of temperature is the kelvin (K), also the celsius (C) or centigrade scale is used. Since the unit degree celsius is exactly equal to the unit kelvin, the temperature expressed in degree celsius can be readily converted to the absolute temperature in kelvin by the following relationship,

$$\text{degree C} = \text{K} - 273.15. \quad (1.29)$$

From the basic units in Table 1.1, the units of a wide range of quantities can be derived, whereby the product and/or quotient of any number of basic units forms the resultant unit of the derived quantity. The units of some of the more common quantities are listed in Table 1.2.

To obtain multiples or decimal fractions of the units, standard prefixes are used, which are collected in Table 1.3.

In order to prevent errors in calculations, it is strongly recommended that in computations only SI-units are used and not their multiples or decimal fractions.

It should be mentioned that, though becoming obsolete, in engineering practice frequently the so-called technical system of units is used. In this system the quantity force, having also the name kilogram, is a basic unit instead of mass. In order to distinguish both kilograms, in the technical system the quantity force is (often) denoted as kilogramforce (abbreviation: kgf). The following relation is defined: $1 \text{ kgf} = 9.80665 \text{ N}$. Some technical units and corresponding SI-units are given in Table 1.4.

In Appendix B a number of conversion factors are collected, arranged according to subject categories.

Table 1.1 Basic SI-units

| quantity | name of unit | symbol |
|---------------------|--------------|--------|
| length | meter | m |
| mass | kilogram | kg |
| time | second | s |
| temperature | kelvin | K |
| electric current | ampère | A |
| luminous intensity | candela | cd |
| amount of substance | mole | mol |

Table 1.2 Derived SI-units

| quantity | name of unit | symbol | definition |
|-----------------|-------------------------------|--------|-------------------------|
| force | newton | N | kg m/s^2 |
| pressure | pascal | Pa | N/m^2 |
| work (energy) | joule | J | $\text{J} = \text{N m}$ |
| power | watt | W | J/s |
| velocity | meter per second | V | m/s |
| acceleration | meter per second squared | a | m/s^2 |
| moment of force | newton meter | M | N m |
| density | kilogram per unit cubic meter | ρ | kg/m^3 |

Table 1.3 Standard multiples and decimal fractions

| multiple/fraction | prefix | symbol |
|-------------------|--------|--------|
| 10^{12} | tera | T |
| 10^9 | giga | G |
| 10^6 | mega | M |
| 10^3 | kilo | k |
| 10^2 | hecto | h |
| 10 | deca | da |
| 10^{-1} | deci | d |
| 10^{-2} | centi | c |
| 10^{-3} | milli | m |
| 10^{-6} | micro | μ |
| 10^{-9} | nano | n |
| 10^{-12} | pico | p |
| 10^{-15} | femto | f |
| 10^{-18} | atto | a |

Table 1.4 Systems of units

| quantity | technical system | | SI-system |
|---------------|-----------------------------|-----------------------------------|---|
| | metric | English | |
| length | m | ft | m |
| time | s | s | s |
| force | kgf | lbf | kg m/s^2 (newton) |
| mass | $\text{kgf s}^2/\text{m}$ | $\text{lbf s}^2/\text{ft}$ (slug) | kg |
| pressure | kgf/m^2 | lbf/ft^2 | N/m^2 |
| work (energy) | kgf m | lbf ft | $\text{kg m}^2/\text{s}^2 = \text{N m}$ (joule) |
| power | kgf m/s | lbf ft/s | $\text{kg m}^2/\text{s}^3 = \text{J/s}$ (watt) |
| density | $\text{kgf s}^2/\text{m}^4$ | $\text{lbf s}^2/\text{ft}^4$ | kg/m^3 |

Chapter 2

THE ATMOSPHERE

2.1 Nature of the atmosphere

The atmosphere is the gaseous shell surrounding to Earth. Atmospheric air consists of a mixture of gases with a total mass of about 5.3×10^{18} kg, which is about one millionth of the mass of the Earth. The normal constituents of air in the lower part of the atmosphere are listed in Table 2.1, where also are given their concentrations and molecular masses.

The molecular mass of a substance may be defined as the mass of one kmol of the substance. The kmol is an amount of matter of a system which holds as many elementary particles (molecules, atoms, etc.) as there are atoms in precisely 12 kg of the isotope ^{12}C . This number amounts to 6.02257×10^{26} kmol $^{-1}$ and is called Avogadro's number.

Chiefly nitrogen and oxygen in the ratio of four-fifths nitrogen to one-fifth oxygen represent 99 % of the total volume of all component gases. Though the volume percentages of carbon dioxide and methane are very small, their presence is especially significant to the temperature at the Earth's surface because these constituents are more absorptive of terrestrial than of solar radiations. They, therefore, are responsible for what is known as the greenhouse or blanketing effect, that is, an elevation of the mean temperature in the lower part of the atmosphere.

In addition to the constant constituents there is always a certain amount of water in the atmosphere, which exists in three states; gaseous (water vapor), liquid (rain and clouds), and solid (snow and hail). The presence of water is also of significance to the above-mentioned greenhouse effect. The proportion of water vapor varies with place on Earth (latitude and longitude), time of day and time of year. On the whole the highest humidity occurs at sea level and in the neighborhood of the Equator.

With respect to the chemical composition, the atmosphere may be classified into the *homosphere* and the *heterosphere* (Figure 2.1). The homosphere extends from sea level to an altitude of about 90 km. Apart from water vapor and ozone, in the homosphere the composition of the air is essentially constant. Consequently, in this region also the mean molecular mass of the air (≈ 29 kg/kmol) is constant.

In the heterosphere, mainly because of molecular dissociation, the molecular mass decreases from about 29 kg/kmol at a height of 90 km, to about 18 kg/kmol at 500 km.

The atmospheric conditions, temperature, pressure, and density, depend strongly on height. For an analysis of these quantities it is appropriate to divide the atmosphere into five layers based on the vertical distribution of the air temperature. The typical variation of the average temperature with altitude is also sketched in

Table 2.1 Normal composition of clean atmospheric air near sea level

| constituent | gas | content, percent by volume | molecular mass, kg/kmol |
|------------------|------------------|-------------------------------|----------------------------|
| Nitrogen | N ₂ | 78.084 | 28.0134 |
| Oxygen | O ₂ | 20.9476 | 31.9988 |
| Argon | Ar | 0.934 | 39.948 |
| Carbon dioxide | CO ₂ | 0.0314 | 44.00995 |
| Neon | Ne | 0.001818 | 20.183 |
| Helium | He | 0.000524 | 4.0026 |
| Methane | CH ₄ | 0.0002 | 16.04303 |
| Krypton | Kr | 0.000114 | 83.80 |
| Sulfur dioxide | SO ₂ | 0 to 0.0001 | 64.0628 |
| Hydrogen | H ₂ | 0.00005 | 2.01594 |
| Nitrous oxide | N ₂ O | 0.00005 | 44.0128 |
| Xenon | Xe | 0.0000087 | 131.30 |
| Ozone | O ₃ | 0 to 0.000007 | 47.9982 |
| Nitrogen dioxide | NO ₂ | 0 to 0.000002 | 46.0055 |
| Iodine | I ₂ | 0 to 0.000001 | 253.8088 |
| Water vapor | H ₂ O | variable | 18.0 |

Figure 2.1.

In ascending order, we distinguish the *troposphere*, the *stratosphere*, the *mesosphere*, the *thermosphere*, and the *exosphere*. The dividing planes between the next four layers are called *tropopause*, *stratopause*, and *mesopause*.

The lowest region of the atmosphere, the troposphere, is characterized by a decreasing temperature with increasing altitude. In this layer the phenomena occur which we call the weather, i.e., the local state of temperature, pressure, humidity, cloudiness, wind, and precipitation. The troposphere extends to about 8 km at the Poles and approximately to 17 km at the Equator. At middle-latitude the tropopause lies at a height of about 11 km, where the average temperature decreases from roughly 15°C at sea level to - 56°C at the tropopause.

In the stratosphere, at first, there is a nearly constant temperature of about - 56°C up to an altitude of about 20 km. This layer may be called the *lower stratosphere*. Above 20 km we have the *upper stratosphere*, where the temperature increases to a maximum value of 0°C at an altitude of about 50 km. This altitude is the stratopause, sometimes referred to as the ozonepause.

It may be remarked that the atmospheric layer up to 20 km, being of major importance to aviation (see Figure 1.7), contains approximately 95% of the total atmospheric mass.

In the mesosphere, reaching from the stratopause to an altitude of 90 km, the temperature decreases to a minimum value of about - 90°C at the *mesopause*.

The stratosphere and the mesosphere are of consequence in the sense that continuously there is a certain amount of ozone. In fact, the temperature increase above

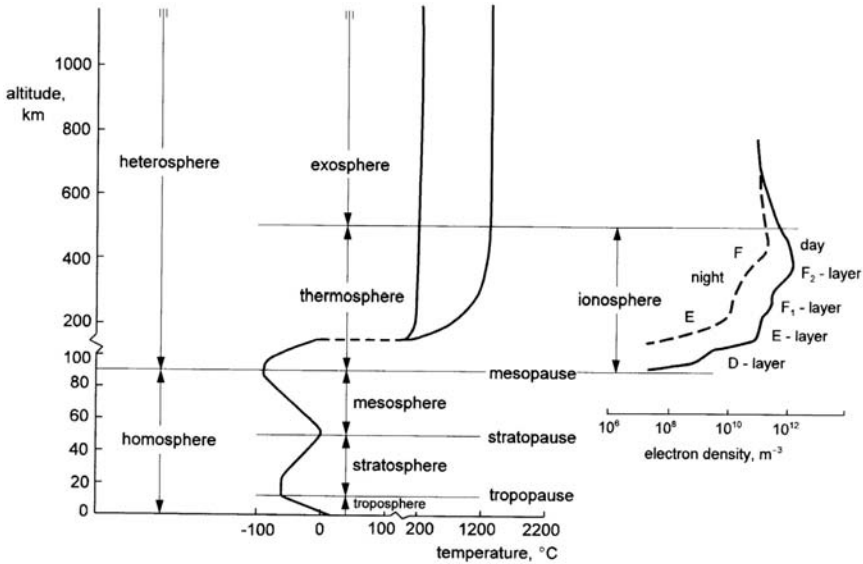


Figure 2.1 Arrangement of atmospheric layers

20 km is related to the absorption of ultraviolet radiation, involving ozone formation. Nevertheless, the proportion of ozone is quite small, the presence of it at these high altitudes is substantial to life on Earth, as it acts as a filter against solar ultraviolet radiation.

The absorption of solar ultraviolet radiation is caused by the dissociation of molecular oxygen (O_2) into atomic oxygen (O). A portion of the atomic oxygen forms ozone (O_3) by combination with molecular oxygen. Finally, ozone and atomic oxygen recombine to form molecular oxygen. The decomposition of ozone to ordinary oxygen causes heating of the atmosphere. The formation and destruction of ozone is a continuous process, resulting in more or less a constant amount of ozone in the stratosphere and mesosphere.

In the thermosphere, the temperature increases quickly with increasing altitude until at about 500 km the so-called *exospheric temperature* is reached. The magnitude of this temperature is dependent on solar activity (Ref. 11).

In the exosphere collisions between molecules are so rare that temperature is only an indication of the kinetic energy of the air particles.

From 90 km upwards, ionization processes occur, i.e., the generation of ions and the accompanying free electrons takes place. Therefore, in Figure 2.1 also is depicted the *ionosphere*, in which layer ionization processes (generation of free electrons and ions) occur due to the absorption of solar radiation incident in this region.

Depending on electron density, the ionosphere is subdivided into four layers, designated D, E, F_1 and F_2 . Figure 2.1 shows that the extent of ionization increases with altitude up to approximately 400 km. Also, the ionization varies with solar

activity and time of the year.

Finally, it should be mentioned that several classifications exist, each using different heights for the positions of the dividing planes between the various layers (Ref. 8).

2.2 Variation of pressure with altitude

The weight of the column of air at rest above a unit area will produce a certain pressure at that surface. The higher one rises in the atmosphere, the smaller will be the weight of the air above the unit area, and the smaller will be the occurring pressure.

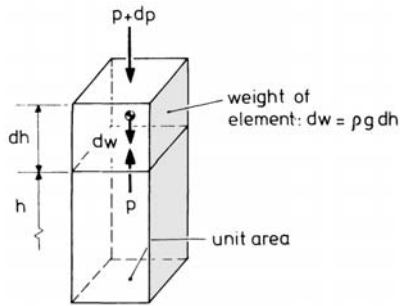


Figure 2.2 Forces acting on an element of air

To obtain an expression for pressure as a function of altitude, consider a unit body of air shown in Figure 2.2. Summing the forces in vertical direction gives

$$p - (p + dp) - \rho g dh = 0 \quad \text{or} \quad dp = -\rho g dh, \quad (2.1)$$

where p is pressure, ρ is density, h is geometrical altitude, and g is the acceleration of gravity. The differential Equation (2.2) is known as the hydrostatic or aerostatic equation, and shows us that with increasing altitude, the pressure decreases at the rate ρg . The combination of the hydrostatic equation and the equation of state for air is a suitable starting point to describe the variation of pressure and density with altitude. Atmospheric air can be assumed to satisfy the equation of state for an ideal gas, i.e.,

$$\frac{p}{\rho} = \frac{R_a}{M} T. \quad (2.2)$$

In the perfect gas law Equation (2.2) R_a is the universal gas constant, M is the molecular mass of the gas, and T is the absolute temperature (kelvin).

Insertion of Equation (2.2) into (2.1) gives

$$dp = -\frac{M p}{R_a T} g dh \quad \text{or} \quad \frac{dp}{p} = -\frac{M g}{R_a T} dh. \quad (2.3)$$

Integration of Equation (2.3) from $h = 0$ (sea level) to an altitude h yields

$$\int_{p_0}^p \frac{dp}{p} = \int_0^h \frac{Mg}{R_a T} dh \quad \text{and} \quad (2.4)$$

$$\ln \frac{p}{p_0} = \int_0^h \frac{Mg}{R_a T} dh. \quad (2.5)$$

Apparently, a calculation of the distribution of atmospheric pressure requires knowledge of:

- the variation of molecular mass with height
- the variation of acceleration of gravity with height
- the variation of temperature with height
- sea level atmospheric pressure, p_0 .

At this point it is appropriate to introduce the geopotential altitude H , which is defined by the following equation,

$$H = \int_0^H dH = \frac{1}{g_0} \int_0^h g dh. \quad (2.6)$$

In this equation, g_0 may be taken equal to the standard sea-level value of the acceleration of gravity (see Section 1.4). Since both H and h are set equal to zero at sea level, the geopotential altitude H is the height in a uniform gravity field at which the potential energy is the same as at a geometrical height h in a variable gravity field.

The relationship between air pressure and geopotential altitude is obtained by combining Equations (2.5) and (2.6):

$$\ln \frac{p}{p_0} = - \int_0^H \frac{Mg_0}{R_a T} dH. \quad (2.7)$$

Clearly, the integration is simplified since the acceleration of gravity g_0 is independent of altitude. The adoption of a particular variation of air temperature with geopotential height will enable us to determine the corresponding pressure ratio variation, provided that the molecular mass M is constant or a known function of altitude.

2.3 Standard atmospheres

The real atmosphere never remains constant. There is always a considerable variation of temperature, pressure and density at any time, height and place on Earth.

Since the performance of airplanes strongly depends on the atmospheric conditions, it will be obvious that the performance of an airplane measured at different moments and places must be related to a common reference. Also, the actual performance of an airplane does not provide a reliable basis of comparison with other airplanes. No more, the results of calculations can be correlated if not the same atmospheric conditions are employed.

In order to satisfy the need for standardization, over the years a number of standard atmospheres have been developed, which all are reflections of what may be expected as mean circumstances.

Then, from the actual performance of an airplane it is possible to deduce what would have been the performance of this airplane under the conditions of a given reference atmosphere. The latter performance data can be compared with those measured at other times and places or can be compared with the performance of some other airplane which has been correspondingly converted to standard conditions.

The atmospheric model used in this book has been adopted for the derivation of the International *Standard Atmosphere* (I.S.A.) in Reference 9. This reference atmosphere is based on the assumption that the air is a perfect gas, which is supposed to be devoid of moisture and dust. Also the assumption is made that the atmosphere is motionless with respect to the Earth.

For the computation of pressure, temperature, density, and other atmospheric properties as functions of altitude, standard conditions are defined at zero-altitude (sea level). Table 2.2 lists the values of primary constants for the International Standard Atmosphere.

The molecular mass of air M follows from Equation (2.2) using the standard values of pressure, density, temperature and the universal gas constant as given in Table 2.2,

$$M = \frac{\rho_0 R_a T_0}{p_0} = 28,96442 \text{ kg/kmol.}$$

The specific gas constant of air is determined from the relationship,

$$R = R_a/M = 287.05 \text{ m}^2/\text{s}^2\text{K.}$$

As $c_p = R \frac{\gamma}{\gamma-1}$ we find

$$c_p = 1004.68 \text{ m}^2/\text{s}^2\text{K} \text{ and } c_v = c_p/\gamma = 717.63 \text{ m}^2/\text{s}^2\text{K.}$$

The variation of temperature with geopotential altitude is presented in Figure 2.3, showing that a sequence of connected constant gradient layers is defined.

In the troposphere and the upper part of the stratosphere the temperature variation can be written as

$$T = T_1 + \lambda(H - H_1), \quad (2.8)$$

Table 2.2 Values of primary constants

| | |
|--------------------------------------|---|
| sea-level pressure | $p_0 = 101325 \text{ N/m}^2$ |
| sea-level temperature | $T_0 = 288.15 \text{ K (15 } ^\circ\text{C)}$ |
| sea-level density | $\rho_0 = 1.225 \text{ kg/m}^3$ |
| acceleration of gravity at sea level | $g_0 = 9.80665 \text{ m/s}^2$ |
| universal gas constant | $R_a = 8314.32 \text{ J/K kmol}$ |
| ratio of specific heats of air | $\gamma = c_p/c_v = 1.4$ |

(c_p = specific heat at constant pressure;
 c_v = specific heat at constant volume)

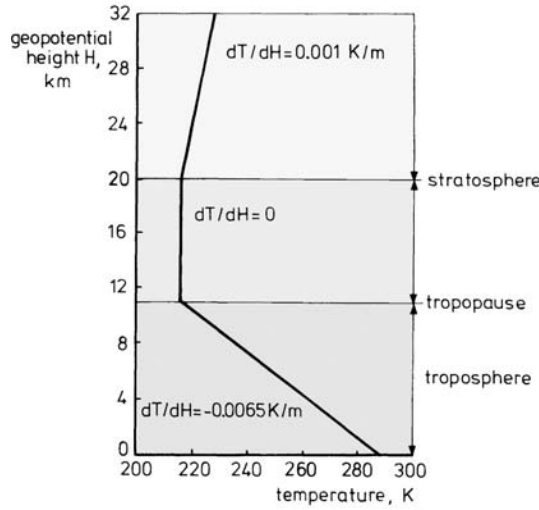


Figure 2.3 Temperature versus geopotential height (I.S.A.)

where $\lambda = dT/dH$ is the temperature gradient and T_1 is the temperature at height H_1 , being the base of the layer. By insertion of Equation (2.8) into (2.7) we obtain

$$\ln \frac{p}{p_1} = - \int_{H_1}^H \frac{g_0}{R[T_1 + \lambda(H - H_1)]} dH = - \frac{g_0}{R\lambda} \ln [T_1 + \lambda(H - H_1)] \Big|_{H_1}^H \quad \text{or}$$

$$\ln \frac{p}{p_1} = - \frac{g_0}{R\lambda} \ln \frac{T_1 + \lambda(H - H_1)}{T_1}. \quad (2.9)$$

Thus, the pressure ratio variation with altitude becomes

$$\frac{p}{p_1} = \left[1 + \frac{\lambda(H - H_1)}{T_1} \right]^{-\frac{g_0}{R\lambda}}. \quad (2.10)$$

The corresponding density ratio variation follows from the equation of state,

$$\frac{\rho}{\rho_1} = \frac{pT_1}{p_1T} = \left[1 + \frac{\lambda(H - H_1)}{T_1} \right]^{-\left[\frac{g_0}{R\lambda} + 1 \right]}. \quad (2.11)$$

In the troposphere the height $H_1=0$, so that the Equations (2.10) and (2.11) reduce to

$$\frac{p}{p_0} = \left[1 + \frac{\lambda H}{T_0} \right]^{-\frac{g_0}{R\lambda}} \quad \text{and} \quad (2.12)$$

$$\frac{\rho}{\rho_0} = \left[1 + \frac{\lambda H}{T_0} \right]^{-\left[\frac{g_0}{R\lambda}+1\right]}. \quad (2.13)$$

In the lower part of the stratosphere the temperature is constant ($\lambda = 0$). Now the pressure ratio is obtained by direct integration of Equation (2.7) between the height of the tropopause H_s and height H ($H \leq 20$ km),

$$\ln \frac{p}{p_s} = - \int_{H_s}^H \frac{g_0}{RT_s} dH = - \frac{g_0}{RT_s} (H - H_s) \quad \text{or} \quad (2.14)$$

$$\frac{p}{p_s} = e^{-\frac{g_0}{RT_s}(H-H_s)}. \quad (2.15)$$

In these equations the subscript "s" denotes the condition at the tropopause.

From the equation of state, we find

$$\begin{aligned} \frac{\rho}{\rho_s} &= \frac{p}{p_s}. \quad \text{Thus} \\ \frac{\rho}{\rho_s} &= e^{-\frac{g_0}{RT_s}(H-H_s)}. \end{aligned} \quad (2.16)$$

In order to determine the value of the geometrical height as a function of geopotential altitude, it is essential to define a relationship between the acceleration of gravity and geometrical height (see Equation (2.6)).

From the discussion in Section 1.4 we know that the acceleration of gravity is the resultant of the gravitational force per unit mass and the centrifugal force per unit mass as caused by the Earth's rotation. Accordingly, it depends upon height and latitude. However, for our aims the acceleration of gravity may be obtained with adequate precision by ignoring the centrifugal force and applying only Newton's law of gravitation as already noticed in Section 1.4. Then we have the following expression

$$\frac{g}{g_0} = \frac{R_e^2}{(R_e + h)^2}. \quad (1.14)$$

Combining Equations (2.6) and (1.14) leads to

$$\int_0^H dH = \int_0^h \frac{R_e^2}{(R_e + h)^2} dh = R_e^2 \int_0^h \frac{dh}{(R_e + h)^2}. \quad (2.17)$$

Performing the integration in Equation (2.17) yields the following relationship between geometrical height and geopotential altitude,

$$H = R_e^2 \int_0^h -d(R_e + h)^{-1} = \frac{R_e h}{(R_e + h)}, \quad \text{or}$$

$$h = \frac{R_e H}{(R_e - H)}. \quad (2.18)$$

The preceding equations in this section and the primary constants in Table 2.2 are used to calculate temperature, pressure, density and geometrical height as functions of geopotential altitude. Figure 2.4 shows how pressure and density in the International Standard Atmosphere vary with height. Numerical values of T , p and ρ are given in the tables in Appendix C. Other quantities listed in Appendix C are the coefficient of dynamic viscosity μ and the speed of sound c . The coefficient of dynamic viscosity is a state variable, which determines the shear stress between air layers moving adjacent to each other at different velocities. The following equation, basically derived from kinetic theory, is used for the computation of μ ,

$$\mu = \frac{\beta T^{3/2}}{T + S}, \quad (2.19)$$

where β is a constant equal to $1.458 \times 10^{-6} \text{ kg s}^{-1} \text{ m}^{-1} \text{ K}^{-1/2}$, and S is Sutherland's constant, equal to 110.4 K.

At sea-level the coefficient of dynamic viscosity is: $\mu_0 = 1.7894 \times 10^{-5} \text{ kg/m s}$. The ratio of μ and the density of air is named kinematic viscosity: $\nu = \mu/\rho$. The speed of sound is the rate at which a small disturbance on the ambient condition travels through the air. The values of c in Appendix C are calculated from (see Appendix D)

$$c = \left(\gamma \frac{R_a}{M} T \right)^{1/2} = (\gamma R T)^{1/2}. \quad (2.20)$$

Its sea-level value becomes: $c = 340.294 \text{ m/s}$.

Since the temperature gradients are linear, it may be a sufficient approximation to consider dc/dH as a constant. E.g., in the troposphere:

$$c = c_0 + \frac{dc}{dH} H. \quad (2.21)$$

Insertion of Equation (2.8) into (2.20) gives

$$c = [\gamma R (T_0 + \lambda H)]^{1/2} = \left[c_0 \left(1 + \frac{\lambda H}{T_0} \right) \right]^{1/2}. \quad (2.22)$$

Using the first two terms of the binomial expansion we get

$$c = c_0 + \frac{c_0 \lambda}{2T_0} H. \quad (2.23)$$

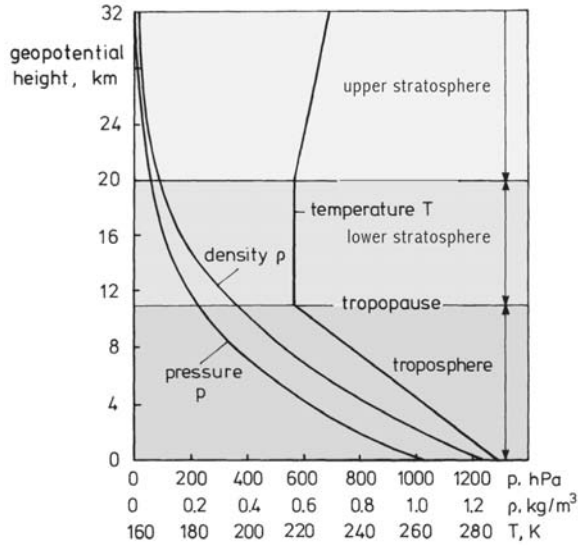


Figure 2.4 Variation of pressure, density and temperature in the International Standard Atmosphere

We thus have in the troposphere:

$$\frac{dc}{dH} = \frac{c_0 \lambda}{2T_0} = -0.00384 \text{ s}^{-1}.$$

2.4 Off-standard atmospheres

Off-standard atmospheres are defined by a temperature distribution which is obtained by changing the temperature of the standard atmosphere with given increment ΔT . The resulting temperatures then are given by

$$T = T_{\text{ISA}} + \Delta T,$$

where the subscript "ISA" denotes a value in the International Standard Atmosphere.

The constant increases in temperature are referred to the so-called geopotential pressure altitude, H_p . The latter altitude corresponds to the reading of an airplane altimeter. This instrument measures the actual air pressure and is calibrated by exposing it to various pressures and marking on the dial the geopotential altitudes that in the International Standard Atmosphere correspond to these pressures (see also Chapter 5). Thus, when the air temperatures are different from those of the standard atmosphere, the altimeter also will read the geopotential pressure altitude. Apparently, the geopotential pressure altitude is the geopotential altitude in the International Standard Atmosphere at which the pressure is equal to the actual pressure. E.g., in the case of an altimeter which is calibrated according to Equation (2.12), we have the following relationship between pressure and geopotential

pressure altitude ($H_p \leq 11,000$ m),

$$H_p = \left[\left[\frac{p}{p_0} \right]^{-\frac{R\lambda}{g_0}} - 1 \right] \frac{T_0}{\lambda}. \quad (2.24)$$

Similarly, for altitudes between 11 and 20 km it follows from Equation (2.14) that

$$H_p = H_s - \frac{RT_s}{g_0} \ln \frac{p}{p_0}. \quad (2.25)$$

Apparently, the altimeter reading furnishes the actual air pressure only. If, in addition, the temperature increment ΔT is known, the air density can be calculated from the equation of state,

$$\frac{p}{R} = \rho_{\text{ISA}} \times T_{\text{ISA}} = \rho(T_{\text{ISA}} + \Delta T) \quad \text{or} \quad (2.26)$$

$$\rho = \frac{\rho_{\text{ISA}}}{1 + \frac{\Delta T}{T_{\text{ISA}}}}. \quad (2.27)$$

Usually, airplane performance data are represented as a function of geopotential pressure altitude and air temperature, $T_{\text{ISA}} + \Delta T$.

Also the so-called *geopotential density altitude*, H_ρ , may be used. This is the geopotential altitude in the International Standard Atmosphere at which the density is equal to the actual air density.

By solving Equation (2.13) for height we obtain the geopotential density altitude in the troposphere as

$$H_\rho = \left[\left[\frac{\rho}{\rho_0} \right]^{-\frac{R\lambda}{g_0 + R\lambda}} - 1 \right] \frac{T_0}{\lambda}. \quad (2.28)$$

In the lower stratosphere, we find from Equation (2.16),

$$H_\rho = H_s - \frac{RT_s}{g_0} \ln \frac{\rho}{\rho_s}. \quad (2.29)$$

Figure 2.5 shows the dependence of H_ρ with T for given values of H_p . By means of this chart, an altimeter reading can be converted into density altitude, provided that the actual air temperature is known.

2.5 Humidity

An upper limit exists concerning the concentration of water vapor that can be present in a fixed volume of air. When a given volume contains the maximum amount of water vapor the air is saturated. By definition, the saturation vapor pressure is the partial pressure at which water vapor can coexist in equilibrium with liquid water. This maximum value of the vapor pressure increases rapidly

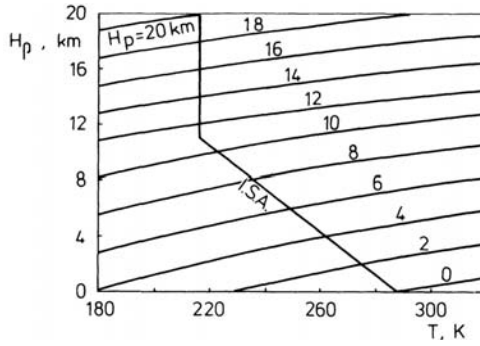


Figure 2.5 Relationship between pressure altitude and density altitude

with increasing temperature. The solid curves in Figure 2.6 represent the variation of the saturation vapor pressure with temperature. This relationship may be approximated by:

$$\left. \begin{aligned} e_{\max_{\text{water}}} &= 611 \times 10^{\frac{7.5T}{237.3+T}} \quad (\text{water vapor} \leftrightarrow \text{water}) \quad \text{and} \\ e_{\max_{\text{ice}}} &= 611 \times 10^{\frac{9.5T}{265.5+T}} \quad (\text{water vapor} \leftrightarrow \text{ice}) \end{aligned} \right\} \quad (2.30)$$

In these expressions T is the temperature in degree celcius, and the saturation vapor pressure is obtained in pascal (N/m^2). From Figure 2.6 we note that below 0°C water vapor can condense into ice as well as into supercooled water. Also note that the vapor pressure of supercooled water is appreciable greater than of ice. According to Dalton's law, the pressure p of moist air is the sum of the partial pressure of dry air p_d and the partial pressure of water vapor e ,

$$p = p_d + e. \quad (2.31)$$

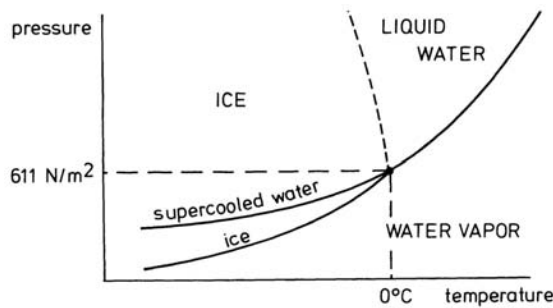


Figure 2.6 Saturation vapor pressure of water and ice

The following quantities are used to express the amount of water vapor in the atmosphere:

- absolute humidity, a
- specific humidity, q

- mixing ratio, x
- relative humidity, H .

Absolute humidity a is the mass of water vapor per cubic meter. Hence, the absolute humidity is equal to the density of water vapor ρ_v . Since, just like air, also water vapor follows the perfect gas law with sufficient approximation, we have

$$a = \rho_v = \frac{M_v e}{R_a T} = \frac{e}{R_v T}. \quad (2.32)$$

In Equation (2.32) M_v and R_v are the molecular mass and the specific gas constant of water vapor, respectively. As $M_v = 18.0$ kg/kmol (Table 2.1), we get

$$R_v = R_a / M_v = 8314.32 / 18.0 = 461.90 \text{ m}^2 / \text{s}^2 \text{K}.$$

The absolute humidity is maximum if at the actual temperature the air is saturated ($e = e_{\max}$). Figure 2.7 gives the maximum absolute humidity against temperature. This graph shows that at 0°C the maximum proportion of water vapor is about 0.004 kg per cubic meter, which value increases to 0.023 kg/m³ at 25°C .

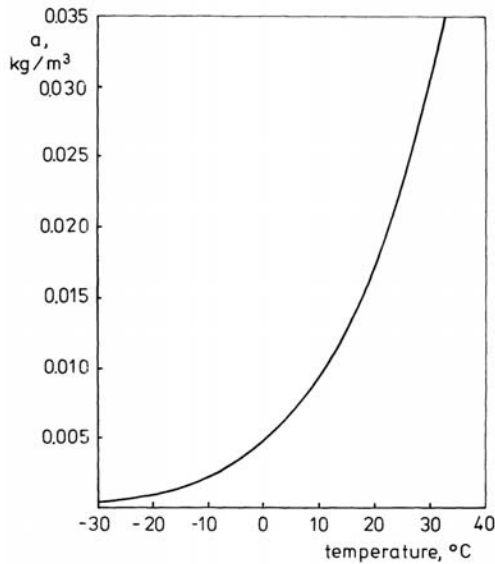


Figure 2.7 Absolute humidity for saturated air

Specific humidity q is the ratio of the density of water vapor to the density of the moist air,

$$q = \frac{\rho_v}{\rho_d + \rho_v}, \quad (2.33)$$

where ρ_d is the density of dry air, which is given by

$$\rho_d = \frac{p_d}{RT} = \frac{p - e}{RT}. \quad (2.34)$$

Insertion of Equation (2.32) and (2.34) into (2.33) yields

$$q = \frac{\frac{e}{R_v T}}{\frac{p-e}{R T} + \frac{e}{R_v T}} = \frac{\frac{R}{R_v} - e}{p - e(1 - \frac{R}{R_v})}. \quad (2.35)$$

Using $R = 287.05 \text{ m}^2/\text{s}^2\text{K}$ and $R_v = 461.90 \text{ m}^2/\text{s}^2\text{K}$, we obtain $R/R_v = 0.622$. It then follows that

$$q = \frac{0.622 e}{p - 0.378 e}. \quad (2.36)$$

The mixing ratio x is the ratio of the density of water vapor to the density of dry air,

$$x = \rho_v / \rho_d. \quad (2.37)$$

This leads to

$$x = \frac{\frac{e}{R_v T}}{\frac{p-e}{R T}} = \frac{\frac{R}{R_v} e}{p - e} = \frac{0.622 e}{p - e}. \quad (2.38)$$

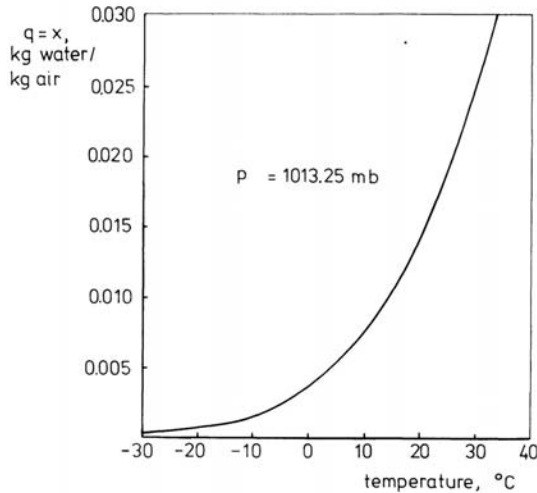


Figure 2.8 Specific humidity and mixing ratio for saturated air

The expressions (2.36) and (2.38) may be approximated by

$$q = x = 0.622 \frac{e}{p}. \quad (2.39)$$

For saturated air, the variation of q ($= x$) versus temperature is plotted in Figure 2.8.

Relative humidity H is defined as the ratio of the actual water vapor pressure to the saturation vapor pressure at that temperature,

$$H = 100 \frac{e}{e_{\max}}, \quad (2.40)$$

where H is expressed in percent.

As clarified in Figure 2.9, lines of constant values of *relative humidity* can be drawn, starting from the line of 100% relative humidity, which corresponds to the saturation vapor pressure curves in Figure 2.6. Evidently, the use of relative humidity requires also a knowledge of the ambient air temperature to have a physical significance.

Instead of relative humidity, the air temperature in combination with the so-called *dew point* may be used to specify the moisture content of the air. As illustrated in Figure 2.9, the dew point is the temperature to which moist air must be cooled isobarically, without addition of moisture, until the saturation point or *frost point* (if below 0°C) is reached.

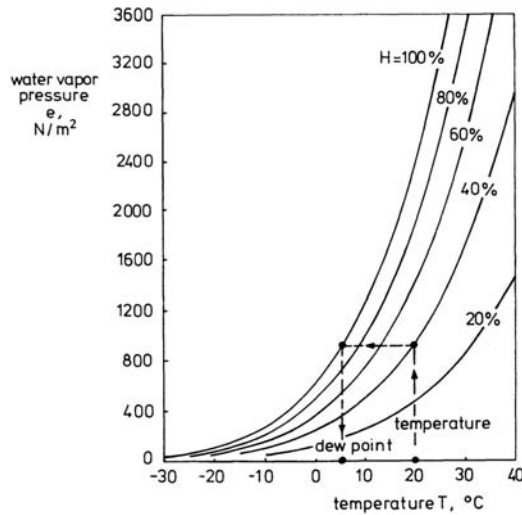


Figure 2.9 Relationship between water vapor pressure, temperature and relative humidity

The magnitude of the difference between the air temperature and the dew point is an indication of how much the moist air will have to be cooled to reach saturation and *condensation*. If the difference between the actual temperature and the dew point is great, extreme cooling is needed to achieve *saturation*, whereas if the difference between the two thermometer readings is small, only slight cooling is required to saturate the air. Clearly, condensation will produce clouds and several forms of precipitation as dew, rain, snow, and so forth. Therefore, the difference between the air temperature and dew point is also a measure for the height at which cloud formation begins.

Finally, we will examine the influence of water vapor on the density of moist air. According to Equation (2.35) we can write

$$\rho = \rho_d + \rho_v = \frac{p-e}{RT} + \frac{e}{R_v T} = \frac{p}{RT} \left[1 - \frac{e}{p} \left(1 - \frac{R}{R_v} \right) \right]. \quad (2.41)$$

By insertion of $R/R_v = 0.622$ into Equation (2.41) we obtain

$$\rho = \frac{P}{RT} \left(1 - 0.378 \frac{e}{p}\right) = \frac{P}{RT_v}, \quad (2.42)$$

where R is the specific gas constant of dry air and T_v is an increased temperature which is called the *virtual temperature* and which is used to account for the effect of humidity on the air density.

From Equation (2.42) it follows that

$$T_v = \frac{T}{1 - 0.378 \frac{e}{p}}. \quad (2.43)$$

Equations (2.42) and (2.43) show that, at a given pressure, moist air is somewhat lighter than dry air. This feature may be of special importance to the thrust or power output of propulsion systems and thus to airplane performance.

2.6 Vertical motion in the atmosphere

Though in all standard atmospheres the air is assumed to be at rest, we all know that the real atmosphere is often in a state of motion. In this section we will therefore consider the vertical displacements of limited masses of air as may occur in the atmosphere.

Since atmospheric pressure decreases with increasing height, the pressure within an isolated mass of air will also decrease when it is lifted into the surrounding air. Then, also its temperature falls because some of the heat energy is used in doing the work required for expansion. To describe this process we may assume that the moving body of air has nearly uniform properties and that its pressure p^* equals constantly the pressure p of the surrounding air, but not necessarily $T^* = T$.

Furthermore, it is assumed that no changes of state occur and that the air expands adiabatically. Then, according to the *first law of thermodynamics* in Appendix D, the process is described by

$$c_p dT^* - \frac{1}{\rho^*} dp^* = 0, \quad (2.44)$$

where c_p is the specific heat at constant pressure of air. By making use of the hydrostatic equation (2.1) and noting that $dp^* = dp$, we find

$$c_p dT^* + \frac{\rho}{\rho^*} g dh = 0. \quad (2.45)$$

Combination of Equation (2.45) and the equation of state (2.2) yields

$$c_p dT^* + \frac{T^*}{T} g dh = 0. \quad (2.46)$$

Hence, the rate of temperature fall is

$$\frac{dT^*}{dh} = -\frac{g T^*}{c_p T}. \quad (2.47)$$

By substitution of $g = 9.80665 \text{ m/s}^2$, $c_p = 1004.68 \text{ m}^2\text{s}^2\text{K}$ (dry air) and $T^*/T = 1$ into Equation (2.47), we find for the rate of change of temperature within the rising mass of air

$$\frac{dT^*}{dh} = -0.0098 \text{ K/m.}$$

Thus, if the expansion process is adiabatic the temperature decrease is about 1 kelvin for each 100 meters rise. This lapse rate holds only for dry or unsaturated air, and is known as the *dry adiabatic rate*.

The water vapor in the moving body of air also cools as it ascends. When it reaches its saturation temperature, condensation will take place with any further cooling. The heat which is released by the condensation is added to the air and the lapse rate is therefore about half the value of the dry adiabatic rate. The temperature lapse rate for saturated air is denoted, therefore, as the *saturation adiabatic rate*.

In Figure 2.10 is sketched the variation of temperature with altitude according to the dry adiabatic rate. From this illustration we can explain what actually can happen when a mass of unsaturated air is elevated. If the atmosphere has a lapse rate which is less than 1 K/100 m, the rising air will always be colder, and thus denser, than the surrounding air. As a result, vertical motion is suppressed so that the moving air will tend to sink back to its initial level. In this case the atmosphere is said to be in a stable condition.

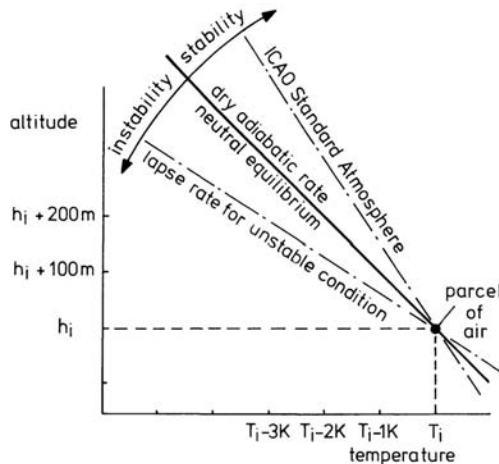


Figure 2.10 Temperature rates

On the other hand, if the observed lapse rate is greater than 1 K/100 m, the rising air will be constantly warmer, and therefore lighter than the surrounding air. In consequence, the rising air tends to move away from its initial position. This is known as an unstable condition. In order to explain the dynamics of lifting and sinking, a moving infinitesimal element of air with dimensions dx , dy and dh will be considered (Figure 2.11). If we assume quasi-static motion ($p^* = p$)

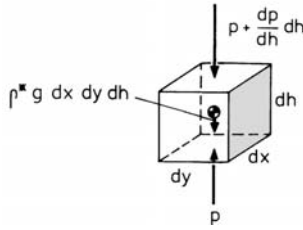


Figure 2.11 Force diagram

and the vertical motion involves no friction forces between the element and its environment, Newton's second law furnishes

$$\rho^* dx dy dh \frac{dw}{dt} = p dx dy - (p + \frac{dp}{dh} dh) dx dy - \rho^* g dx dy dh. \tag{2.48}$$

In this equation w is the vertical velocity of the element of air. Dividing the terms by $\rho^* dx dy dh$ gives

$$\frac{dw}{dt} = -\frac{1}{\rho^*} \frac{dp}{dh} - g. \tag{2.49}$$

Inserting the hydrostatic Equation (2.1) and the equation of state (2.2) into Equation (2.49), we obtain

$$\frac{dw}{dt} = g \left(\frac{T^*}{T} - 1 \right). \tag{2.50}$$

This result indicates that the vertical velocity tends to increase (unstable condition) if starting from the original level, the ratio T^*/T increases. Indeed, this requires that the prevailing lapse rate is greater than the dry adiabatic rate.

In the special circumstance that the lapse rate in the atmosphere is the same as the dry adiabatic rate, the temperature within the moving air constantly coincides with the temperature of the surrounding air. Consequently, there is no density difference, and the air will not restore to or displace from its momentary position. This condition is called neutral equilibrium.

As explained earlier, in the case of moving air which is saturated, the rate of cooling is about 0.5 K/100 m. To examine the stability, now, the actual temperature variation in the atmosphere must be compared to the saturation adiabatic rate.

When the actual temperature lapse rate lies between that of the dry adiabatic rate and that of the saturation adiabatic rate, so-called *conditional instability* prevails (Figure 2.12). This term expresses that there is a stable condition for unsaturated air and an unstable condition for saturated air.

Although air normally gets colder as we go up in the atmosphere, the air temperature also can rise with increasing height. This causes decided atmospheric stability. Then we have a *temperature inversion* (negative lapse rate) which may be produced by advection of warm air currents or by cooling through contact with a cold ground surface.

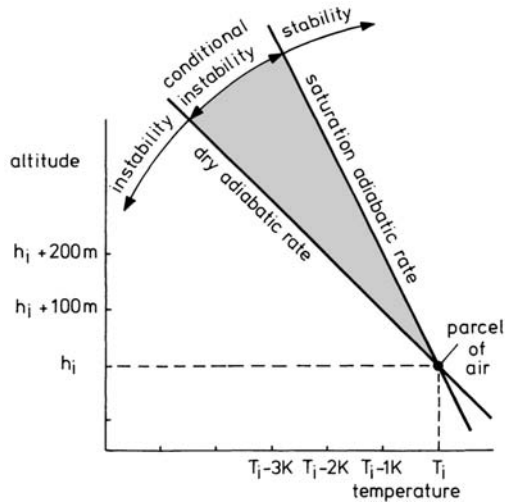


Figure 2.12 Conditional Instability

The vertical movements brought about by unstable atmospheric conditions are called *convection*. This type of air currents can emerge near the Earth's surface when local heating of the ground causes a lapse rate which is greater than the dry adiabatic rate. The rising air may be used by glider pilots to gain altitude while gliding (Figure 2.13a).

The height at which the rising air reaches its saturation temperature is called the convective condensation level (Figure 2.13b). If above this level conditional instability exists, the air may continue its upward motion thereby cooling at the saturation adiabatic rate. Then condensation of some of the moisture takes place and clouds may be formed due to the presence of condensation nuclei in the atmosphere. By reason of this, clouds consist of an enormous amount of droplets of water.

As illustrated in Figures 2.13a and b, the rapid updrafts due to instability give localized clouds with vertical development. The cooling and condensation needed for cloud formation may also be caused by slow rising of a whole layer of stable air. E.g., due to the horizontal movement of air (wind) against a mountain or over a front, which is a wedge of cold air moving under the influence of gravity beneath a warm air mass (Figure 2.13c). This gives slow condensation processes and therefore layerlike clouds.

Usually, cloud types are divided into four families according to the regions where particular forms are found (Figure 2.14).

The distance from the ground to the base of the clouds is called the ceiling. In the case of fog, which is a cloud at the Earth's surface, the ceiling will be at zero altitude.

It is quite obvious that the presence of clouds or fog is extremely important to aviation because it reduces the pilot's range of vision from the flight deck. In this

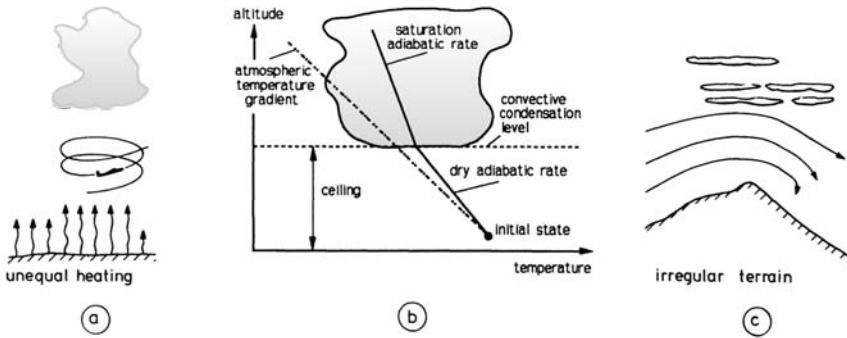


Figure 2.13 Cloud formation

respect, also information on the visibility is included in all aviation weather reports. According to its definition, visibility in a definite direction is the maximum distance to which prominent suitable objects like trees or houses, located in that direction and observed against the horizon sky, can be seen.

It is also important to know that water droplets are present in clouds, even when the air temperature is below freezing point. Only at temperatures below -15°C to -20°C clouds are composed mostly of *ice crystals*.

Supercooled water droplets exist in a highly unstable state and when excited will rapidly be transformed into ice. The freezing of water droplets which are intercepted by the airplane results in the formation of ice on various surfaces of the airplane. Also when the humidity is high and the air temperature is near freezing point, acceleration of the air flow around the wing and propeller blades may cause sufficient fall of temperature to start the freezing process.

Ice formation has always been a hazard to aviation since it affects the flying characteristics and the performance of airplanes by loss of lift, added drag, added weight and loss of thrust. Icing can also stop the air vents, leading to the flight instruments. It should be stated here that modern airplanes are equipped with full de-icing.

2.7 Wind

Wind is the horizontal movement of air relative to the Earth, and is one of the primary atmospheric factors affecting airplane performance.

The direction of wind is that direction from which the wind comes. If the wind is blowing from the southwest, its direction is indicated as southwest (SW). Figure 2.15 shows the generally used wind direction scales.

Wind velocity is reported either in knots or in meters per second. Surface winds may also be expressed in terms of the *Beaufort scale of wind force*. Originally, this system was used to estimate wind velocity by observing its effect on the condition of the sea surface. Table 2.3 gives the relationship between Beaufort number and wind speeds as defined for wind at a height of 10 meters above the ground. The

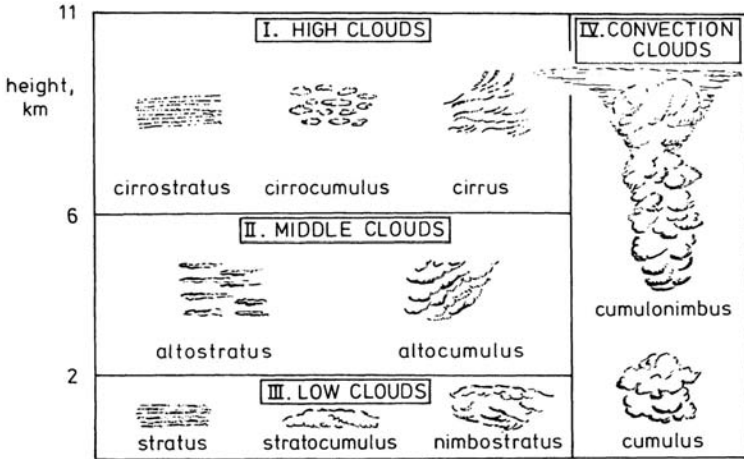


Figure 2.14 Basic cloud families

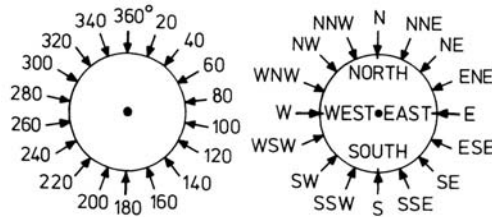


Figure 2.15 Wind direction scales

table also includes the description of winds.

As a whole there is a systematic meridional circulation of the atmosphere, which is caused by the uneven distribution of solar heat over the Earth. Figure 2.16 represents the general circulation on the Northern Hemisphere. Equatorial surfaces heat most. This causes the lower air to expand. Owing to this expansion the sea-level pressure at the Equator is reduced and a higher pressure in upper levels over the Equator is created. Then, at higher elevations air flows from the Equator and in lower levels toward the Equator.

Due to the rotation of the Earth from west to east, the Coriolis force, (see Section 1.3), deflects the air which is moving from the Equator to the right. This leads to a high pressure zone at about latitude 30° , where calm and variable winds occur. The winds blowing Equatorward become the well-known Northeast trades in the neighborhood of the Equator. Light winds occur in the equatorial low pressure zone between the two belts of trade winds.

The cooling in the Polar regions causes the air to contract, resulting in a high pressure at the ground and a relative low pressure in upper levels. The air moving southward from the North Pole is deflected into an easterly flow. The air which is forced Poleward from the high pressure zone at latitude 30° is turned to the west

and becomes the familiar prevailing Westerlies. As a result, a low pressure zone is also found around latitude 60° .

Table 2.3 Beaufort scale

| Beaufort number | wind velocity (knots) | description of wind |
|-----------------|-----------------------|---------------------|
| 0 | < 1 | calm |
| 1 | 1-3 | light air |
| 2 | 4-6 | light breeze |
| 3 | 7-10 | gentle breeze |
| 4 | 11-16 | moderate |
| 5 | 17-21 | fresh |
| 6 | 22-27 | strong |
| 7 | 28-33 | near gale |
| 8 | 34-40 | gale |
| 9 | 41-47 | strong gale |
| 10 | 48-55 | storm |
| 11 | 56-63 | violent storm |
| 12 | > 63 | hurricane |

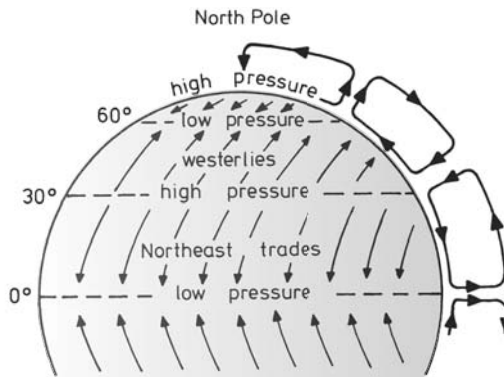


Figure 2.16 General circulation of Northern Hemisphere

Near the Earth's surface the forces that determine wind direction and wind speed are the force due to the horizontal pressure gradient, the Coriolis force and the friction force. The latter force arises from the relative motion between air and ground surface. The magnitude of the wind speed at lower altitudes is strongly affected by this friction force, which tends to decrease the wind velocity. The retarding effect of the surface is largest near the ground and remains of significance up to about 1000 meters above ground level. The region where the surface friction occurs may be called the *planetary boundary layer*.

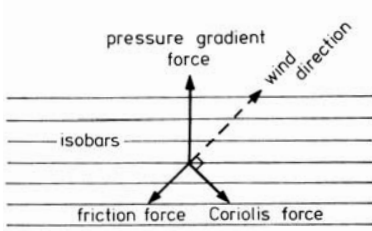


Figure 2.17 Change of wind direction due to Coriolis force

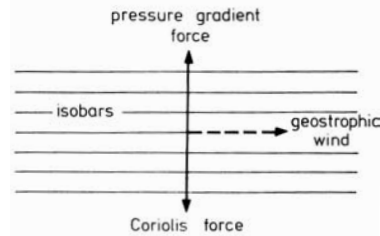


Figure 2.18 The geostrophic wind on the Northern Hemisphere

Since the Coriolis force is proportional to the wind velocity, this apparent force increases with increasing height. In the so-called surface boundary layer, which reaches to about a height of 100 meters, the Coriolis force is negligible small in comparison with the friction force and the pressure gradient force. In this layer the wind velocity increases continuously with increasing height, starting from the zero-velocity boundary value at ground level, whereby the air moves in a direction perpendicular to the isobars.

Above the surface boundary layer the wind speed increases further and wind blowing Poleward is deflected in an easterly direction under the influence of the Coriolis force. This situation is depicted in Figure 2.17, where equilibrium of forces is assumed. The reduction of the wind velocity due to the friction force and the angle that the wind makes with the isobars depend on the type and roughness of the ground surface.

Above the planetary boundary layer the surface friction is no longer effective. Then, finally, the wind direction becomes parallel to the isobars. Under these circumstances the Coriolis force is balanced by the pressure gradient force (Figure 2.18).

The equation which expresses this condition for the case of straight isobars, is the so-called geostrophic wind equation:

$$\frac{1}{\rho} \frac{dp}{ds} = 2\omega_e V_w \sin \phi, \quad (2.51)$$

where dp/ds is the horizontal pressure gradient if s is measured across the isobars, V_w is the geostrophic wind velocity and ϕ is latitude.

A qualitative description of the direction of the geostrophic wind is given by the law of *Buys-Ballot*, which states that in the Northern Hemisphere, if you face the wind the atmospheric pressure decreases toward your right and increases toward your left. In the Southern Hemisphere the opposite is true.

Information services for air navigation all over the world regularly report meteorological data that comprise wind directions and velocities at various altitudes. On the average the wind speed increases up to the tropopause (Figure 2.19a).

Also the presence of the so-called *jet streams* in the upper troposphere and lower stratosphere should be mentioned. These relative strong winds, having velocities

of 300–400 km/h, are concentrated within a narrow flow and follow a meandering path at particular latitudes.

The increase in wind velocity with height in the surface boundary layer often is represented by power laws, according to the relationship

$$V_w = \bar{V}_{w1} \left(\frac{h}{h_1} \right)^n, \quad (2.52)$$

where \bar{V}_{w1} is the average wind velocity at a fixed reference height h_1 . For wind blowing over a relatively smooth surface and in conditions of normal lapse rates, the exponent n is approximately equal to $1/7$ (Reference 12). Figure 2.19b displays the form of the wind profile according to Equation (2.52), using $\bar{V}_{w1} = 5$ m/s at $h_1 = 2$ m.

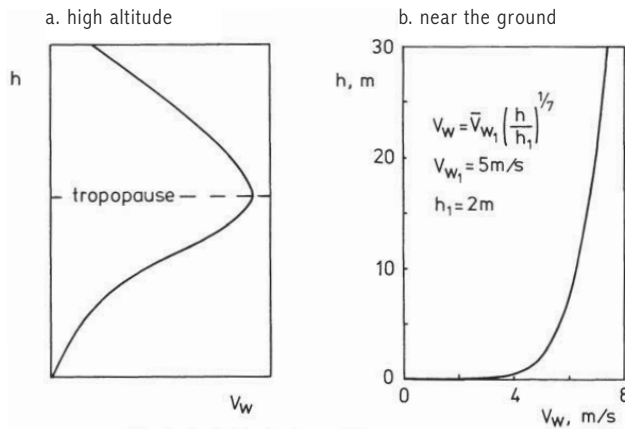


Figure 2.19 Typical wind velocity profiles

When the wind blows over a rough surface or when the air flows in layers adjacent to each other at different speeds, irregular motions in the atmosphere may be induced. The type of small-scale motion which is superimposed on a basic flow is called *turbulence* or *gustiness*. A similar form is the convective turbulence which is produced in the case of unstable atmospheric conditions.

On an unclouded day the turbulence is not visible so that it will be felt by an airplane without any visual warning. Under these conditions the term *clear-air turbulence* is used. In general we can designate local wind shear at heights near the tropopause as being the most important cause of clear-air turbulence.

2.8 Atmospheric fronts

In the previous section we have observed that the circulation of the atmosphere is basically the migration of extensive air masses over long distances.

By air masses are meant far-reaching bodies of air, wherein the atmospheric conditions are approximately consistent at each level, and of which the physical properties originate from the characteristics of their source regions on Earth.

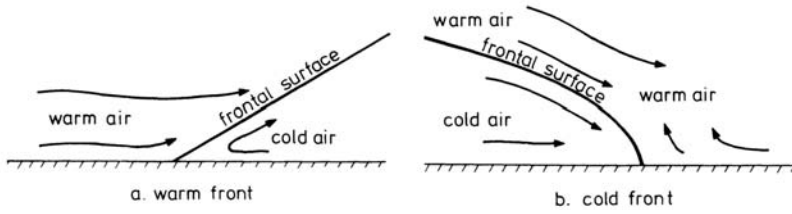


Figure 2.20 Vertical cross-section through atmospheric fronts

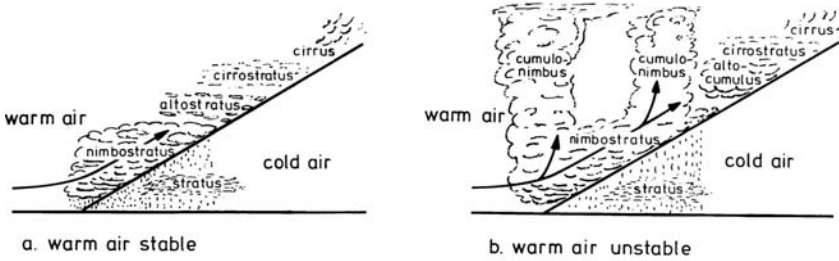


Figure 2.21 Warm front cloud systems

During its motion, the air has a tendency to maintain its commencing properties, or else is modified somewhat by the nature of the ground surface over which it travels.

When air masses of different temperature meet each other, a rather thin transition layer or surface of discontinuity is formed between them. The colder, heavier air moves underneath the warmer light air, thereby forming a wedge of cold air under the action of gravity (Figure 2.20). The dividing plane between the two air masses is called the frontal surface. The intersection of the frontal surface with the ground surface is called a front.

A front is designated by the relative temperature of the air mass, which moves toward the other. Thus, if warmer air is displacing colder air, it is called a *warm front* (Figure 2.20a). In the same way, a cold front is a front along which colder air replaces warmer air (Figure 2.20b).

Logically, a warm front causes higher temperatures at the places over which it proceeds, and a cold front brings lower temperatures. Each front has its own special quality of cloud, precipitation and wind conditions.

Figure 2.21a shows the cloud system in a warm front with the warm air stable. In this case the air slowly advances over the sloping frontal surface and extensive cloud formation occurs. First cirrus clouds come into sight, and then cirrostratus and altostratus, in sequence. Ultimately, nimbostratus clouds are developed, and precipitation drops down. Low stratus clouds may cover the nimbostratus.

The humidity of the cold air is increased to near-saturation by the precipitation, through which further cooling during the night may produce fog over large areas. If the warm air is conditionally unstable, altocumulus and cumulonimbus clouds come after the cirrus forms and thunderstorm activeness may be encountered

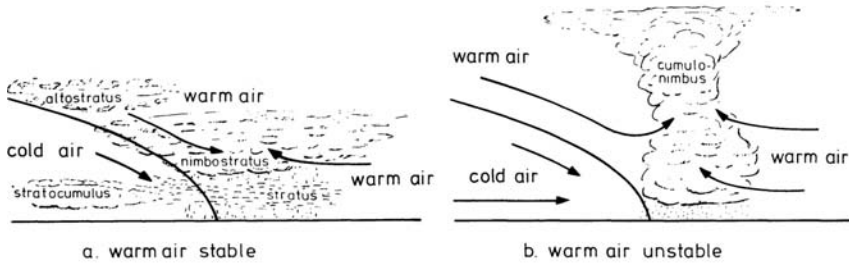


Figure 2.22 Fast-moving cold front cloud formation

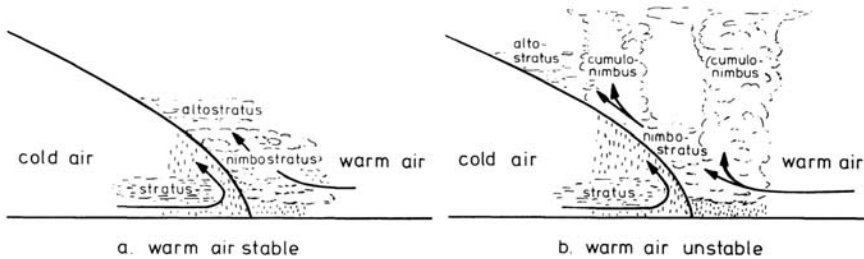


Figure 2.23 Vertical cross-section of clouds in slow moving cold fronts

ahead of the front, together with convective showers (Figure 2.21b).

The wind directions and velocities above and under the frontal surface commonly differ significantly.

Two types of cold fronts are distinguished, fast-moving cold fronts and stationary or slow-moving cold fronts.

Figure 2.22a indicates that the motions in a fast-moving cold front consist of declining movements at both sides of the frontal surface, causing variable surface winds behind the front. In the warm air ahead of the front upward movements take place.

If the warm air is stable, the sky becomes overcast with altostratus and nimbostratus clouds, from which rain falls.

An unstable condition of the warm air (Figure 2.22b) leads to the development of cumulonimbus clouds, thunderstorm activity, and showers along and ahead of the front.

The cloud formation in a slow-moving cold front is of the same kind as in a warm front (Figure 2.23); warm air sloping upward delivers altostratus and nimbostratus clouds. Also, there may be sufficient upward movements in the cold air to produce low stratus clouds behind the front. When the warm air is conditionally unstable cumulonimbus clouds with thunderstorm activity may arise.

In the case that a cold front meets a warm front, we may have the situation of an occluded front. The manner in which the occlusion works out depends on the relative temperature of the cold air masses underlying the two frontal surfaces.

In a so-called *cold front occlusion* (Figure 2.24a), the air behind the cold front

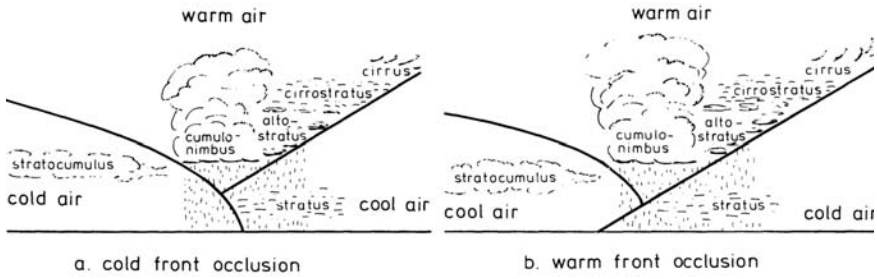


Figure 2.24 Occluded fronts

is the colder, and therefore displaces the cool air behind the warm front. On the other hand, as shown in Figure 2.24b, in a warm front occlusion the air behind the cold front is less cold than the air beneath the warm front so that now the cold front climbs over the wedge of the warm front.

We end this section with the remark that, apparently, an appreciation of the boundaries between air masses of different characteristics is very important since their frontal disturbances involve special weather conditions which may cause serious aviation hazards in the form of gusts, low ceilings, poor visibilities, and ice accretion.

Chapter 3

EQUATIONS OF MOTION

3.1 Translational motion

Newton's second law of motion can be written as

$$\vec{F} = \frac{d(M\vec{V})}{dt}, \quad (3.1)$$

where \vec{F} is the resultant of all external forces applied to the body, M is its mass, and \vec{V} is the linear velocity vector of the center of gravity of the body relative to an inertial frame of reference.

Starting from Equation (3.1), in Appendix A the derivation is given of the general equation of translational motion for an arbitrary deformable body of mass M (see Equation (A.46) of Appendix A). Of course, all airplanes are flexible, that is, the relative positions of the various parts of the structure change somewhat under the influence of the forces acting in flight. However, it is very beneficial to the complexity of the problem to disregard these deformations. This simplification is generally justified and, as has been mentioned already in Chapter 1, shall also be used here in analyzing the performance of airplanes.

Assuming a rigid body of constant mass, Equation (3.1) becomes the familiar form

$$\vec{F} = M \frac{d\vec{V}}{dt} = M\vec{a}. \quad (3.2)$$

According to Appendix A, the rotational motion of a rigid body is governed by

$$\vec{M}_{cg} = \frac{d\vec{B}_{cg}}{dt}. \quad (3.3)$$

This equation says that the external moment applied to a body is equal to the time derivative of its angular momentum relative to the center of gravity of the body.

In this section the translational motion of rigid airplanes of constant mass will be described by using the body axis system. For this purpose the vector equation (3.2) is transformed analogous to Equation (A.20) of Appendix A. Then we have

$$\vec{F} = M \left(\frac{\delta\vec{V}}{\delta t} + \vec{\Omega} \times \vec{V} \right), \quad (3.4)$$

where $\frac{\delta\vec{V}}{\delta t}$ is the time derivative of the velocity vector with respect to the body axis system, and $\vec{\Omega}$ is the angular velocity of the airplane.

If the unit vectors in our airplane fixed reference frame are $\vec{i}, \vec{j}, \vec{k}$ and if u, v, w and p, q, r are the components of \vec{V} and $\vec{\Omega}$ along the body axes, respectively, then

$$\vec{V} = u\vec{i} + v\vec{j} + w\vec{k} \quad \text{and} \quad (3.5)$$

$$\vec{\Omega} = p\vec{i} + q\vec{j} + r\vec{k}. \quad (3.6)$$

If further the corresponding components of the external force are given by

$$\vec{F} = F_x\vec{i} + F_y\vec{j} + F_z\vec{k}, \quad (3.7)$$

we obtain from Equation (3.4) the following three scalar equations:

$$\left. \begin{aligned} F_x &= M\left(\frac{du}{dt} + wq - vr\right) \\ F_y &= M\left(\frac{dv}{dt} + ur - wp\right) \\ F_z &= M\left(\frac{dw}{dt} + vp - uq\right) \end{aligned} \right\}. \quad (3.8)$$

The resultant external force \vec{F} includes the aerodynamic force \vec{R} , originating from the interaction between airflow and airplane surfaces, the thrust \vec{T} of the propulsive system, and the weight \vec{W} of the airplane,

$$\vec{F} = \vec{R} + \vec{T} + \vec{W}. \quad (3.9)$$

We also may consider the so-called *resultant aerodynamic force* \vec{A} , being the vector sum of two constituents; the aerodynamic force \vec{R} and the thrust \vec{T} ,

$$\vec{A} = \vec{R} + \vec{T}. \quad (3.10)$$

By reference to Figure 3.1, we see that the components of the weight along the body axes are:

$$\left. \begin{aligned} W_x &= -W \sin \theta \\ W_y &= W \cos \theta \sin \phi \\ W_z &= W \cos \theta \cos \phi \end{aligned} \right\}. \quad (3.11)$$

Now Equation (3.8) for the translational motion may be written as

$$\left. \begin{aligned} -W \sin \theta + A_x &= M\left(\frac{du}{dt} + wq - vr\right) \\ W \cos \theta \sin \phi + A_y &= M\left(\frac{dv}{dt} + ur - wp\right) \\ W \cos \theta \cos \phi + A_z &= M\left(\frac{dw}{dt} + vp - uq\right) \end{aligned} \right\}, \quad (3.12)$$

where A_x, A_y and A_z are the scalar components of the resultant aerodynamic force \vec{A} .

3.2 Rotational motion

In order to derive similar expressions for the rotational motion, we will evaluate Equation (A.57) of Appendix A, which equation describes the total angular momentum relative to the center of gravity of the airplane as

$$\vec{B}_{cg} = \int_M \vec{r} \times (\vec{\Omega} \times \vec{r}) dM, \quad (3.13)$$

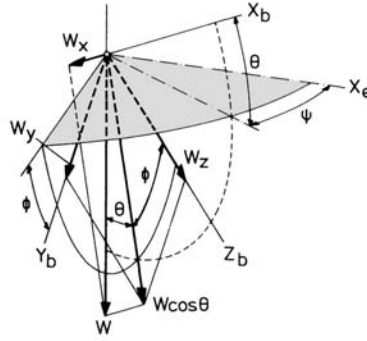


Figure 3.1 Components of airplane weight along body axes

where \vec{r} is the position vector of a mass element with respect to the center of gravity of the airplane. Using the following basic law for the vector triple product,

$$\vec{r} \times (\vec{\Omega} \times \vec{r}) = \vec{\Omega}(\vec{r} \cdot \vec{r}) - \vec{r}(\vec{\Omega} \cdot \vec{r}),$$

we can rewrite Equation (3.13) as

$$\vec{B}_{cg} = \int_M \vec{\Omega}(\vec{r} \cdot \vec{r}) dM - \int_M \vec{r}(\vec{\Omega} \cdot \vec{r}) dM. \quad (3.14)$$

If the coordinates of a mass element in the body axis system are x, y, z , then

$$\vec{r} = x\vec{i} + y\vec{j} + z\vec{k}. \quad (3.15)$$

In terms of the coordinates x, y, z , the dot products in Equation (3.14) become

$$\vec{r} \cdot \vec{r} = x^2 + y^2 + z^2,$$

$$\vec{\Omega} \cdot \vec{r} = px + qy + rz.$$

Substituting the latter relations into Equation (3.14) yields

$$\vec{B}_{cg} = \vec{\Omega} \int_M (x^2 + y^2 + z^2) dM - \int_M \vec{r}(px + qy + rz) dM. \quad (3.16)$$

If we write

$$\vec{B}_{cg} = B_x\vec{i} + B_y\vec{j} + B_z\vec{k} \quad (3.17)$$

the components of \vec{B}_{cg} along the body axes are:

$$\left. \begin{aligned} B_x &= p \int_M (y^2 + z^2) dM - q \int_M xy dM - r \int_M xz dM \\ B_y &= -p \int_M yx dM + q \int_M (x^2 + z^2) dM - r \int_M yz dM \\ B_z &= -p \int_M zx dM - q \int_M zy dM + r \int_M (x^2 + y^2) dM \end{aligned} \right\}. \quad (3.18)$$

In Equation (3.18) appear the so-called moments of inertia of the body:

$$\left. \begin{aligned} I_x &= \int_M (y^2 + z^2) dM \\ I_y &= \int_M (x^2 + z^2) dM \\ I_z &= \int_M (x^2 + y^2) dM \end{aligned} \right\}, \quad (3.19)$$

and the *products of inertia*:

$$\left. \begin{aligned} I_{xy} &= I_{yx} = - \int_M xy dM \\ I_{yz} &= I_{zy} = - \int_M yz dM \\ I_{xz} &= I_{zx} = - \int_M xz dM \end{aligned} \right\}. \quad (3.20)$$

Equations (3.19) and (3.20) give the nine components of the *tensor of inertia* \vec{I} of the body. Hence, we may write

$$\left. \begin{aligned} B_x &= p I_x + q I_{xy} + r I_{xz} \\ B_y &= p I_{xy} + q I_y + r I_{yz} \\ B_z &= p I_{xz} + q I_{yz} + r I_z \end{aligned} \right\}. \quad (3.21)$$

Apparently, Equation (3.13) also can be expressed as the dot product of the tensor \vec{I} and the vector $\vec{\Omega}$,

$$\vec{B}_{cg} = \int_M \vec{r} \times (\vec{\Omega} \times \vec{r}) dM = \vec{I} \cdot \vec{\Omega}. \quad (3.22)$$

Accordingly, the rotational Equation (A.58) of Appendix A can be expressed as

$$\vec{M}_{cg} = \frac{d\vec{B}_{cg}}{dt} = \vec{I} \cdot \frac{d\vec{\Omega}}{dt} + \vec{\Omega} \times \vec{B}_{cg}, \quad (3.23)$$

where \vec{M}_{cg} is the external (aerodynamic) moment on the airplane, acting about the center of gravity. If \vec{M}_{cg} is resolved into its components along the body axes, the following three scalar equations are obtained:

$$\left. \begin{aligned} M_x &= \frac{dp}{dt} I_x + \frac{dq}{dt} I_{xy} + \frac{dr}{dt} I_{xz} + qB_z - rB_y \\ M_y &= \frac{dp}{dt} I_{xy} + \frac{dq}{dt} I_y + \frac{dr}{dt} I_{yz} + rB_x - pB_z \\ M_z &= \frac{dp}{dt} I_{xz} + \frac{dq}{dt} I_{yz} + \frac{dr}{dt} I_z + pB_y - qB_x \end{aligned} \right\}. \quad (3.24)$$

These equations are indicated as Euler's equations of rotational motion, where M_x is the rolling moment, M_y the pitching moment, and M_z the yawing moment. For most airplanes the simplification can be made that the distribution of the mass of the airplane is symmetric with respect to the XZ -plane. Then: $I_{yz} = I_{xy} = 0$, and the components of \vec{M}_{cg} become:

$$\left. \begin{aligned} M_x &= \frac{dp}{dt} I_x + (I_z - I_y)qr + I_{xz} \left(\frac{dr}{dt} + pq \right) \\ M_y &= \frac{dq}{dt} I_y + (I_x - I_z)pr + I_{xz} (p^2 - r^2) \\ M_z &= \frac{dr}{dt} I_z + (I_y - I_x)pq + I_{xz} \left(\frac{dp}{dt} - qr \right) \end{aligned} \right\}. \quad (3.25)$$

The systems of Equations (3.12) and (3.25), and the kinematic relations (1.22) describe the motion of a rigid airplane with constant mass.

In a general sense, we have to consider accelerated motion of the airplane on the basis of a detailed knowledge of the force and moment components. Such studies make up the essence of the subject termed *flight dynamics*. Both, a number of problems in the field of stability and control, and airplane performance fall under the heading of flight dynamics. Concerning airplane performance, for example, the prediction of takeoff and landing distances and the determination of optimum flight trajectories under circumstances in which the interchange between kinetic and potential energies is of importance to the computational results, pertain to this class of questions.

On the other hand, one should remember that during most of its flying time, an airplane can be assumed to be in quasi-steady motion. Therefore, as a topic of particular interest, in the following section the equations describing the most general motion of an airplane in steady flight are presented.

3.3 The most general steady motion

In Section 1.9 steady flight has been defined as the flight in which both magnitude and direction of forces and moments acting on the airplane remain constant.

Starting from this definition, we can examine the resulting motion, provided that the atmospheric conditions are independent of flight altitude (poor assumption in case of prolonged flight).

Steady motion requires that the time derivatives of all the variables involved in Equations (3.12) and (3.25) are zero:

$$\frac{du}{dt} = \frac{dv}{dt} = \frac{dw}{dt} = \frac{dp}{dt} = \frac{dq}{dt} = \frac{dr}{dt} = 0 \quad \text{and} \quad \frac{d\theta}{dt} = \frac{d\phi}{dt} = 0. \quad (3.26)$$

These conditions lead to the following equilibrium equations:

$$\left. \begin{aligned} -W \sin \theta + A_x &= M(wq - vr) \\ W \cos \theta \sin \phi + A_y &= M(ur - wp) \\ W \cos \theta \cos \phi + A_z &= M(vp - uq) \\ M_x &= (I_z - I_y)qr + I_{xz}pq \\ M_y &= (I_x - I_z)pr + I_{xz}(p^2 - r^2) \\ M_z &= (I_y - I_x)pq - I_{xz}qr \end{aligned} \right\}. \quad (3.27)$$

It follows from the requirements (3.26) that only the angular velocity $d\psi/dt$ may have a finite value. Then, according to the definition of the angle of yaw in Figure 1.14, the resultant angular velocity of the airplane is about the vertical axis,

$$\Omega = \frac{d\psi}{dt}.$$

For steady motion the kinematic relations (1.22) reduce to (see Figure 1.20)

$$\left. \begin{aligned} p &= -\frac{d\psi}{dt} \sin \theta \\ q &= +\frac{d\psi}{dt} \cos \theta \sin \phi \\ r &= +\frac{d\psi}{dt} \cos \theta \cos \phi \end{aligned} \right\}. \quad (3.28)$$

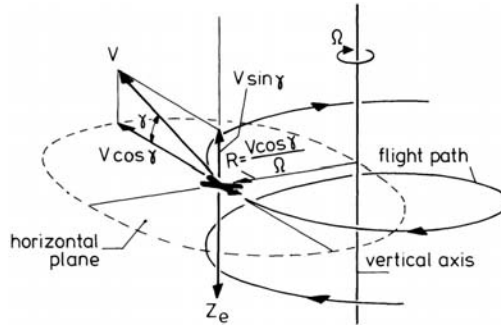


Figure 3.2 Helicoidal motion

It is seen from the equations (3.28) that not only the direction, but also the magnitude of the resultant angular velocity remains unchanged. Expressed in terms of the angles defining the orientation of the air-path axes, we have

$$\Omega = \frac{d\chi}{dt} \quad \text{and} \quad \frac{d\gamma}{dt} = \frac{d\mu}{dt} = 0. \quad (3.29)$$

Evidently, the flight-path angle γ and the aerodynamic angle of roll μ are also independent of time. Consequently, the same holds true for the angle of attack α and the angle of sideslip β since at a given velocity the aerodynamic force solely depends on the attitude of the airplane relative to the velocity vector, and this orientation is fully determined by the angles α and β .

As shown in Figure 3.2, the condition that velocity V , angle γ , and angular velocity Ω are constants, implies that the most general steady motion of an airplane is a nonsymmetric flight in which the center of gravity of the airplane travels at constant velocity along a helical path with vertical axis, having a constant radius and pitch (spiral climb).

In performance considerations, the forces in Equation (3.27) are conveniently expressed in terms of their components along the air-path axes. In doing so, we derive for the steady helicoidal motion the following force equations (Figure 3.3):

$$\left. \begin{aligned} -D + T \cos \alpha_T \cos \beta - W \sin \gamma &= 0 \\ -S - T \cos \alpha_T \sin \beta + W \cos \gamma \sin \mu - C \cos \mu &= 0 \\ -L - T \sin \alpha_T + W \cos \gamma \cos \mu + C \sin \mu &= 0 \end{aligned} \right\}. \quad (3.30)$$

These equations give the force components along the X_a , Y_a and Z_a -axis, respectively. As can be seen from Figure 3.3, the sideslip is toward the inner side of the curvilinear path ($\beta > 0$).

The thrust angle α_T in Equation (3.30) includes the angle of attack and the fixed inclination η of the thrust vector to the X_b -axis. The force C is the horizontal centrifugal force, which is given by (see Equation (1.16))

$$C = \frac{W}{g} V \Omega \cos \gamma = \frac{W}{g} \frac{V^2}{R} \cos^2 \gamma, \quad (3.31)$$

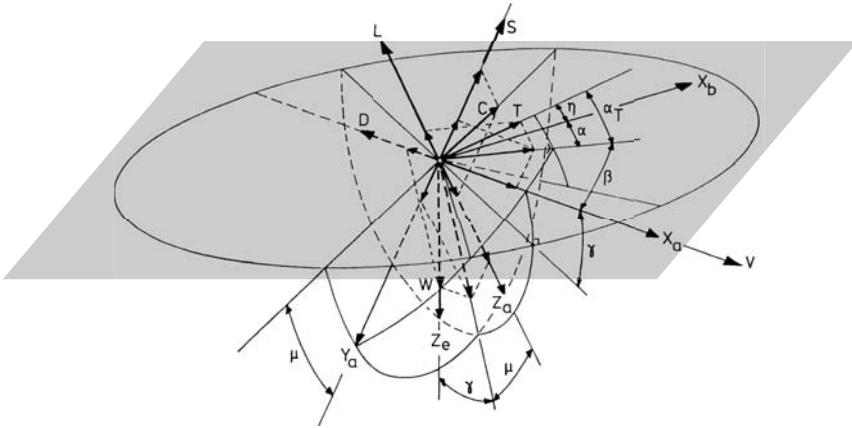


Figure 3.3 Forces acting on the airplane in steady helicoidal motion

where R is the radius of curvature (Figure 3.2). The side force S is the cross component of the aerodynamic force R due to the sideslipping motion, and acts along the negative Y_a -axis at a positive angle of sideslip. The paramount contributions to the force S originate from the fuselage and the vertical tailplane. Also the propulsive system may produce a contribution to the side force.

3.4 Special types of flight

a. Steady straight nonsideslipping flight

In this particular case all the lateral variables are zero: $\beta = 0, C = 0, S = 0$. Insertion of these conditions into Equation (3.30) learns us that also the aerodynamic angle of roll is zero ($\mu = 0$).

The force equations (3.30) are then reduced to

$$\left. \begin{aligned} -D + T \cos \alpha_T - W \sin \gamma &= 0 \\ -L - T \sin \alpha_T + W \cos \gamma &= 0 \end{aligned} \right\} \quad (3.32)$$

In addition, we have the requirement that the moments generated by the aerodynamic forces must be fully balanced by appropriate settings of the control surfaces (trimmed flight condition where $M_x = M_y = M_z = 0$). Use of the controls, of course, will affect the aerodynamic characteristics of the airplane. However, in considering particular flight types, we shall assume that the contributions from control surface deflections to lift, drag, and side force are sufficiently small in magnitude so that they can be neglected. Moreover, because we are primarily concerned with the translational motion of the airplane, we can usually limit ourselves to the application of the force equations only.

The above-mentioned conclusion that $\mu = 0$ implies that the Y_a -axis lies in the horizontal plane so that the plane of symmetry of the airplane coincides with one and the same vertical plane (Figure 3.4).

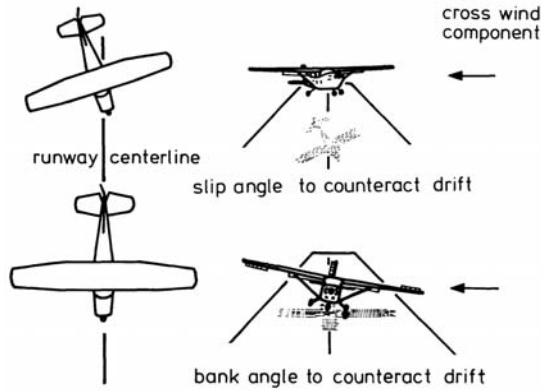


Figure 3.5 Landing in cross wind

the positive Y_a -axis. Therefore, in the flat turn the nose of airplane lies to the right of the velocity vector ($\beta < 0$). From Figure 3.7 we now get the following force equations:

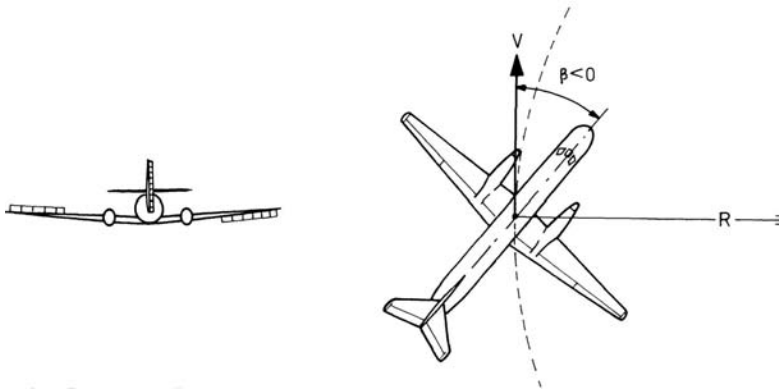


Figure 3.6 The flat turn

$$\left. \begin{aligned} -D + T \cos \alpha_T \cos \beta &= 0 \\ S - T \cos \alpha_T \sin \beta - C &= 0 \\ -L - T \sin \alpha_T + W &= 0 \end{aligned} \right\} \quad (3.34)$$

In the flat turn the occupants of the airplane are submitted to annoying transversal accelerations.

Moreover, it appears that the radius of curvature in the flat turn is relatively large so that the pilot will use this maneuver only when he wants to change his pathway over the Earth slowly (Reference 1). In regular cases, however, the course of an airplane is always changed by executing a *banked turn* as will be discussed in the following.

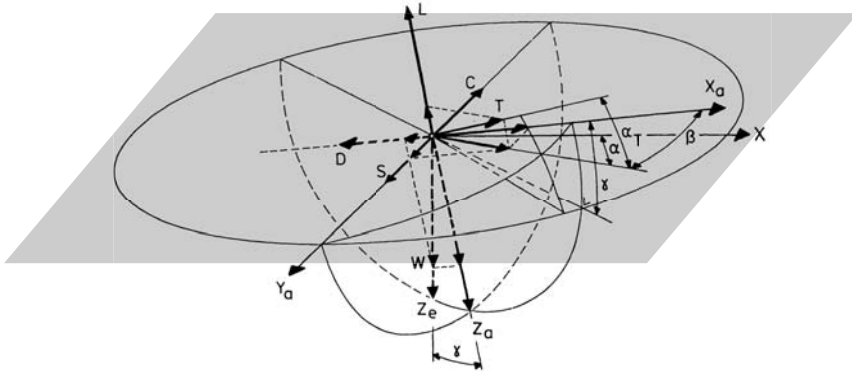


Figure 3.7 Forces in the flat turn

d. *Steady nonsideslipping banked turn*

This type of flight is called the *true banked* or *coordinated turn*, and is the natural maneuver to change the pathway of an airplane. In a coordinated turn to the right, the pilot brings the airplane into an inclined position by banking it to the right.

As the condition for a coordinated turn is that the airplane may not be yawed, the Y_a -axis and the Y_b -axis coincide. Then, analogous to Equation (1.19), the relation between angle of bank Φ , aerodynamic angle of roll μ , and the flight-path angle γ is given by

$$\sin \Phi = \sin \mu \cos \gamma. \quad (3.35)$$

Owing to the absence of sideslip the side force S is zero so that the resultant aerodynamic force acts in the plane of symmetry of the airplane. Accordingly, also the vector sum of the weight W and the centrifugal force C lies in the plane of symmetry (Figure 3.8).

The equilibrium equations now read:

$$\left. \begin{aligned} T \cos \alpha_T - D - W \sin \gamma &= 0 \\ W \cos \gamma \sin \mu - C \cos \mu &= 0 \\ -T \sin \alpha_T - L + W \cos \gamma \cos \mu + C \sin \mu &= 0 \end{aligned} \right\}. \quad (3.36)$$

The second equation of (3.36) shows that in the coordinated turn the component of the centrifugal force along the Y_a -axis is balanced solely by a lateral component of the weight of the airplane. Consequently, the occupants experience only an additional force in a direction perpendicular to their seats, and there will be no tendency of sliding in a lateral direction.

Often, the system of equations (3.36) may be expressed as follows:

$$\left. \begin{aligned} T \cos \alpha_T - D - W \sin \gamma &= 0 \\ -T \sin \alpha_T \sin \mu + L \sin \mu - C &= 0 \\ -T \sin \alpha_T \cos \mu - L \cos \mu + W \cos \gamma &= 0 \end{aligned} \right\}. \quad (3.37)$$

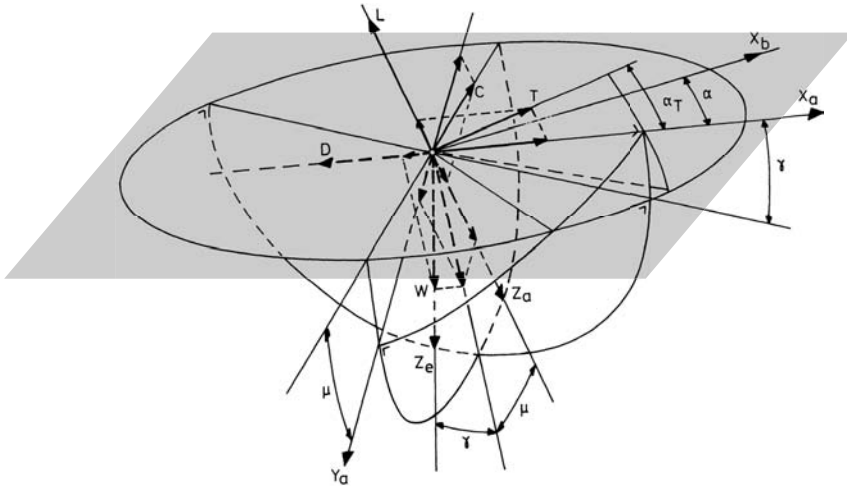


Figure 3.8 Forces in the coordinated turn

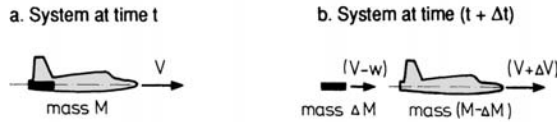


Figure 3.9 Ejection of airplane mass

The first of these equations gives again the equilibrium of forces along the X_a -axis. The second equation gives the summation of the radial forces in the horizontal plane, whilst the third equation gives the summation of the forces acting perpendicular to the X_a -axis in the vertical plane.

3.5 Translational equation for variable mass

In considering the motion of an airplane, we have to allow for the fact that in powered flight the propulsion system consumes fuel, by which the mass of the airplane is decreasing continually.

In order to formulate the equation for translational motion for a rigid airplane ejecting mass, we consider an airplane in horizontal straight flight that at time t has a mass M and a velocity V relative to an inertial frame of reference (Figure 3.9a).

Suppose that at time $t + \Delta t$ the airplane has a mass $M - \Delta M$ and a velocity $V + \Delta V$. Further, suppose that mass ΔM , ejected in the time Δt , has a velocity w relative to the airplane (Figure 3.9b).

By Newton's second law of motion, the total external force acting on the complete mass system at time t is equal to the rate of change of linear momentum of the

system. In the limit as Δt tends to zero we have

$$F = \lim_{\Delta t \rightarrow 0} \frac{(M - \Delta M)(V + \Delta V) + \Delta M(V - w) - MV}{\Delta t} = M \frac{dV}{dt} - w \frac{dM}{dt}. \quad (3.38)$$

Thus for an airplane that is losing mass, the equation of motion can be written as

$$F + w \frac{dM}{dt} = M \frac{dV}{dt}. \quad (3.39)$$

The term dM/dt may be replaced by the fuel flow rate, m_f

$$\frac{dM}{dt} = -m_f, \quad (3.40)$$

where the minus sign indicates that the airplane mass is decreasing. Substitution of Equation (3.40) into (3.39) gives

$$F - m_f w = M \frac{dV}{dt}. \quad (3.41)$$

We conclude that Equation (3.2) can be used to consider the motion of an airplane in powered flight, provided that the linear momentum of the fuel flow rate relative to the airplane is included in the entire external force.

Chapter 4

AERODYNAMIC BASIS

4.1 Aerodynamic coefficients

The aerodynamic forces R and the moment M_{cg} , acting on a moving airplane are produced by pressure forces and viscous forces. The pressure forces happen due to the asymmetric pressure distribution about the wing and the other airplane component parts, whereas the viscous forces arise because of shear stresses at the outer surface of the airplane.

Figure 4.1 shows the pressure distribution over a wing section slanted at a normal (low) incidence angle to the freestream in a steady flow. According to Bernoulli's equation for compressible isentropic flow in Appendix D, the variation of the static pressure p along a streamline is given by

$$p_t = p \left[1 + \frac{\gamma - 1}{2} \frac{\rho}{p} V^2 \right]^{\frac{\gamma}{\gamma - 1}} = \text{constant.} \quad (4.1)$$

Along the streamline which follows the surface of the wing section, the velocity lowers from the freestream value ahead of the wing till zero at the stagnation point on the nose of the wing, where the static pressure becomes equal to the freestream total pressure p_t .

Following the streamline from the nose along the upper surface of the wing section, the velocity increases and the local static pressure decreases. At some point the velocity reaches its highest value and the static pressure its lowest value. Past this point the velocity decreases again and the local static pressure comes back to the freestream static pressure. Similar variations of local velocity and pressure occur along the lower surface. Owing to the difference between the amount of upper and lower surface camber, and also because the wing section is at an angle of incidence, the velocity of the air flowing over the upper surface is greater than the velocity along the lower surface. Consequently, the pressure on the upper surface will be lower than that acting on the lower surface. As a result, a resultant force is produced due to shape and angle of attack of the wing section.

The surface shear stress τ_0 is the force per unit area acting tangentially on the surface of a body due to the frictional effects between body and surrounding air flow. Figure 4.2 illustrates the cause of the shear stress, namely, the fact that the fluid particles adjacent to a solid boundary are brought to rest and those close to it are slowed down markedly. This effect decays quickly across the flow so that always there is a velocity gradient in the flow adjacent to the surface of the body. The layer in which the velocity of the air particles increases from zero at the surface to the local velocity about the body is normally very thin (thickness < 1 cm).

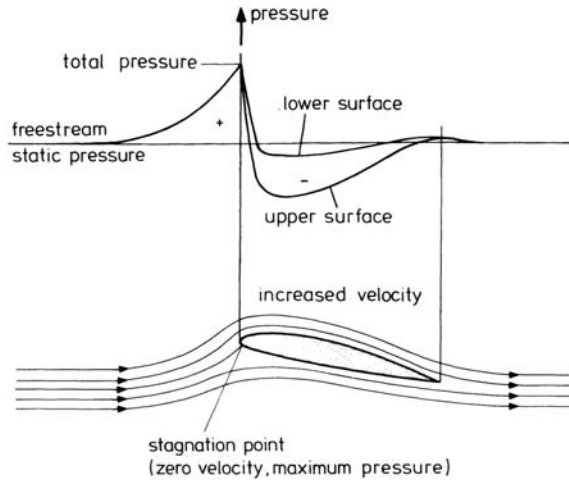


Figure 4.1 Pressure distribution over a wing section

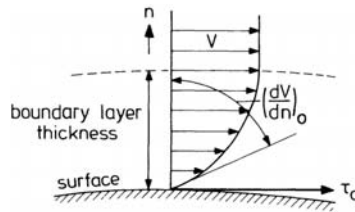


Figure 4.2 Velocity profile across the boundary layer

The velocity differences between the laminae of air are fundamentally due to cohesion and interaction between fluid particles. It allows motion only by sliding action between adjacent layers which induces shear forces. The resultant effect of all these forces is the skin friction drag of the body. The layer of air adhering to the surface in which friction is essential is indicated as the boundary layer. As will be explained in Section 4.3, the concept of boundary layer flow is a useful tool for the understanding of drag characteristics. Point of departure thereby, is the idea that viscosity manifests only in a restricted region and not throughout the main flow.

Hence the flow pattern around a body may be divided into two regions, that is, a thin boundary layer in which friction is important, and a region beyond this in which the air behaves as a frictionless fluid.

Experimentally, it has been observed that the shear stress τ_0 is given by the product of the slope of the velocity profile at the surface and the coefficient of dynamic viscosity μ ,

$$\tau_0 = \left(\frac{dV}{dn} \right)_0 \mu. \quad (4.2)$$

For the simple type of laminar flow where successive layers of air slide over one

another in the form of parallel layers, the coefficient μ is a physical property, approximately proportional to $T^{1/2}$ over the normal range of air temperatures (see Chapter 2). Clearly, for a given μ , the velocity gradient at the surface is the deciding factor in the determination of the skin friction drag.

From the preceding discussion we may expect that the aerodynamic force and moment are determined by the following quantities:

- general shape of the airplane
- size of the airplane surface, S
- airplane condition
- control surface deflections
- attitude of the airplane relative to the freestream
- airspeed, V
- density of the air, ρ
- coefficient of dynamic viscosity, μ .

To these variables should be added the speed of sound in air, c , which defines the freestream *Mach number*, $M = V/c$. As we will see later, the Mach number is a convenient parameter for indicating the importance of the compressibility of the air on the pressure distribution over the airplane surface (see Section 4.3).

A working method to derive expressions for the aerodynamic force R and moment M_{cg} is the technique called *dimensional analysis*. This technique is based on the principle that in a physical equation the dimensions should be the same on both sides.

Therefore, we state that the aerodynamic force on the airplane depends on S , V , ρ , c and μ ,

$$R = f(S, V, \rho, c, \mu). \quad (4.3)$$

Since R has dimensions of a force, the right side of Equation (4.3) must also have dimensions of a force. The only possibility to secure dimensional uniformity is writing the latter equation in the following manner,

$$R = K(S^a V^b \rho^d c^e \mu^f), \quad (4.4)$$

where a , b , d , e and f are unknown constants and K is a function of the remaining dimensionless variables, which cannot be brought into Equation (4.3). Then, in terms of mass [M], length [L] and time [T], we have

$$\frac{ML}{T^2} = K(L^2)^a \left(\frac{L}{T}\right)^b \left(\frac{M}{L^3}\right)^d \left(\frac{L}{T}\right)^e \left(\frac{M}{LT}\right)^f. \quad (4.5)$$

Clearly, the exponent of the mass on the left-hand side of Equation (4.5) is 1, and on the right-hand side $d + f$. Thus,

$$1 = d + f. \quad (4.6)$$

Similarly, for the length we get

$$1 = 2a + b - 3d + e - f, \quad (4.7)$$

and for the time

$$-2 = -b - e - f. \quad (4.8)$$

The latter three equations contain five unknowns. Assuming that S , V and ρ are of primary significance, we can solve the Equations (4.6) to (4.8) for a , b and d in terms of e and f . We find

$$\left. \begin{aligned} a &= 1 - f/2 \\ b &= 2 - e - f \\ d &= 1 - f \end{aligned} \right\}. \quad (4.9)$$

Substitution of these exponents into Equation (4.4) gives

$$R = K(S)^{1-f/2}(V)^{2-e-f}(\rho)^{1-f}c^e\mu^f. \quad (4.10)$$

Grouping factors of particular exponents yields

$$R = K\rho V^2 S \left(\frac{c}{V}\right)^e \left(\frac{\mu}{\rho V S^{1/2}}\right)^f. \quad (4.11)$$

Since the dimension of $S^{1/2}$ is correspondent to a length ℓ , we may write

$$R = K\rho V^2 S \left(\frac{c}{V}\right)^e \left(\frac{\mu}{\rho V \ell}\right)^f. \quad (4.12)$$

We note that the ratio V/c is the freestream Mach number. The quantity $\rho V \ell / \mu$, which is called the *Reynolds number* (denoted by the symbol Re), indicates the relative importance of the shear and inertia forces within the flow; the lower the value of Re the more relative important are the viscous forces. Hence,

$$R = K\rho V^2 S \left(\frac{1}{M}\right)^e \left(\frac{1}{Re}\right)^f. \quad (4.13)$$

For convenience we set

$$K \left(\frac{1}{M}\right)^e \left(\frac{1}{Re}\right)^f = \frac{C_R}{2}.$$

Now we can write

$$R = C_R \frac{1}{2} \rho V^2 S = C_R q S. \quad (4.14)$$

Equation (4.14) states that the aerodynamic force is determined by a coefficient C_R times the dynamic pressure $\frac{1}{2}\rho V^2 = q$ times an area S .

For airplanes the convention is to use the area of the wing planform as the surface of reference. This area is called wing area and is further explained in Section 4.2. Evidently, Equation (4.14) represents also the lift, drag and side force components of the aerodynamic force:

$$\left. \begin{aligned} L &= C_L \frac{1}{2} \rho V^2 S \\ D &= C_D \frac{1}{2} \rho V^2 S \\ S &= C_S \frac{1}{2} \rho V^2 S \end{aligned} \right\}. \quad (4.15)$$

Here the coefficients C_L , C_D and C_S are known as the coefficients of lift, drag and side force, respectively.

When the technique of dimensional analysis is applied to the moment M_{cg} , the following expression easily is found,

$$M_{cg} = C_M \frac{1}{2} \rho V^2 S \bar{c}, \quad (4.16)$$

where C_M is the nondimensional moment coefficient. According to universal practice, the length factor \bar{c} is taken equal to the mean aerodynamic chord of the wing (see Section 4.2).

The way in which in aerodynamics the coefficients C_L , C_D , C_S and C_M are determined is, of course, beyond the scope of this text. At this place, suffice it to say that even for a given airplane these coefficients by no means are constants, but that they are dependent on airplane condition, control surface deflections, Mach number, Reynolds number and attitude of the airplane.

The side force given in Equation (4.15) occurs only when there is an angle of sideslip. However, sideslipping flight is virtually always an unwanted flight condition. Therefore, so-called coordinated flight conditions ($\beta = 0$) are of primary importance.

4.2 Airfoil and wing characteristics

A cross-section of the wing parallel to the plane of symmetry of the airplane is called *airfoil or wing section*, and is so shaped as to generate lift without excessive drag. Figure 4.3 provides an impression of the development of wing section shapes over the years. Of special significance is the supercritical airfoil developed for use on the modern high-subsonic transports. This advanced wing section has a flatter upper surface, a more convex underside, and an increased camber near the trailing edge.

The improved shape gives a more evenly distributed pressure over the surface, permitting the section to be thicker without causing more drag at high-subsonic airspeeds than its predecessors. More recently was designed the GAW-2 airfoil for application on the low-subsonic general aviation airplanes. This airfoil type produces reduced drag coefficients and an increased maximum lift coefficient. Figure 4.4 gives the nomenclature in defining the shape of an airfoil. The mean camber line determines the amount of curvature and is the line that is situated in

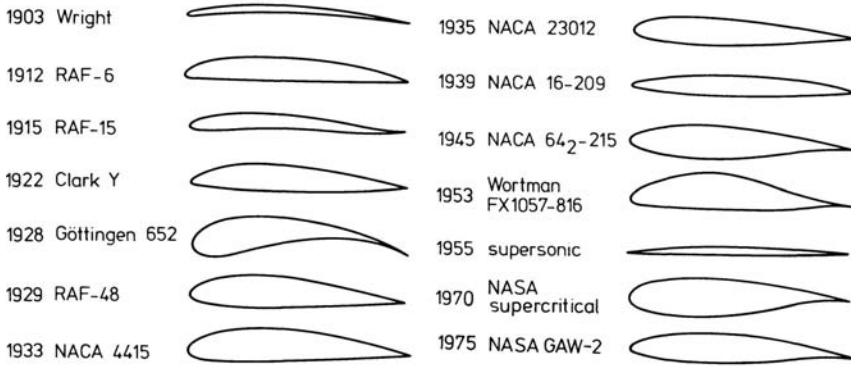


Figure 4.3 Historical review of airfoil shapes

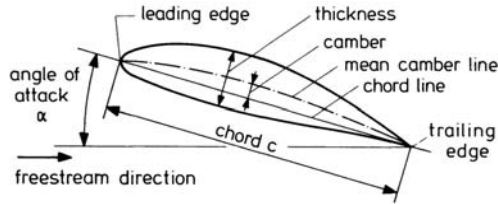


Figure 4.4 Airfoil geometry and nomenclature

the middle between upper and lower surfaces. The ends of the mean camber line are the leading edge and the trailing edge points. The chord line is the straight line joining the two ends of the mean camber line. The chord is the distance between leading edge and trailing edge points, measured along the chord line. The angle between the freestream direction and the chord line is the angle of attack α . The two-dimensional lift, drag and moment coefficients are, according to Equations (4.15) and (4.16),

$$c_\ell = \frac{\ell}{\frac{1}{2}\rho V^2 c} \quad (4.17)$$

$$c_d = \frac{d}{\frac{1}{2}\rho V^2 c} \quad (4.18)$$

$$c_m = \frac{m}{\frac{1}{2}\rho V^2 c^2}, \quad (4.19)$$

where ℓ , d and m are the lift, drag and pitching moment of the aerodynamic force per unit width of the wing, respectively (Figure 4.5). The moment m is usually specified in reference to the quarter-chord point. At low velocities, this point is very close to the aerodynamic center of the airfoil. The latter point is the point about which the pitching moment for a given freestream velocity is essentially independent of the angle of attack. Characteristic curves, showing the variations of lift, drag and moment coefficients with angle of attack, are sketched in Figure 4.6.

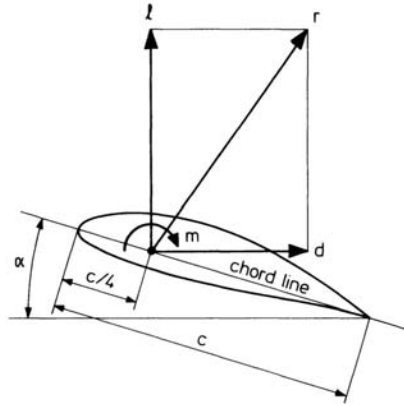


Figure 4.5 Aerodynamic force and moment on airfoil

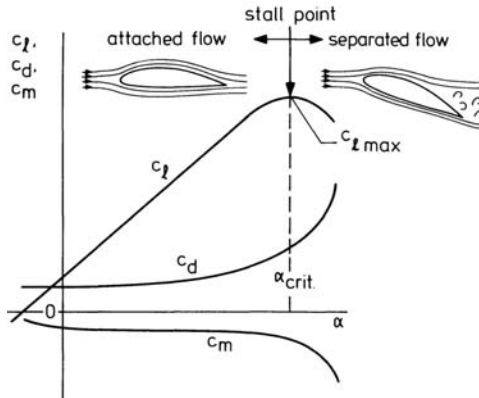


Figure 4.6 Typical c_l - α , c_d - α , c_m - α curves for cambered airfoil

Apparently, up to a large angle of attack, the c_l versus α curve may be represented by a straight line. Notice also that the moment coefficients have negative values. As the angle of attack is increased up to the stall point, $c_{l \max}$ is reached. Beyond this critical angle of attack, the airflow separates from the upper surface, with the result that the lift coefficient is strongly reduced. Computational methods have been developed for the determination of the coefficients c_l , c_d and c_m . Also, a large amount of experimental airfoil data from wind tunnel tests is available in literature; see e.g. Reference 13.

Figure 4.7 shows the most important parameters specifying the geometry of an airplane wing. The wing span b is the length in Y -direction between the wing tips. The wing area S , is the area of the wing projected onto the XY -plane, and may be written as

$$S = \int_{-b/2}^{b/2} c(y) dy, \quad (4.20)$$

where c is the chord length, which often varies with the Y -coordinate. The ratio c_t/c_r is named the taper ratio. As illustrated in Figure 4.8, the wing area, arbitrarily, comprises also the central part of the wing covered by the fuselage.

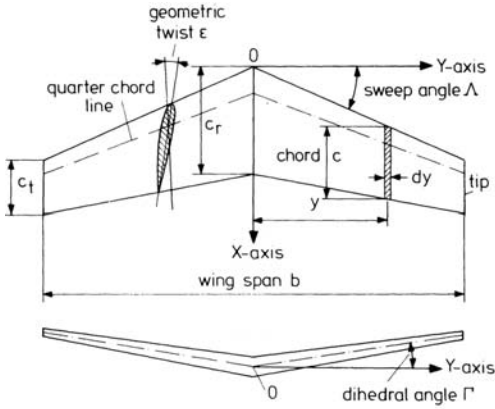


Figure 4.7 Wing geometry

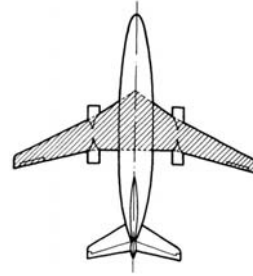


Figure 4.8 Wing area

The mean geometric chord, c_{mg} , is the arithmetic mean of the chord lengths,

$$c_{mg} = \frac{S}{b}. \quad (4.21)$$

The ratio of the wing span to the mean geometric chord is known as the aspect ratio and given the symbol A ,

$$A = \frac{b}{c_{mg}} = \frac{b^2}{S}. \quad (4.22)$$

A wing parameter of importance in quantifying the moment coefficient is the mean aerodynamic chord \bar{c} , which is defined as

$$\bar{c} = \frac{1}{S} \int_{-b/2}^{b/2} c^2(y) dy. \quad (4.23)$$

As with wing area S , we usually specify $c(y)$ over the part of the wing occupied by the fuselage by extending the leading and trailing edges to the plane of symmetry of the airplane.

Geometric twist ϵ , is the variation in direction of a section chord line relative to the direction of the chord line at the root section of the wing. We may modify the spanwise distribution of lift by twisting the wing to give a desired angle-of-attack variation along the span.

The dihedral angle Γ is the angle between the quarter-chord line and its projection on the XY -plane. Dihedral is applied as a means to improve lateral stability. The last term denotes the ability of the airplane to restore to its original attitude after an unwanted displacement about the X_b -axis, without pilot assistance.

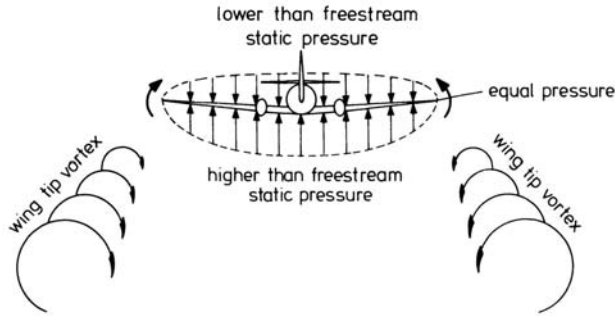


Figure 4.9 Finite wing flow

We end our enumeration of wing geometrical parameters with the sweep angle Λ , which may be represented by the angle between the Y -axis and the projection of the wing leading edge onto the XY -plane. Sweeping the wing is an important measure to reduce the magnitude of the freestream velocity normal to the leading edge, which component determines the velocity and pressure distributions over the wing sections.

Next we have to consider the influence of the finite width of the wing on lift and drag coefficients, when using two-dimensional airfoil data.

Since the pressure on the bottom surface is greater than that on the top surface, there will arise a circular motion of air around the wing tips, and consequently, a reduced lift coefficient at a given angle of attack (Figure 4.9).

In exchange for this loss of lift, we get from the spanwise inflow above the wing and the outflow below the wing, two discrete wing tip vortices in the flow downstream of the wing.

A theoretical analysis yields the following approximate formula for the value of the wing lift-curve slope at subsonic velocities (Reference 14):

$$\frac{dC_L}{d\alpha} = \frac{2\pi}{\frac{2}{A} + \sqrt{\left(\frac{2}{A}\right)^2 + \frac{1}{\cos^2 \Lambda} - M^2}}. \quad (4.24)$$

Now we can examine the example where we want to achieve the same lift coefficient from a wing placed in a three-dimensional flow as predicted by the aerodynamic properties of the composing wing sections.

From Figure 4.10, we see that this is obtained by increasing the angle of attack of the wing in the actual three-dimensional flow by a small value $\Delta\alpha$ over that for the wing in two-dimensional flow. The latter flow condition is the same as would prevail for a wing of infinite span.

In terms of drag, the effect of the increased angle of attack is expressed as follows; the drag coefficient for the wing in the three-dimensional flow is equal to the two-dimensional drag coefficient C_{Dp} plus the induced drag coefficient C_{Di} :

$$C_D = C_{Dp} + C_{Di}. \quad (4.25)$$

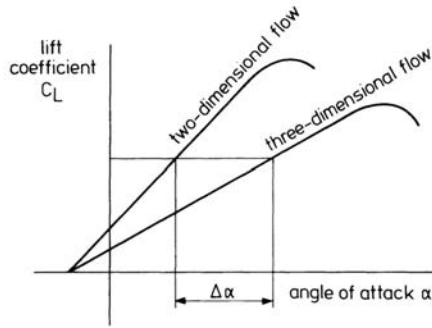


Figure 4.10 Wing lift coefficient as a function of angle of attack

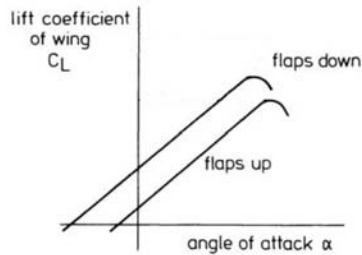


Figure 4.11 Effect of flap deflection on lift curve

The coefficient C_{Dp} in Equation (4.25) is called the profile drag coefficient (due to pressure drag and skin friction drag in the two-dimensional situation at the given lift coefficient C_L).

In order to raise the maximum lift coefficient C_{Lmax} during takeoff and landing, aerodynamic devices are affixed to the wing. The most usual devices to facilitate takeoff and landing are trailing-edge flaps, which may also extend the wing area. In particular, the increase in C_{Lmax} is obtained by a change in airfoil shape and/or by increased camber.

The effects of the use of flaps is indicated in Figure 4.11, where it is shown that the lift coefficients are increased over the whole range of angles of attack, and that the critical angle of attack may be slightly decreased from that of the wing with flaps up. Flaps also increase the wing drag. Therefore, full flap deflection

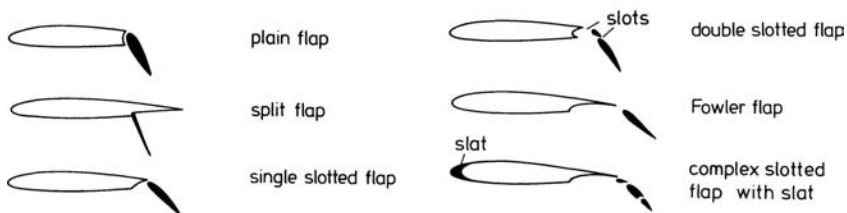


Figure 4.12 Types of wing flaps

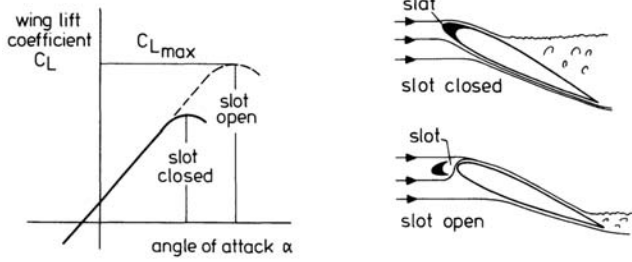


Figure 4.13 Effect of a slot on wing lift curve

is applied to decelerate the airplane during the landing maneuver. The different types of trailing-edge flaps are shown in Figure 4.12. The maximum lift coefficient may also be increased by use of a slot formed by an auxiliary device called slat, which is placed in front of the wing leading edge. The air flowing through the slot is accelerated, through which flow separation is delayed and so increasing the critical angle of attack and the maximum lift coefficient. The effect of the presence of a slot on the lift coefficient is illustrated in Figure 4.13. Notice that a slot extends C_{Lmax} without any shift of the lift curve. Detrimental to the view from the flight deck is the higher stall angle required.

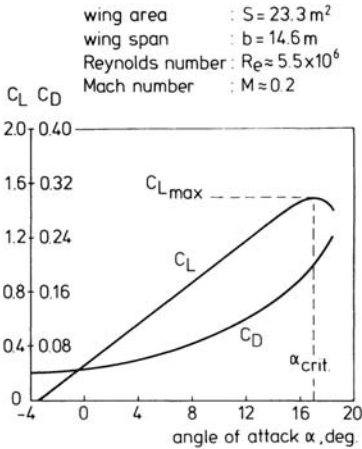


Figure 4.14 Aerodynamic characteristics of a low-subsonic airplane (estimated)

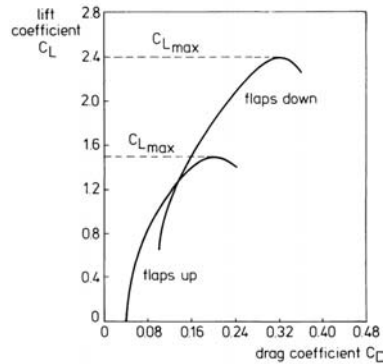


Figure 4.15 Lift-drag polar for a low subsonic airplane (estimated)

4.3 The lift-drag polar

Figure 4.14 shows the lift and drag coefficients as a function of angle of attack for a low-subsonic airplane in clean configuration (fixed landing gear). Note that these curves have essentially the same form as for a wing section. At an angle of

attack of about 16° , separation of the flow from the wing begins, which leads to a substantial loss of lift and increase in airplane drag. Therefore, the airplane can only fly at an angle of attack below α_{crit} .

By elimination of α from the relations $C_L = f(\alpha)$ and $C_D = f(\alpha)$, the lift-drag polar is obtained,

$$C_D = f(C_L). \quad (4.26)$$

The lift-drag polar which results from Figure 4.14 is given in Figure 4.15. In addition, also the lift-drag polar for the airplane with wing flaps down is plotted. Due to the deflection of the flaps, the maximum lift-coefficient is increased considerably. Using the relationship (4.26) we should remember that a lift-drag polar is only of significance if the following parameters are known:

- actual shape of the airplane (control surface deflections and airplane condition)
- Reynolds number
- flight Mach number.

In most performance calculations, it turns out that drag increments due to control surface deflections are negligible. Therefore, throughout this text the effects of these trim forces on the lift-drag polar will be omitted.

Concerning the airplane condition, typical configurations may be distinguished to be present in the various flight phases encountered by the airplane. This means that lift-drag polars will be used that are representative for the condition of the airplane during particular flight phases, such as:

- takeoff (flaps partly deflected and landing gear down)
- cruise (flaps and landing gear retracted)
- landing (flaps fully deflected and landing gear down).

From the remarks made above, it is evident that any presentation of a lift-drag polar should be accompanied by a record of the several associated conditions on which the curve depends. The lift-drag polars of a transport airplane with retractable landing gear, as given in Figure 4.16, show that in addition to the increase of drag coefficient due to flap deflection, also the landing gear furnishes a considerable contribution to the total drag of the airplane.

As has previously been noted, the viscous effects in the flow manifest in the presence of a boundary layer. An important effect on the boundary layer condition has the Reynolds number. At low Reynolds numbers the flow in the boundary layer is laminar, i.e. streamline (see Figure 4.2). At high Reynolds numbers, mostly turbulent flow prevails. In turbulent flow there are oscillations of air particles across the boundary layer, by which there is an exchange of kinetic energy among the laminae and a transfer of energy from the freestream to the boundary layer. Figure 4.17 shows the velocity profiles across the boundary layer for both laminar and

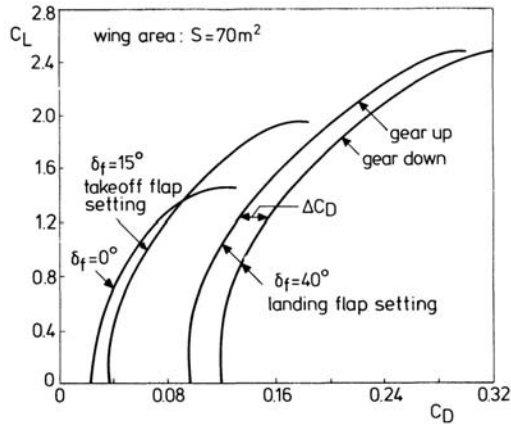


Figure 4.16 Typical lift-drag polars for propeller-driven transport airplane (estimated)

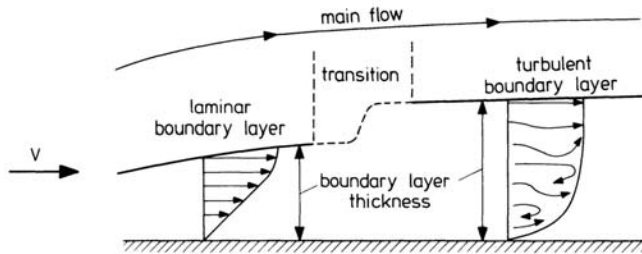


Figure 4.17 Typical laminar and turbulent boundary layer velocity profiles

turbulent flow. Assuming the same flow conditions, the turbulent boundary layer is thicker than the laminar boundary layer. Another important difference is that near the surface the velocity gradient of the turbulent layer is much greater than that of the laminar boundary layer. Then, Equation (4.2) tells us that transition to turbulence must result in an increase in skin friction drag.

Referenced to the wing chord, as characteristic linear measure, airplanes experience Reynolds numbers of 5×10^6 to 10^8 or higher. At these typical high Reynolds numbers, turbulent flow is present over a very large portion, let's say, 90 % of the wing chord.

In Figure 4.18 is sketched the development of the boundary layer over the upper surface of a wing. Over the front portion, near the leading edge, there is always a laminar boundary layer. The thickness of this layer increases when the flow moves from the nose of the wing. Then very soon after the point for minimum local air pressure, transition to turbulence occurs which is accompanied by a drastic thickening of the boundary layer. The turbulent boundary layer goes on to grow in thickness with increasing downstream distance. When moving over the rear portion of the wing surface, the air particles must press against both the viscous forces and the increasing local pressures. At a certain point the flow collapses and

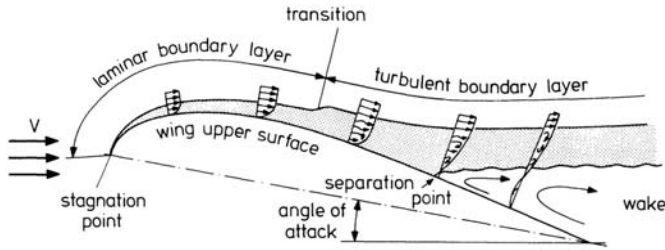


Figure 4.18 Development of the boundary layer over the wing

a wake emanates from the flow separation.

At lower angles of attack, separation occurs generally close to the trailing edge. As the angle of attack is increased, the boundary layer thickness increases, the separation point shifts forward, and the drag coefficient builds up. Finally a complete break-away of the flow occurs, which sets an upper limit to the lift coefficient.

As the Reynolds number increases, the boundary layer becomes turbulent further upstream. At the same time, separation is delayed, resulting in a smaller wake. The size of the wake is a measure of the drag caused by the separation. The smaller the wake, the smaller the pressure drag component, and hence, the smaller the total drag coefficient. On the other hand, the maximum lift coefficient that can be obtained increases slightly with increasing Reynolds number.

At this point it is worth noting that in order to detect an approaching stall of an airplane, there must be an adequate stall warning, with flaps and landing gear in any normal position, in straight and turning flight. The warning may be furnished either through the inherent behavior of the airplane or by an artificial stall warning device. The latter system generally consists of a pressure vent near the leading edge of the wing, located so that just prior to the stall point the stagnation pressure crosses the aperture and the pressure there varies quickly in consequence. This large pressure change is used to produce an acoustic signal or warning light to advise the pilot that the angle of attack is near the stall angle. The stall warning begins at a speed exceeding the stalling speed and continues until stall occurs.

The stall angle may also be determined by a small vane on the side of the fuselage near the nose. The vane can rotate freely so that it is aligned to the flight path, whereby the vane angle is converted into an electrical signal that is transmitted to an indicator in the cockpit.

Returning to the preceding discussion on the Reynolds number, we can summarize its effects as follows:

1. For a given condition of the wing (roughness of the surface) and shape of the wing sections (pressure distribution over the surface), the value of the Reynolds number determines the location of both the transition and the separation point.
2. With increasing Reynolds number, the transition point moves forward and the separation point moves backward over the wing. As a result, the general

trends are a somewhat higher value of maximum lift coefficient and a lower profile drag coefficient when the Reynolds number becomes greater.

Concerning the variations of maximum lift coefficient and profile drag coefficient, it is important to note that these coefficients vary merely at a very small rate within the normal ranges of Reynolds numbers encountered in the various flight phases. This observation implies that, usually, it will be sufficient to consider in each flight phase a mean value of the Reynolds number.

Let us now look at the effects of flight Mach number on the lift-drag polar. For that we consider the pressure disturbances in the air produced by an airplane (Figure 4.19). When the airplane is flying at a low airspeed, the air in front of the airplane is subjected to these disturbances amply before the airplane appears so that the air will flow smoothly about the airplane. This situation may be illustrated by Figure 4.19a, where for convenience the airplane is represented by a point source with zero dimensions. The circles indicate the locations of the pressure disturbances which have been created by the source at certain moments and are transmitted at the speed of sound. Obviously, the disturbances are closer together in the direction of motion.

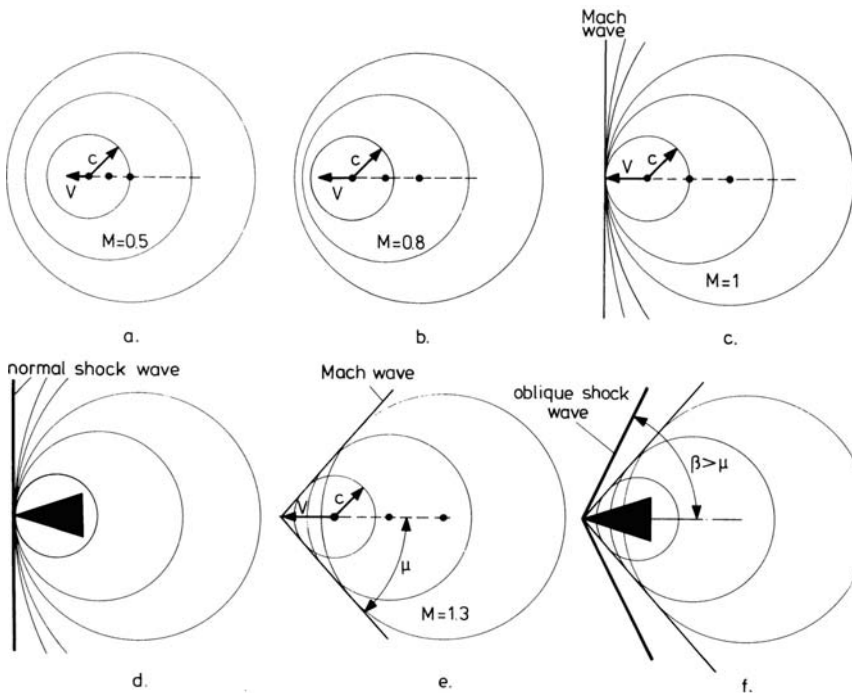


Figure 4.19 Pressure perturbations from a moving source

As the airspeed comes to the speed of sound, the pressure disturbances are confined to a smaller area ahead of the source, and the time between the arrival of the

disturbances and the appearance of the source diminishes. This means that some adjustment must take place in a very short time (Figure 4.19b).

As the airspeed equals the speed of sound, the pressure disturbances and the source move at the same speed (Figure 4.19c). Now, the disturbances form a so-called *Mach wave*, which is the limiting case of an infinitely weak shock wave. Ahead of a source with finite dimensions, such as an airplane, a normal shock wave occurs (Figure 4.19d). According to Appendix D, a shock wave is an almost sudden increase in pressure, temperature and density, and a decrease in velocity and total pressure. As a result, there is a change in pressure distribution over the surface from that experienced at low airspeeds, and hence, there is a change in the aerodynamic coefficients of the airplane. In Figure 4.19e we see the condition in which the speed of the point source exceeds the speed of sound. Now, the Mach wave is the line tangent to all the circles of disturbances. From Figure 4.19e we obtain

$$\mu = \sin^{-1} \left[\frac{c}{V} \right] = \sin^{-1} \left[\frac{1}{M} \right]. \quad (4.27)$$

where the angle μ is the *Mach angle*, being the angle the Mach wave makes with the direction of the flight velocity. As shown in Figure 4.19f, at the nose of a high speed airplane, an oblique shock wave is produced, which is inclined at an angle, $\beta > \mu$ (see Appendix D).

In Figure 4.20 the various flight regimes are classified in terms of Mach number. For Mach numbers smaller than approx. 0.5, we have low-subsonic flow, where in aerodynamics the air is treated as though it is incompressible (constant air density). For Mach numbers between 0.5 and 0.8, say, we have high-subsonic flow, where the compressibility of the air cannot be ignored. Transonic flow concerns the speed regime in which the flow pattern changes from subsonic to supersonic. This regime covers the Mach numbers between 0.8 and 1.2 approximately. For Mach numbers greater than 1.2, we have supersonic flow, where compressibility effects are of paramount importance. Now the velocity of the main flow about the airplane in every place exceeds the speed of sound and oblique shock waves occur.

For Mach numbers exceeding 5, we speak about hypersonic flow. Owing to the high temperatures developed around the nose of a body in a hypersonic flow, dissociation and ionization processes occur, causing that the assumption of a perfect gas is no longer valid.

Figure 4.21 illustrates the development of shock waves about an airfoil. Up to a flight Mach number of about $M = 0.5$ the flow is subsonic everywhere (Figure 4.21a). Since the local Mach number M^* will be higher than the flight Mach number, a particular flight Mach number comes about at which locally sonic flow first occurs on the surface (Figure 4.21b). The corresponding flight Mach number is termed the critical Mach number, M_{crit} .

As the flight Mach number increases further, regions of supersonic flow come forth, which end through the occurrence of normal shock waves (Figures 4.21c

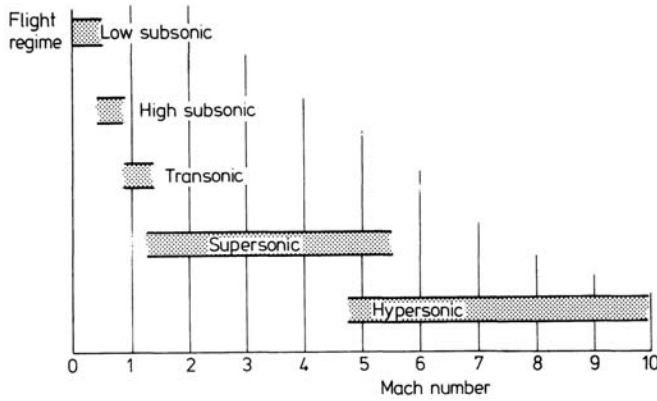


Figure 4.20 Fields of aerodynamics

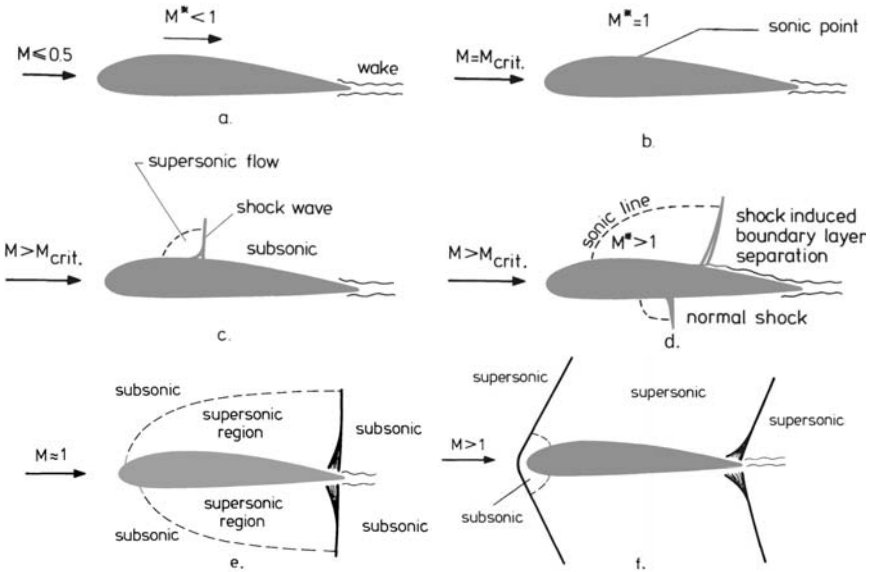


Figure 4.21 Shock wave formation about an airfoil

and d). The normal shock on the upper surface in Figure 4.21d produces an increased static pressure behind the wave. Usually, the boundary layer is unable to withstand the large pressure rise across the wave. Then, separation of the boundary layer flow occurs, which causes an increase in wake thickness and so in section drag and a reduction of the maximum lift coefficient. This type of separation is known as *shock induced boundary layer separation*.

Figure 4.21e shows the flow pattern at a flight Mach number close to $M = 1$, where large regions are supersonic. At supersonic airspeeds, finally, an oblique shock wave is present around the nose and at the trailing edge of the airfoil (Figure 4.21f).

The actual variation of the drag coefficient at constant-lift coefficient versus Mach number for a supersonic airplane is illustrated by the curves in Figure 4.22a. The corresponding lift-drag polars are plotted in Figure 4.22b. The curves show that up to a Mach number of about 0.9, the lift-drag polar remains fairly the same. The slight decrease in drag coefficient at constant lift coefficient in Figure 4.22a is caused by the circumstance that the effect of an increasing Mach number is to increase the slope of the C_L - α curve (Figure 4.23). Note also that, on the other hand, an increasing Mach number leads to a lower $C_{L_{\max}}$ value.

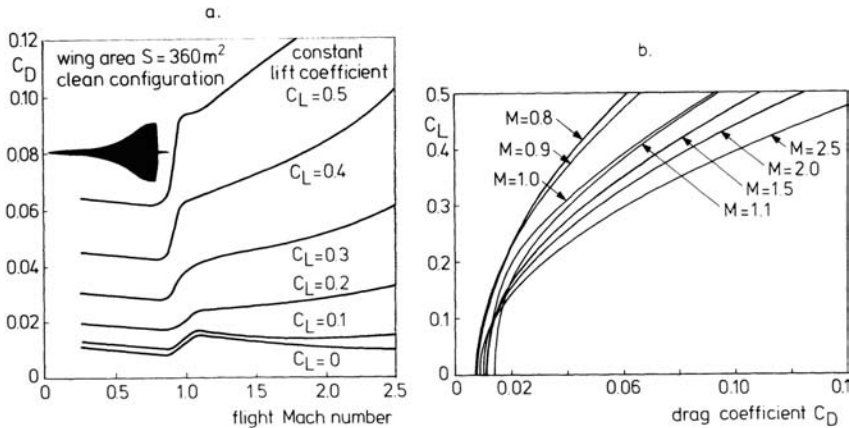


Figure 4.22 Aerodynamic properties of a supersonic airplane

The extra drag at transonic and supersonic flight Mach numbers in Figure 4.22, is called wave drag and results from the formation of shock waves. The shock waves convert a substantial part of the freestream kinetic energy into heat, which results in airplane drag. In addition, the interaction between shock wave and boundary layer at high-subsonic and transonic speeds creates a further increase in the drag coefficients. The flight Mach number at which the drag coefficient at constant lift coefficient begins to rise sharply, is named the *drag-divergence Mach number*, M_d ($M_d > M_{\text{crit}}$).

An effective means of increasing the drag-divergence Mach number of high-subsonic airplanes is the use of supercritical airfoils. Another adequate means is the application of wing sweep (Figure 4.24), which also delays the shock formation on the wing surface. As was mentioned earlier, this behavior is due to the fact that the velocity and pressure distribution around the wing sections is a function of the velocity perpendicular to the leading edge. From Figure 4.24a it can be seen that for a swept wing the operative Mach number normal to the front edge of the wing, M_n , is related to the airspeed by

$$M_n = \frac{V_n}{c} = \frac{V}{c} \cos \Lambda. \quad (4.28)$$

Hence, sweeping the wings of high-subsonic airplanes will, in principle, increase the critical Mach numbers by a factor $1/\cos \Lambda$.

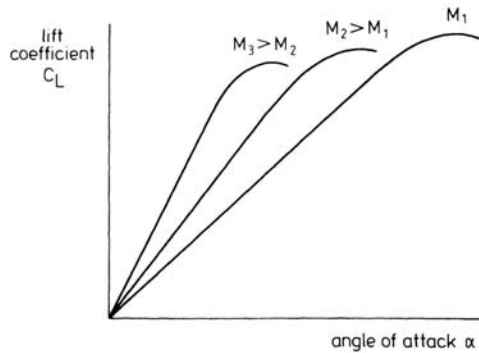


Figure 4.23 Effect of Increasing flight Mach number

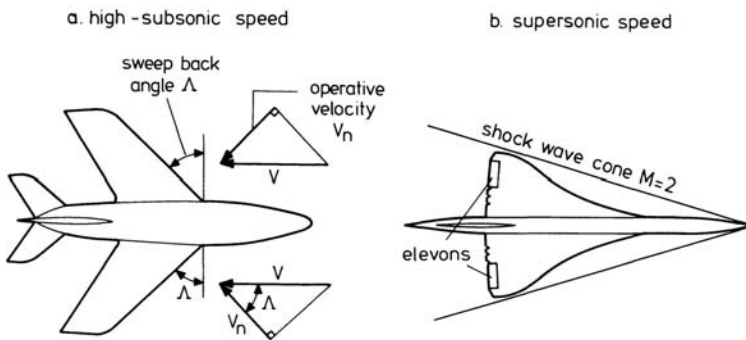


Figure 4.24 Effect of speed on the shape of an airplane

The wave drag occurring in transonic and supersonic flight lessens markedly with the slenderness of the body. In consequence, supersonic airplanes show a slender fuselage and low aspect ratio wings with thin airfoils.

The combination of a large sweep angle and a reduced aspect ratio may then result in a slender delta wing. Pitch and roll control may be provided by elevons on the trailing edges of the delta wing (Figure 4.24b). Elevons work together as elevators and differentially as ailerons.

If the wing fits within the shock wave cone from the fuselage nose, as shown in Figure 4.24b, the operative velocity at the wing leading edges is subsonic, which condition furnishes less wave drag.

At low speeds and high angles of attack, the delta wing reveals a special flow condition as shown in Figure 4.25. Because of the sharp leading edge and the large sweep angle, the flow over the delta wing forms leading edge vortices. The formation of these vortices create a high-lift effect and obviate total flow separation. As a result, a delta wing shows a very large stall angle.

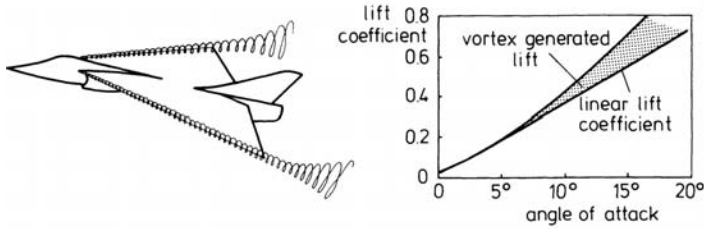


Figure 4.25 Excess lift due to delta-wing vortex flow from leading edges

4.4 Parabolic lift-drag polar

The total drag of an airplane may be divided into the drag of the wing D_w and the sum of the component drags D_n ,

$$D = D_w + D_n. \quad (4.29)$$

Referring to Equation (4.25), we can write the wing drag as the sum of the induced drag D_i and the profile drag D_p . With this, Equation (4.29) becomes

$$D = D_i + D_p + D_n. \quad (4.30)$$

The nature of the induced drag (or drag due to lift), has already been discussed in Section 4.2. The profile drag consists of pressure drag, skin friction drag and wave drag. The wave drag is zero for subsonic airspeeds below the critical Mach number. Pressure drag, skin friction drag and wave drag together, form also the drag of the airplane components. Since the drag coefficient of each component part, C_{Dn} , is based on a certain area S_n as the reference area, the total airplane drag is given by

$$C_D \frac{1}{2} \rho V^2 S = C_{Di} \frac{1}{2} \rho V^2 S + C_{Dp} \frac{1}{2} \rho V^2 S + (\sum C_{Dn} S_n) \frac{1}{2} \rho V^2. \quad (4.31)$$

Accordingly, the drag coefficient of an airplane is (see Figure 4.26)

$$C_D = C_{Di} + C_{Dp} + \frac{\sum C_{Dn} S_n}{S}, \quad (4.32)$$

where the quantity $\frac{\sum C_{Dn} S_n}{S}$ is called the *parasite drag coefficient*.

Theoretical aerodynamics predicts that the induced drag coefficient is directly proportional to the square of the lift coefficient C_L , and inversely proportional to the aspect ratio A and a wing efficiency factor ϕ ,

$$C_{Di} = \frac{C_L^2}{\pi A \phi}. \quad (4.33)$$

The factor ϕ depends primarily on the wing planform since it indicates how close the elliptic spanwise lift distribution is obtained. For an elliptic lift distribution

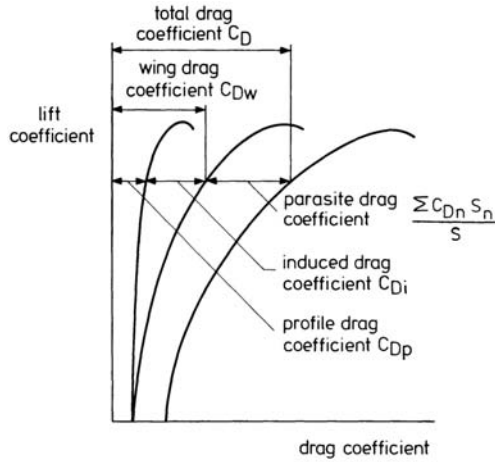


Figure 4.26 Components of drag coefficient

$\phi = 1$ (minimum induced drag coefficient). In all other cases ϕ will be less than one. Thus, the drag coefficient of the airplane is

$$C_D = \frac{C_L^2}{\pi A \phi} + C_{Dp} + \frac{\sum C_{Dn} S_n}{S}. \quad (4.34)$$

Since also the profile drag and parasite drag coefficients are dependent on the angle of attack, Equation (4.34) may be written as

$$C_D = \frac{C_L^2}{\pi A \phi} + X C_L^2 + \left[C_{Dp} + \frac{\sum C_{Dn} S_n}{S} \right]_{C_L=0}. \quad (4.35)$$

The term $X C_L^2$ represents the assumed parabolic change of the profile and parasite drag coefficients with lift coefficient. The quantity in parentheses is termed zero-lift drag coefficient and given the symbol C_{D0} .

Then, Equation (4.35) can be transformed into

$$C_D = C_{D0} + \frac{C_L^2}{\pi A e}, \quad (4.36)$$

where the factor e follows from

$$\frac{1}{e} = X \pi A + \frac{1}{\phi}, \quad (4.37)$$

and is called the *Oswald's efficiency factor*. Apparently, this factor accounts for the variation of the profile and parasite drag coefficients with lift coefficient, and the effect of the actual spanwise lift distribution on induced drag coefficient. For most airplane types the value of e varies between 0.6 and 0.9. Sometimes, Equation (4.37) is expressed in the form

$$C_D = C_{D0} + k C_L^2, \quad (4.38)$$

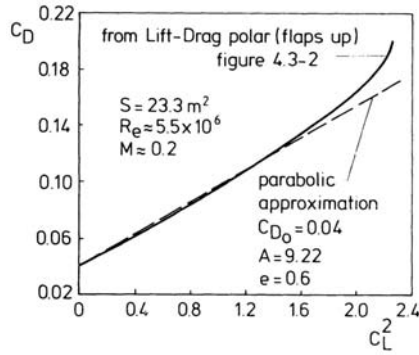


Figure 4.27 Parabolic approximation of lift-drag polar of low-subsonic airplane

where $k = 1/(\pi Ae)$ is called the *induced drag factor*.

In Figure 4.27 the drag coefficient of Figure 4.15 is plotted against C_L^2 . The deviation from the parabolic form is represented by the divergence from the straight (dotted) line. We see that a considerable part of the lift-drag polar is indeed a parabola, but there is some extra drag at lift coefficients beyond about 1.0.

The parabolic lift-drag polar can be used not only at subsonic speeds, but also at both transonic and supersonic airspeeds, if in Equation (4.38) the values of C_{D_0} and k are adjusted appropriately. Anticipating later discussions, it may here be noted that in many respects the performance of airplanes are determined by the following aerodynamic ratios: C_L/C_D , C_L^3/C_D^2 , and C_L/C_D^2 . In particular the maximum values of these ratios are of importance.

For maximum C_L/C_D we differentiate this ratio with respect to C_L and set the first derivative equal to zero, i.e.

$$\frac{d(C_L/C_D)}{dC_L} = \frac{C_D - C_L \frac{dC_D}{dC_L}}{C_D^2} = 0.$$

Since $C_D \neq 0$, we have the condition

$$\frac{dC_D}{dC_L} = \frac{C_D}{C_L}. \quad (4.39)$$

Using the parabolic lift-drag polar, Equation (4.36), we obtain

$$\frac{2C_L}{\pi Ae} = \frac{C_{D_0} + C_L^2/\pi Ae}{C_L} \quad \text{or} \quad C_L = \sqrt{C_{D_0}\pi Ae}. \quad (4.40)$$

Substitution of the latter result into Equation (4.36) yields (see Figure 4.28)

$$C_D = 2C_{D_0} \quad \text{and} \quad (4.41)$$

$$\left(\frac{C_L}{C_D}\right)_{\max} = \frac{\sqrt{C_{D_0}\pi Ae}}{2C_{D_0}} = \frac{1}{2}\sqrt{\frac{\pi Ae}{C_{D_0}}}. \quad (4.42)$$

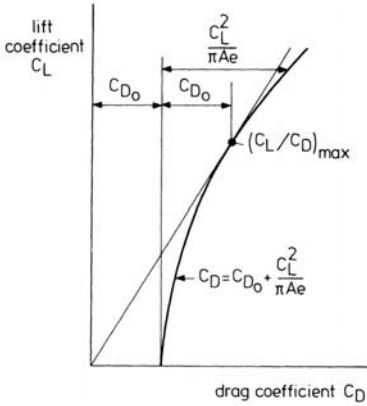


Figure 4.28 Maximum value of C_L/C_D

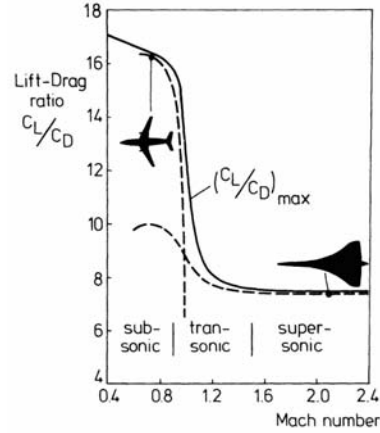


Figure 4.29 Maximum lift-to-drag ratios

For maximum C_L^3/C_D^2 in like manner, differentiation furnishes the general condition

$$\frac{dC_D}{dC_L} = \frac{3C_D}{2C_L} \quad (4.43)$$

Making use of the parabolic lift-drag polar gives

$$\frac{2C_L}{\pi A e} = \frac{3}{2} \left[\frac{C_{D_0} + C_L^2/(\pi A e)}{C_L} \right] \quad \text{or} \quad C_L = \sqrt{3C_{D_0}\pi A e} \quad (4.44)$$

Substitution of Equation (4.44) into (4.36) yields

$$C_D = 4C_{D_0} \quad \text{and} \quad (4.45)$$

$$\left(\frac{C_L^3}{C_D^2} \right)_{\max} = \frac{3C_{D_0}\pi A e \sqrt{3C_{D_0}\pi A e}}{16C_{D_0}^2} = \frac{3\sqrt{3}}{16} \pi A e \sqrt{\frac{\pi A e}{C_{D_0}}} \quad (4.46)$$

Similarly, for maximizing C_L/C_D^2 , setting $\frac{d(C_L/C_D^2)}{dC_L} = 0$ yields the condition

$$\frac{dC_D}{dC_L} = \frac{1}{2} \frac{C_D}{C_L} \quad (4.47)$$

Then in case of a parabolic lift-drag polar, we find

$$C_L = \sqrt{\frac{1}{3}C_{D_0}\pi A e}, \quad (4.48)$$

$$C_D = \frac{4}{3}C_{D_0} \quad \text{and} \quad (4.49)$$

$$\left(\frac{C_L}{C_D^2} \right)_{\max} = \frac{\sqrt{\frac{1}{3}C_{D_0}\pi A e}}{\frac{16}{9}C_{D_0}^2} = \frac{3\sqrt{3}}{16} \sqrt{\frac{\pi A e}{C_{D_0}^3}} \quad (4.50)$$

We end this subject by remarking that, especially, the maximum lift-to-drag ratio, $(C_L/C_D)_{\max}$, is a significant aerodynamic quantity of an airplane. In Figure 4.29 are depicted the order of magnitude values of this ratio for transport airplanes. The curve of Figure 4.29 shows that the attainable value of $(C_L/C_D)_{\max}$ is about 16 at subsonic velocities. The maximum lift-to-drag ratio falls off abruptly in the transonic region and approaches to a value of approximately 7.5 in the supersonic region.

Chapter 5

AIR DATA INSTRUMENTS

5.1 Introduction

The instrument panel in the cockpit may consist of a large number of indicators, which provide essential data on the flight condition and the orientation of the airplane relative to the Earth. Likewise, these readings present to the pilot complex information for control and guidance of the airplane.

Generally, the various instruments and flight systems can be divided into four categories, namely,

- *Air data instruments*, which include the altimeter, the vertical-speed indicator, the airspeed indicator, the Machmeter, and the air thermometer.
- *Engine instruments*, like tachometers (engine-speed indicators), temperature and pressure gauges, and fuel-flow meters.
- *Blind flying instruments*, under which fall for example the turn and slip indicator, the direction indicator, and the artificial horizon.
- *Avionics systems*, such as applied for communication, navigation, flight control, and flight management.

In the light of the aim of this course book, however, only the air data instruments are inside the scope of our inquiry. This means that the principles of the engine instruments and the gyroscopic devices of the third category, will not be discussed here. Also, for any explanation of the avionics systems, the interested reader is referred to the literature dealing with these special topics.

5.2 The altimeter

The altimeter indicates the vertical distance of the airplane above ground level. As shown schematically in Figure 5.1, the instrument is simply a pressure measuring device since it is actuated by the static pressure of the atmosphere.

Essentially, the altimeter is made up of an air-tight case, where a differential-pressure capsule is placed. The capsule is made up of two diaphragms which are connected and sealed at their edges to form a hollow room.

The instrument chamber is connected to a static pressure tapping on the airplane so that the interior of the case is at the ambient air pressure. The diaphragm unit is evacuated, with the result that it will expand when the air pressure decreases. A linkage structure conveys the displacement of the capsule to the indicator pointer.

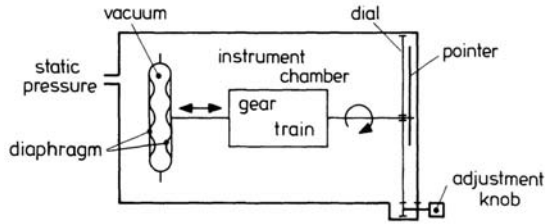


Figure 5.1 Principle of altimeter

To provide an indication of height instead of pressure, the scale is calibrated according to the pressure-height relationship in the International Standard Atmosphere (I.S.A.). Then, for use in the troposphere, the calibration equation in terms of *geopotential pressure height* is (see Section 2.4)

$$H_p = \left[\left(\frac{p}{p_0} \right)^{-\frac{R\lambda}{g_0}} - 1 \right] \frac{T_0}{\lambda}, \quad (5.1)$$

where

the pressure at sea level $p_0 = 101325 \text{ N/m}^2$.

the temperature at sea level $T_0 = 288.15 \text{ K}$,

the gas constant $R = 287.05 \text{ m}^2/\text{s}^2\text{K}$,

the temperature gradient $\lambda = -0.0065 \text{ K/m}$,

the acceleration of gravity at sea level $g_0 = 9.80665 \text{ m/s}^2$.

Naturally, in the stratosphere and mesosphere calibration equations different from Equation (5.1) must be used. E.g., an altimeter which is to be used up to an altitude of 20 km will have to be calibrated according to Equation (5.1) up to 11,000 m and thereafter will have to use the following calibration equation:

$$H_p = H_s - \frac{RT_s}{g_0} \ln \frac{p}{p_s} \quad (5.2)$$

where the subscript "s" denotes tropopause ($H_s = 11,000 \text{ m}$).

Noteworthy is the fact that, although in the International Standard Atmosphere height is defined in terms of meter, the altimeter scale almost always uses the foot as a measure of altitude. On the other hand, horizontal length such as range of vision and takeoff and landing distances are normally expressed in SI-units (meter or km).

As we have pointed out already in chapter 2, the pressure occurring at the geopotential pressure height H_p , as measured by the altimeter in any atmosphere is equal to the pressure at the same geopotential height H in the International Standard Atmosphere.

It will be clear that when the atmospheric conditions depart from the values assumed in the International Standard Atmosphere an altimeter is in error, that is, the geopotential pressure altitude differs from the actual geopotential height. Thus,

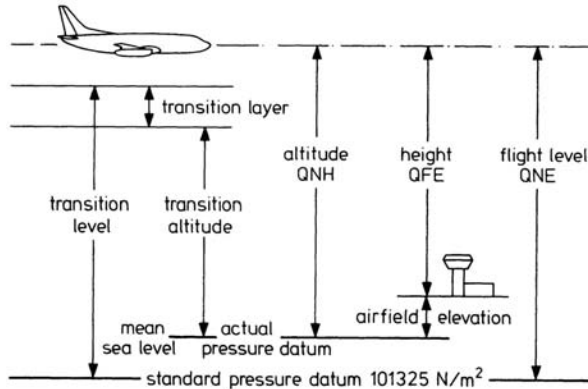


Figure 5.2 Definition of altimeter settings

the quantity geopotential pressure height provides the actual air pressure but furnishes only an approximation of the geometric or true height above the ground. The greatest error is caused by the influence of the sea-level pressure p_0 . In order to correct the altimeter reading for the occurring pressure at ground level, the altimeter is provided with a subsidiary scale. Now the datum pressure at which the altimeter will read zero altitude can be set on this subscale. This may be accomplished by means of a manually operated adjustment knob on the instrument (Figure 5.1). The adjustment knob can be turned until the altimeter reads the elevation of the airport above mean sea level (MSL) or zero height at the airport level.

Three settings of the datum pressure on the subscale can be distinguished, which are designated by the following codes (Figure 5.2):

QNE - setting the standard sea-level pressure of 101325 N/m².

QNH - pressure setting such that the altimeter reads altitude above mean sea level at the airport level.

QFE - pressure setting such that the altimeter reads zero height at the airport level.

The QNE setting is used for test work and for normal flight operations above a prescribed transition altitude. Then the altimeter is a pressure measuring apparatus and a means to secure the vertical separation of airplanes.

The QNH and QFE settings are applied for takeoff and landing maneuvers and for low-level flights at or below transition altitude.

It will be clear from the foregoing that the vertical position of an airplane during climb after takeoff is expressed in terms of altitude (feet) until it arrives at the transition altitude above which the vertical position is given in terms of pressure level, usually called *flight level* (FL). E.g., FL 100 means that the altimeter indicates a geopotential pressure height of 10,000 ft. Likewise, on approach the vertical position is given in terms of flight level until the airplane reaches the transition level

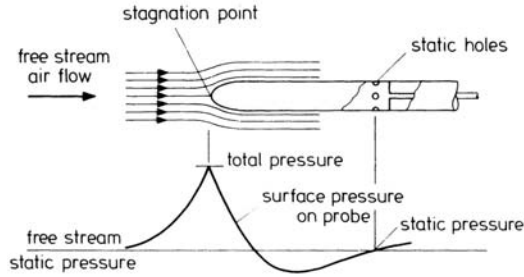


Figure 5.3 Static probe and pressure distribution (subsonic speed)

below which the vertical position is expressed again in terms of altitude.

The reading of the altimeter may also be subject to inaccuracies in the instrument itself. Permissible limits of this instrumental error are maintained by a current calibration procedure.

The freestream static pressure which is fed to the altimeter is measured by means of a static pressure probe, or alternatively by a set of static vents in the side of the fuselage of the airplane. The probe is directed forward and may be mounted on the forebody, wing, or vertical tail.

Figure 5.3 shows the static probe and the pressure distribution along the streamlines following the surface of the probe.

According to Appendix D, the variation of the static pressure along a streamline may be described by Bernoulli's equation for compressible isentropic flow,

$$p_t = p \left[1 + \frac{\gamma - 1}{2\gamma} \frac{\rho}{p} V^2 \right]^{\frac{\gamma}{\gamma - 1}} = \text{constant}, \quad (5.3)$$

where p_t is the total pressure and p , ρ and V are the local values of static pressure, air density, and flow velocity, respectively.

From Figure 5.3, we see that ahead of the probe the local static pressure equals the freestream static pressure. There, the local velocity is equal to the freestream velocity. Approaching the nose of the probe the velocity decreases and the static pressure increases. At the stagnation point the velocity is zero and the local static pressure equals the total pressure.

Moving from the nose along the surface of the probe, the velocity increases again and the local static pressure decreases. At some point behind the nose of the probe the velocity and pressure return to their freestream values. At that point there are static holes which are connected with the altimeter.

The pressure at the instrument and at the measurement point may be different due to system lag during alterations of height or speed. Moreover, the presence of the airplane and/or the positioning of the probe in the pressure field may cause a local pressure at the measurement point which differs from the freestream value. To avoid or minimize this so-called position error, the freestream static pressure must be measured outside the pressure field of the airplane.

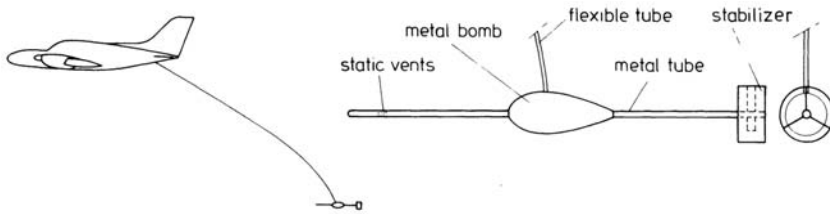


Figure 5.4 Trailing static tube

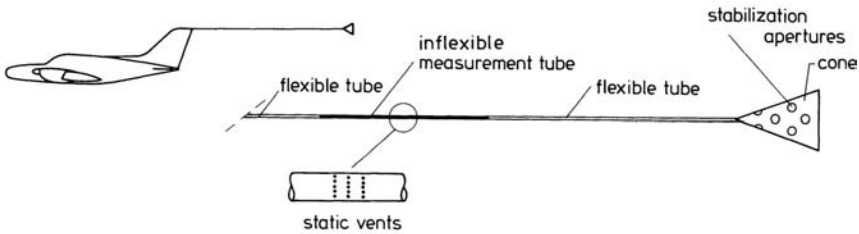


Figure 5.5 Trailing static cone

When executing flight-test work, a usual way of obtaining the proper static pressure is to trail a static tube at some distance below the airplane (Figure 5.4). Since this device is limited to a maximum airspeed of approximately 450 km/h, as an alternative, a static cone can be trailed behind the airplane (Figure 5.5). Position error is dependent on altitude and airspeed so that it differs all through the entire operating range of the airplane. Therefore, a convenient method of measurement of position error corrections is to fly in formation with a reference airplane having a well-calibrated static system. Then immediate comparison of the indicated altitude can be made between the two altimeter readings.

For a detailed discussion on the determination of error corrections, the reader is referred to Reference 15.

5.3 The vertical-speed indicator

The vertical-speed indicator displays whether the airplane is continuing level flight, or measures the rate of climb or descent.

As sketched in Figure 5.6, in the vertical-speed indicator the static pressure source is connected directly to the diaphragm capsule and to the instrument chamber via a capillary tube.

When level flight is maintained, the pressure inside the capsule equals the pressure in the casing and the instrument reading is zero.

During climb or descent, the pressure led into the instrument changes continuously. However, the capillary tube controls the rate of air flow into or out of the instrument chamber and so the pressure surrounding the capsule. Due to the restrained choke, the pressure change in the instrument chamber is delayed relative to the pressure in the diaphragm capsule. In other words, the diaphragm unit con-

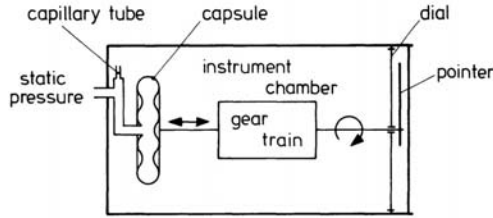


Figure 5.6 Principle of vertical-speed Indicator

tracts or expands in terms of a rate of change of pressure. This deflection of the capsule is calibrated to yield an indication of vertical speed.

For test work, almost always, use is made of the altimeter reading to establish the rate of climb or descent by measuring the time interval Δt to cover a certain vertical distance ΔH .

In the absence of vertical wind, the rate of climb, RC , at the mean height between two successive measurement points may be approximated by

$$RC = \frac{\Delta H}{\Delta t}. \quad (5.4)$$

In calculating the rate of climb, we must take into account that the (true) height interval ΔH in Equation (5.4) differs from the indicated height interval ΔH_p when the actual atmosphere does not conform to the standard reference conditions.

Generally, from the aerostatic equation (Equation (2.1)) and the equation of state $p/\rho = RT$,

$$dp = -\frac{p}{RT}g_0 dH = -\frac{p}{RT_{ISA}}g_0 dH_p, \quad \text{or} \quad (5.5)$$

$$dH = dH_p \frac{T}{T_{ISA}}. \quad (5.6)$$

In Equation (5.6), T_{ISA} is the temperature in the International Standard Atmosphere and T is the prevailing temperature at the same altitude H_p . Combining Equations (5.4) and (5.6) yields the following expression,

$$RC = \frac{\Delta H}{\Delta t} = \frac{T}{T_{ISA}} \frac{\Delta H_p}{\Delta t}, \quad (5.7)$$

where ΔH_p is the measured height interval, and T and T_{ISA} are the temperatures at the mean geopotential pressure altitude.

5.4 The airspeed indicator

The determination of airspeed is based on the measurement of the differential pressure,

$$p_t - p = q_c, \quad (5.8)$$

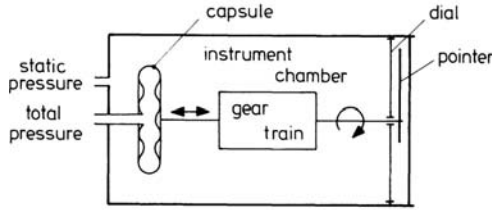


Figure 5.7 Principle of airspeed Indicator



Figure 5.8 Pitot probe

where p_t is the total pressure and p is the freestream static pressure. The difference between these pressures, q_c , is termed *impact pressure*.

As depicted in Figure 5.7, the pressures p_t and p are fed separately into the instrument and the pressure difference is measured by employing an air-tight case in which a diaphragm unit is placed. The total pressure is sensed by a pitot probe, which has an orifice at the stagnation point on the nose (Figure 5.8). Often, the pitot probe is combined with the static probe, which assembly is called a pitot-static probe or pressure head (Figure 5.9). The relationship between the impact pressure q_c and the airspeed V is obtained by substitution of Equation (5.3) into Equation (5.8),

$$q_c = p_t - p = p \left[\left(1 + \frac{\gamma - 1}{2\gamma} \frac{\rho}{p} V^2 \right)^{\frac{\gamma}{\gamma - 1}} - 1 \right] \quad \text{or} \quad (5.9)$$

$$V = \sqrt{\frac{2\gamma}{\gamma - 1} \frac{p}{\rho} \left[\left(1 + \frac{p_t - p}{p} \right)^{\frac{\gamma - 1}{\gamma}} - 1 \right]}. \quad (5.10)$$

Besides the pressure difference ($p_t - p$), in Equation (5.10) also are present the air pressure p and density ρ so that the resulting airspeed at a given value of ($p_t - p$) is a function of altitude. To derive a unique calibration equation for the airspeed indicator, the concept of *calibrated airspeed* V_c is used. By definition, V_c is obtained by making the assumptions that in Equation (5.10) $p = p_0$ is the pressure sea-level reference value of 101325 N/m^2 and $\rho = \rho_0$ is the density sea-level reference value of 1.225 kg/m^3 . Thus, airspeed indicators are calibrated to

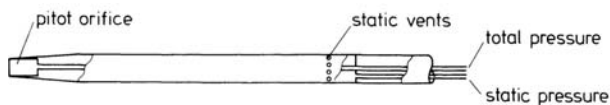


Figure 5.9 Pitot-static probe

the equation

$$p_t - p = p_0 \left[\left(1 + \frac{\gamma - 1}{2\gamma} \frac{\rho_0}{p_0} V_c^2 \right)^{\frac{\gamma}{\gamma - 1}} - 1 \right]. \quad (5.11)$$

Evidently, the calibrated airspeed V_c is only equal to the *true airspeed* V , when the actual atmospheric conditions match the standard sea-level reference conditions. From Equations (5.10) and (5.11), we see that the true airspeed can be determined from its relation to calibrated airspeed and the prevailing values of pressure and density,

$$V = \sqrt{\frac{2\gamma}{\gamma - 1} \frac{p}{\rho} \left[\left[1 + \frac{p_0}{p} \left[\left(1 + \frac{\gamma - 1}{2\gamma} \frac{\rho_0}{p_0} V_c^2 \right)^{\frac{\gamma}{\gamma - 1}} - 1 \right] \right]^{\frac{\gamma - 1}{\gamma}} - 1 \right]}. \quad (5.12)$$

Apparently, the computation of true airspeed requires that calibrated airspeed, geopotential pressure altitude, and air temperature are measured.

At low subsonic airspeeds, a simplified procedure for the determination of the true airspeed can be established by assuming that the measured pressure difference is related to the airspeed by Bernoulli's equation for incompressible isentropic flow (see Appendix D),

$$p_t - p = \frac{1}{2} \rho V^2 \quad \text{or} \quad V = \sqrt{\frac{2}{\rho} (p_t - p)}. \quad (5.13)$$

In this case, the airspeed indicator reading is called *equivalent airspeed*, V_e . This quantity satisfies Equation (5.13) at sea level for standard sea-level density,

$$p_t - p = \frac{1}{2} \rho_0 V_e^2 \quad \text{or} \quad V_e = \sqrt{\frac{2}{\rho_0} (p_t - p)}. \quad (5.14)$$

From Equations (5.13) and (5.14), we also find the relation

$$V = V_e \sqrt{\frac{\rho_0}{\rho}}. \quad (5.15)$$

An insight into the accuracy of the true airspeed when calculated by means of Equation (5.15) instead of Equation (5.12) can be obtained by comparing these equations for a given instrument reading. Thus, from Equations (5.11) to (5.13)

$$\frac{V_{\text{compr}}}{V_{\text{inc}}} = \sqrt{\frac{\frac{\gamma}{\gamma - 1} \left[\left[1 + \frac{p_0}{p} \left[\left(1 + \frac{\gamma - 1}{2\gamma} \frac{\rho_0}{p_0} V_c^2 \right)^{\frac{\gamma}{\gamma - 1}} - 1 \right] \right]^{\frac{\gamma - 1}{\gamma}} - 1 \right]}{\frac{p_0}{p} \left[\left(1 + \frac{\gamma - 1}{2\gamma} \frac{\rho_0}{p_0} V_c^2 \right)^{\frac{\gamma}{\gamma - 1}} - 1 \right]}}. \quad (5.16)$$

This equation shows that the ratio between the resulting compressible and incompressible airspeeds varies with the calibrated airspeed and the static pressure.

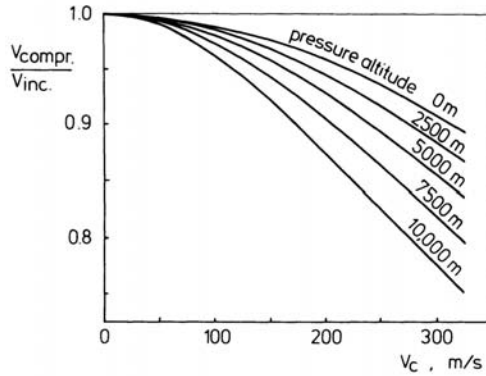


Figure 5.10 Compressibility correction to airspeed

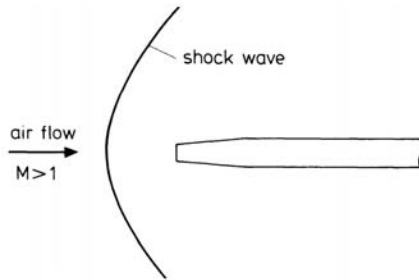


Figure 5.11 Pitot probe in supersonic flow

The effect of compressibility is visualized in Figure 5.10, where the ratio (5.16) is plotted as functions of calibrated airspeed and geopotential pressure altitude. The curves confirm that the relevance of the equivalent airspeed is limited to low-subsonic airspeeds.

At supersonic speeds, a normal shock will appear ahead of the pitot probe as shown in Figure 5.11. With the relations $M = V/c$, $c = \sqrt{\gamma RT}$, and $p/\rho = RT$, we get

$$M = \frac{V}{\sqrt{\gamma p}}. \quad (5.17)$$

Substitution of Equation (5.17) into Equation (5.3) yields the freestream total pressure in terms of static air pressure and flight Mach number

$$p_t = p \left(1 + \frac{\gamma - 1}{2} M^2 \right)^{\frac{\gamma}{\gamma - 1}}. \quad (5.18)$$

The shock wave causes that the total pressure p_t^* measured at the stagnation point on the probe is less than the freestream total pressure p_t . As derived in Appendix D, the ratio of the total pressure behind the shock to the freestream static pressure

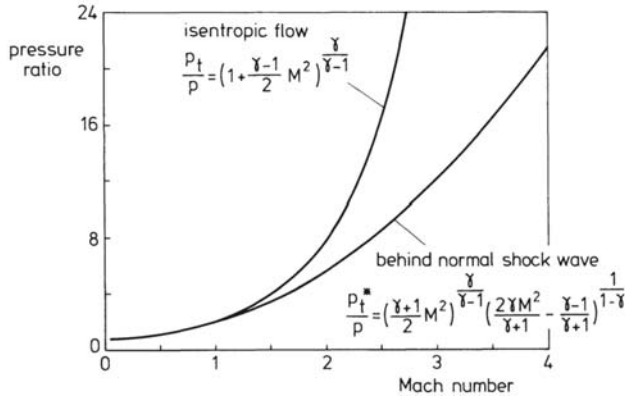


Figure 5.12 Total pressure for isentropic flow and behind normal shock wave ($\gamma = 1.4$)

is related to the flight Mach number by the following equation, which is called the Rayleigh formula,

$$\frac{p_t^*}{p} = \left(\frac{\gamma+1}{2} M^2 \right)^{\frac{\gamma}{\gamma-1}} \left(\frac{2\gamma M^2}{\gamma+1} - \frac{\gamma-1}{\gamma+1} \right)^{\frac{1}{1-\gamma}}. \quad (5.19)$$

In Figure 5.12 are plotted the ratios p_t/p and p_t^*/p versus Mach number. The curves show that the difference between the total pressure for isentropic flow and behind a normal shock grows larger as the freestream (supersonic) Mach number becomes greater. E.g., the ratio p_t^*/p_t decreases from 1.0 at $M = 1$ to 0.721 at $M = 2$ ($\gamma = 1.4$).

Since also at supersonic speeds the freestream static pressure can be obtained by applying a pitot-static probe or via a static source located on the surface of the fuselage of the airplane, we find that the measured impact pressure difference is given by

$$p_t^* - p = p \left[\left(\frac{\gamma+1}{2} M^2 \right)^{\frac{\gamma}{\gamma-1}} \left(\frac{2\gamma M^2}{\gamma+1} - \frac{\gamma-1}{\gamma+1} \right)^{\frac{1}{1-\gamma}} - 1 \right]. \quad (5.20)$$

Using the sea-level reference values $p = p_0$ and $\rho = \rho_0$, we obtain the following relationship from Equations (5.17) and (5.20),

$$p_t^* - p = p_0 \left[\left(\frac{\gamma+1}{2\gamma} \frac{\rho_0}{p_0} V_c^2 \right)^{\frac{\gamma}{\gamma-1}} \left(\frac{2}{\gamma+1} \frac{\rho_0}{p_0} V_c^2 - \frac{\gamma-1}{\gamma+1} \right)^{\frac{1}{1-\gamma}} - 1 \right]. \quad (5.21)$$

This is the calibration equation of the airspeed indicator for supersonic flight. The reading of the airspeed indicator is called the indicated airspeed V_i . Possible inaccuracies emanating from instrument errors and from the pitot-static system constitute the difference between indicated airspeed and calibrated airspeed. Finally, the various airspeeds considered in this section are summarized below:

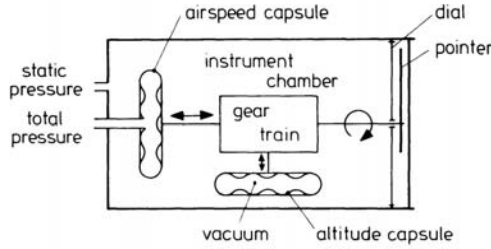


Figure 5.13 Principle of Machmeter

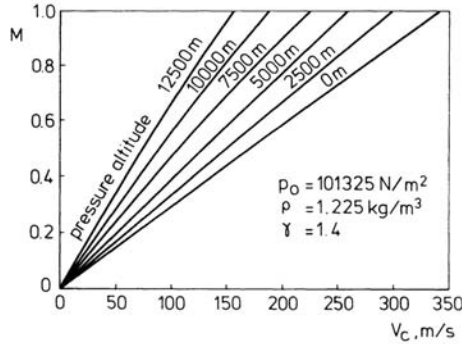


Figure 5.14 Mach number versus calibrated airspeed for various geopotential pressure altitudes

- V true airspeed, T.A.S.
- V_c calibrated airspeed, C.A.S.
- V_e equivalent airspeed, E.A.S.
- V_i indicated airspeed, I.A.S.

We close this section with the observation that airspeed indicator scales almost always use the knot (nautical mile per hour) as a measure of airspeed.

5.5 The machmeter

The *Machmeter* is the instrument which measures the flight Mach number, $M = V/c$. Equations (5.18) and (5.20) indicate that in both the supersonic and subsonic speed regime, the flight Mach number can be determined by measuring the pressure ratio $(p_t - p)/p$. Figure 5.13 shows that the Machmeter is a compound flight instrument which consists of an airspeed indicator and an altimeter. The pressure difference $p_t - p$ is measured by means of the airspeed capsule and the static pressure is obtained from the movement of the altitude capsule. The deflections of the two mechanisms are combined and then transmitted to the indicator pointer.

The result of the previous section also show that the flight Mach number can be computed from known values of V_c and H_p . Figure 5.14 gives the subsonic flight Mach number as a function of the calibrated airspeed for various geopotential

pressure altitudes, calculated from Equations (5.11) and (5.18).

5.6 Ambient air temperature measurement

The prediction of airplane performance and the operation of airplanes requires that the freeair static pressure and the total pressure are known. In addition, the ambient or freeair static temperature at the flight altitude is needed for getting the true airspeed or to compute the density of the air for instance.

The air thermometer on an airplane commonly is made up of a temperature probe attached to the outer surface of the airplane and an indicator in the cockpit.

Mostly, the temperature sensed by the temperature probe is higher than the ambient air temperature because of the adiabatic heating effect of the air flow on the temperature sensing element.

If the air at the measurement point could be brought to rest by an adiabatic process, the total temperature, T_t , would be registered, which quantity is a direct function of the ambient temperature and the flight Mach number in both subsonic and supersonic flow (see Appendix D),

$$T_t = T \left(1 + \frac{\gamma - 1}{2} M^2 \right). \quad (5.22)$$

In actual circumstances, however, the instrument usually displays a temperature which is somewhat less than the total temperature. This phenomenon, which is due to a heat flow from the sensor to the surrounding body, is conveniently expressed by the ratio

$$K = \frac{T_i - T}{T_t - T}, \quad (5.23)$$

where T_i is the indicated temperature and K is the recovery factor of the probe, denoting the relative amount of the adiabatic temperature rise which is accomplished by the thermometer. If the recovery factor is included in Equation (5.22), we obtain

$$T_i = T \left(1 + K \frac{\gamma - 1}{2} M^2 \right). \quad (5.24)$$

A graphic representation of Equation (5.24) is given in Figure 5.15, where is shown the variation of the ratio T_i/T versus M^2 for six K -values. As used in this diagram, the recovery factor of typical installations ranges from 0.5 to 1.0.

The value of K for a particular thermometer can be determined from calibration tests in a wind tunnel or by the execution of flight tests. For example, from flight runs at a constant altitude, the relationship between T_i and M^2 can be established by direct measurement of flight Mach number and indicated temperature. Then, as may be seen from Figure 5.15, extrapolation to $M = 0$ of the curve through the test data gives the ambient temperature at the measurement height, whilst the slope of the curve furnishes the associated value of K .

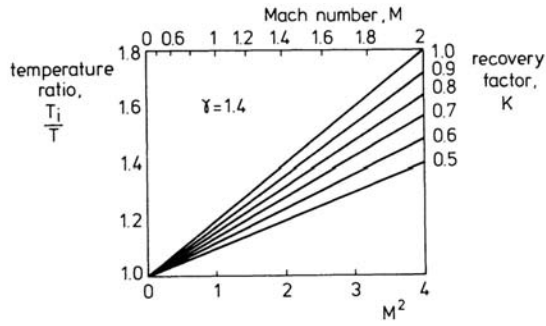


Figure 5.15 Relationship between measured and ambient temperature

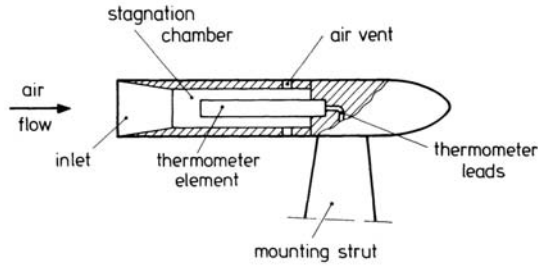


Figure 5.16 Sketch of the total temperature probe

Present-day installations for measuring the air temperature are virtually always total temperature probes, having a tube shaped stagnation chamber in which a sensing element is placed (Figure 5.16). The thermometer element usually consists of a temperature sensitive resistor included in a electrical bridge circuit. These electric thermometers supply a current arising from the bridge unbalance. This current is a function of the resistance and, thus, a measure of the prevailing temperature (References 16 and 17).

Chapter 6

PROPULSION

6.1 Types of airplane propulsion systems

The four types of main propulsion systems to be considered here are the reciprocating piston engine with propeller, the turbojet, the turboprop (the turbo-engine and propeller combination), and the turbofan.

These all are named airbreathing engines because of the fact that they employ the oxygen from the atmospheric air to burn the fuel.

All these devices also have the common property that they generate a propulsive force through application of Newton's third law (action = reaction), by accelerating air backwards with respect to the airplane. In accordance with Newton's second law of motion (see Appendix A), the magnitude of the thrust supplied is equal to the time rate of change of linear momentum given to the mass of air or gas (air mixed with combustion products).

The piston engine plus propeller is used today in the small general aviation airplanes only. These engines have four or six cylinders, are aircooled and operate on the four-stroke cycle principle. The cylinders are virtually always arranged in horizontally opposed pairs (Figure 6.1). Fuel may be supplied by individual injection to each cylinder or by a carburetor which mixes the fuel and air to the right proportions and leads this mixture to the cylinders via the inlet manifold. Each cylinder has an intake valve and an exhaust valve and inside the cylinder is a piston moving up and down by the high gas pressures obtained from burning the mixture of fuel and air. The pistons drive the crankshaft via connecting rods, which change the reciprocating motion of the pistons to the rotational motion of the crankshaft.

The power delivered to the crankshaft is called shaft brake power, which designation has as origin the measurement of the engine output by coupling the crankshaft

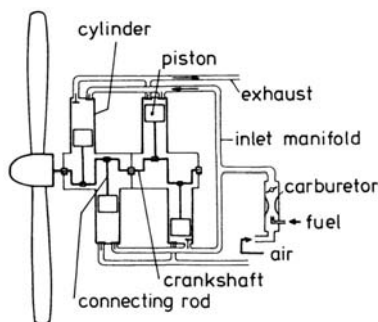


Figure 6.1 Four-cylinder piston engine with propeller

to a brake system (dynamometer). On the other hand, it is also possible to determine the shaft power in flight by means of a torque meter (Reference 16).

The crankshaft, in turn, drives the propeller, which device produces the thrust by accelerating atmospheric air with respect to the airplane.

The useful power available for propulsion is given by the product of thrust T and airspeed V . This quantity is called *power available* and denoted by the symbol P_a . The ratio of power available to shaft brake power is the propulsive efficiency of the propeller,

$$\eta_j = \frac{TV}{P_{br}} = \frac{P_a}{P_{br}}. \quad (6.1)$$

We shall discuss the subject of propeller efficiency further in Chapter 7. It is suffice here to realize that the piston engine converts the heat energy in the fuel to shaft brake power and that this power then is used by the propeller to effectuate power available. There are, thus, two separate and different conversion processes involved; an *energy conversion* process and a *power conversion process*.

The usefulness of the piston engine and propeller combination is limited to low subsonic airspeeds. The development of the turbojet in the thirties and forties of the twentieth century came as an answer to the demand for higher flight speeds. In this engine, a mass flow of air is heated by burning fuel and ejected rearward as a blast of hot gas at high velocity. In Figure 6.2 is sketched the basic layout of the turbojet. It consists of five distinct components; air intake, compressor, combustor, turbine and exhaust nozzle. The core of the engine comprising the compressor, combustor and turbine may be termed the *gas generator*. A picture of the typical changes in pressure, temperature and velocity of the air or gas flowing through the engine is also shown in Figure 6.2. The changes in intake and nozzle are only effectuated by way of the form of the passages through which the fluid flows.

Due to external compression, the air enters the intake at a velocity which is somewhat lower than the flight speed. In the intake the air is slowed down further, giving a substantial pressure and temperature rise of the air.

Two types of compressor may be found; centrifugal and axial (Figure 6.3). In the centrifugal compressor the air is taken in near the center of an impeller, which flings the air in the direction of the circumference. This gives a high pressure at the compressor exit.

In modern gas turbine engines, mostly the axial flow compressor is found, which consists of a series of rotating many-bladed fans. These fans rotate between sets of fixed stator blades. Each set of fixed and rotating blades forms a compressor stage and delivers a certain increase in pressure. Therefore, in the compressor which may incorporate a large number of stages, the passing air obtains a very high pressure rise. This is accompanied by a considerable increase in temperature.

In the combustor heat energy of fuel is released in the air flow, providing a high turbine entry temperature. Normally, there is a maximum turbine entry temperature because of the critical thermal load of the blades of the turbine. To keep

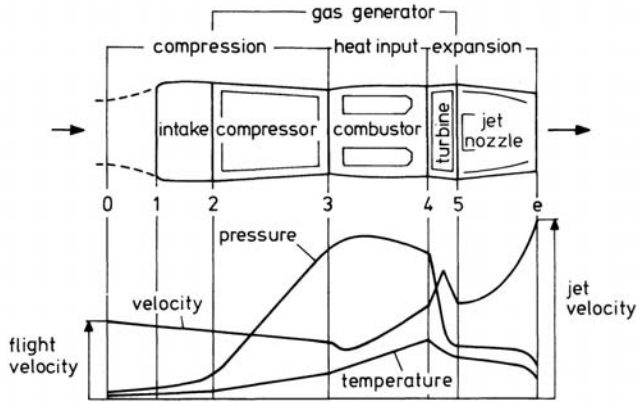


Figure 6.2 Typical layout of the turbojet

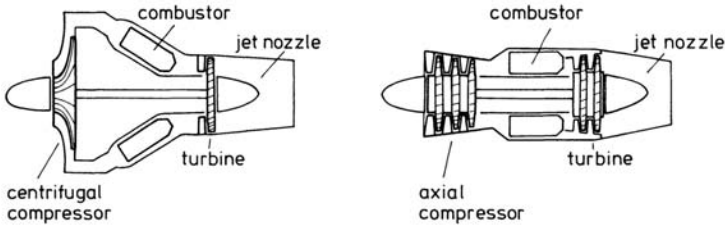


Figure 6.3 Typical compressor types

the gas temperature at the turbine inlet within acceptable limits, much more air is used in the turbojet than is required for combustion. This large mass flow is also needed to get a high thrust.

In passing through the turbine, energy is extracted from the gas flow in order to drive the compressor. This is coupled with a drop in pressure and temperature in the turbine. Most turbojets have two compressors, one after the other, each driven by an independent turbine through concentric unconnected shafts (Figure 6.4). As each rotating assembly, consisting of a turbine, a drive shaft and a compressor or fan is a spool, the arrangement shown in Figure 6.4 is called a *two-spool engine*. The remaining energy from the gas generator is expanded in the nozzle and exhausted as a high-velocity jet. If the turbojet is designed for use at subsonic airspeeds, the nozzle is convergent. In the case of an engine aimed to fly at supersonic

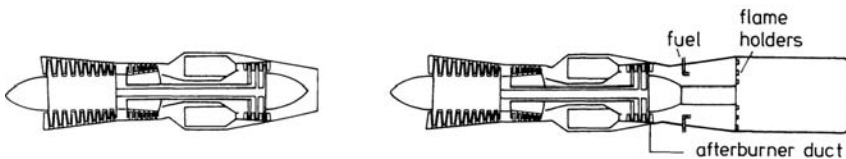


Figure 6.4 Two-spool turbojet without and with afterburner

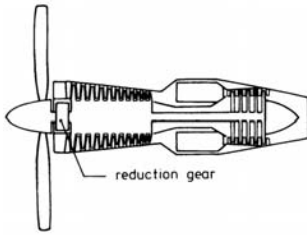


Figure 6.5 Turboprop

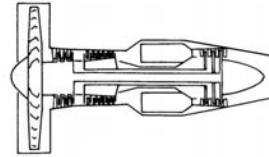


Figure 6.6 Two-spool turbofan

velocities, a convergent-divergent exhaust nozzle is used to obtain maximum jet velocity.

Gas turbine engines may be equipped with a reheat system or *afterburner*. In the case of afterburning, supplementary fuel is injected into the exhaust nozzle as is also illustrated in Figure 6.4. Burning of extra fuel is possible because the exhaust gas entering the nozzle comprises an excess of unburned oxygen. Afterburning is a method to achieve a temporary increase in thrust for takeoff and climb or for transition from subsonic to supersonic flight velocities.

In contrast to the piston engine, the various processes in the turbojet are continuous. In combination with the absence of reciprocating parts, the turbojet runs smoother and enables more heat energy to be released.

Another essential difference between jet and propeller propulsion is the nature of the rearward mass flow. In the case of the propeller a large mass flow of cold air is transported at a relatively low speed, whereas the turbojet produces a thrust by accelerating a relative small amount of hot gas to a very high velocity. This implies, as will be explained in subsequent sections, that the turbojet is only effective at high flight speeds, whereas the propeller is an efficient means of producing thrust at low-subsonic airspeeds.

The problem of the inefficiency of the turbojet at low flight speeds can be solved through extracting most of the power from the hot gases by means of an enlarged turbine, and then to supply the power to a propeller. This arrangement is called a *turboprop*. Figure 6.5 shows the layout of a single shaft engine, where turbine, compressor and propeller are all mechanically connected. A reduction gear is present between the compressor and the propeller since the propeller must rotate at a much lower speed than the gas generator in order to avoid extreme tip speeds. Normally it will be possible to use the residual energy after the turbine to eject the gases from an exhaust nozzle at a rather high speed and so to generate some extra thrust.

A compromise between the turboprop and the turbojet is the *turbofan*, which engine type operates efficiently in the high subsonic speed range. In this case a ducted fan takes the place of the propeller of the turboprop. As sketched in Figure 6.6, usually, the fan is placed at the front of the engine, where it is an integral part of the low-speed compressor. This arrangement is designated as front fan. Part of the air impelled by the fan passes through the bypass duct and is discharged as a

cold jet. The rest of the fan flow goes through the engine and forms the hot flow. A characteristic design figure for a turbofan is the bypass ratio, which is the ratio of the mass flow rate of the cold (secondary) flow passing through the bypass duct to the mass flow rate of the hot (primary) flow passing through the gas generator. In formula

$$B = \frac{m_c}{m_h}, \quad (6.2)$$

where B denotes the bypass ratio and m_c and m_h are the mass flow rates of the cold and hot stream, respectively.

Since $m = m_c + m_h$, we also have the relationships

$$\frac{m_c}{m} = \frac{B}{B+1} \quad \text{and} \quad \frac{m_h}{m} = \frac{1}{B+1}. \quad (6.3)$$

Today's turbofan engines have a bypass ratio between 4 and 8. Advanced propulsion systems with a bypass ratio beyond the current values are called ultra-high bypass ratio (UHBR) engines.

To accelerate the cold stream, a large percentage of the energy available from the gas generator is supplied as shaft power to the fan. Therefore, in principle, the turbofan is similar to the turboprop except that its bypass ratio is much lower. Nevertheless, in addition to the thrust produced by the hot jet, the fan also accelerates such a large mass of cold air that it supplies a generous contribution to the total thrust. An added benefit of bypassing of air is reduced jet-generated noise.

6.2 The piston engine

The working cycle of the four-stroke piston engine requires two revolutions of the crankshaft; two strokes down and two strokes up. The four events are illustrated in Figure 6.7 in the form of a plot of pressure versus volume:

The intake stroke (1). The piston travels from the cylinder head (top dead center) to the bottom of the cylinder (bottom dead center). An amount of fuel and air is sucked into the cylinder through the open intake valve.

The compression stroke (2). The piston moves upward to the top of the cylinder, and the charge is almost isentropically compressed from the inlet-manifold pressure p_2 to a pressure p_3 . When the piston approaches the top of the stroke, the mass of gas confined in the cylinder is ignited by the ignition system. Between points 3 and 4, combustion takes place at approximately constant volume and the pressure increases to p_4 .

The power stroke (3). The high pressure pushes the piston downward and the burning gas expands more or less isentropically to the pressure p_5 . Just before the piston reaches the bottom of the stroke the exhaust valve opens and the pressure inside the cylinder drops to the value p_6 ($p_6 = p_1$).

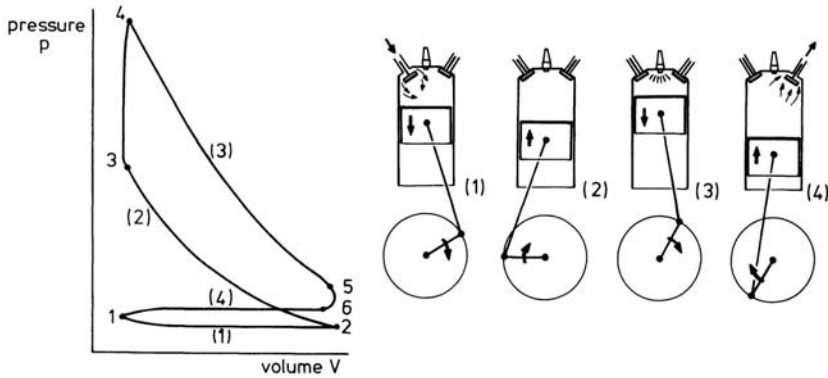


Figure 6.7 Working cycle of the four-stroke piston engine

The exhaust stroke (4). The piston again moves upward and the burned gases in the cylinder are forced out through the exhaust valve.

The compression ratio of the piston engine is the volume of space in the cylinder when the piston is at bottom dead center divided by the volume when the piston is at top dead center.

The cycle or thermal efficiency is the ratio of the power developed in the engine and the heat release per unit time or thermal input,

$$\eta_{\text{th}} = \frac{NP_i}{Q} = \frac{NP_i}{m_f H}, \quad (6.4)$$

where N is the number of cylinders and P_i is the indicated power, which is the power developed in one cylinder. The thermal input Q can be written as the product of the fuel mass flow rate m_f and the heating value of the fuel H . For aviation fuels the heating value is about 4.3×10^7 Joule/kg.

The conversion of the heat energy released during combustion to mechanical power, usually, is analyzed by considering the *Otto-cycle*, which consists of four ideal processes (Figure 6.8). Point 2 in Figure 6.8 stands for the mixture of air and fuel in the cylinder at the inlet-manifold pressure that is compressed isentropically along the line 2-3. From 3 to 4 heat is added to the charge by burning the fuel at constant volume, thereby considerably increasing the pressure. Then, the gases are expanded isentropically along the line 4-5 to the pressure p_5 . Finally, from 5 to 2, the cycle is completed by the discharge of the gases at constant volume.

When making use of the Poisson relations between p , T and ρ (see Appendix D), the highest thermal efficiency is easily obtained as

$$\eta_{\text{th}} = 1 - \frac{1}{\varepsilon^{\gamma-1}}, \quad (6.5)$$

where ε is the compression ratio of the engine and γ is the ratio of the specific heats of the fuel-air mixture. Depending on the composition of the gas, the value of γ varies between 1.2 and 1.4.

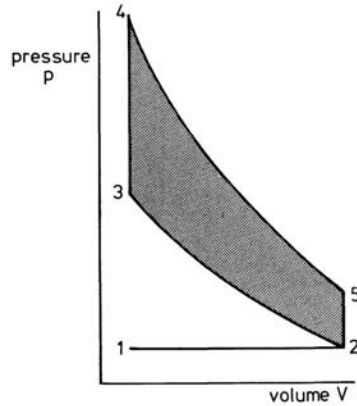


Figure 6.8 The Otto-cycle

It should be noted that due to heat and friction losses, the actual value of the thermal efficiency is lower than that forecasted by Equation (6.5).

The net work per cylinder done during one cycle, W_i , is represented by the hatched area in Figure 6.8 since this work is given by

$$W_i = \oint p \, dV. \quad (6.6)$$

At an engine speed n (revolutions per second), the number of power strokes in one second is $n/2$. Hence,

$$P_i = W_i \frac{n}{2}. \quad (6.7)$$

When we neglect the friction losses between the moving parts of the engine, the power delivered to the shaft, P_{br} , may be set equal to the total indicated power,

$$P_{br} = N P_i. \quad (6.8)$$

Combination of Equations (6.7) and (6.8) yields

$$P_{br} = N W_i \frac{n}{2}. \quad (6.9)$$

The power P_i and the work W_i are habitually related to each other by means of the mean effective pressure, p_e , which quantity is defined by

$$p_e = \frac{W_i}{\frac{\pi}{4} D^2 S}, \quad (6.10)$$

where D is the diameter of the piston (the bore) and S is the length of the displacement of the piston (the stroke). Clearly, the pressure p_e in Equation (6.10) is a fictitious parameter, which is broadly used as an index in determining the shaft brake power. Insertion of Equation (6.10) into (6.9) yields

$$P_{br} = p_e \frac{\pi}{4} D^2 S \frac{n}{2} N, \quad (6.11)$$

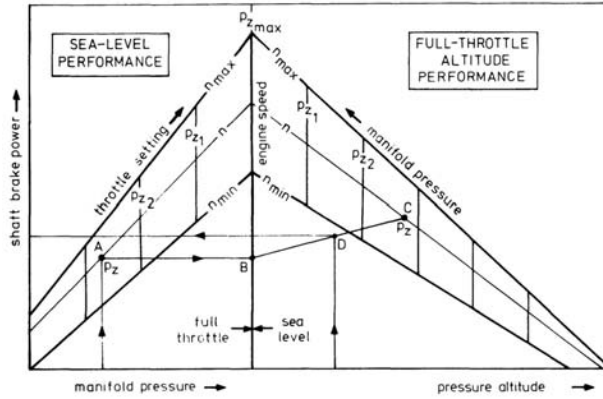


Figure 6.9 Standard power diagram (I.S.A.)

where the quantity $\frac{\pi}{4}D^2SN$ is the total volume displaced by the piston during one stroke (the total piston displacement of the engine).

Apparently, the shaft brake power delivered by a given engine is a function of mean effective pressure and engine speed,

$$P_{br} = P_{br}(p_e, n). \quad (6.12)$$

Further thermodynamic analysis learns that the pressure p_e varies proportional to the quotient of pressure and temperature of the fuel-air mixture at the beginning of the compression stroke (point 2 in Figure 6.8). This means that p_e depends on the density of the atmospheric air and the throttle setting δ ($0 \leq \delta \leq 1.0$). Accordingly, we have

$$P_{br} = P_{br}(H, \delta, n) = P_{br}(H, \Gamma), \quad (6.13)$$

where $\Gamma = \Gamma(\delta, n)$ is the engine control setting.

The charts as generally supplied by the engine manufacturers are of the form sketched in Figure 6.9. In this so-called *standard power diagram* the shaft brake power in International Standard Atmosphere is given, assuming a mixture control which furnishes maximum power.

In the left hand diagram is given the power at sea level: $P_{br0} = P_{br0}(\delta, n)$. The throttle setting is expressed in terms of inlet manifold pressure p_z . The power is limited by the maximum permissible engine speed and maximum inlet manifold pressure, which corresponds to the full-throttle condition (fully opened throttle valve; $\delta = 1.0$). The effect of altitude on full-throttle power is shown in the right hand diagram of Figure 6.9 ($P_{br0} = P_{br0}(H, n)$). The chart gives also the prevailing inlet manifold pressures. In the full-throttle condition and for a given engine speed the shaft brake power decreases with increasing height due to the decreasing air density.

An empirical relationship often used to account for the effect of altitude is:

$$\frac{P_{br}}{P_{br0}} = 1.132 \frac{\rho}{\rho_0} - 0.132,$$

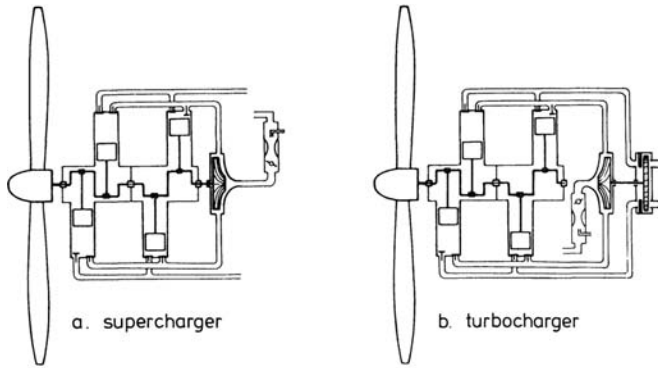


Figure 6.10 Supercharging

where the subscript "0" denotes sea-level condition. In order to determine the power at altitude for a part-throttle condition for given values of altitude, engine speed, inlet manifold pressure, and air temperature, the following procedure is employed:

1. Locate point A on sea-level curve for the known values of inlet manifold pressure and engine speed and transfer to B.
2. Locate point C on full-throttle altitude curve for the given inlet manifold pressure and engine speed.
3. Determine power output at the required height (point D) by linear interpolation between points B and C. Note that along the straight line B-C the power increases somewhat due to the decreasing air temperature.
4. Modify the power P_{br} (I.S.A.) at point D for the deviation of air temperature T from standard altitude temperature $T_{I.S.A.}$ by the following empirical formula:

$$P_{br} = P_{br}(I.S.A.) \sqrt{\frac{T_{I.S.A.}}{T}}, \quad (6.14)$$

where P_{br} is the actual power output and T and $T_{I.S.A.}$ are expressed in kelvin.

To improve the performance of a normally aspirated engine a supercharger is used, which provides a greater pressure at the intake valve. The supercharger is usually positioned between carburetor and inlet manifold. It may be driven by the crankshaft as sketched in Figure 6.10a. Alternatively, there may be a turbocharger, a supercharger impelled by a small turbine which in turn is driven by the exhaust gas stream. The latter assembly is more economic than a gear-driven supercharger since it utilizes the heat energy present in the exhaust gases.

Figure 6.11 shows a picture of the standard power diagram of a supercharged engine. Depending on engine speed, the maximum inlet manifold pressure is

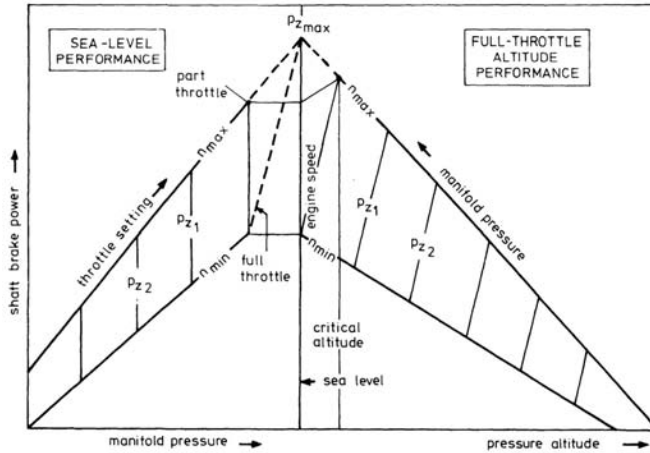


Figure 6.11 Standard power diagram (supercharged)

increased at sea level and hence the altitude performance. In order to avoid unacceptable high engine loads, it is not possible to use the high inlet manifold pressures at lower altitudes. Therefore, limitations are put on the inlet manifold pressure, and only when altitude is gained it is licensed to open the throttle gradually in order to compensate for the loss in atmospheric pressure.

The altitude at which the throttle becomes fully open is termed the critical altitude of the engine for the given engine speed and inlet manifold pressure. Above the critical altitude, the power output decreases with increasing height due to the reduction of air density as in the case of an aspirated engine.

An important engine characteristic is the amount of fuel required to generate the shaft brake power. This may be expressed as the fuel weight flow rate, F , divided by shaft brake power,

$$c_P = \frac{F}{P_{br}} = \frac{m_f g}{P_{br}}, \quad (6.15)$$

where c_P is the specific fuel consumption, which has the dimensions N/Wh or N/kWh.

A comparison of Equation (6.15) with Equations (6.4) and (6.8) reveals that the specific fuel consumption is an inverse criterion of thermal efficiency,

$$c_P = \frac{g}{H \eta_{th}}. \quad (6.16)$$

The working cycle of the piston engine gives a high thermal efficiency over a wide range of inlet manifold pressures, engine speeds, and flight altitudes. A cruising thermal efficiency of 35% ($c_P = 2.4$ N/kWh) is fairly representative of airplane piston engines. The thermal efficiency, however, is only half the problem since the conversion of shaft brake power into power available is also coupled with

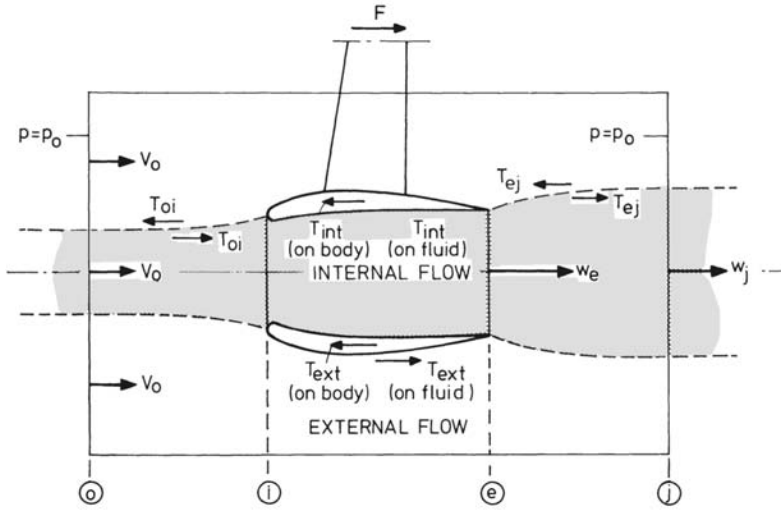


Figure 6.12 Thrust and drag of a turbojet

losses. The overall efficiency of the complete propulsion process can be written as

$$\eta_{\text{tot}} = \frac{TV}{m_f H} = \frac{TV}{P_{\text{br}}} = \frac{P_{\text{br}}}{m_f H} = \eta_j \eta_{\text{th}}, \quad (6.17)$$

where, according to Equation (6.1), $\eta_j = TV/P_{\text{br}}$ is the propulsive efficiency.

6.3 Definition of thrust for jet propulsion

In order to explain the customary definition of thrust for jet propulsion, a nacelle mounted turbojet engine is considered in Figure 6.12.

Since the resultant force in a steady flow is conveniently established by the application of the momentum equation (see Appendix D), in Figure 6.12 a control volume is specified around the engine, which extends far upstream where the pressure and velocity have their freestream values p_0 and V_0 . The side boundaries are parallel to the velocity V_0 and are, just like the aft control surface, sufficiently far removed from the engine that the local pressures are equal to the freestream pressure p_0 . In Figure 6.12 also are distinguished the air flows passing through and around the engine duct.

The air mass flow rate of the internal flow crossing the boundary at the front is given by $m = \rho_0 V_0 A_0$. The mixture of air and combustion products crosses the aft plane through an area A_j with a velocity w_j .

The force obtained as a result from the time rate of change of linear momentum of the fluid that passes through the engine, and by assuming uniform flow over the area A_j , is given by the equation

$$F_1 = T_{0i} + T_{\text{int}} + T_{0e} = (m + m_f)w_j - mV_0, \quad (6.18)$$

where T_{oi} and T_{ej} are component forces in the direction parallel to the freestream velocity arising from the pressure forces acting on the boundary of the pre-entry streamtube and the post-exit streamtube, respectively. The force T_{int} is called the intrinsic thrust, and is associated with the pressure and friction forces acting on the internal surfaces of the nacelle and engine.

The first term on the right-hand side of Equation (6.18) includes also the linear momentum of the fuel flow rate, $m_f w_j$, as seen relative to the engine. It should be noticed that in the derivation of the forces in Equation (6.18) all pressures are referred to the freestream pressure as a datum.

The force obtained as a result from the rate of increase of momentum of the air which passes around the outside of the nacelle is given by

$$F_2 = -T_{oi} + T_{\text{ext}} - T_{ej}, \quad (6.19)$$

where T_{ext} is called the extrinsic thrust, which is the force in the direction parallel to the freestream velocity arising from the pressure and friction forces acting on the external surface of the nacelle.

The net engine force F , which is imparted to the airplane structure is the sum of the forces exerted over the internal and external surfaces of the engine-nacelle combination,

$$F = T_{\text{int}} + T_{\text{ext}}. \quad (6.20)$$

Combining Equation (6.18) to (6.20) yields

$$F = F_1 + F_2 = (m + m_f)w_j - mV_0 + F_2. \quad (6.21)$$

Conventionally, the net force acting on the airplane in its flight direction is divided into thrust and drag.

Such division is a matter of definition. If we define $-F_2$ as nacelle (or airplane) drag, then Equation (6.21) tells us that the thrust is given by the force F_1 . This means that the thrust is defined as the time rate of change of momentum of the flow through the engine between the stations 0 and j in Figure 6.12.

However, there is an inconvenience in this definition of the thrust due to the difficulty which is encountered when we want to determine the velocity w_j . Certainly for a convergent nozzle, there is in fact hardly a physical post-exit streamtube because of the exchange of energy between internal and external flows.

In order to avoid this complication, engine manufacturers normally express the thrust as the rate of increase of momentum between the stations o and e in Figure 6.12,

$$T = T_{oi} + T_{\text{int}} = (m + m_f)w_e - mV_0 + A_e(p_e - p_0). \quad (6.22)$$

The thrust so defined depends on the conditions in the undisturbed stream and at the nozzle exit, which both are known or determinable.

When applying the momentum equation for the jet

$$A_e(p_e - p_0) + T_{ej} = (m + m_f)(w_j - w_e), \quad (6.23)$$

we readily find the following expression for the net engine force

$$F = (m + m_f)w_e - mV_0 + A_e(p_e - p_0) - (T_{oi} - T_{ext}). \quad (6.24)$$

Apparently, using Equation (6.22) for the calculation of the thrust requires that the drag is defined by the last term of the right-hand side of Equation (6.24). Clearly, the physical complexity of the problem is now confined to the determination of T_{ext} and T_{oi} as the components of the drag force. Anyway, Equation (6.22) will form the basis for our evaluations of engine thrust throughout this book.

According to our discussion in Section 3.5 the linear momentum of the fuel flow rate relative to the engine can be omitted in Equation (6.22). We thus obtain

$$T = m(w_e - V_0) + A_e(p_e - p_0). \quad (6.25)$$

A convenient form for the thrust equation is obtained when we introduce the equivalent jet velocity, $(w_e)_{eq}$, defined by

$$(w_e)_{eq} = w_e + \frac{A_e}{m}(p_e - p_0). \quad (6.26)$$

Using this definition we get

$$T = m((w_e)_{eq} - V_0). \quad (6.27)$$

An important measure for the relationship between the thrust and the size of the engine is the thrust per unit air weight flow rate or *specific thrust*

$$\psi_T = \frac{T}{mg} = \frac{(w_e)_{eq} - V_0}{g}. \quad (6.28)$$

With this definition the specific thrust has the dimension of second.

If the nozzle exit pressure equals the ambient pressure, then we obtain

$$\psi_T = \frac{T}{mg} = \frac{w_e - V_0}{g}. \quad (6.29)$$

Expressing the thrust as the product of weight flow rate of the air through the engine and specific thrust, will be useful for our subsequent discussions on turbojet performance.

6.4 Ideal turbojet cycle

The working cycle of the turbojet is different from that of the piston engine in Figures 6.8 insofar that the combustion process in the gas turbine engine is very nearly isobaric with an increase in volume of the gas.

In examining the thermodynamic behavior of the fluid as it flows through the turbojet, we will consider here the *ideal turbojet cycle* or *Brayton-cycle*. The idealization implies that the following assumptions are made:

- a. The working fluid behaves as a perfect gas with constant specific heats, which are equal to those of air.
- b. All compression and expansion processes are isentropic.
- c. Combustion takes place at constant total pressure.
- d. In the exhaust nozzle the flow is expanded to the freestream static pressure.

The resulting cycle is shown in Figure 6.13 in terms of pressure versus specific volume. Specific volume, v , is the volume per unit mass of the working fluid and hence the inverse of the density, $v = 1/\rho$. The various engine components are assigned by numerical engine stations as defined in Figure 6.2.

As shown in Appendix D, static pressure and temperature and velocity of an airstream are equivalent to the total pressure and temperature. Hence, in studying the conditions of the flow through the engine the kinetic energy is taken into account implicitly by using the total properties.

If p_t denotes the total pressure, p the static pressure, and M the flow Mach number, we have for isentropic compression or expansion,

$$p_t = p \left[1 + \frac{\gamma-1}{2} M^2 \right]^{\frac{\gamma}{\gamma-1}}. \quad (6.30)$$

For adiabatic and isentropic compression or expansion the total temperature is given by

$$T_t = T \left[1 + \frac{\gamma-1}{2} M^2 \right], \quad (6.31)$$

where again subscript t denotes the stagnation state.

Starting from the freestream conditions p_0 , T_0 , and M_0 or V_0 in point 0 of Figure 6.13, the air passes successively through the following engine components:

1. The intake (0-2). The pressure rises from p_0 to about $p_{t2} = p_{t0}$ at the inlet of the compressor. The increase in pressure is due to the external and internal deceleration of the air relative to the engine, and is called the ram pressure rise,

$$p_{t2} = p_{t0} = p_0 \left[1 + \frac{\gamma-1}{2} M_0^2 \right]^{\frac{\gamma}{\gamma-1}}. \quad (6.32)$$

Likewise, the temperature at engine station 2 equals the freestream total temperature

$$T_{t2} = T_{t0} = T_0 \left[1 + \frac{\gamma-1}{2} M_0^2 \right]. \quad (6.33)$$

2. The compressor (2-3). From Equations (6.30) and (6.31) we obtain

$$\frac{T_t}{T} = \left[\frac{p_t}{p} \right]^{\frac{\gamma-1}{\gamma}}. \quad (6.34)$$

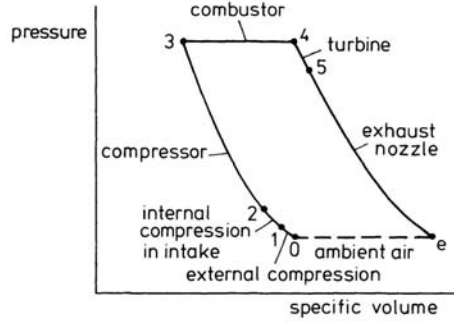


Figure 6.13 Ideal cycle for gas turbine engine (Brayton-cycle)

But, according to Appendix D, $T/(p)^{\frac{\gamma-1}{\gamma}} = \text{constant}$ for an isentropic process so that Equation (6.34) becomes

$$\frac{T_t}{(p_t)^{\frac{\gamma-1}{\gamma}}} = \text{constant}. \quad (6.35)$$

Applying Equation (6.35) to the isentropic compression process, we have the compressor outlet temperature given by

$$T_{t3} = T_{t2}(\epsilon_c)^{\frac{\gamma-1}{\gamma}}, \quad (6.36)$$

where $\epsilon_c = p_{t3}/p_{t2}$ is the pressure ratio of the compressor.

3. The combustor (3-4). As a consequence of the simplification that the drop in total pressure during combustion is zero, we get

$$p_{t4} = p_{t3}. \quad (6.37)$$

From the steady flow energy equation in Appendix D, we find for the heat added to the flow per unit time

$$Q = m_f H = mc_p(T_{t4} - T_{t3}), \quad (6.38)$$

where H is the heating value of the fuel, T_{t4} the turbine entry temperature, and c_p is the specific heat of air at constant pressure.

4. The turbine (4-5). The temperature at the turbine exit is found from the condition that turbine power equals compressor power. In formula

$$mc_p(T_{t4} - T_{t5}) = mc_p(T_{t3} - T_{t2}), \quad \text{or} \quad (6.39)$$

$$T_{t5} = T_{t4} - (T_{t3} - T_{t2}). \quad (6.40)$$

The pressure at the turbine outlet is given by

$$p_{t5} = p_{t4} \left[\frac{T_{t5}}{T_{t4}} \right]^{\frac{\gamma}{\gamma-1}}. \quad (6.41)$$

5. The exhaust nozzle (5-e). If we assume that in flowing through the nozzle the pressure of the gas falls to ambient pressure, the Mach number at the nozzle exit can be found from Equation (6.30),

$$\frac{p_{te}}{p_e} = \frac{p_{t5}}{p_0} = \left[1 + \frac{\gamma-1}{2} M_e^2 \right]^{\frac{\gamma}{\gamma-1}}, \quad \text{or} \quad (6.42)$$

$$M_e = \sqrt{\frac{2}{\gamma-1} \left[\left[\frac{p_{te}}{p_0} \right]^{\frac{\gamma-1}{\gamma}} - 1 \right]}. \quad (6.43)$$

Referring to Equations (6.30) and (6.31), we see that the temperature T_e can be written as

$$T_e = \frac{T_{te}}{1 + \frac{\gamma-1}{2} M_e^2} = \frac{T_{te}}{\left[\frac{p_{te}}{p_0} \right]^{\frac{\gamma-1}{\gamma}}}. \quad (6.44)$$

Using Equation (2.20) for the speed of sound, the jet velocity becomes

$$w_e = M_e \sqrt{\gamma R T_e} = \sqrt{\frac{2\gamma R}{\gamma-1} T_{te} \left[1 - \left[\frac{p_0}{p_{te}} \right]^{\frac{\gamma-1}{\gamma}} \right]}. \quad (6.45)$$

An expression for the specific thrust is obtained by substituting Equation (6.45) into Equation (6.29)

$$\psi_T = \frac{1}{g} \left[\sqrt{\frac{2\gamma R}{\gamma-1} T_{te} \left[1 - \left[\frac{p_0}{p_{te}} \right]^{\frac{\gamma-1}{\gamma}} \right]} - V_0 \right]. \quad (6.46)$$

The thermal efficiency of the working cycle of the turbojet is defined as the increase in kinetic energy of the gas stream in unit time divided by the heat energy added to the flow in unit time,

$$\eta_{th} = \frac{\frac{1}{2} m (w_e^2 - v_0^2)}{m_f H}. \quad (6.47)$$

The energy equation in terms of total temperature reads (Appendix D)

$$T_t = T + \frac{V^2}{2c_p}. \quad (6.48)$$

Substitution of Equation (6.48) into Equation (6.47) yields

$$\eta_{th} = 1 - \frac{1}{(\varepsilon)^{\frac{\gamma-1}{\gamma}}}, \quad (6.49)$$

where ε is the overall pressure ratio of the cycle,

$$\varepsilon = \frac{p_{t3}}{p_0} = \frac{p_{t3}}{p_{t2}} \frac{p_{t2}}{p_0} = \varepsilon_c \left[1 + \frac{\gamma-1}{2} M_0^2 \right]^{\frac{\gamma}{\gamma-1}}. \quad (6.50)$$

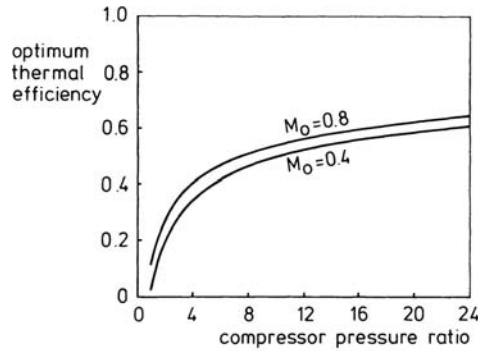


Figure 6.14 Thermal efficiency for Brayton-cycle

A graphic representation of Equation (6.49) is given in Figure 6.14. This chart emphasizes the importance of applying a high overall pressure ratio, that is, a high flight Mach number and a high engine speed in order to accomplish a satisfactory thermal efficiency.

The optimum thermal efficiency as given by Equation (6.49) is independent of the temperature to which the gas stream is raised in the burner. It should be realized, however, that the compression of the air goes together with an increase in temperature. The higher the overall compression ratio, the less the amount of fuel which can be supplied to the combustion chamber without going beyond the bounds of the turbine entry temperature. Thus, the maximum pressure ratio increases with increasing turbine entry temperature and with that the maximum attainable thermal efficiency.

The propulsive efficiency of the turbojet engine is defined as the ratio of power available to the increase in kinetic energy of the gas stream,

$$\eta_j = \frac{P_a}{P_j} = \frac{TV_0}{\frac{1}{2}m(w_e^2 - V_0^2)}. \quad (6.51)$$

Substituting Equation (6.25) into Equation (6.51) yields ($p_e = p_0$)

$$\eta_j = \frac{m(w_e - V_0)V_0}{\frac{1}{2}m(w_e^2 - V_0^2)} = \frac{2}{1 + \frac{w_e}{V_0}} = \frac{2}{2 + \frac{T}{mV_0}}. \quad (6.52)$$

The overall efficiency of the entire propulsion process is given by

$$\eta_{\text{tot}} = \frac{TV_0}{m_f H} = \frac{TV_0}{\frac{1}{2}m(w_e^2 - V_0^2)} \frac{\frac{1}{2}m(w_e^2 - V_0^2)}{m_f H} = \eta_j \eta_{\text{th}}. \quad (6.53)$$

In the case of jet propulsion the fuel consumption is related to the thrust,

$$F = c_T T, \quad (6.54)$$

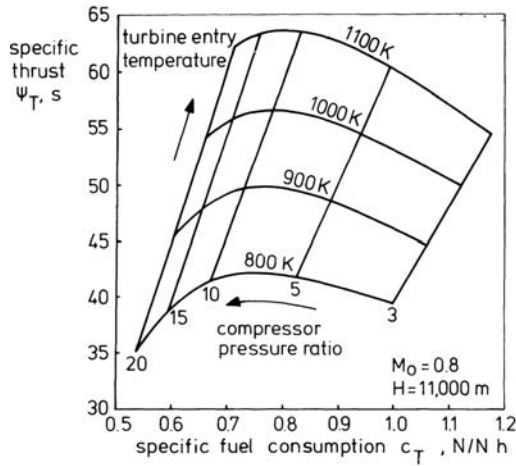


Figure 6.15 Ideal turbojet cycle performance

where F is the fuel weight flow rate and c_T is the thrust specific fuel consumption, or in short specific fuel consumption (SFC), which has the dimensions of N/N s or N/N h.

The specific fuel consumption is related to the overall efficiency by

$$c_T = \frac{F}{T} = \frac{g}{H} \frac{V_0}{\eta_{\text{tot}}}. \quad (6.55)$$

Specific fuel consumption is an important engine characteristic since it is a measure of the efficiency of the engine. A low value of c_T means a high overall efficiency.

We conclude this section with presenting Figure 6.15, where are shown typical results of a series of design point calculations which apply to a subsonic flight condition of $H = 11,000$ m (I.S.A.) and $M_0 = 0.80$.

In Figure 6.15 is plotted specific fuel consumption versus specific thrust for a range of compressor pressure ratios and turbine entry temperatures. The curves indicate that specific thrust and specific fuel consumption increase with increasing turbine entry temperature. At a constant T_{t4} , however, an increase in pressure ratio ϵ_c causes a reduction in specific fuel consumption.

6.5 Component efficiencies

In Section 6.4 we saw that for a given flight condition of altitude and airspeed, both specific thrust and specific fuel consumption of the ideal turbojet cycle were completely determined by compressor pressure ratio and turbine entry temperature.

The actual performance, however, will also depend on the efficiencies of the engine components. Deviations from the ideal behavior arise mainly from the effects

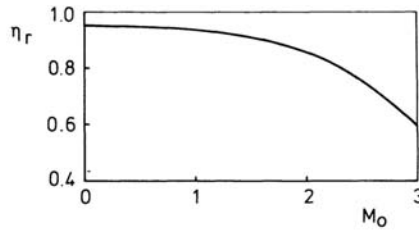


Figure 6.16 Typical variation of Intake pressure recovery factor

of friction and turbulence in the flow, through which for example we have non-isentropic compression in the intake and compressor, and nonisentropic expansion in the turbine. In the following a short description of most of the imperfections is given.

In the intake the air is decelerated to a very low velocity before it flows into the compressor. Because, at least in principle, there is no heat transfer, the total temperature remains constant as the flow velocity reduces from the flight speed ahead of the intake to the low velocity at the compressor inlet. In the case of subsonic intakes, viscous effects result in a reduction of total pressure, whilst for supersonic intakes a further cause for total pressure loss is the occurrence of shock waves.

To describe the efficiency of the intake, the ratio of total pressure at the compressor inlet to the freestream total pressure may be used,

$$\eta_r = \frac{p_{t2}}{p_{t0}}. \quad (6.56)$$

The quantity η_r is termed the *pressure recovery factor* of the intake.

A typical variation of η_r with flight Mach number for well-designed intakes is shown in Figure 6.16.

Alternatively, the *intake adiabatic efficiency* may be employed, which is defined by

$$\eta_d = \frac{(T_{t2})_{is} - T_0}{T_{t2} - T_0}, \quad (6.57)$$

where T_{t2} is the actual temperature at the compressor inlet and $(T_{t2})_{is}$ is the total temperature which would have been reached after isentropic compression from p_0 to p_{t2} .

Since $T_{t2} = T_{t0}$, we find from Equations (6.30) and (6.31) that

$$\eta_d = \frac{\left[\frac{p_{t2}}{p_0}\right]^{\frac{\gamma-1}{\gamma}} - 1}{\frac{\gamma-1}{2}M_0^2} \quad \text{or} \quad \frac{p_{t2}}{p_0} = \left[1 + \eta_d \frac{\gamma-1}{2}M_0^2\right]^{\frac{\gamma}{\gamma-1}}. \quad (6.58)$$

Combination of Equation (6.56) and Equation (6.58) produces the relationship:

$$\eta_d = \frac{(\eta_r)^{\frac{\gamma-1}{\gamma}} \left[1 + \frac{\gamma-1}{2}M_0^2\right] - 1}{\frac{\gamma-1}{2}M_0^2}. \quad (6.59)$$

For subsonic intakes, both η_r and η_d are experienced to be virtually constant with flight Mach number. At supersonic airspeeds it is most common to specify the intake losses by means of the intake pressure recovery factor as a function of Mach number M_0 .

The efficiency of the compressor may be expressed in terms of the compressor isentropic efficiency, which is the ratio of the ideal and actual compressor powers,

$$\eta_c = \frac{mc_p((T_{t3})_{is} - T_{t2})}{mc_p(T_{t3} - T_{t2})} = \frac{(T_{t3})_{is} - T_{t2}}{T_{t3} - T_{t2}}. \quad (6.60)$$

Equation (6.60) expresses that for a given compressor pressure ratio, the actual total temperature rise exceeds the isentropic value so that the actual compression process requires more power than the ideal process.

The temperature rise for a given compressor pressure ratio ϵ_c , from Equation (6.60), is found as follows,

$$T_{t3} - T_{t2} = \frac{T_{t2}}{\eta_c} \left[(\epsilon_c)^{\frac{\gamma-1}{\gamma}} - 1 \right]. \quad (6.61)$$

A disadvantage of the isentropic efficiency is the fact that it is dependent on the magnitude of the compressor pressure ratio. For this reason, we may use the concept of polytropic efficiency, which is the isentropic efficiency of an infinitely small pressure change such that it has a fixed value throughout the entire process. Then

$$\eta_{pol} = \frac{(dT_t)_{is}}{dT_t} = \text{constant}. \quad (6.62)$$

Also, from Equation (6.35), we have for an isentropic process

$$\frac{(dT_t)_{is}}{T_t} = \frac{\gamma-1}{\gamma} \frac{dp_t}{p_t}. \quad (6.63)$$

Combination of Equations (6.62) and (6.63) gives

$$\eta_{pol} \frac{dT_t}{T_t} = \frac{\gamma-1}{\gamma} \frac{dp_t}{p_t}. \quad (6.64)$$

Integrating between the limits 2 and 3 furnish

$$\eta_{pol} = \frac{\ln(p_{t3}/p_{t2})^{\frac{\gamma-1}{\gamma}}}{\ln(T_{t3}/T_{t2})}, \quad \text{or} \quad (6.65)$$

$$\frac{T_{t3}}{T_{t2}} = (\epsilon_c)^{\frac{\gamma-1}{\eta_{pol} \gamma}}. \quad (6.66)$$

Substitution of Equation (6.66) into Equation (6.61) produces the following relation between the polytropic and the isentropic efficiency of the compression process,

$$\eta_c = \frac{(\epsilon_c)^{\frac{\gamma-1}{\gamma}} - 1}{(\epsilon_c)^{\frac{\gamma-1}{\eta_{pol} \gamma}} - 1}. \quad (6.67)$$

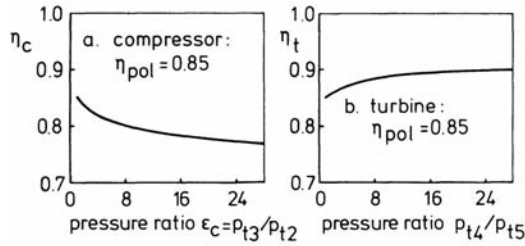


Figure 6.17 Isentropic efficiencies

Nonisentropic expansion in the turbine makes that for a given turbine pressure ratio the gas comes out at a higher temperature than in the ideal case. This behavior may be expressed by the *turbine isentropic efficiency*, which is defined as the ratio of the actual and ideal turbine powers,

$$\eta_t = \frac{mc_p(T_{t4} - T_{t5})}{mc_p(T_{t4} - (T_{t5})_{is})} = \frac{T_{t4} - T_{t5}}{T_{t4} - (T_{t5})_{is}}. \quad (6.68)$$

Combining Equations (6.41) and (6.68) results in an expression for the turbine pressure ratio at a given temperature drop,

$$\frac{p_{t5}}{p_{t4}} = \left[1 - \frac{T_{t4} - T_{t5}}{\eta_t T_{t4}} \right]^{\frac{\gamma}{\gamma-1}}. \quad (6.69)$$

Similarly, since for an expansion $\eta_{pol} = dT_t/(dT_t)_{is}$, it follows that

$$\frac{p_{t5}}{p_{t4}} = \left[\frac{T_{t5}}{T_{t4}} \right]^{\frac{\gamma}{\eta_{pol}(\gamma-1)}}. \quad \text{Consequently,} \quad (6.70)$$

$$\eta_t = \frac{1 - \left[\frac{p_{t5}}{p_{t4}} \right]^{\frac{\eta_{pol}(\gamma-1)}{\gamma}}}{1 - \left[\frac{p_{t5}}{p_{t4}} \right]^{\frac{\gamma-1}{\gamma}}}. \quad (6.71)$$

Typical variations of η_c and η_t as functions of pressure ratio are given in Figure 6.17 for a polytropic efficiency of 0.85. The curves show that η_c decreases and η_t increases with increasing pressure ratio.

Another factor that can affect the output of the actual turbojet cycle is the variation of specific heat c_p with the conditions of the gas. Under normal working conditions, generally, c_p is a function of temperature alone.

Figure 6.18 shows the variation of c_p with temperature for air and typical combustion gases (Reference 23). The curves indicate that c_p rises somewhat with increasing temperature and with increasing fuel-air ratio. The opposite is true of the specific heat ratio, $\gamma = c_p/c_v$, since this quantity is given by (see Chapter 2)

$$\frac{1}{\gamma} = 1 - \frac{R_a}{Mc_p} \quad (6.72)$$

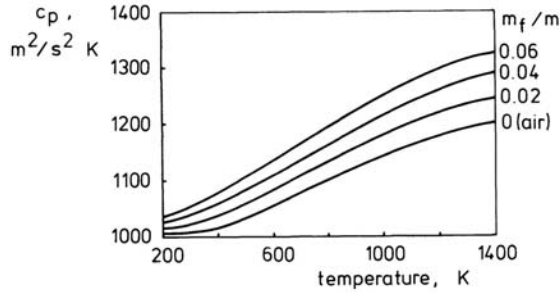


Figure 6.18 Dependence of specific heat on temperature

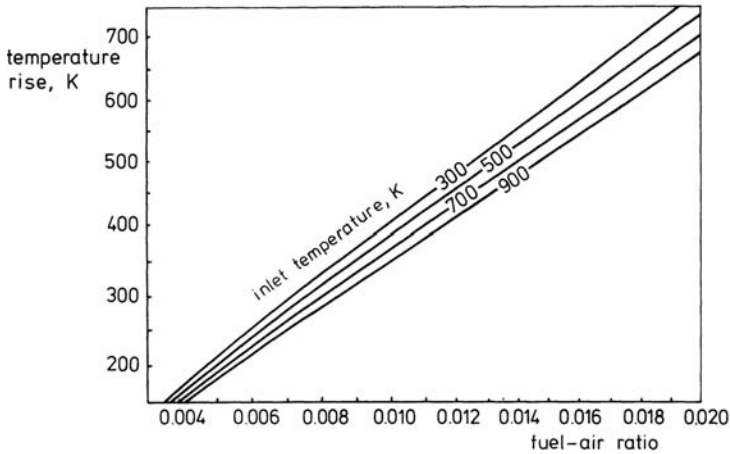


Figure 6.19 Temperature rise for standard fuel

where R_a is the universal gas constant and M the molecular mass of the gas.

It is important to note that the molecular mass of combustion gases is approximately equal to that of air so that γ is related to c_p by Equation (6.72) with $R = R_a/M = 287 \text{ m}^2/\text{s}^2\text{K}$. For design calculations, it is common practice to use the following mean values of c_p and γ for the compression and expansion processes, intake and compressor (air): $c_p = 1005 \text{ m}^2/\text{s}^2\text{K}$, $\gamma = 1.4$, turbine and nozzle (gas): $c_p = 1147 \text{ m}^2/\text{s}^2\text{K}$, $\gamma = 1.333$.

In order to establish the fuel consumption for given values of T_{i3} and T_{i4} , it is essential to match the heat energy, that is, to balance the sum of the heat energy in the air mass flow rate at the inlet of the combustion chamber and the fuel mass flow rate at the fuel temperature to that in the combustion gas at the turbine entry temperature. The required computations may be facilitated by applying a chart as given in Figure 6.19, which shows the temperature increase ($T_{i4} - T_{i3}$) as a function of fuel-air ratio for a number of initial temperatures T_{i3} (from Reference 23). These data concern complete burning of a reference fuel. When making use of Figure 6.19, the fuel mass flow rate is easily obtained from the product of fuel-air ratio and air mass flow rate.

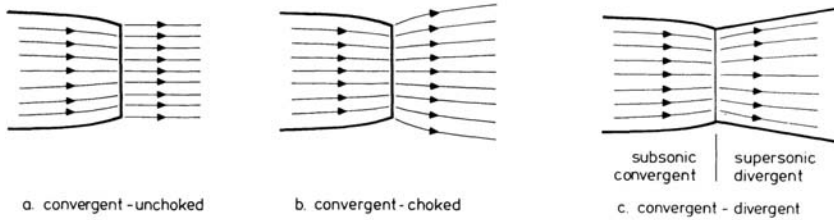


Figure 6.20 Exhaust nozzles

The combustion process involves two losses, a loss due to imperfect conversion of fuel to heat energy and a drop in total pressure. A discussion of these subjects, however, is left to the more advanced studies of propulsion.

Finally, it should be mentioned that some refinement of the ideal performance may be obtained by taking into consideration the design of the exhaust nozzle. In this connection, it is important to recognize that a gas turbine engine designed for subsonic flight speeds, usually, has a convergent nozzle (Figure 6.20).

Since the expansion process in the exhaust nozzle is nearly isentropic, we can make use of Equation (6.30) to write

$$p_{t5} = p_{te} = p_e \left[1 + \frac{\gamma - 1}{2} M_e^2 \right]^{\frac{\gamma}{\gamma - 1}}. \quad (6.73)$$

According to Appendix D, in the case of a convergent nozzle a critical pressure ratio is distinguished, which yields sonic velocity at the nozzle exit. Insertion of $M_e = 1$ into Equation (6.73) yields

$$\left[\frac{p_{te}}{p_e} \right]_{\text{cr}} = \left[\frac{\gamma + 1}{2} \right]^{\frac{\gamma}{\gamma - 1}}. \quad (6.74)$$

For air, taking $\gamma = 1.4$, the critical pressure ratio is 1.893; for gas, using $\gamma = 1.333$, $(p_{te}/p_e)_{\text{cr}}$ equals 1.851. These values apply of course only to the case of isentropic expansion in the nozzle.

For pressure ratios below the critical value, the pressure p_e in Equation (6.73) may be set equal to p_0 . Then

$$\frac{p_{te}}{p_0} < \left[\frac{\gamma + 1}{2} \right]^{\frac{\gamma}{\gamma - 1}}. \quad (6.75)$$

When the latter condition exists we have *unchoked flow*. This implies that $M_e < 1$ and $p_e = p_0$ so that the jet flows out as a cylindrical stream (Figure 6.20a). Because of the equality $p_e = p_0$ the pressure term in Equation (6.25) for the thrust is zero, and the nozzle exit Mach number is given by Equation (6.43).

When the actual nozzle pressure ratio is greater than the critical value, we have

$$\frac{p_{te}}{p_0} > \left[\frac{\gamma + 1}{2} \right]^{\frac{\gamma}{\gamma - 1}}. \quad (6.76)$$

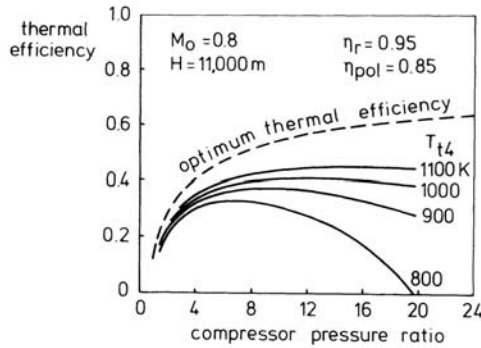


Figure 6.21 Thermal efficiency

Now we speak of *choked flow* since the mass flow rate has its maximum value. The Mach number is unity at the exit plane, and the static pressure at the nozzle exit becomes

$$\frac{p_{te}}{p_e} = \left[\frac{\gamma + 1}{2} \right]^{\frac{\gamma}{\gamma - 1}}, \quad (6.77)$$

where $p_e > p_0$.

For most control settings and flight conditions of interest to gas turbine engines the flow at the nozzle exit will be choked so that the flow behind the exit plane will expand further (Figure 6.20b).

To achieve optimum thrust under such conditions, clearly, the nozzle would have to be convergent-divergent (Figure 6.20c). Especially at supersonic flight speeds, where high pressure ratios occur, it is essential to use a convergent-divergent nozzle in order that the pressure p_e matches the ambient pressure p_0 .

Figure 6.21 presents again the thermal efficiencies of turbojet cycles, but now with typical efficiency values for intake, compressor and turbine, and with application of convergent nozzles. As assumed in Figure 6.15, the flight Mach number is 0.8 and the flight altitude 11,000 meters (I.S.A.). To simplify matters, it is adopted that the working fluid behaves throughout the engine as a perfect gas with fixed thermodynamic properties, which are equal to those of air. Also the assumptions are made of perfect combustion and isentropic expansion of the flow in the exhaust nozzle.

It is seen from Figure 6.21 that as the compressor pressure ratio is enlarged for a given turbine entry temperature the thermal efficiency is increased until a peak value is achieved. Further increase in pressure ratio then diminishes the thermal efficiency. Apparently, there is a maximum pressure ratio corresponding to some given turbine entry temperature.

In order to demonstrate how the specific fuel consumption and specific thrust are affected by the efficiencies of intake, compressor and turbine, results of design point calculations are presented in Figure 6.22, using the same basic figures and assumptions as in Figure 6.21. Looking at the actual and ideal performance in

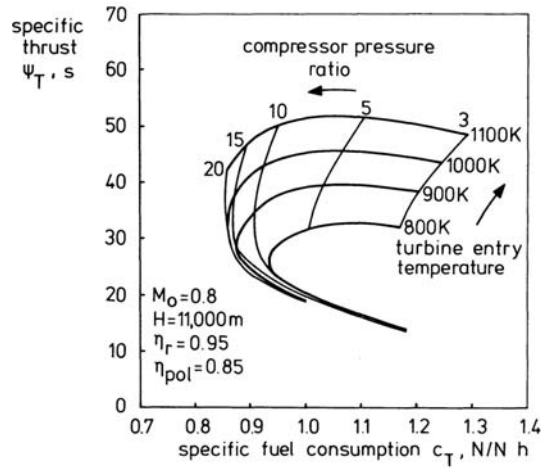


Figure 6.22 Turbojet cycle performance

Figure 6.22 and 6.15, we see that the picture is largely the same, except that noticeable performance penalties arise from the imperfections.

6.6 Typical turbojet performance

The reader is reminded that in Sections 6.4 and 6.5 we have been considering the design point performance. This term indicates the performance when the engine is running at the particular compressor pressure ratio, turbine entry temperature, atmospheric conditions and forward speed for which the components are designed. For a given engine the remaining problem is then to provide the *off-design performance*, being the performance over the entire operating range of control settings, airspeeds and atmospheric conditions.

The methods of attaining of such data are wholly beyond the scope of this book. Here we will merely illustrate the typical effects of the operational variables on the performance of the turbojet.

The engine speed is controlled by the fuel flow rate. However, for a given supply of fuel, thrust and specific fuel consumption are affected by the conditions of the air entering the intake. These conditions are defined by four variables: (1) airspeed V_0 or flight Mach number M_0 , (2) ambient pressure p_0 or geopotential pressure altitude H_p , (3) ambient temperature T_0 , and (4) humidity q . Thus we can write

$$\left. \begin{aligned} T &= T(\Gamma, M_0, H_p, T_0, q) \\ c_T &= c_T(\Gamma, M_0, H_p, T_0, q) \end{aligned} \right\}. \quad (6.78)$$

The symbol Γ in these equations is used for the engine control setting, which, usually, is represented by compressor rpm (revolutions per minute) instead of fuel flow rate.

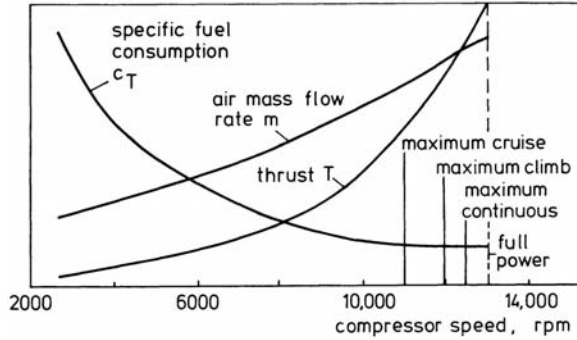


Figure 6.23 Typical static performance of turbojet

When standard atmospheric conditions are assumed, the state of the incoming airstream is completely described by flight Mach number and altitude, and the relations (6.78) reduce to

$$\left. \begin{aligned} T &= T(\Gamma, M_0, H) \\ c_T &= c_T(\Gamma, M_0, H) \end{aligned} \right\} \quad (6.79)$$

Figure 6.23 depicts how static thrust, air mass flow rate and specific fuel consumption vary with control setting. The three quantities show a strong dependence on compressor speed, owing to the increase of compressor pressure ratio and air mass flow rate with increasing compressor rpm.

It should be noticed that the engine rating *full power* in Figure 6.23 can be used only for a limited duration (for example, five minutes) in order to avoid a risk of damage to the engine. Therefore, the manufacturer designates a number of ratings at which the engine may be running for short periods and at which the engine may be operated continuously. E.g., the maximum thrust permitted for continuous operation, which is often named *maximum except takeoff (METO)-power*. The maximum control setting permitted in the cruise portion of the flight may be called *maximum cruise*.

Typical variations in thrust and specific fuel consumption with change in engine control setting and Mach number for a turbojet operating at a fixed altitude, are shown in Figure 6.24. It is seen that for any given Mach number thrust increases significantly with increasing engine rating.

As Mach number increases from static, thrust at constant rotational speed decreases because the increase of jet velocity with flight speed is relatively small. Hence, the difference between w_e and V_0 goes down as airspeed increases so that according to Equation (6.28) the specific thrust will become less.

At higher airspeeds, a beneficial effect of an increasing mass rate of air flow through the system more than balances, and thrust starts to rise. As a result, in the subsonic speed regime the thrust is more or less constant with airspeed.

Figure 6.24 also shows how specific fuel consumption varies with Mach number. Apparently, some change for the worse occurs with increasing airspeed.

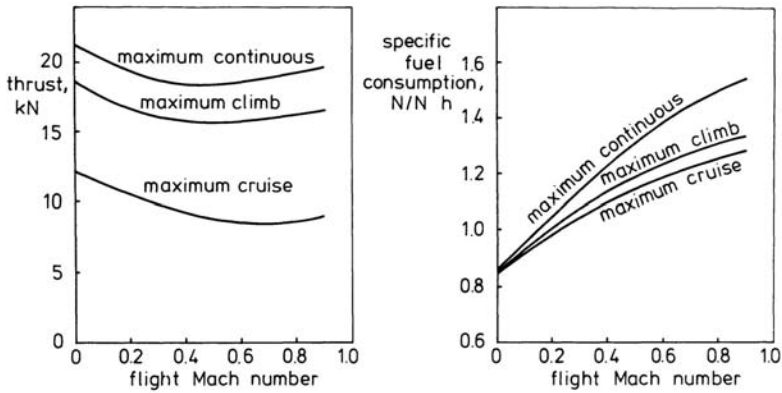


Figure 6.24 Sea-level performance of typical turbojet engine

With respect to the observation that the thrust is approximately independent of airspeed, mention must be made of the circumstance that at supersonic airspeeds the air mass flow rate becomes so large that a substantial increase in thrust takes place. The curves in Figure 6.25 illustrate the strong dependence of turbojet thrust on airspeed at Mach numbers greater than one.

It is also seen from Figure 6.25 that thrust decreases markedly with increasing altitude. As shown in Figure 6.26, the same influence of altitude on thrust is found for a typical subsonic turbojet. Specific fuel consumption, however, manifests some improvement as the airplane gains altitude. The minimum value of the specific fuel consumption occurs in the stratosphere (I.S.A.).

The effect of altitude on thrust can be explained by considering the separate influences of atmospheric pressure and temperature. Looking back to the cycle analysis in Section 6.4, it may be understood that specific thrust is not dependent on the magnitude of the ambient pressure, but only on pressure ratio and the ambient temperature. Thereby, it appears that specific thrust increases as the ambient temperature becomes less. This means that as height is gained in the troposphere, the reduction of temperature will cause an increase in specific thrust. On the contrary, at a given engine control setting and flight Mach number the mass flow rate decreases with increasing altitude due to the decreasing air density. Owing to this opposing influence of altitude on specific thrust and mass flow, the variation of thrust with altitude may be written as

$$\frac{T}{T_0} = \left[\frac{\rho}{\rho_0} \right]^n, \quad (6.80)$$

where the subscript "0" designates sea-level condition. For turbojet thrust, in the troposphere (I.S.A.), the power n is about 0.75, giving a thrust at the tropopause which is approximately 40% of its sea-level value (Figure 6.27).

In the lower stratosphere (I.S.A.), where the air temperature is constant, the thrust

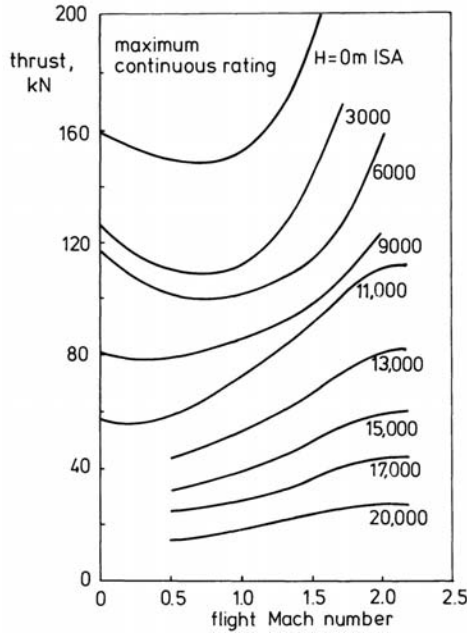


Figure 6.25 Typical performance of turbojet designed for use at supersonic speeds

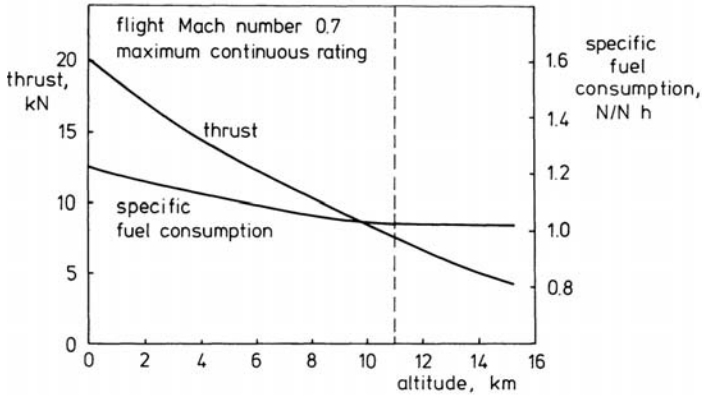


Figure 6.26 Altitude performance of typical turbojet engine

varies in proportion to the density of the air,

$$\frac{T}{T_s} = \frac{\rho}{\rho_s}, \tag{6.81}$$

where the subscript "s" denotes the condition at the tropopause.

At a given geopotential pressure altitude, a significant variable in the thrust equations is the temperature. From previous discussions we know that when the air temperature increases, air mass flow rate and specific thrust decrease. Consequently, less thrust will be delivered by the engine. In Figure 6.28 calculation

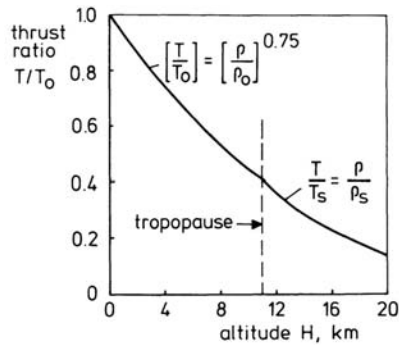


Figure 6.27 Variation of thrust with altitude

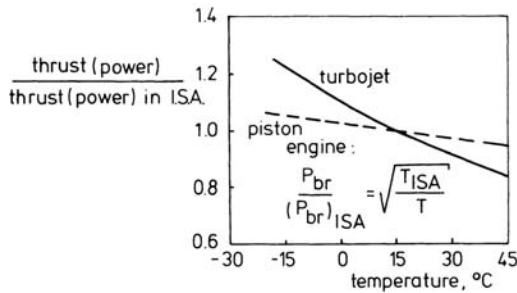


Figure 6.28 Effect of air temperature on thrust and power

results for the ratio of thrust in standard and in off-standard atmosphere are plotted against air temperature. Also is shown that the power of the piston engine is less sensitive to temperature variations than turbojet thrust.

Clearly, during warm days it may be necessary to restore the thrust. A temporary increase in thrust can be obtained by liquid injection, through which the air entering the engine is cooled by means of vaporization of a mixture of water and methanol. Addition of the coolant to the flow is usually achieved by spraying the liquid into the compressor inlet or directly into the combustion chamber.

Finally, the effect of the presence of humidity in the atmosphere must be mentioned. Investigations in Reference 24 indicate, however, that the effect of humidity on turbojet performance is generally small. The test results for which the static performance data of a turbojet at sea level were determined at constant engine speed and air temperature, show a decrease of about 5 percent in thrust for the large variation in specific humidity from zero to 0.04 (Figure 6.29). In order to illustrate the humidities that might be encountered in the operation of airplanes, the calculated variation of saturation specific humidity with altitude is also presented in Figure 6.29.

For comparison, in Figure 6.29 also is depicted the effect of humidity on the shaft power of the piston engine (Reference 25). It is clearly seen that there is a much greater effect of atmospheric humidity on piston engine power.

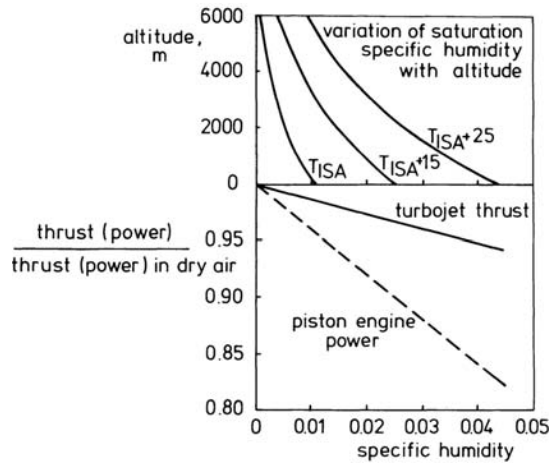


Figure 6.29 Effect of humidity on engine performance

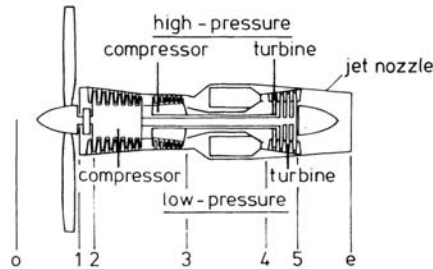


Figure 6.30 Two-spool turboprop

6.7 The turboprop engine

Figure 6.30 shows a two-spool configuration of the turboprop. This arrangement has a separate high-pressure compressor/turbine system, which is mechanically independent of the low-pressure compressor/turbine system. The low-pressure turbine extracts from the gas flow the useful power to drive the propeller.

We proceed with an examination of the thermodynamic processes in the gas generator. For simplicity's sake, we shall assume that the pressure of the gas falls completely to ambient pressure in going through the turbines.

Working through the cycle the points will be numbered as in Figure 6.30. Thus, the total temperature at the compressor inlet comes from

$$T_{t2} = T_0 \left[1 + \frac{\gamma-1}{2} M_0^2 \right], \quad (6.82)$$

where T_0 is the ambient temperature and M_0 the flight Mach number. Likewise, the total pressure at station 2 is given by

$$p_{t2} = p_0 \left[1 + \eta_d \frac{\gamma-1}{2} M_0^2 \right]^{\frac{\gamma}{\gamma-1}}, \quad (6.83)$$

where η_d is the adiabatic efficiency of the intake. By inserting Equation (6.66) into Equation (6.39), we obtain the turbine power required to drive the compressor per unit air weight flow rate as

$$\frac{P_c}{mg} = \frac{c_p}{g} T_{t2} \left[(\epsilon_c)^{\frac{\gamma-1}{\eta_{\text{pol}}\gamma}} - 1 \right], \quad (6.84)$$

where $\epsilon_c = p_{t3}/p_{t2}$ is the compressor pressure ratio and η_{pol} the polytropic efficiency of the compressor. Note that in deriving Equation (6.84) use is made of the assumption that c_p is constant throughout the engine. The quantity P_c/mg may be called *specific compressor power*.

We can use Equation (6.70) to solve for the total specific turbine power

$$\frac{P_t}{mg} = \frac{c_p}{g} T_{t4} \left[1 - \left[\frac{p_{t5}}{p_{t4}} \right]^{\frac{\eta_{\text{pol}}(\gamma-1)}{\gamma}} \right], \quad (6.85)$$

where now η_{pol} is the polytropic efficiency of the turbine.

Admitting here the simplification of assuming that in the turbine the flow expands to ambient pressure, the specific output of the engine from Equations (6.84) and (6.85) then turns out to be

$$\psi_P = \frac{P_{\text{br}}}{mg} = \frac{c_p}{g} \left[T_{t4} \left[1 - \left[\frac{p_0}{p_{t4}} \right]^{\frac{\eta_{\text{pol}}(\gamma-1)}{\gamma}} \right] - T_{t2} \left[(\epsilon_c)^{\frac{\gamma-1}{\eta_{\text{pol}}\gamma}} - 1 \right] \right]. \quad (6.86)$$

As in the case of the piston engine, the specific fuel consumption of the turboprop is expressed as the fuel weight flow rate divided by shaft brake power. Using Equation (6.38) produces the following expression

$$c_P = \frac{F}{P_{\text{br}}} = \frac{m_f g}{\psi_P mg} = \frac{c_p (T_{t4} - T_{t3})}{H \psi_P}, \quad (6.87)$$

where c_P has the dimensions N/Wh or N/kWh.

In Figure 6.31 are presented specific shaft power and specific fuel consumption of the gas generator for matched expansion in the power turbine ($p_{t5} = p_e = p_0$). These have been calculated for a range of turbine entry temperatures and compressor pressure ratios and apply to a flight Mach number of $M_0 = 0.4$ and an altitude of 4000 m (I.S.A.). Used is the assumption that c_p and γ have everywhere the same values as in ambient air.

It is seen again that in a gas turbine engine an increase in turbine entry temperature results in a considerable increase in specific output. The curves in Figure 6.31 also show that there is for any given turbine entry temperature, an optimal compressor pressure ratio producing maximum specific power. Increase in pressure ratio beyond this optimum reduces specific power, but provides an improvement

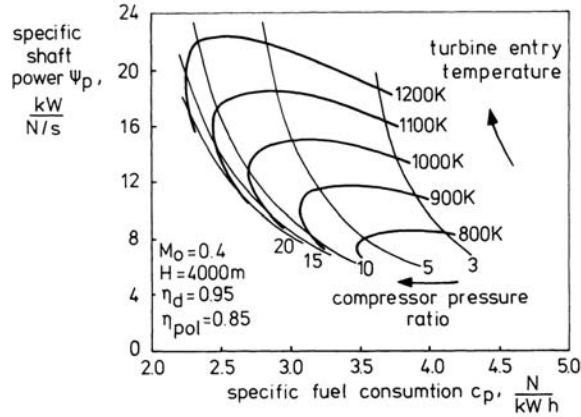


Figure 6.31 Gas generator cycle performance

of specific fuel consumption. The curves also make clear that for any given turbine entry temperature there exists an optimal value of compressor pressure ratio yielding the minimum specific fuel consumption.

Comparison of the curves in Figure 6.31 and in Figure 6.22 shows a complete similarity, only that at a given pressure ratio, the specific fuel consumption in the turboprop tends to improve somewhat with increasing turbine entry temperature, whereas in the turbojet there is an attendant increase in specific fuel consumption. The actual turboprop performance differs from the gas generator output in Figure 6.31 in that some of the useful power becomes available as jet thrust. This is due to the fact that when designing a turboprop, the pressure of the gas at the turbine exit is always chosen greater than ambient pressure in order to use the pressure drop after the turbines to eject the gases from a jet nozzle (Figure 6.30). In cruise the power produced from the exhaust thrust may amount to 10-20 percent of the useful power.

The contribution of the jet thrust, T_j , to the power output is usually expressed in terms of an apparent increase in shaft power.

The definition of the so-called *equivalent shaft power*, P_{eq} follows from

$$P_a = TV_0 = \eta_j P_{br} + T_j V_0, \quad (6.88)$$

where P_a is the power available for propulsion, and η_j the propulsive efficiency. Hence,

$$P_{eq} = \frac{P_a}{\eta_j} = P_{br} + \frac{T_j V_0}{\eta_j}. \quad (6.89)$$

When the airplane is not moving, it is assumed that the propeller generates a fixed amount of thrust per unit shaft power. Thus, the static equivalent shaft power can be expressed as

$$P_{eq} = P_{br} + \frac{T_j}{K}. \quad (6.90)$$

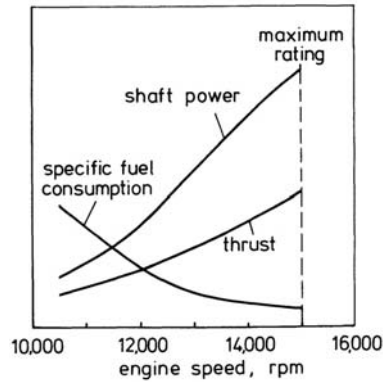


Figure 6.32 Static performance at sea level of turboprop

For an average propeller, the factor K is approximately 15 N/kW. Although the output of the turboprop often is specified in terms of equivalent shaft power, it might be worthwhile for any analysis to detail both shaft power and jet thrust.

From the above discussion it may be clear that the performance of a turboprop is dependent on the same parameters as those used for turbojet performance. When the restriction is made of operation in the International Standard Atmosphere, we can write

$$\left. \begin{aligned} P_{br} &= P_{br}(\Gamma, M_0, H) \\ T_j &= T_j(\Gamma, M_0, H) \\ c_p &= c_p(\Gamma, M_0, H) \end{aligned} \right\}. \quad (6.91)$$

Figure 6.32 shows schematically the static performance of the turboprop at sea level as a function of control setting.

The typical variations of shaft power, jet thrust, and specific fuel consumption with flight Mach number are illustrated by the curves in Figure 6.33a. The shaft power and specific fuel consumption show some improvement with increasing forward speed, whereas the thrust strongly decreases as the airspeed increases.

The qualitative effect of altitude on turboprop performance is sketched in Figure 6.33b. It can be seen that there is a loss of power and thrust and an improvement in specific fuel consumption with increasing altitude.

Like the thrust of the turbojet, also the equivalent shaft power of the turboprop at any given altitude may be related to its sea-level value by the relationship

$$\frac{P_{eq}}{(P_{eq})_0} = \left[\frac{\rho}{\rho_0} \right]^n, \quad (6.92)$$

where again in the troposphere, the exponent n has a value of approximately 0.75. At a given pressure altitude, the effect of an increase in air temperature is a loss of shaft power and jet thrust, and a worsening of specific fuel consumption (see also Figure 6.28).

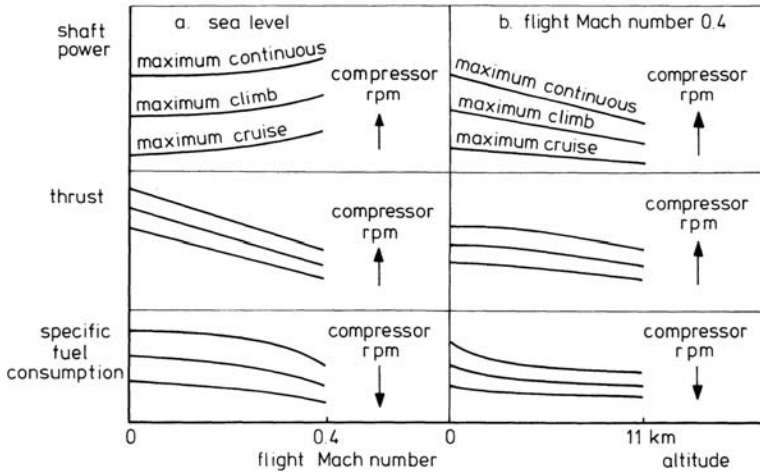


Figure 6.33 Typical turboprop performance

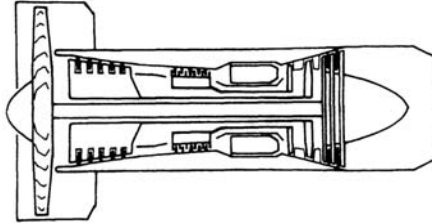


Figure 6.34 Three-spool turbofan

6.8 The turbofan

In the turboprop engine, the available energy from the gas generator is converted to one of greater mass flow rate and lower exhaust velocity, than it was directly expanded in the hot nozzle. As sketched in Figure 6.6, this is accomplished by combining the ideas of the turbojet and the turboprop.

In the two-spool layout of Figure 6.6 the fan is driven by a low-pressure turbine. This configuration is suitable for mediate compressor pressure ratios and bypass ratios. At very high values of these parameters, the three-spool system of Figure 6.34 may be required to keep the fan rotational speed within acceptable bounds.

To understand the workings of gas turbine engines it will be useful to follow a numerical example of the method of calculating turboprop specific thrust and specific fuel consumption. Therefore we shall determine the design point performance of a hypothetical two-spool turboprop engine with convergent nozzle, for a flight Mach number of 0.8 and an altitude of 11,000 m (I.S.A.).

The four design parameters for the engine are:

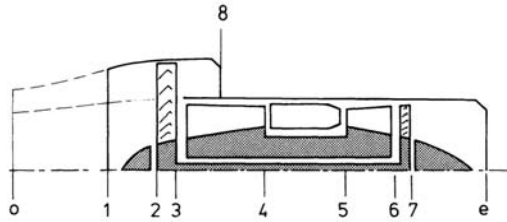


Figure 6.35 Turbofan station designations

| | |
|---------------------------------|--------|
| bypass ratio | 3.5 |
| total compressor pressure ratio | 20 |
| fan pressure ratio | 1.7 |
| turbine entry temperature | 1300 K |

Using the engine stations as numbered in Figure 6.35, we have at the fan inlet with $T_0 = 217$ K and $\gamma = 1.4$

$$T_{t2} = T_0 \left[1 + \frac{\gamma - 1}{2} M_0^2 \right] = 217(1 + 0.2 \times 0.64) = 245 \text{ K.}$$

If the pressure recovery factor of the intake is 0.95, the pressure ratio at station 2 has the following value:

$$\frac{p_{t2}}{p_0} = \eta_r \left[1 + \frac{\gamma - 1}{2} M_0^2 \right]^{\frac{\gamma}{\gamma - 1}} = 0.95(1 + 0.2 \times 0.64)^{3.5} = 1.448.$$

At the fan exit we have

$$T_{t3} = T_{t2} \left[\frac{p_{t3}}{p_{t2}} \right]^{\frac{\gamma - 1}{\eta_{\text{pol}} \gamma}} = 245(1.7)^{0.336} = 293 \text{ K,}$$

where for the polytropic efficiency a value of 0.85 is used.

The related pressure ratio is

$$\frac{p_{t3}}{p_0} = \frac{p_{t3}}{p_{t2}} \frac{p_{t2}}{p_0} = 1.7 \times 1.448 = 2.462.$$

Thus, the cold nozzle pressure ratio is

$$\frac{p_{t3}}{p_0} = 2.462.$$

When the expansion processes in the nozzles are accepted to be 100% efficient, the critical pressure ratio, from Equation (6.74) is

$$\frac{p_{t3}}{p_8} = \left[\frac{\gamma + 1}{2} \right]^{\frac{\gamma}{\gamma - 1}} = (1.2)^{3.5} = 1.893.$$

Since $p_{t3}/p_0 > p_{t3}/p_8$ the cold nozzle is choked so that $M_8 = 1.0$ and $p_8 > p_0$. Hence,

$$T_8 = T_{t3} \left(\frac{2}{\gamma+1} \right) = 293 \left(\frac{1}{1.2} \right) = 244 \text{ K},$$

$$\frac{p_8}{p_0} = \frac{p_8}{p_{t3}} \frac{p_{t3}}{p_0} = \frac{2.462}{1.893} = 1.301.$$

The cold nozzle outlet velocity is

$$w_8 = M_8 \sqrt{\gamma R T_8} = 1 \sqrt{1.4 \times 287 \times 244} = 313 \text{ m/s}.$$

The contribution of the cold stream to the specific thrust of the engine is given by

$$\frac{T_c}{mg} = \frac{m_c(w_8 - V_0)}{mg} + \frac{A_8(p_8 - p_0)}{mg},$$

where $V_0 = M_0 \sqrt{\gamma R T_0} = 0.8 \sqrt{1.4 \times 287 \times 217} = 236 \text{ m/s}$.

Using the familiar relationships $m_c = \rho_8 w_8 A_8$, $\rho_8 = \frac{p_8}{R T_8}$ and $\frac{m_c}{m} = \frac{B}{B+1}$, it readily follows that

$$\frac{T_c}{mg} = \frac{B}{B+1} \frac{1}{g} \left[(w_8 - V_0) + \sqrt{\frac{R T_8}{\gamma}} \left[1 - \frac{p_0}{p_8} \right] \right].$$

Putting in numerical values yields

$$\frac{T_c}{mg} = \frac{3.5}{(3.5+1)} \frac{1}{9.81} \left[(313 - 236) + \sqrt{\frac{287 \times 244}{1.4}} \left[1 - \frac{1}{1.301} \right] \right] = 10.2 \text{ s}.$$

The pressure ratio of the high-pressure compressor is

$$\frac{p_{t4}}{p_{t3}} = \frac{p_{t4}}{p_{t2}} \frac{p_{t2}}{p_{t3}} = \frac{20}{1.7} = 11.765.$$

The total temperature at the outlet from the high-pressure compressor comes from

$$T_{t4} = T_{t3} \left[\frac{p_{t4}}{p_{t3}} \right]^{\frac{\gamma-1}{\eta_{\text{pol}} \gamma}} = 293 (11.765)^{0.336} = 671 \text{ K},$$

where again is adopted: $\eta_{\text{pol}} = 0.85$.

The high-pressure turbine temperature drop follows from the equality of compressor and turbine powers. Admitting the assumption that throughout the engine the specific heats of the working fluid have the same values as in atmospheric air ($c_p = 1005 \text{ m}^2/\text{s}^2\text{K}$, $\gamma = 1.4$, $R = 287 \text{ m}^2/\text{s}^2\text{K}$), we obtain

$$T_{t5} - T_{t6} = \frac{1}{\eta_m} (T_{t4} - T_{t3}),$$

where η_m is the mechanical efficiency. This factor takes into account the losses which occur when power is transmitted from the turbine to the compressor. Setting $\eta_m = 0.98$, we find the temperature behind the high-pressure turbine to be

$$T_{t6} = T_{t5} - \frac{1}{\eta_m}(T_{t4} - T_{t3}) = 1300 - \frac{1}{0.98}(671 - 293) = 914 \text{ K.}$$

The low-pressure turbine temperature drop follows from the power demand of the low-pressure compressor,

$$m_h(T_{t6} - T_{t7}) = \frac{1}{\eta_m}m(T_{t3} - T_{t2}).$$

Remembering that $m/m_h = B + 1$, and using $\eta_m = 0.98$

$$T_{t7} = T_{t6} - \frac{(B+1)}{\eta_m}(T_{t3} - T_{t2}) = 914 - \frac{(3.5+1)}{0.98}(293 - 245) = 694 \text{ K.}$$

To calculate the hot nozzle pressure ratio we write

$$\frac{p_{t7}}{p_0} = \frac{p_{t7}}{p_{t5}} \frac{p_{t5}}{p_{t4}} \frac{p_{t4}}{p_{t3}} \frac{p_{t3}}{p_0}.$$

The total turbine pressure ratio is given by

$$\frac{p_{t7}}{p_{t5}} = \left[\frac{T_{t7}}{T_{t5}} \right]^{\frac{\gamma}{\eta_{\text{pol}}(\gamma-1)}}.$$

With a turbine polytropic efficiency of 85% we get

$$\frac{p_{t7}}{p_{t5}} = \left[\frac{694}{1300} \right]^{4.118} = 0.07544.$$

The pressure loss in the combustor is assumed to be 5% of the compressor delivery pressure, so that

$$\frac{p_{t5}}{p_{t4}} = 0.95.$$

With the substitution of these numbers, the nozzle pressure ratio becomes

$$\frac{p_{t7}}{p_0} = 0.07544 \times 0.95 \times 11.765 \times 2.462 = 2.076.$$

It appears that also the hot nozzle is choked so that $M_e = 1.0$ and $p_e > p_0$. Accordingly,

$$T_e = T_{t7} \left(\frac{2}{\gamma+1} \right) = 694 \left(\frac{1}{1.2} \right) = 578 \text{ K,}$$

$$\frac{p_e}{p_0} = \frac{p_e}{p_{t7}} \frac{p_{t7}}{p_0} = \frac{2.076}{1.893} = 1.097.$$

The jet velocity of the hot stream is

$$w_e = M_e \sqrt{\gamma R T_e} = 1 \sqrt{1.4 \times 287 \times 578} = 482 \text{ m/s.}$$

The contribution of the hot stream to the specific thrust of the engine is given by

$$\frac{T_h}{mg} = \frac{m_h(w_e - V_0)}{mg} + \frac{A_e(p_e - p_0)}{mg}.$$

Recalling that $m_h/m = 1/(B+1)$, we find

$$\begin{aligned} \frac{T_h}{mg} &= \frac{1}{B+1} \frac{1}{g} \left[(w_e - V_0) + \sqrt{\frac{RT_e}{\gamma}} \left[1 - \frac{p_0}{p_e} \right] \right] \\ &= \frac{1}{(3.5+1)} \frac{1}{9.81} \left[(482 - 236) + \sqrt{\frac{287+578}{1.4}} \left[1 - \frac{1}{1.097} \right] \right] = 6.3 \text{ s.} \end{aligned}$$

The total specific thrust is

$$\psi_T = \frac{T_c}{mg} + \frac{T_h}{mg} = 10.2 + 6.3 = 16.5 \text{ s.}$$

The specific fuel consumption comes by dividing the fuel weight flow rate by the thrust

$$c_T = \frac{m_f g}{T}.$$

The fuel flow equation may be written as

$$\eta_b m_f H = m_h c_p (T_{t5} - T_{t4}),$$

where H is the heating value of the fuel ($H = 4.31 \times 10^7$ J/kg) and η_b is the combustion efficiency, which is introduced to take into account the incomplete burning of the fuel flow. Combining the latter two equations leads to

$$c_T = \frac{1}{B+1} \frac{c_p}{H \eta_b} \frac{(T_{t5} - T_{t4})}{\psi_T}.$$

Assuming $\eta_b = 0.95$, we obtain

$$c_T = \frac{1005(1300 - 671)3600}{(3.5+1)4.31 \times 10^7 \times 0.95 \times 16.5} = 0.76 \text{ N/Nh.}$$

The above calculations indicate that bypassing of air results in a low specific thrust compared with the turbojet (see Figure 6.22). On the other hand, the figure obtained for the specific fuel consumption illustrates that at a flight Mach number $M_0 = 0.8$ the efficiency of the turbofan is markedly better than that of the turbojet. To explain the principal flight regimes for application of a specific engine type, particularly, the propulsive efficiency may be used. According to Equation (6.51), the propulsive efficiency is given by the ratio of power available to the increase in kinetic energy of the flow. In terms of the equivalent jet velocity, we have

$$\eta_j = \frac{2}{1 + \frac{(w_e)_{\text{eq}}}{V_0}}, \quad \text{and also} \quad (6.93)$$

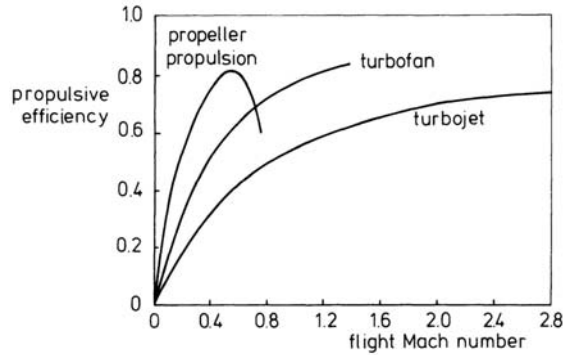


Figure 6.36 Typical trends of propulsive efficiency

$$\eta_j = \frac{2}{2 + \frac{T}{mV_0}}. \quad (6.94)$$

Clearly, propulsive efficiency increases with increasing flight speed and mass flow rate, and decreases with decreasing jet velocity.

A comparison of propulsive efficiency values for the various types of engines is sketched in Figure 6.36. Since turbojet thrust is produced at high jet velocities, the higher the flight speed, the higher is its propulsive efficiency. Due to the increased mass flow rate and reduced mean exhaust velocity of the turbofan, this engine type is best in the high-subsonic speed range. At low-subsonic flight speeds, the propeller remains much to be preferred to the other forms of propulsion.

Of course, the ultimate basis on which the engine types must be compared is the overall efficiency, which follows from the product of propulsive efficiency and thermal efficiency.

The thermal efficiency is determined by the parameters defining the thermodynamic cycle of the flow, through which it is mainly within the control of the engine designer. Obviously, measures to improve the propulsive efficiency are only valuable if there is a resultant increase in overall efficiency.

The way in which for a turbofan with given gasgenerator, thrust and specific fuel consumption vary with bypass ratio, is sketched in Figure 6.37. Two flight conditions, takeoff and cruise at the tropopause (I.S.A.) are shown. The main features are that thrust increases and specific fuel consumption decreases by application of a greater bypass ratio.

The typical variation of thrust and specific fuel consumption with flight Mach number and control setting, is explained by the curves in Figure 6.38. Compressor speed, expressed as percentage of maximum, is used to specify the engine control setting. From these plots we may see that in comparison with the turbojet there are vital reductions in specific fuel consumption (cf. Figure 6.24). On the other hand, the turbofan thrust shows a significant decrease with airspeed.

The variation of turbofan thrust with altitude may also be represented by Equation (6.80). Now, the value of the exponent depends on bypass ratio, and because of

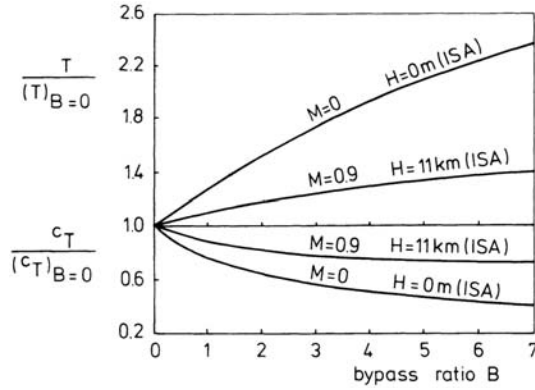


Figure 6.37 Effect of bypass ratio on performance of turbofan

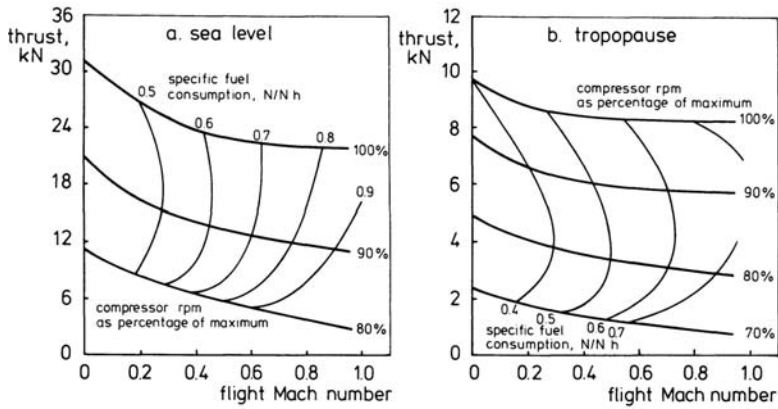


Figure 6.38 Typical turbofan engine performance

the large mass flow rates involved, n is usually near one.

Finally, it should be realized that the calculations made in this section concern the bare engine. The airplane performance equations, of course, require the use of the installed thrust and specific fuel consumption, which include both the detrimental effects associated with the integration of engine and airplane structure and the losses owing to bleeding compressed air and power extraction. However, a detailed analysis of all these effects is not simple and certainly beyond the scope of this text.

Chapter 7

PROPELLER PERFORMANCE

7.1 Propeller thrust and efficiency

As illustrated in Figure 7.1, an airplane propeller consists of two or more blades of which the blade sections are airfoil shaped. The propeller blades convert the shaft power of the engine into a thrust by pushing air backward, whereby the propeller thrust is given by the time rate of change of momentum of the air that passes through the propeller. The control surface 0 in Figure 7.1 is far upstream of the propeller where air pressure and flow velocity have their freestream values p_0 and V_0 . The aft plane e is sufficiently far downstream that the local pressure equals the freestream pressure p_0 . Then

$$T = m(w_e - V_0), \quad (7.1)$$

where w_e is the final slipstream velocity.

Equation (7.1) defines the thrust which is obtained in the absence of the airframe. Therefore, this force may be called the *freeair thrust*.

The work done by the thrust per unit time is the power available P_a , and the ratio of P_a to shaft power P_{br} is the propulsive efficiency of the propeller (see also Equation (6.1)),

$$\eta_j = \frac{P_a}{P_{br}} = \frac{TV_0}{P_{br}}. \quad (7.2)$$

Consequently, the variation of thrust with airspeed is given by

$$T = \eta_j \frac{P_{br}}{V_0}. \quad (7.3)$$

From our discussion in Chapter 6 we know that at a given altitude and engine control setting, it is a good approximation to assume that the shaft power is independent of forward velocity. If we also assume that η_j has a constant value, the

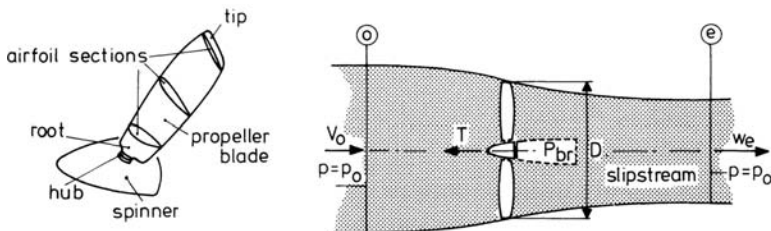


Figure 7.1 Shape and propulsive action of airplane propeller

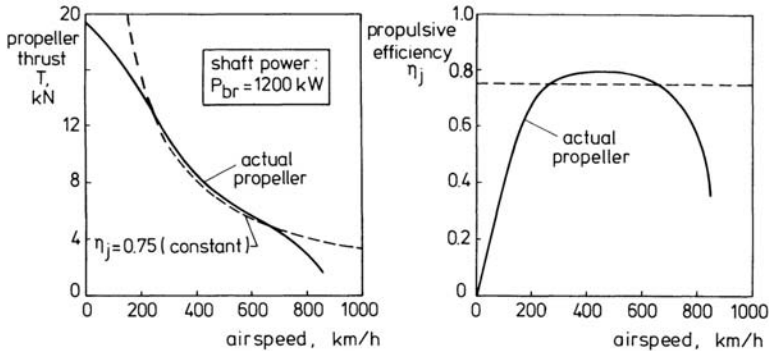


Figure 7.2 Typical propeller performance

thrust predicted by Equation (7.3) will strongly diminish as airspeed increases. This strong dependence of thrust on airspeed holds also for an actual propeller, as sketched in Figure 7.2. At zero velocity the actual propeller generates a finite thrust, which is called *static thrust*. Under this condition, the propulsive efficiency from Equation (7.2) is zero. In the first instance η_j increases considerably with airspeed, but beyond 200 km/h the propulsive efficiency remains more or less constant until, at about 700 km/h, the efficiency is seriously impaired as the blade tips approach the speed of sound.

Essentially, the speed of the propeller blade tip relative to the air is the vector sum of the forward velocity V_0 in the direction of the propeller axis and the rotational velocity ωR , directed perpendicular to the propeller axis (Figure 7.3). The magnitude of the propeller tip speed is thus given by

$$V_t = \sqrt{V_0^2 + (\omega R)^2} = \sqrt{V_0^2 + (\pi n_p D)^2}, \quad (7.4)$$

where R is the blade radius, ω is the angular velocity and n_p is the number of revolutions per second of the propeller ($\omega = 2\pi n_p$). On the small airplanes with piston-engine, the propeller may be connected directly with the engine crankshaft. In this case the propeller speed n_p equals the engine speed n . On turboprop airplanes there is always a gearbox, which makes that the propeller turns much more slowly than the turbine shaft that drives it so that the ratio n_p/n is less than one.

As the tip speed V_t approaches the speed of sound, the compressibility effects will dramatically reduce the propulsive efficiency of the propeller. This factor limits the use of the current propellers to a maximum flight Mach number of about 0.6 (see Figures 7.2 and 6.36).

Some further insight into the fundamental relationship between thrust, shaft power, propulsive efficiency and airspeed can be obtained from a classic treatment which is known as the *momentum theory*. As depicted in Figure 7.4, the assumption is made that the flow passing through the propeller forms a well-defined streamtube, where the propeller is replaced by an actuator disk. Furthermore, this theory assumes that the pressures and velocities are evenly distributed over the disk area

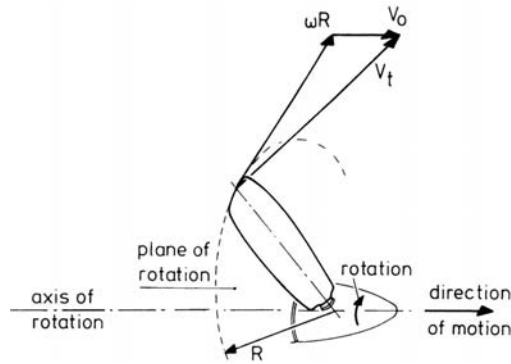


Figure 7.3 Propeller tip speed

and that the flow is incompressible and irrotational. By the action of the propeller the freestream velocity V_0 is increased to the slipstream velocity $(V_0 + V_{a3})$, and a certain contraction of the air flow passing through the disk occurs.

As the flow approaches the disk, the freestream velocity V_0 increases to a value $(V_0 + V_a)$ at the disk. At the same time the static pressure p_0 falls to p_1 just in front of the disk. In the slipstream behind the disk the velocity rises to a value $(V_0 + V_{a3})$. The pressure increases to p_2 on passing through the disk and decays to the freestream value p_0 in the slipstream.

Since the thrust is given by the time rate of change of axial momentum, we get

$$T = \rho \frac{\pi}{4} D^2 (V_0 + V_a) V_{a3}, \quad (7.5)$$

where ρ is the ambient density and D is the diameter of the disk.

The thrust acting on the disk is also given by

$$T = \frac{\pi}{4} D^2 (p_2 - p_1). \quad (7.6)$$

Application of Bernoulli's equation (Appendix D) on each side of the actuator disk yields

$$\left. \begin{aligned} p_0 + \frac{1}{2} \rho V_0^2 &= p_1 + \frac{1}{2} \rho (V_0 + V_a)^2 & \text{and} \\ p_2 + \frac{1}{2} \rho (V_0 + V_a)^2 &= p_0 + \frac{1}{2} \rho (V_0 + V_{a3})^2 \end{aligned} \right\} \quad (7.7)$$

From Equations (7.6) and (7.7), we find

$$T = \rho \frac{\pi}{4} D^2 (V_0 + \frac{1}{2} V_{a3}) V_{a3}. \quad (7.8)$$

Comparing Equations (7.5) and (7.8), we obtain

$$V_a = \frac{1}{2} V_{a3}. \quad (7.9)$$

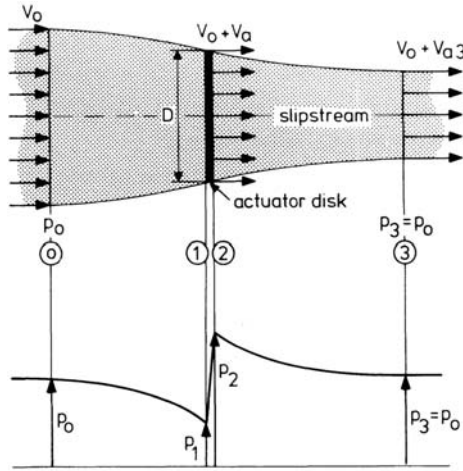


Figure 7.4 Velocities and pressures of the momentum theory

The latter equality shows that half the total increment in velocity occurs in front of the disk. The shaft power may be expressed as the increase in kinetic energy of the air mass flow rate,

$$P_{br} = \frac{1}{2} \rho \frac{\pi}{4} D^2 (V_0 - V_a) [(V_0 + V_{a3})^2 - V_0^2] = \rho \frac{\pi}{4} D^2 (V_0 - V_a)^2 V_{a3}. \quad (7.10)$$

By combining Equations (7.5) and (7.10) we get the following expression for the propulsive efficiency (cf. Equation (6.52))

$$\eta_j = \frac{TV_0}{P_{br}} = \frac{V_0}{V_0 + V_a} = \frac{1}{1 + \frac{V_a}{V_0}} \quad \text{or} \quad (7.11)$$

$$\eta_j = \frac{2}{2 + \frac{V_{a3}}{V_0}}. \quad (7.12)$$

Evidently, the propulsive efficiency can also be expressed in terms of the thrust,

$$\eta_j = \frac{2}{1 + \sqrt{1 + \frac{T}{\frac{1}{2} \rho \frac{\pi}{4} D^2 V_0^2}}}. \quad (7.13)$$

Emphasis is made that Equations (7.12) and (7.13) represent the theoretical upper limit of the attainable propulsive efficiency since the underlying theory does not include rotational kinetic energy in the slipstream and assumes that the axial velocity is uniform over the disk.

Clearly, the value of the momentum theory lies especially in providing a qualitative appreciation of the way in which propellers are likely to act under different design and operating conditions. E.g., Equation (7.12) indicates that at a given airspeed the propulsive efficiency increases as the slipstream velocity decreases. Further, Equation (7.13) tells us that in order to achieve this improvement of η_j at a constant value of the thrust, the propeller diameter must be enlarged.

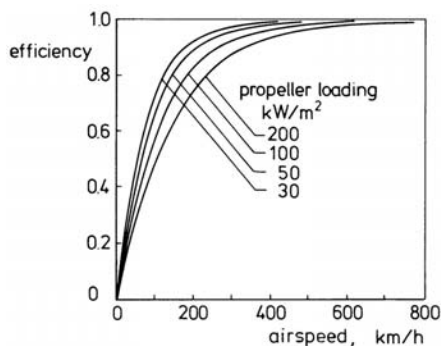


Figure 7.5 Variation of propulsive efficiency with airspeed

Another result of the momentum theory is illustrated by Figure 7.5, where is plotted the propulsive efficiency as a function of airspeed for various values of the loading of the propeller, $P_{br}/\frac{\pi}{4}D^2$. It is seen that lower efficiencies may be expected as this quantity increases.

The values of $P_{br}/\frac{\pi}{4}D^2$ considered in Figure 7.5 represent the loading of propellers which are currently in service. The order of magnitude of these loadings is such that all existing propellers may be typified as lightly loaded. This term is used to indicate that their performance may be effectively examined to the neglect of the rotational kinetic energy in the slipstream. Under this condition the propulsive efficiency, especially, is determined by losses owing to the profile drag of the blades.

A second category of losses comes about in consequence of the fact that the propeller blades are also subject to induced drag. The general cause of losses is of course that not all kinetic energy in the slipstream can be recovered and converted into thrust. The portion that axial and rotational kinetic energy contributes to the total losses is dependent on the number of blades, tip speed and propeller loading. Because of the need to conserve fuel, in the last decades of the twentieth century the propeller has been considered again as a propulsor for large commercial air transports (Reference 28). Figure 7.6 shows schematically the various advanced turboprop concepts which have been proposed for future application at high- subsonic airspeeds. The powerplants incorporate a sophisticated gas generator and one or two multibladed small-diameter propellers known as *propfans*. To reduce compressibility losses, the thickness-to-chord ratios of the blades are roughly half those of the modern conventional propeller blades. In addition, the blade tips show a large angle of sweep. The development programs were directed toward tractor and pusher configurations and concerned single-rotating propfans and counterrotating systems. The counterrotating propfan consists of two rows of blades rotating in opposite directions. These systems have the potential of a recovery of the swirl losses because the rotational velocities of the front row may be removed by the rear half. Both single and counterrotating propfans have advanced gearboxes capable of transmitting high engine powers and pitch-change mechanisms capable

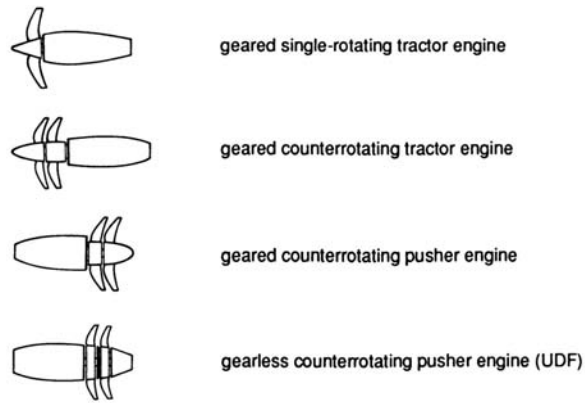


Figure 7.6 Advanced turboprop systems

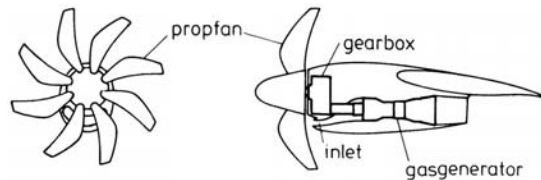


Figure 7.7 Propfan powerplant

of governing the eight to ten highly loaded fan blades (Figure 7.7). Of importance was also the program for a gearless counterrotating pusher engine, the unducted fan (UDF), where the propfans are directly connected to counterrotating turbine stages. From aerodynamic and acoustic considerations, there is a strong need to limit the tip speed of the blades. This requirement explains the relative small fan diameters, which together with the high engine powers involved cause a propeller loading of about three times that of the conventional turboprops. This implies correspondingly high torque forces that are responded by imparting a large amount of angular momentum to the slipstream. The resulting high rotational kinetic energy in the airflow contributes directly to the reduced losses of the system and leads to the indication “highly loaded” for this class of propellers.

Flight tests have shown that actually significant improvements in propulsive efficiency can be achieved. However, interior and exterior noise problems seem to introduce prohibitive objections for practical applications.

7.2 Propeller geometry

Under normal flight conditions the direction of the propeller axis may be considered as coinciding with the direction of the flight velocity (Figure 7.8). If induced velocities in the flow through the propeller are neglected, then, as in Equation (7.4), the velocity of a blade section relative to the air is composed of a translation with airspeed V_0 and a simultaneous rotation about the propeller axis with

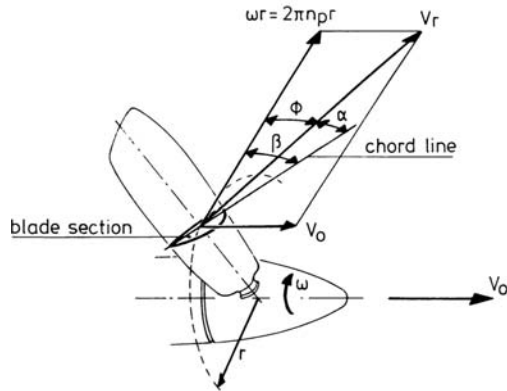


Figure 7.8 Motion of a propeller blade section

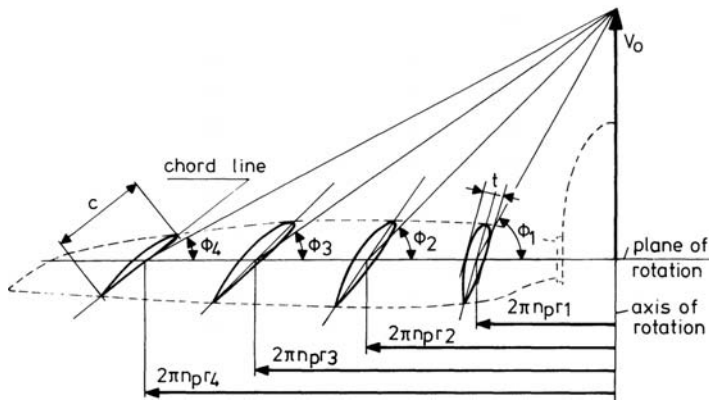


Figure 7.9 Variation of advance angle and blade angle from hub to tip

rotational speed ωr :

$$V_r = \sqrt{V_0^2 + (\omega r)^2} = \sqrt{V_0^2 + (2\pi n_p r)^2}. \quad (7.14)$$

Evidently, the component V_0 has the same value at each blade section, whilst the rotational speed is proportional to the distance r from the propeller axis to the blade section.

The angle between the relative velocity V_r and the plane of propeller rotation is called the *advance angle*, ϕ . From Figure 7.8 we find

$$\tan \phi = \frac{V_0}{\omega r} = \frac{V_0}{2\pi n_p r}. \quad (7.15)$$

For given values of airspeed V_0 and angular velocity ω , the advance angle decreases from the root to the tip of the blade since the root sections are revolving slower than the tip sections (Figure 7.9).

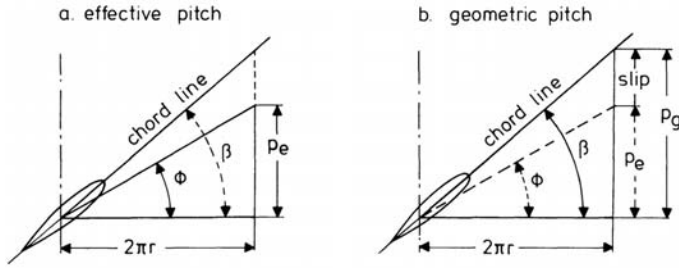


Figure 7.10 Effective and geometric propeller pitch

The advance angle of the tip section is given by

$$\tan \phi_t = \frac{V_0}{\omega R} = \frac{V_0}{\pi n_p D}. \quad (7.16)$$

The dimensionless quantity $V_0/(n_p D)$ is called the *advance ratio* and given the symbol J ,

$$J = \frac{V_0}{n_p D} = \pi \tan \phi_t. \quad (7.17)$$

After one revolution of the propeller axis, the propeller has advanced a certain distance in the direction of flight. This length is called the *effective pitch*, p_e , of the helical motion performed by each point on the propeller (Figure 7.10a).

The effective pitch of the propeller is related to the advance angle and propeller speed by

$$p_e = 2\pi r \tan \phi = 2\pi r \frac{V_0}{2\pi n_p r} = \frac{V_0}{n_p}. \quad (7.18)$$

It can be further seen that

$$J = \frac{V_0}{n_p D} = \frac{p_e}{D}. \quad (7.19)$$

Hence the advance ratio is a measure of the effective pitch. A low value of J implies a fine pitch and a high J a coarse pitch.

The angle from the plane of propeller rotation to the well-defined chord line of the blade section is the *blade angle* β (see Figure 7.8). The angle β is the sum of the advance angle and the angle of attack,

$$\beta = \phi + \alpha. \quad (7.20)$$

At this point we state that a low drag behavior of the propeller requires that the angle of attack at each blade radius has approximately the same value as will be explained in the next section. For that reason, the propeller blades always appear to be twisted with the smallest blade angle at the tip and the greatest at the hub, owing to the increase in advance angle (see Figure 7.9).

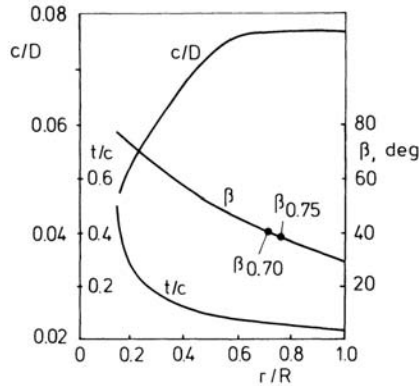


Figure 7.11 Geometric data of a propeller blade

Figure 7.11 shows for a given propeller the variation of the blade angle along the blade radius, which, customarily, is designated by specifying β at 75% or 70% of the radial distance. The higher the airspeed for which a propeller is designed, the greater the angle $\beta_{0.75}$ or $\beta_{0.70}$ and thus all blade angles at which the blade sections are set.

The blade angles are often given in terms of the geometric pitch p_g . This parameter is obtained from the geometry of Figure 7.10b. When expressed in terms of $\beta_{0.75}$ we get

$$p_g = 2\pi r \tan \beta = 2\pi \frac{3}{4} R \tan \beta_{0.75}. \quad \text{Thus,} \quad (7.21)$$

$$\beta_{0.75} = \tan^{-1} \left[\frac{4}{3} \frac{p_g}{\pi D} \right]. \quad (7.22)$$

Geometric pitch is the distance that the propeller would travel per complete turning if it were rotated in a solid medium. The difference between the geometric pitch and the effective pitch is called *propeller slip*.

Figure 7.11 shows also the typical distribution of maximum blade thickness-to-chord ratio, t/c , and relative chord length, c/D . Especially, structural requirements make that near the root the thickness of the blade sections is relatively large. Also, for structural reasons the chord lengths over the outer part of the blade radius is kept constant.

7.3 Blade element theories

The calculation of propeller characteristics from experimental airfoil data is known as the blade element theory. In order to determine the forces at any blade radius, the blades are divided into radial elements of width dr and chord length c (Figure 7.12).

The method requires that the blade elements can be considered individually. In other words, the blade element theory assumes that there are no forces acting in

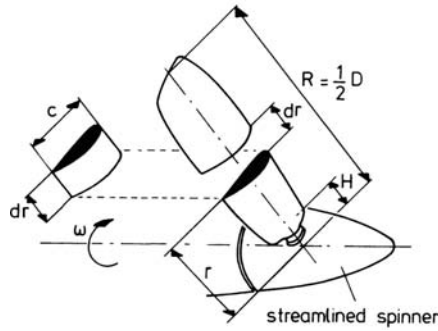


Figure 7.12 Blade element

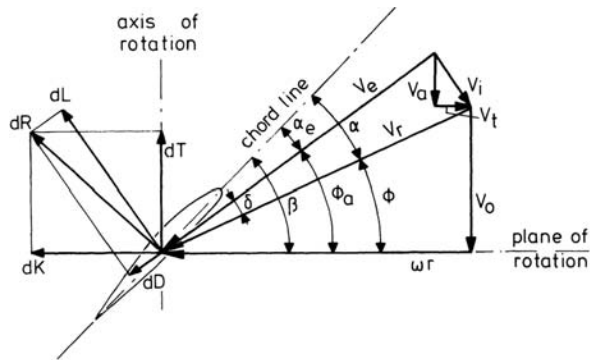


Figure 7.13 Blade element velocity and force diagram

radial direction so that each element is subjected to two-dimensional flow. The velocity and force diagram of a blade element at a radius r is depicted in Figure 7.13. Under the influence of the forces produced by the propeller, an extra velocity V_i is induced at the blade element, which shifts the relative velocity V_r through an angle δ . The axial component $V_a = V_i \cos \phi_a$ is related to the thrust generated by the blade element while the presence of the component $V_t = V_i \sin \phi_a$ represents the rotation imparted to the slipstream. Apparently, the effect of V_i is to lower the angle of attack α to the effective angle of attack α_e .

The *effective velocity* V_e experienced by the blade element is obtained by the relative velocity V_r and the induced velocity V_i . As indicated in Figure 7.13, the induced velocity is approximately perpendicular to V_e , giving

$$V_e = \sqrt{V_0^2 + (\omega r)^2 - V_i^2} \tag{7.23}$$

The angle formed by the effective velocity and the plane of rotation may be called the aerodynamic advance angle ϕ_a .

From Figure 7.13, the following relations are apparent:

$$\left. \begin{aligned} \beta &= \phi + \alpha \\ \alpha_e &= \beta - \phi_a \\ \phi_a &= \phi + \delta \\ \alpha &= \delta + \alpha_e \end{aligned} \right\}. \quad (7.24)$$

By definition, the lift dL is perpendicular to V_e , and the drag dD is precisely in the direction of V_e .

The vector sum of dL and dD forms the aerodynamic force dR . The component of dR parallel to the propeller axis furnishes the thrust produced by a single blade element,

$$dT = dL \cos \phi_a - dD \sin \phi_a. \quad (7.25)$$

The force opposing the rotation of the blade element is

$$dK = dL \sin \phi_a + dD \cos \phi_a. \quad (7.26)$$

The power required to rotate the blade element is given by

$$dP_p = \omega r dK = \omega r (dL \sin \phi_a + dD \cos \phi_a). \quad (7.27)$$

Substituting the relationships $dL = c_\ell \frac{1}{2} \rho V_e^2 cdr$ and $dD = c_d \frac{1}{2} \rho V_e^2 cdr$ in Equations (7.25) and (7.27) gives the expressions for dT and dP_p respectively:

$$dT = \frac{1}{2} \rho V_e^2 c (c_\ell \cos \phi_a - c_d \sin \phi_a) dr \quad (7.28)$$

$$dP_p = \frac{1}{2} \rho V_e^2 \omega r c (c_\ell \sin \phi_a + c_d \cos \phi_a) dr. \quad (7.29)$$

Emphasis is made that the coefficients c_ℓ and c_d are functions of angle of attack α_e , helical Mach number $M_e = V_e/c$, and Reynolds number (see Chapter 4),

$$c_\ell = c_\ell(\alpha_e, M, \text{Re}) \quad (7.30)$$

$$c_d = c_d(\alpha_e, M, \text{Re}). \quad (7.31)$$

Essentially, the difficulty in determining thrust and propeller power at given propeller operating conditions is to find the value of α_e at each radial station. This angle, in turn, is dependent on the induced velocity. Although V_i is normally relatively small, it is essential to account for its effect when the aim is to obtain accurate results.

We may attack the problem by using the simple momentum theory of Section 7.1, which predicts that the axial component of the induced velocity at the propeller plane has a value of one-half the final velocity in the slipstream. This enables us to express the propulsive force produced by all blade elements located at a radial distance r from the propeller axis as (cf. Equation (7.8))

$$BdT = 2\pi r dr \rho (V_0 + V_i \cos \phi_a) 2V_i \cos \phi_a, \quad (7.32)$$

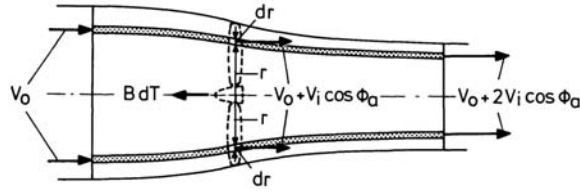


Figure 7.14 Annular stream tube

where B represents the number of propeller blades.

In deriving Equation (7.32) the assumption is made that the total thrust BdT is given by the average time rate of change of axial momentum of the air flowing through an annular stream tube, which at the propeller plane has a radius r and is dr wide.

The preceding system of equations can now be solved to obtain the value of the effective angle of attack. Once the angle α_e has been found, the propeller thrust and propeller power are obtained by integrating Equations (7.28) and (7.29) between $r = H$ (propeller hub) and $r = R$ (propeller tip). Thus

$$T = B \int_H^R dT = B \int_H^R \frac{1}{2} \rho V_e^2 c (c_\ell \cos \phi_a - c_d \sin \phi_a) dr \quad (7.33)$$

$$P_p = B \int_H^R dP_p = B \int_H^R \frac{1}{2} \rho V_e^2 \omega r c (c_\ell \sin \phi_a - c_d \cos \phi_a) dr. \quad (7.34)$$

The above combination of theories is called *momentum blade element theory*. This technique furnishes a rapid method for calculating the performance of propellers of known design. However, such factors as non-uniform flow, blade interference effects, and tip losses are ignored by this approach. For that, other blade element theories are available of which most elements are based on treatments enunciated in the first half of this century (see References 29-35). A detailed discussion of these so-called vortex theories, however, is rather complicated and certainly beyond the intended scope of this course book.

Momentum blade element theory requires the input of airfoil aerodynamic data for the calculation of thrust and power. The last fifty years, the airfoils employed for propellers have been largely restricted to the NACA 16-series sections (Figure 7.15). These airfoil types were developed in the late thirties by the National Advisory Committee for Aeronautics (NACA) in the U.S.A., and found exclusive use in propellers. We note that in 1958 a new name was given to the NACA research agency: National Aeronautics and Space Administration (NASA).

More recently became available two new series of blade sections, developed in the U.K. and in the U.S.A. for use on the modern generation turboprop airplanes (References 36 and 37). Their increased performance characteristics are illustrated in Figure 7.15, where a comparison is made between the lift-to-drag ratios of a con-

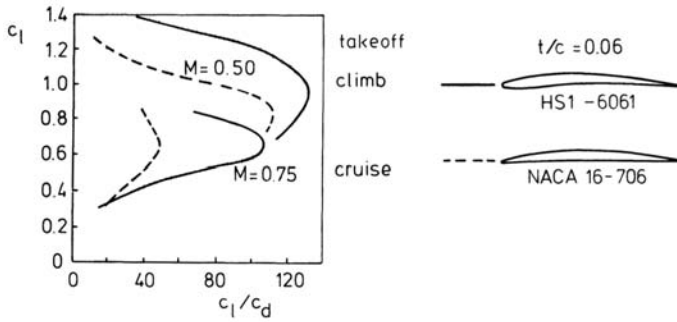


Figure 7.15 Typical lift/drag ratios of propeller blade section airfoils

ventional section and an advanced propeller blade section airfoil (from Reference 36).

Notice also that significantly higher values of maximum lift/drag ratio are obtained on a propeller blade section than are achieved in the case of an airplane wing section. This phenomenon might be explained by considering the effect of reduced boundary layer thickness due to the centrifugal field in which the blade sections are operating.

At this point, let us return to our discussion on propeller geometry of the preceding section in order to make a few remarks about the necessity for twisting the propeller blades. According to its definition, the propulsive efficiency of the propeller is given by

$$\eta_j = \frac{TV_0}{P_{br}} = \frac{TV_0}{P_p}. \quad (7.35)$$

The blade element theory uses a similar notion, the blade element efficiency,

$$\eta_j = \frac{dTV_0}{dP_p}. \quad (7.36)$$

Through insertion of Equations (7.28) and (7.29) into Equation (7.36), and by making use of the relationship $V_0 = \omega r \tan \phi$ (see Figure 7.13), we obtain

$$\eta_e = \left[\frac{c_\ell \cos \phi_a - c_d \sin \phi_a}{c_\ell \sin \phi_a + c_d \cos \phi_a} \right] \tan \pi. \quad (7.37)$$

We gain further insight by adopting in Equation (7.37) the approximation that the induced velocity at the blade section is sufficiently small so that ϕ_a may be replaced by ϕ . Now Equation (7.37) can readily be manipulated into the following form:

$$\eta_e = \frac{\tan \phi}{\tan(\phi + \delta)}, \quad (7.38)$$

where $\tan \delta = c_d/c_\ell$.

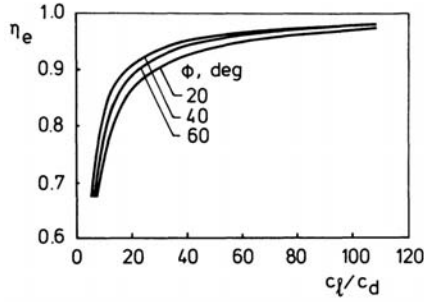


Figure 7.16 Propeller blade element efficiency versus lift/drag ratio

Figure 7.16 shows the relationship of blade element efficiency with lift/drag ratio and advance angle. Apparently, the magnitude of the angle ϕ has only a relatively small influence on the efficiency of the blade element. Therefore, we may consider a mean curve in Figure 7.16. This unique relation between η_e and c_l/c_d reveals that the optimum angle of attack is that angle for which the lift/drag ratio attains its maximum value. Hence, if the propeller blade has the same airfoil section throughout its entire length, the optimum angle of attack must be uniform along the blade, which results in a decreasing blade angle from hub to tip. Though, mostly, the blade sections are not shaped equally, it continues in force that propeller blades are twisted strongly (Figure 7.11).

The results of the blade element theory may also be used to explain the term activity factor, or shortly AF, which evaluates the distribution of the blade area along the radius and expresses the ability of a propeller blade to absorb power.

The factor AF may be defined by

$$AF = \frac{10^5}{D^5} \int_{0.2R}^R cr^3 dr = \frac{10^5}{16} \int_{0.2}^{1.0} \frac{c}{D} \left[\frac{r}{R} \right]^3 d \left(\frac{r}{R} \right), \quad (7.39)$$

where the lower limit of integration represents the outer radius of the hub.

The meaning of Equation (7.39) can be explained by examining Figure 7.13. When neglecting again the induced velocity, the power required to rotate the blade element may be expressed as (cf. Equation (7.29))

$$dP_p = \frac{1}{2} \rho V_r^2 \omega r c (c_\ell \sin \phi + c_d \cos \phi) dr. \quad (7.40)$$

Using the relationship $V_r = \omega r \sec \phi$, Equation (7.40) can be written as

$$dP_p = \left(\frac{1}{2} \rho \omega^3 \sec^2 \phi \right) (c_\ell \sin \phi + c_d \cos \phi) c r^3 dr. \quad (7.41)$$

For given working conditions and blade section shape, the factors between brackets are constants so that for the whole blade the power absorption capacity is proportional to $\int_{0.2R}^R cr^3 dr$. To make this quantity dimensionless, it is divided by

D^5 . The constant 10^5 in Equation (7.39) is only used to give the activity factor a convenient magnitude.

Thus, for a given propeller and operating at given conditions, the ability to absorb power is directly correlated to the activity factor, so that

$$P_p = \text{constant} \times B \times \text{AF},$$

where the product $B \times \text{AF}$ is called the *total activity factor*, TAF.

For a blade having a constant chord length, we find from Equation (7.39), $\text{AF} = 1560 c/D$. For the propeller blade considered in Figure 7.11 the activity factor becomes $\text{AF} = 121$.

The thrust producing capability of a propeller blade is characterized by the integrated design lift coefficient,

$$C_{Li} = 4 \int_{0.2}^{1.0} c_{\ell i} \left[\frac{r}{R} \right]^3 d \left(\frac{r}{R} \right), \quad (7.42)$$

where $c_{\ell i}$ is the design lift coefficient of a blade element at zero incidence, defining the sectional camber. A propeller blade with a high C_{Li} -value is able to generate more thrust for the same chord length distribution.

7.4 Propeller charts

From the preceding discussions it may be appreciated that for a propeller with a given number of blades and given blade shape, the thrust will be determined by the density of air, the propeller speed, the propeller diameter, the freestream velocity, the blade setting, the speed of sound, and the viscosity of the air. Therefore,

$$T = T(\rho, n_p, D, V_0, \beta_{0.75}, c, \mu). \quad (7.43)$$

Utilizing the technique of dimensional analysis as described in Chapter 4, we may write

$$T = K(\rho^a n_p^b D^d V_0^e c^f \mu^g). \quad (7.44)$$

Then, in term of the units mass $[M]$, length $[L]$ and time $[T]$, we have

$$\frac{ML}{T^2} = K \left[\frac{M}{L^3} \right]^a \left[\frac{1}{T} \right]^b [L]^d \left[\frac{L}{T} \right]^e \left[\frac{L}{T} \right]^f \left[\frac{M}{LT} \right]^g. \quad (7.45)$$

By equating exponents we obtain

$$\begin{aligned} 1 &= a && +g \\ 1 &= -3a && +d + e + f && -g \\ -2 &= && -b && -e - f && -g. \end{aligned} \quad (7.46)$$

When we solve the three equations for the exponents a , b and d in terms of e , f and g , we get

$$\begin{aligned}
 a &= 1 & -g \\
 b &= 2 - e - f & -g \\
 d &= 4 - e - f & -2g.
 \end{aligned} \tag{7.47}$$

Using these powers in Equation (7.44) yields

$$T = K\rho n_p^2 D^4 \left[\frac{V_0}{n_p D} \right]^e \left[\frac{c}{V_0} \right]^f \left[\frac{\mu}{\rho V_0 D} \right]^g \quad \text{or} \tag{7.48}$$

$$T = K\rho n_p^2 D^4 J^e \left[\frac{1}{M_0} \right]^f \left[\frac{1}{Re} \right]^g. \tag{7.49}$$

If we set

$$K J^e \left[\frac{1}{M_0} \right]^f \left[\frac{1}{Re} \right]^g = C_T,$$

we can write Equation (7.49) as

$$T = C_T \rho n_p^2 D^4, \tag{7.50}$$

where C_T is the dimensionless thrust coefficient of which the value may vary with blade angle $\beta_{0.75}$, advance ratio J , flight Mach number M_0 and Reynolds number Re .

Carrying out a similar dimensional analysis on propeller power, we find

$$P_p = C_P \rho n_p^3 D^5, \tag{7.51}$$

where C_P is the power coefficient.

Hence for a given propeller it follows that

$$C_T = C_T(\beta_{0.75}, J, M_0, Re) \tag{7.52}$$

$$C_P = C_P(\beta_{0.75}, J, M_0, Re). \tag{7.53}$$

Now, as shown in Figure 7.17, the propeller chart may give the values of C_T and C_P as functions of $\beta_{0.75}$ and J . Here, the points on the various curves C_P versus J for constant value of $\beta_{0.75}$ that correspond to the same value of C_T are connected.

The data in this figure represent experimental results obtained at fixed values of Mach number and Reynolds number.

By making use of Equations (7.50) and (7.51) we can express the propulsive efficiency in the form

$$\eta_j = \frac{TV_0}{P_p} = \frac{C_T \rho n_p^2 D^4 V_0}{C_P \rho n_p^3 D^5} = \frac{C_T}{C_P} J. \tag{7.54}$$

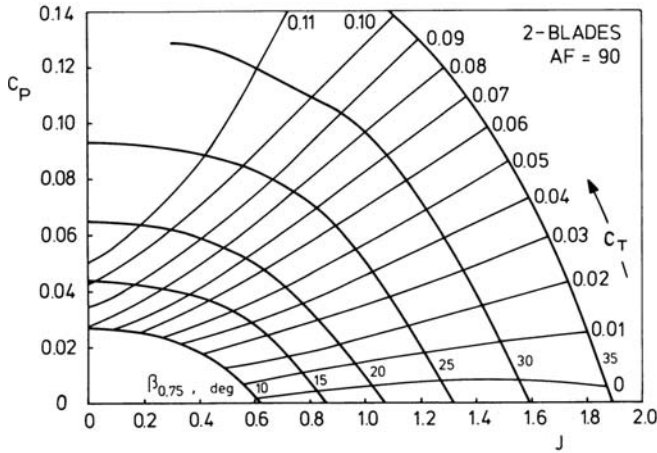


Figure 7.17 Propeller chart (NACA 16 blade section series)

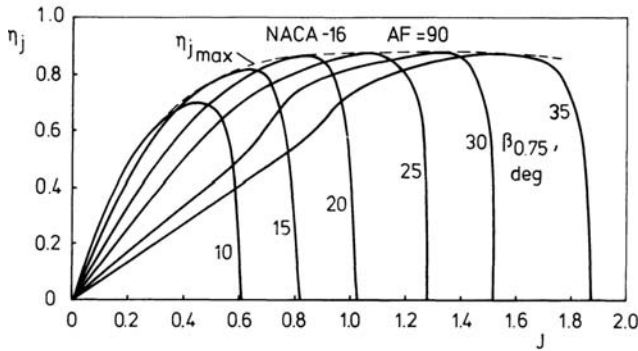


Figure 7.18 Propulsive efficiency

Figure 7.18 gives the propeller performance in terms of η_j , J and $\beta_{0.75}$. The optimum performance curve is indicated by the dashed line, joining the points of maximum propulsive efficiency. Notice that the graph refers to the same propeller as considered in Figure 7.17.

Inspection of Figure 7.18 shows that the blade setting has a marked influence on the propulsive efficiency. On a so-called *fixed-pitch propeller* the blade angle $\beta_{0.75}$ has one particular value so that optimum efficiency occurs for a given design condition of V_0 and n_p . It is also seen that for this type of propeller a high efficiency is gained in only a very narrow range of advance ratios. For example, low efficiencies are obtained at takeoff and climb if the propeller is designed for cruising conditions. On the other hand, the airplane may be equipped with a climb propeller, which has a smaller blade angle or lower pitch. This increases performance during takeoff and climb, but decreases performance during cruise.

Apparently, for optimum propulsive efficiency it would be of advantage to provide a pitch-change mechanism to change the blade setting as the advance ratio

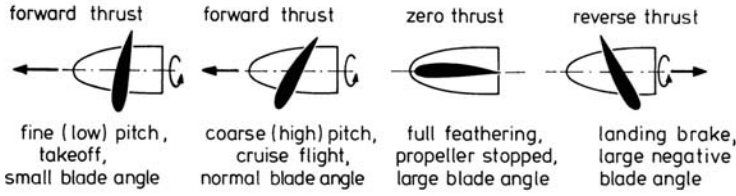


Figure 7.19 Application of pitch control

varies. This requirement has resulted in a solution which is known as the variable-pitch propeller. As can be seen from the curves in Figure 7.18, the *variable-pitch propeller* furnishes improved performance over a broad range of operating conditions. This explains that nowadays fixed-pitch propellers only are used on the small single-engine airplanes.

An airplane equipped with a variable-pitch propeller has an engine throttle control for the engine output and a pitch control to regulate the propeller speed. A so-called constant speed propeller is equipped with a governor, which changes the blade angles in response to any departure in propeller speed from the value selected by the pilot.

Constant speed propellers on most of the larger modern airplanes have the possibility for full feathering in flight, that is, the blades can be turned edge-on to the oncoming air to prevent the occurrence of high windmilling-drag in case of engine failure (Figure 7.19). Also, the pitch-change mechanism may be designed to permit the selection of a large negative blade angle after landing, thus creating reverse thrust for rapid deceleration of the airplane during ground run.

The governor adjusts the propeller speed by changing the blade setting to ensure that the power required by the propeller equals the shaft power at the selected rotational speed:

$$P_p = P_{br}. \quad (7.55)$$

For given values of ρ , V_0 , D , n_p , and P_{br} the power coefficient and the advance ratio follow from

$$C_P = \frac{P_{br}}{\rho n_p^3 D^5} \quad (7.56)$$

$$J = \frac{V_0}{n_p D}. \quad (7.57)$$

Now the blade angle $\beta_{0.75}$ and the thrust coefficient C_T are known from the propeller chart in Figure 7.17. The thrust, finally, is found from Equation (7.50).

It is worth mentioning that the piston-engine generates its shaft power evenly over a wide range of engine speeds (Figure 7.20). For airborne operation, a piston-engine uses approximately 40% of the rpm-range in which the propeller blade angle varies between about 20° at flight idle to 45° at maximum airspeed. The turbo-prop, on the contrary, operates within a narrow range of high rotational speeds in

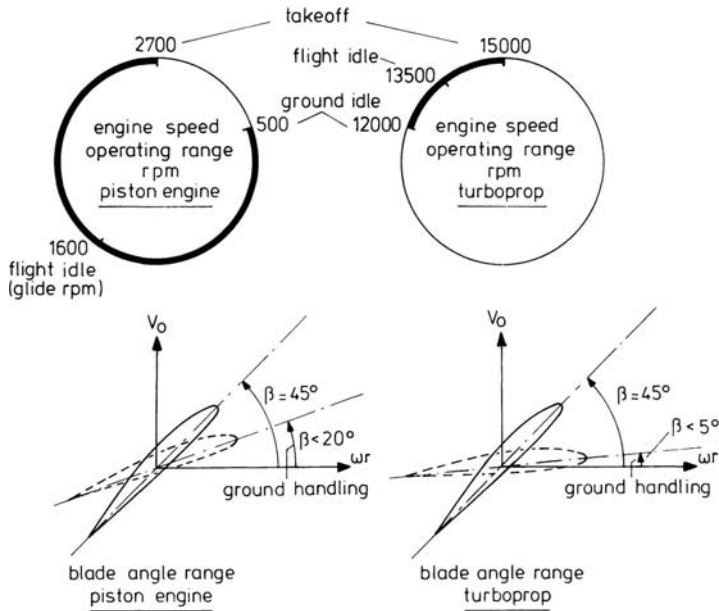


Figure 7.20 Engine and propeller operating range

order to achieve its low specific fuel consumption characteristics. Consequently, the turboprop-propeller blade angle during a glide at minimum power is smaller than that of a piston-engine propeller. The blade angle of a turboprop propeller therefore changes from about 5° to 45° in only 10% of the flight range of engine speeds so that the blades change angle at a much faster rate than the blades of a piston-engine propeller. This implies that the turboprop provides a better thrust response to control lever movement than a piston-engine.

We close this section with remarking that also the control of the turboprop may differ from that of the reciprocating engine since the pilot of a turboprop airplane, generally, has the disposal of only one control lever, which regulates the fuel flow to the engine. In this case, the fuel control operates in conjunction with the pitch control in the flight range of the engine speeds to ensure that the operating limits of the engine will not be exceeded. It is convenient to specify the output of such a turboprop system in terms of compressor speed (see Chapter 6). When the engine is operating at rotational speeds below flight idle, it is said to be in the ground-handling or beta-range (Figure 7.20). In this low-power region, the propeller blade angle is controlled directly by the pilot's control lever and may be varied progressively from forward thrust through zero to reverse for braking and taxiing.

7.5 Installed propeller performance

From the existing methods on propeller performance prediction, generally, the freeair thrust is obtained. However, the installation of propeller and engine in the airplane leads naturally to a flow through the propeller disk which differs from the isolated behavior. The mutual interference of propeller slipstream and airframe results in two important installation effects:

- The presence of nacelle and wing or fuselage behind the propeller causes a retardation of the air flow through the propeller disk.
- The airframe parts which are immersed in the slipstream deliver a higher drag than the freestream value, because of the higher local flow velocities.

In order to take account of these effects when executing airplane performance calculations, the effective thrust, T_{eff} is used. This is the thrust of the isolated propeller corrected for all effects emanating from the presence of airframe parts in the slipstream.

Since the drag of a propeller-driven airplane is defined for zero thrust, the actual or propeller efficiency becomes

$$\eta_p = \frac{T_{\text{eff}} V_0}{P_{\text{br}}}. \quad (7.58)$$

We may simplify the problem by looking only at the increment in profile drag of the airframe parts that are exposed to the propeller slipstream. From Equation (7.5) and (7.9), the freeair thrust is

$$T = \rho \frac{\pi}{4} D^2 (V_0 + \frac{\Delta V}{2}) \Delta V, \quad (7.59)$$

where ΔV is the increase in velocity in the slipstream.

The increase in dynamic pressure of the flow through the propeller disk is given by

$$\Delta q = \frac{1}{2} \rho [(V_0 + \Delta V)^2 - V_0^2]. \quad (7.60)$$

Combining Equations (7.59) and (7.60) yields

$$\Delta q = \frac{T}{\frac{\pi}{4} D^2}. \quad (7.61)$$

If the airframe parts immersed in the slipstream of one propeller have a parasite drag area $\Sigma(C_{D_s} S_s)$, the increase in airplane drag per propeller can be expressed in the form

$$\Delta D = \Delta q \Sigma(C_{D_s} S_s) = \frac{T}{\frac{\pi}{4} D^2} \Sigma(C_{D_s} S_s). \quad (7.62)$$

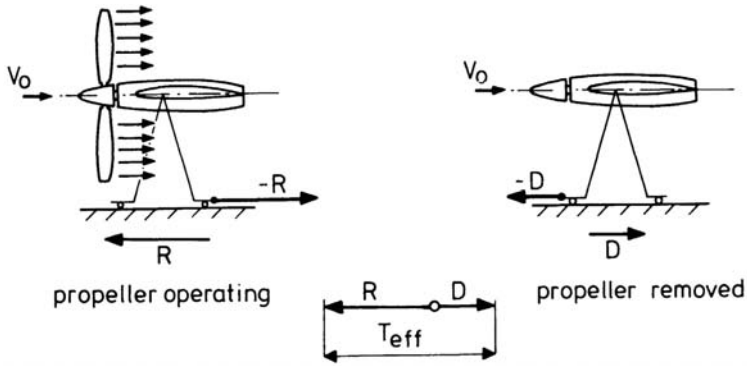


Figure 7.21 Measurement of effective thrust in windtunnel

Now we are able to relate the propeller efficiency and the propulsive efficiency as follows

$$\eta_p = \frac{(T - \Delta D)V_0}{P_{br}} = \frac{TV_0}{P_{br}} \left(1 - \frac{\Delta D}{T}\right) = \eta_j \left[1 - \frac{\Sigma(C_{Ds}S_s)}{\frac{\pi}{4}D^2}\right]. \quad (7.63)$$

In practice, the drag coefficient in Equation (7.63) usually is treated as a constant, irrespective of the operating conditions. Based on wetted area, $C_{Ds} = 0.004$ may be used (Reference 14).

Propeller efficiencies given in propeller charts may be derived from windtunnel tests on the propeller with spinner mounted in front of the proper nacelle-wing combination (Figure 7.21). In this case the effective thrust is the measured resultant force of the propeller-body combination plus the drag of the body measured without the propeller.

Chapter 8

THE AIRPLANE IN SYMMETRIC FLIGHT

8.1 Fundamental equations

In view of the importance of symmetric flight in airplane performance considerations, it is appropriate to extend the analyses of Chapter 3 to this type of flight.

In this section we shall devote our attention to examining the fundamental equations which govern the accelerated motion of the center of gravity of a rigid airplane along a curved flight path.

As depicted in Figure 8.1, at a given point on the trajectory, the X_a -axis and the Z_a -axis of the air-path axis system and the X_b -axis of the body axis system are set up. The X_a -axis is tangent to the flight path and the Z_a -axis lies in the vertical plane through the X_a -axis, perpendicular to the local flight direction.

The flight condition at one instant along the trajectory is characterized by the following kinematic and geometric parameters:

- Airspeed V , which is the velocity vector of the center of gravity of the airplane. The velocity vector coincides with the X_a -axis and lies in the plane of symmetry of the airplane.
- Angle α_T , which defines the inclination of the thrust vector to the X_a -axis.
- Flight-path angle γ , which is the angle between the X_a -axis and its projection on the horizontal plane. The angle γ is positive if the airplane climbs relative to the air, and negative if the airplane descends. Thus, from vertical climb to vertical dive the flight-path angle varies from $\pi/2$ to $-\pi/2$ (Figure 8.2).
- Angle of attack α , which is the angle between the X_b -axis of the body axis system and the X_a -axis. The angle of attack represents the attitude of the

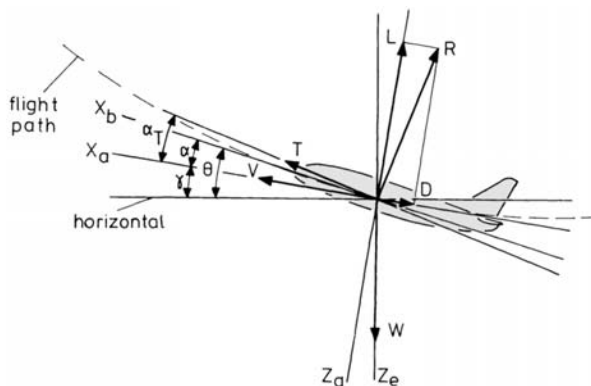


Figure 8.1 Airplane In symmetric flight

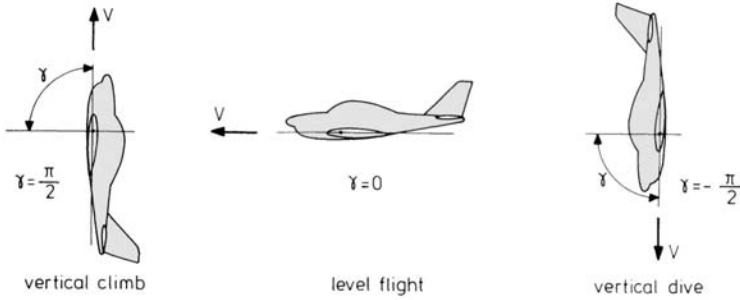


Figure 8.2 Sign of flight-path angle

airplane relative to the oncoming air, and is positive if the X_b -axis is turned in positive sense to the X_a -axis.

- Angle of pitch θ , which is the angle between the X_b -axis and the horizontal. According to the sign convention for the flight-path angle, the angle θ has a positive value if the X_b -axis lies above the horizontal plane, and negative when it is below this plane.

In symmetric flight the angle of pitch, the angle of attack and the flight-path angle are related by

$$\theta = \alpha + \gamma. \quad (8.1)$$

In Figure 8.1 also are indicated the three principal forces acting on the airplane that determine its performance. These forces are:

- Airplane weight W , which acts vertically downward.
- Thrust T , which is assumed to make an angle α_T with the X_a -axis.
- Aerodynamic force R , and its components lift L and drag D . The forces L and D act along the negative Z_a -axis and negative X_a -axis, respectively.

Applying Newton's second law of motion along the X_a -axis yields the equation

$$\frac{W}{g} \frac{dV}{dt} = T \cos \alpha_T - D - W \sin \gamma, \quad (8.2)$$

where dV/dt is the acceleration tangent to the flight path.

Along the Z_a -axis, we have

$$\frac{W}{g} \frac{V^2}{R} = T \sin \alpha_T + L - W \cos \gamma, \quad (8.3)$$

where R is the local radius of curvature of the flight path.

The left-hand side of Equation (8.3) is the centrifugal force due to the curvilinear motion (see Section 1.3). With the familiar relationship $V = R d\gamma/dt$, the centrifugal force can also be expressed as

$$\frac{W}{g} \frac{V^2}{R} = \frac{W}{g} V \frac{d\gamma}{dt}. \quad (8.4)$$

The lift can be written as (see Chapter 4)

$$L = C_L q S = C_L \frac{1}{2} \rho V^2 S, \quad (8.5)$$

where C_L is the lift coefficient, $q = \frac{1}{2} \rho V^2$ is the dynamic pressure and S is the wing area. Similarly, we have

$$D = C_D q S = C_D \frac{1}{2} \rho V^2 S, \quad (8.6)$$

where C_D is the drag coefficient.

Consequently, the equations of motion for an airplane in symmetric flight are found to be

$$\frac{W}{g} \frac{dV}{dt} = T \cos \alpha_T - C_D \frac{1}{2} \rho V^2 S - W \sin \gamma \quad (8.7)$$

$$\frac{W}{g} \frac{V^2}{R} = \frac{W}{g} V \frac{d\gamma}{dt} = T \sin \alpha_T + C_L \frac{1}{2} \rho V^2 S - W \cos \gamma. \quad (8.8)$$

Since the weight of the airplane decreases continuously due to the consumption of fuel by the engine(s), we have the relationship

$$F = -\frac{dW}{dt}, \quad (8.9)$$

where F denotes the fuel weight flow rate.

In this connection, it should be remarked that in principle the motion of the airplane must be determined for the case of a body with variable mass. From our discussion in Section 3.5, we know that Equations (8.7) and (8.8) are correct if the rate of increase of linear momentum of the fuel flow relative to the airplane is included in the expression for the thrust. For airbreathing engines, however, this contribution to the entire time rate of change of linear momentum is such small that we may ignore the effect of a variable mass in Equations (8.7) and (8.8).

In the absence of wind, the variation of true altitude per unit time is the rate of climb RC of the airplane, which is equal to the vertical component of the airspeed V ,

$$RC = \frac{dh}{dt} = V \sin \gamma. \quad (8.10)$$

The rate of climb is positive when the airplane ascends relative to the air, and negative when the airplane descends.

When we consider an airplane that flies in the International Standard Atmosphere (I.S.A.), the atmospheric conditions are completely determined by the geopotential altitude H . Also, we will use the approximation that $h = H$ in Equation (8.10). Further, we make the assumption that at each point of time the aerodynamic forces in accelerated flight equate the air loads in steady flow with the momentary values

of angle of attack, airspeed and altitude. Then, from the discussions in Section 4.1, we know that for an airplane with given configuration the coefficients C_L and C_D in Equation (8.7) and (8.8) are functions of angle of attack, flight Mach number and Reynolds number,

$$C_L = C_L(\alpha, M, \text{Re}) \quad (8.11)$$

$$C_D = C_D(\alpha, M, \text{Re}). \quad (8.12)$$

Since $M = M(V, H)$ and $\text{Re} = \text{Re}(V, H)$, it follows that

$$C_L = C_L(\alpha, V, H) \quad (8.13)$$

$$C_D = C_D(\alpha, V, H). \quad (8.14)$$

Similarly, from Chapter 6, we have

$$T = T(\Gamma, V, H) \quad (8.15)$$

$$F = F(\Gamma, V, H). \quad (8.16)$$

Finally, the angle α_T in the equations of motion is a function of the angle of attack,

$$\alpha_T = \alpha_T(\alpha). \quad (8.17)$$

From the foregoing it is thus evident that Equations (8.7) and (8.8) contain the following variables:

$$t, W, \alpha, V, H, \gamma, \Gamma.$$

If we take the time t as independent variable, the other six are the dependent variables, which define the flight condition at each point of time.

To find these six unknowns, four equations (Equations (8.7) to (8.10)) are available so that the course of the flight is fully determined if two dependent variables are prescribed as a function of time.

The two variables which can be chosen freely, are called *control variables*, and the remaining four variables are the state variables.

The functions which describe the time history of the control variables are called *control laws*, e.g.,

$$\left. \begin{array}{l} \alpha = \alpha(t) \\ \Gamma = \Gamma(t) \end{array} \right\} \quad (8.18)$$

With these two control laws we have a system of six equations to solve the six unknowns.

The two basic controls on the airplane about which the pilot has the disposal in symmetric flight, namely, the elevator to adjust the angle of attack (pitch control) and the engine control lever to select the power output (engine control), allow the realization of the prescribed control laws (Figure 8.3).

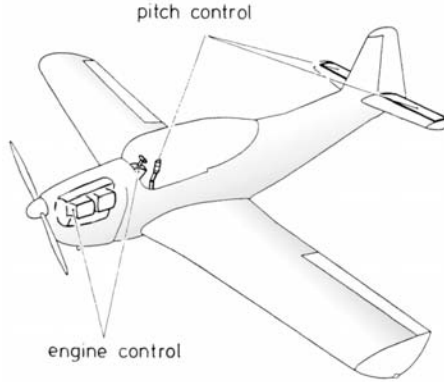


Figure 8.3 Controls In symmetric flight

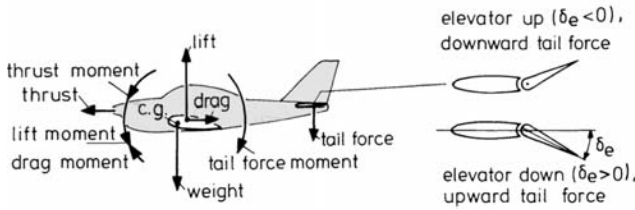


Figure 8.4 Pitch control

The name given to the combination of the two control laws in Equation (8.18) is *flight technique* or *flight program*.

To the preceding system of equations describing the translational motion in symmetric flight, we can add Equation (3.24) for the rotational motion.

Since in symmetric flight we are concerned with longitudinal motion only, this moment equation reduces to

$$M_y = \frac{dq}{dt} I_y = \frac{d^2\theta}{dt^2} I_y, \tag{8.19}$$

in which $\theta = \alpha + \gamma$.

The longitudinal control about the lateral axis is provided by the tail load carried by the horizontal stabilizer (Figure 8.4). The magnitude of the tail force depends on the elevator deflection. This tail force is, in addition to aerodynamic force R , thrust T and weight W , the fourth force acting on the airplane in symmetric flight. The tail force must be counteracted by the lift when it is directed downward. Clearly, the higher the downward tail load the higher the total lift, which implies more drag. This means that in symmetric flight the lift and drag coefficients in general have the following functional relationships:

$$\begin{aligned} C_L &= C_L(\alpha, V, H, \delta_e) \\ C_D &= C_D(\alpha, V, H, \delta_e) \end{aligned} \tag{8.20}$$

Thus, by inserting Equation (8.19) into the system of equations we are faced with only one extra variable so that the number of control variables continues to be two.

Though the use of Equation (8.19) may be needed, it is often possible to assume that the elevator deflection δ_e is instantly reactive to the prescribed control law $\alpha = \alpha(t)$. Equation (8.19) can then be omitted. This simplification implies that the effect of elevator deflection on the resultant aerodynamic force is neglected.

8.2 Integral and point performance

Equations (8.7) to (8.19) describe the unsteady airplane motion along a curvilinear path. They can be applied to determine the so-called *path performance* or *integral performance* values, which are related to the course of the flight. Examples of integral performance values are time to climb to a certain altitude, range and endurance in cruise, and takeoff and landing distances.

On the other hand, we distinguish the *point performance* of an airplane. This name identifies the study of performance parameters which occur at a given point of time or at a given point on the flight path.

Hence, the designation "point performance" refers to instantaneous quantities such as maximum and minimum speed in level flight, maximum climb angle and rate of climb, and minimum radius of turn.

Studies of integral performance and point performance both may fall within the category of flight dynamics. Recall from Chapter 3 that this term classifies the study of performance problems in which the exchange between kinetic and potential energies is of significance. In particular, the integral and point performance achieved when flying along optimum trajectories, but also the unsteady motion during takeoff and landing belong to the class of dynamic performance.

Generally, Equations (8.7) and (8.8), which form a system of nonlinear differential equations, are not very suitable for analytical integration. To make these equations amenable to treatment, several simplifications and approximations are generally introduced. In this light, as an engineering approach, integral performance values from general translational motion of an airplane in accelerated flight are often determined by the use of the simplifying assumption that the airplane executes a quasi-steady flight.

In this text, we are interested mainly in the last-mentioned case where the acceleration can be assumed to be zero. The airplane's performance concerning such steady-state flight conditions are called *static performance*. This last type of performance analysis leads in many applications to sufficient accurate computations of the parameters which define the performance capabilities of an airplane.

On the other hand, when predicting the integral performance of airplanes, the variations of airplane weight and/or altitude may be neglected. E.g., these assumptions may be reasonable in the case that the time passed in a specific flight phase is very short, such as in takeoff and landing maneuvers.

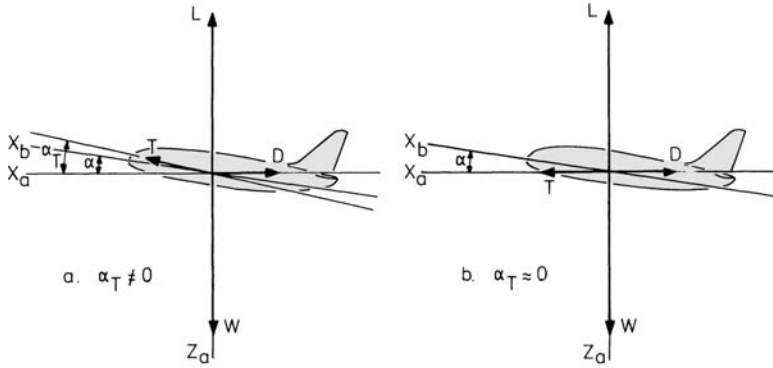


Figure 8.5 Equilibrium of forces in quasi-steady level symmetric flight

8.3 Air loads

All loads applied to an airplane that is airborne are produced through accelerations of the vehicle as a result of a control action by the pilot (maneuvering loads) or by encountering atmospheric turbulence (gust loads).

To enter into the details of the idea of air load we consider an instant along a horizontal flight path (Figure 8.5a). When symmetric flight is maintained at constant airspeed and altitude, all forces are in balance. For this condition the flight-path angle γ in Equations (8.7) and (8.8) is zero. Then, the left-hand sides of these equations are zero, yielding

$$0 = T \cos \alpha_T - C_D \frac{1}{2} \rho V^2 S \quad (8.21)$$

$$0 = T \sin \alpha_T + C_L \frac{1}{2} \rho V^2 S - W. \quad (8.22)$$

Since for most conventional airplane types the angle α_T is very small, we may assume that $\cos \alpha_T = 1$ and $\sin \alpha_T = 0$. Then, from Equations (8.21) and (8.22), we find that at each instant during the flight the thrust is equal to the drag and the weight is equal to the lift (Figure 8.5b),

$$T = D = C_D \frac{1}{2} \rho V^2 S = C_D \frac{1}{2} \rho_0 V_e^2 S \quad (8.23)$$

$$W = L = C_L \frac{1}{2} \rho V^2 S = C_L \frac{1}{2} \rho_0 V_e^2 S. \quad (8.24)$$

In these equations V_e is the equivalent airspeed (E.A.S.) and ρ_0 is the standard sea-level density (I.S.A.). Now assume that, starting from the quasi-steady level flight condition in Figure 8.6a, the pilot moves the elevator in the negative direction. From Figure 8.4 this results in a positive pitching (clockwise) motion of the airplane, through which at the given flight speed the angle of attack is suddenly increased by $\Delta\alpha$. Consequently, equilibrium of forces no longer exists and an

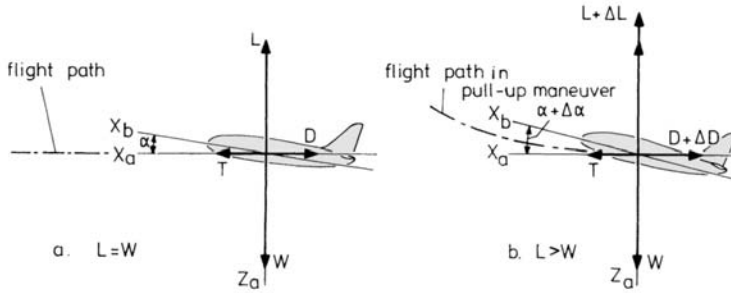


Figure 8.6 Lift in steady and accelerated flight

acceleration will take place, which causes a curvature of the flight path (Figure 8.6b). The increased values of lift and drag may be expressed as

$$L' = L + \Delta L = (C_L + \Delta C_L) \frac{1}{2} \rho V^2 S \quad (8.25)$$

$$D' = D + \Delta D = (C_D + \Delta C_D) \frac{1}{2} \rho V^2 S. \quad (8.26)$$

In describing the air load, the *load factor* is used, which parameter refers to the ratio of the resultant aerodynamic force to the weight of the airplane,

$$n = \frac{|A|}{W}, \quad (8.27)$$

where n denotes the load factor and A is the vector sum of the aerodynamic force R and the thrust T .

However, as portrayed in Figure 8.6b, the increase in lift will be of prime significance and therefore the loads from accelerations normal to the X_a -axis.

Consequently, the load factor in its usual form is obtained by dividing the lift by the weight,

$$n = \frac{L'}{W} = 1 + \frac{\Delta C_L}{C_L}. \quad (8.28)$$

The equation of motion along the Z_a -axis can be written as

$$\frac{W}{g} a_n = L' - W, \quad (8.29)$$

where a_n is the acceleration toward the center of curvature (centripetal acceleration). Equations (8.28) and (8.29) give for this acceleration normal to flight path,

$$a_n = g(n - 1). \quad (8.30)$$

In quasi-steady level symmetric flight a_n is zero, meaning that the lift equals the weight of the airplane and that the load factor is equal to one.

As pointed out already, a load factor other than one may occur as a result of a maneuver or due to an external cause in the form of a gust.

Obviously, the greatest maneuvering load factors will occur if the maximum amount of lift is generated. In other words, if the angle of attack is increased up to the critical angle of attack. Hence

$$n = \frac{C_{L_{\max}} \frac{1}{2} \rho V^2 S}{W}. \quad (8.31)$$

As will be explained in the next section, the maximum lift coefficient is related to the minimum stalling speed V_{MS} by

$$W = C_{L_{\max}} \frac{1}{2} \rho V_{MS}^2 S. \quad (8.32)$$

Thus from Equations (8.31) and (8.32), the value of n that can be achieved from maneuvering, can be expressed as

$$n = \frac{V^2}{V_{MS}^2}. \quad (8.33)$$

Equation (8.33) shows that the obtainable load factor strongly increases with increasing airspeed.

8.4 Stalling speeds

Most performance requirements are specified in reference to the *minimum stalling speed*, V_{MS} , that is the minimum speed in a stall, of the airplane.

The minimum stalling speed is defined in the airworthiness requirements as the minimum speed reached during a prescribed stall maneuver with the airplane in a given configuration. In conducting the stall maneuver, the following procedure is utilized (Figure 8.7): The airplane is flown at a steady speed 20% to 40% above the anticipated minimum stalling speed with the engine(s) at idle. The flight speed is reduced with elevator control until the speed is slightly above the minimum stalling speed. Then the elevator control is pulled back so that the airplane is slowed down at a constant deceleration dV/dt (stall entry rate) until the minimum airspeed is reached. This speed is recognized by uncontrollable downward pitching motions, owing to breaking away of flow from the upper surface of the wing.

As sketched in Figure 8.7, in approaching the stall, the load factor first remains roughly constant and the lift coefficient gradually increases according to the equation

$$\frac{W}{g} a_n = C_L \frac{1}{2} \rho V^2 S - W \quad (8.34)$$

or with Equation (8.30)

$$C_L = \frac{n W}{\frac{1}{2} \rho V^2 S} \quad (8.35)$$

Immediately beyond the point of time at which the maximum lift coefficient occurs, the load factor drops considerably, indicating that stalling phenomena are advancing quickly.

As soon as the airplane is stalled, the pilot recovers the motion by pitching down the nose, producing an increase in airspeed.

Since the resulting minimum stalling speed depends strongly on the magnitude of the stall entry rate, a sufficient number of stall maneuvers are executed to obtain enough data points to define the minimum stalling speed at a prescribed value of $dV/dt = -1$ knot per second (Figure 8.8a). The stall entry rate is defined as the slope of the line connecting the minimum stalling speed and a value 10% above V_{MS} . That is:

$$\frac{dV}{dt} = \frac{V_{MS} - 1.1 V_{MS}}{\Delta t} \tag{8.36}$$

Furthermore, minimum stalling speeds are determined for every flap and landing gear position that is used in the various flight phases.

Besides V_{MS} , also the minimum speed at which the lift equals the weight of the airplane can be deduced from the measurement data,

$$V_S = \sqrt{\frac{W}{S} \frac{2}{\rho} \frac{1}{C_{Lmax}}} \tag{8.37}$$

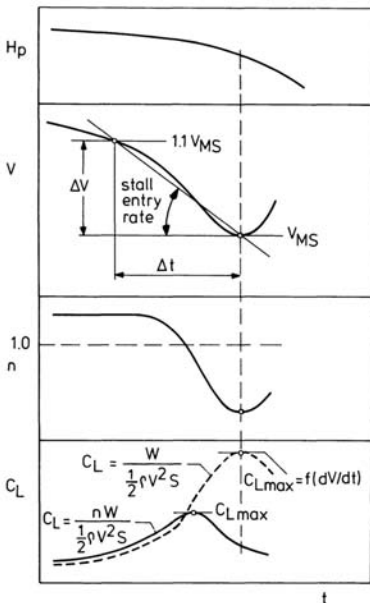


Figure 8.7 Determination of minimum stalling speed

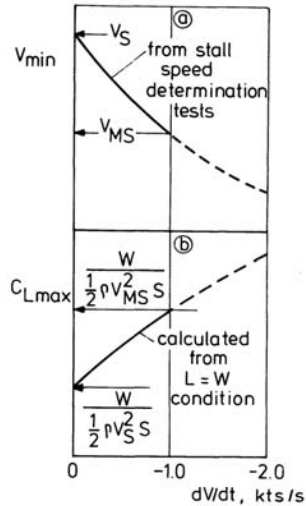


Figure 8.8 Effect of stall entry rate

The speed V_S is called the *one-g stalling speed* or simply *stalling speed*, and is thus the minimum steady speed in free air under one-g conditions at minimum

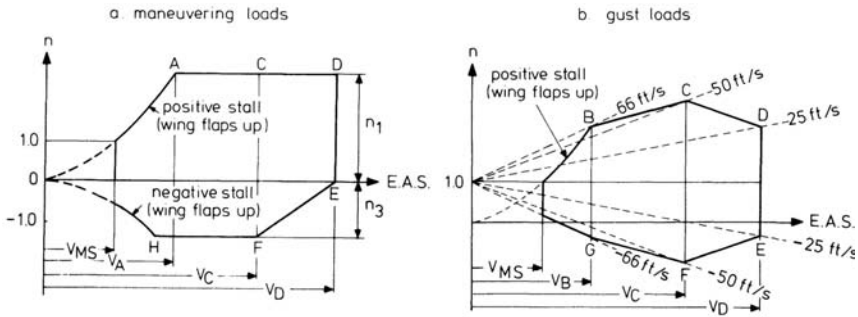


Figure 8.9 Basic load factor envelopes

engine control setting. Typically, V_{MS} may be as low as $0.94 V_S$ at $dV/dt = -1$ knot/s.

In Figure 8.7, the minimum stalling speed has also been reduced to an apparent maximum lift coefficient by using the $L = W$ condition,

$$C_{Lmax} = \frac{W}{\frac{1}{2}\rho V_{MS}^2 S}. \tag{8.38}$$

It is evident that the C_{Lmax} -value thus obtained is a function of the stall entry rate (Figure 8.8b).

Using $V_{MS} = 0.94V_S$, we find that the latter maximum lift coefficient may be quoted at a value some 13% higher than the C_{Lmax} obtained by calculation methods or wind tunnel tests. Whenever appropriate in this text, a tacit enlargement of the "physical" C_{Lmax} -values in this manner will be supposed.

8.5 Load factor envelopes

All existing airworthiness requirements prescribe that the airframe, the load-carrying structure of the airplane, is strong enough to withstand certain *limit load factors* on the boundaries of a representative flight envelope.

The basic maneuvering envelope which defines the symmetrical flight maneuvering loads for which the airframe is constructed, is shown in Figure 8.9a. The various design speeds, as selected by the airplane designer, are given in terms of equivalent airspeeds (E.A.S.). The curve 0A is the stall line and represents the load factor according to Equation (8.33).

The design maneuvering speed V_A is obtained at the positive limit maneuvering load factor n_1 :

$$V_A = V_{MS}\sqrt{n_1}, \tag{8.39}$$

where V_{MS} is the minimum stalling speed with wing flaps retracted.

In Figure 8.9a, the speed V_C is the design cruising speed, V_D is the design diving speed, and V_F is the design speed with flaps fully deflected.

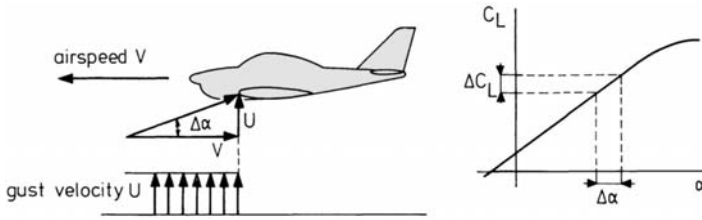


Figure 8.10 Effect of vertical gust on angle of attack

A pull-down maneuver, a sudden decrease of the angle of attack, yields a load factor less than one and can even cause a negative load factor. Since the negative value of $C_{L_{\max}}$ is generally less than the positive $C_{L_{\max}}$, the negative limit maneuvering load factor n_3 in Figure 8.9a is lower than its positive counterpart. Values of the limit maneuvering load factors as used for strength requirements are roughly as follows:

$$n_1 = 2.5 \quad \text{and} \quad n_3 = -1.0 \quad \text{for civil transport airplanes}$$

$$n_1 = 8.0 \quad \text{and} \quad n_3 = -3.5 \quad \text{for military airplanes.}$$

The airplane is also assumed to be subjected to symmetrical vertical gusts when flying through turbulent air. As sketched in Figure 8.10, in the simplest case there may be a sudden sharp-edged gust with speed U . Then, the alteration of the lift coefficient is

$$\Delta C_L = \frac{dC_L}{d\alpha} \Delta\alpha = \pm \frac{dC_L}{d\alpha} \frac{U}{V}, \quad (8.40)$$

where the minus sign refers to a downward gust.

Substitution of Equation (8.40) into (8.28) and using Equation (8.24) yields the following expression for the gust load factor

$$n = 1 \pm \frac{dC_L}{d\alpha} \frac{\frac{1}{2}\rho_0 U_e V_e}{W/S}, \quad (8.41)$$

where U_e is the gust velocity expressed in terms of an equivalent velocity.

Conform the airworthiness requirements listed at the end of this section, the gust load factors must be computed from

$$n = 1 \pm K \frac{dC_L}{d\alpha} \frac{\frac{1}{2}\rho_0 U_e V_e}{W/S}, \quad (8.42)$$

in which K is an adjusting factor, referred to as gust alleviation factor. This factor takes account of the fact that actual gust velocity profiles will never be sharp-edged but will have a more uniform shape so that, depending on airplane size and weight, there will be some response by the airplane.

Equations (8.41) and (8.42) clearly demonstrate that gust load factors are of special importance to high-speed airplanes having low wing loadings. Hence, in the

presence of high gust velocities the flight will be executed at a much slower speed than in still air.

The limit gust load factor, according to the current airworthiness standards, must correspond to particular positive and negative values of U_e . An example of a basic gust load factor envelope is given in Figure 8.9b. The dashed lines show the gust load factors for given gust velocities. The gust velocities used at the design cruising speed are assumed to be 50 ft/s (15.24 m/s) equivalent speed at altitudes between sea level and 20,000 ft (6096 m). These gust velocities may be reduced linearly from 50 ft/s at 20,000 ft to 25 ft/s (7.62 m/s) at 50,000 ft (15240 m). Also positive and negative gusts of 25 ft/s at the design diving speed V_D must be considered at altitudes between sea level and 20,000 ft. Above 20,000 ft this value may be reduced linearly to 12.5 ft/s (3.81 m/s) at 50,000 ft. Furthermore, rough air gusts of ± 66 ft/s (20.12 m/s) must be considered at altitudes between sea level and 20,000 ft. This maximum gust velocity may be reduced linearly from 66 ft/s at 20,000 ft to 38 ft/s at 50,000 ft.

At given altitude and airplane weight, the maximum gust velocity determines the speed V_B in Figure 8.9b. This is the speed at which the assumed gust velocity causes the airplane to stall. The speed V_B is called the design speed for maximum gust velocity or rough airspeed.

The limit load factors considered in this section represent the maximum air loads which might be expected in normal operation. Airworthiness requirements are also specified in terms of ultimate load factors, being the limit load multiplied by a factor of safety. This measure provides that the structure does not fail before the ultimate load is reached. Normally, a factor of safety of 1.5 must be applied to the prescribed limit load factors.

Finally, it is worth noting that the airworthiness standards encompass much more items than the requirements on design strength as described above.

"Airworthiness" has to do generally with a chain of involvements contributing to an overall aviation safety level. This is achieved by controlling the various stages in the life of an airplane; reaching from its design phase via type certification to its operation by the airline and specification of maintenance standards. Airworthiness requirements are promulgated by national authorities and are based primarily on past experience. All existing rules remain subject to continuous updating as a consequence of implementation of new experience and advanced developments. For conventional civil airplanes, the two codes of current requirements most frequently cited are:

- FAR; Federal Aviation Regulations issued by the Federal Aviation Administration (FAA) of the United States of America.
- JAR; Joint Airworthiness Requirements produced by a number of European countries and published by the Civil Aviation Authority, England on behalf of the Airworthiness Authorities Steering Committee (AASC).

Moreover, there exist similar codes of requirements published for military airplanes.

Chapter 9

PERFORMANCE IN STEADY SYMMETRIC FLIGHT

9.1 Basic relations

Consider an instant along the flight path of an airplane in steady symmetric climbing flight, as shown in Figure 9.1a. Summing forces parallel to the flight path, we have

$$T \cos \alpha_T - D - W \sin \gamma = 0, \quad (9.1)$$

and perpendicular to the flight path, we get

$$T \sin \alpha_T + L - W \cos \gamma = 0. \quad (9.2)$$

For most airplane types and in normal flight conditions, the component $T \sin \alpha_T$ in Equation (9.2) is relatively small in comparison with the other terms. Therefore, it is useful to ignore this force and to assume that the thrustline inclination from the flight path is zero so that the propulsive force T points into the direction of the velocity V (Figure 9.1b). Then, Equations (9.1) and (9.2) reduce to

$$T - D - W \sin \gamma = 0 \quad (9.3)$$

$$L - W \cos \gamma = 0. \quad (9.4)$$

Although not essential, it is often convenient to multiply Equation (9.3) with air-speed V ,

$$TV - DV - WV \sin \gamma = 0. \quad (9.5)$$

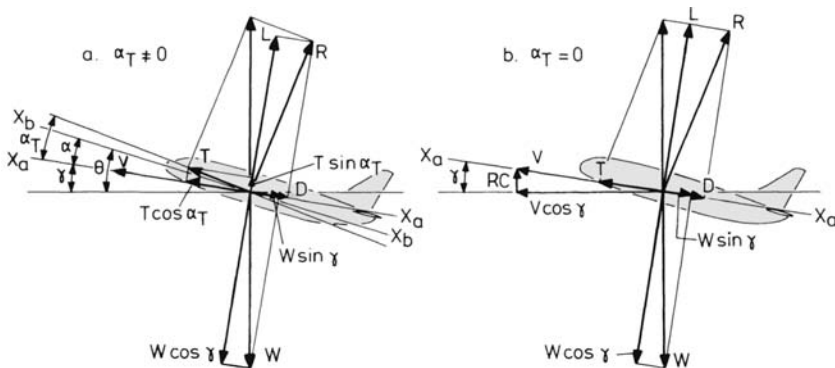


Figure 9.1 Airplane In steady symmetric flight

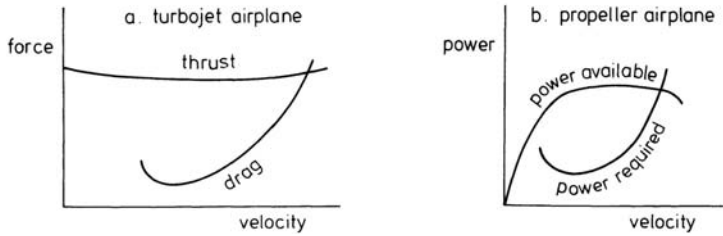


Figure 9.2 Performance diagram

Equation (9.5) expresses the work per unit time done by the forces in the direction of flight, and is frequently used in this form.

By introduction of the rate of climb RC of the airplane,

$$RC = V \sin \gamma, \quad (9.6)$$

Equation (9.5) becomes

$$TV = DV + W(RC). \quad (9.7)$$

The left-hand side of Equation (9.7) is the power delivered by the powerplant at the airspeed V . This quantity is called power available P_a ,

$$P_a = TV. \quad (9.8)$$

The term DV on the right-hand side of Equation (9.7) is the power required for flight at velocity V or shortly power required P_r ,

$$P_r = DV. \quad (9.9)$$

The difference between power available and power required is the excess power,

$$P_c = P_a - P_r. \quad (9.10)$$

Thus, the excess power P_c refers to the power that in steady flight is used to climb

$$P_c = W(RC). \quad (9.11)$$

In Chapter 8, we demonstrated that at a given point of time (given airplane weight and altitude) the flight condition depends on the following four variables:

- angle of attack, α
- airspeed, V
- flight-path angle, γ
- engine control setting, Γ .

When α (elevator stick position) and Γ (control lever position) are chosen, then the flight-path angle and airspeed can be obtained from the Equations (9.3) to (9.5).

To solve these equations, the *performance diagram* or *Penaud diagram* may be used, where, for a given altitude, airplane weight, configuration and engine control setting, the drag or power required and the thrust or power available are plotted against airspeed.

Figure 9.2 shows typical shapes of performance curves in terms of both force and power. Putting together the two curves of thrust and drag is useful when analyzing turbojet and turbofan powered airplanes since their engines are rated in terms of thrust (Figure 9.2a). On the other hand, piston- and turboprop engines are rated in terms of shaft power. Then, it is more convenient to examine their performance by combining the curves of power required and power available rather than force curves (Figure 9.2b).

Before discussing the deductions which can be made from the performance diagram, let us first consider the nature of the power and force curves separately as their variations with flight velocity are essential to the resultant performance.

9.2 Drag and power required

From Equations (9.4) and (9.9), and using the relationships $L = C_L \frac{1}{2} \rho V^2 S$ and $D = C_D \frac{1}{2} \rho V^2 S$, we easily find that

$$V = \sqrt{\frac{W}{S} \frac{2}{\rho} \frac{1}{C_L} \cos \gamma} \quad (9.12)$$

$$D = \frac{C_D}{C_L} W \cos \gamma \quad (9.13)$$

$$P_r = W \sqrt{\frac{W}{S} \frac{2}{\rho} \frac{C_D^2}{C_L^3} \cos^3 \gamma}. \quad (9.14)$$

These expressions show that for a low-subsonic airplane with a given weight and flying at a given altitude (given air density), the airspeed V , drag D and power required P_r , are functions of angle of attack α and flight-path angle γ . In its turn, the flight-path angle depends via the thrust term in Equation (9.3) on the engine control setting Γ .

In climbing flight, of course, the flight-path angle is unequal to zero. Nevertheless, performance analyses are customarily simplified by neglecting the effect of γ on V , D and P_r . Also in this book, we shall assume that the flight-path angle is sufficiently small so that its cosine may be replaced by unity, unless otherwise stated. The approximation $\cos \gamma = 1$ means that at a given height, the lift and drag coefficients and thus the drag and power required are functions of airspeed only. In other words, these relationships are given by single curves which apply to all engines control settings.

A main point to note is that, although $\cos \gamma = 1$, the sine of the flight-path angle remains unequal to zero. With this conventional assumption, Equations (9.12) to (9.14) reduce to

$$V = \sqrt{\frac{W}{S} \frac{2}{\rho} \frac{1}{C_L}} \quad (9.15)$$

$$D = \frac{C_D}{C_L} W \quad (9.16)$$

$$P_r = W \sqrt{\frac{W}{S} \frac{2}{\rho} \frac{C_D^2}{C_L^3}} \quad (9.17)$$

Table 9.1 Drag and power required for a low-subsonic airplane

| airplane weight | | | W = 20,000 N | | | |
|-----------------|-------|-----------|-----------------------|---------|------|------------|
| wing area | | | S = 25 m ² | | | |
| flight altitude | | | H = 0 m (I.S.A.) | | | |
| C_L | C_D | C_L/C_D | V, m/s | V, km/h | D, N | P_r , kW |
| 1.5 | 0.210 | 7.14 | 29.5 | 106.2 | 2801 | 82.63 |
| 1.4 | 0.164 | 8.54 | 30.5 | 109.8 | 2342 | 71.43 |
| 1.3 | 0.143 | 9.09 | 31.7 | 114.1 | 2200 | 69.74 |
| 1.2 | 0.124 | 9.68 | 33.0 | 118.8 | 2066 | 68.18 |
| 1.0 | 0.097 | 10.31 | 36.1 | 130.0 | 1940 | 70.03 |
| 0.8 | 0.076 | 10.53 | 40.4 | 145.4 | 1899 | 76.72 |
| 0.6 | 0.061 | 9.84 | 46.7 | 168.1 | 2033 | 94.94 |
| 0.4 | 0.049 | 8.16 | 57.1 | 205.6 | 2451 | 139.95 |
| 0.3 | 0.045 | 6.67 | 66.0 | 237.6 | 2999 | 197.93 |
| 0.2 | 0.042 | 4.76 | 80.8 | 290.9 | 4202 | 339.52 |

As a first example, let us consider a propeller-driven small airplane of 20,000 N weight with a wing area of 25 m². In Table 9.1 are calculated the drag and power required values at sea level (I.S.A.), starting from chosen values of lift coefficient C_L . For each C_L the airspeed V is calculated from Equation (9.15), using $\rho_0 = 1.225 \text{ kg/m}^3$ (see Appendix C). Since our example concerns an airplane designed for low-subsonic airspeeds, the corresponding values of C_D follow directly from the known lift-drag polar (Figure 9.3). Now, from Equation (9.16) the drag is determined. Finally, power required is calculated from Equation (9.17). The results of Table 9.1 are plotted as a function of airspeed in Figure 9.4. On the two curves special points can be distinguished which correspond to particular points on the lift-drag polar:

- Minimum airspeed in steady flight (point A). From Equation (9.15), we see that the airspeed decreases as the lift coefficient increases so that the minimum airspeed is obtained for maximum lift coefficient, $C_{L\text{max}}$. Then,

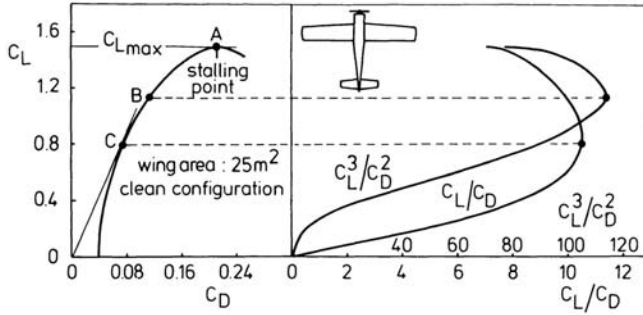


Figure 9.3 Typical lift-drag polar of a propeller-driven airplane

according to Equation (8.37), the minimum airspeed is the stalling speed V_S .

- Minimum power required (point B). Figure 9.4 shows clearly that the power required curve reaches a minimum value at an airspeed greater than the stalling speed V_S . From Equation (9.17) we see that minimum power required occurs at an angle of attack for maximum climb factor, $(C_L^3/C_D^2)_{max}$.
- Minimum drag (point C). The angle between any radius from the origin to a point on the power required curve in Figure 9.4 is a measure for P_r/V and so for the drag (see Equation (9.9)). The point C on the power required curve that corresponds to minimum drag is thus found by drawing a straight line from the origin tangent to the P_r -curve, as shown in Figure 9.4. Hence, minimum drag is always obtained at a higher airspeed and a lower lift coefficient (smaller angle of attack) than minimum power required.

Equation (9.16) tells us that minimum drag will be obtained when the airplane is flying at an angle of attack for which C_L/C_D is the maximum.

An analytical representation of drag and power required curves can be obtained by using the parabolic approximation for the lift-drag polar,

$$C_D = C_{D0} + \frac{C_L^2}{\pi A e}, \tag{9.18}$$

where C_{D0} is the zero-lift drag coefficient, A is the wing aspect ratio and e is the Oswald's efficiency factor (see Section 4.4). Introducing the parabolic drag equation, we can write Equation (9.13) as

$$D = C_{D0} \frac{1}{2} \rho V^2 S + \frac{C_L^2}{\pi A e} \frac{1}{2} \rho V^2 S. \tag{9.19}$$

From the basic equation $L = W$, we have

$$C_L = \frac{W}{\frac{1}{2} \rho V^2 S}. \tag{9.20}$$

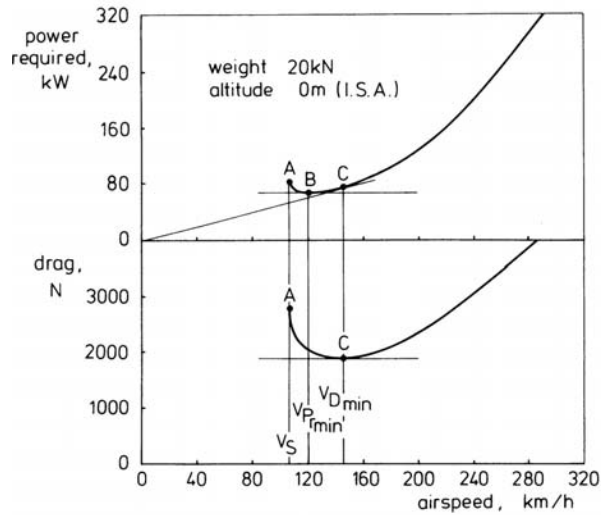


Figure 9.4 Drag and power required for low-subsonic airplane

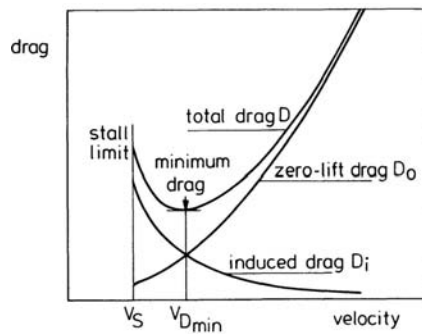


Figure 9.5 Drag components in level flight

Substituting Equation (9.20) into Equation (9.19) yields

$$D = C_{D0} \frac{1}{2} \rho V^2 S + \frac{W^2}{\pi A e \frac{1}{2} \rho V^2 S} = D_0 + D_i \quad (9.21)$$

In Equation (9.21), D_0 is the zero-lift drag and D_i is the induced drag of the airplane. Examination of this expression indicates that at a given altitude the zero-lift drag increases with V , while the induced drag decreases with increasing flight velocity. These two contributions to the total drag D are sketched as separate functions of airspeed in Figure 9.5.

The speed for minimum drag corresponds to the condition $dD/dV = 0$. Differentiating Equation (9.21) with respect to V and setting the derivative equal to zero, we readily obtain

$$V_{D\min} = \sqrt{\frac{W}{S} \frac{2}{\rho} \frac{1}{\sqrt{C_{D0} \pi A e}}} \quad (9.22)$$

Insertion of this expression into Equation (9.21) produces

$$D_0 = D_i = W \sqrt{\frac{C_{D0}}{\pi A e}} \quad \text{and} \quad (9.23)$$

$$D_{\min} = 2W \sqrt{\frac{C_{D0}}{\pi A e}}. \quad (9.24)$$

Equation (9.23) shows that at the velocity for minimum airplane drag, corresponding to $C_D = 2C_{D0}$ and $C_L = \sqrt{C_{D0}\pi A e}$, zero-lift and induced drags are equal (see Figure 9.5).

Notice that Equation (9.24) can also be derived by combining the expression for maximum lift-to-drag ratio, Equation (4.42), with Equation (9.16),

$$D_{\min} = \frac{W}{(C_L/C_D)_{\max}} = 2W \sqrt{\frac{C_{D0}}{\pi A e}}. \quad (9.25)$$

Similarly, using Equations (9.18) and (9.20) leads to the following expression for the power required

$$P_r = C_D \frac{1}{2} \rho V^3 S = C_{D0} \frac{1}{2} \rho V^3 S + \frac{W^2}{\pi A e \frac{1}{2} \rho V S}. \quad (9.26)$$

For minimum power required, $dP_r/dV = 0$. Taking the derivative of Equation (9.26) with respect to V , equating it to zero, leads to the following expression for the speed for minimum power required

$$V_{P_{\min}} = \sqrt{\frac{W}{S} \frac{2}{\rho} \frac{1}{\sqrt{3C_{D0}\pi A e}}}. \quad (9.27)$$

Substituting Equation (9.27) into Equation (9.26) furnishes the expression for minimum power required. Thus

$$P_{r\min} = \frac{4}{3} W \sqrt{\frac{W}{S} \frac{2}{\rho} \sqrt{\frac{3C_{D0}}{(\pi A e)^3}}}. \quad (9.28)$$

Note that substitution of the expression for maximum climb factor, Equation (4.46), into Equation (9.17) also will produce Equation (9.28).

By combining Equations (9.22) and (9.27), we find the relationship,

$$V_{D\min} = \sqrt[4]{3} V_{P_{\min}}. \quad (9.29)$$

Apparently, based on the parabolic lift-drag polar, the minimum drag speed is 1.32 times the speed for minimum power required.

As we shall see later on in this text, $V_{D\min}$ and $V_{P_{\min}}$ represent very important flight conditions because of operational as well as economical reasons.

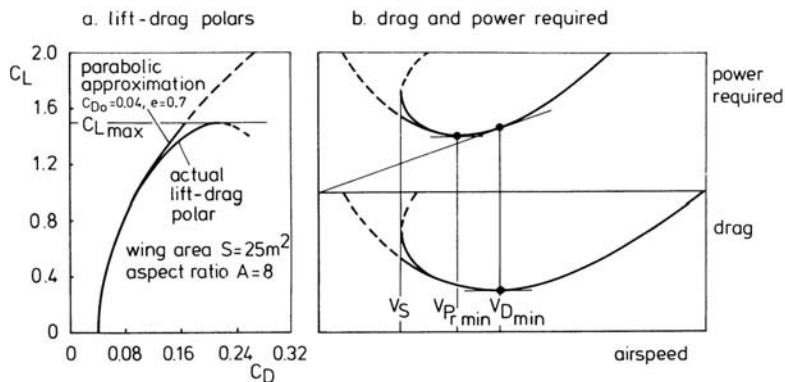


Figure 9.6 Parabolic approximation of lift-drag polar

Figure 9.6a displays the parabolic approximation of the lift-drag polar of our illustrative propeller-driven small airplane. The values of C_{D0} and e are determined by drawing the parabola that fits best the empirical curve.

We see from Figure 9.6a that at a certain value of the lift coefficient, the drag coefficient ceases to be parabolic with C_L . As the lift coefficient increases past a value of about 1.0, the actual drag coefficient increases strongly from that expected from the parabolic behavior. Beyond the stalling point the C_L drops again as the angle of attack is further increased.

The parabolic lift-drag polar on the other hand, is simply broken off at the maximum lift coefficient. At this point a large deviation from the actual drag coefficient occurs.

Therefore, as is clearly seen by inspection of the illustrative diagrams in Figure 9.6b, the shapes of the P_r - and D -curves at airspeeds near the stalling speed are somewhat different for the two types of C_L versus C_D -curves. For the actual lift-drag polar the drag and power required values will be greater than obtained from its parabolic approximation. Furthermore, the actual P_r - and D -curves are convex in a way that they have vertical tangents at the stalling speed.

Figure 9.7a presents typical parabolic lift-drag polars for a high-subsonic commercial turbofan airplane. The same data are in Figure 9.7b by means of the zero-lift drag coefficient C_{D0} and the induced drag factor $k = 1/(\pi Ae)$ as functions of flight Mach number. The curves illustrate that the drag coefficients rise sharply at Mach numbers greater than 0.70.

The procedure of calculating the drag and power required curves is accomplished in Table 9.2 for the aerodynamic data of Figure 9.7, assuming an airplane weight of 2500 kN, a wing area of 365 m², and a flight altitude of 9000 m (I.S.A.). The Mach number corresponding to a given forward velocity is given by

$$M = \frac{V}{c} = \frac{V}{\sqrt{\gamma RT}}, \quad (9.30)$$

where T is air temperature = 229.65 K. The lift coefficient follows from Equation

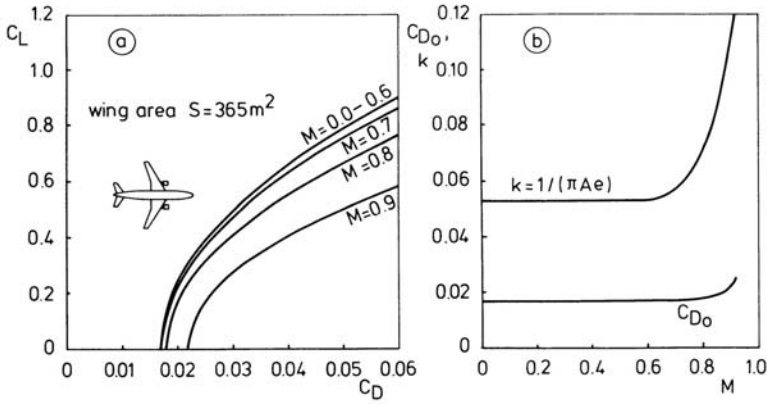


Figure 9.7 Lift-drag polars for high-subsonic transport airplane

Table 9.2 Drag and power required for a high-subsonic airplane

| airplane weight | | $W = 2500 \text{ kN}$ | | | | |
|-----------------|-------------|--------------------------------|--------|-----------|------------|-------------|
| wing area | | $S = 365 \text{ m}^2$ | | | | |
| flight altitude | | $H = 9,000 \text{ m (I.S.A.)}$ | | | | |
| C_L | $V,$ m/s | M | C_D | C_L/C_D | $D,$ kN | P_r kW |
| 1.40 | 144.9 | 0.477 | 0.1229 | 11.39 | 219.4 | 31795 |
| 1.20 | 156.5 | 0.515 | 0.0933 | 12.86 | 194.4 | 30426 |
| 1.00 | 171.5 | 0.564 | 0.0700 | 14.29 | 175.0 | 30013 |
| 0.80 | 191.7 | 0.631 | 0.0513 | 15.58 | 160.4 | 30756 |
| 0.70 | 204.9 | 0.675 | 0.0441 | 15.89 | 157.3 | 32235 |
| 0.60 | 221.4 | 0.729 | 0.0389 | 15.42 | 162.1 | 35885 |
| 0.50 | 242.5 | 0.798 | 0.0360 | 13.89 | 180.0 | 43650 |
| 0.45 | 255.6 | 0.841 | 0.0370 | 12.16 | 205.7 | 52565 |
| 0.40 | 271.1 | 0.892 | 0.0386 | 10.36 | 241.3 | 65403 |

(9.20) with $\rho = 0.4663 \text{ kg/m}^3$ (see Appendix C).

For each pair of C_L and M values, the drag coefficient is found through the drag equation

$$C_D = C_{D0} + kC_L^2. \tag{9.31}$$

The numerical results are plotted in Figure 9.8. From a comparison with Figure 9.4, it is apparent that there is no fundamental difference in the general shapes of the power required and drag curves for propeller-driven and jet-driven airplanes.

As a third example, in Table 9.3 the drag and power required curves are produced for a supersonic airplane with a weight of 85 kN and a wing area of 35 m². The flight is executed at an altitude of 11,000 m (I.S.A.). At this height the air density

Table 9.3 Drag and power required for a supersonic airplane

| | | airplane weight | | | | | $W = 85,000 \text{ N}$ |
|------|-------------|-----------------|--------|-----------|------------|-------------|---------------------------------|
| | | wing area | | | | | $S = 35 \text{ m}^2$ |
| | | flight altitude | | | | | $H = 11,000 \text{ m (I.S.A.)}$ |
| M | $V,$ m/s | C_L | C_D | C_L/C_D | $D,$ kN | P_r kW | |
| 0.47 | 138.1 | 0.7000 | 0.2095 | 3.34 | 25.4 | 3513 | |
| 0.50 | 147.5 | 0.6271 | 0.1697 | 3.70 | 23.0 | 3394 | |
| 0.60 | 177.0 | 0.4355 | 0.0839 | 5.19 | 16.4 | 2897 | |
| 0.80 | 236.1 | 0.2447 | 0.0308 | 7.96 | 10.7 | 2522 | |
| 1.00 | 295.1 | 0.1567 | 0.0273 | 5.75 | 14.8 | 4366 | |
| 1.10 | 324.6 | 0.1295 | 0.0386 | 3.36 | 25.3 | 8213 | |
| 1.20 | 354.1 | 0.1088 | 0.0343 | 3.18 | 26.8 | 9476 | |
| 1.60 | 472.1 | 0.0612 | 0.0252 | 2.43 | 35.0 | 16530 | |
| 2.20 | 649.2 | 0.0324 | 0.0195 | 1.66 | 51.3 | 33271 | |

$= 0.3639 \text{ kg/m}^3$ and the air temperature $= 216.65 \text{ K}$. Figure 9.9 furnishes the aerodynamic data for the vehicle. In the calculations, values of Mach number are chosen. The corresponding airspeeds follow from Equation (9.30) and the lift coefficients are given by Equation (9.20). From Equation (9.31) the lift coefficient at a given Mach number determines the drag coefficient and so the drag and power required.

The graphic representation of the calculation results is given in Figure 9.10. The curves portray that there is a dramatic rise in drag and power required due to compressibility when the airplane flies at transonic and supersonic speeds. Since the drag coefficient decreases with increasing supersonic flight velocity, the drag rises above $M = 1.1$ at a slower rate than below the sonic speed.

9.3 Thrust and power available

Figure 9.11 indicates the typical variation of thrust with flight Mach number for turbojets, turbofans and propeller propulsion systems. The data are presented as the fraction of the thrust at a given Mach number to the static thrust ($V = 0$).

The curves show that throughout the subsonic flight regime the thrust of a turbojet is reasonably constant with airspeed (cf. Figure 6.24). On the other hand, propeller thrust declines rapidly with increasing Mach number. For moderate bypass ratios, the curves for the turbofans have shapes in the middle between that of turbojets and propeller propulsion systems.

As depicted in Figure 9.12a, the behavior of the propeller thrust results in a power available remaining relatively constant with airspeed, except at high and low forward velocities where the propulsive efficiency falls off (see Figure 7.2). In contrast, the almost constant value of turbojet thrust causes that its power available increases essentially linearly with airspeed (Figure 9.12b). Obviously, if the air-

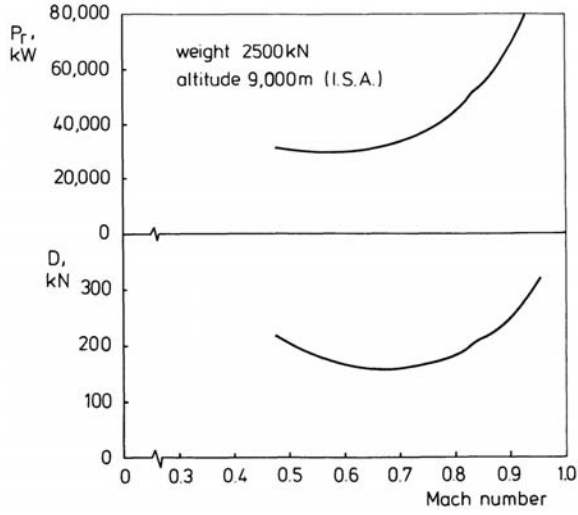


Figure 9.8 High-subsonic transport airplane drag and power required

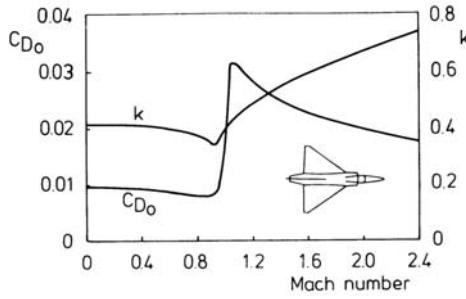


Figure 9.9 Aerodynamic data for supersonic airplane (estimated)

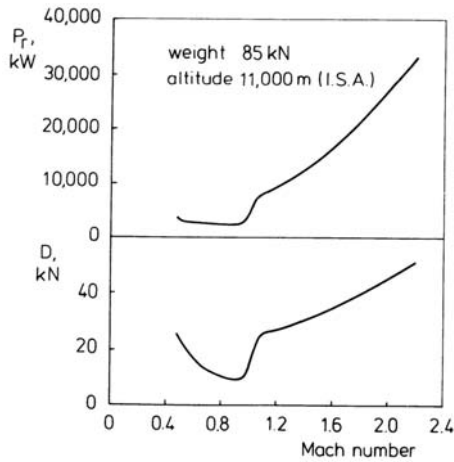


Figure 9.10 Power required and drag for a supersonic airplane

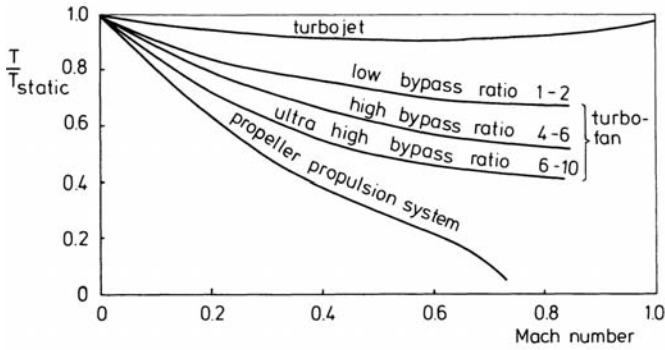


Figure 9.11 Typical variation of thrust with Mach number

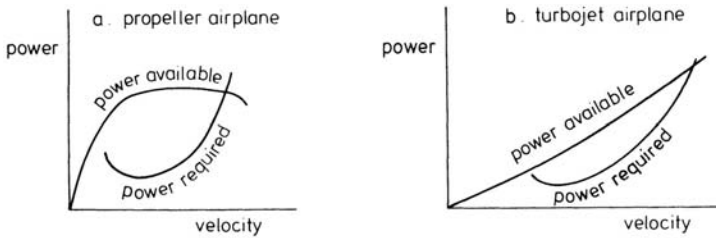


Figure 9.12 Typical power available curves

plane is equipped with turbofan engines, the power available curve will lie approximately halfway between that of the pure turbojet and propeller propulsion systems.

Since the performance characteristics of turbojet and turbofan engines are specified in terms of thrust, the power available curves for these engine types are simply obtained from $P_a = TV$. For propeller-driven airplanes the calculation procedure is definitely more complicated as the available power is obtained from the product of shaft brake power of the engine and propulsive efficiency of the propeller,

$$P_a = \eta_j P_{br} \tag{9.32}$$

First of all, we will explain the derivation of the power available versus V-curve for an airplane with piston-engine and propeller. This type of airplane may be equipped with a constant speed propeller or a fixed-pitch propeller. In both cases, power available is determined at a given inlet manifold pressure. Thus, as explained in Section 6.2, for the flight at a given altitude, shaft brake power as a function of engine rpm is known from the standard power diagram.

For the combination of piston-engine and constant speed propeller, the pilot can control the inlet manifold pressure and the propeller blade angle separately such that the engine speed remains constant.

Accordingly, at a given altitude (given air density), shaft brake power is directly known from selected values of inlet manifold pressure and engine speed.

Table 9.4 Power available and thrust for piston-engine and constant speed propeller

| | | flight altitude $H = 0$ m (I.S.A.) | | | | | | |
|--------------|---------------|---|--------|-------|-------|----------|---------------|------------|
| | | propeller diameter $D = 2.60$ m | | | | | | |
| | | propeller gear ratio $n_p/n = 1.0$ | | | | | | |
| | | inlet manifold pressure $p_z = 115140$ N/m ² | | | | | | |
| | | engine speed $n = 2300$ rpm | | | | | | |
| V , m/s | V , km/h | P_{br} kW | C_P | J | C_T | η_j | P_a , kW | T , N |
| 10 | 36 | 295 | 0.0360 | 0.100 | 0.090 | 0.250 | 73.75 | 7375 |
| 20 | 72 | 295 | 0.0360 | 0.201 | 0.081 | 0.452 | 133.34 | 6667 |
| 30 | 108 | 295 | 0.0360 | 0.301 | 0.070 | 0.585 | 172.58 | 5753 |
| 40 | 144 | 295 | 0.0360 | 0.401 | 0.061 | 0.680 | 200.60 | 5015 |
| 50 | 180 | 295 | 0.0360 | 0.502 | 0.054 | 0.753 | 222.14 | 4443 |
| 60 | 216 | 295 | 0.0360 | 0.602 | 0.048 | 0.803 | 236.89 | 3948 |
| 70 | 252 | 295 | 0.0360 | 0.702 | 0.044 | 0.858 | 253.11 | 3616 |
| 80 | 288 | 295 | 0.0360 | 0.803 | 0.040 | 0.892 | 263.14 | 3289 |

In Table 9.4 is carried out the calculation of power available and thrust for our illustrative propeller-driven small airplane of the preceding section, using the chosen set of data.

The procedure of finding power available and propeller thrust at successive values of airspeed is illustrated in the following.

1. For the selected values of inlet manifold pressure and engine speed we find the shaft brake power from the standard power diagram in Figure 9.13.
2. The power coefficient of the propeller is computed from the equilibrium condition $P_p = P_{br}$:

$$C_P = \frac{P_{br}}{\rho n_p^3 D^5}.$$

3. The advance ratio at each chosen value of airspeed V is obtained from the relationship

$$J = \frac{V}{n_p D}.$$

4. The value of C_T for the C_P and J found in steps 2 and 3 is taken from Figure 9.14, and the propulsive efficiency is computed from

$$\eta_j = \frac{C_T}{C_P} J.$$

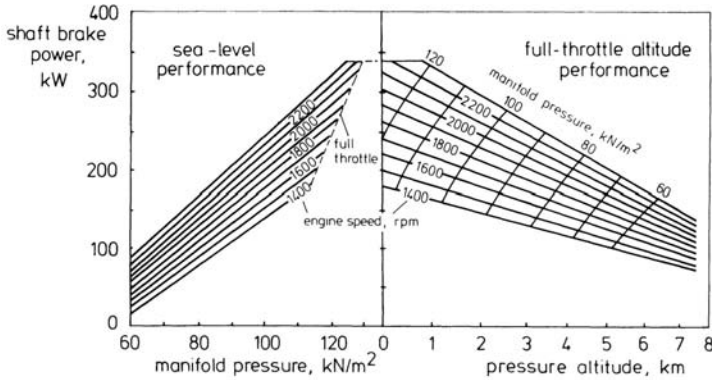


Figure 9.13 Standard power diagram of piston-engine (illustrative)

5. Power available and thrust are determined by using the two equations

$$P_a = \eta_j P_{br} \quad \text{and} \quad T = \eta_j \frac{P_{br}}{V}.$$

When dealing with a fixed-pitch propeller the blade angle $\beta_{0.75}$ is constant. This implies that the power required for rotation and so the propeller speed will vary with forward velocity.

At flight speeds lower than a chosen design speed the propeller power requirements slow the rotational speed down, and at higher airspeeds it is necessary to reduce the engine control setting in order to avoid overspeeding of the engine.

When starting from given values of airspeed, the determination of power available and thrust requires a very cumbersome calculation method since the engine speed, defined by the equilibrium condition $P_p = P_{br}$ can only be found by trial and error. A working procedure to determine successive points of the power available curve for a piston-engine with a fixed-pitch propeller is to start from chosen values of engine speed. Then, in combination with the selected inlet manifold pressure, shaft brake power is directly known, and the resulting airspeed follows from the condition $P_p = P_{br}$.

The values of power available and thrust can now be found in four steps:

1. Determine P_{br} from the standard power diagram for each chosen value of engine speed.
2. Compute the power coefficient from

$$C_P = \frac{P_{br}}{\rho n_p^3 D^5}.$$

3. Take from the propeller chart the values of J and C_T which correspond to this C_P and the selected blade angle $\beta_{0.75}$ and compute V and η_j by using

$$V = J n_p D \quad \text{and} \quad \eta_j = \frac{C_T}{C_P} J.$$

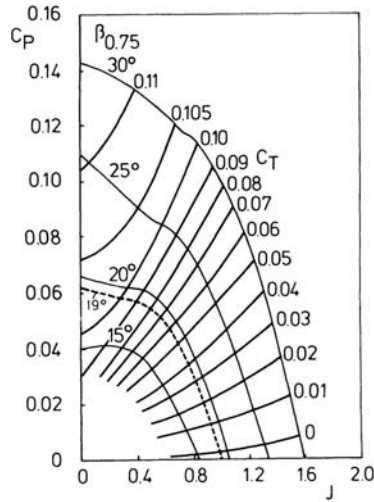


Figure 9.14 Propeller chart of 2-bladed propeller (estimated)

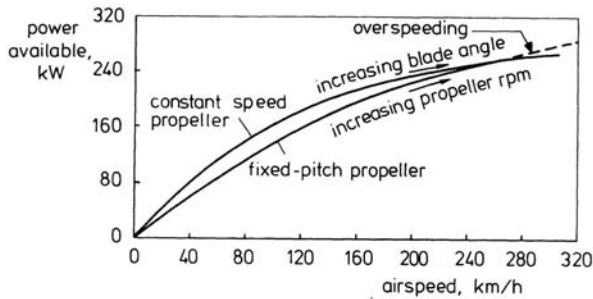


Figure 9.15 Power available curves for piston-engine propeller combination

4. Compute the available power and thrust by using

$$P_a = \eta_j P_{br} \quad \text{and} \quad T = \eta_j \frac{P_{br}}{V}$$

The procedure is executed in Table 9.5 for the airplane of the preceding example, but now for the case of a constant propeller blade setting. The numerical results in Tables 9.4 and 9.5 are plotted in Figure 9.15, showing that the curve for the fixed-pitch propeller is not very different from that for the constant speed propeller, except that there will be less excess power.

In a turboprop, most of the gas generator power is extracted from the gas stream through the engine by the turbine to drive the propeller, while a small portion is used to develop jet thrust through expansion of the exhaust gases in the nozzle. Therefore, the power available produced by the turboprop is the sum of the power delivered by the propeller plus the power equivalent of the jet thrust,

$$P_a = \eta_j P_{br} + T_j V, \tag{9.33}$$

Table 9.5 Power available and thrust for piston-engine and fixed-pitch propeller

| | | flight altitude $H = 0$ m (I.S.A.) | | | | | | | |
|------------|-----------|---|------|-------|------|-------|----------|--------|------|
| | | propeller diameter $D = 2.60$ m | | | | | | | |
| | | inlet manifold pressure $p_z = 115140$ N/m ² | | | | | | | |
| | | propeller blade angle $\beta_{0.75} = 19^\circ$ | | | | | | | |
| $n_p = n,$ | $P_{br},$ | C_P | J | C_T | V | V | η_j | $P_a,$ | $T,$ |
| rpm | kW | | | | m/s | km/h | | kW | N |
| 1800 | 233 | 0.0593 | 0.18 | 0.102 | 14.0 | 50.4 | 0.309 | 72.0 | 5143 |
| 1900 | 245 | 0.0530 | 0.54 | 0.074 | 40.2 | 144.7 | 0.749 | 183.5 | 4565 |
| 2000 | 258 | 0.0479 | 0.60 | 0.066 | 52.0 | 187.2 | 0.826 | 213.0 | 4096 |
| 2100 | 270 | 0.0433 | 0.66 | 0.056 | 60.1 | 216.2 | 0.853 | 230.5 | 3835 |
| 2200 | 283 | 0.0394 | 0.71 | 0.048 | 67.7 | 243.7 | 0.871 | 246.5 | 3641 |
| 2300 | 295 | 0.0360 | 0.74 | 0.043 | 73.8 | 265.7 | 0.875 | 258.0 | 3496 |

where the shaft power P_{br} and the additional jet thrust T_j may be known from the engine brochure and η_j can be found according to the procedure for the constant speed propeller in Table 9.4.

9.4 The performance diagram

Figure 9.16 shows the two performance curves in terms of power for our illustrative small airplane with piston-engine and constant speed propeller. Power required and power available are taken from the previous Tables 9.1 and 9.4.

The maximum forward velocity at which level unaccelerated flight can be maintained, is determined by the condition that $P_c = 0$ in Equation (9.10). Thus

$$P_a = P_r. \quad (9.34)$$

In Figure 9.16, this equality holds for the intersection of the P_a and P_r -curves. At all speeds lower than the maximum level flight speed V_{max} , power available exceeds power required for level flight. The excess power can be used for increasing the potential energy of the vehicle, i.e., climbing flight and/or for increasing kinetic energy, i.e., accelerated flight.

Now, suppose the pilot wishes to slow down the airspeed in order to change to a steady climbing flight. For that, he must pull back the control stick to operate the elevators such that the angle of attack is increased. In the first instant, before the airspeed is altered, increased lift and drag are produced. The extra lift causes an upward directed acceleration and the excess drag reduces the flight velocity. Ultimately, the control action may lead to a new state of steady climbing flight where, from Equations (9.10) and (9.11), the rate of climb is given by

$$RC = \frac{P_a - P_r}{W}. \quad (9.35)$$

Using Equation (9.35), the rate of climb follows directly from the excess power in Figure 9.16.

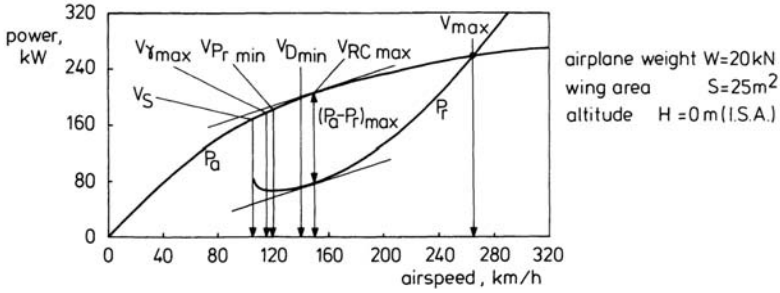


Figure 9.16 Performance diagram for small propeller-driven airplane

Table 9.6 Calculation of rate of climb

| V , km/h | P_a , kW | P_r kW | P_c kW | RC m/s |
|---------------|---------------|-------------|-------------|-------------|
| 106.2 | 170.0 | 82.6 | 87.4 | 4.37 |
| 120.0 | 183.0 | 68.0 | 115.0 | 5.75 |
| 140.0 | 197.0 | 74.0 | 125.0 | 6.15 |
| 160.0 | 210.0 | 88.0 | 122.0 | 6.10 |
| 180.0 | 221.0 | 107.0 | 114.0 | 5.70 |
| 200.0 | 231.0 | 132.0 | 99.0 | 4.95 |
| 220.0 | 240.0 | 165.0 | 75.0 | 3.75 |
| 240.0 | 248.0 | 204.0 | 44.0 | 2.20 |
| 260.0 | 256.0 | 247.0 | 9.0 | 0.45 |
| 280.0 | 262.0 | 293.0 | -31.0 | -1.55 |

This procedure is carried out in Table 9.6 and the resulting RC is plotted versus V in Figure 9.17a. The maximum rate of climb is then found to be $RC_{max} = 6.2$ m/s. Naturally, the maximum rate of climb is of great importance to minimize the time for the airplane to attain its cruise altitude.

From the curve in Figure 9.17a, we also see that the best speed for climbing is $V_{RCmax} = 150$ km/h.

Since the rate of climb is maximum at the airspeed at which the excess power is maximum, the optimum speed for maximum rate of climb can also be found in Figure 9.16 as the abscissa where the two power curves have parallel tangents.

Another curve that can be used to display the climb performance is the hodograph, which is the plot of the rate of climb against the horizontal component of the airspeed, $V_h = V \cos \gamma$ (Figure 9.17b). In the latter diagram, a radius vector from the origin and intersecting the curve has the slope:

$$\frac{RC}{V_h} = \frac{V \sin \gamma}{V \cos \gamma} = \tan \gamma.$$

Hence, the angle between the abscissa and a straight line from the origin to the

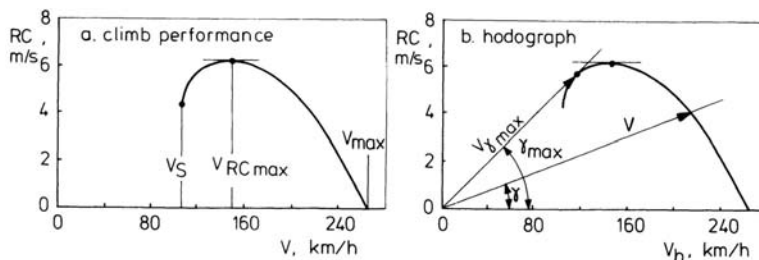


Figure 9.17 Rate of climb versus airspeed and climb performance hodograph

RC curve represents the flight-path angle or angle of climb,

$$\gamma = \tan^{-1} \left[\frac{RC}{V_h} \right] = \sin^{-1} \left[\frac{RC}{V} \right].$$

It is also apparent that the length of the radius vector from the origin to any point on the curve serves as a measure of the airspeed V .

Furthermore, it is seen that the maximum climb angle in steady symmetric flight is determined by the tangent to the hodograph. From Figure 9.17b, $\gamma_{\max} = 9.93^\circ$.

The corresponding speed for steepest climbing is found as $V_{\gamma_{\max}} = 120$ km/h.

The flight with maximum climb angle is of importance to minimize the horizontal distance for the airplane to arrive at a particular altitude.

We further notice that the airspeed for best climb angle is less than the speed for best rate of climb.

As matters of interest, the airspeeds for minimum drag, $V_{D_{\min}}$, and minimum power required, $V_{P_{r\min}}$, have also been marked in Figure 9.16. It is seen that $V_{RC_{\max}}$ is greater than the minimum drag speed and that $V_{\gamma_{\max}}$ is nearby the minimum power required speed.

At the engine control setting considered in Figure 9.16, a large excess power is available at the stalling speed, through which the airplane will climb if steady flight is maintained. In order to perform a level flight at the stall, of course, the engine must be throttled back until power available equals power required.

Another point to note with respect to the flight at low airspeeds is that in case the pilot desires to increase the rate of climb, the control stick has to be pushed forward in order to attain an increased airspeed. This control action will lead to the wanted effect of a higher rate of climb owing to the greater vertical distance between the performance curves in Figure 9.16. The region wherein this phenomenon occurs is referred to as the *region of reversed command*. This situation is connected with the problem of speed instability, which complication shall be discussed in Section 11.3.

In Figure 9.18, the performance curves of Figure 9.16 are repeated. In addition, the power available curve for the fixed-pitch propeller of the previous Table 9.5 is drawn. The blade setting of the latter propeller is such that both propulsion systems provide the same maximum level flight speed.

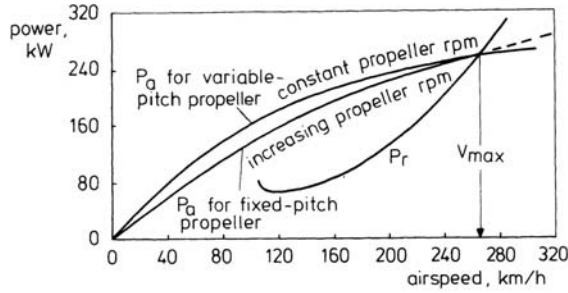


Figure 9.18 Performance diagrams for small propeller-driven airplane

As we have learned in the preceding section, due to the decrease in engine speed with decreasing airspeed, shaft brake power and so power available is lower for the fixed-pitch propeller. Consequently, the rate of climb and the climb angle at each flight velocity will be less for the airplane with fixed-pitch propeller.

From our discussion in Section 9.1, we know that it is convenient in considering the performance of jet propelled airplanes to work with thrust and drag curves. This type of performance diagram is presented in Figure 9.19 for our illustrative high-subsonic turbofan transport of Table 9.2. The thrust curve is sketched according to the typical variation of high-bypass ratio turbofan thrust.

The intersection of the thrust and drag curves in Figure 9.19 defines the maximum airspeed for level flight,

$$T = D. \tag{9.36}$$

At velocities below V_{max} , the excess thrust determines directly the angle of climb since from Equation (9.3) we find that

$$\sin \gamma = \frac{T - D}{W}. \tag{9.37}$$

This equation indicates that the maximum climb angle is obtained for maximum excess thrust. Inspection of Figure 9.19 shows that for the jet airplane steepest climbing occurs in the proximity of the minimum drag speed.

The high thrust to weight ratios for jet airplanes allow relative large climb angles. Therefore, in the light of Equations (9.12) to (9.14), it is worthwhile to examine the validity of the approximation that γ is sufficiently small to assume that $\cos \gamma$ is equal to one.

The effect of this approximation can best be studied by considering steady symmetric flight conditions at a given airspeed. Then, the performance diagram directly yields the climb angle and the rate of climb, using drag and power required for level flight.

At a given airspeed, the lift coefficient in level flight is greater than in climbing flight ($C_L = W/(qS)$ instead of $C_L = W \cos \gamma/(qS)$). Consequently, also the drag coefficient and so the drag and power required in level flight are greater than in climbing flight.

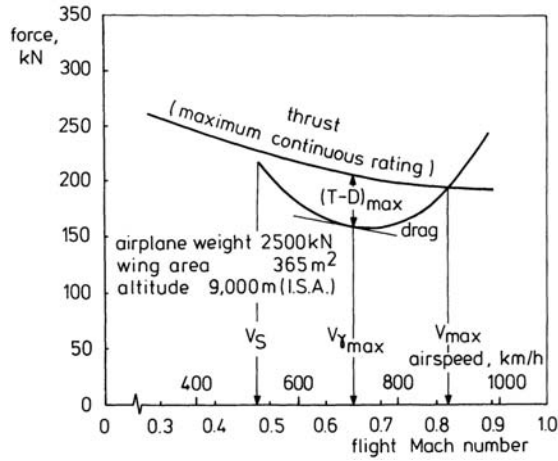


Figure 9.19 Performance diagram for turboprop transport airplane

It is thus evident that when using the performance diagram, we have the safe situation that climb angle and rate of climb are underestimated.

Apparently, the increased drag and power required values result from the use of wrong lift coefficients (wrong induced drag coefficients). Hence we may provide a relationship between the actual climb angle and the climb angle using $\cos \gamma = 1$ by writing:

$$\sin \gamma = \frac{T-D}{W} = \frac{T-D_1}{W} + \frac{\Delta D_i}{W}. \quad (9.38)$$

where the subscript "1" denotes the case $\cos \gamma = 1$ and ΔD_i is the surplus of induced drag.

However, $\Delta D_i = \Delta C_{Di} \frac{1}{2} \rho V^2 S$; hence, from Equation (9.38)

$$\sin \gamma = \sin \gamma_1 + \Delta C_{Di} \frac{\frac{1}{2} \rho V^2 S}{W}.$$

Now since $C_{Di} = k C_L^2$,

$$\sin \gamma = \sin \gamma_1 + k (C_{L1}^2 - C_L^2) \frac{\frac{1}{2} \rho V^2 S}{W}.$$

Substituting $C_{L1} = W / (\frac{1}{2} \rho V^2 S)$ and $C_L = W \cos \gamma / (\frac{1}{2} \rho V^2 S)$, results in the expression:

$$\sin \gamma = \sin \gamma_1 + k \sin^2 \gamma \frac{W}{\frac{1}{2} \rho V^2 S}. \quad (9.39)$$

The problem may be adequately described by setting $\gamma = \gamma_1$ in the second term on the right-hand side of Equation (9.39), so that

$$\frac{\sin \gamma}{\sin \gamma_1} = \frac{RC}{RC_1} = 1 + k \sin \gamma_1 \frac{W}{\frac{1}{2} \rho V^2 S}. \quad (9.40)$$

To illustrate the result of the preceding analysis we now look as an example at a typical turbofan transport with a wing loading of 6850 N/m^2 . For this airplane the induced drag factor is $k = 0.053$ and the maximum sea-level climb angle $\gamma_1 = 15^\circ$. If the corresponding speed for steepest climbing is 425 km/h , we have from Equation (9.40),

$$\frac{\sin \gamma}{\sin \gamma_1} = \frac{RC}{RC_1} = 1 + 0.053 \times 0.2588 \frac{6850}{0.5 \times 1.225 \times (425/3.6)^2} = 1.011.$$

From this numerical result, we see that the error is only 1.1 %. Nevertheless, if desired, the result can easily be improved by iteration.

9.5 Performance prediction using analytical expressions

The performance diagram enables us to determine graphically the point performance for airplanes for which the lift-drag polar and the variation of thrust or power available with forward speed are known in any arbitrary form.

In Section 9.2, we described an analytical procedure for deriving the drag and power required curves from the approximation that the drag coefficient increases parabolically with the lift coefficient (see Equations (9.21) and (9.26)).

In order to obtain a complete analytical representation of the performance curves we have to introduce also simplifying assumptions with regard to the shape of the thrust and power available curves.

Obviously, such analytical methods of performance computation will only provide an assessment of the actual performance and are especially of importance to obtain an insight into the effects on performance of the various parameters.

As discussed in Chapter 6, the thrust of a turbofan engine is produced by the cold air flowing through the bypass duct and the hot air passing through the exhaust nozzle (see Figure 6.6). Typically, the turbofan thrust decreases with airspeed, which behavior may be conveniently described by:

$$\frac{T}{T_{\text{static}}} = 1 - k(V)^{\frac{1}{2}}, \quad (9.41)$$

where k is a constant for a given bypass ratio, control setting and altitude.

Although it is a laborious task, from Equations (9.21) and (9.41), formulae for the performance of the airplane can be derived.

Returning to Figure 9.11, we see that the variation of turbofan thrust with airspeed lies between that of the turboprop and the turbojet. Moreover, Figure 9.11 shows that the turbofan becomes more and more a turboprop as the bypass ratio is enlarged, and that the turbofan resembles a pure turbojet if its bypass ratio is low. Therefore, it is convenient in analyzing performance using analytical expressions for thrust and drag, to consider successively the extreme cases of propulsion by a propeller and a pure jet.

As we have learned in Section 9.3, for a constant speed propeller the power available is essentially constant throughout the speed range of the airplane. Hence, power available for propeller-driven airplanes may be assumed to be independent of airspeed, provided that engine control setting and altitude remain unchanged. The variation of power available with altitude may be described by a relationship similar to Equation (6.92), namely,

$$\frac{P_a}{P_{a0}} = \left(\frac{\rho}{\rho_0} \right)^n, \quad (9.42)$$

in which the subscript "0" designates sea-level condition and the power n is less than 1.0 (in the troposphere).

Returning again to Figure 9.11, we note that the thrust of a subsonic turbojet engine is relatively constant with flight velocity. Accordingly, it appears worthwhile to assume that the thrust of a jet-powered airplane has a constant value throughout the subsonic speed range. As stated previously (see Equation (6.80)), we may relate the thrust of the turbojet at any given altitude to its sea-level value by

$$\frac{T}{T_0} = \left(\frac{\rho}{\rho_0} \right)^n. \quad (9.43)$$

Figure 9.20a shows schematically the performance diagram with the assumption P_a is constant. On the power required curve are indicated special points which correspond to definite points on the lift-drag polar, sketched in Figure 9.20b. The meanings of these points are reviewed in Table 9.7, where points 2, 3 and 6 require some further explanation.

The angle inclined between any straight line through point O' in Figure 9.20a and intersecting the power required curve and the horizontal P_a -line is approximately a measure of the climb angle since, from Equations (9.6) and (9.35), γ is given by

$$\gamma = \sin^{-1} \left[\frac{RC}{V} \right] = \sin^{-1} \left[\frac{P_a - P_r}{W V} \right]. \quad (9.44)$$

Hence, at point 2 we find the speed for steepest climbing and the corresponding maximum climb angle as this point is located by the tangent from point O' to the P_r -curve. The exact location of point 2, clearly, depends on the magnitude of power available.

Recalling Equation (9.35) for the rate of climb, we find that when power available is unchanging, the maximum rate of climb is given by

$$RC_{\max} = \frac{P_a - P_{r\min}}{W}. \quad (9.45)$$

Point 3 in Figure 9.20 a indicates the speed at which the power required curve has a minimum value. Substitution of Equation (9.17) into Equation (9.45) results in

$$RC_{\max} = \frac{P_a}{W} - \sqrt{\frac{W}{S} \frac{2}{\rho} \frac{1}{(C_L^3/C_D^2)_{\max}}}. \quad (9.46)$$

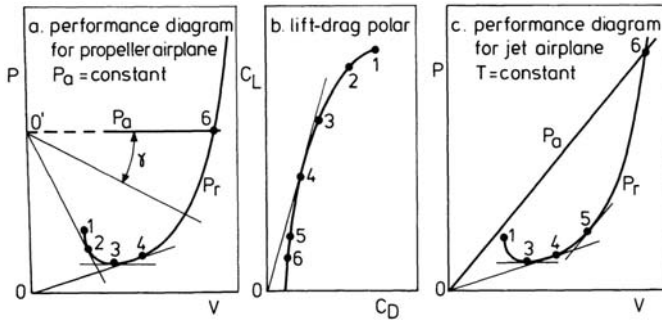


Figure 9.20 Idealized performance diagrams

Table 9.7 Point performance in steady symmetric flight

| performance | | lift-drag polar | equation |
|-------------------------|----------------------------|------------------------------|---|
| $P_a = \text{constant}$ | $T = \text{constant}$ | | |
| 1 | stalling speed | $C_{L\text{max}}$ | $V = \sqrt{\frac{W}{\rho} \frac{2}{C_L}}$ |
| 2 | maximum climb angle | — | $\sin \gamma = \frac{P_a - P_r}{WV}$ |
| minimum power required | | | $P_r = W \sqrt{\frac{W}{\rho} \frac{2}{C_L} \frac{C_D^2}{C_L^3}}$ |
| 3 | maximum rate of climb | $(C_L^3/C_D^2)_{\text{max}}$ | $RC = \frac{P_a - P_r}{W}$ |
| minimum drag | | | $D = \frac{C_D}{C_L} W$ |
| 4 | — | $(C_L/C_D)_{\text{max}}$ | |
| 5 | — | maximum climb angle | $\sin \gamma = \frac{T - D}{W}$ |
| 5 | — | maximum rate of climb | $RC = \frac{P_a - P_r}{W}$ |
| 6 | maximum level flight speed | — | $P_a = P_r$ $L = W$ |

Thus, we see that point 3 on the lift-drag polar represents the angle of attack at which the climb factor C_L^3/C_D^2 is maximum.

Regarding point 6, it should be noticed that an analytical prediction of the maximum level flight speed starting from a given value of P_a and using Equations (9.34), (9.17) and (9.31) is very complicated as it requires the solution of a fourth power equation in C_L .

A working approach to the problem is to specify V_{max} and then to determine the power available needed to satisfy the equilibrium condition $P_a = P_r$.

Figure 9.20c shows the performance diagram in terms of power for a jet airplane with constant thrust. In this case power available varies linearly with airspeed. The meanings of the special points in Figures 9.20b and 9.20c are also listed in Table 9.7, where now the points 4, 5 and 6 may need some additional explanation.

For the climb angle (point 4) we can write, from Equations (9.37) and (9.16),

$$\sin \gamma = \frac{T-D}{W} = \frac{T}{W} - \frac{C_D}{C_L}. \quad (9.47)$$

At constant thrust, the climb angle appears to be maximum at the minimum drag speed and thus at the maximum lift-to-drag ratio,

$$\sin \gamma_{\max} = \frac{T}{W} - \frac{1}{(C_L/C_D)_{\max}}. \quad (9.48)$$

In reference to Figure 9.20b, the point at which C_L/C_D is maximum is found by drawing a line from the origin tangent to the lift-drag polar.

Maximum rate of climb occurs at point 5, where the excess power is maximum. Clearly, the location of the corresponding point on the lift-drag polar depends on the magnitude of the thrust, which defines the slope of the P_a -line in Figure 9.20c. Combining Equations (9.15) and (9.47) results in the following expression for the rate of climb,

$$RC = V \sin \gamma = \sqrt{\frac{W}{S} \frac{2}{\rho} \frac{1}{C_L}} \left[\frac{T}{W} - \frac{C_D}{C_L} \right]. \quad (9.49)$$

The maximum rate of climb can be obtained by setting the first derivative of Equation (9.49) with respect to C_L equal to zero, i.e.,

$$\frac{dRC}{dC_L} = \frac{d}{dC_L} \left[\sqrt{\frac{W}{S} \frac{2}{\rho} \frac{1}{C_L}} \left[\frac{T}{W} - \frac{C_D}{C_L} \right] \right].$$

Carrying out this differentiation yields the condition for maximum rate of climb that

$$\frac{T}{W} = 3 \frac{C_D}{C_L} - 2 \frac{dC_D}{dC_L}. \quad (9.50)$$

For a parabolic variation of C_D with C_L we can substitute Equation (9.18) into Equation (9.50) to give

$$\frac{T}{W} = 3 \frac{C_{D0}}{C_L} - \frac{C_L}{\pi A e}. \quad (9.51)$$

This quadratic equation in C_L can be solved to obtain the lift coefficient for maximum rate of climb,

$$C_{Lc} = \frac{\pi A e T}{2W} \left[-1 + \sqrt{1 + 12 \frac{C_{D0}}{\pi A e} \left(\frac{W}{T} \right)^2} \right]. \quad (9.52)$$

The maximum level steady flight speed at point 6 is described by the conditions:

$$W = C_{Lc} \frac{1}{2} \rho V^2 S \quad (9.53)$$

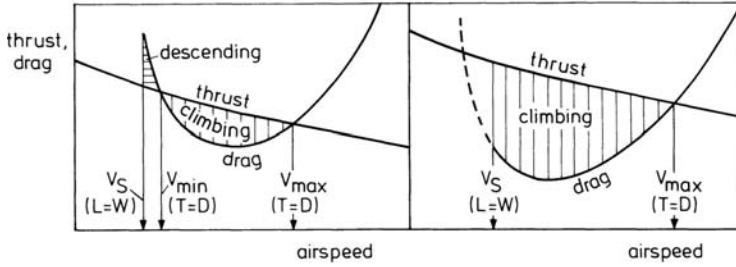


Figure 9.21 Minimum airspeed

$$T = C_D \frac{1}{2} \rho V^2 S. \tag{9.54}$$

Substituting Equation (9.21) into Equation (9.54) yields a quadratic equation in V_{\max} ,

$$T = C_{D0} \frac{1}{2} \rho V_{\max}^2 S + \frac{W^2}{\pi A e \frac{1}{2} \rho V_{\max}^2 S}, \tag{9.55}$$

which can be solved to obtain an expression for the maximum level flight speed,

$$V_{\max} = \sqrt{\frac{T}{\rho C_{D0} S} \left[1 \pm \sqrt{4 \frac{C_{D0}}{\pi A e} \left(\frac{W}{T} \right)^2} \right]}. \tag{9.56}$$

In principle, there are two solutions for the level steady flight speed. The plus sign in Equation (9.56) represents the high-speed intersection of the thrust and drag curves, and the minus sign is coupled with the possibility of a low-speed intersection (Figure 9.21). In the latter case, the stalling speed cannot be reached in level steady flight. On the other hand, there are speeds, depending on airplane weight, configuration, altitude and engine rating, at which the equation $T = D$ cannot be satisfied at a lift coefficient less than or equal to $C_{L_{\max}}$. Then the minimum airspeed equals the stalling speed.

Chapter 10

EFFECT OF ALTITUDE

10.1 Effect of altitude on drag and power required

The effect of altitude on point performance in steady symmetric flight arises from the decrease in air density with increasing altitude. The attendant modification of the performance diagram may be examined by repeating the construction of the two performance curves for each altitude in the way described in Sections 9.2 and 9.3. However, the influence of altitude on drag and power required curves can best be studied by considering flight conditions at different altitudes but at the same angle of attack. Using the subscript "1" to denote the conditions at altitude H_1 , the relevant equations are:

$$V_1 = \sqrt{\frac{W}{S} \frac{2}{\rho_1} \frac{1}{C_L}}, \quad D_1 = \frac{C_D}{C_L} W, \quad P_{r1} = W \sqrt{\frac{W}{S} \frac{2}{\rho_1} \frac{C_D^2}{C_L^3}}.$$

At an altitude $H_2 > H_1$, designated by the subscript "2", we have

$$V_2 = \sqrt{\frac{W}{S} \frac{2}{\rho_2} \frac{1}{C_L}}, \quad D_2 = \frac{C_D}{C_L} W, \quad P_{r2} = W \sqrt{\frac{W}{S} \frac{2}{\rho_2} \frac{C_D^2}{C_L^3}}.$$

Let us assume that we can neglect the effect on the lift-drag polar of the alteration of the flight Mach number that is coupled with the altitude variation at constant dynamic pressure. Then, the lift and drag coefficients also remain unchanged, and we obtain,

$$\frac{V_2}{V_1} = \sqrt{\frac{\rho_1}{\rho_2}} \quad (10.1)$$

$$\frac{D_2}{D_1} = 1 \quad (10.2)$$

$$\frac{P_{r2}}{P_{r1}} = \sqrt{\frac{\rho_1}{\rho_2}}. \quad (10.3)$$

The ratios (10.1) to (10.3) show that at a given angle of attack the values of air-speed and power required increase with increasing altitude, whereas the drag is independent of height. To illustrate the results of this analysis, consider as an example an airplane powered by two turboprop engines, having the following characteristics:

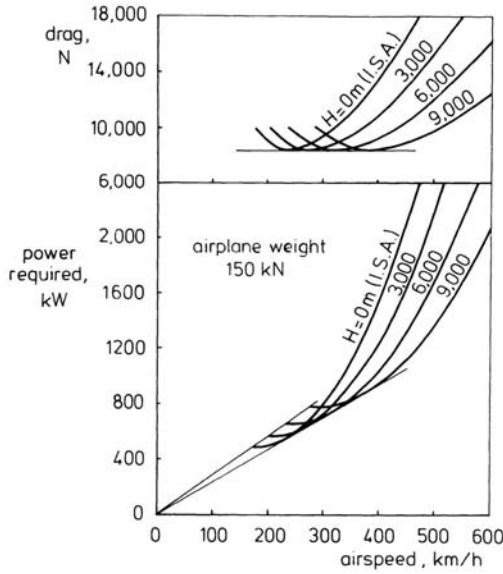


Figure 10.1 Altitude effects on drag and power required

| | | |
|----------------------------|----------------|--------------------------------|
| airplane weight | W | $= 150,000 \text{ N}$ |
| wing area | S | $= 70 \text{ m}^2$ |
| wing aspect ratio | A | $= 12$ |
| lift-drag polar | C_D | $= C_{D0} + C_L^2 / (\pi A e)$ |
| zero-lift drag coefficient | C_{D0} | $= 0.013$ |
| Oswald's efficiency factor | e | $= 0.76$ |
| maximum lift coefficient | $C_{L_{\max}}$ | $= 1.5.$ |

Figure 10.1 presents drag and power required curves for four altitudes. According to Equations (10.1) and (10.2), the drag curves experience a horizontal translation to the right when altitude increases. The power required curves show a shift to the right as well as an upward displacement. In this respect, from Equation (10.1) and (10.3), we can write,

$$\frac{P_{r2}}{P_{r1}} = \frac{V_2}{V_1}. \tag{10.4}$$

Equation (10.4) shows that corresponding points for a given angle of attack lie at a straight line through the origin. Consequently, all power required curves have only one joint tangent, which defines the locations of the points for minimum drag ($D_{\min} = (P_r/V)_{\min}$).

10.2 Rate of climb and climb angle

Figure 10.2a shows a graph of representative power available curves for our illustrative turboprop airplane of the preceding section. Sketched are typical variations

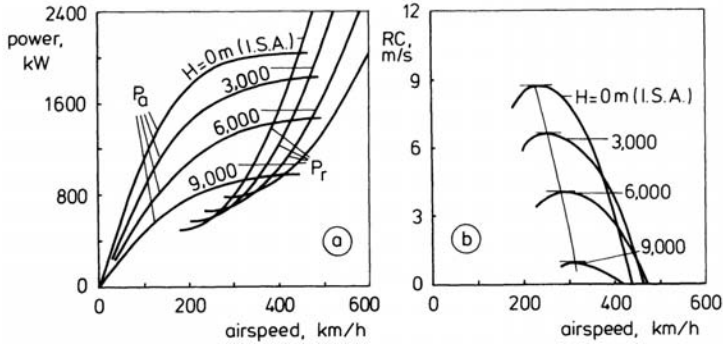


Figure 10.2 Performance diagrams and rate of climb curves

of P_a with V for a given engine control setting, where it is assumed that at each velocity the available power varies with height according to Equation (9.42). Also plotted is the set of power required curves, as given in the previous Figure 10.1. Figure 10.2a shows that the variations of power required and power available with altitude result in a decrease in the vertical distances between the performance curves. We also see that the stalling speed (T.A.S.) increases, whilst the maximum level steady flight speed first remains more or less unchanged, and later falls off with increasing altitude.

The altitude effects on the RC vs V -curves, resulting from the performance curves, are shown in Figure 10.2b. These plots show that as altitude increases the maximum rate of climb decreases.

This is illustrated by Figure 10.3, where is plotted RC_{\max} against altitude. It appears that the latter curve is practically linear. A point to note is that in the case of a supercharged piston engine the linear decrease of maximum rate of climb with altitude is only valid above the critical altitude of the engine since from thereon the power output decreases linearly with air density. This behavior is illustrated by the dashed lines in Figure 10.3.

The altitude at which maximum rate of climb becomes equal to zero is called the *absolute ceiling* or *theoretical ceiling* of the airplane. At this height the P_a -curve is tangent to the P_r -curve, i.e., the highspeed and the low-speed intersections of the performance curves coincide and no positive excess power exists (Figure 10.3). Note that the theoretical ceiling depends on airplane configuration, airplane weight and engine control setting.

The time to climb from sea level to any given altitude H is given by the integral

$$t = \int_0^H \frac{dH}{dH/dt} = \int_0^H \frac{dH}{RC}. \quad (10.5)$$

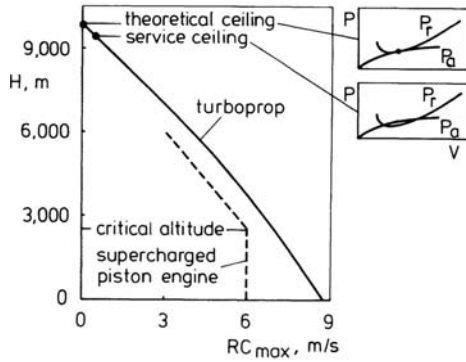


Figure 10.3 Maximum rate of climb versus altitude

Hence, the minimum time to arrive at the theoretical ceiling, H_{th} is

$$t_{\min} = \int_0^{H_{th}} \frac{dH}{RC_{\max}}. \tag{10.6}$$

Since maximum rate of climb diminishes to zero at the theoretical ceiling, the time needed for reaching this altitude becomes infinite. This makes the idea of the theoretical ceiling inadequate for use as a criterion for the climbing capability of an airplane. Therefore, as a practical upper limit of flight altitude, the *service ceiling* is used, which is defined as that altitude at which the maximum rate of climb is reduced to 0.5 m/s (100 ft/min). In our example in Figure 10.3 the difference between the two ceilings is seen to be 500 meters.

Let us assume for the sake of discussion that power available would be independent of airspeed. Then, the maximum rate of climb is given by Equation (9.46), which is repeated here for convenience,

$$RC_{\max} = \frac{P_a}{W} - \sqrt{\frac{W}{S} \frac{2}{\rho} \frac{1}{(C_L^3/C_D^2)_{\max}}}. \tag{10.7}$$

This equation clearly shows that, at a given engine control setting, the maximum rate of climb diminishes with increasing height due to the fact that both P_a and ρ lessen. Equation (10.7) also indicates that for P_a is constant with airspeed, the angle of attack for maximum rate of climb does not vary with altitude. Hence, the equilibrium condition $W = C_L \frac{1}{2} \rho V^2 S$ requires that the dynamic pressure must remain fixed (Figure 10.4a). Accordingly, we draw the interesting conclusion that the equivalent airspeed for maximum rate of climb is invariable with height,

$$V_{e_{RC_{\max}}} = \sqrt{\frac{W}{S} \frac{2}{\rho_0} \frac{1}{(C_L)(C_L^3/C_D^2)_{\max}}}. \tag{10.8}$$

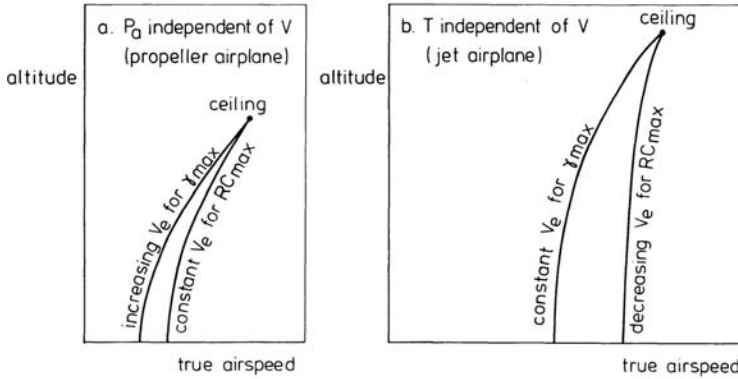


Figure 10.4 Typical variations of climb speed with altitude

The corresponding variation of true airspeed is

$$V_{RC_{\max}} = \sqrt{\frac{W}{S} \frac{2}{\rho} \frac{1}{(C_L)(C_L^3/C_D^2)_{\max}}}. \quad (10.9)$$

It must be emphasized that this reasoning is only valid as far as P_a is independent of airspeed. When the actual variations of power available are taken into account, the fastest climb will occur at a somewhat higher equivalent airspeed than predicted by Equation (10.8).

As was seen in Chapter 9, in the case of a propeller-driven airplane we cannot derive analytic expressions for the steepest climb conditions. However, from Figure 9.17b one thing is sure; at sea level the airspeed for steepest climb is lower than that for maximum rate of climb and lies very close to the stalling speed. Since the airspeeds for steepest climb and fastest climb must coincide at the theoretical ceiling, we conclude that the equivalent airspeed for steepest climb will increase with altitude (Figure 10.4a).

We will proceed to examine the effect of altitude on the two special climb speeds for jet airplanes, assuming that the engine thrust is constant with airspeed. Then, the maximum climb angle is given by Equation (9.48), which is rewritten below,

$$\sin \gamma_{\max} = \frac{T}{W} - \frac{1}{(C_L/C_D)_{\max}}. \quad (10.10)$$

This equation shows that at constant engine control setting the climb angle will decrease as the altitude increases. At the theoretical ceiling of the airplane, the steepest climb angle becomes zero,

$$\sin \gamma_{\max} = \frac{T_{th}}{W} - \frac{1}{(C_L/C_D)_{\max}} = 0. \quad (10.11)$$

Obviously, the angle of attack for steepest climb is independent of altitude so that now we have the special condition that the airspeed for best angle of climb

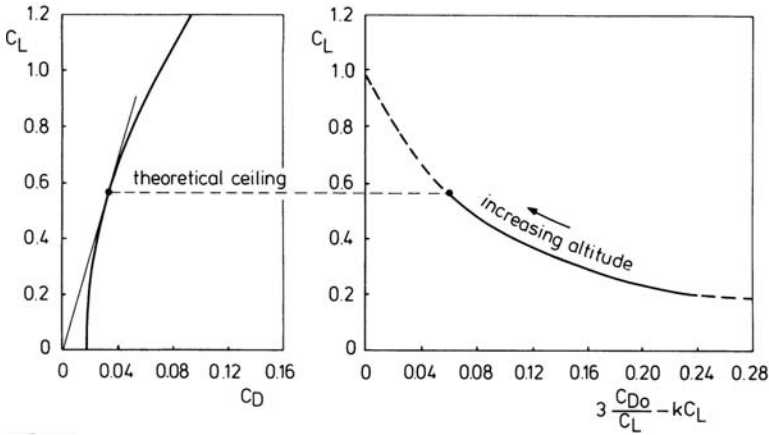


Figure 10.5 Lift coefficient for fastest climb

corresponds to a constant equivalent airspeed,

$$V_{e\gamma_{\max}} = \sqrt{\frac{W}{S} \frac{2}{\rho_0} \frac{1}{(C_L/C_D)_{\max}}} \quad (10.12)$$

Also with respect to the airspeed for fastest climb, a different behavior occurs compared with the case of propeller propulsion. According to Equation (9.50), the condition for maximum rate of climb reads,

$$\frac{T}{W} = 3 \frac{C_D}{C_L} - 2 \frac{dC_D}{dC_L} \quad (10.13)$$

For an airplane with parabolic lift-drag polar, $C_D = C_{D0} + kC_L^2$, Equation (10.13) can be written as (see also Equation (9.51))

$$\frac{T}{W} = 3 \frac{C_{D0}}{C_L} - k C_L \quad (10.14)$$

The condition (10.14) is plotted in Figure 10.5 for an airplane that has a drag equation with $C_{D0} = 0.017$ and $k = 0.053$.

An important thing to notice is that the lift coefficient for maximum rate of climb increases with increasing altitude, owing to the fact that the thrust falls off when height is gained. This observation implies that the equivalent airspeed for best rate of climb also falls off with height although the corresponding true airspeed may increase somewhat with height (Figure 10.4b). At the theoretical ceiling, we have

$$\frac{T_{th}}{W} = \frac{C_D}{C_L} \quad (10.15)$$

Substitution of Equation (10.15) into Equation (10.13) confirms the result of the previous Equation (10.11) that at the theoretical ceiling the airplane flies at that angle of attack where the ratio C_L/C_D is the maximum.

Although the foregoing results are based on the assumption of a thrust which is independent of airspeed, they certainly indicate the typical features of the climb speeds for γ_{\max} and RC_{\max} .

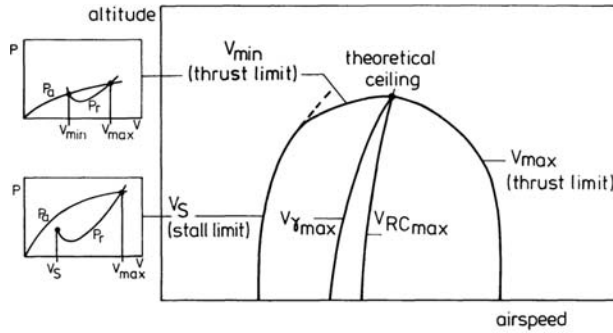


Figure 10.6 Typical flight speed boundaries for subsonic airplane

10.3 Stall, propulsion and buffet boundaries

For the case of constant engine control setting and given airplane weight and configuration, the influence of height on the possible flight speeds is sketched in Figure 10.6. For the sake of completeness, also are indicated the typical variations of the climb speeds.

The altitude effects on the high-speed and low-speed boundaries due to engine output and stall characteristics are, basically, identical for the various types of subsonic airplanes with turbo-engines and for airplanes with aspirated (nonsupercharged) piston engines.

With regard to minimum airspeed, two different altitude regions must be distinguished. At lower heights, the magnitude of power available is such that a steady flight with maximum lift coefficient can be executed without losing height (see also Figure 9.21). Therefore, in this region, the minimum airspeed is equal to the stalling speed, which follows from

$$V_S = \sqrt{\frac{W}{S} \frac{2}{\rho} \frac{1}{C_{L_{\max}}}}. \quad (10.16)$$

At heights near the theoretical ceiling, power available has been reduced to the extent that power required for steady level flight at maximum lift coefficient exceeds P_a . In this region, the minimum airspeed is determined by the low-speed intersection of the performance curves, whereby the required angle of attack is smaller than the critical angle of attack. This condition is also depicted in Figure 10.6.

The high-speed boundary is formed by the maximum level steady flight speeds. In accordance with the performance diagrams in the previous Figure 10.2, the maximum airspeed in Figure 10.6 initially remains approximately constant and then becomes smaller with increasing altitude down to the speed $V_{\gamma_{\max}} = V_{RC_{\max}}$ at the theoretical ceiling.

Let us first examine in some detail the variation of V_{\max} with altitude for propeller-

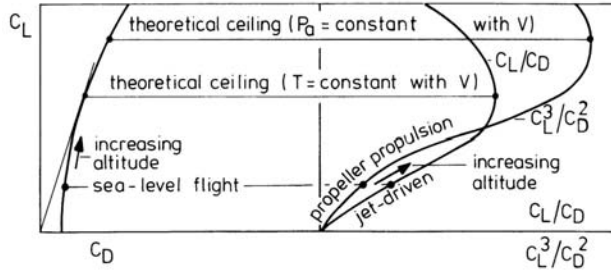


Figure 10.7 Lift coefficient for maximum airspeed

driven airplanes. In this case, we may use our approximation that P_a is constant with airspeed. Using Equation (9.17) and the condition $P_a = P_r$, we get the relationship

$$P_a = W \sqrt{\frac{W}{S} \frac{2}{\rho} \frac{C_D^2}{C_L^3}} \quad (10.17)$$

Solving Equation (10.17) for the climb factor yields

$$\frac{C_L^3}{C_D^2} = \frac{W^3}{S} \frac{2}{\rho} \frac{1}{P_a^2} \quad (10.18)$$

Equation (10.18) indicates that because ρ and P_a decrease with increasing altitude, the climb factor will increase up to its maximum value $(C_L^3/C_D^2)_{\max}$ when the airplane is at the theoretical ceiling. As can be seen in Figure 10.7, there will be an attendant increase in angle of attack so that also the lift and drag coefficients at which the airplane flies will become greater as altitude increases.

The relationship between the maximum level steady flight speed and the changing values of ρ , P_a and α is given by

$$P_a = C_D \frac{1}{2} \rho V_{\max}^3 S \quad \text{or} \quad (10.19)$$

$$V_{\max} = \sqrt[3]{\frac{P_a}{S} \frac{2}{\rho} \frac{1}{C_D}} \quad (10.20)$$

In studying the variation of V_{\max} with altitude on the basis of Equation (10.20), we have to include an assumption about the relationship between power available and height. To this end, we consider the following three characteristic altitude changes of P_a :

- a. Power available is directly proportional to air density. In this case, it is seen from Equation (10.20) that V_{\max} decreases continuously with height, as sketched in Figure 10.8a.

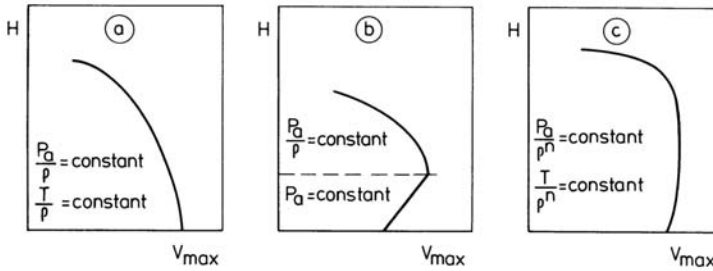


Figure 10.8 Altitude effects on maximum airspeed

- b. Power available is independent of altitude. Now, the decrease of ρ will dominate the increase of C_D , resulting in a rise in V_{\max} (Figure 10.8b). This condition can be used in the case of airplanes with supercharged piston engines at heights below the critical altitude of the engines.

Beyond the critical height, the piston engine output varies linearly with density. Consequently, V_{\max} will inevitably decrease so that from thereon the V_{\max} vs H -curve is similar to the curve in Figure 10.8a.

- c. The ratio P_a/ρ increases with height according to Equation (9.42). Under this condition, we may find that at first V_{\max} increases somewhat. Above a certain altitude the influence of the increasing C_D will dominate and, accordingly, V_{\max} will fall off (Figure 10.8c). This behavior is typical for turboprop airplanes.

The same traits are true of the turbojet airplane. From the condition of equilibrium $T = D$ at V_{\max} , we obtain

$$T = \frac{C_D}{C_L} W \quad \text{whence} \quad (10.21)$$

$$\frac{C_L}{C_D} = \frac{W}{T}. \quad (10.22)$$

Using the approximation that T is constant with V , we find that in consequence of the fact that the thrust falls off with altitude, the lift-to-drag ratio in Equation (10.22) will increase up to $(C_L/C_D)_{\max}$ at the theoretical ceiling (Figure 10.7). Now the relation between V_{\max} , ρ , T and α is governed by

$$T = C_D \frac{1}{2} \rho V_{\max}^2 S \quad \text{or} \quad (10.23)$$

$$V_{\max} = \sqrt{\frac{T}{S} \frac{2}{\rho} \frac{1}{C_D}}. \quad (10.24)$$

If the assumption is made that the thrust decreases in direct proportion to ambient density, it follows from Equation (10.24) that V_{\max} decreases with height, as shown in Figure 10.8a.

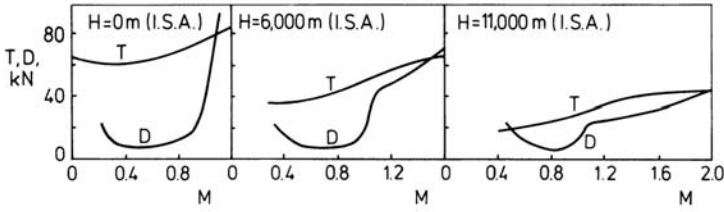


Figure 10.9 Performance diagrams of supersonic airplane

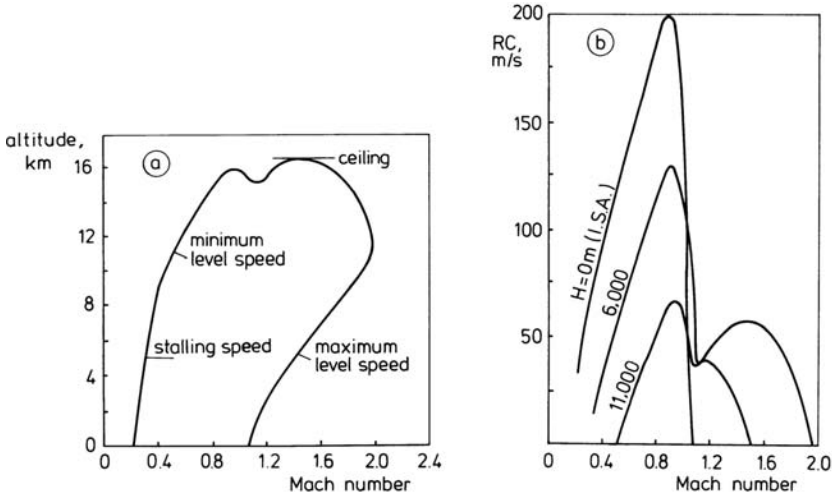


Figure 10.10 Altitude effects on performance of supersonic airplane

In point of fact, V_{max} will be almost constant up to a large flight altitude. This picture of the maximum level flight speed variation is shown in Figures 10.6 and 10.8c and comes about because of the increase in the ratio T/ρ with altitude (see Equations (6.80) and (9.43)).

In Figure 10.9 are presented the performance diagrams for three altitudes for a supersonic airplane with a weight of 82 kN and having its jet thrust augmented by afterburning.

The altitude effects resulting from these graphs are shown in Figure 10.10.

In contrast with its subsonic counterparts, the maximum level steady flight speed appears to increase strongly when a supersonic airplane climbs from sea level to a higher altitude. The reason for this lies in the combined effect of an increasing thrust and decreasing drag coefficient with supersonic flight velocity. Figure 10.10a shows that the very highest airspeed is reached near the tropopause (I.S.A.).

Apparently, high excess powers are present at both subsonic and supersonic speeds, through which in each of the two speed regimes a maximum rate of climb speed can be recognized (Figure 10.10b).

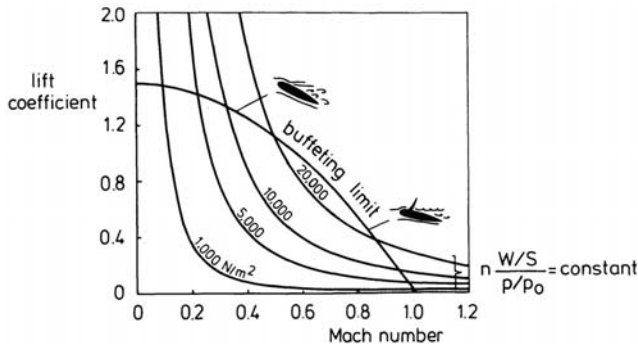


Figure 10.11 Mach number effect on stall

The flight regime of an airplane is also determined by its buffet characteristics. Buffeting concerns an undesirable shaking of the airplane and its controls, which is caused by the turbulence in the flow when the boundary layer separates from the outer surface of the airplane. Boundary layer separation can happen at any airspeed. Therefore, buffeting can affect the low-speed as well as the high-speed boundary.

Generally, there is a marked tendency for the stalling angle of attack to go down with increasing flight Mach number. The actual maximum usable angles of attack, of course, can only be obtained from flight testing over the entire Mach number range of a specific type of airplane. In Figure 10.11 is sketched the typical variation of the maximum attainable lift coefficient against flight Mach number for a high-subsonic type of airplane (buffeting limit).

At low Mach numbers, buffeting occurs as the stall is approached, and the maximum achievable lift coefficient is close to the $C_{L_{max}}$ -value of the airplane.

As described in Chapter 4, when an airplane exceeds the critical Mach number, shock waves on the airplane surface will be formed. Due to the large pressure increase through the waves, shock-induced boundary layer separation comes about and the resulting turbulence in the wake may cause buffeting. The objectionable phenomena also include pitching and yawing oscillations from rapid changes of pressure distribution. In consequence of this, buffeting becomes more pronounced and maximum C_L decreases with increasing Mach number up to transonic speeds, at which it may cause a complete collapse of the lift.

In Figure 10.11 also are plotted curves of constant values of $n \frac{W/S}{P/P_0}$, where n is the load factor. The curves are calculated from

$$nW = C_L \frac{1}{2} \gamma p M^2 S, \quad (10.25)$$

which is a basic lift equation for level flight if the load factor is not equal to unity (see Section 8.3).

Clearly, plots such as in Figure 10.11 can be used to determine the operating envelope of an airplane with respect to buffeting since for any given wing loading, altitude and load factor there is a minimum and maximum Mach number defined

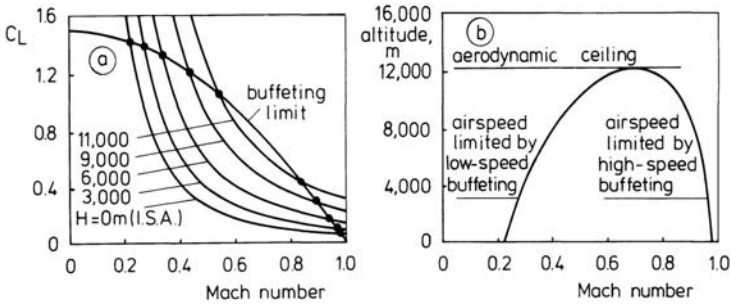


Figure 10.12 Mach number effect on level flight speed limits

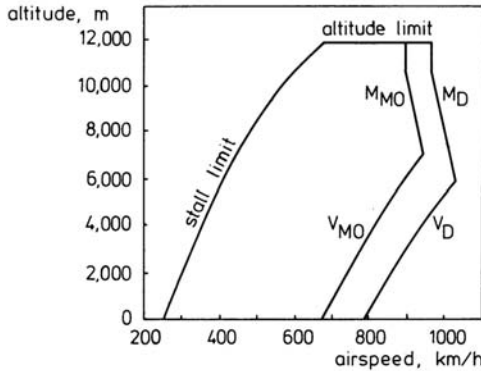


Figure 10.13 Flight envelope of jet airplane

by the points at which the buffet boundary crosses the appropriate $n \frac{W/S}{\rho/P_0}$ vs M -curve.

In order to determine the operational envelope where level steady flight speeds can be maintained, our hypothetical buffet boundary is plotted again in Figure 10.12a. Superimposed on the buffet plot are now C_L vs M -curves for level steady flight, calculated from the condition $W = C_L \frac{1}{2} \gamma \rho M^2 S$, using $W/S = 5 \text{ kN/m}^2$. We clearly see that the range of possible level flight speeds becomes smaller as altitude increases. At a certain altitude the low-speed and high-speed stall coincide. This altitude is called the *aerodynamic ceiling* of the airplane.

Figure 10.12b shows the resulting flight Mach numbers as a function of altitude. It is evident that these flight speed limits depend on airplane configuration, weight and load factor.

10.4 Flight envelope

The flight envelope describes the area of altitude and airspeed where an airplane is constrained to operate (Figure 10.13). Within the boundaries of this diagram fall all the possible combinations of airspeed, altitude and load factor.

The flight envelope is defined by the various limitations on the performance of the

airplane, such as available engine power, stalling, buffet characteristics, structural considerations and requirements on external noise production.

The selected high-speed boundary depends highly on the chosen value of the design cruising speed V_C , which is the maximum equivalent or calibrated level flight speed at which the structure is strong enough to withstand prescribed loads imposed by allowable flight maneuvers and gusts encountered in rough air. The conditions defining the flight loads are specified in the airworthiness regulations. As explained in the previous Section 8.5, the basic maneuvering and gust envelopes (V - n diagrams) define the symmetrical flight loads for which the airplane structure is designed.

From the speed-altitude operating limits in Figure 10.13, which refer to jet airplanes, the following boundaries are recognized:

- The maximum operating speed V_{MO} , which is the calibrated airspeed that may not be deliberately exceeded in any type of flight. The airspeed V_{MO} is so established that it is not greater than the design cruising speed V_C . Flying at V_{MO} , the associated flight Mach number increases with altitude and an altitude may be reached at which it would be impossible to fly because of compressibility effects. For this reason, there is a maximum operating Mach number M_{MO} which cuts off V_{MO} so that the airplane remains free from undesirable flying qualities associated with buffeting.
- The design diving speed V_D and the design diving Mach number M_D , which limit the maximum level flight speeds at which the airplane is designed to remain controllable and to withstand particular flight loads. The difference between V_D and V_{MO} and between M_D and M_{MO} is the safety margin for unintentional increments of speed.
- The maximum flight altitude for airplanes with a pressurized cabin. This altitude limit is determined by the maximum pressure differential load for which the airplane structure is designed.
- The stall limit, which is formed by the calibrated minimum stalling speed, that is the calibrated minimum steady flight speed with power off at which the airplane is controllable. The maneuver conducted to measure this speed has previously been described in section 8.4.

Remember that at constant indicated airspeed the flight Mach number will increase with altitude. Therefore, the calibrated minimum stalling speed may increase with altitude due to the effects of near-stall buffeting on maximum lift coefficient. It is also important to remember that the stall boundary depends strongly on airplane weight and configuration.

For supersonic airplanes similar flight speed limitations occur. In addition to the boundaries indicated in Figure 10.13, maximum speed may be limited by detri-

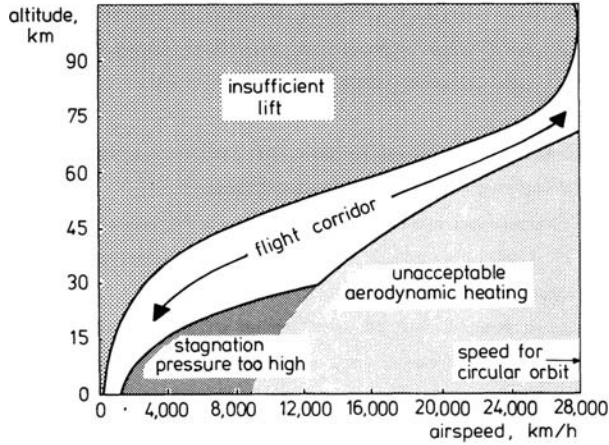


Figure 10.14 Flight corridor

mental effects of compressibility on flying qualities. Also, the serious deterioration of the strength of materials due to aerodynamic heating in supersonic flight may constrain the achievable level flight speed.

The relationship between the temperature at the stagnation points on the leading edge of the wing or at the nose of the fuselage and the flight Mach number is given by the expression, as derived in Appendix D,

$$T_t = T \left[1 + \frac{\gamma - 1}{2} M^2 \right], \quad (10.26)$$

where T_t represents the total temperature at a stagnation point and T is the ambient temperature.

For instance, let us assume a flight in the lower stratosphere (I.S.A.) at a Mach number of 2.5. Then Equation (10.26) yields: $T_t = 488\text{K} = 215^\circ\text{C}$. This figure may confirm that extra structural problems are present in supersonic airplane design as a result of kinetic heating of the skin surfaces.

In order to warrant safe and economic operations throughout the entire range of flight speeds, each airplane is furnished with a flight manual, specifying the conditions under which the airplane can be used safely.

The possible area of altitude and airspeed where hypersonic airplanes may operate is depicted in Figure 10.14.

The maximum altitude boundary is attained when the sum of aerodynamic lift and centrifugal force becomes insufficient to balance the component of the airplane weight perpendicular to the flight path. On the other hand, for a given airspeed the airplane cannot fly below a certain altitude where the adverse effects of high total pressures or high skin temperatures on structural strength, become too great. When an airplane is flying along a curvilinear path in a great-circle plane, the

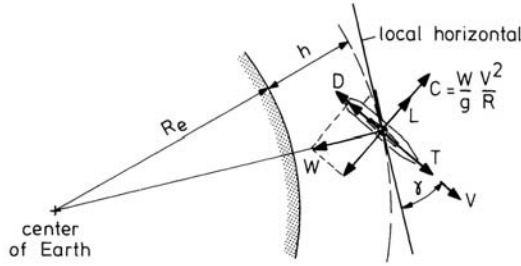


Figure 10.15 High-altitude and high-velocity flight In great-circle plane

upper boundary can be found from the equality

$$C_L \frac{1}{2} \rho V^2 S + \frac{W V^2}{g R} = W \cos \gamma, \quad (10.27)$$

where R is the radius of curvature of the flight path and γ is the angle the flight path makes with the local horizontal (Figure 10.15).

With the assumption of a small flight-path angle ($\cos \gamma = 1$), we can transform Equation (10.27) into the form

$$C_L \frac{1}{2} \rho V^2 S + \frac{W}{g} \frac{V^2}{(R_e + h)} = W. \quad (10.28)$$

In this equation R_e is the radius of the (spherical) Earth and h is the flight altitude. Substitution of Equation (1.18) into Equation (10.28) produces the following expression for the relationship between the flight velocity V and the altitude h ,

$$C_L \frac{1}{2} \rho V^2 S = W_0 \frac{g}{g_0} \left[1 - \frac{V^2}{V_c^2} \right], \quad (10.29)$$

where W_0 is the weight of the airplane at sea level and V_c is the circular velocity. As exemplified in Figure 10.14, there exists a narrow flight corridor which links atmospheric flight to space flight and visa versa. Through the flight corridor a lifting vehicle can reach the circular velocity and become a satellite or can perform a lifting re-entry trajectory.

The three boundaries in Figure 10.14 are determined for the value $W_0 / (C_L S) = 4800 \text{ N/m}^2$, a permissible total pressure of $p_t / p_0 = 2$, and a maximum allowable total temperature of $1900 \text{ }^\circ\text{C}$. For the variation of temperature, pressure and density with altitude in the upper atmosphere, the data in Reference 38 are used.

Chapter 11

FLIGHT AND AIRPLANE CONDITION EFFECTS

11.1 Effect of weight

To study the effect of changing the weight of an airplane, we consider here steady symmetric flight at an initial weight W_1 . For the purpose of calculating new values of airspeed, drag and power required at a weight W_2 , let the flight altitude and the angle of attack remain fixed. If further possible effects of compressibility are ignored, we can utilize the fact that C_L and C_D are invariable at constant angle of attack. Then, from Equations (9.15) to (9.17), we have the following ratios,

$$\frac{V_2}{V_1} = \sqrt{\frac{W_2}{W_1}}. \quad (11.1)$$

$$\frac{D_2}{D_1} = \frac{W_2}{W_1}. \quad (11.2)$$

$$\frac{P_{r2}}{P_{r1}} = \sqrt{\left[\frac{W_2}{W_1}\right]^3}. \quad (11.3)$$

Thus, starting from the weight W_1 , for each angle of attack the new speed V_2 , drag D_2 and power required P_{r2} can be calculated.

Figure 11.1 shows the effect of weight on drag and power required curves of our illustrative turboprop airplane with a wing area of 70 m^2 , a parabolic lift-drag polar, $C_D = 0.023 + 0.035C_L^2$ and a maximum lift coefficient of 1.5.

As can be seen from Equations (11.1) and (11.2), all corresponding points on the drag curves which have the same angle of attack are located on a quadratic curve through the origin,

$$\frac{D_2}{D_1} = \left[\frac{V_2}{V_1}\right]^2. \quad (11.4)$$

Similarly, from Equations (11.1) and (11.3), we find that with changing weight all corresponding points on the power required curves move along a third order curve through the origin,

$$\frac{P_{r2}}{P_{r1}} = \left[\frac{V_2}{V_1}\right]^3. \quad (11.5)$$

It is important to realize again that the foregoing relations hold only at low-subsonic velocities and that at high-subsonic and supersonic velocities the effect

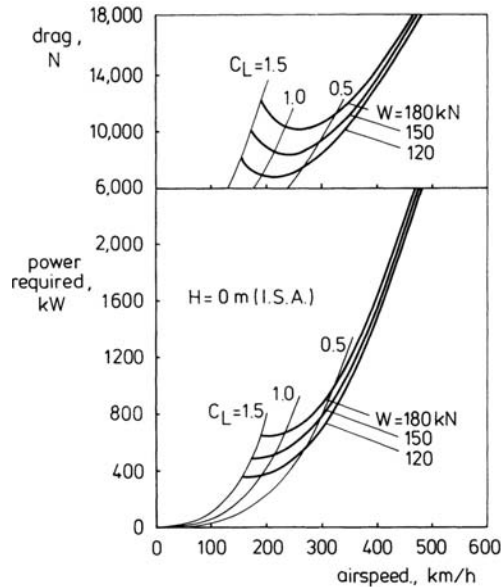


Figure 11.1 Effect of weight on drag and power required

of weight must be determined by calculating the drag and power required curves according to the procedure described in Section 9.2.

Using a parabolic lift-drag polar, the effect of changing the weight of the airplane can also be examined from Equation (9.26) which is repeated below for convenience,

$$P_r = C_{D_0} \frac{1}{2} \rho V^3 S + \frac{W^2}{\pi A e \frac{1}{2} \rho V S}. \quad (11.6)$$

Inspection of Equation (11.6) shows that the weight only affects that part of power required that is associated with induced drag. Since at constant weight the relative importance of this part of power required increases with decreasing velocity and air density, the effect of changes in weight on performance are especially noticeable at lower airspeeds and/or greater heights (Figure 11.2).

As far as the minimum airspeed is determined by stalling, from Equation (11.1), we have

$$\frac{V_{S2}}{V_{S1}} = \sqrt{\frac{W_2}{W_1}}. \quad (11.7)$$

A change in weight, particularly, has a considerable influence on climb performance. Of special interest is of course the effect of weight on the maximum rate of climb. From Equation (9.35), we find that

$$RC_{\max} = \frac{(P_a - P_r)_{\max}}{W} \quad (11.8)$$

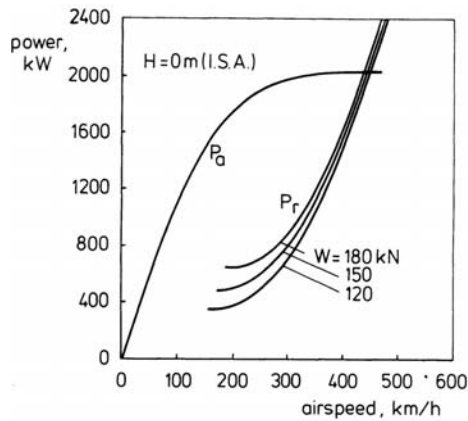


Figure 11.2 Effect of weight on performance diagram

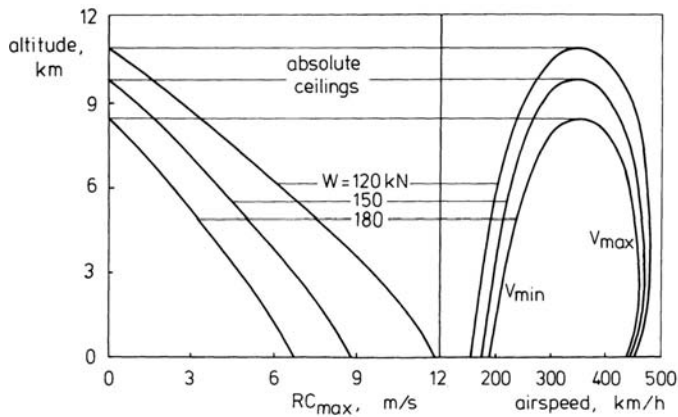


Figure 11.3 Effect of weight on performance

It will be appreciated that at each flight speed the numerator of Equation (11.8) decreases with increasing weight. Consequently, the total outcome of Equation (11.8) is a dramatic reduction of the maximum rate of climb. Also, there is a higher speed for fastest climb as the weight increases. Obviously, the same effects on maximum climb angle and steepest climb speed will occur.

In the high-speed range, the first term of the right-hand side of Equation (11.6) prevails so that there the influence of a change in weight on maximum level flight speed will be much smaller, certainly at low altitudes. This is confirmed by the performance curves in Figure 11.2, which show that there is only a slight reduction in maximum airspeed as weight increases.

For our example airplane, a complete picture of the effect of weight on performance in level steady flight and climb is presented in Figure 11.3. It can be seen that also the absolute ceiling goes down significantly with weight.

Table 11.1 Takeoff climb requirements for transport airplanes

| number of engines | minimum climb gradient | | |
|---|------------------------|------|------|
| | 2 | 3 | 4 |
| first segment | | | |
| (T.O.-power and flaps, landing gear down) | > 0.0 % | 0.3% | 0.5% |
| second segment | | | |
| (T.O.-power and flaps, landing gear up) | 2.4% | 2.7% | 3.0% |
| third segment | | | |
| (METO-power, flaps and landing gear up) | 1.2% | 1.4% | 1.5% |

From the preceding discussion it may be clear that for each flight, the maximum allowable weight of the airplane and so the maximum load the airplane can carry is determined by requirements on takeoff and landing distances, climb performance, and en route obstacle clearance. Therefore, a close relationship exists between actual takeoff weight and the airworthiness standards.

To illustrate this connection, Table 11.1 gives the minimum climb requirements to be achieved by transport airplanes with the critical engine out, as specified in the Federal Aviation Regulations (FAR) (see Section 8.5). The climb requirements are expressed as climb gradients, that is to say, in terms of $\sin \gamma = \frac{RC}{V}$, and expressed in percent. As portrayed in Figure 11.4, the takeoff path with engine failure is broken down into three climb segments. The takeoff reference speeds V_{LOF} and V_2 in Figure 11.4 are specified in terms of the calibrated minimum stalling speed V_{MS} for the appropriate airplane configuration and weight. To ensure a safe climbout, the speed at liftoff, V_{LOF} , normally, is 15 to 25 percent higher than the minimum stalling speed. Dependent on the type of powerplant and number of engines, the minimum value of the speed at the obstacle height, the takeoff safety speed V_2 , may not be less than $1.15 V_{MS}$ or $1.2 V_{MS}$ (Chapter 16).

From a complete investigation of each segment, weight limits are determined which are available to the pilot in the form of graphs where the takeoff weight is given in terms of humidity, pressure altitude, and ambient temperature (Figure 11.5). In conclusion we can say that for safe operation the pilot should know exactly at which weight he is flying. He also should have a good understanding of the performance characteristics under different conditions of number of operative engines, engine control setting, flap setting, and landing gear position. The typical effects of the latter conditions will be discussed in the following sections.

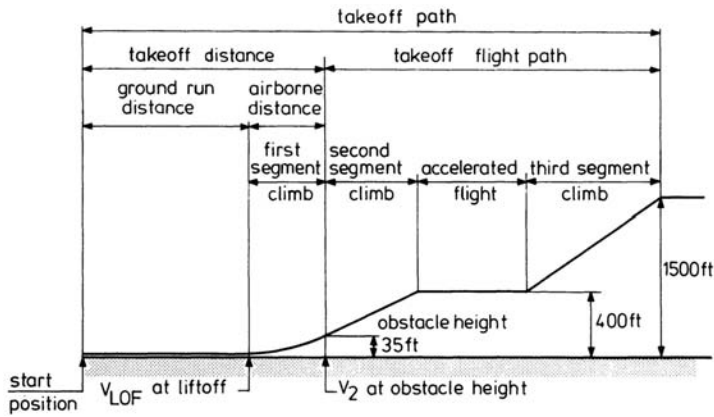


Figure 11.4 Takeoff performance for transport airplane

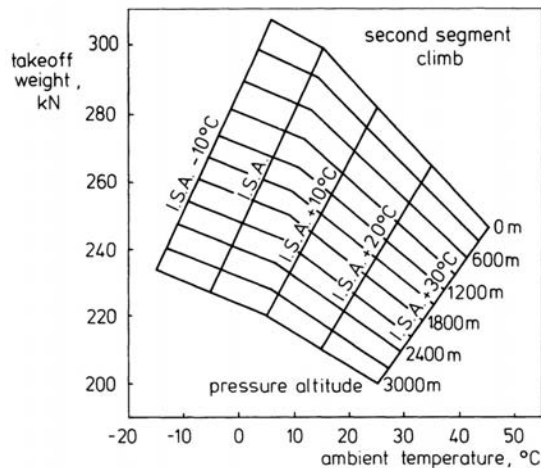


Figure 11.5 Weight-altitude-temperature (WAT)-curves for transport airplane

11.2 Effect of engine failure

Malfunction of one or more engines on multi-engine airplanes leads, as a matter of course, to a considerable loss in power available. E.g., in the case of a two-engine airplane, after engine failure we have only half the commencing thrust. With the resulting reduction in excess thrust and power, maximum level flight speeds, maximum rates of climb and ceilings deteriorate.

In Figure 11.6 are sketched the qualitative effects of the number of operative engines on maximum rate of climb for a two-engine and a four-engine airplane. It is important to notice that engine failure must be considered for multi-engine airplanes in all flight phases. With respect to cruise flying, especially, the lowering of the theoretical and practical ceilings is of great importance to flight safety. Needless to say that the load the airplane carries as well as the selected route must

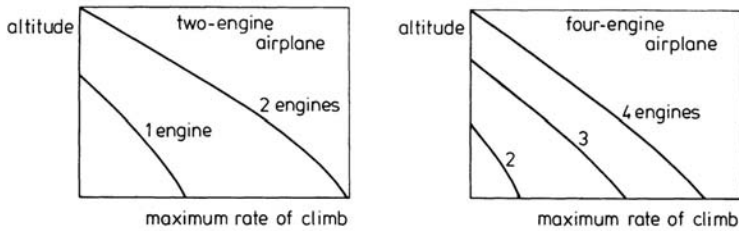


Figure 11.6 Effect of the number of operating engines on maximum rate of climb

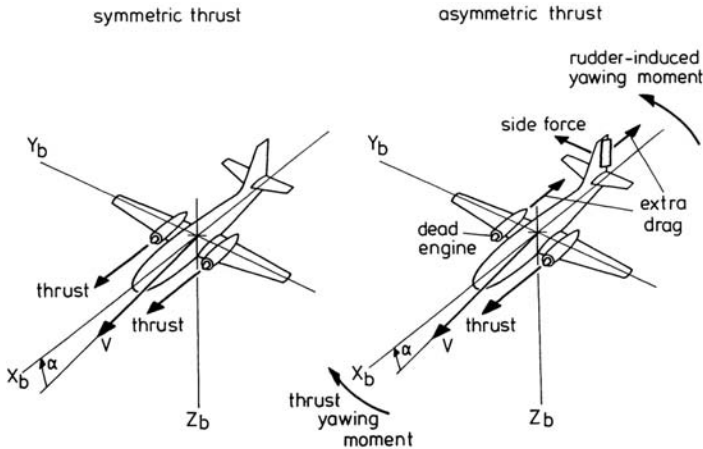


Figure 11.7 Engine failure on a twin-engined airplane

warrant the condition that there is no risk of en route terrain collisions. A point to note is that on four-engine airplanes the occurrence of two inoperative engines in cruising flight must be awaited.

Failure of an engine in flight not only means loss of thrust, but also an increment in drag as caused by (Figure 11.7):

- additional drag from control surface deflections
- additional drag produced by the dead engine.

For a propeller airplane it is important to avoid the existence of windmilling drag. A propeller being windmilled by the oncoming air and thus driving the inoperative engine causes a considerable additional drag.

Also, there is a great risk of further damage to the engine. Fortunately, windmilling drag can be almost completely eliminated by feathering the propeller (see Chapter 7).

The methods of calculating windmilling drag are beyond the scope of this presentation. For information about this subject the reader is referred to Reference 39.

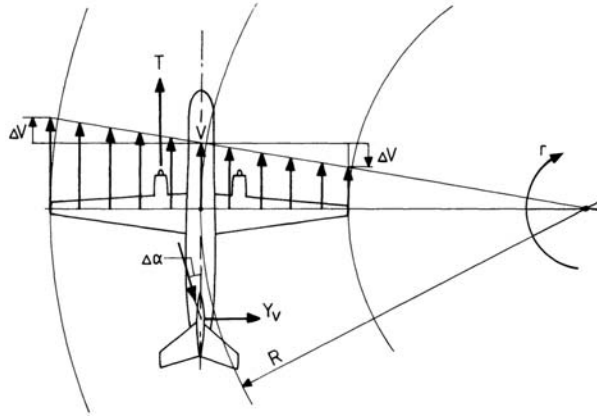


Figure 11.8 Yawing motion

As portrayed in Figure 11.7, failure of the starboard engine of a twin-engined airplane causes an unbalanced thrust yawing moment to the right. Under this condition, there will be a direct tendency to yaw toward the dead engine.

Assuming a pure yawing motion, the angle of sideslip remains zero so that the velocity vector of the center of gravity lies in the plane of symmetry (Figure 11.8). The airplane travels along a curvilinear flight path of which the radius is given by

$$R = \frac{V}{r}, \quad (11.9)$$

where r is the angular velocity of the yawing motion.

From Figure 11.8, it is seen that the wing tips of the airplane have velocity differences from the flight speed by an amount

$$\Delta V = r \frac{b}{2}. \quad (11.10)$$

The changes in local velocity along the span due to the yawing velocity will cause an increase in lift and drag on the outer wing and a decrease in lift and drag on the inner wing. Also a side force Y_v occurs due to a change in the angle of attack at the vertical stabilizer.

Clearly, the yawing motion considered in Figure 11.8 will create a rolling moment to the right and, although to a lesser degree, also a yawing moment to the left (Figure 11.9).

Furthermore, in the case of failure of a wing-mounted propeller engine, the asymmetric lift from the part of the wing submerged in the slipstream of the propeller will cause an additional rolling moment toward the dead engine (Figure 11.10).

The resulting yawing moment to the right in combination with the rolling moment in the same direction will cause, if allowed to continue uncontrolled, a spiral dive. Evidently, when engine failure occurs the yawing motion must be stopped

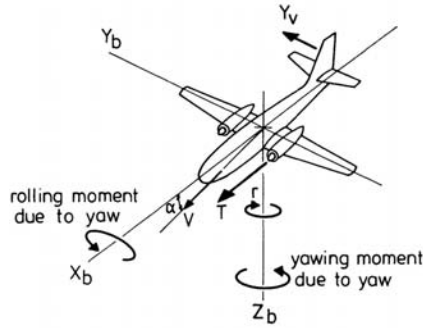


Figure 11.9 Asymmetric force and moments resulting from yawing motion

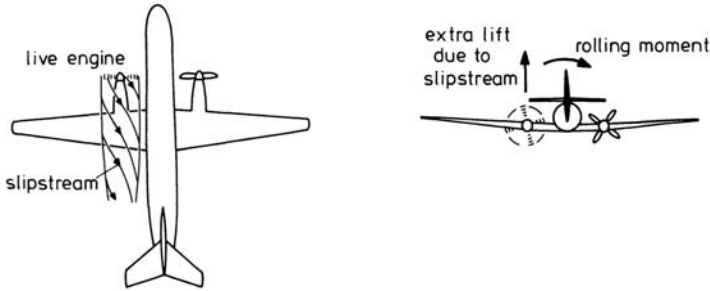


Figure 11.10 Rolling moment caused by asymmetric lift on wing

promptly. A resolute application of rudder deflection toward the live engine will be required to generate a rudder-induced yawing moment (see Figure 11.7). Also a deflection of the ailerons will be needed to overcome the rolling moment. Figure 11.11 shows a new condition of steady straight level flight, which may be established by applying a sideslip angle β and giving the airplane a slight angle of bank Φ toward the live engine.

From Figure 11.11, we now obtain the following force equations, expressed in terms of their components along the air-path axes (cf. Equation (3.33)),

$$\left. \begin{aligned} -D + T \cos \beta &= 0 \\ -S - T \sin \beta + W \sin \Phi + S_v &= 0 \\ -L + W \cos \Phi &= 0 \end{aligned} \right\} \quad (11.11)$$

The forces S and S_v in the equations are the lateral forces due to the sideslipping motion and rudder deflection, respectively. Recall that for consistency with lift and drag, the forces S and S_v are taken positive in the direction of the negative Y_a -axis. Normally, a sideslip at $\beta > 0$ produces a side force to port ($S > 0$). According to Equation (4.15), we have $S = C_S \frac{1}{2} \rho V^2 S$, where C_S is the lateral force coefficient which varies essentially linearly with angle of sideslip.

Note that $\Phi < 0$ in Figure 11.11 because the bank angle customarily is taken positive when the airplane is rotating clockwise about its longitudinal axis.

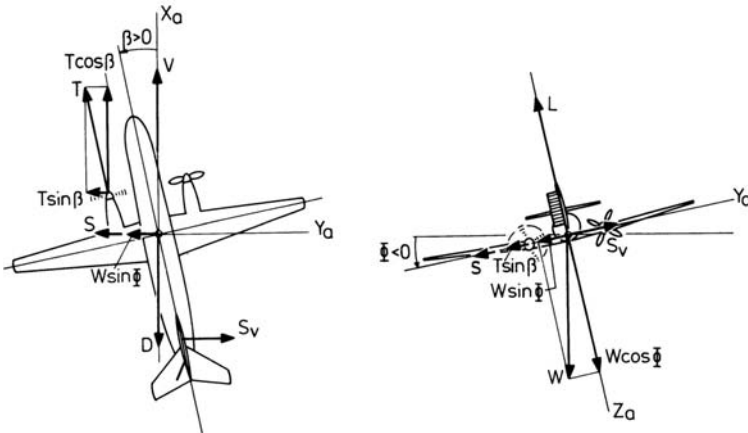


Figure 11.11 Steady straight level sideslipping flight with bank angle

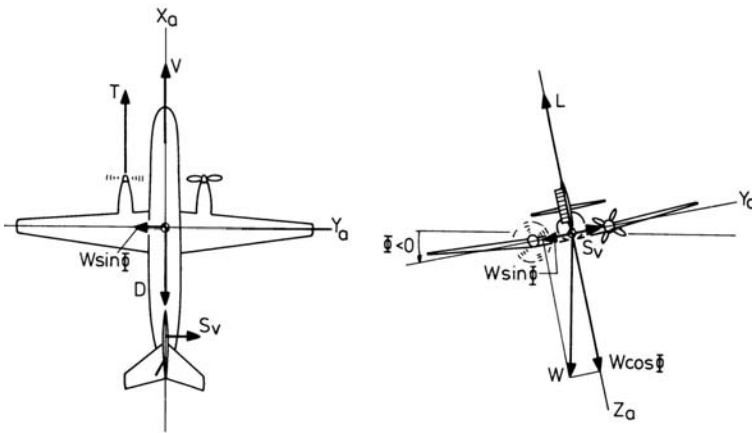


Figure 11.12 Steady straight level nonslipping flight with bank angle

Of special relevance is the flight condition at an angle of sideslip $\beta = 0$ and $\Phi \neq 0$. The force equations (11.11) then become (Figure 11.12)

$$\left. \begin{aligned} -D + T &= 0 \\ +W \sin \Phi + S_y &= 0 \\ -L + W \cos \Phi &= 0 \end{aligned} \right\} \quad (11.12)$$

In this flight condition the lowest airplane drag will occur, furnishing maximum flight speed.

Emphasis is made that the maximum side force the rudder can establish, decreases with decreasing airspeed. The airspeed at which the maximum amount of moment exerted by full rudder equals the unbalanced yawing moment developed by the inoperative engine, determines the lowest speed at which the airplane can be flown

while keeping straight. The latter airspeed is called the minimum control speed, V_{MC} , and represents the minimum speed for fully controlled flight at a given airplane weight, configuration and altitude, and at any particular engine control setting. Clearly, the airspeed always must be maintained above the *minimum control speed* in a flight with one or more engines inoperative. During the takeoff maneuver, especially, the minimum control speed is an essential factor and must be at least 10% below the takeoff safety speed V_2 at the obstacle height in Figure 11.4. When engine failure occurs the operative engine(s) will be called on to generate extra thrust or power by choosing a higher control setting. We shall look at the effect of changes of engine control setting on airplane performance in some detail in the next section.

11.3 Effect of changes of engine control setting

In order to get increased thrust or power, a higher engine control setting must be selected by the pilot. The occurrence of engine failure, as discussed in the preceding section, is an example of a condition in which additional thrust from the live engine may be asked to maintain height and/or airspeed.

Also in the flight with all engines operating, the pilot can affect the engine output by changing the engine control setting. In Figure 11.13 are sketched typical performance curves for an airplane powered by turboprop engines. The power available curves are drawn for a number of characteristic power settings.

As we have learned in Chapter 8, airspeed and engine control setting in climbing flight can be chosen independently of each other, whereas in steady level flight the flight condition is fully determined by one of the variables, α , V or Γ . Thus, when flying at a given altitude, particular values of flight speed and engine control setting are coupled. This is illustrated in Figure 11.13 by the intersections A to F, which define the relationship between engine control setting and level flight velocity.

When the engine throttles are fully opened, emergency or full power will be obtained. This condition is represented in Figure 11.13 by the upper power available curve. As mentioned earlier in Chapter 6, full power can be allowed for a short time only. The maximum rating permitted for unlimited duration is therefore lower and is known as METO (maximum except takeoff) or maximum continuous.

The effects of lowering the engine control setting are apparent from Figure 11.13; a decreasing maximum level flight speed and a decrease in rate of climb at each airspeed. Also note that at low engine ratings the minimum flight speed is determined by the low-speed intersection of the P_a and P_r -curves. Then, steady level flight at either of two velocities is possible. One faster and one slower than the airspeed at which maximum excess power occurs (see also Figure 9.21).

Operating at the greater airspeed is known as flying the normal or front side of the power curve, while operation in the low-speed region is called flying the back side

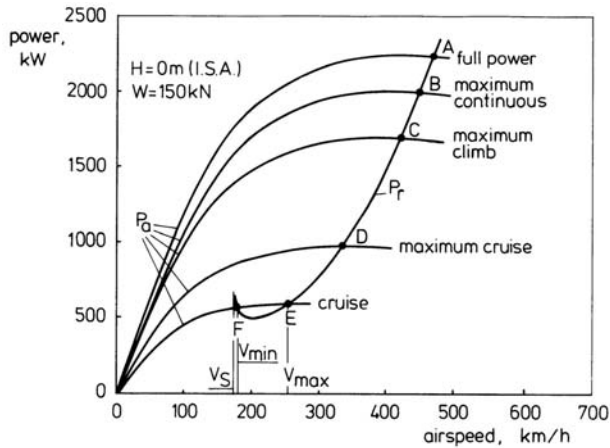


Figure 11.13 Performance diagram for various engine control settings

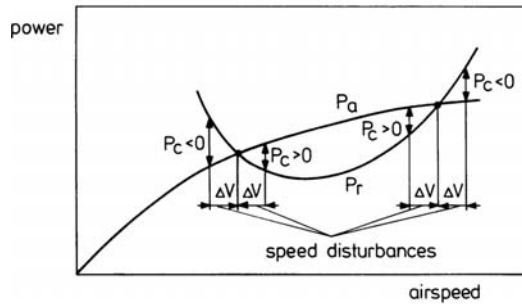


Figure 11.14 Variation of level flight speed at fixed engine control setting

of the power curve or flying in the region of reversed command (see Chapter 9). To explain this, suppose the pilot is flying in the high-speed region and that due to an external cause, the airplane experiences a sudden change in airspeed from the equilibrium condition in point E in Figure 11.13.

In the case that the pilot maintains level flight at a fixed engine control setting, there will be a negative excess power when speed increases and a positive excess power when speed falls off (Figure 11.14). Hence, in both situations the airplane will tend to restore the original airspeed. Apparently, the equilibrium condition in point E is stable. On the other hand, in the low-speed region, e.g. in point F in Figure 11.13, any speed disturbance will tend to diverge the speed further from its original value.

What is argued above about the behavior of the speed following a speed disturbance is all we can state from considering equilibrium conditions. The transition from one steady flight condition to another is, as a matter of course, intrinsically connected with unsteady motions and should be studied by means of the full system of equations of motion as derived in Chapter 3. However, consistent with the scope of this text, we need not concern ourselves with the dynamic behavior of

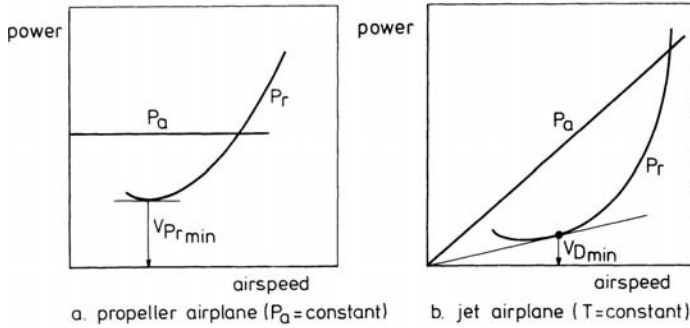


Figure 11.15 Selection of flight region

the airplane in response to the forces and moments developed. In any case, flying in the low-speed region must be avoided in all circumstances in which loss of airspeed or altitude may be dangerous.

The boundary between the two speed regions is found at the airspeed where the performance curves have parallel tangents which, of course, is at the fastest climb speed.

Provided that power available is constant with airspeed the transition point occurs at the minimum power required speed (Figure 11.15a). Likewise, in the case of a jet airplane the transition point is approximately the speed for minimum drag (Figure 11.15b). The jet picture in Figure 11.15b illustrates that besides the variation of power available with airspeed, there is a second characteristic of a jet airplane that is different from a propeller-driven airplane. Meant is the relative stretching and flatness of the power required curve in the low-speed region.

In order to assure a sufficient degree of *speed stability*, the pilot will select a flight speed greater than the minimum drag speed. Generally, for jet airplanes as well as propeller airplanes:

$$V \geq V_M = 1.1V_{D\min}, \quad (11.13)$$

where V_M is called *minimum comfortable airspeed*.

If an airplane is cruising at $V < V_M$ a loss of speed due to a disturbance will require immediate elevator control as well as thrust increase to avoid undesired speed deviations and/or loss of altitude.

Assuming a parabolic variation of C_L with C_D , we obtain from Equations (11.13), (9.22) and (10.16) the ratio of the minimum comfortable airspeed to the stalling speed as

$$\frac{V_M}{V_S} = 1.1 \sqrt{\frac{C_{L\max}}{\sqrt{C_{D0}} \pi A e}}. \quad (11.14)$$

Equation (11.14) shows that for jet airplanes relative high values of the ratio V_M/V_S will occur, owing to their comparative low values of zero-lift drag coefficient C_{D0} and wing aspect ratio A . This is especially true for supersonic airplanes

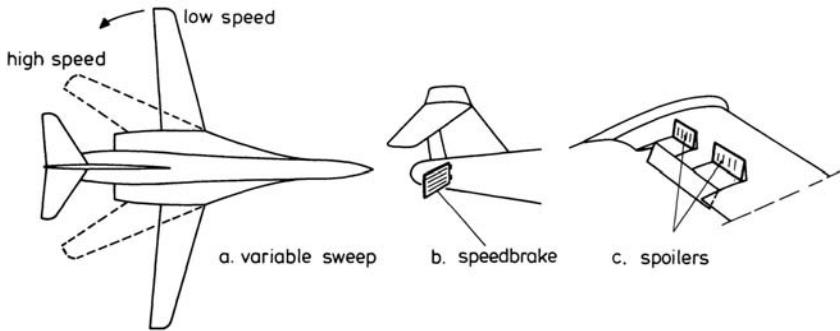


Figure 11.16 Reduction of minimum drag speed

with slender delta wings.

The necessity to correct the engine control setting continually arises at all flight speeds lying in the low-speed region and at which the pilot tries to maintain a straight flight path. A critical situation may be the approach path before landing, where application of an automatic throttle control system may be needed to solve the problem artificially.

Equation (11.14) indicates that lack of sufficient speed stability can also be attacked by increasing the zero-lift drag coefficient and/or wing aspect ratio. In the case of highly swept supersonic wings, variable wing geometry can be a suitable design feature providing, among other things, an improved aspect ratio and thus a reduced approach speed (Figure 11.16a). In order to stabilize the descent speed on approach by drag increase, the airplane uses high-drag devices. In addition to wing flaps and landing gear, the airplane may be equipped with speed-brakes in the form of extensible panels attached to the fuselage (Figure 11.16b). Also use may be made of spoilers. The latter high-drag devices are opening panels in the upper surface of the wing positioned spanwise between fuselage and ailerons (Figure 11.16c). They are extended symmetrically across the plane of symmetry of the airplane. When used in combination with flaps, a large extra drag results.

Besides for providing a high drag, spoilers are used to supply additional roll control. For this purpose, only the spoilers on the downgoing wing are up to cancel the lift at that wing and thus rolling the airplane. They also have a practical meaning, in the case of a glider, as a control to vary the lift-to-drag ratio and with that the glide angle (Chapter 13). Further, during ground run with spoilers opened, the lift is destroyed to increase the frictional force between wheels and ground surface (Chapter 16).

11.4 Effect of airplane configuration

In this section we shall illustrate the effect of landing gear position and flap deflection on low-altitude flight performance.

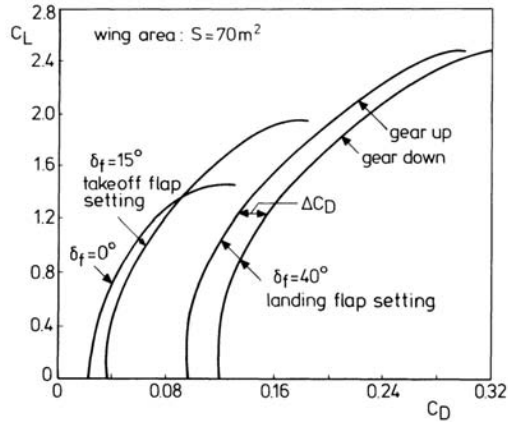


Figure 11.17 Typical low-speed lift-drag polars

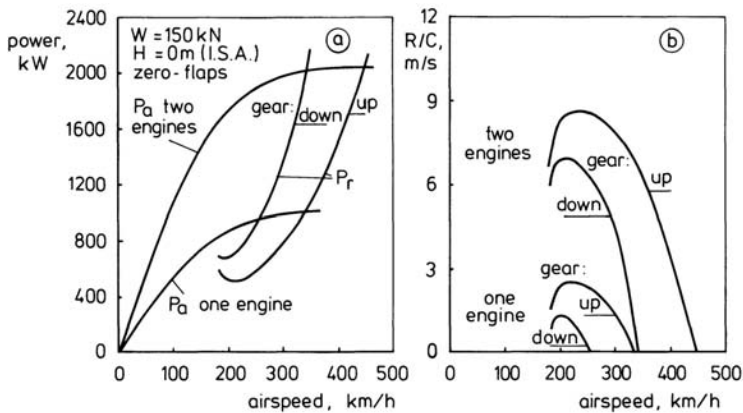


Figure 11.18 Effect of undercarriage-drag on climb performance

The importance of landing gear down and flap deflection will be considered on the basis of the typical set of lift-drag polars in Figure 4.16, which are reshown in Figure 11.17 for convenience. The curves, which apply to a hypothetical two-engine turboprop airplane, show that a considerable contribution to the drag coefficient is supplied by the landing gear; approximately a doubling of the zero-lift drag coefficient of the clean airplane. As explained earlier in Chapter 4, we also see that a flapped configuration affects both drag and lift coefficients. Let us assume that our turboprop airplane has a weight of 150 kN and that it flies at sea level (I.S.A.). Figure 11.18a shows the corresponding graph of power required versus airspeed for the clean airplane and for the configuration with landing gear down. Also are sketched representative power available curves at maximum continuous engine rating, considering the flight with two operative engines and the case of one inoperative engine with propeller feathered. Expressed in terms of rate of climb against airspeed, the power data in Figure 11.18a look as plotted in Figure

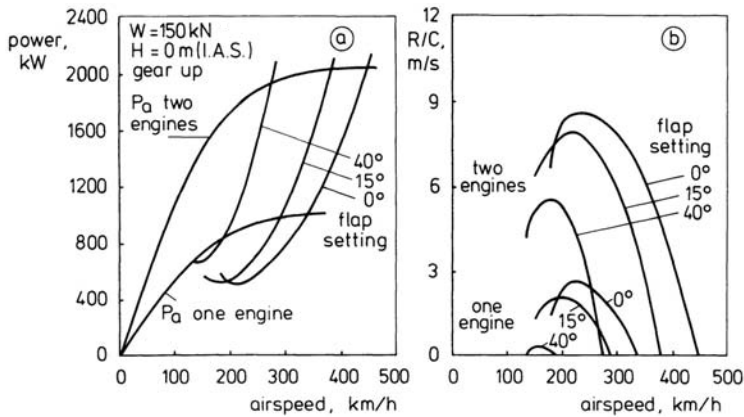


Figure 11.19 Effect of flap-angle on climb performance

11.18b. It appears that the landing gear drag causes a considerable deterioration of the performance of the airplane. Especially, in the case of engine failure, the influence of the landing gear on maximum rate of climb is dramatic.

The effect of flap deflection on the performance curves and rate of climb is presented in Figure 11.19, for the case of one and two operative engines. At a fixed airspeed V , the lift coefficient C_L is also fixed by the condition $L = W$, or

$$C_L = \frac{W}{S} \frac{2}{\rho V^2}. \quad (11.15)$$

This conclusion implies that at a given flight velocity, the drag coefficient C_D increases with increasing flap angle. As a consequence, power required enlarges and, hence, rate of climb worsens as the flap setting becomes greater.

On the other hand, flaps reduce the stalling speed V_S by increasing the maximum lift coefficient $C_{L_{\max}}$ and/or wing area S . The relationship between these quantities again follows from the condition that lift equals weight in steady flight

$$V_S = \sqrt{\frac{W}{S} \frac{2}{\rho C_{L_{\max}}}}. \quad (11.16)$$

Apparently, when taking off, the effect of flap deflection is twofold; it decreases the ground run distance by a reduced liftoff speed and it increases the airborne distance through reduced rate of climb. Nevertheless, a flapped configuration can produce a shortening of the takeoff distance (Figure 11.4). However, the flap angle for minimum takeoff distance varies considerably with runway and ambient conditions so that the selection of the optimum flap setting requires extensive calculations.

Concerning the use of flaps it is important to notice that the maximum flap angle that can be applied is usually limited by the climbout performance. To illustrate

this statement, we recall that according to the Federal Aviation Regulations (FAR) for transport category airplanes, compliance with the climb gradient requirements at an airspeed $V_2 = 1.20V_{MS}$ and at one engine inoperative, must be shown (see Section 11.1). From Figure 11.19b, we find that at a flap angle of 40° , the climb gradient is insufficient ($\gamma < 2.4\%$). This observation also explains why during takeoff the flaps virtually always are partly deflected ($\delta_f = 10^\circ - 15^\circ$). For small airplanes even zero flap setting may be selected.

On the other hand, during landing operations it is necessary to apply full flaps in order to furnish a high drag required to handle the airplane on the approach path and during the ground run after landing. When an expedited descent is required also a flap setting beyond the normal landing setting ($\delta_f = 50^\circ - 90^\circ$) may be used.

It is worth to mention that all movable aerodynamic devices affixed to the airplane for producing high lift or high drag, usually have a speed limitation for extension. Also the landing gear, when used as a speedbrake, has such a speed limit, but when locked down it might be used up to higher airspeeds.

We end this section by emphasizing that, although the evaluation of the low-speed capabilities in the foregoing example pertains to a propeller-driven airplane, the picture for jet-powered airplanes is practically the same.

Chapter 12

TURNING PERFORMANCE

12.1 Governing equations

As mentioned earlier in Section 3.4, the basic maneuver to change the flight path heading is the true banked or coordinated turn. For that reason, in discussing the maneuverability of airplanes, the emphasis is primarily on steady curvilinear flight with wings banked and without sideslip, as visualized in the previous Figure 3.8. Remember that in the coordinated turn we have the special conditions that the inward centripetal force required to pull the airplane toward the center of the turn is accomplished by the horizontal component of the lift and that both the resultant aerodynamic force ($R + T$) and the vector sum of the weight and the outward centrifugal force ($W + C$) are in the plane of symmetry of the airplane.

In accordance with our approach to analyzing point performance in Chapters 9 to 11, we shall continue to adopt that the thrust vector is tangent to the flight path ($\alpha_T = 0$). Then, from the system of equations (3.36), we find that the instantaneous conditions on the spiral flight path are described by (Figure 12.1):

$$T - D - W \sin \gamma = 0 \quad (12.1)$$

$$W \cos \gamma \sin \mu - C \cos \mu = 0 \quad (12.2)$$

$$-L + W \cos \gamma \cos \mu + C \sin \mu = 0. \quad (12.3)$$

Rather than the conventional air-path axis system used for symmetric flight, it is more convenient to employ for turning flight an additional axis system with axes X_t , Y_t , and Z_t . With the origin of the system at the center of gravity of the airplane, the X_t -axis coincides with the X_a -axis (and thus with the velocity vector). The Y_t -axis lies in the horizontal plane along the radius of curvature. The Z_t -axis lies in the vertical plane and is perpendicular to both the X_t and Y_t axes (see Figure 12.1).

Resolving the forces along the latter coordinate system produces the following series of equations (cf. Equation (3.37)):

$$T - D - W \sin \gamma = 0 \quad (12.4)$$

$$L \sin \mu - C = 0 \quad (12.5)$$

$$-L \cos \mu + W \cos \gamma = 0. \quad (12.6)$$

In examining the instantaneous flight condition in a coordinated turn, it is customary to assume level flight ($\gamma = 0$) since the resulting performance in level turning flight can be used to represent the performance in all normal climbing and descending turns. Then, from Equation (3.35), we see that the aerodynamic angle of roll equals the angle of bank ($\mu = \Phi$). Further, the centrifugal force C is given by

$$C = \frac{W V^2}{g R} \quad (12.7)$$

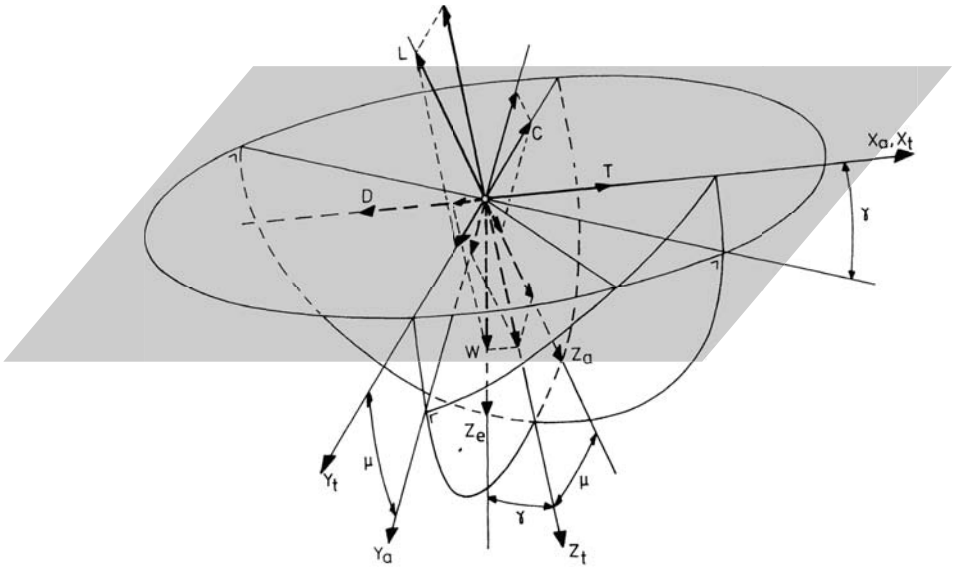


Figure 12.1 Forces In the coordinated turn

where R is the turning radius and g is the acceleration of gravity ($g = g_0 = 9.80665 \text{ m/s}^2$).

Thus, the governing force equations alter, for steady level turning flight, to

$$T - D = 0 \tag{12.8}$$

$$L \sin \Phi - \frac{W V^2}{g R} = 0 \tag{12.9}$$

$$-L \cos \Phi + W = 0. \tag{12.10}$$

These equations can also be found directly from Figure 12.2, where are shown the forces in a turn to the right when looking from behind and down on the airplane. The figure illustrates that in a true banked turn the centripetal force is completely balanced by the centrifugal force. This condition provides that the airplane has no tendency to move either inward or outward so that the airplane travels along a circular path. Figure 12.2 also shows that the weight is balanced by the vertical component of the lift and that the drag equals the thrust.

Substitution of the relationships $L = C_L \frac{1}{2} \rho V^2 S$ and $D = C_D \frac{1}{2} \rho V^2 S$ into Equations (12.8) to (12.10) yields

$$T = C_D \frac{1}{2} \rho V^2 S \tag{12.11}$$

$$\frac{W V^2}{g R} = C_L \frac{1}{2} \rho V^2 S \sin \Phi \tag{12.12}$$

$$W = C_L \frac{1}{2} \rho V^2 S \cos \Phi. \tag{12.13}$$

For given values of W and ρ , the three Equations (12.11) to (12.13) contain five

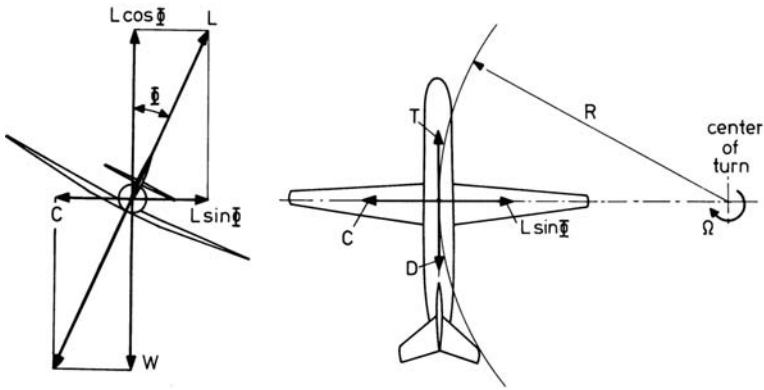


Figure 12.2 The airplane in a steady level true banked turn

variables: α , V , Γ , R and Φ so that the flight condition is determined by two control variables.

In the next section we will express the various performance items in terms of angle of attack α (C_L and C_D), and the angle of bank Φ .

12.2 Equations for the performance in a coordinated turn

The airspeed in a constant altitude turn, from Equation (12.13), is given by

$$V = \sqrt{\frac{W}{S} \frac{2}{\rho} \frac{1}{C_L} \frac{1}{\cos \Phi}} \quad (12.14)$$

The drag follows from Equation (12.11) and (12.13) as

$$D = W \frac{C_D}{C_L} \frac{1}{\cos \Phi} \quad (12.15)$$

An expression for the power required is found by multiplying Equation (12.15) with Equation (12.14) to give

$$P_r = DV = W \sqrt{\frac{W}{S} \frac{2}{\rho} \frac{C_D^2}{C_L^3} \frac{1}{\cos^3 \Phi}} \quad (12.16)$$

The Equations (12.14) to (12.16) can also be expressed in terms of angle of attack and load factor. According to its definition, the load factor n follows from Equation (12.10) as

$$n = \frac{L}{W} = \frac{1}{\cos \Phi} \quad (12.17)$$

which shows that the load factor changes inversely as the cosine of the bank angle.

Using Equation (12.17), we can write

$$V = \sqrt{\frac{n W^2}{S \rho C_L}} \quad (12.18)$$

$$D = nW \frac{C_D}{C_L} \quad (12.19)$$

$$P_r = nW \sqrt{\frac{n W^2 C_D^2}{S \rho C_L^3}}. \quad (12.20)$$

Expressions for the radius of turn are obtained from Equations (12.12) and (12.13), whence

$$R = \frac{W^2}{S \rho g C_L \sin \Phi} \quad \text{and} \quad (12.21)$$

$$R = \frac{V^2}{g \tan \Phi} \quad \text{or} \quad (12.22)$$

$$R = \frac{W^2}{S \rho g C_L} \frac{1}{\sqrt{n^2 - 1}} \quad \text{and} \quad (12.23)$$

$$R = \frac{V^2}{g \sqrt{n^2 - 1}}. \quad (12.24)$$

These equations tell us that the larger the bank angle or the load factor and the lower the airspeed in a turn, the smaller the radius of turn will be.

The rate of turn can be found from Equations (12.22) and (12.24) as

$$\Omega = \frac{V}{R} = \frac{g \tan \Phi}{V} = \frac{g \sqrt{n^2 - 1}}{V} \quad (12.25)$$

It might be interesting to mention that well-defined rates of turn are in common use. These turning rates are expressed in terms of the number of degrees the airplane changes heading in one second, namely,

Rate 1 $\Phi = 3^\circ/\text{s}$

Rate 2 $\Phi = 6^\circ/\text{s}$

Rate 3 $\Phi = 12^\circ/\text{s}$

Rate 4 $\Phi = 24^\circ/\text{s}$.

When turning at Rate 1, the airplane executes what is known as a *standard rate turn*, where a complete reversal of flight direction (180° turn) takes one minute.

From Equation (12.25), we see that the time needed to execute a 180° turn (π radians) is given by

$$T_\pi = \frac{\pi}{\Omega} = \frac{\pi V}{g \tan \Phi} = \frac{\pi V}{g \sqrt{n^2 - 1}}. \quad (12.26)$$

Equation (12.26) shows that the lower the airspeed the smaller the angle of bank (load factor) required for a desired turning time T_π . For example, at an airspeed of 300 km/h (162 knot), the angle of bank for a Rate 1 turn ($T_\pi = 1$ minute) is 24° ,

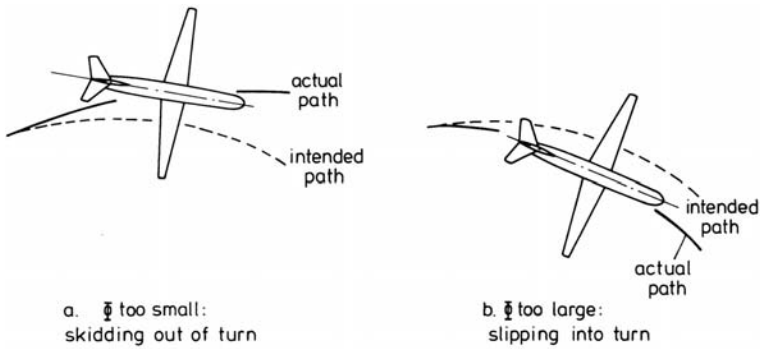


Figure 12.3 Turn with Incorrect angle of bank

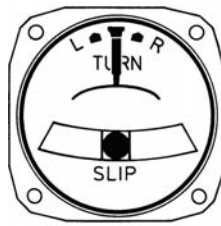


Figure 12.4 Turn and slip Indicator

and at $V = 150 \text{ km/h}$ (81 knot) we find: $\Phi = 12.5^\circ$.

If for a given rate of turn the angle of bank is too small, the unbalanced centrifugal force will pull the airplane to the outside of the turn. Under this condition the airplane is said to be skidding out of turn, whereby the nose of the airplane will swing toward the inside of the flight path (Figure 12.3a). On the other hand, if the airplane banking is too large for the rate of turn the airplane will be pulled to the inside of the turn, and the nose will swing toward the outside; slipping into turn (Figure 12.3b).

Obviously, during an incorrect banked turn, also the occupants will tend to slide inward or outward on their seats.

To indicate to the pilot whether or not the angle of bank is correct for a particular rate of turn, the instrument panel in the cockpit is equipped with a turn and slip indicator. This instrument is actually a combination of two separate mechanisms, which are brought together in one casing; a turn needle and a ball which can move freely in a curved transparent tube. The dial presentation of a conventional turn and slip indicator is sketched in Figure 12.4.

The turn needle is a gyroscopically controlled pointer mechanism and indicates the rate at which the airplane is turning about its vertical axis. We leave the description of the way in which the turn indicator works to specialized books on aircraft instruments. For instance, see Reference 16.

For our aim it is merely of interest to understand the operation of the slip indicator.

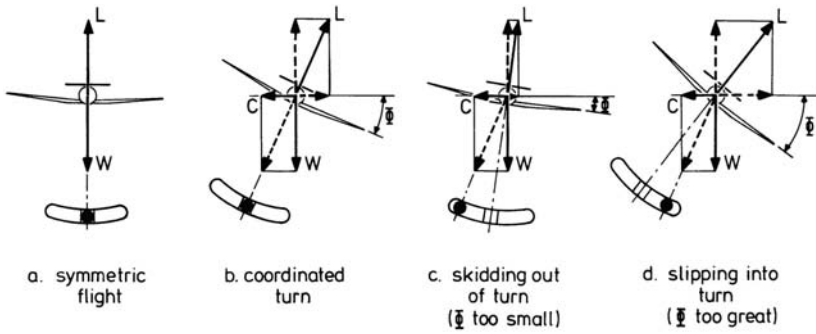


Figure 12.5 Slip Indicator

Therefore, let us examine Figure 12.5, where the position of the ball in the tube indicates skid or slip and is determined by the gravitational forces acting on the ball.

During symmetric flight as well as in a coordinated turn, the ball is in the lowest point of the tube because the resultant of the gravitational forces acts in the plane of symmetry of the airplane (Figures 12.5a and b). If the gravitational forces are unbalanced, such as during a skid or a slip, the ball moves away from the center position in the direction of the horizontal excess force (Figures 12.5c and d).

The influence of banking and turning on drag and power required curves can be examined by considering flight conditions at different load factors (angles of bank) but at a fixed angle of attack (fixed lift and drag coefficients). From Equations (12.14) to (12.20), the following simple ratios are obtained when flight conditions at load factors n_1 and n_2 are considered:

$$\frac{V_2}{V_1} = \sqrt{\frac{n_2}{n_1}} = \sqrt{\frac{\cos \Phi_1}{\cos \Phi_2}} \quad (12.27)$$

$$\frac{D_2}{D_1} = \frac{n_2}{n_1} = \frac{\cos \Phi_1}{\cos \Phi_2} \quad (12.28)$$

$$\frac{P_{r2}}{P_{r1}} = \sqrt{\left[\frac{n_2}{n_1}\right]^3} = \sqrt{\left[\frac{\cos \Phi_1}{\cos \Phi_2}\right]^3}. \quad (12.29)$$

These ratios indicate that at a given angle of attack the values of airspeed, drag and power required increase as the load factor or the angle of bank becomes greater.

In Figure 12.6 are plotted drag and power required curves at various angles of bank for the former illustrative two-engine airplane with turboprops. The lift-drag polar of the airplane is given in the previous Figure 11.17. The curves in Figure 12.6 relate to the clean configuration (flaps and gear up), an airplane weight of 150,000 N, and an altitude of 0 m (I.S.A.). The following technique was used to obtain the drag and power required curves at a given angle of bank:

1. Values of C_L were chosen.

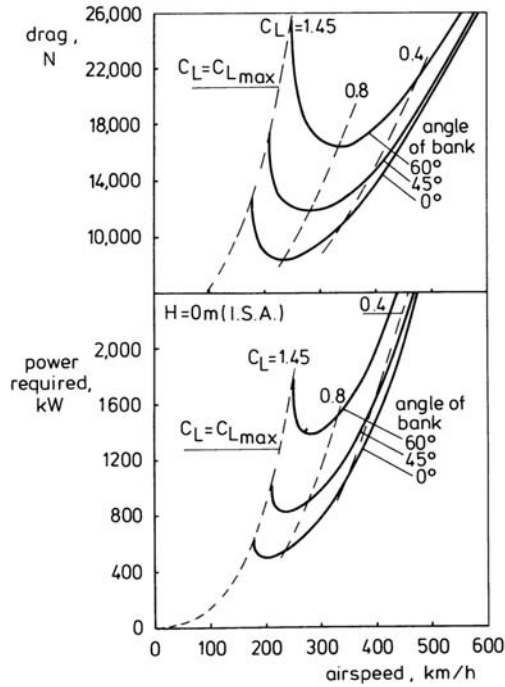


Figure 12.6 Drag and power required at various angles of bank

2. The associated values of C_D were determined from the lift-drag polar in Figure 11.17.
3. At each C_L , the airspeed was found from Equation (12.14), using $\rho_0 = 1.225 \text{ kg/m}^3$.
4. Drag and power required were computed from Equations (12.15) and (12.16), respectively.

This procedure of finding drag and power required at successive values of C_L was repeated for several values of angle of bank, and in this fashion the system of curves in Figure 12.6 was determined. Clearly, also the stalling speed in a turn, $V_{S\Phi}$, increases proportional to the square root of the load factor,

$$V_{S\Phi} = \sqrt{\frac{n W 2}{2 \rho C_{L\max}}} = V_S \sqrt{n}, \quad (12.30)$$

where V_S is the stalling speed in symmetric flight.

The dashed lines in Figure 12.6 are formed by the points on the drag and power required curves that correspond to a given lift coefficient.

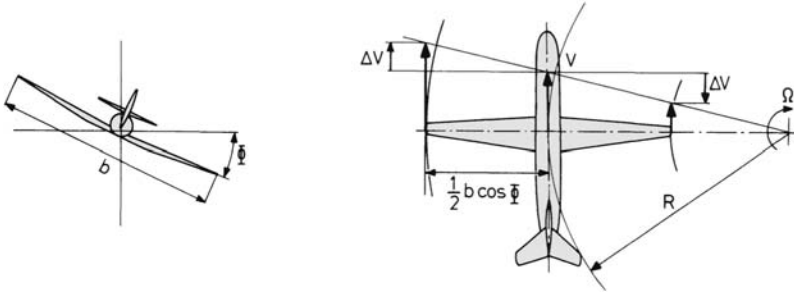


Figure 12.7 The airplane in circular motion

From the Equations (12.27) to (12.29), we find that

$$\frac{D_2}{D_1} = \left[\frac{V_2}{V_1} \right]^2, \quad (12.31)$$

$$\frac{P_{r2}}{P_{r1}} = \left[\frac{V_2}{V_1} \right]^3. \quad (12.32)$$

Apparently, all corresponding points on the drag and power required curves are located on quadratic and third order curves, respectively.

The circling motion, in principle, has two effects on the drag characteristics of the airplane. The first is a change in the flow direction relative to the airplane, and the second is that the outer wing travels faster than the inner wing (Figure 12.7). Usually, the second of these is the most important effect, implying the occurrence of nonuniform lift and drag distributions over the wing span, which give rise to moments affecting the rotation of the airplane (see also Section 11.2). These additional moments have to be trimmed by extra control surface deflections, resulting in more drag.

The difference between the wing tip velocity and the flight speed is given by (see Figure 12.7)

$$\Delta V = \Omega \frac{b}{2} \cos \Phi. \quad (12.33)$$

By substituting $\Omega = V/R$, we can write

$$\frac{\Delta V}{V} = \frac{1}{2} \frac{b}{R} \cos \Phi. \quad (12.34)$$

In order to provide a quantitative impression of the velocity ratio $\Delta V/V$, we notice that according to Equation (12.21), the turning radius will be least when the airplane flies at $C_{L\max}$ and $\Phi = 90^\circ$. Putting these values in Equation (12.21), we obtain

$$R_{\text{lim}} = \frac{W}{S} \frac{2}{\rho} \frac{1}{g} \frac{1}{C_{L\max}} = \frac{V_S^2}{g}. \quad (12.35)$$

It is important to realize that actually, of course, this theoretical lower limit of the radius of turn can never be reached since, as will be demonstrated in Section 12.4,

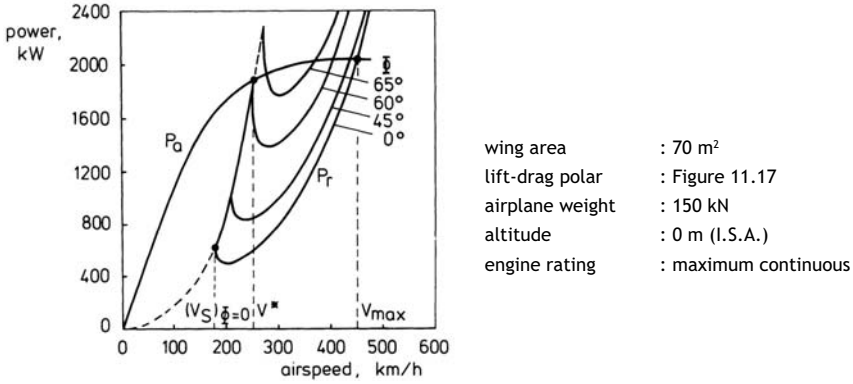


Figure 12.8 Performance diagrams for turning flight

the maximum attainable angle of bank depends directly on the thrust-to-weight ratio T/W .

Nevertheless, we can use Equation (12.35) to judge the importance of the problem. E.g., for an airplane having a stalling speed V_S of 60 m/s and a wing span of 25 m, we get: $R_{lim} = 360$ m and $\Delta V/V = 0.035$.

The latter result may indicate that in actual practice $\Delta V/V \ll 1$ so that the maneuvering capability of an airplane can be determined, to a first approximation, by neglecting the effects of rotation on trim drag.

Finally, we may remark that in turning flight an additional trim drag also may occur because of the fact that at the same airspeed the lift coefficient must be increased over that required for symmetric flight according to the equation:

$$C_L = \frac{n W}{\frac{1}{2} \rho V^2 S} \tag{12.36}$$

The required equilibrium of moments about the lateral axis calls for a greater elevator angle and hence more drag is produced. However, in the present discussion we shall also neglect this effect on the drag characteristics of the airplane.

12.3 Calculation of turning performance

The preceding analysis on turning performance can best be summarized by looking at an illustrative example. Therefore, in Figure 12.8 are shown sea-level performance diagrams at a given engine control setting and at various angles of bank for the turboprop airplane of Section 12.2.

In order that the airplane executes a level-flight turn, power required must be equal to power available at each airspeed. Owing to this requirement, we make the interesting observation that in Figure 12.8 the total range of flight speeds, from the stalling speed $(V_S)_{\Phi=0}$ up to the maximum level flight speed V_{max} , can be divided into two distinct parts, from $(V_S)_{\Phi=0}$ to V^* and from V^* to V_{max} .

Table 12.1 Calculation of turning performance

| V , km/h | C_D | C_L | L , kN | n | Φ , deg. | R , m | T_π , s |
|---------------|-------|-------|-------------|------|------------------|------------|----------------|
| 176 | 0.124 | 1.45 | 150.0 | 1.00 | 0.0 | ∞ | ∞ |
| 200 | 0.124 | 1.45 | 192.2 | 1.28 | 38.6 | 395 | 22 |
| 240 | 0.124 | 1.45 | 276.6 | 1.84 | 57.1 | 293 | 14 |
| 260 | 0.118 | 1.44 | 321.8 | 2.15 | 62.3 | 279 | 12 |
| 300 | 0.079 | 1.26 | 374.9 | 2.50 | 66.4 | 309 | 11 |
| 340 | 0.056 | 0.99 | 378.3 | 2.52 | 66.6 | 393 | 13 |
| 380 | 0.040 | 0.71 | 339.5 | 2.26 | 63.7 | 561 | 17 |
| 420 | 0.030 | 0.45 | 262.8 | 1.75 | 55.2 | 967 | 26 |
| 450 | 0.024 | 0.20 | 150.0 | 1.00 | 0.0 | ∞ | ∞ |

In the first region $(V_S)_{\Phi=0} < V < V^*$, the airplane can execute a turn at maximum lift coefficient. Since power available prevails in this interval, the pilot must lower the engine control setting until the power available becomes equal to the power required. The value of P_a can be found from

$$P_a = (C_D)_{C_{L\max}} \frac{1}{2} \rho V^3 S. \quad (12.37)$$

It should be noticed that limiting values of lift coefficient from buffet onset phenomena may be relevant to the possible stalling speeds in a turn. When a stall occurs during a turn, there is a tendency for the airplane to follow a descending spiral path in its stalled-state. This yawing-rolling motion is called *spin*. To guard against the danger of a turning stall, it is usual practice to keep the permissible maximum angle of attack below the critical value.

In the second region $(V^* < V < V_{\max})$, the airplane cannot perform a level turn at $C_{L\max}$ because of limitations imposed by the power available curve in Figure 12.8. Now, at a given airspeed the allowable turning drag coefficient follows from

$$C_D = \frac{P_a}{\frac{1}{2} \rho V^3 S}. \quad (12.38)$$

Starting from the conditions as specified by the Equations (12.37) and (12.38), the turning performance can be deduced from the envelope of the performance curves in Figure 12.8, which for the sake of clearness are repeated separately in Figure 12.9a.

The calculation procedure is demonstrated in Table 12.1. At each combination of airspeed, drag coefficient, and lift coefficient, the lift is computed from $L = C_L \frac{1}{2} \rho V^2 S$, the load factor from $n = L/W$, the angle of bank from $(\Phi = \cos^{-1}(1/n))$, the radius of turn from $R = V^2/g \tan \Phi$, and the time in a 180° turn from $T_\pi = \pi R/V$. The results tabulated in Table 12.1 are plotted in Figures 12.9b to 12.9d. Evidently, at V_S and V_{\max} the airplane is in steady level symmetric flight, where $n = 1$, $\Phi = 0$, $R = \infty$, $\Omega = 0$ and $T_\pi = \infty$. The curves show that the airspeed

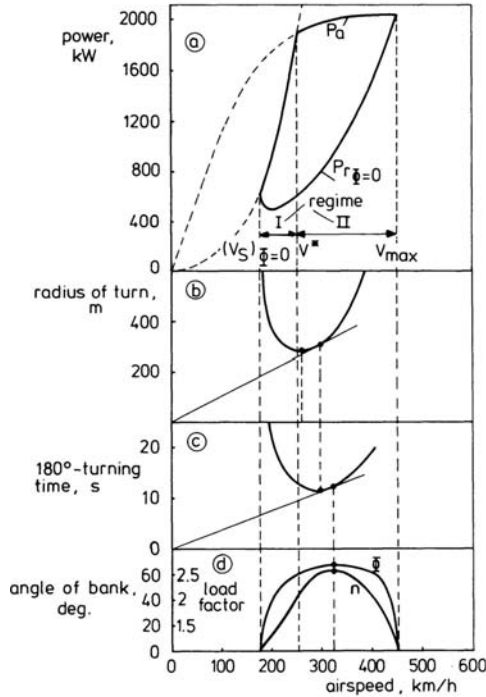


Figure 12.9 Turning performance

for minimum turning radius is not the same as that for minimum turning time. Likewise, the speed for fastest turn differs from the speed at which the bank angle and load factor are maximum. Apparently, we have:

$$V_{R_{\min}} < V_{T_{\pi \min}} < V_{n_{\max}}$$

To prove that this order has a general validity, we write

$$T_{\pi} = \frac{\pi R}{V}$$

This expression indicates that the location of the airspeed for fastest turn is found by drawing the tangent from the origin to the R - V curve in Figure 12.9b, giving $V_{T_{\pi \min}} > V_{R_{\min}}$. From Equation (12.26), the angle of bank is $\tan \Phi = \frac{\pi}{g} \frac{V}{T_{\pi}}$ so that we find that the tangent to the T_{π} - V curve in Figure 12.9c locates the point where the angle of bank and the load factor are maximum, yielding $V_{n_{\max}} > V_{T_{\pi \min}}$. To this point in our discussion, only sea-level turning performance has been exemplified. In order to demonstrate the impact on maneuverability due to altitude effects, let us return to our transport airplane with turbofan engines of which the aerodynamic data are given in Figure 9.7, and having a wing area of 365 m², a weight of 2500 kN, and a maximum sea-level T/W of 0.25. Since for this high-subsonic airplane compressibility drag may occur, at each flight velocity the lift

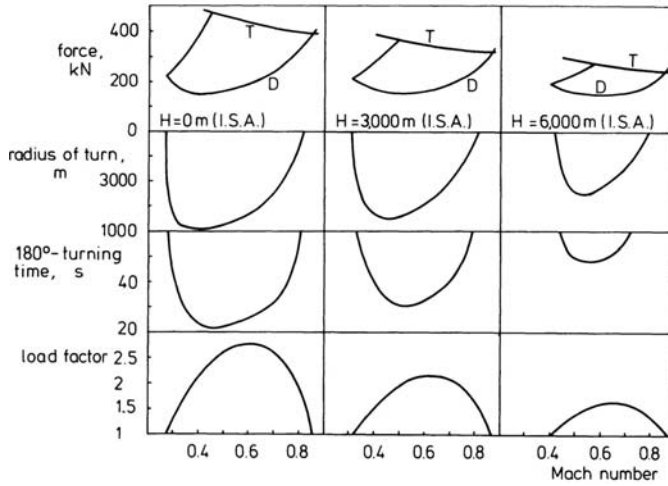


Figure 12.10 Effect of altitude on turning performance

and drag coefficients must be determined from the lift-drag polar for the turning flight Mach number.

Figure 12.10 shows for three altitudes the radius of turn, turning time and load factor as functions of airspeed for this turbofan airplane, when flying at constant engine control setting. As the general tendency is for the thrust to decrease with altitude, also the resulting turning performance deteriorates strongly with increasing height.

12.4 Analytic expressions for best turning performance

As we have seen in the preceding section, the airspeeds for maximum bank angle or load factor and minimum turning radius, define a speed region where optimum conditions are present for performing a turn.

Therefore, an interesting way of looking at the turning performance problem is to estimate the performance features at the boundaries of this velocity range. Here, this will be done by means of analytic expressions, which for their developments require the adoption of simplifying assumptions with regard to the variation of thrust and power available with flight speed.

We first consider the estimation of the bank angle. Inserting $T = D$ and $P_a = P_r$ into Equations (12.15) and (12.16) results in the following expressions,

$$\cos \Phi = \frac{W C_D}{T C_L} \quad \text{and} \quad (12.39)$$

$$\cos \Phi = \left[\frac{W \frac{2}{\rho} (C_D^2 / C_L^3)}{(P_a / W)^2} \right]^{\frac{1}{3}}. \quad (12.40)$$

If we take up the case of a subsonic jet airplane, we recall from Figure 9.11 that the thrust for this type of airplane is more or less constant with airspeed. Using

the idealized behavior that T does not vary with airspeed, then from Equation (12.39), we draw the conclusion that the steepest turn (maximum bank angle and maximum load factor) occurs when is flown at the angle of attack for maximum lift-to-drag ratio, $(C_L/C_D)_{\max}$.

Likewise, it appears from Equation (12.40) that in the case of a propeller-driven airplane for which we can make the working approximation that power available is independent of airspeed, the steepest turn is obtained in the flight at the angle of attack for maximum climb factor, $(C_L^3/C_D^2)_{\max}$.

Furthermore, we see that at constant engine control setting, the maximum angle of bank falls off with altitude due to the decrease of thrust or power available and air density with height. Note that the height has the same deteriorating influence on the associated values of turning radius and turning time, as can be seen from Equations (12.21) and (12.26). The related airspeed, on the contrary, will show a gradual increase with altitude, as may be appreciated when we consider the equilibrium condition that the drag is equal to the thrust (see Equation (12.11)):

$$V = \sqrt{\frac{T}{\rho} \frac{2}{S} \frac{1}{C_D}}. \quad (12.41)$$

In terms of power available, we have

$$V = \sqrt[3]{\frac{P_a}{\rho} \frac{2}{S} \frac{1}{C_D}}. \quad (12.42)$$

In analyzing the variation of the airspeeds for steepest turn, $V_{\Phi_{\max}}$, we may assume that the ratios T/ρ and P_a/ρ both increase somewhat with height (see Chapter 9). Under these conditions, we find at constant C_D an increasing value of $V_{\Phi_{\max}}$.

The foregoing analysis shows anew that the maneuverability of an airplane improves as the flight altitude is decreased. When drawing this conclusion, however, it is important to remember that the maximum achievable load factor may be greater than the maximum allowable load factor. As mentioned in Chapter 8, the value of the limit maneuvering load factor is based on strength requirements and may vary from 2.5 for transports up to roughly 7 for fighter airplanes. Moreover, passenger comfort in civil airplanes and the possibility of physical damage of the human body due to large accelerations and decelerations in combat airplanes may limit the maneuverability (Reference 44).

From Equation (12.21), the condition for the tightest turn (minimum radius of turn) can be expressed as

$$R_{\min} = \frac{W}{S} \frac{2}{\rho} \frac{1}{g} \frac{1}{(C_L \sin \Phi)_{\max}}. \quad (12.43)$$

where, for a jet powered airplane, the relationship between C_L and Φ may be given by Equation (12.39). Elimination of the bank angle from Equations (12.39) and

(12.43) yields

$$R_{\min} = \frac{W}{S} \frac{1}{\rho g} \frac{1}{\left[C_L \sqrt{1 - \left[\frac{W}{T} \right]^2 \left[\frac{C_D}{C_L} \right]^2} \right]_{\max}}. \quad (12.44)$$

This expression shows that at a given engine control setting and altitude (given value of T/W), the tightest turn occurs at an angle of attack which lies between the angle of attack for maximum lift coefficient and that for maximum lift-to-drag ratio.

The exact lift coefficient for minimum turning radius can be derived by differentiating the quantity between brackets in Equation (12.44) with respect to C_L and setting the result equal to zero,

$$\frac{d}{dC_L} \left[C_L \sqrt{1 - \left[\frac{W}{T} \right]^2 \left[\frac{C_D}{C_L} \right]^2} \right] = 0.$$

This yields the following condition:

$$\frac{C_D}{C_L} \frac{dC_D}{dC_L} = \left(\frac{T}{W} \right)^2. \quad (12.45)$$

Introducing in Equation (12.45) a parabolic variation of C_L with C_D , that is $C_D = C_{D0} + C_L^2/(\pi Ae)$, we find the lift coefficient as

$$C_L = \sqrt{\frac{1}{2} \left(\frac{T}{W} \right)^2 (\pi Ae)^2 - C_{D0} \pi Ae}. \quad (12.46)$$

From Equation (12.46), it is apparent that the lift coefficient for the tightest turn decreases with increasing height so that its largest value occurs at sea level, where the thrust is at a maximum. At low heights, however, the lift coefficient demanded by Equation (12.46) generally exceeds the maximum lift coefficient of the airplane so that only an actual minimum turning radius can be realized at the (calibrated) stalling speed in the turn, $V_{S\Phi}$. This observation also emphasizes the significance of a large value of the maximum lift coefficient in obtaining a small turning radius. At the theoretical ceiling, where $R = \infty$, we have $T/W = C_D/C_L$ in Equation (12.45), yielding $dC_D/dC_L = C_D/C_L$, which is the condition for maximum lift-to-drag ratio (see Section 4.4). Therefore, the airspeed $V_{R\min}$ normally increases from $V_{S\Phi}$ at sea level up to the minimum drag speed in level flight, $V_{D\min}$, at the theoretical ceiling.

In the same manner, we can readily produce an expression, giving the lift coefficient for minimum radius of turn analogous to Equation (12.46), for a propeller-driven airplane with power available independent of airspeed.

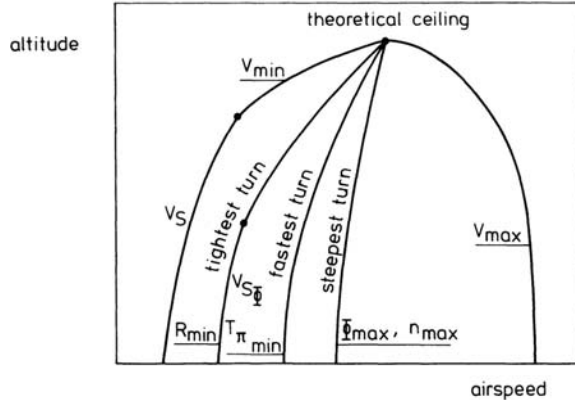


Figure 12.11 Effect of altitude on airspeeds for optimum turning performance

The required lift coefficient then turns out to be

$$C_L = \sqrt{\frac{27 (P_a/W)^4}{64 \left[\frac{W}{S} \frac{2}{\rho}\right]^2} (\pi A e)^4 - C_{D0} \pi A e} \tag{12.47}$$

Now, the reader can easily make certain for himself that the lift coefficient given by the last equation will vary from $C_L = C_{L_{max}}$ at sea level down to $C_L = \sqrt{3C_{D0} \pi A e}$ at the theoretical ceiling, where is flown at the minimum power required speed.

As a consequence, there is again the tendency for the airspeed for tightest turn to increase with altitude.

It will also be evident from the foregoing analyses that as a result of the difference in wing loading and in the variation of thrust with airspeed for jet-powered and propeller-driven airplanes, there is the particular quality of the latter airplane types that most of the speeds for best turning performance are somewhat less than those of their jet-driven counterparts.

We end this section with Figure 12.11, where the qualitative relationships are sketched between the three airspeeds for best turning performance. For the sake of completeness, the minimum and maximum level flight speeds have also been indicated.

12.5 Climbing and descending turns

Sometimes it may be needed to execute a climbing or descending turn, e.g., when height must be altered in a flight over a restricted area.

From Equations (12.4) to (12.6), the expressions for the airspeed, drag, power required and load factor in a climbing turn may be written as follows:

$$V = \sqrt{\frac{W}{S} \frac{2}{\rho} \frac{1}{C_L} \frac{\cos \gamma}{\cos \mu}} \tag{12.48}$$

$$D = \frac{C_D}{C_L} W \frac{\cos \gamma}{\cos \mu} \quad (12.49)$$

$$P_r = W \sqrt{\frac{W}{S} \frac{2 C_D^2 \cos^3 \gamma}{\rho C_L^3}} \quad (12.50)$$

$$n = \frac{\cos \gamma}{\cos \mu}. \quad (12.51)$$

According to Equation (3.35), the aerodynamic angle of roll μ in these expressions is related to the bank angle Φ and the flight-path angle γ by

$$\sin \mu = \frac{\sin \Phi}{\cos \gamma}. \quad (12.52)$$

Comparing Equations (12.49) and (12.50) with Equations (12.15) and (12.16) shows that for climbing flight, the drag and power required at given angle of attack and bank angle are unequal to the corresponding values for a constant altitude turn. Nevertheless, for small flight-path angles, say, $\gamma < 15^\circ$, it is acceptable to assume $\cos \gamma = 1$ so that drag and power required are given by Equations (12.15) and (12.16). With this, the following approximations to the flight-path angle and the rate of climb in a climbing turn hold:

$$\sin \gamma = \frac{T - D}{W} = \frac{T}{W} - \frac{C_D}{C_L} \frac{1}{\cos \Phi} \quad (12.53)$$

$$RC = \frac{P_a - P_r}{W} = \frac{P_a}{W} - \sqrt{\frac{W}{S} \frac{2 C_D^2}{\rho C_L^3} \frac{1}{\cos^3 \Phi}}. \quad (12.54)$$

Of course, the extension of a symmetric climb with a turn will have the effect that the rate of climb becomes less than that in straight flight, provided that during the maneuver the engine control setting remains unchanged.

Similarly, a greater rate of descent occurs in a descending turn than in a symmetric descent. As we have remarked in Chapter 3, in order to lose height in approaching for landing, small airplanes may perform a straight sideslipping flight. In this respect it may be more effective to execute a descending turn and in particular a slipping turn, where the airplane is subjected to a large drag.

The latter maneuver is characterized by the fact that the bank angle is too large for the rate of turn. Under this condition the airplane slips into the turn with its nose pointing toward the outside of the turn (see Figure 12.3b). Figure 12.12 gives by way of illustration the forces acting on the airplane in a slipping level turn to the right ($\beta > 0$). When resolving the forces along the X_t , Y_t and Z_t axes, we get the following equations for level slipping turning flight:

$$-D + T \cos \beta = 0 \quad (12.55)$$

$$L \sin \Phi - T \sin \beta \cos \Phi - S \cos \Phi - C = 0 \quad (12.56)$$

$$-L \cos \Phi - T \sin \beta \sin \Phi - S \sin \Phi + W = 0. \quad (12.57)$$

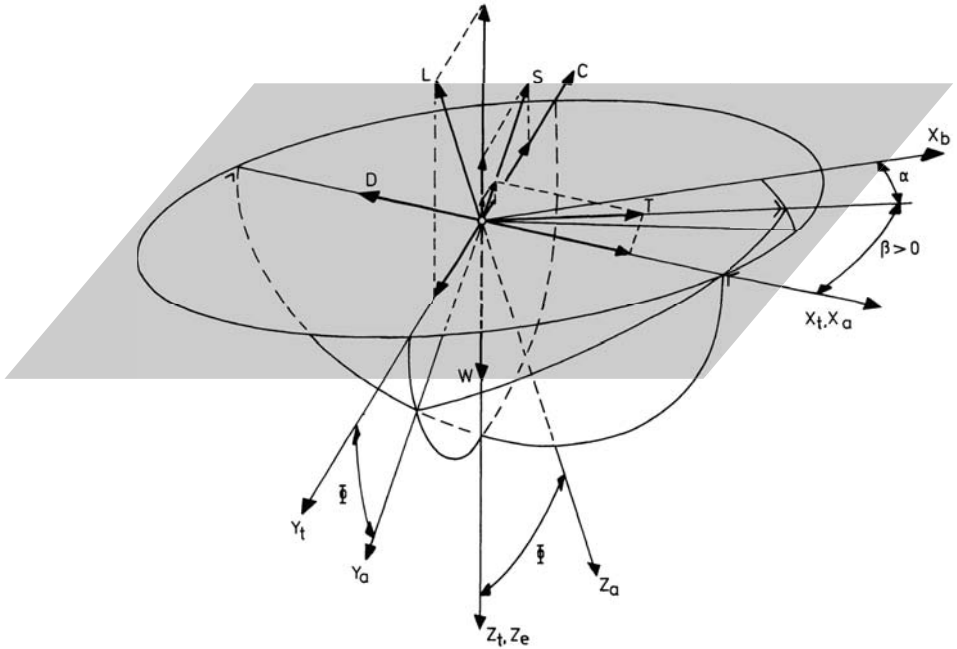


Figure 12.12 Forces In a slipping turn

A special type of flight is the gliding turn, which for example is carried out by a glider pilot when circling in rising air to gain height and also as a means to lose height when descending toward the airfield for landing. We shall look at this type of maneuver in Chapter 13.

As we have previously mentioned, in a turn the outer wing will move faster than the inner wing, and therefore will produce more lift. As a consequence, it may be found necessary to apply opposite aileron deflections in order to maintain the desired angle of bank. This intervention of the pilot is called *holding off bank*.

A point to note is that this phenomenon is different in climbing and descending turns. To explain this, we consider the three rotations of the airplane about its body axes.

Recalling that $\Omega = \Psi$, we find from Equation (1.22) the angular velocities as follows (see also Figure 1.20).

$$\text{rate of roll } p = -\Omega \sin \theta \quad (12.58)$$

$$\text{rate of pitch } q = \Omega \cos \theta \sin \phi \quad (12.59)$$

$$\text{rate of yaw } r = \Omega \cos \theta \cos \phi. \quad (12.60)$$

In these equations θ is the angle of pitch and ϕ is the angle of roll. Note that the rate of turn Ω is positive when pointing along the positive Z_e -axis (vertically downward).

In a climbing turn ($\theta > 0$), the airplane is besides pitching and yawing, also rolling outward. Conversely, in a descending turn the airplane is rolling inward.

The roll to the outside of the turn in a climb increases the angle of attack at the outer wing above that of the inner wing. In combination with its higher velocity, the outer wing generates more lift so that the airplane may have a tendency to overbank.

The inward roll of the descending turn causes a greater angle of attack at the inner wing. The additional lift obtained in this fashion may balance the extra lift furnished by the outer wing due to its higher speed. Accordingly, in a descending turn the problem of hold off bank generally is absent.

Chapter 13

GLIDING FLIGHT

13.1 Symmetric flight

Gliding flight, by definition, is the flight with zero thrust. Naturally, this is true in the case of an engineless glider or sailplane, but also when an airplane is flying with the engine(s) at idling, the propulsive force usually is sufficiently small that its contribution to the resultant aerodynamic force can be ignored. Furthermore, zero thrust can be expected when an airplane has shortage of fuel or when a single-engine airplane has engine failure.

Setting $T = 0$ in Equations (9.1) and (9.2), we obtain the following equations (see also Figure 9.1)

$$-D - W \sin \gamma = 0 \quad (13.1)$$

$$L - W \cos \gamma = 0. \quad (13.2)$$

Equations (13.1) and (13.2) describe the equilibrium of forces for symmetric unpowered flight and show that the weight must be balanced by the lift and drag only. Since the drag is directed along the negative X_a -axis, a state of equilibrium exists if the weight furnishes a force component in the direction of flight. In other words, the airplane must travel downward so that $\gamma < 0$ (Figure 13.1).

When an airplane flies at a negative flight-path angle, it is said to be in either a descent or a dive. The term descent is used when the flight path makes a relatively small angle with the horizontal plane, whilst a dive concerns the occurrence of a steep slope of the flight path. Descents and dives may be executed in the flight with either power-on or power-off. The subject of the present chapter is the glide, which is thus a descending or diving flight with $T = 0$.

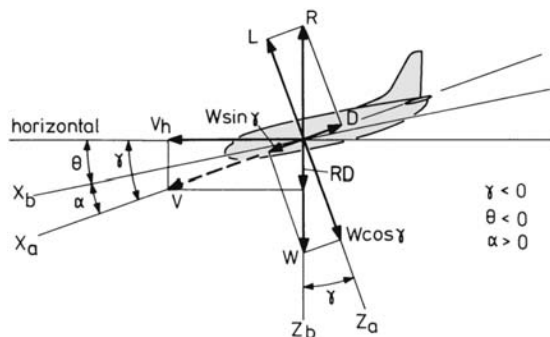


Figure 13.1 Steady symmetric glide conditions

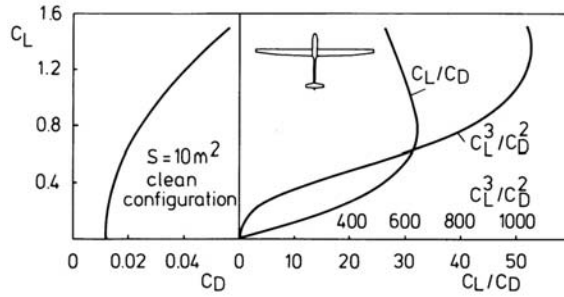


Figure 13.2 Plot of parabolic lift-drag polar for glider

In order to avoid the use of negative flight-path angles in formulae, one conventionally defines

$$\gamma_d = -\gamma. \quad (13.3)$$

Hence the angle γ_d is counted positive downward and is called the angle of descent or angle of glide.

Similarly, a negative rate of climb may be replaced by a positive rate of descent (rate of sink),

$$RD = -RC. \quad (13.4)$$

Substituting $\gamma_d = -\gamma$ into Equations (13.1) and (13.2) and using the familiar expressions; $L = C_L \frac{1}{2} \rho V^2 S$ and $D = C_D \frac{1}{2} \rho V^2 S$, we obtain in a glide

$$D = C_D \frac{1}{2} \rho V^2 S = W \sin \gamma_d \quad (13.5)$$

$$L = C_L \frac{1}{2} \rho V^2 S = W \cos \gamma_d. \quad (13.6)$$

From Equation (13.6), the airspeed can be written as

$$V = \sqrt{\frac{W}{S} \frac{2}{\rho} \frac{1}{C_L} \cos \gamma_d}. \quad (13.7)$$

Dividing Equation (13.5) by Equation (13.6) gives

$$\tan \gamma_d = C_D / C_L. \quad (13.8)$$

From Equations (13.7) and (13.8), the rate of descent in gliding flight is found to be

$$RD = V \sin \gamma_d = V \frac{C_D}{C_L} \cos \gamma_d = \sqrt{\frac{W}{S} \frac{2}{\rho} \frac{C_D^2}{C_L^3} \cos^3 \gamma_d}. \quad (13.9)$$

In the Equations (13.7) to (13.9), note that - at low subsonic flight speeds and ignoring Reynolds number effects - the quantities V , γ_d and RD are fully determined

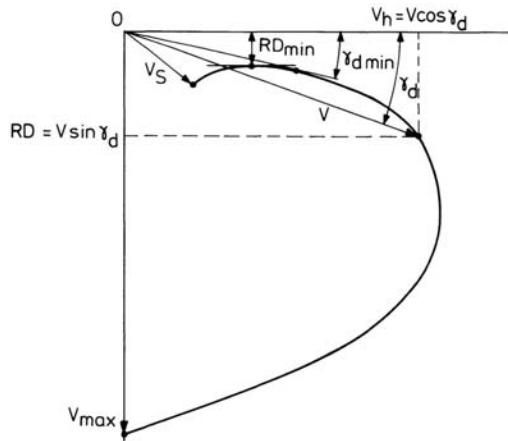


Figure 13.3 Hodograph curve for gliding flight

by the angle of attack of the airplane, which single control variable in its turn is controlled by the elevator.

Equations (13.7) to (13.9) form the basis of our analyses on performance in gliding flight. In the following we proceed by examining the variations of V , γ_d and RD with angle of attack for a specified type of glider. Let us assume that this airplane has a parabolic lift-drag polar with $C_D = 0.012 + 0.02C_L^2$ and a maximum lift coefficient of 1.5.

Figure 13.2 shows a graph of the drag equation, where also are plotted the variations of the lift-to-drag ratio C_L/C_D and the climb factor C_L^3/C_D^2 with lift coefficient. The computations are made in Table 13.1, presuming a flight at an altitude of 2,000 m (I.S.A.) and a wing loading of 400 N/m^2 . The airplane data specified for our numerical example may illustrate the general features that airplanes designed for gliding have a comparatively low wing loading, a low induced drag factor (large wing aspect ratio), and a small C_{D0} value.

A graphic representation of the point performance in symmetric flight is sketched in Figure 13.3 in the form of the hodograph curve. As we have seen in Chapter 9, this diagram is a plot of the vertical velocity $RD = V \sin \gamma_d$ versus the horizontal velocity $V_h = V \cos \gamma_d$.

Clearly, the length of the vector from the origin O to a point on the hodograph represents the magnitude of the airspeed along the flight path that corresponds to that point. The angle confined between a radius vector and the horizontal axis is a measure of the angle of descent.

From an inspection of the hodograph curve, the following features are apparent:

- From the stalling speed at maximum lift coefficient, the airspeed increases continuously with decreasing lift coefficient. When flying at $C_L = 0$, the airplane is in a steady vertical dive ($\gamma_d = 90^\circ$), where the flight velocity is maximum.

Table 13.1 Calculation of glide performance

| airplane weight | | $W = 4,000 \text{ N}$ | | | | | |
|-----------------|--------|--------------------------------|---------------|--------------------|---------------|---------------|---------------|
| wing area | | $S = 10 \text{ m}^2$ | | | | | |
| altitude | | $H = 2,000 \text{ m (I.S.A.)}$ | | | | | |
| configuration | | clean | | | | | |
| C_L | C_D | C_L/C_D | C_L^3/C_D^2 | γ_d deg. | V , km/h | RD , m/s | V_h km/h |
| 1.50 | 0.0570 | 26.3 | 1038.8 | 2.176 | 82.8 | 0.874 | 82.8 |
| 1.40 | 0.0512 | 27.3 | 1046.8 | 2.094 | 85.7 | 0.871 | 85.7 |
| 1.30 | 0.0458 | 28.4 | 1047.4 | 2.018 | 89.0 | 0.870 | 88.9 |
| 1.20 | 0.0408 | 29.4 | 1038.1 | 1.947 | 92.6 | 0.874 | 92.6 |
| 1.10 | 0.0362 | 30.4 | 1015.7 | 1.885 | 96.7 | 0.884 | 96.7 |
| 1.00 | 0.0320 | 31.3 | 976.6 | 1.833 | 101.5 | 0.901 | 101.4 |
| 0.90 | 0.0282 | 31.9 | 916.7 | 1.795 | 107.0 | 0.930 | 106.9 |
| 0.80 | 0.0248 | 32.3 | 832.5 | 1.776 | 113.4 | 0.976 | 113.4 |
| 0.70 | 0.0218 | 32.1 | 721.7 | 1.784 | 121.3 | 1.049 | 121.2 |
| 0.60 | 0.0192 | 31.3 | 585.9 | 1.833 | 131.0 | 1.164 | 130.9 |
| 0.50 | 0.0170 | 29.4 | 432.5 | 1.947 | 143.5 | 1.354 | 143.4 |
| 0.40 | 0.0152 | 26.3 | 277.0 | 2.176 | 160.4 | 1.692 | 160.3 |
| 0.30 | 0.0138 | 21.7 | 141.8 | 2.634 | 185.2 | 2.364 | 185.0 |
| 0.20 | 0.0128 | 15.6 | 48.8 | 3.662 | 226.7 | 4.022 | 226.3 |
| 0.10 | 0.0122 | 8.2 | 6.7 | 6.956 | 319.8 | 10.757 | 317.4 |
| 0.00 | 0.0120 | 0.0 | 0.0 | 90.000 | 926.8 | 257.435 | 0.0 |

- The minimum value for the rate of descent occurs at that point where the hodograph has a horizontal tangent.
- The point on the hodograph that corresponds to the minimum angle of descent is found by drawing a line from the origin tangent to the curve.

An expression for the terminal-speed in the vertical dive is obtained by substituting $C_D = C_{D0}$ and $\sin \gamma_d = 1$ in Equation (13.5), which furnishes

$$V_{\max} = \sqrt{\frac{W}{S} \frac{2}{\rho} \frac{1}{C_{D0}}} \quad (13.10)$$

For our illustrative glider we find $V_{\max} = 927 \text{ km/h}$, which value will strongly exceed the design diving speed for which the airplane is designed to withstand. A typical value of the maximum allowable airspeed for a glider is of the order of 250 km/h (Reference 45).

Minimum rate of descent is of interest to the pilot when he wants to perform a flight with maximum endurance, that is, the maximum length of time that the

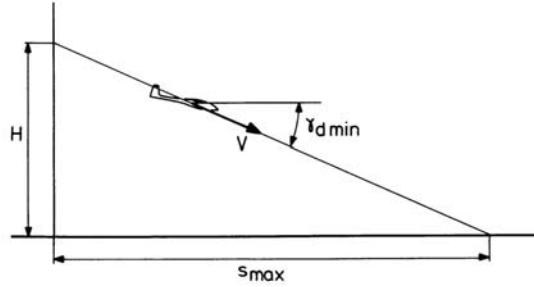


Figure 13.4 Maximum distance covered in quasi-steady glide

glider can stay in the air,

$$t_{\max} = \int_H^0 \frac{-dH}{RD_{\min}} = \int_H^0 \frac{dH}{RD_{\min}}. \quad (13.11)$$

Minimum angle of descent is of importance to the pilot if he wants to glide as far as possible (Figure 13.4),

$$s_{\max} = \int_H^0 \frac{dH}{\tan \gamma_{d\min}} = \frac{H}{\tan \gamma_{d\min}}. \quad (13.12)$$

From Equation (13.8) we see that the smallest angle of descent, and hence the maximum horizontal distance that the glider can travel, is obtained when the angle of attack is such that the lift-to-drag ratio is the maximum, so that

$$s_{\max} = H \left[\frac{C_L}{C_D} \right]_{\max}. \quad (13.13)$$

Notice that there is no effect of weight on the minimum angle of descent and so on maximum range. On the other hand, weight affects the airspeed at a given height and lift coefficient and with that the corresponding endurance.

From Table 13.1, we observe that when considering a glide in the normal range of airspeeds, the angle of descent remains small enough to assume $\cos \gamma_d = 1$. Using this approximation in the Equations (13.7) to (13.9) yields the following expressions for gliding flight:

$$V = \sqrt{\frac{W}{S} \frac{2}{\rho} \frac{1}{C_L}} \quad (13.14)$$

$$\gamma_d = \tan^{-1} \left[\frac{C_D}{C_L} \right] = \sin^{-1} \left[\frac{C_D}{C_L} \right] \quad (13.15)$$

$$RD = \sqrt{\frac{W}{S} \frac{2}{\rho} \frac{C_D^2}{C_L^3}}. \quad (13.16)$$

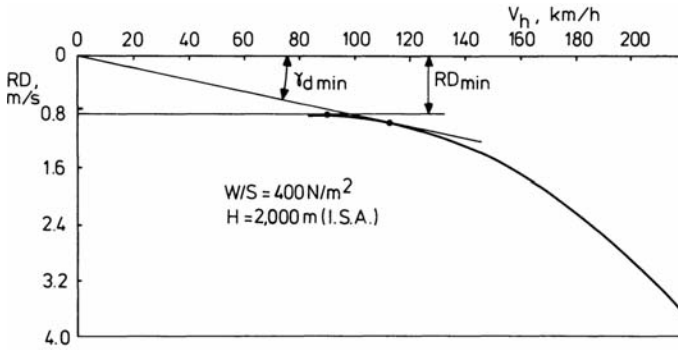


Figure 13.5 Glide performance hodograph assuming $\cos \gamma_d = 1$

Equation (13.16) shows that with the assumption $\cos \gamma_d = 1$, the minimum rate of descent is obtained when the climb factor C_L^3/C_D^2 is the maximum. We also see that at the speed for best glide angle the airplane drag is minimum,

$$D_{\min} = W \sin \gamma_{d\min} = \frac{W}{(C_L/C_D)_{\max}} \quad (13.17)$$

Likewise, it follows that at the speed for minimum rate of descent, the power required is minimum,

$$P_{r\min} = (DV)_{\min} = (WV \sin \gamma_d)_{\min} = W(RD_{\min}). \quad (13.18)$$

Figure 13.5 gives again the hodograph for our illustrative glider, but now calculated from Equations (13.14) to (13.16), and for the speed range extending from the stall to about the maximum allowable airspeed.

With the adoption of a parabolic lift-drag polar, $C_D = C_{D0} + C_L^2/(\pi Ae)$, the airspeeds for best glide angle and for minimum rate of descent can easily be deduced from Equation (13.14) as

$$V_{\gamma_{d\min}} = \sqrt{\frac{W}{S} \frac{2}{\rho} \frac{1}{\sqrt{C_{D0}} \pi Ae}} \quad \text{and} \quad (13.19)$$

$$V_{RD_{\min}} = \sqrt{\frac{W}{S} \frac{2}{\rho} \frac{1}{\sqrt{3} C_{D0} \pi Ae}}. \quad (13.20)$$

For our glider the lift coefficients for flattest glide and for minimum rate of descent are 0.78 and 1.34, respectively. As discussed in Chapter 4, a large part of the lift-drag polar is indeed roughly parabolic, but there may be some additional drag at lift coefficients above about 1.0. This means that the actual minimum rate of descent tends to be worse than the parabolic drag equation forecasts.

13.2 Effect of altitude

To investigate the effect of altitude on the performance in gliding flight, two flight conditions at different altitudes but at the same angle of attack are considered. The

latter requirement says that the lift and drag coefficients remain constant as the altitude varies, provided that slight Reynolds number effects on the lift-drag polar can be ignored. Since from Equation (13.8) the glide angle is completely determined by the lift-to-drag ratio, we discover that this angle also remains unchanged. Using the subscripts "1" and "2" to denote the set of conditions at altitudes H_1 and H_2 , the ratio of the horizontal velocities is

$$\frac{V_{h2}}{V_{h1}} = \frac{\sqrt{\frac{W}{S} \frac{2}{\rho_2} \frac{1}{C_L} \cos \gamma_d \cos \gamma_d}}{\sqrt{\frac{W}{S} \frac{2}{\rho_1} \frac{1}{C_L} \cos \gamma_d \cos \gamma_d}} = \sqrt{\frac{\rho_1}{\rho_2}} \quad (13.21)$$

Similarly, for the ratio of the vertical velocities we obtain

$$\frac{RD_2}{RD_1} = \frac{\sqrt{\frac{W}{S} \frac{2}{\rho_2} \frac{1}{C_L} \cos \gamma_d \sin \gamma_d}}{\sqrt{\frac{W}{S} \frac{2}{\rho_1} \frac{1}{C_L} \cos \gamma_d \sin \gamma_d}} = \sqrt{\frac{\rho_1}{\rho_2}} \quad (13.22)$$

Combining Equations (13.21) and (13.22) yields

$$\frac{V_{h2}}{V_{h1}} = \frac{RD_2}{RD_1} \quad (13.23)$$

Let us now consider Figure 13.6a, where for our illustrative glider are shown the hodograph curves for three altitudes. According to Equation (13.23), corresponding points on the curves shift to the left and upward along a straight line through the origin when altitude decreases (increasing air density). Consequently, all curves have a joint tangent which defines the minimum angle of glide. Note that the related airspeed decreases with decreasing height. Likewise, we find that at a given angle of attack the rate of descent and the corresponding airspeed both fall off with decreasing altitude.

Looking at Equations (13.11) to (13.16), we see that the flight program for maximum range as well as for maximum endurance requires that the pilot controls the airplane in such a way that throughout the glide the dynamic pressure remains constant. In other words, the equivalent airspeed must be kept constant and the airplane executes a quasi-steady flight, where the true airspeed increases when the airplane descends.

It will be evident from the foregoing discussion that plotting the hodograph curves on the basis of equivalent airspeeds will lead again to a single curve applying at all altitudes (Figure 13.6b).

In this respect, it is worth to note that the pilot is faced with two sorts of speed data. The airspeed indicator, in principle, displays equivalent airspeeds, whereas the readings of the vertical-speed indicator are close to true speeds.

Widely used for indicating the vertical velocity of a glider is the mechanical variometer, which is - like the vertical-speed indicator discussed earlier in Chapter 5 - a pressure operated device. As shown in Figure 13.7, one side of the variometer is connected to the static pressure tapping on the glider and the other to a vacuum-insulated capacity. When the airplane descends, the increasing air pressure forces

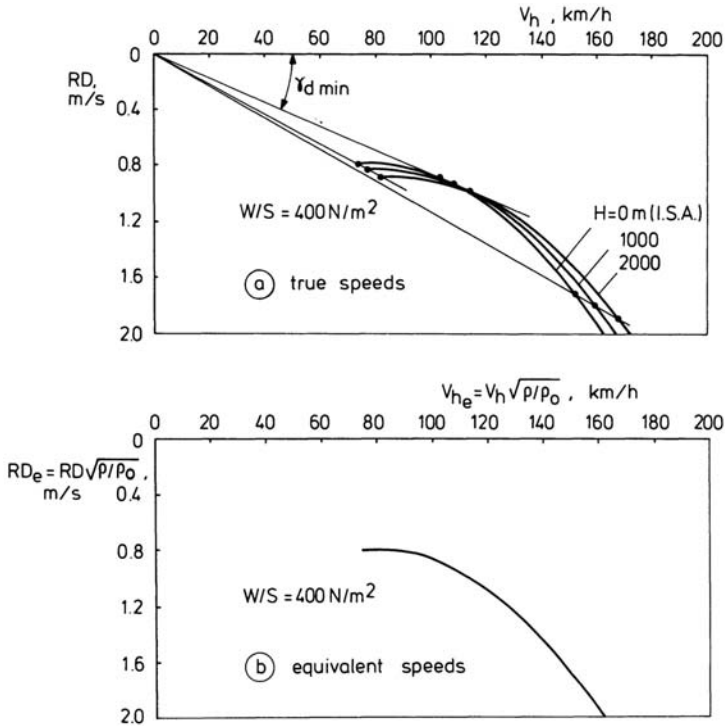


Figure 13.6 Effect of altitude on glide performance

air to flow into the device through the clearance between the vane and the case; the flow direction, naturally, is reversed when climbing. The pointer, which is directly connected to the vane, shows a displacement owing to the different pressures acting on the two sides of the vane.

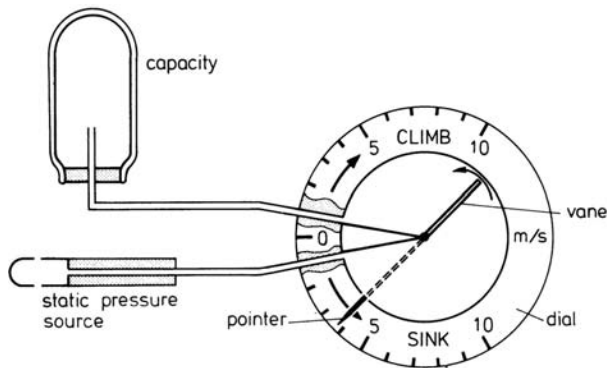


Figure 13.7 Principle of varlometer

So far, hodograph curves have been considered, which relate low-subsonic flight speeds. However, as the angle of glide and/or the wing loading of the airplane are

greater, the glide will be executed at a higher airspeed.

Of special note is the orbiter stage of the United States Space Shuttle. The Orbiter is a reusable delta-winged space vehicle/glider, powered by three rocket engines, which are contained in the aft fuselage (Figure 13.8). The liquid propellants for these engines are carried in an external jettisonable tank, attached to the vehicle at liftoff. In addition, two jettisonable and reusable solid rocket boosters are mounted on the fuel tank for liftoff. The complete Space Shuttle system is launched vertically, with all engines operating.

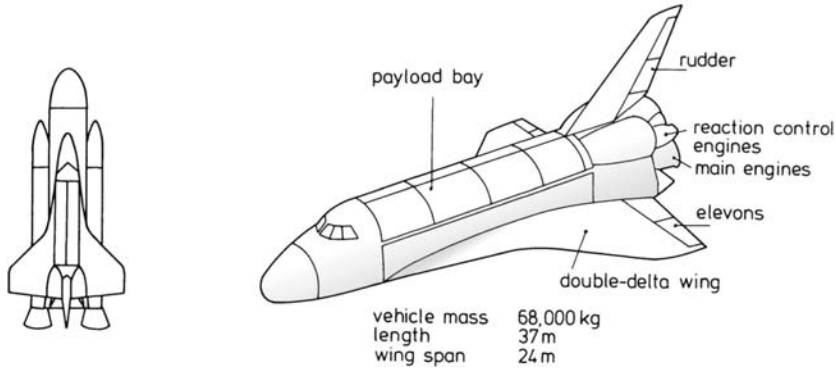


Figure 13.8 Space shuttle system and orbiter

The Orbiter can deliver to Earth orbit a crew of seven persons and a mass of 29,500 kg payload. After completion of a mission, the orbiter reenters the atmosphere and returns to the surface of the Earth where it lands as a conventional airplane.

In the upper layer of the atmosphere, the spacecraft is steered by a reaction control system, but in the lower more dense atmosphere, the vehicle is controlled aerodynamically by rudder and elevons. When traveling back from orbit to Earth, the Orbiter behaves as a lifting vehicle, performing a glide through the flight corridor, as shown in the previous Figure 10.14. During the return to sea level the orbital speed range is encountered so that the lift-drag polar will strongly depend on flight Mach number,

$$C_L = C_L(\alpha, M) \quad (13.24)$$

$$C_D = C_D(\alpha, M). \quad (13.25)$$

Not only the Orbiter, but also the conventional jet airplanes with their high wing loadings attain flight speeds at which the effects of compressibility cannot be ignored. Consequently, the glide performance of all these airplane types can no longer be represented by a single hodograph curve as in Figure 13.6b. If we want to determine their hodograph curves, we now have for the point performance (given values of altitude and airplane weight) at a given flight Mach number:

$$V = Mc \quad (13.26)$$

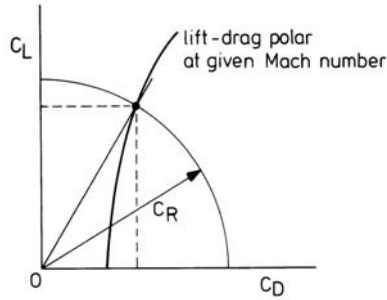


Figure 13.9 Establishing the angle of attack from known value of C_R

$$C_L = \frac{W}{S} \frac{2}{\rho V^2} \cos \gamma_d = f_1(\alpha) \quad (13.27)$$

$$C_D = C_{D0} + k C_L^2 = f_2(\alpha) \quad (13.28)$$

$$\gamma_d = \tan^{-1} \left[\frac{C_D}{C_L} \right] = f_3(\alpha) \quad (13.29)$$

$$RD = V \sin \gamma_d = f_4(\alpha). \quad (13.30)$$

Since Equations (13.27) to (13.30) contain the angle of attack in implicit form, we must solve the problem iteratively starting from $\cos \gamma_d = 1$.

The angle of attack can also be determined graphically from the condition $R = W$ or (cf. Equation (4.14))

$$C_R = \frac{W}{\frac{1}{2} \gamma \rho M^2 S}. \quad (13.31)$$

For the lift-drag polar at a given Mach number we have at each angle of attack the relationship (Figure 13.9)

$$C_R = \sqrt{C_L^2 + C_D^2}. \quad (13.32)$$

Since at a given airplane weight, altitude and Mach number, the value of C_R is known from Equation (13.31), we obtain the corresponding values of C_L and C_D at that point on the lift-drag polar where the curve intersects a circle having a radius C_R and of which the center is located at the origin O .

13.3 Effect of wind

it is important to realize that in our discussions on gliding flight so far the atmosphere is supposed to be at rest with respect to the Earth.

As we have learned in Chapter 1, in the presence of wind, the velocity of the airplane relative to the ground or ground speed V_g , is the vector sum of the airspeed V and the wind velocity V_w (see Figure 1.21).

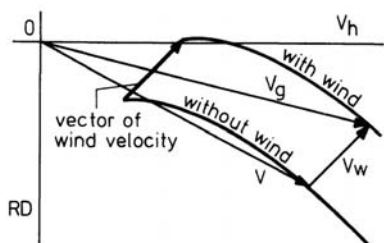


Figure 13.10 Hodograph for gliding with and without wind

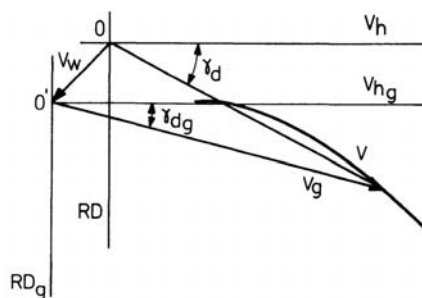


Figure 13.11 Effect of wind in the hodograph diagram

In considering the effect of wind on gliding, for simplification, we shall assume a steady wind. We shall also assume that the wind blows in a direction parallel to the plane of symmetry of the airplane. Under these conditions, the wind velocity can be added to the flight velocities given by the hodograph curve in still air to give the ground speed.

In Figure 13.10 the hodograph curve of Figure 13.5 is plotted again, together with a hodograph illustrating the effect of a steady wind. The latter curve shows that as a result of the upward component of the wind velocity, a positive rate of climb is possible. Apparently, the presence of wind may be of great importance to gliding since in the case of an upwind that is greater than the rate of descent, the airplane will climb relative to the Earth.

The resulting type of flight is known as *soaring*, which mostly is performed using rising currents of warm air. These vertical updrafts usually are called thermals and occur due to local heating of the Earth's surface by the Sun (see Section 2.6). Obviously, to gain the maximum rate of climb in a thermal, the pilot must select the airspeed which provides the minimum rate of descent with respect to the air.

Figure 13.11 illustrates the usual technique to find the performance in soaring against wind from the hodograph curve in still air. For this purpose, ground speed V_g is measured relative to replaced axes of which the origin is shifted over a distance equal to the wind velocity and in a direction opposite to the wind direction. The angle γ_{dg} is the actual glide angle (glide angle relative to the Earth's surface). Figure 13.12 illustrates the effects of horizontal and vertical wind velocities on flattest glide. If the pilot wants to achieve the best glide angle over the ground in the presence of an upwind, then the best airspeed to glide will correspond to point A in Figure 13.12a, such that $O'A$ is the tangent to the hodograph curve. In the case of a downwind the origin is displaced upward and the minimum angle of glide is found by drawing the tangent $O'B$.

When a pilot wants to fly at the best angle of glide relative to the ground in the presence of a headwind or tailwind, then points C and D in Figure 13.12b represent the best airspeeds.

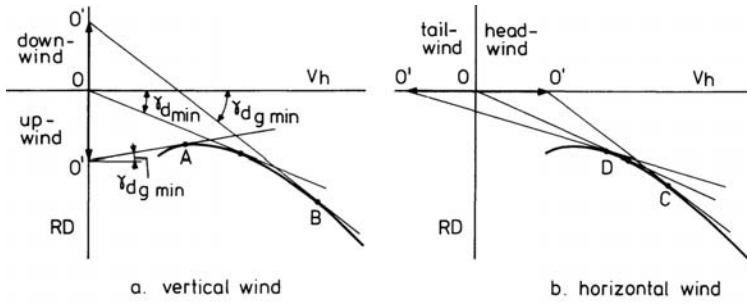


Figure 13.12 Vertical and horizontal wind velocities In the hodograph diagram

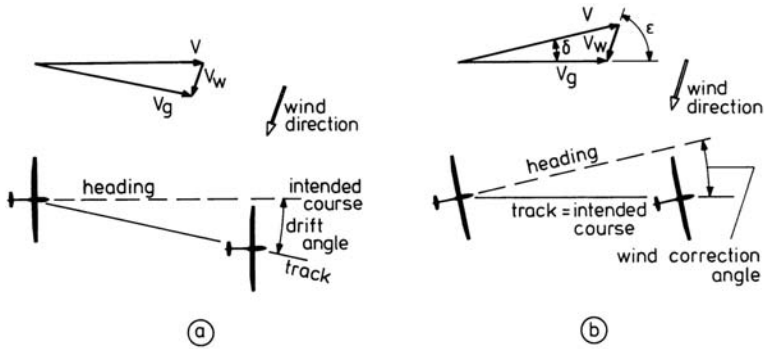


Figure 13.13 Effect of wind on heading

Emphasis is made that the foregoing analyses are based on a wind blowing in a direction parallel to the flight path. Under most circumstances, however, the wind velocity will be directed at some angle to the desired flight path of the airplane over the ground. Figure 13.13a shows, as an example, the path of an airplane in level flight as resulting from its airspeed and a horizontal wind velocity. Since the wind is blowing from the left, the airplane will drift to the right, through which the velocity vector of the ground speed is at a drift angle with the intended course. Therefore, in addition to the preceding simplified treatment of the effect of wind, it is worth to recognize that the pilot often must counteract the wind velocity by changing the heading of the airplane in order that the track coincides with the intended course. The latter situation is depicted in Figure 13.13b. Apparently, the ground speed is given by

$$V_g = V \cos \delta - V_w \cos \epsilon, \tag{13.33}$$

where δ is the angle between the flight velocity vector and the track, the so-called *wind correction angle*, and ϵ is the angle between the wind velocity vector and the desired path. Equation (13.33) can be manipulated to yield

$$V_g = V \sqrt{1 - \left[\frac{V_w}{V} \right]^2 \sin^2 \epsilon - V_w \cos \epsilon}. \tag{13.34}$$

An inspection of Equation (13.34) indicates that a wind directed perpendicular to the track reduces the flight speed relative to the ground, although it has no component along the track. Clearly, this effect occurs because the heading of the airplane is into the wind in order that the actual flight path over the ground shall be in the right direction.

13.4 Turning flight

In the preceding section, we have seen that a glider can gain height by flying in ascending warm air masses. Owing to their small horizontal dimensions, the glider pilot must execute turning flights to utilize these thermals.

A horizontal cross-section through a thermal may be taken as circular, with the greatest vertical velocity at the center and falling off toward the outside. The most appropriate radius of turn and the associated values of angle of bank and airspeed for optimum climb performance will then depend on the manner in which the vertical velocity in the thermal varies with radius.

For this reason, the relationship between the minimum rate of descent and the radius of turn of the airplane is of importance.

To investigate this connection, let us consider the equations governing the translational motion of the airplane in a steady coordinated turn. Then, by substitution of $T = 0$ and $\gamma = -\gamma_d$ in Equations (12.4) to (12.6), we obtain

$$-D + W \sin \gamma_d = 0 \quad (13.35)$$

$$L \sin \mu - C = 0 \quad (13.36)$$

$$-L \cos \mu + W \cos \gamma_d = 0, \quad (13.37)$$

where, from Equation (3.31), the centrifugal force C is

$$C = \frac{W}{g} V \Omega \cos \gamma_d = \frac{W}{g} \frac{V^2}{R} \cos^2 \gamma_d. \quad (13.38)$$

With the substitution of Equation (13.38), $D = C_D \frac{1}{2} \rho V^2 S$ and $L = C_L \frac{1}{2} \rho V^2 S$, the equations for turning in a glide become

$$C_D \frac{1}{2} \rho V^2 S = W \sin \gamma_d \quad (13.39)$$

$$C_L \frac{1}{2} \rho V^2 S \sin \mu = \frac{W}{g} V \Omega \cos \gamma_d = \frac{W}{g} \frac{V^2}{R} \cos^2 \gamma_d \quad (13.40)$$

$$C_L \frac{1}{2} \rho V^2 S \cos \mu = W \cos \gamma_d. \quad (13.41)$$

For a given airplane weight and atmospheric conditions, Equations (13.39) to (13.41) contain five variables, namely: α , V , γ_d , μ and R so that each instantaneous flight condition is defined by the selection of two control variables.

Expressing the performance items in terms of angle of attack (C_L and C_D) and the aerodynamic angle of roll μ , we readily find

$$V = \sqrt{\frac{W}{S} \frac{2}{\rho} \frac{1}{C_L} \frac{\cos \gamma_d}{\cos \mu}} \quad (13.42)$$

$$\tan \gamma_d = \frac{C_D}{C_L} \frac{1}{\cos \mu} \quad (13.43)$$

$$RD = \sqrt{\frac{W}{S} \frac{2 C_D^2 \cos^3 \gamma_d}{\rho C_L^3 \cos^3 \mu}} \quad (13.44)$$

$$n = \frac{L}{W} = \frac{\cos \gamma_d}{\cos \mu} = \frac{C_L}{C_D} \sin \gamma_d \quad (13.45)$$

$$R = \frac{V^2 \cos \gamma_d}{g \tan \mu} = \frac{W}{S} \frac{2}{\rho} \frac{1}{g C_L} \frac{1}{\sin \mu} \cos^2 \gamma_d \quad (13.46)$$

$$\Omega = \frac{V \cos \gamma_d}{R} = \frac{g \tan \mu}{V} \quad (13.47)$$

$$T_\pi = \frac{\pi}{\Omega} = \frac{\pi R}{V \cos \gamma_d}. \quad (13.48)$$

However, in consonance with our earlier experience that in a normal glide the angles of descent remain small, we may assume that $\cos \gamma_d$ is approximately equal to unity in the equations listed above. Moreover, because we are considering coordinated turns, we get from Equation (3.35) that in consequence of the assumption $\cos \gamma_d = 1$, the aerodynamic angle of roll μ is equal to the angle of bank Φ . Then the governing series of equations reduce to

$$V = \sqrt{\frac{W}{S} \frac{2}{\rho} \frac{1}{C_L} \frac{1}{\cos \Phi}} \quad (13.49)$$

$$\tan \gamma_d = \frac{C_D}{C_L} \frac{1}{\cos \Phi} \quad (13.50)$$

$$RD = \sqrt{\frac{W}{S} \frac{2 C_D^2}{\rho C_L^3} \frac{1}{\cos^3 \Phi}} \quad (13.51)$$

$$n = \frac{L}{W} = \frac{1}{\cos \Phi} = \frac{C_L}{C_D} \sin \gamma_d \quad (13.52)$$

$$R = \frac{V^2}{g \tan \Phi} = \frac{W}{S} \frac{2}{\rho} \frac{1}{g C_L} \frac{1}{\sin \Phi} \quad (13.53)$$

$$\Omega = \frac{V}{R} = \frac{g \tan \Phi}{V} \quad (13.54)$$

$$T_\pi = \frac{\pi}{\Omega} = \frac{\pi R}{V}. \quad (13.55)$$

The effect of banking on the hodograph curve can be examined by considering again two flight conditions at different bank angles but at a fixed angle of attack. Assuming that at constant α also the lift and drag coefficients remain the same, we find

$$\frac{V_{h2}}{V_{h1}} = \left[\frac{\cos \Phi_1}{\cos \Phi_2} \right]^{1/2} = \left[\frac{n_2}{n_1} \right]^{1/2} \quad (13.56)$$

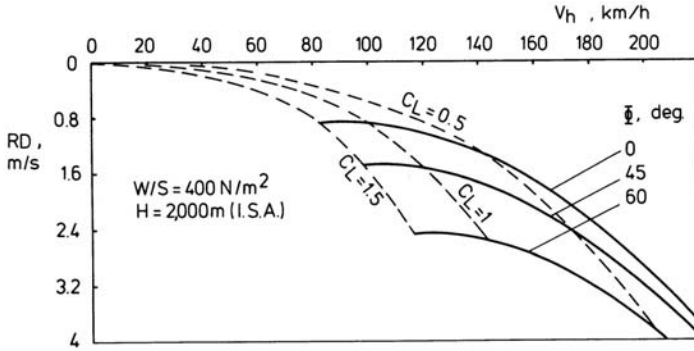


Figure 13.14 Effect of angle of bank on hodograph curve

$$\frac{RD_2}{RD_1} = \left[\frac{\cos \Phi_1}{\cos \Phi_2} \right]^{3/2} = \left[\frac{n_2}{n_1} \right]^{3/2} \quad \text{and} \quad (13.57)$$

$$\frac{RD_2}{RD_1} = \left[\frac{V_{h2}}{V_{h1}} \right]^3, \quad (13.58)$$

where the subscripts "1" and "2" indicate the conditions at bank angles Φ_1 and Φ_2 , respectively.

The hodograph curves of Figure 13.14 show the performance of our illustrative glider when turning at fixed angles of bank. The curves are deduced from the hodograph curve in straight flight, in the way described before. The points on the curves that correspond to the same value of C_L are joined by dashed lines.

Figure 13.15 presents the rate of descent as a function of radius of turn for various angles of bank, as calculated from Equations (13.51) and (13.53). Here the points are connected that correspond to the same value of V .

The upper dashed line in Figure 13.15 represents the minimum rate of descent which can be obtained at each particular radius of turn. Along this line the air-speed and the bank angle increase as the radius of turn decreases.

A mathematical formulation of the relationship between RD and R is derived by elimination of the angle of bank from Equations (13.51) and (13.53). This yields the equation

$$RD = \sqrt{\frac{W}{S} \frac{2}{\rho} \left[\frac{C_D^2}{\left[C_L^2 - \left(\frac{W}{S} \frac{2}{\rho} \frac{1}{g} \frac{1}{R} \right)^2 \right]^{3/2}} \right]}. \quad (13.59)$$

Apparently, at given values of airplane weight, air density and radius of turn, the minimum rate of descent will be obtained when the term between brackets in Equation (13.59) is a minimum.

An expression for the corresponding lift coefficient is derived by taking the derivative of that term with respect to C_L and equating it to zero. Using the parabolic

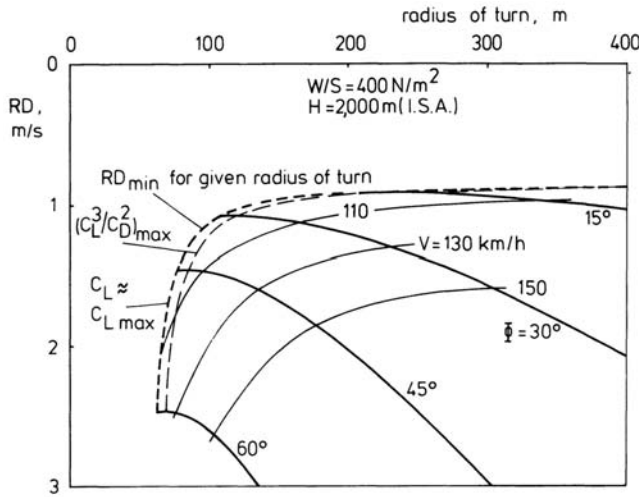


Figure 13.15 Rate of descent versus radius of turn for various angles of bank

drag equation, $C_D = C_{D0} + C_L^2/(\pi Ae)$, the optimum lift coefficient for minimum rate of descent is found to be

$$C_L = \sqrt{3C_{D0}\pi Ae + 4\left(\frac{W}{S} \frac{2}{\rho} \frac{1}{g} \frac{1}{R}\right)^2} \tag{13.60}$$

This equation shows that for minimum rate of descent the glider should obviously fly at a large lift coefficient that varies between the value at which the climb factor is the maximum ($R = \infty$) and a value close to the maximum lift coefficient ($R = R_{min}$).

In order to demonstrate the determination of the maximum rate of climb, we will assume the presence of a very simple thermal in which the variation of the vertical velocity with radius r is given by

$$V_W = V_{Wmax} \left[1 - \frac{r}{r_{max}} \right] \tag{13.61}$$

The linear velocity profile of this thermal is shown as the upper line in Figure 13.16, assuming $V_{Wmax} = 4$ m/s and $r_{max} = 200$ m.

By taking various points at particular radii on the thermal line and subtracting from the vertical air velocity the minimum rate of descent of the glider in still air when turning at the same radius (see the upper dashed curve in Figure 13.15), we find the lower curve in Figure 13.16. This curve shows the eventual result since it gives the rate of climb relative to the Earth versus radius of turn when circling concentrically with the thermal.

Clearly, the maximum rate of climb for our example is achieved at a radius of about 80 m. According to Figure 13.15, the corresponding lift coefficient is approximately 1.5 ($= C_{Lmax}$). Using these figures in Equation (13.53) learns that

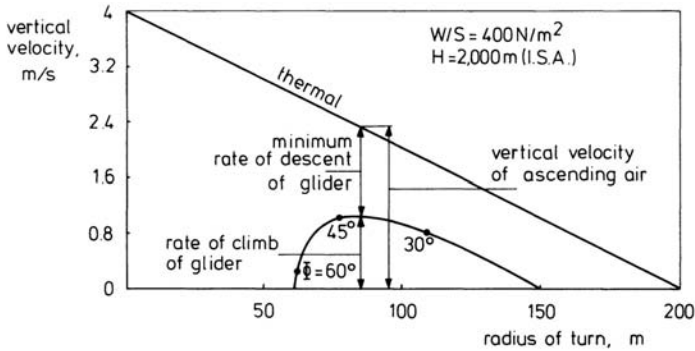


Figure 13.16 Determination of maximum rate of climb in a given thermal

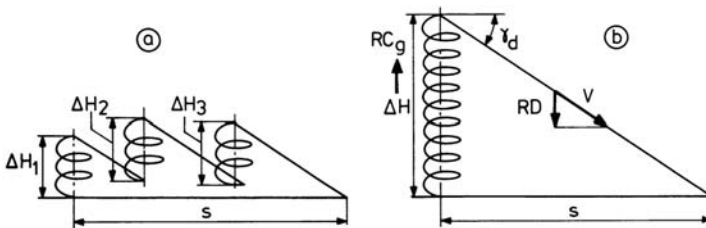


Figure 13.17 Representation of cross-country flying

optimum climb performance is achieved at an angle of bank of 43° and an air-speed of 97 km/h.

We end this section by noting that it may be possible to execute a glide which combines turning in thermals with some "dolphin" flying. The latter term denotes the performance condition in which a glider flies through a series of updrafts during a straight glide. Then the resulting flight path exhibits a series of leaps, somewhat comparable with the manner of moving on of a dolphin.

13.5 Cross-country flight

The normal flight of a glider consists of a series of climbs made by turning in thermals and a series of straight symmetric glides between the thermals (Figure 13.17a).

In Section 13.4 we have demonstrated how to determine the maximum rate of climb in a given thermal. Here we will consider the problem of maximizing the average speed for the whole flight.

For that end, all the climbs and all the straight glides are taken together and represented by a single climb followed by a single glide. Further, the assumption is made that the start and the end of the flight are at the same height and that the glide takes place in still air (Figure 13.17b).

Presuming that the mean rate of climb of the airplane in the thermal is RC_g and

the gain of height is ΔH , then the time spent in the climb is

$$t_C = \frac{\Delta H}{RC_g} \tag{13.62}$$

Similarly, the time gone in the glide is

$$t_D = \frac{\Delta H}{RD} \tag{13.63}$$

Thus the total time for the whole flight becomes

$$t_C + t_D = \Delta H \left(\frac{1}{RC_g} + \frac{1}{RD} \right) = \frac{\Delta H}{RC_g \times RD} (RC_g + RD) \tag{13.64}$$

The distance traveled can be expressed as the average speed \bar{V} times the total time. Hence, the horizontal distance s becomes

$$s = \bar{V}(t_C + t_D) \cos \gamma_d \tag{13.65}$$

Making use of the relationships $s = \Delta H / \tan \gamma_d$ and $RD = V \sin \gamma_d$, we obtain

$$\bar{V} = \frac{\Delta H}{(t_C + t_D)} \frac{V}{RD} \tag{13.66}$$

By combination of Equations (13.64) and (13.66), we find the average speed as

$$\bar{V} = RC_g \frac{V}{(RC_g + RD)} \tag{13.67}$$

Clearly, the problem is to select the flight speed \bar{V} in the glide so as to make \bar{V} an extremity at a known value of the rate of climb RC_g . Therefore, consider the hodograph diagram in Figure 13.18a where from a point A, such that the length OA expresses RC_g , a line is drawn to a point B on the hodograph curve.

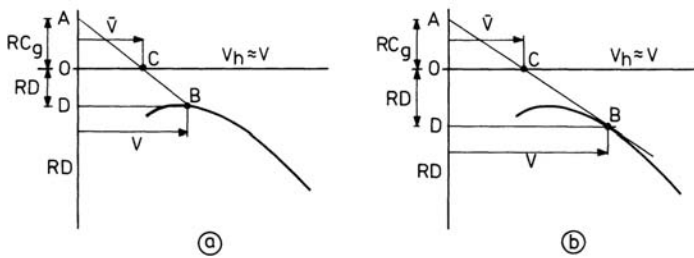


Figure 13.18 The average cross-country speed in the hodograph diagram

With the approximation that $V_h \approx V$, the distance DB represents the flight speed V during the glide.

Observing that the triangles AOC and ADB are similar, we find that the relationship between the various speeds in Figure 13.18a corresponds to Equation (13.67)

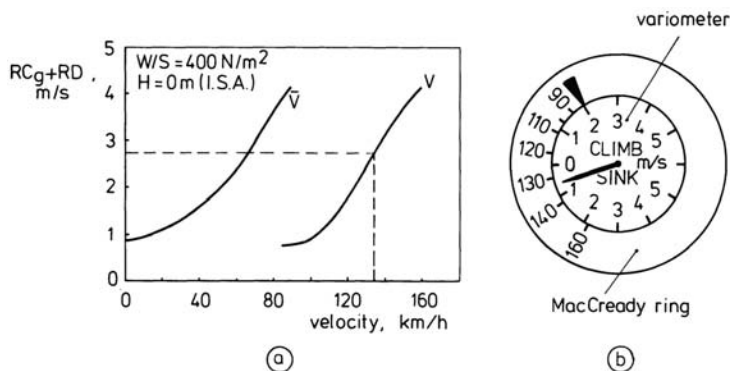


Figure 13.19 Determination of the optimum airspeed during glide between thermals

if the speed \bar{V} is represented by OC . It is also clear that the optimum value for \bar{V} is found by drawing the tangent from point A to the hodograph curve (Figure 13.18b).

By considering a large number of rate of climb values RC_g in Figure 13.5, for our illustrative glider the curves of Figure 13.19a can be produced.

A convenient tool in optimizing a cross-country flight is the MacCready ring, which is a rotatable ring added to the variometer (Figure 13.19b).

When gliding between the thermals, the datum mark on the ring is set opposite the figure on the rate of climb scale which equals the prevailing value of RC_g . The ring is calibrated such that the connection between the airspeeds V on the ring and the rates of descent RD on the variometer scale corresponds to the relationship between V and $(RC_g + RD)$ in Figure 13.19a. This makes that, for a given wing loading and height, the pointer designates directly the airspeed for optimum cross-country flying on the ring. It should be understood that the airspeed thus found depends entirely on the pilot's assessment of RC_g (2 m/s in Figure 13.19b).

Modern gliders may be equipped with water tanks so that their weight can be increased by carrying water ballast. This provision can lead to an improved cross-country performance, at least as the vertical velocities in the thermals are sufficiently large.

To illustrate the influence of the extra weight on the optimum value for the speed \bar{V} we consider Figure 13.20, where are sketched the hodograph curves for an airplane weight W_1 and for an increased weight W_2 .

From Equations (13.14) and (13.16), it is immediately apparent that the two hodograph curves relating to the higher wing loading are obtained by multiplying corresponding V and RD values on the initial curves by the factor $\sqrt{W_2/W_1}$.

It is interesting to note that the effect of an increased weight on the hodograph curve is precisely the same as the effect of an increase in altitude, i.e., the curve is displaced downward and to the right (cf. Figure 13.6a).

As depicted in Figure 13.20, the rate of climb RC_g in a given thermal will decrease

and the best speed in the glide V will increase with weight. This visualization of the problem indicates that in the case of strong thermals, the average speed \bar{V} may increase and hence the presence of ballast in the airplane promises to be beneficial (Figure 13.20a). When, on the other hand, the thermals are quite weak, it does not pay to fly with ballast, and jettisoning water may be gainful (Figure 13.20b).

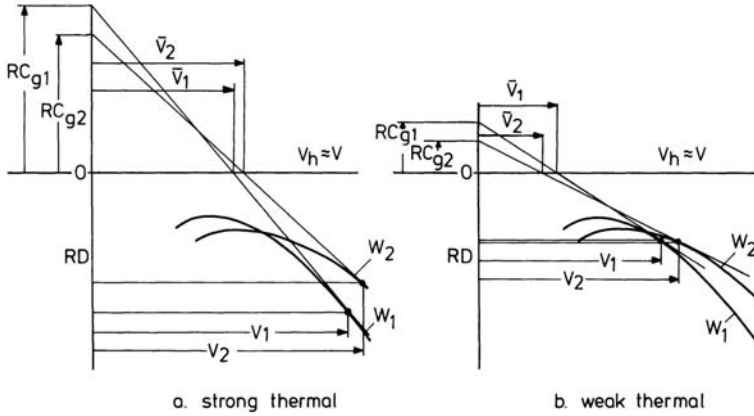


Figure 13.20 Effect of airplane weight on optimum speed

Chapter 14

SYMMETRIC CLIMB AND DESCENT

14.1 Quasi-steady symmetric flight

To this point, we have dealt mainly with point performance problems. For the remainder of this book, emphasis will be placed on the path performance or integral performance values, which, as we have defined in Chapter 8, are related to the course of the flight. With regard to the climb to a particular altitude, three integral performance values are of paramount importance, namely,

- the length of time required to climb
- the horizontal distance covered during climb
- the amount of fuel consumed during climb.

In the absence of wind, the time rate of change of altitude is the rate of climb of the airplane, which is equal to the vertical component of the airspeed,

$$\frac{dh}{dt} = RC = V \sin \gamma \quad \text{and} \quad (14.1)$$

$$dt = \frac{dh}{RC} = \frac{dH}{RC}. \quad (14.2)$$

The time to climb from an altitude H_1 to an altitude H_2 is obtained by integrating Equation (14.2) between H_1 and H_2

$$t = \int_{H_1}^{H_2} \frac{dH}{RC}, \quad (14.3)$$

where, for a given airplane, RC is a function of airplane weight, engine control setting, selected flight speed and altitude. The related range (= horizontal distance) in the absence of wind is given by

$$s = \int_{t_1}^{t_2} V \cos \gamma dt = \int_{H_1}^{H_2} \frac{dH}{\tan \gamma}. \quad (14.4)$$

The weight of the fuel consumed during a climb from H_1 to H_2 is

$$W_f = \int_{t_1}^{t_2} F dt = \int_{H_1}^{H_2} \frac{F}{RC} dH, \quad (14.5)$$

where F is the fuel weight flow rate.

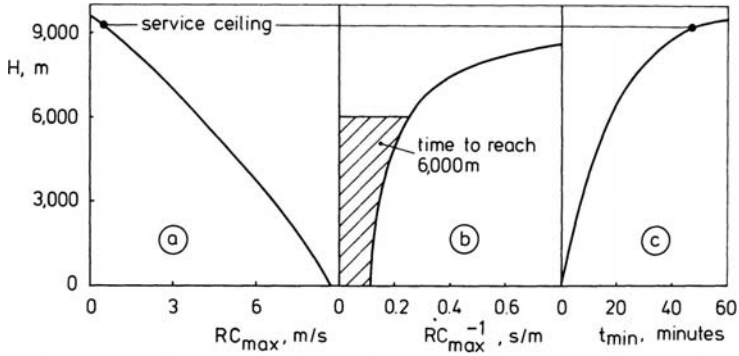


Figure 14.1 Time to climb determination

Let us look at the determination of the minimum time to climb from sea level to a given altitude, using the approach of quasi-steady flight conditions. Then, Equation (14.3) tells us that to minimize t , the rate of climb must be maximum at each altitude (cf. Equation (10.6)),

$$t_{\min} = \int_0^H \frac{dH}{RC_{\max}}. \quad (14.6)$$

Assuming that the maximum rate of climb decreases linearly with height, we can write

$$\frac{RC_{\max}}{RC_{\max_0}} = \frac{H_{th} - H}{H_{th}}, \quad (14.7)$$

where the subscripts "0" and "th" denote sea level and theoretical ceiling, respectively.

Using this relationship, Equation (14.6) can be integrated to give

$$t_{\min} = \frac{H_{th}}{RC_{\max_0}} \ln \frac{1}{\left(1 - \frac{H}{H_{th}}\right)}. \quad (14.8)$$

When no analytic expression is obtainable that relates RC_{\max} to H , the integration of Equation (14.6) can be accomplished graphically. Then, as shown in Figure 14.1b, the minimum time to climb to a given altitude is derived by plotting the curve RC_{\max}^{-1} against H and determining the shaded area on the left-hand side of the curve. The present relationship is based on the RC_{\max} versus H -curve in Figure 14.1a. This curve is repeated from the previous Figure 10.3, and concerns our illustrative two-engine turboprop airplane of Chapter 10. The result in Figure 14.1c shows that the minimum time needed to reach the service ceiling ($H = 9250$ m) is 47.5 minutes.

The time required to climb to a given altitude may also be obtained by adding increments in time between altitude intervals,

$$t = \sum_{i=1}^n \left[\frac{\Delta H}{RC_i} \right]. \quad (14.9)$$

Table 14.1 Calculation of time to climb

| H , m | RC_{\max} , m/s | RC_i , m/s | Δt_i , min | t , min | H , m | RC_{\max} , m/s | RC_i , m/s | Δt_i , min | t , min |
|------------|----------------------|-----------------|-----------------------|--------------|------------|----------------------|-----------------|-----------------------|--------------|
| | | | | 0.00 | | | 5.05 | 1.65 | 12.42 |
| 0 | 8.60 | | | | 5000 | 4.80 | | | |
| | | 8.50 | 0.98 | 0.98 | | | 4.60 | 1.81 | 14.23 |
| 500 | 8.40 | | | | 5500 | 4.40 | | | |
| | | 8.25 | 1.01 | 1.99 | | | 4.15 | 2.01 | 16.24 |
| 1000 | 8.10 | | | | 6000 | 3.90 | | | |
| | | 7.90 | 1.05 | 3.04 | | | 3.65 | 2.28 | 18.52 |
| 1500 | 7.70 | | | | 6500 | 3.40 | | | |
| | | 7.55 | 1.10 | 4.14 | | | 3.25 | 2.56 | 21.08 |
| 2000 | 7.40 | | | | 7000 | 2.90 | | | |
| | | 7.20 | 1.16 | 5.30 | | | 2.65 | 3.15 | 24.23 |
| 2500 | 7.00 | | | | 7500 | 2.40 | | | |
| | | 6.80 | 1.23 | 6.53 | | | 2.15 | 3.88 | 28.11 |
| 3000 | 6.60 | | | | 8000 | 1.90 | | | |
| | | 6.35 | 1.31 | 7.84 | | | 1.65 | 5.05 | 33.16 |
| 3500 | 6.10 | | | | 8500 | 1.40 | | | |
| | | 5.90 | 1.41 | 9.25 | | | 1.10 | 7.58 | 40.74 |
| 4000 | 5.70 | | | | 9000 | 0.80 | | | |
| | | 5.50 | 1.52 | 10.77 | | | 0.65 | 6.41 | 47.15 |
| 4500 | 5.30 | | | | 9250 | 0.50 | | | |

In this summation form of Equation (14.6), RC_i is the average value of the rate of climb within each interval ΔH . The mean and cumulative values for the airplane considered in Figure 14.1, are tabulated in Table 14.1. When using this numerical procedure, it is fairly simple to include the effect of the variation of airplane weight due to the consumption of fuel. For this purpose, at the end of each interval ΔH , the weight of the fuel consumed is determined, $\Delta W_{fi} = F_i \Delta t_i$, where F_i is the average value of the fuel weight flow rate within an interval ΔH . Then, the rate of climb in the adjacent interval is calculated at an airplane weight, $W_{i+1} = W_i - \Delta W_{fi}$. Of course, the total fuel consumed during climb can be found from $W_f = \Sigma \Delta W_{fi}$.

We conclude this section with the observation that the downward flight with engine(s) working differs from the climb only in that at the descent speed the sign of the flight-path angle is negative so that the thrust will be less than the drag. Therefore, the formulae for descending flight are included in the preceding general performance theory and need not to be developed separately.

Descent programs may be expressed as a constant engine control setting and constant Mach number schedule until a particular operating speed is reached, after which a constant E.A.S. is maintained. Needless to say that local air traffic con-

trol regulations may cause considerable alterations to recommended schedules.

14.2 The unsteady quasi-rectilinear climb

In Figure 14.1 and Table 14.1, the determination of minimum time to climb was carried out using quasi-steady-state climb data. In fact, the airspeed at which the maximum rate of climb occurs, increases with height, as can be seen in Figure 10.4. This implies that we must use a portion of the available excess power to accelerate the airplane along its flight path.

In order to examine the effect of the dynamic behavior of the airplane on the rate of climb, we consider the equation of motion in the direction of flight (cf. Equation (8.7)),

$$\frac{W}{g} \frac{dV}{dt} = T - D - W \sin \gamma, \quad (14.10)$$

where the thrust vector lies along the velocity vector.

Assuming quasi-rectilinear flight, we have normal to the flight path the following approximate equilibrium condition, determining the angle of attack,

$$L = W \cos \gamma. \quad (14.11)$$

With the assumption of a small flight-path angle, so that $\cos \gamma$ can be set equal to unity, Equation (14.11) reduces to

$$L = W. \quad (14.12)$$

Equation (14.10) can be rewritten by multiplying with V as

$$\frac{W}{g} V \frac{dV}{dh} \frac{dh}{dt} = TV - DV - WV \sin \gamma. \quad (14.13)$$

Using $dh/dt = V \sin \gamma = RC$, $TV = P_a$ and $DV = P_r$, and rearranging Equation (14.13) yields

$$RC \left[1 + \frac{V}{g} \frac{dV}{dh} \right] = \frac{P_a - P_r}{W}, \quad (14.14)$$

where the numerator of the right-hand term is the excess power, that can be used for climb and acceleration. The excess power per unit airplane weight is called the *specific excess power*.

When performing a quasi-steady climb, the excess power is used for climbing only. Neglecting the possible effects of accelerations on the lift-drag polar, allows that power required in Equation (14.14) can be taken equal to its value in quasi-steady flight at the same momentary conditions. Hence,

$$\frac{P_a - P_r}{W} = RC_s. \quad (14.15)$$

where the subscript "s" is used to denote a quasi-steady flight condition. When we put Equation (14.15) into Equation (14.14), we obtain

$$RC = \frac{RC_s}{1 + \frac{V}{g} \frac{dV}{dH}} = \frac{RC_s}{1 + \frac{V}{g_0} \frac{dV}{dH}}, \quad (14.16)$$

where the acceleration of gravity g_0 has the standard sea-level value (9.80665 m/s²). The denominator of the far right-hand term represents the effect of the acceleration of the airplane along the flight path on the actual rate of climb RC , and is called the *kinetic energy correction factor*.

Division of Equation (14.16) by V yields a similar expression for the climb angle

$$\sin \gamma = \frac{\sin \gamma_s}{1 + \frac{V}{g_0} \frac{dV}{dH}}, \quad (14.17)$$

where γ and γ_s are the angles of climb in actual flight and in quasi-steady climb, respectively.

The results derived above can be applied to particular climb programs, like the climb at constant equivalent airspeed, which we go through as a first example of an unsteady airplane motion. In this case the relationship between airspeed V (T.A.S.) and equivalent airspeed (E.A.S.) is

$$V = V_e(\rho_0/\rho)^{1/2}. \quad (14.18)$$

In the climb with constant equivalent airspeed the true airspeed continually increases with height so that the airplane is gaining kinetic energy ($dV/dH > 0$). Consequently, the actual rate of climb values are smaller than their quasi-steady-state counterparts ($RC < RC_s$).

Using Equation (14.18) and $V_e = \text{constant}$, the kinetic energy correction factor can be written as

$$1 + \frac{V}{g_0} \frac{dV}{dH} = 1 + \frac{1}{2g_0} \frac{dV^2}{dH} = 1 + \frac{V_e^2}{2g_0} \frac{d(\rho_0/\rho)}{dH}. \quad \text{Then} \quad (14.19)$$

$$\frac{RC}{RC_s} = \frac{\sin \gamma}{\sin \gamma_s} = \frac{1}{1 + \frac{V_e^2}{2g_0} \frac{d(\rho_0/\rho)}{dH}}. \quad (14.20)$$

For the International Standard Atmosphere, the density ratio ρ_0/ρ and altitude H are related by the previous Equations (2.13) and (2.16).

Using the equation of state $p = \rho RT$, the relationship $\frac{1}{2}\rho V^2 = \frac{1}{2}\gamma p M^2$ and the hydrostatic equation $dp = -\rho g_0 dH$, we can easily develop the following detailed expression for the kinetic energy correction factor in terms of the instantaneous flight Mach number,

$$1 + \frac{V}{g_0} \frac{dV}{dH} = 1 + \frac{\gamma M^2}{2} \left[1 + \frac{R}{g_0} \frac{dT}{dH} \right]. \quad (14.21)$$

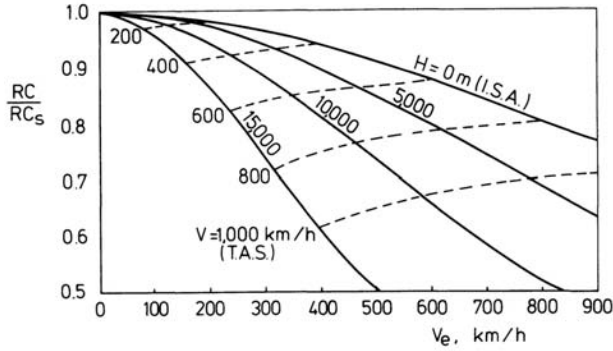


Figure 14.2 Kinetic energy correction

When we put Equation (14.21) into Equation (14.20), we find in the troposphere (I.S.A.) with $dT/dH = -0.0065$ K/m (see Figure 2.3),

$$\frac{RC}{RC_s} = \frac{\sin \gamma}{\sin \gamma_s} = \frac{1}{1 + 0.567M^2}. \quad (14.22)$$

In the lower stratosphere (I.S.A.), where $dT/dH = 0$, we obtain

$$\frac{RC}{RC_s} = \frac{\sin \gamma}{\sin \gamma_s} = \frac{1}{1 + 0.7M^2}. \quad (14.23)$$

Note that in the climb with constant equivalent airspeed, the Mach number in Equations (14.22) and (14.23) increases with altitude according to $\frac{1}{2}\rho_0 V_e^2 = \frac{1}{2}\gamma p M^2$, or

$$M = V_e \sqrt{\frac{\rho_0}{\gamma p}}. \quad (14.24)$$

In Figure 14.2 is plotted the ratio RC/RC_s against equivalent airspeed for a number of altitudes. The points on the curves that correspond to the same value of V are connected by dashed lines. Clearly, the kinetic energy correction factor increases with increasing airspeed and altitude.

Climb programs commonly consist of a constant E.A.S. schedule until the cruise Mach number is reached, followed by a climb at this Mach number toward the cruise altitude. Therefore, as a second example of a practical flight technique we consider the climb at constant flight Mach number.

Using $V^2 = M^2 c^2 = M^2 \gamma RT$, we find that

$$1 + \frac{V}{g_0} \frac{dV}{dH} = 1 + \frac{1}{2} \gamma M^2 \frac{R}{g_0} \frac{dT}{dH}. \quad (14.25)$$

For a climb in the troposphere (I.S.A.), we get

$$\frac{RC}{RC_s} = \frac{\sin \gamma}{\sin \gamma_s} = \frac{1}{1 - 0.133M^2}. \quad (14.26)$$

Climbing in this region at constant Mach number means a decreasing airspeed with altitude. Equation (14.26) confirms that which we would expect: $RC > RC_s$ and $\gamma > \gamma_s$.

In the lower part of the stratosphere (I.S.A.), the airspeed remains unchanged and hence $RC = RC_s$.

14.3 Optimum climb

In Section 14.1, we demonstrated the usual method for obtaining the minimum time to climb to a given altitude. The relationship between maximum rate of climb in quasi-steady flight and altitude for a given engine control setting was used to establish the required length of time.

In Section 14.2, we made clear that the actual rate of climb values may differ from the corresponding quasi-steady-state values because some of the excess power must be used to accelerate the airplane along its flight path. Therefore, the conventional approach may be inadequate for high-subsonic and supersonic airplanes since the problem not only concerns climbing to a given height but also attaining effectively any desired airspeed at that height.

The mathematical method which is capable of handling the problem of optimizing the dynamic performance of airplanes is the optimal control theory or the calculus of variations. A discussion of this subject, however, is definitely beyond the scope of this book. The interested reader is referred to References 46 and 47, which contain detailed teaching texts in the field of airplane performance optimization.

As mentioned already in Section 14.1, there are three dynamic performance problems of special interest. They are fastest climb or least time to climb, steepest climb or minimum range during climb, and most economical climb where the smallest amount of fuel is consumed. A fairly simple approach to these climb trajectories is to formulate the dynamics of the airplane in terms of its total energy. This is the so-called *energy-state approximation* that will be explained briefly in this section. The present dynamic model neglects accelerations normal to the flight path and assumes a flight in a single vertical plane and a no-wind condition (References 48 and 49).

Then the total energy of the airplane, E , is given by the sum of the potential energy and the kinetic energy. Thus

$$E = WH + \frac{1}{2} \frac{W}{g_0} V^2. \quad (14.27)$$

The total energy per unit airplane weight is termed *energy height* and denoted here by the symbol H_e ,

$$H_e = H + \frac{V^2}{2g_0}. \quad (14.28)$$

The energy height is a measure of the geopotential and geometric altitude that can be attained if the airplane loses all its kinetic energy and trades it for increased potential energy.

By differentiating Equation (14.28) with respect to time, and using $dH/dt = V \sin \gamma$, we obtain

$$\frac{dH_e}{dt} = \frac{dH}{dt} + \frac{V}{g_0} \frac{dV}{dt} = V \left[\sin \gamma + \frac{1}{g_0} \frac{dV}{dt} \right]. \quad (14.29)$$

Combining Equations (14.10), (14.15) and (14.29) furnishes

$$\frac{dH_e}{dt} = \frac{(T - D)V}{W} = RC_s. \quad (14.30)$$

This remarkable result says that the time derivative of the energy height is equal to the rate of climb of the airplane in quasi-steady flight. Therefore, dH_e/dt is also called specific excess power.

From Equations (14.3) and (14.16), the time to climb can be expressed as

$$t = \int_{H_1}^{H_2} \frac{\left[1 + \frac{V}{g_0} \frac{dV}{dH} \right] dH}{RC_s}. \quad (14.31)$$

By differentiating Equation (14.28) with respect to H and substituting the result into Equation (14.31), we can write the time to climb from one energy height to another as follows:

$$t = \int_{H_{e_1}}^{H_{e_2}} \frac{dH_e}{RC_s}. \quad (14.32)$$

By the same token, Equations (14.4) and (14.5) can also be transformed into integrals with independent variable H_e ,

$$s = \int_{H_{e_1}}^{H_{e_2}} \frac{dH_e}{\tan \gamma_s} \quad (14.33)$$

$$W_f = \int_{H_{e_1}}^{H_{e_2}} \frac{F}{RC_s} dH_e. \quad (14.34)$$

Thus the trajectories for minimum time, steepest climb and minimum expenditure of fuel between any two altitude/airspeed combinations are optimized by maximizing the quasi-steady-state performance parameters RC_s , RC_s/F , and γ_s at each energy height. In this connection, it is important to remember that the time-history of the airplane motion is fully determined if two control variables are specified as a function of time, and appropriate boundary conditions are known, e.g., the initial

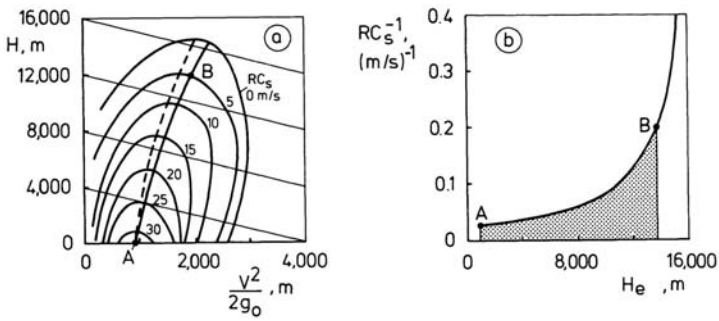


Figure 14.3 Determination of minimum flight time from an Initial to a final energy height

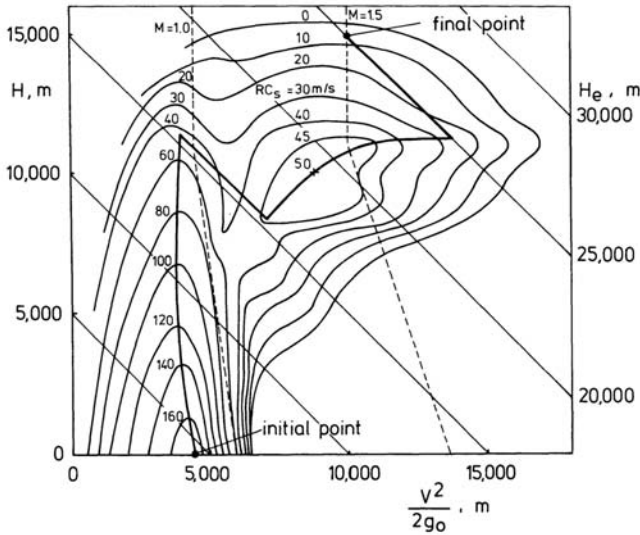


Figure 14.4 Curves of constant rate of climb for a supersonic airplane

flight condition (see Chapter 8).

The importance of the energy height concept is exemplified here by applying this approach to the minimum time to climb problem. Therefore, typical contours of constant RC_s are plotted in Figure 14.3a for a high-subsonic airplane and in Figure 14.4 for a supersonic airplane. These curves are constructed by determining the RC_s values for a series of altitudes, assuming a constant engine control setting and airplane weight. The RC_s equal to zero contours represent the level flight speed envelopes as portrayed in the previous Figures 10.6 and 10.10.

The plots in Figures 14.3a and 14.4 are enhanced by superimposing lines of constant energy height, which are calculated from Equation (14.28). Since a base of H versus $V^2/(2g_0)$ is used, the constant H_e lines are straight.

From Equation (14.32) it follows that the condition for minimum time to climb is

given by

$$\left[\frac{\partial(RC_s)}{\partial V} \right]_{H_e} = 0. \quad (14.35)$$

In other words, the minimum flight time in Figures 14.3a and 14.4 is obtained when flying through the points on the RC_s curves that are tangent to the constant energy height lines. The loci of these points of tangency describe the optimum trajectories. Note that in the supersonic case, the optimum path consists of a number of stages. Successively we have in Figure 14.4: an accelerated climb from the initial condition to an appropriate energy height, a zoom dive through the transonic speed range along a constant energy height line, a continued accelerated climb at supersonic speeds, and a zoom climb to the final point at almost constant energy height.

To calculate t_{\min} , first plot RC_s^{-1} against H_e for various points along the trajectory, as constructed in Figure 14.3b for the high-subsonic airplane. The shaded area under the curve represents the minimum flight time from $V = V_A$ at sea level ($H = 0$) to $V = V_B$ at $H_e = 13800$ m.

As indicated by the dashed line in Figure 14.3a, the quasi-steady fastest climb schedule occurs at altitude/airspeed combinations at which the RC_s curves are tangent to the horizontal lines of constant geopotential altitude. Apparently, this trajectory does not differ seriously from the unsteady climb schedule so that the associated times to climb will only be slightly different. In contrast, the supersonic airplane in Figure 14.4 has a significantly different time schedule and in this case the energy concept leads to substantial savings in flight time.

14.4 Effects of vertical wind gradients

In this section the situation is considered in which the airplane is faced with the occurrence of a varying wind velocity during climb and descent. The variations of wind speed with height and time are called *wind shear*. It is the object of the following analysis to show the importance of wind on climb angle and rate of climb and to derive a suitable means of correcting for its effect.

For simplicity, we shall presume the presence of an increasing or decreasing headwind or tailwind which varies with height only: $V_W = V_W(H)$.

From Figure 14.5a, we find at an airspeed V and headwind V_W the components of the ground speed along the axes of the Earth axis system as (cf. Equation (1.26))

$$V_{X_g} = V \cos \gamma - V_W \quad (14.36)$$

$$V_{Y_g} = 0 \quad (14.37)$$

$$V_{Z_g} = V \sin \gamma. \quad (14.38)$$

The associated acceleration of the airplane is described by the two equations:

$$\frac{dV_{X_g}}{dt} = \frac{dV}{dt} \cos \gamma - V \sin \gamma \frac{d\gamma}{dt} - \frac{dV_W}{dt} \quad (14.39)$$

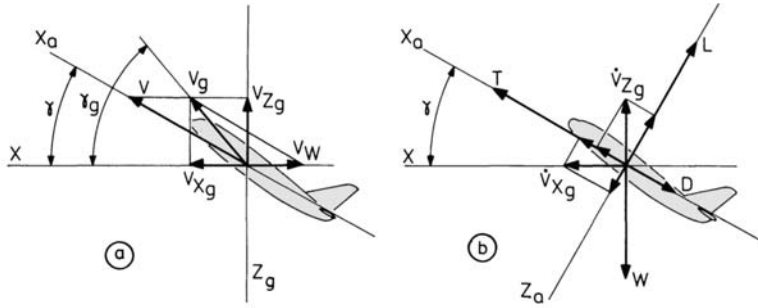


Figure 14.5 Effect of wind on velocities and accelerations

$$\frac{dV_{Z_g}}{dt} = \frac{dV}{dt} \sin \gamma + V \cos \gamma \frac{d\gamma}{dt}. \tag{14.40}$$

In Equation (14.39), the term dV_W/dt is the time rate of change of the wind velocity as experienced by the airplane.

The components of the acceleration along the air-path axes are given by (Figure 14.5b)

$$\frac{dV_{X_a}}{dt} = \frac{dV_{X_g}}{dt} \cos \gamma + \frac{dV_{Z_g}}{dt} \sin \gamma \tag{14.41}$$

$$\frac{dV_{Z_a}}{dt} = \frac{dV_{X_g}}{dt} \sin \gamma + \frac{dV_{Z_g}}{dt} \cos \gamma. \tag{14.42}$$

After substitution of Equations (14.39) and (14.40) into Equations (14.41) and (14.42), we get

$$\frac{dV_{X_a}}{dt} = \frac{dV}{dt} - \frac{dV_W}{dt} \cos \gamma \tag{14.43}$$

$$\frac{dV_{Z_a}}{dt} = V \frac{d\gamma}{dt} + \frac{dV_W}{dt} \sin \gamma. \tag{14.44}$$

Thus, in the presence of a wind gradient, the equations of motion for the airplane in symmetric flight read:

$$\frac{W}{g} \left[\frac{dV}{dt} - \frac{dV_W}{dt} \cos \gamma \right] = T - D - W \sin \gamma \tag{14.45}$$

$$\frac{W}{g} \left[V \frac{d\gamma}{dt} + \frac{dV_W}{dt} \sin \gamma \right] = L - W \cos \gamma. \tag{14.46}$$

Note that with $dV_W/dt = 0$, the equations of motion become identical to the Equations (8.7) and (8.8), which were derived in Chapter 8 for the no-wind condition. Hence, we can conclude that the motion of the airplane relative to the air is not affected by a horizontal wind with a constant velocity. However, when the magnitude of the wind velocity varies with altitude, also the motion of the airplane relative to the air changes. This may be seen by writing,

$$\frac{dV}{dt} = \frac{dV}{dH} \frac{dH}{dt} = \frac{dV}{dH} V \sin \gamma \quad \text{and} \tag{14.47}$$

$$\frac{dV_W}{dt} = \frac{dV_W}{dH} \frac{dH}{dt} = \frac{dV_W}{dH} V \sin \gamma, \quad (14.48)$$

where dV_W/dH is the vertical wind gradient.

Assuming a quasi-rectilinear climb and using $g = g_0$, we obtain by putting Equations (14.47) and (14.48) into Equation (14.45),

$$\frac{W}{g_0} \left[\frac{dV}{dH} V \sin \gamma - \frac{dV_W}{dH} V \sin \gamma \cos \gamma \right] = T - D - W \sin \gamma. \quad (14.49)$$

Assuming also that the flight-path angle is sufficiently small, so that its cosine can be replaced by unity, we can change Equation (14.49) into the forms:

$$\sin \gamma \left[1 + \frac{V}{g_0} \frac{dV}{dH} - \frac{V}{g_0} \frac{dV_W}{dH} \right] = \frac{T - D}{W} = \sin \gamma_s \quad \text{and} \quad (14.50)$$

$$RC \left[1 + \frac{V}{g_0} \frac{dV}{dH} - \frac{V}{g_0} \frac{dV_W}{dH} \right] = \frac{(T - D)V}{W} = RC_s. \quad (14.51)$$

Examining Equations (14.50) and (14.51), we note that the effect of a wind gradient ($dV_W/dH \neq 0$) can be treated in a similar fashion as the effect of accelerated flight. Furthermore, we note that in the case of a headwind that increases with height ($dV_W/dH > 0$), a wind gradient has the tendency to improve the climb performance, at least as V is held constant. Due to the resulting decrease in acceleration with respect to the ground there is a conversion from kinetic to potential energy, through which both the climb angle and the rate of climb will increase. Conversely, a negative wind gradient ($dV_W/dH < 0$) will reduce the climb performance.

As discussed in Chapter 2, due to the surface friction effect of the ground on the wind, for an open area there will normally be a continuous increase in wind velocity from ground level up to some height (see Figure 2.19). Clearly, large wind gradients may occur close to the ground so that wind shear effects are of special significance when taking off or landing in wind.

Before closing this section, we remark that variations in the horizontal wind direction will change the magnitude of the headwind or tailwind component and therefore will have a similar effect as a change of wind velocity with height.

14.5 Limitations on vertical velocity

The adjustment of the pressures within the air spaces in our head to varying atmospheric pressure during climb and descent can be experienced as unpleasant and even as painful.

Of special significance is the matching of the air pressure in the middle ear cavity (Figure 14.6). When the exterior pressure changes, the eardrum bulges outward if the atmospheric pressure is decreasing, and inward if it is increasing. Equalization of pressures is obtained by means of the *Eustachian tube*, which connects the middle ear with the oral cavity.

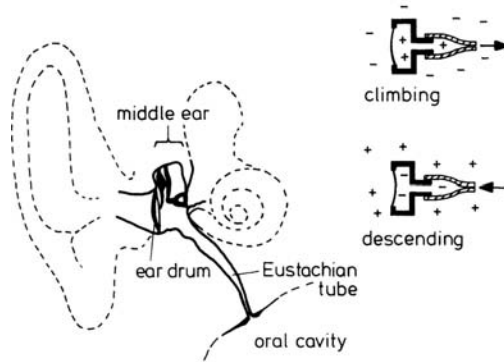


Figure 14.6 The Eustachian tube

When climbing, the higher pressure in the middle ear causes air to escape through the Eustachian tube. This occurs each time a pressure difference of about 2000 Pa is built up between the inside and outside air. The process of balancing the pressure in the middle ear is fairly automatic and the occupant is aware only of a click as the air passes through the Eustachian tube.

When descending, however, the equalization process is most often more difficult. In going from lower to higher atmospheric pressure, the Eustachian tube does not open of itself and yawning, swallowing, or blowing with mouth and nose closed is required in order that compensating air can enter the middle ear. But if there is a common cold or a sore throat, the Eustachian tube may be blocked. In such circumstances, overinflation of the eardrums occurs and severe pain will be experienced during descent.

Generally, the influence of ambient pressure changes on the ears fail to appear if the time rate of change of pressure is kept within the following limits:

$$-30 < dp/dt < 18 \text{ Pa/s.} \quad (14.52)$$

In relating the change in pressure to the rate of climb of the airplane, we write

$$RC = \frac{dH}{dt} = \frac{dH}{dp} \frac{dp}{dt}. \quad (14.53)$$

By making use of the hydrostatic equation: $dp = -\rho g_0 dH$, we can express the rate of climb as

$$RC = -\frac{1}{\rho g_0} \frac{dp}{dt}. \quad (14.54)$$

Obviously, the vertical velocities determined by Equations (14.52) and (14.54) decrease as altitude decreases. E.g., the maximum allowable rate of climb at sea level should not exceed 2.5 m/s (500 ft/min) and the rate of descent 1.5 m/s (300 ft/min).

The use of pressurized airplanes has greatly solved the problem mentioned above. In this case, the limit on the vertical velocities of the airplane is determined by the rate of change of cabin pressure. At the normal cruising altitude, the cabin pressure, p_c , is equivalent to a geopotential pressure altitude of approximately 1800 m ($\approx 6,000$ ft), i.e., $p_c/p_0 = 0.8$. Under this condition, the minimum time needed to increase the cabin pressure to the sea-level standard value becomes

$$t = \frac{p_0(1 - p_c/p_0)}{dp/dt} = \frac{101325(1 - 0.8)}{18} = 1125 \text{ s (18.8 minutes)}.$$

Note that this length of time is independent of the cruising altitude. For instance, during a descent from 9,000 m, the mean allowable rate of descent of the airplane is $9,000/1125 = 8$ m/s (1575 ft/min).

Chapter 15

CRUISE PERFORMANCE

15.1 Range and endurance

As depicted in Figure 15.1, here, the term range is used for the horizontal straight-line distance an airplane travels in cruising flight, whereas the distance traversed in climb, cruise, and descent is called *total range*, *stage length* or *block distance*. Maximum total range is the distance an airplane can fly between takeoff and landing as limited by its fuel capacity. The fuel consumption per unit time is

$$F = \frac{dW_f}{dt}, \quad (15.1)$$

where W_f is the total fuel load.

Since $dW_f = -dW$, the fuel weight flow rate is related to the weight of the airplane by (see also Chapter 8)

$$F = -\frac{dW}{dt}. \quad (15.2)$$

The range is obtained from the following definite integral,

$$R = \int_{t_1}^{t_2} V dt = \int_{W_1}^{W_2} -\frac{V}{F} dW = \int_{W_2}^{W_1} \frac{V}{F} dW, \quad (15.3)$$

where V/F is the specific range (range per unit weight of fuel). The subscripts "1" and "2" refer to the initial and final conditions at start and end of cruise, respectively.

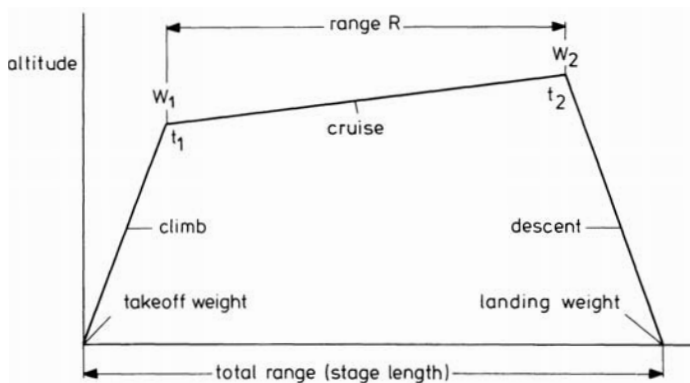


Figure 15.1 Mission nomenclature

The term *endurance* is used for the length of time spent in cruising flight. The endurance can be written as

$$E = \int_{t_1}^{t_2} dt = \int_{W_1}^{W_2} -\frac{dW}{F} = \int_{W_2}^{W_1} \frac{dW}{F}. \quad (15.4)$$

At this point it is important to remember that in symmetric flight, the time history of the flight condition depends on the specification of two control laws, that is to say, the description of the variation of two control variables with time (see Chapter 8).

Generally, both control variables are held constant throughout the cruise so that the flight condition only changes due to the influence of fuel consumption on airplane weight.

For airplanes propelled by airbreathing engines, however, there is only a slow variation of airplane weight. This observation allows us to consider the flight as a continuous succession of uniform motions under slowly varying conditions. In other words, the instantaneous values of V/F and F can be determined as though the airplane is in quasi-steady-state flight.

The procedure for determining F and V/F as a function of airplane weight may be illustrated by reference to Figures 15.2a and 15.2b for a propeller-driven and a jet-driven airplane, respectively. In both cases it is assumed that the airplane is performing a level flight at constant engine control setting.

In the case of propeller propulsion, the problem requires the computation of the level flight speed at a number of airplane weights from the equilibrium condition $P_a = P_r$. To each flight velocity, there corresponds a particular value of propulsive efficiency η_j and specific fuel consumption c_p . Then, successive engine powers can be found by using Equation (6.1),

$$P_{br} = \frac{P_a}{\eta_j}. \quad (15.5)$$

The corresponding fuel weight flow rates can be computed from Equation (6.15),

$$F = c_p P_{br}. \quad (15.6)$$

Analogously, for the jet picture we may use the respective points of intersection of the thrust and drag curves to give the successive values of airspeed V , thrust T , and specific fuel consumption c_T . According to the definition of c_T , Equation (6.54), the fuel weight flow rates can be obtained from

$$F = c_T T. \quad (15.7)$$

Now, Equations (15.3) and (15.4) can be evaluated graphically to give the values of range and endurance for the chosen cruise technique of constant altitude and constant engine control setting.

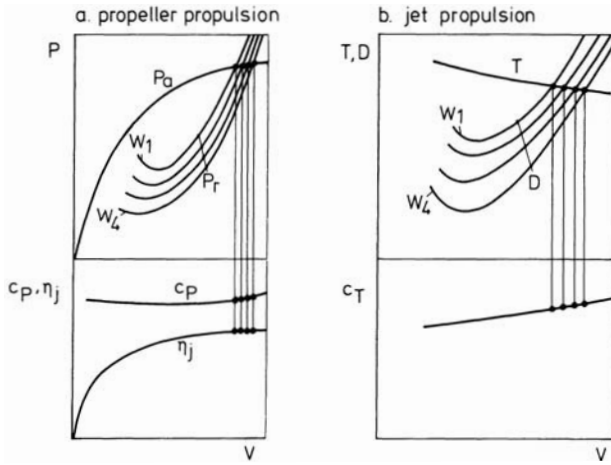


Figure 15.2 Determination of V/F and F (flight at constant altitude and engine control setting)

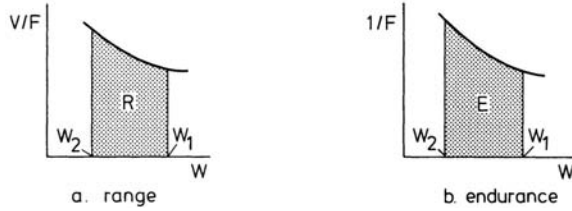


Figure 15.3 Calculation of range and endurance

Range follows from plotting V/F against W , as shown in Figure 15.3a. The shaded area under the curve from the final cruise weight W_2 to the initial cruise weight W_1 represents the range. Similarly, the endurance follows from the plot of $1/F$ versus W , as shown in Figure 15.3b.

If the preceding calculation procedure is done systematically a so-called *cruise chart* can be deduced as exemplified in Figure 15.4. The diagram gives for a specified altitude the typical variations of specific range with airspeed and airplane weight, showing the various cruise techniques.

In Figure 15.4, the constant engine rating program is represented by the line AB, the constant speed program by the line AC, and the maximum range program by the line AD, all for the same initial cruising speed. Of these, the most realistic cruise program is to maintain a constant airspeed at a fixed altitude (line AC). In this connection, it may be remarked that, practically, the range achieved by this cruise technique is virtually the same as that gained by the maximum range program (Reference 50).

The instantaneous airspeeds which give the greatest distance on a given quantity of fuel (line AD), may be called maximum range speeds or economic speeds, V_{ec} . Obviously, for a particular cruise program, the relationship between specific range

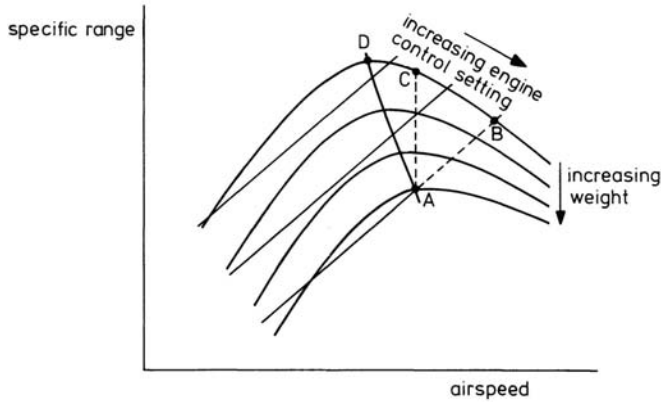


Figure 15.4 Typical specific range performance at a specified altitude

and airplane weight follows directly from the chart and so the resulting range for a given amount of fuel.

15.2 Approximate analytic expressions for range and endurance (propeller propulsion)

To obtain analytic expressions for range and endurance, we note that specific range and fuel weight flow rate can be related to the characteristics of the airplane and propulsion system by using Equations (15.5) and (15.6). Assuming quasi-level and quasi-steady flight, we can write

$$F = c_P P_{br} = c_P \frac{P_a}{\eta_j} = c_P \frac{P_r}{\eta_j} = c_P \frac{DV}{\eta_j}. \quad (15.8)$$

Making use of the relationships of Chapter 9 that $V = \sqrt{\frac{W}{S} \frac{2}{\rho} \frac{1}{C_L}}$ and $D = \frac{C_D}{C_L} W$, we obtain

$$\frac{V}{F} = \frac{\eta_j C_L}{c_P C_D} \frac{1}{W} \quad (15.9)$$

$$F = \frac{c_P W}{\eta_j} \sqrt{\frac{W}{S} \frac{2}{\rho} \frac{C_D^2}{C_L^3}}. \quad (15.10)$$

Substituting Equation (15.9) into Equation (15.3), and Equation (15.10) into Equation (15.4) gives

$$R = \int_{W_2}^{W_1} \frac{\eta_j C_L}{c_P C_D} \frac{dW}{W} \quad (15.11)$$

$$E = \int_{W_2}^{W_1} \frac{\eta_j}{c_P W} \frac{dW}{\sqrt{\frac{W}{S} \frac{2}{\rho} (C_D^2/C_L^3)}}. \quad (15.12)$$

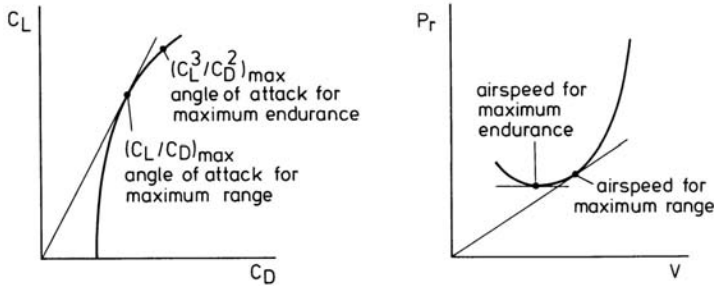


Figure 15.5 Best range and endurance conditions in level flight for propeller-driven airplanes

An examination of Equations (15.11) and (15.12) reveals that from an analytical point of view it is interesting to consider the cruise technique where the angle of attack is held constant throughout the flight. Furthermore, η_j and c_p usually exhibit only small variations over the band of cruising speeds so that it is possible to assume that they have constant average values.

Then, Equation (15.11) can be integrated to give an approximate analytic expression for the range,

$$R = \frac{\eta_j C_L}{c_P C_D} \int_{W_2}^{W_1} \frac{dW}{W} = \frac{\eta_j C_L}{c_P C_D} \left| \ln W \right|_{W_2}^{W_1} = \frac{\eta_j C_L}{c_P C_D} \ln \frac{W_1}{W_2}. \quad (15.13)$$

This expression is the classic Breguet formula for range, derived by the Frenchman Louis-Charles Breguet (1880-1955).

Inspection of Equation (15.13) learns that to maximize range, flight must be carried out at the angle of attack at which C_L/C_D is the maximum. This is the flight condition for minimum airplane drag (Figure 15.5).

Also note that Equation (15.13) can be used for both constant altitude and climbing flight. If the altitude is kept constant, then we see from the relationship $W = C_L \frac{1}{2} \rho V^2 S$ that the airspeed must be steadily reduced as fuel is consumed. On the other hand, if the airspeed is held constant, the cruising height must be gradually increased during the course of the flight. Therefore, the latter cruise technique is commonly referred to as cruise-climb flight. It should be remarked that this type of flight may not be tolerable in many situations because of the requirements of air traffic control (A.T.C.).

For propeller airplanes powered by piston engines, the term η_j/c_P in Equation (15.13) remains nearly constant when airspeed or altitude are changed. Consequently, there will be no difference in range when the two cruise programs are compared; only an increase in cruising speed for the cruise-climb flight.

For turboprop airplanes, however, high cruising altitudes are essential, since at a given engine rating the specific fuel consumption decreases with height. Also it is important that at the economic airspeed the engines operate at their maximum

permitted cruise rating in order to achieve the lowest possible specific fuel consumption. Obviously, the only way to attain the optimum cruising condition is to fly at a high altitude.

To obtain a closed form solution for the endurance we shall consider the realistic cruise technique of a flight at constant altitude. Then, carrying out the integration of Equation (15.12), with η_j and c_P assumed constant throughout the flight, produces the following formula

$$\begin{aligned} E &= \frac{\eta_j}{c_P} \sqrt{\frac{C_L^3/C_D^2}{\frac{1}{S} \frac{2}{\rho}}} \int_{W_2}^{W_1} \frac{dW}{W\sqrt{W}} = \frac{\eta_j}{c_P} \sqrt{\frac{C_L^3/C_D^2}{\frac{1}{S} \frac{2}{\rho}}} \left[\frac{-2}{\sqrt{W}} \right]_{W_2}^{W_1} \\ &= \frac{\eta_j}{c_P} \sqrt{\frac{C_L^3/C_D^2}{\frac{1}{S} \frac{2}{\rho}}} \left[\frac{2}{\sqrt{W_2}} - \frac{2}{\sqrt{W_1}} \right]. \end{aligned} \quad (15.14)$$

Introducing the airspeed at the starting point of the cruising flight, that is

$$V_1 = \sqrt{\frac{W_1}{S} \frac{2}{\rho} \frac{1}{C_L}}, \quad (15.15)$$

we modify Equation (15.14) to obtain

$$E = 2 \frac{\eta_j C_L}{c_P C_D} \frac{1}{V_1} \left[\sqrt{\frac{W_1}{W_2}} - 1 \right]. \quad (15.16)$$

Combination of Equations (15.13) and (15.16) yields the following expression for the average velocity during the flight

$$V_{av} = \frac{R}{E} = \frac{V_1 \ln(W_1/W_2)}{2(\sqrt{W_1/W_2} - 1)}. \quad (15.17)$$

Equation (15.14) indicates that for best endurance, the airplane must fly at the angle of attack at which C_L^3/C_D^2 is the maximum. This is the flight condition for minimum power required and minimum fuel weight flow rate.

Inspection of Figure 15.5 shows that level flight speeds less than the speed for best endurance are in the region of reversed command. As was demonstrated in Section 11.3, flying in this region introduces the problem of speed instability. Because of this phenomenon the actual cruising speed lies somewhat above the minimum power required speed, e.g., $V_{cr} \geq 1.1V_{D_{min}}$ (cf. Equation (11.13)).

15.3 Approximate analytic expressions for range and endurance (jet propulsion)

Assuming quasi-steady level flight and using the relationship $D = \frac{C_D}{C_L} W$, the thrust can be written as

$$T = D = \frac{C_D}{C_L} W. \quad (15.18)$$

With Equation (15.7) and the relationship $V = \sqrt{\frac{W}{S} \frac{2}{\rho} \frac{1}{C_L}}$, the specific range is found to equal

$$\frac{V}{F} = \frac{1}{c_T W} \sqrt{\frac{W}{S} \frac{2}{\rho} \frac{C_L}{C_D}}. \quad (15.19)$$

Substituting Equation (15.19) into Equation (15.3) yields

$$R = \int_{W_2}^{W_1} \frac{1}{c_T W} \sqrt{\frac{W}{S} \frac{2}{\rho} \frac{C_L}{C_D}} dW. \quad (15.20)$$

The corresponding integral, expressing the endurance is obtained by insertion of Equations (15.7) and (15.18) into Equation (15.4),

$$E = \int_{W_2}^{W_1} \frac{1}{c_T} \frac{C_L}{C_D} \frac{dW}{W}. \quad (15.21)$$

In deriving analytic expressions for range and endurance, first, we shall consider cruising at a fixed height and at a constant angle of attack. Moreover, we shall continue to assume that the specific fuel consumption remains constant for the duration of the flight. The analysis will be further simplified by neglecting the variation of the effects of compressibility on the aerodynamic characteristics of the airplane as the flight speed reduces during the course of the flight.

Integrating Equation (15.20), we find

$$\begin{aligned} R &= \frac{1}{c_T} \sqrt{\frac{2}{S\rho} \frac{C_L}{C_D}} \int_{W_2}^{W_1} \frac{dW}{\sqrt{W}} = \frac{2}{c_T} \sqrt{\frac{2}{S\rho} \frac{C_L}{C_D}} \left| \sqrt{W} \right|_{W_2}^{W_1} \\ &= \frac{2}{c_T} \sqrt{\frac{2}{S\rho} \frac{C_L}{C_D}} [\sqrt{W_1} - \sqrt{W_2}]. \end{aligned} \quad (15.22)$$

It should be remarked that $\sqrt{\rho}$ is present in the denominator of Equation (15.22), and that this is the essential reason why high cruising altitudes are desired for jet powered airplanes. By using Equation (15.15), we can rewrite Equation (15.22) as follows,

$$R = \frac{2}{c_T} \sqrt{\frac{W_1}{S} \frac{2}{\rho} \frac{C_L}{C_D}} \left[1 - \sqrt{\frac{W_2}{W_1}} \right] = 2 \frac{V_1}{c_T} \frac{C_L}{C_D} \left[1 - \sqrt{\frac{W_2}{W_1}} \right], \quad (15.23)$$

where V_1 is the initial airspeed.

Performing the integration of Equation (15.21) gives

$$E = \frac{1}{c_T} \frac{C_L}{C_D} \int_{W_2}^{W_1} \frac{dW}{W} = \frac{1}{c_T} \frac{C_L}{C_D} \left| \ln W \right|_{W_2}^{W_1} = \frac{1}{c_T} \frac{C_L}{C_D} \ln \frac{W_1}{W_2}. \quad (15.24)$$

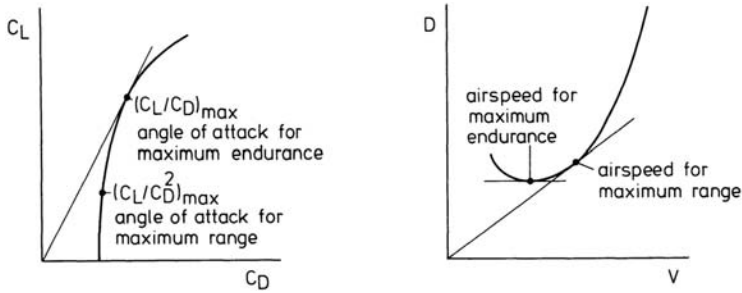


Figure 15.6 Best range and endurance conditions in level flight for jet-powered airplanes

From Equations (15.23) and (15.24) the average airspeed during the flight is found to be

$$V_{av} = \frac{R}{E} = \frac{2V_1(1 - \sqrt{W_2/W_1})}{\ln(W_1/W_2)} \quad (15.25)$$

An inspection of Equations (15.22) and (15.24) shows that:

- For best range, the airplane should be flown at the angle of attack for maximum C_L/C_D^2 . From the relationships $V = \sqrt{\frac{W}{\rho} \frac{2}{S} \frac{1}{C_L}}$ and $D = \frac{C_D}{C_L} W$, it may be seen that this requirement corresponds to the flight condition for minimum D/V (Figure 15.6).
- At a given angle of attack, range increases with altitude up to the typical cruising altitude. The favorable effect of a higher altitude is augmented by the tendency of the specific fuel consumption to decrease with increasing altitude up to the tropopause (I.S.A.).
- Maximum endurance will be obtained when C_L/C_D is the maximum. This is the flight condition for minimum airplane drag (Figure 15.6).

A second cruise technique of interest for turbojet and turbofan airplanes is the flight at constant airspeed and angle of attack. For this cruise technique, we pointed out in Section 15.2 that as fuel is burned, the airplane should ascend in altitude.

The flight-path angle occurring in this cruise-climb schedule, however, is normally sufficiently small so as to approve the use of the level-flight conditions that lift is equal to weight and thrust is equal to drag.

From Equations (15.3), (15.7) and (15.18), we then have

$$R = \int_{W_2}^{W_1} \frac{V}{c_T} \frac{C_L}{C_D} \frac{dW}{W}. \quad (15.26)$$

If again c_T and C_L/C_D are assumed to have constant values throughout the flight, Equation (15.26) can be readily integrated to give the expression

$$R = \frac{V}{c_T} \frac{C_L}{C_D} \ln \frac{W_1}{W_2}, \quad (15.27)$$

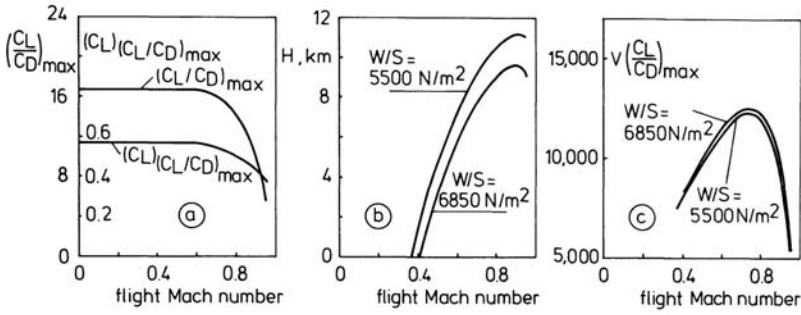


Figure 15.7 Condition for maximum $V(C_L/C_D)$

where the quantity $\frac{V}{c_T} \frac{C_L}{C_D}$ is called the *range factor*.

Sometimes it may be convenient to express the range in terms of the overall efficiency of the propulsion system. According to Equation (6.55), we have

$$\eta_{tot} = \frac{gV}{Hc_T}. \tag{15.28}$$

Insertion of Equation (15.28) into Equation (15.27) gives

$$R = \eta_{tot} \frac{H}{g} \frac{C_L}{C_D} \ln \frac{W_1}{W_2}. \tag{15.29}$$

As mentioned earlier in Chapter 6, the heating value H of all common aviation fuels (hydrocarbon fuels) is about 4.3×10^7 Joule/kg so that the ratio H/g in Equation (15.29) is about 4390 km.

Equations (15.27) and (15.29) are also labeled Breguet range equations, although Breguet's name was originally associated with range performance of airplanes driven by the combination of piston-engines and propellers. In this light, it is worthwhile to remark that Equation (15.29) also holds for propeller-driven airplanes. This statement can easily be verified by substitution of Equations (6.16) and (6.17) into Equation (15.13).

At constant airspeed and angle of attack, the endurance is directly found as

$$E = \frac{R}{V} = \frac{1}{c_T} \frac{C_L}{C_D} \ln \frac{W_1}{W_2}. \tag{15.30}$$

Obviously, the greatest endurance will be obtained when C_L/C_D is the maximum. Also note that Equation (15.30) is identical to the expression for the endurance in level flight (see Equation (15.24)).

Equation (15.27) indicates that for a given initial weight and fuel load, the airplane should fly at that altitude and airspeed at which the product $V(C_L/C_D)$ is a maximum, provided that variations in specific fuel consumption can be neglected.

The derivation of this flight condition will be demonstrated from a numerical example. For this, we return to our illustrative turbofan airplane with its lift-drag polars given in the previous Figure 9.7. From this data, the curves in Figure 15.7a are deduced, which give the maximum lift-to-drag ratio and the associated lift coefficient as a function of flight Mach number. The graph manifests the characteristic behavior that both quantities drop off sharply at Mach numbers greater than 0.6. In Figure 15.7b are plotted the required altitudes (I.S.A.) versus M as computed from the relationship $W = C_L \frac{1}{2} \gamma \rho M^2 S$ where C_L is the lift coefficient at which C_L/C_D is the maximum. The related airspeeds follow from $V = Mc$. The final result is shown in Figure 15.7c, in the form of a plot of the product $V(C_L/C_D)_{\max}$ against flight Mach number. Clearly, there is an optimum flight Mach number and an optimum altitude at a given airplane weight. Figure 15.7b also demonstrates that as the weight of the airplane decreases during cruise the airplane should climb in altitude to maintain the optimum flight condition.

Note from Equation (15.27) that with the assumptions of constant c_T and C_L/C_D , the range has no absolute maximum. Without compressibility drag, a constrained optimum is obtained when the magnitude of the airspeed is specified. In this case, the maximum range will also occur when C_L/C_D is the maximum. This condition requires that the instantaneous height should be that height at which the minimum drag speed becomes equal to the chosen airspeed.

When our cruise-climb flight is conducted in the lower stratosphere (I.S.A.), where the speed of sound is constant, a fixed airspeed also means a fixed flight Mach number. Consequently, the aerodynamic ratio in Equation (15.27) is exactly constant (see Chapter 4). If we look at the force equation

$$T = C_D \frac{1}{2} \rho V^2 S, \quad (15.31)$$

we see that the thrust is directly proportional to the air density. However, at a constant value of T/ρ , turbo-engine performance in the lower stratosphere (I.S.A.) is such that engine control setting is fixed. As a result, also specific fuel consumption remains unchanged (see Chapter 6). Therefore, the desired flight program is realized if the pilot simply maintains constant readings on the Mach meter and the engine-speed indicator. The appropriate expression for the range is then obtained by substituting Equation (15.31) into Equation (15.27). The resulting form becomes

$$R = \frac{1}{c_T} \sqrt{\frac{T}{S} \frac{2 C_L^2}{\rho C_D^3}} \ln \frac{W_1}{W_2}. \quad (15.32)$$

We observe that the condition for maximum range when flying in the lower stratosphere (I.S.A.) at a given engine control setting and airspeed exists when C_L^2/C_D^3 is the maximum.

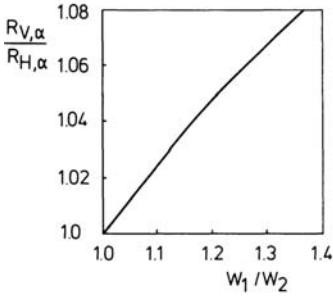


Figure 15.8 Relative range

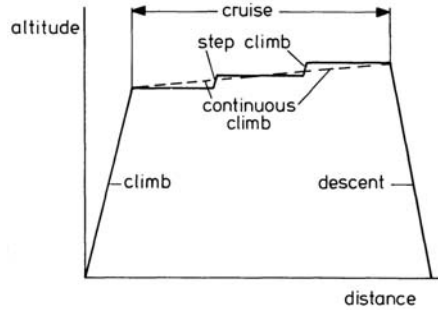


Figure 15.9 Stepped altitude flight

A third constrained optimum is derived for a specified altitude at the starting point of the cruise-climb flight. Then, insertion of Equation (15.15) into Equation (15.27) leads to the expression

$$R = \frac{1}{c_T} \sqrt{\frac{W_1}{S}} \frac{2 C_L}{\rho_1 C_D^2} \ln \frac{W_1}{W_2}, \tag{15.33}$$

where ρ_1 is the air density at the initial height H_1 .

Examination of the above equation reveals that to obtain maximum range, flight must be executed at maximum C_L/C_D^2 .

Taking the initial height of the cruise-climb flight to be the cruising height of the constant altitude flight and assuming the same angle of attack and specific fuel consumption, we can derive a simple relationship between the two ranges. Dividing Equation (15.27) by Equation (15.23) yields

$$\frac{R_{V,\alpha}}{R_{H,\alpha}} = \frac{\ln(W_1/W_2)}{2(1 - \sqrt{W_2/W_1})}. \tag{15.34}$$

The above ratio is presented in Figure 15.8. The graph indicates that the increase in range by performing a cruise-climb flight becomes greater as the weight ratio W_1/W_2 increases. In other words, flying cruise-climb appears to be more economical than level flight, especially when the airplane executes a long-distance flight. In practice, a cruise-climb flight may be approximated by a sequence of level flight segments (Figure 15.9). However, when the cruise is executed under the jurisdiction of flight traffic control regulations, each altitude change needs approval. Then cruising altitudes as well as cruising speeds and headings are assigned by air traffic control in order that sufficient spacing is ensured vertically, longitudinally, and laterally for safe flight.

15.4 Effect of wind on cruise performance

In this section we shall pay some attention to the effect of wind on cruising performance. For simplicity, we shall consider the presence of a constant headwind or tailwind only, directed along the flight path.

From our analysis in Chapter 14, we know that if an airplane flies in a steady wind, the motion is governed by the same equations as used in still air. Thus, drag and power required curves are unaffected although now ground speed differs from airspeed.

In level and quasi-level flight, the relationship between ground speed V_g , airspeed V , and wind velocity V_W , is given by (cf. Equation (1.24))

$$V_g = V - V_W, \quad (15.35)$$

where, according to our sign convention, a headwind is taken positive and a tailwind negative.

Wind does not affect the endurance of an airplane because it is a function only of fuel consumption per unit time. On the contrary, wind has a pronounced effect on range.

The specific range with respect to the ground can be expressed as

$$\frac{V_g}{F} = \frac{V - V_W}{F} = \frac{V}{F} \left[1 - \frac{V_W}{V} \right]. \quad (15.36)$$

Equation (15.36) indicates that the with-wind and zero-wind specific ranges are different. For example, when $V = V_W$ the distance traveled relative to the ground is zero. Clearly, the presence of wind also affects the economic speed. This can be investigated by considering the following relationships:

$$\frac{V_g}{F} = \frac{V_g}{c_P P_{br}} = \frac{\eta_j}{c_P} \left[\frac{V - V_W}{P_r} \right]. \quad (15.37)$$

$$\frac{V_g}{F} = \frac{V_g}{c_T T} = \frac{1}{c_T} \left[\frac{V - V_W}{D} \right]. \quad (15.38)$$

Note that Equations (15.37) and (15.38) concern the specific range of propeller-driven airplanes and jet powered airplanes, respectively.

As shown in Figure 15.10, with wind the economic speeds with respect to the ground are found by determining new origins on the airspeed axes and drawing tangents to the power required curve and the drag curve. From the constructions shown, it is seen that for both airplane types the airspeed for maximum specific range with a headwind is greater than in still-air conditions. The reverse is true when flying with a tailwind. Further, it may be understood from Figure 15.10 that maximum specific range, and so the maximum range, is increased by a tailwind and decreased by a headwind.

An expression for the range relative to the ground with a wind of velocity V_W is given by

$$R = \int_{W_2}^{W_1} \frac{V_g}{F} dW = \int_{W_2}^{W_1} \frac{(V - V_W)}{F} dW = \int_{W_2}^{W_1} \frac{V}{F} dW - V_W \int_{W_2}^{W_1} \frac{dW}{F} \quad \text{or}$$

$$R = R_{(V_W=0)} - V_W E. \quad (15.39)$$

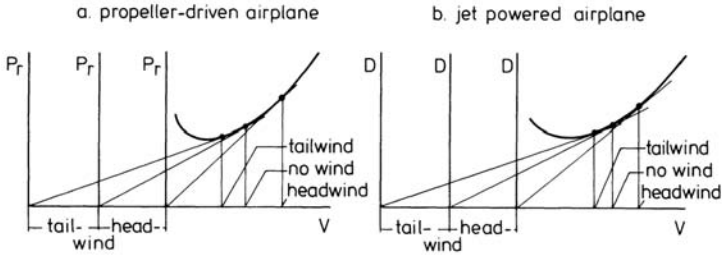


Figure 15.10 Effect of steady headwind and tailwind on airspeed for maximum specific range

Again this equation shows that range is affected advantageously by a tailwind and adversely by a headwind. Therefore, it will be clear that the actual fuel load of the airplane not only is determined by the flight distance but also by the prevailing winds along the flight path. These may be known from meteorological forecasts, completed with seasonal wind data for the airway.

15.5 Weight breakdown

The total weight of the airplane W_{to} , may be written as the sum of the structural weight W_c , the weight of the propulsion system W_e , the payload W_p , the fuel weight W_f , and the weight of the reserve fuel W_{fr} . Thus,

$$W_{to} = W_c + W_e + W_p + W_f + W_{fr}. \tag{15.40}$$

The total weight is the weight at takeoff brake release (TOW), and depends on the loading condition. TOW should not exceed the maximum takeoff weight (MTOW), which is generally determined by structural considerations.

The reserve fuel must be onloaded above the trip fuel to provide for changes in the intended flight profile or flight program and for diversion to an alternate airport due to a balked landing at the airport of destination. The amount of reserve fuel is usually determined by the operator in accordance with operational procedures. Typically, the procedure allows for a flight to alternate and a standard stacking time (Figure 15.11).

Payload is the weight of passengers and cargo. The sum of the payload and trip fuel may be called the useful load W_u .

$$W_u = W_p + W_f. \tag{15.41}$$

The structural weight will include not only the weight of the airframe but also the weight of fixed and removable equipment, furnishings, and the weight of the complete crew. The structural weight and the weight of the propulsion system may be combined into the operational empty weight (OEW) or basic operational weight W_b ,

$$W_b = W_c + W_e. \tag{15.42}$$

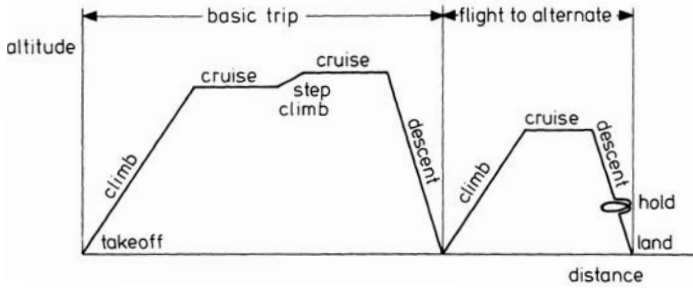


Figure 15.11 Typical flight profile

Thus, W_b is the weight of the airplane fully equipped excluding only payload and fuel,

$$W_{to} = W_b + W_p + W_f + W_{fr}. \quad (15.43)$$

If we divide through by the total weight, we obtain the weight breakdown in terms of weight fractions,

$$1 = \frac{W_b}{W_{to}} + \frac{W_p}{W_{to}} + \frac{W_f}{W_{to}} + \frac{W_{fr}}{W_{to}}. \quad (15.44)$$

Because of their usefulness, weight fractions are often employed in airplane performance and design considerations. For example, when we assume that the entire journey length is performed in cruising flight, from Equations (15.27) and (15.29), the ratio W_f/W_{to} can be written as

$$\frac{W_f}{W_{to}} = 1 - e^{-\frac{R}{\bar{v}_T(C_L/C_D)}} = 1 - e^{-\frac{R}{\eta_{to} \frac{H}{g}(C_L/C_D)}}, \quad (15.45)$$

where now R is the total range. Equations (15.45) and (15.44) show that the aim is obviously to make the range factor as large as possible and to keep the fraction W_b/W_{to} low in order to obtain a large payload fraction. The weight fraction W_b/W_{to} may be regarded as the structural efficiency since the lighter the airplane is built, the greater is the useful load fraction.

Typical weight fractions for a stage length of 6500 km are shown in Figure 15.12 for a high-subsonic turbofan airplane and a supersonic transport with turbojet engines. Due to its lower range factor, the fuel fraction for the supersonic airplane is higher than for the turbofan airplane. Consequently, the payload fraction for the supersonic transport is considerably smaller, notwithstanding its higher structural efficiency.

We also conclude from Equation (15.45) that at a given range factor, a greater fuel fraction is required as the range becomes longer. This implies that for a given airplane the payload fraction decreases with range as can be seen from Equation (15.44).

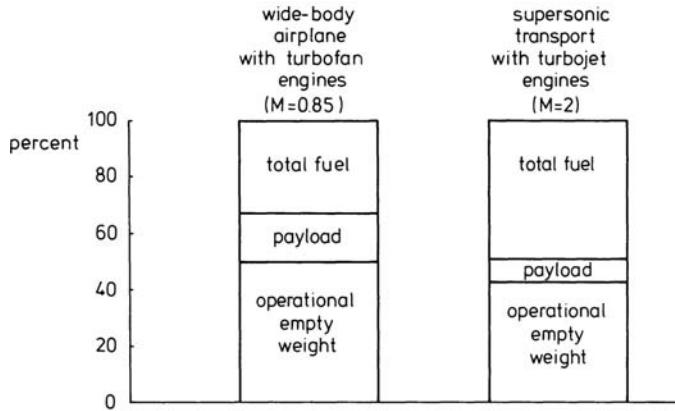


Figure 15.12 Typical weight breakdowns

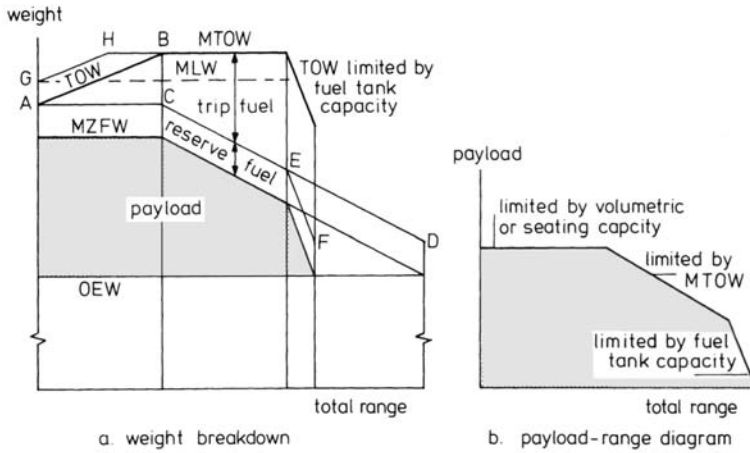


Figure 15.13 Payload-range characteristics

In Figure 15.13a the weight breakdown is sketched with respect to stage length in still air for a typical transport airplane. The line AB gives the takeoff weight at the maximum payload that can be carried. Point B corresponds to the maximum stage length with maximum payload. This range is called the design range. Increasing the total range above the design range requires that payload is replaced by fuel. This is represented by the line CD. At point D the ultimate range is reached (zero payload and reserve fuel unconsumed). Usually, the fuel tank capacity is such that the range cannot be increased beyond point E. The line EF, finally, indicates that some further increase of the total range is possible by reducing the takeoff weight when consuming the full fuel load.

The line GH in Figure 15.13a represents a limit to the takeoff weight that may be dictated on short ranges by the maximum allowable weight of the airplane at the landing. The maximum landing weight (MLW) is imposed by structural design re-

quirements. Another weight limit is the maximum zero fuel weight (MZFW), the maximum allowable weight of the airplane without fuel. Normally, the maximum landing weight is greater than the maximum zero fuel weight plus the reserve fuel. Otherwise, payload might be restricted by the limited strength of the landing gear or airframe structure under particular landing conditions.

The payload-range relationship of Figure 15.13a is separately portrayed in Figure 15.13b. The latter curve may be regarded as the basis of the economic value of a transport airplane.

15.6 The economic performance of transport airplanes

In this section are summarized the most valuable parameters determining the commercial merit of a transport airplane. These performance items are given below and will be explained in the order listed:

- block time, E_B
- block speed, V_B
- transport product, P_R
- transport productivity, P_h
- revenue-earning capacity, P_y

The *block time* is the total time elapsing from starting engines at the departure airport to engines off at the destination place. Thus, the block time includes taxi time from the loading point to the takeoff runway, checks, takeoff, ascent to cruising height, cruise, descent, final circuits, approach and landing, and taxi time to the terminal point.

The *block speed* is the block distance divided by the block time,

$$V_B = \frac{R}{E_B}. \quad (15.46)$$

Evidently, the block speed is lower than the cruising speed. According to Reference 51, the relationship between block time, block distance and cruising speed can be written as

$$E_B = \frac{R}{V_{cr}} + \Delta t, \quad (15.47)$$

where R is the block distance, V_{cr} is the cruising speed and Δt is the length of time that accounts for the field operations and the lower airspeeds in flight phases other than the cruise.

Combining Equations (15.46) and (15.47) results in the following expression for the block speed,

$$V_B = \frac{R}{\frac{R}{V_{cr}} + \Delta t}. \quad (15.48)$$

Typical variations of block time and block speed with total range are plotted in Figure 15.14, using $\Delta t = 50$ minutes. The graphs show that at a given cruising

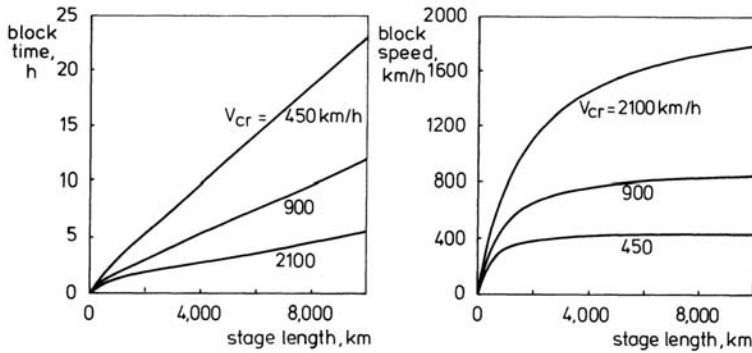


Figure 15.14 Block time and block speed versus range

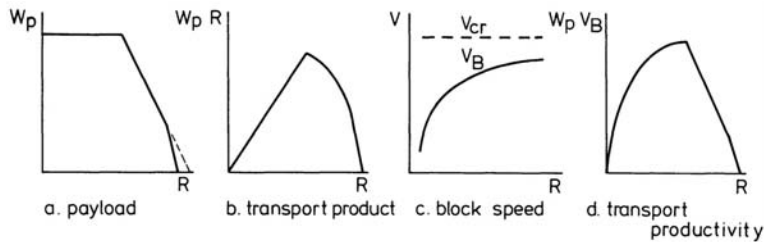


Figure 15.15 Economic parameters for transport airplane

speed both block time and block speed increase with increasing block distance, and that raising the cruising speed is more beneficial as the range is greater. Obviously, the revenues which are gained by transport of passengers and/or freight are dependent on payload as well as range. Therefore, the transport performance is given by the product of payload and range,

$$P_R = W_p R, \tag{15.49}$$

where P_R is named the *transport product* and may be expressed in the units tonkm or passengerkm.

For a transport airplane with payload-range characteristic as depicted in Figures 15.13b and 15.15a, the variation of the transport product versus stage length is as shown in Figure 15.15b. It is of interest to note that the peak value of the transport product occurs at a flight distance which is equal to half the ultimate range. In the case that the latter distance is shorter than the design range, the optimum value occurs at the design range. Also note that the revenues are directly proportional to the load factor, the ratio of the payload actually carried over a given route distance to that payload that could have been carried over the same distance. The reader should note that the term "load factor" is also used in Chapter 8 in the context of the loads from flight maneuvers on the airplane structure.

The *transport productivity* is defined as the transport product delivered per unit

time. Usually, it is based on block time, so that we can write

$$P_h = \frac{W_p R}{E_B} = W_p V_B. \quad (15.50)$$

From the combination of the payload range diagram in Figure 15.15a and the block speed-range relationship in Figure 15.15c, we obtain the curve of Figure 15.15d. This shows the typical variation of transport productivity with block distance. From the diagrams, we see that the maximum value of P_h occurs at the design range.

The *revenue-earning capacity* is the transport product per year. If U is the annual flight utilization of the airplane in hours, we have

$$P_y = P_h U = W_p V_B U. \quad (15.51)$$

For long-haul routes, the annual utilization might reach a value of 4500 hours. This figure gradually decreases as the route distance (block time) becomes shorter (Reference 52).

Besides the preceding parameters, the specific costs of operating a commercial airplane, that is to say, the costs per tonkm or costs per hour are as much of importance to its economic value.

The operating costs are usually broken down into direct and indirect costs. The direct operating costs (DOC) are those which are associated with flying operations. These may include maintenance, crew, airplane service, landing fees, depreciation of capital invested, insurance, and fuel. The indirect operating costs (IOC), on the other hand, are independent of the characteristics of the airplane since they are connected with the costs of operating an airline. They may encompass management, administration, sales, housing, and depreciation of ground properties and equipment.

Beyond doubt, when considering the economic value of an airplane we shall specially be interested in the direct operating costs as a criterion.

As a means of estimating DOC for comparative purposes, standard methods were published by the Society of British Aircraft Constructors (SBAC) in 1959 and by the Air Transport Association of America (ATA) in 1967 (References 52 and 53). To reflect the effects of inflation and changing technology, renewed and updated cost models have been developed recently. See, for example, References 54 and 55. These sources will aid the reader in obtaining a proper understanding of the airplane related cost problem.

Chapter 16

AIRFIELD PERFORMANCE

16.1 The takeoff maneuver

The takeoff can be defined as the maneuver by which the airplane is accelerated from rest on the runway to the climbout speed V_C over a 10.7 m (35 ft) obstacle (screen height) for civil transports or a 15.2 m (50 ft) obstacle for light propeller-driven and military airplanes (Figure 16.1).

The takeoff distance may be considered to consist of two main parts: (1) the ground run distance, and (2) the airborne distance.

The ground run comprises the pre-rotation phase and the rotation phase, where the airplane successively accelerates from standstill to the rotation speed V_R and from V_R to the liftoff speed V_{LOF} . The rotation speed is the speed at which the pilot initiates upward rotation of the airplane and is perhaps the most important reference speed for the pilot since varying V_R can greatly affect the takeoff distance and the overall safety level of the takeoff maneuver.

During the first part of the ground run, the airplane incidence remains fairly unchanged. Beyond the rotation speed the angle of attack is gradually increased from the ground attitude toward the liftoff condition such that at V_{LOF} the lift equals the weight and the airplane becomes airborne.

The airborne distance is usually divided into the transition to climbing flight and the rectilinear climb to the screen height. In the transition phase, where the flight-path angle is increased from zero at V_{LOF} to that of steady climb at screen speed V_C , is flown with an incremental lift coefficient in order to provide sufficient lift to accomplish an adequate curvature of the flight path.

During the takeoff maneuver flap deflection and engine control setting remain constant. However, to improve climb performance, the landing gear is retracted soon after the airplane has become airborne.

After passing the screen, the airplane travels along the takeoff flight path until it reaches a safe flight condition at an altitude of about 450 m (1500 ft), where the continued climb to cruising altitude begins (see Figure 11.4).

According to the airworthiness requirements, for multi-engine civil transport airplanes the occurrence of single engine failure during the takeoff ground run must be awaited. To warrant nevertheless adequate safety and handling, a number of reference speeds are of significance in airfield performance computations. These speeds are indicated in Figure 16.2 in the order in which they normally occur during the takeoff maneuver.

The decision speed V_1 is selected such that when at this speed an engine failure is recognized, the pilot is able to abort the takeoff and make a full stop on the

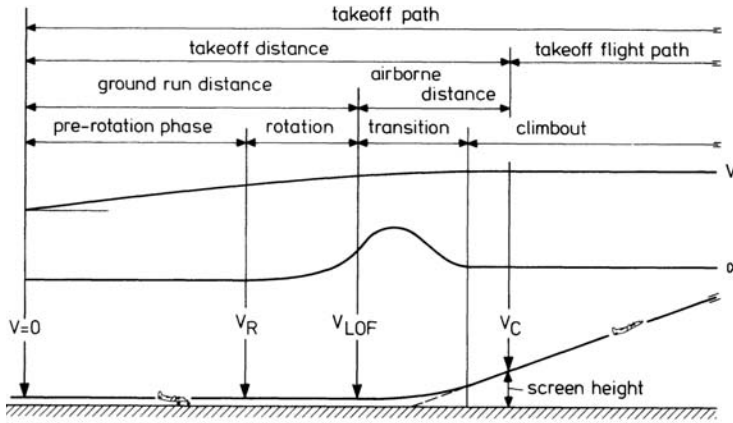


Figure 16.1 The takeoff maneuver

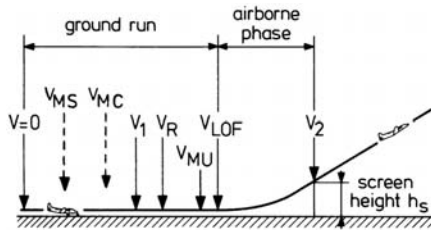


Figure 16.2 Takeoff reference speeds for conventional transports

runway, or to continue the takeoff to the screen height with one engine out, in the same distance (Figure 16.3a).

Takeoff distances based on this condition are called *balanced field lengths*. The scheduled takeoff distances are usually determined by the balanced field lengths or by the distances over the screen height for the all-engines case multiplied by a factor 1.15, whichever is greater.

The decision speed V_1 is determined by computing the so-called *accelerate stop* and *accelerate-climb distances* as functions of the engine failure speed, V_{EF} . The former distance is the length required to accelerate to V_{EF} and thereafter stop the airplane on the runway. The other distance is the length required to accelerate to V_{EF} and then continue the takeoff over the screen height with one engine inoperative.

Plotting the two distances as sketched in Figure 16.3b yields the balanced field length and the decision speed. If an engine should stop at a speed below V_1 the pilot should abandon the takeoff, whereas, if an engine fails beyond V_1 the pilot should continue the takeoff because of the fact that there may remain not enough runway length for deceleration to standstill.

The decision speed may be recommended to be somewhat less for wet runway conditions than for dry conditions to guarantee that the same accelerate-stop dis-

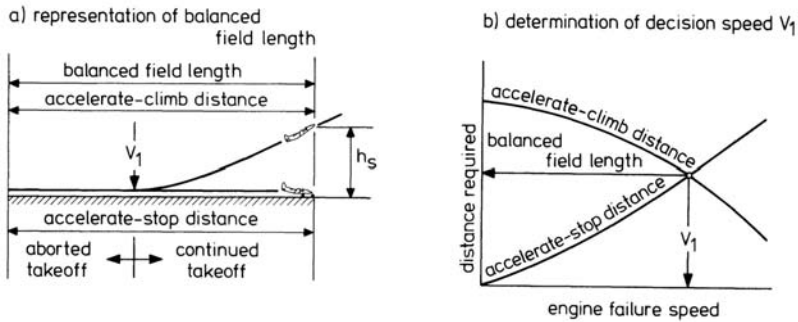


Figure 16.3 Balanced field length concept

tance can be achieved.

Returning to Figure 16.2, we see that the decision speed is higher than the minimum control speed, V_{MC} , the minimum speed above which it is possible to maintain adequate airplane control for takeoff (see Section 11.2). We also see that the decision speed is lower than the rotation speed V_R . In its turn, the minimum acceptable value of V_R may not be less than $1.05 V_{MC}$.

The airworthiness requirements also distinguish the minimum liftoff or unstick speed V_{MU} , the calibrated minimum speed at which the airplane can safely lift off the ground, and continue the takeoff. The actual liftoff speed V_{LOF} depends on the rotation speed V_R . The latter speed must be chosen such that $V_{LOF} \geq 1.1V_{MU}$ with all engines operating or $V_{LOF} \geq 1.05V_{MU}$ with one engine out. The requirements prevent a rotation to an attitude exceeding that at the demonstrated V_{MU} and with that the occurrence of a ground stall and so insufficient ability to liftoff. Further, V_R must allow the takeoff safety speed V_2 to be reached at the screen. The speed V_2 is referenced as the lowest speed to ensure an adequate and safe climbout with the critical engine inoperative and the live engine(s) developing full takeoff thrust. For turboprop airplanes the requirements quote: $V_2 \geq 1.1V_{MC}$ and $V_2 \geq 1.2V_{MS}$ for two-engine and three-engine airplanes and $V_2 \geq 1.15V_{MS}$ for airplanes with more than three engines. For jet-driven airplanes the takeoff safety speed shall not be less than: $V_2 = 1.1V_{MC}$ and $V_2 = 1.2V_{MS}$ irrespective of the number of engines. The speed V_{MS} , is the minimum stalling speed measured in a flight where the airspeed is steadily reduced at a rate of 1 knot per second, as already defined in Section 8.4. For further details and the regulations in the nontransport categories the reader should consult the airworthiness requirements.

16.2 Takeoff ground run

The forces on the airplane during ground run are shown in Figure 16.4. The weight of the airplane is balanced by the lift and the reaction force of the ground surface on the wheels. Thrust is opposed by the rolling friction between wheels and ground surface in addition to the drag of the airplane.

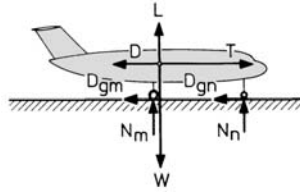


Figure 16.4 Forces acting during takeoff ground run

The frictional force D_g may be written as

$$\begin{aligned} D_g &= D_{gm} + D_{gn} = \mu_r(N_m + N_n) \\ &= \mu_r(W - L) = \mu_r(W - C_{Lg}\frac{1}{2}\rho V^2 S), \end{aligned} \quad (16.1)$$

where C_{Lg} is the lift coefficient in the ground run attitude and μ_r is the coefficient of rolling friction. Typically, μ_r may be taken as 0.02 for a concrete or asphalted runway and 0.05 for an airstrip with short cut grass.

The equation of motion in forward direction is (assuming zero wind and no runway slope)

$$\frac{W}{g} \frac{dV}{dt} = T - D - D_g = T - C_{Dg}\frac{1}{2}\rho V^2 S - D_g, \quad (16.2)$$

where C_{Dg} is the drag coefficient in the ground running condition. Both C_{Lg} and C_{Dg} will vary during the rotation phase of the ground run.

Combining Equations (16.1) and (16.2), the acceleration of the airplane during ground run at a speed V becomes

$$\frac{dV}{dt} = g \left[\frac{T}{W} - \mu_r - (C_{Dg} - \mu_r C_{Lg}) \frac{\frac{1}{2}\rho V^2}{W/S} \right]. \quad (16.3)$$

Denoting $dV/dt = a$ and using $V = ds/dt$, the distance traveled in accelerating from rest to the liftoff speed can be expressed in the form

$$s_g = \int_0^{V_{LOF}} \frac{V dV}{a} = \int_0^{V_{LOF}} \frac{V dV}{g \left[\frac{T}{W} - \mu_r - (C_{Dg} - \mu_r C_{Lg}) \frac{\frac{1}{2}\rho V^2}{W/S} \right]}. \quad (16.4)$$

This equation shows that the distance s_g depends on the acceleration during the ground run, which is a function of V .

Introduction of the lift coefficient $(C_L)_{LOF}$ defined by the condition that the lift at V_{LOF} is equal to the weight of the airplane

$$W = L = (C_L)_{LOF} \frac{1}{2}\rho V_{LOF}^2 S, \quad (16.5)$$

yields for the ground run distance

$$s_g = \int_0^{V_{LOF}} \frac{V dV}{g \left[\frac{T}{W} - \mu_r - \frac{(C_{Dg} - \mu_r C_{Lg})}{(C_L)_{LOF}} \frac{V^2}{V_{LOF}^2} \right]}. \quad (16.6)$$

The length of the ground run may be determined by stepwise integration of Equation (16.4), that is, calculate the acceleration of the airplane at a number of forward speeds and then plot V/a against V as shown in Figure 16.5. The area under the curve from $V = 0$ to $V = V_{LOF}$ is the value for s_g .

The ground run distance may be estimated analytically by assuming that the thrust to weight ratio T/W is represented by a mean value of the thrust \bar{T} (W is assumed constant during takeoff). Further, we assume that the angle of attack is constant. In the case of a nose-wheel type landing gear, this is achieved by keeping the nose wheel on the ground until liftoff. Under this condition the quantity $(C_{Dg} - \mu_r C_{Lg})$ in Equation (16.4) may be assumed constant throughout the ground run.

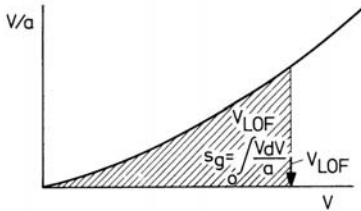


Figure 16.5 Graphic determination of ground run distance

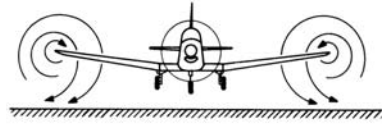


Figure 16.6 Effect of ground on tip vortices

Integrating Equation (16.6) between $V = 0$ and $V = V_{LOF}$, we have

$$s_g = \frac{W/S}{\rho g(C_{Dg} - \mu_r C_{Lg})} \ln \frac{\frac{\bar{T}}{W} - \mu_r}{\frac{\bar{T}}{W} - \mu_r - \frac{(C_{Dg} - \mu_r C_{Lg})}{(C_L)_{LOF}}} \quad (16.7)$$

The actual value of \bar{T} may be described by the relationship $\bar{T} = kT_{static}$, where the factor k is a function of the ratio T_{LOF}/T_{static} . The latter ratio depends on the type of propulsion system owing to the different variation of thrust with forward speed (see Figure 9.11). Another approach to the analytic estimation of the ground run distance is the use of a mean acceleration \bar{a} , giving the same distance as the actual variable acceleration.

Then, from Equation (16.4), we get

$$s_g = \frac{V_{LOF}^2}{2\bar{a}} \quad (16.8)$$

Usually, \bar{a} is taken as the acceleration at a speed $V_{LOF}/\sqrt{2} = 0.7V_{LOF}$.

It should be remarked that in determining the aerodynamic forces and moments on the airplane during the ground run, we have to account for the effects of the proximity of the ground on the flow field around the airplane. The presence of the ground reduces the induced downwash from the tip vortices since there cannot be a flow going into the ground (Figure 16.6). Consequently, the airplane's C_L - α and C_D - α curves change as sketched in Figure 16.7 (see also Figure 4.10),

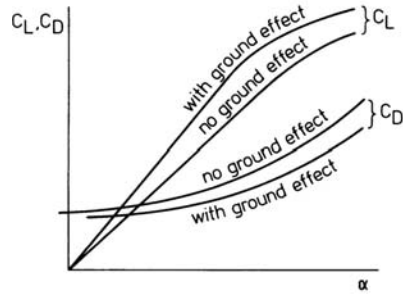


Figure 16.7 Typical effect of ground on lift and drag coefficient

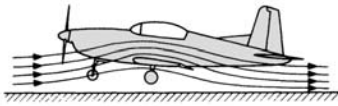


Figure 16.8 Effect of ground on downwash

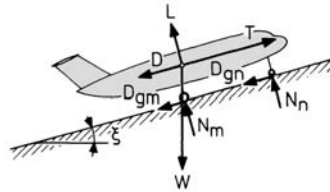


Figure 16.9 Presence of a runway slope

through which at a given altitude of the airplane the lift coefficient increases and the (induced) drag coefficient decreases.

The proximity of the ground also may have an effect on the contribution of the horizontal stabilizer to longitudinal stability at large angles of attack. The ground surface straightens the flow streamlines, thereby decreasing the downwash behind the wing (Figure 16.8). This results in a greater angle of attack at the tail, which requires an increased upward deflection of the elevator to keep the airplane in equilibrium.

The ground effects decrease with increasing wing aspect ratio and are dependent on the relative distance between wing and ground surface (Reference 56).

Practically, ground effects are of importance during ground run and may be ignored when the airplane is airborne.

Before leaving our examination of the ground run distance, let us call some attention to the effect of a runway slope. Looking at the forces in Figure 16.9, the equation of motion reads:

$$\frac{W}{g} \left(\frac{dV}{dt} \right)_{\zeta} = T - D - \mu_r (W \cos \zeta - L) - W \sin \zeta, \tag{16.9}$$

where ζ is the runway slope, uphill positive.

Adopting in Equation (16.9) the approximation that $\cos \zeta = 1$, we obtain

$$\left(\frac{dV}{dt} \right)_{\zeta} = g \left[\frac{T}{W} - \mu_r - (C_{Dg} - \mu_r C_{Lg}) \frac{\frac{1}{2} \rho V^2}{W/S} - \sin \zeta \right]. \tag{16.10}$$

By combining Equation (16.10) with Equation (16.3), the relationship between the accelerations with and without runway slope can be written as

$$\left(\frac{dV}{dt}\right)_\zeta = \frac{dV}{dt} - g \sin \zeta. \quad (16.11)$$

Any numerical consideration on the effect of $g \sin \zeta$ on the magnitude of the acceleration may show the strong influence of a runway slope on the length of the ground run.

16.3 The airborne phase of the takeoff maneuver

The airborne distance depends strongly on the way in which the pilot controls the airplane and can, therefore, only be evaluated when the two control laws are specified. One of these is already defined by the condition that the engine control setting is constant during the takeoff maneuver. The second control law may concern the time-history of the lift coefficient, the normal acceleration, or the rate of pitch, from the moment the airplane leaves the ground until it reaches the steady climbing attitude at the end of the transition.

An accurate determination of the flight path between the liftoff point and the screen height is usually made by step by step calculations, adopting a particular control law.

Also analytic procedures are developed, assuming $C_L = \text{constant}$ or $d\theta/dt = \text{constant}$ during transition. For a detailed description of these techniques, the reader is referred to References 57 and 58.

In order to examine the airplane motion in the transition flare, let us return to Equations (8.7) and (8.8), which can be written as (Figure 16.10a)

$$\frac{W}{g} V \frac{dV}{ds} = T \cos \alpha_T - D - W \sin \gamma \quad (16.12)$$

$$\frac{W}{g} \frac{V^2}{R} = L + T \sin \alpha_T - W \cos \gamma. \quad (16.13)$$

Assuming that the thrust and the velocity vectors are coincident ($\alpha_T = 0$) and that the flight-path angles are small ($\sin \gamma = \gamma$ and $\cos \gamma = 1$), the governing equations of motion reduce to (Figure 16.10b)

$$\frac{W}{g} V \frac{dV}{ds} = T - D - W \gamma \quad (16.14)$$

$$\frac{W}{g} \frac{V^2}{R} = L - W. \quad (16.15)$$

Here, a simple analytic approach to the problem is made by supposing that the path is circular of radius R . Accordingly, we have to consider the transition on

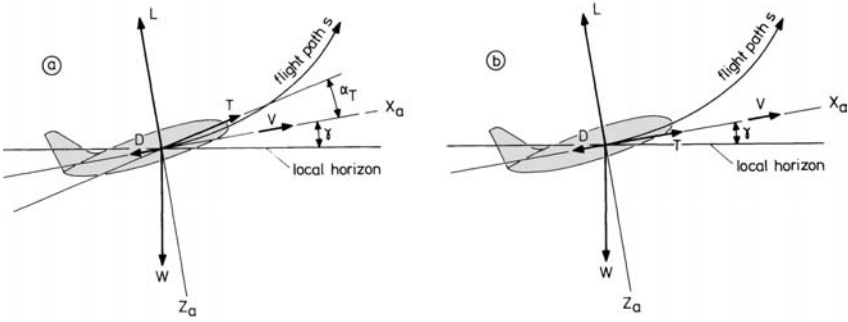


Figure 16.10 Equilibrium of forces during transition

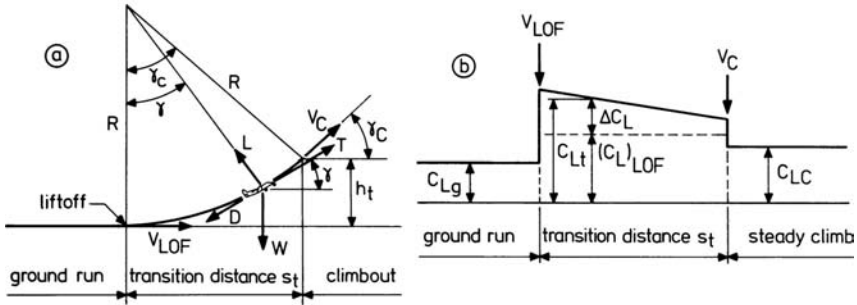


Figure 16.11 Schematic for transition to steady climb

the condition that at the liftoff point the pilot instantaneously increases the angle of attack and thereby applies an increment of lift, forcing the airplane to follow a curved path (Figure 16.11a).

Just after liftoff, the transition lift coefficient, C_{L_t} , may be expressed as

$$(C_{L_t})_{LOF} = (C_L)_{LOF} + \Delta(C_L)_{LOF}, \tag{16.16}$$

where $(C_L)_{LOF}$ is defined by Equation (16.5).

The lift coefficient at any point on the transition flight path may then be written as (Figure 16.11b)

$$C_{L_t} = (C_L)_{LOF} + \Delta C_L. \tag{16.17}$$

When we insert Equations (16.5) and (16.17) into Equation (16.15), we get

$$\frac{1}{gR} = \frac{1}{V_{LOF}^2} - \frac{1}{V^2} + \frac{\Delta C_L}{\frac{2W}{\rho S}}. \tag{16.18}$$

This expression shows that due to the increase in flight velocity, the value of ΔC_L and so of C_{L_t} must decrease during the transition (see Figure 16.11b).

By combining Equations (16.5), (16.15) and (16.16), we can express the radius R as

$$R = \frac{\frac{2W}{\rho S}}{\rho g \Delta(C_L)_{LOF}} = \frac{V_{LOF}^2}{g} \frac{(C_L)_{LOF}}{\Delta(C_L)_{LOF}} = \frac{V_{LOF}^2}{g(n_{LOF} - 1)}, \tag{16.19}$$

where n_{LOF} is the load factor at liftoff.
When the flight-path angle reaches the value

$$\gamma_C = \left(\frac{T-D}{W} \right)_C, \quad (16.20)$$

the transition is completed and a steady climb at an airspeed V_C begins. At that point of the flight path the instantaneous value of the transition lift coefficient is suddenly reduced to a value C_{LC} associated with the steady speed V_C ,

$$C_{LC} = \frac{W}{S} \frac{2}{\rho} \frac{1}{V_C^2}. \quad (16.21)$$

If R and γ_C are known, it is an easy matter to obtain from the geometrical pattern in Figure 16.11a the following relationships:

$$s_t = R \gamma_C \quad (16.22)$$

$$h_t = R(1 - \cos \gamma_C) = R \frac{\gamma_C^2}{2} = \frac{1}{2} s_t \gamma_C. \quad (16.23)$$

Note that in Equation (16.23) we have employed the trigonometric relationship $1 - \cos \alpha = 2 \sin^2(\alpha/2)$. With $dh = \gamma ds$, the speed increment attained during transition follows from integrating Equation (16.14),

$$\int_{V_{LOF}}^{V_C} \frac{W}{2g} dV^2 = \int_0^{s_t} (T-D) ds - \int_0^{h_t} W dh \quad \text{or} \quad (16.24)$$

$$\frac{V_C^2 - V_{LOF}^2}{2g} = \int_0^{s_t} \left(\frac{T-D}{W} \right) ds - h_t. \quad (16.25)$$

If the specific excess thrust $(T-D)/W$ in Equation (16.25) is assumed constant and equal to its value at V_{LOF} , we obtain

$$\frac{V_C^2 - V_{LOF}^2}{2g} = \gamma_{LOF} s_t - h_t, \quad (16.26)$$

where γ_{LOF} is the steady flight-path angle at the speed V_{LOF} ,

$$\gamma_{LOF} = \left(\frac{T-D}{W} \right)_{LOF}. \quad (16.27)$$

As the variation of the airspeed during transition usually is very small, it is permissible to make the approximation that $\gamma_C = \gamma_{LOF}$. Then, after substitution of Equations (16.19), (16.22), and (16.23) into Equation (16.26), the following expression is derived:

$$\frac{V_C}{V_{LOF}} = \left[1 + \gamma_{LOF}^2 \frac{(C_L)_{LOF}}{\Delta(C_L)_{LOF}} \right]^{\frac{1}{2}}. \quad (16.28)$$

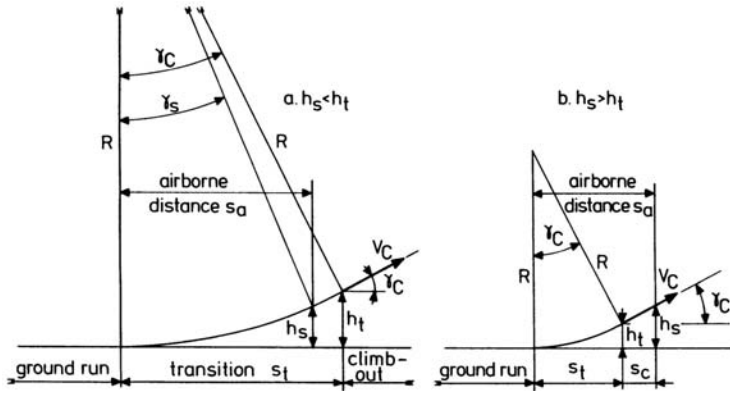


Figure 16.12 Transition and screen height

The quantity $(\Delta C_L)_{LOF}$ is often expressed in terms of the normal acceleration a_n or the load factor n_{LOF} at liftoff (see also Section 8.3),

$$\frac{W}{g} \frac{V_{LOF}^2}{R} = \frac{W}{g} (a_n)_{LOF} = W(n_{LOF} - 1) = \Delta(C_L)_{LOF} \frac{1}{2} \rho V_{LOF}^2 S \quad (16.29)$$

or with Equation (16.5),

$$\frac{(a_n)_{LOF}}{g} = n_{LOF} - 1 = \frac{\Delta(C_L)_{LOF}}{(C_L)_{LOF}}. \quad (16.30)$$

As an example we may take $(C_L)_{LOF} = C_{Lmax}/1.44$ ($V_{LOF} = 1.2V_{MS}$) and an instantaneous rotation at liftoff to an angle of attack such that $(C_L)_{LOF} = 0.8C_{Lmax}$. This gives

$$\frac{(a_n)_{LOF}}{g} = \frac{(C_L)_{LOF} - (C_L)_{LOF}}{(C_L)_{LOF}} = 0.8 \times 1.44 - 1 = 0.152, \text{ and } n_{LOF} = 1.152.$$

This result represents a typical value for the normal acceleration as the practical upper limit may be about $0.2g$ ($n_{LOF} = 1.2$).

Sometimes, the screen height is cleared before transition to the steady climb attitude is completed. Then the flight-path angle at the screen and the airborne distance follow from the relationships (Figure 16.12a):

$$h_s = R(1 - \cos \gamma_s) = R\gamma_s^2/2 \quad \text{and} \quad s_a = R\gamma_s. \quad (16.31)$$

If h_s is greater than h_t , then the airborne distance is (Figure 16.12b)

$$s_a = s_t + s_c, \quad (16.32)$$

where $s_c = (h_s - h_t)/\tan \gamma_c$ is the climb distance.

16.4 Effect of wind on takeoff

The effect of wind on the takeoff length is examined by considering a steady headwind of speed V_w . The acceleration relative to the ground and the distance traveled along the runway are given by

$$a_g = \frac{dV_g}{dt} = V_g \frac{dV_g}{ds_g} \quad (16.33)$$

$$(s_g)_w = \int_0^{(V_g)_{LOF}} \frac{V_g dV_g}{a_g}. \quad (16.34)$$

In these equations V_g is the ground speed ($V_g = V - V_w$). At a constant wind velocity we have $dV_g = dV$ and $a_g = a$ so that the ground run distance with headwind V_w becomes

$$\begin{aligned} (s_g)_w &= \int_{V_w}^{V_{LOF}} \frac{(V - V_w)dV}{a} = \int_0^{V_{LOF}} \frac{V dV}{a} - \int_0^{V_w} \frac{V dV}{a} - V_w \int_{V_w}^{V_{LOF}} \frac{dV}{a} \\ &= s_g - s_{g0} - V_w(t_g)_w, \end{aligned} \quad (16.35)$$

where s_g is the ground run distance from standstill to V_{LOF} in the absence of wind, s_{g0} is the distance from $V = 0$ to $V = V_w$, and $(t_g)_w$ is the time elapsed from $V = V_w$ to $V = V_{LOF}$.

Equation (16.35) shows that a headwind reduces the ground run distance required to attain the liftoff speed V_{LOF} .

A steady headwind has the same effect on the elapsed time. From $a = dV_g/dt$, we can write

$$(t_g)_w = \int_0^{(V_g)_{LOF}} \frac{dV_g}{a} = \int_{V_w}^{V_{LOF}} \frac{dV}{a} = \int_0^{V_{LOF}} \frac{dV}{a} - \int_0^{V_w} \frac{dV}{a} = t_g - t_{g0}, \quad (16.36)$$

where t_g is the time during ground run in still air and t_{g0} is the time elapsed from $V = 0$ to $V = V_w$.

The analyses of the effect of wind in Chapter 14 have learned us that the presence of a headwind that increases with height is to increase the rate of climb and therefore to decrease the horizontal distance required to attain a particular height. In rough considerations, the effect of a wind gradient during the airborne phase is accounted for as the effect of a constant headwind with a velocity equal to that at half the height of the screen. Now the airborne distance with headwind V_w is

$$(s_a)_w = s_a - V_w t_a, \quad (16.37)$$

where t_a is the airborne phase time. At an average airspeed \bar{V} , we get

$$\frac{(s_a)_w}{s_a} = \frac{s_a - V_w \frac{s_a}{\bar{V}}}{s_a} = 1 - \frac{V_w}{\bar{V}}. \quad (16.38)$$

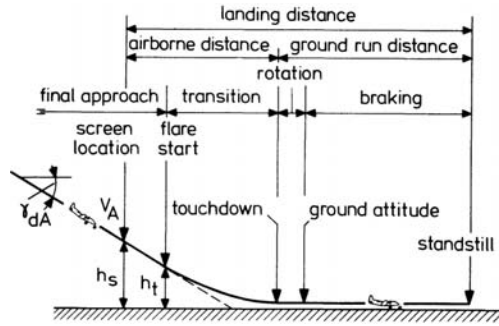


Figure 16.13 Landing maneuver

This expression shows that the effect of a headwind V_w during transition and climb may be obtained by multiplying the airborne distance in still air by the factor $(1 - (V_w/\bar{V}))$, where $\bar{V} = (V_{LOF} + V_C)/2$.

It must not be forgotten that our analyses have been based on the presence of a headwind, and that it is of frequent occurrence that the wind makes some angle with the runway. Therefore, as a final note, during a so-called crosswind takeoff there is a tendency of the airplane to rotate about the vertical axis through its center of gravity. In order to hold heading, wings level and wheels on the ground during ground run, use of rudder and aileron is necessary.

After liftoff, heading is changed adequately to maintain straight track from the runway (see Figure 13.13). Typically, maximum safe crosswind-component velocities may vary from about 15 knots (7.7 m/s) for light airplanes up to 30 knots (15.4 m/s) or more for civil transports.

Similarly, high crosswind components during approach and landing also will require application of rudder and aileron to overcome the forces acting sidewise on the airplane (see Figure 3.5).

16.5 The landing maneuver

The landing is the maneuver by which the airplane is brought from a steady approach speed V_A over a 15 m (50 ft) obstacle at the runway threshold (screen location) to standstill on the runway (Figure 16.13).

Airworthiness requirements stipulate that the steady approach speed shall not be less than $1.3V_{MS}$, where V_{MS} is now the calibrated minimum stalling speed for the airplane in the landing configuration.

For analysis, the landing distance can be divided into four parts:

1. The part of the final approach in the direction of the extended runway centerline. The distance covered during this phase is the horizontal length of the flight path between the screen location and the point where the transition flare starts. During approach flight landing gear and wing flaps are extended.

2. The flare to transit the airplane to a horizontal motion by the time the airplane arrives at ground level. During the flare the engine control setting is progressively throttled back to flight idling so that at touchdown the thrust is zero and the associated touchdown speed V_T is below the speed V_A at the screen. Further, we may assume that under touchdown conditions the vertical velocity of the airplane is zero and the lift equals the weight.
3. A free roll during which the airplane is rotated down to the ground altitude.
4. The major ground run where the retarding force is increased by application of the wheel brakes and additional aerodynamic and propulsive means.

Commonly, the required field length is specified as 10/6 times the shortest landing distance obtained from tests conducted on a dry runway. The factor 10/6 is used as a safety factor to take care of possible deviations in regular operation. For wet runway operation, it has become usual to impose an extra 15 percent on the landing distance.

Finally, we remark that the effects of wind on the landing distance are very similar to those on the takeoff distance. The presence of a headwind component shortens the landing distance, whereas a tailwind component increases the landing distance.

16.6 The airborne distance of the landing maneuver

The airborne distance is the horizontal length between the screen location and the touchdown point at the end of the flare.

The approach part covers a distance (see Figure 16.13)

$$s_d = \frac{h_s - h_t}{\tan \gamma_{dA}}, \quad (16.39)$$

where γ_{dA} is the slope of the descent path.

The governing equations for steady descending flight are (Figure 16.14)

$$-D + T \cos \alpha_T + W \sin \gamma_{dA} = 0 \quad (16.40)$$

$$-L - T \sin \alpha_T + W \cos \gamma_{dA} = 0. \quad (16.41)$$

Assuming again $\alpha_T = 0$ and $\cos \gamma_{dA} = 1$, and using the relationships $L = C_{LA} \frac{1}{2} \rho V_A^2 S$ and $D = C_{DA} \frac{1}{2} \rho V_A^2 S$, we find

$$C_{LA} = \frac{W}{S} \frac{2}{\rho} \frac{1}{V_A^2} \quad (16.42)$$

$$\sin \gamma_{dA} = \left[\frac{C_D}{C_L} \right]_A - \frac{T}{W}. \quad (16.43)$$

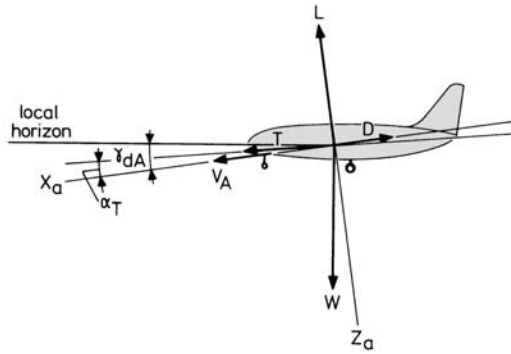


Figure 16.14 Forces in steady symmetric descent

If the engines are idling during final approach (glide approach), then the airspeed V_A corresponds to a fixed slope of the flight path :

$$\gamma_{dA} = \sin^{-1} \left[\frac{C_D}{C_L} \right]_A. \quad (16.44)$$

When performing a power-on approach, the slope of the flight path can be chosen independent of the angle of attack. The powered descent is always executed in regular service operations of transport airplanes, which normally fly toward the runway by means of the *Instrument Landing System* (ILS). This navigational system provides vertical guidance above and below an approach path established at a fairly small angle of descent of about 3 degrees. Clearly, this condition requires that the engines deliver a rather high thrust. Maintaining adequate thrust is also needed to control the flight path and to cope safely with an aborted final approach or a balked landing.

An assessment of the flare distance s_f and the height h_f can be made by representing the landing flare by a circular arc (Figure 16.15a). This requires, as we know from the analysis in Section 16.3, that the angle of attack at the beginning of the flare is instantaneously increased to (Figure 16.15b)

$$(C_{Ll})_A = C_{LA} + \Delta C_{LA}. \quad (16.45)$$

In this case the formulae for the radius of curvature of the flare are identical to those in Equation (16.19), except that here V_{LOF} must be replaced by V_A , so that

$$R = \frac{2 \frac{W}{S}}{\rho g \Delta C_{LA}} = \frac{V_A^2}{g} \frac{C_{LA}}{\Delta C_{LA}} = \frac{V_A^2}{g(n_A - 1)}. \quad (16.46)$$

Since at the end of the flare the flight path is tangential to the ground surface, the horizontal distance covered by the flare and the initial height of the flare can be expressed as

$$s_f = R\gamma_{dA} \quad \text{and} \quad h_f = R(1 - \cos \gamma_{dA}) = R \frac{\gamma_{dA}^2}{2} = \frac{1}{2} s_f \gamma_{dA}. \quad (16.47)$$

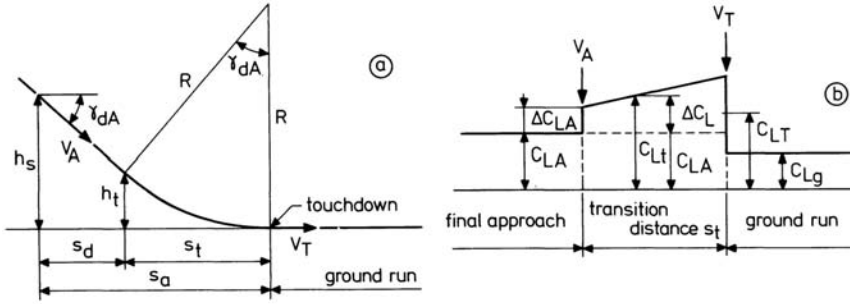


Figure 16.15 Schematic for landing flare analysis

Using appropriate values for γ_{dA} , V_A and n_A , we find from Equations (16.46) and (16.47) the dimensions of the landing flare.

From known values of s_t and h_t it is possible to estimate the reduction in speed by integration of Equation (16.14),

$$\int_{V_A}^{V_T} \frac{W}{2g} dV^2 = \int_0^{s_t} (T - D) ds - \int_{h_t}^0 W \gamma ds. \quad (16.48)$$

With $\gamma ds = -\gamma_d ds = dh$, we obtain

$$\int_0^{s_t} \left(\frac{T - D}{W} \right) ds = \frac{V_T^2 - V_A^2}{2g} - h_t. \quad (16.49)$$

Using a mean value for the excess thrust during the transition phase, we may write

$$\frac{V_T^2 - V_A^2}{2g} = \frac{(\overline{T - D})}{W} s_t + h_t. \quad (16.50)$$

In order to transform Equation (16.50) into a suitable form, we set the excess thrust $(\overline{T - D})$ equal to the mean of its values at the start and the end of the flare. At the speed V_A , from Equation (16.40), we have

$$(T - D)_A = -W \gamma_{dA}, \quad (16.51)$$

and at touchdown we find with $W = C_{LT} \frac{1}{2} \rho V_T^2 S$, $D = C_{DT} \frac{1}{2} \rho V_T^2 S$ and $T = 0$,

$$(T - D)_T = -D_T = -W \left[\frac{C_D}{C_L} \right]_T. \quad (16.52)$$

The mean value of the specific excess thrust is therefore

$$\frac{(\overline{T - D})}{W} = \frac{(T - D)_A + (T - D)_T}{2W} = -\frac{1}{2} \left[\gamma_{dA} + \left[\frac{C_D}{C_L} \right]_T \right]. \quad (16.53)$$

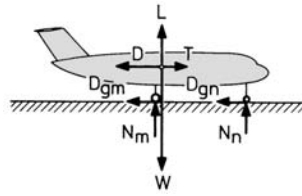


Figure 16.16 Forces acting during landing ground run

Insertion of Equation (16.53) into Equation (16.50) produces the following expression for the flare distance

$$\frac{V_A^2 - V_T^2}{2g} = \frac{1}{2} s_t \left[\gamma_{dA} + \left[\frac{C_D}{C_L} \right]_T \right] - h_t. \quad (16.54)$$

As mentioned already in Section 16.5, to comply with most airworthiness regulations, the airspeed V_A at the start of the transition flare is more than or equal to $1.3 V_{MS}$. Usually, the pilot technique is such that at touchdown the airspeed is reduced to about $1.15 V_{MS}$.

16.7 The landing ground run

After touchdown an adjustment in incidence must be made to settle the airplane in its ground attitude. This requires some rotation of the airplane, during which a free roll is traversed before the wheel brakes are applied.

However, for the sake of simplicity, we shall neglect the distance covered during the rotation phase. In other words, we shall presume that at touchdown the pilot instantaneously accomplishes an angle of attack reduction to the ground attitude value at which $C_L = C_{Lg}$ (see Figure 16.15b).

In Figure 16.16 are shown the forces on the airplane during the landing ground run. The equation of motion in forward direction reads:

$$\frac{W}{g} \frac{dV}{dt} = T - D - D_g, \quad \text{where} \quad (16.55)$$

$$D_g = \mu(N_n + N_m) = \mu(W - L) \quad (16.56)$$

is the frictional force resulting from the adhesion forces acting between the tires and the ground (Figure 16.17a). When a brake torque is applied to a wheel, it is reacted by an increased frictional force, through which the wheel is forced to slow its rotational speed ωr relative to the forward speed V of the wheel. At a brake torque Q , the rotational motion, approximately, is governed by

$$I \frac{d\omega}{dt} = D_g r - Q, \quad (16.57)$$

where I is the moment of inertia of the wheel with respect to its axis of rotation, ω the angular velocity of the braked wheel, and r is the wheel radius.

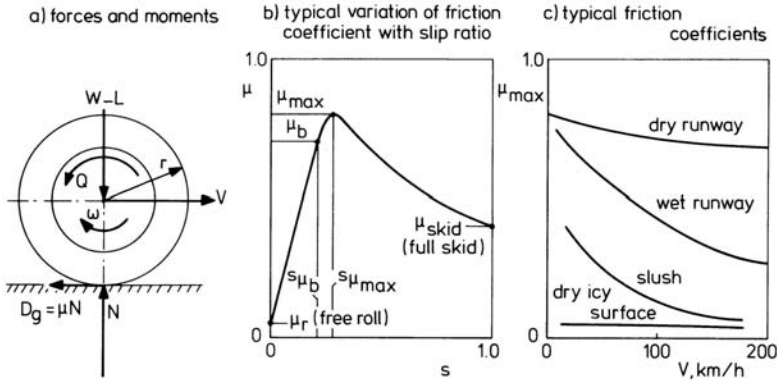


Figure 16.17 Application of brake torque on a rolling wheel

For steady braking, from Equation (16.57), we have the condition

$$D_g = \mu N = Q/r, \tag{16.58}$$

where Q/r is the brake force μ applied to the wheel.

The generated friction coefficient μ varies with the so-called *braking slip ratio*, s , defined by

$$s = \frac{V - \omega r}{V}. \tag{16.59}$$

The variation of μ with s is illustrated in Figure 16.17b. As the slip ratio increases, the friction coefficient rises from its free roll value μ_r at $s = 0$ to a peak value μ_{\max} at a slip ratio $s_{\mu \max}$.

It should be remarked that up to this slip ratio, practically, there is only an apparent slip due to the elastic deformation of the tire.

After $s_{\mu \max}$ is reached, unless the brake is released, the slip ratio increases rapidly which leads to skidding of the wheel at $s = 1.0$ and a low value of the associated friction coefficient, μ_{skid} .

From Figure 16.17b and Equation (16.57), it can also be understood that for $s < s_{\mu \max}$ the wheel rotational motion is in a condition of stable equilibrium. On the contrary, in the region $s > s_{\mu \max}$, any rotational speed disturbance will tend to diverge the slip ratio further from its original value.

From the foregoing discussion it is evident that rolling wheels are forced by braking action to slow their angular velocity from the free roll condition ($\omega = V/r$) to a locked condition ($\omega = 0$), provided the brake forces continuously exceed the produced frictional forces.

When the brakes are controlled manually, it is not easy for a pilot to adjust and maintain a consistent braking condition at $s_{\mu \max}$. This problem is largely solved by the use of anti-skid devices in which brake control is achieved automatically by reference to the slip ratio. These systems avoid excessive tire wear and effectuate an optimum friction coefficient μ_b at a slip ratio below $s_{\mu \max}$ (see Figure

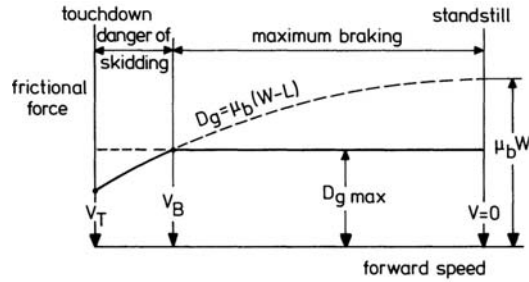


Figure 16.18 Attainable frictional force during ground run

16.17b). Modern systems may produce a value of μ_b up to 90 percent of μ_{\max} . As portrayed in Figure 16.17c, the attainable value of the friction coefficient depends strongly on the surface condition of the runway and the forward speed (Reference 39, Vol. 3).

At the start of the ground run only a fraction of the available brake torque can be applied owing to the low normal force on the wheels at high forward speeds. Therefore, the ground run must be divided into two parts (Figure 16.18). During the first part, we can assume that the friction coefficient is constant and equal to μ_b . This implies that the brake force must be gradually increased with decreasing forward velocity. During the second part, the “torque-limited” brake force, Q_{\max}/r , is insufficient to generate the maximum attainable frictional force,

$$Q_{\max}/r < \mu_b(W - L). \quad (16.60)$$

Under this condition, the brakes can operate at full capacity and a constant frictional force is obtained at a decreasing friction coefficient as the airplane slows down,

$$D_{g \max} = Q_{\max}/r = \mu(W - L). \quad (16.61)$$

On a dry runway, the frictional force $D_{g \max}$ may be 30 to 40 percent of the weight of the airplane.

The speed V_B at which the lift is sufficiently reduced that full braking is permitted, follows from the equality

$$D_{g \max} = \mu_b(W - C_{Lg} \frac{1}{2} \rho V_B^2 S), \quad (16.62)$$

where C_{Lg} is the lift coefficient in the ground running condition.

Thus, in the speed range from V_T down to V_B , the wheels can be made to skid except if use is made of automatic brakes.

The distance covered from the touchdown speed to rest, in general, is given by

$$s_b = \int_{V_T}^0 \frac{V dV}{a}, \quad (16.63)$$

where $a = dV/dt < 0$.

For an accurate calculation of s_b , Equation (16.63) can be evaluated by step by step integration. In the following, however, we will develop analytic expressions which allow direct calculation of the ground run distance. For that end, we assume automatic brakes, zero thrust, and a constant angle of attack throughout the ground run. Then from Equations (16.55), (16.56), and (16.63), we readily obtain for the ground run distance between the speeds V_T and V_B ,

$$s_{b1} = \int_{V_T}^{V_B} \frac{V dV}{g \left[-\mu_b - (C_{Dg} - \mu_b C_{Lg}) \frac{1/2 \rho V^2}{W/S} \right]}, \quad (16.64)$$

where the lift and drag coefficients C_{Lg} and C_{Dg} are, of course, the appropriate values considering the effect of ground proximity.

Using the condition $W = C_{LT} \frac{1}{2} \rho V_T^2 S$, we can transform Equation (16.64) into the form

$$\begin{aligned} s_{b1} &= \int_{V_T}^{V_B} \frac{V dV}{-g \mu_b \left[1 + \frac{(C_{Dg} - \mu_b C_{Lg}) V^2}{\mu_b C_{LT} V_T^2} \right]} \\ &= \int_{V_T}^{V_B} \frac{V dV}{-g \mu_b \left[1 + Z(V^2/V_T^2) \right]}, \end{aligned} \quad (16.65)$$

where $Z = (C_{Dg} - \mu_b C_{Lg}) / (\mu_b C_{LT})$. Integrating Equation (16.65) yields

$$s_{b1} = \frac{V_T^2}{2g \mu_b Z} \ln \frac{1+Z}{1+Z(V_B^2/V_T^2)}. \quad (16.66)$$

Below the speed V_B , the acceleration is given by

$$a = \frac{dV}{dt} = \frac{g}{W} (-C_{Dg} \frac{1}{2} \rho V^2 S - D_{g \max}). \quad (16.67)$$

From Equation (16.63), with V_T replaced by V_B , the ground run distance between the speed V_B and standstill is

$$s_{b2} = \int_{V_B}^0 \frac{V dV}{-\frac{g}{W} (C_{Dg} \frac{1}{2} \rho V^2 S + D_{g \max})}. \quad (16.68)$$

Integration gives

$$s_{b2} = \frac{W}{C_{Dg} \rho g S} \ln \left[\frac{C_{Dg} \frac{1}{2} \rho V_B^2 S}{D_{g \max}} + 1 \right]. \quad (16.69)$$

The results of the analysis in this section manifest that for a short ground run distance we need a large deceleration force.

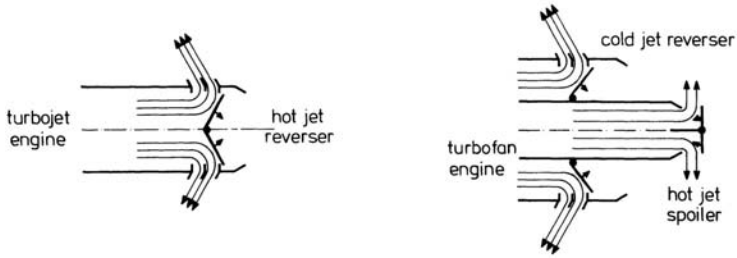


Figure 16.19 Thrust reversal

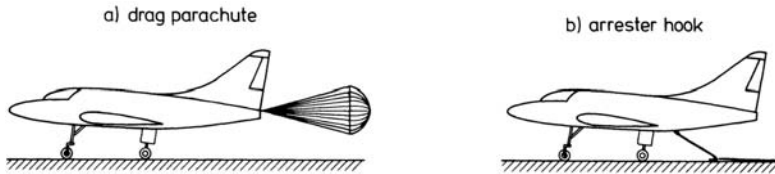


Figure 16.20 Special types of braking devices

An adequate aid in dissipating kinetic energy of jet-driven airplanes is to divert the exhaust gas flow of the engines in a forward direction by means of thrust reversers (Figure 16.19). In the case of a turbofan engine, negative thrust is obtained by reversing the cold jet through the fan. Because this airflow provides enough reverse thrust, the hot jet is then only directed in a normal direction to avoid it neutralizing the reversal effect from the cold jet.

On propeller-driven airplanes, reverse thrust is accomplished by using reversible pitch propellers (see Figure 7.19).

In addition to wheel brakes and propulsive means, ground spoilers on the wings are used to destroy or reduce the lift. This condition increases the ground friction drag as the normal force on the wheels is increased (see also Section 11.3).

Another aerodynamic means to increase the retardation force during the landing run is the braking parachute for use on high performance (military) airplanes (Figure 16.20a). A very special form of a brake system is a cable laid across the flight deck of an aircraft carrier for catching the arrester hook on the airplane (Figure 16.20b).

Appendices

Appendix A

NEWTONIAN MECHANICS

A.1 Newton's laws of motion

The essential equations describing the motion of bodies are based on Newton's laws of motion. Below are stated these laws for a particle, i.e., a constant mass concentrated in a point.

Law 1: Every particle continues in a state of rest or uniform motion in a straight line unless compelled to do otherwise by forces acting on it.

Law 2: The time rate of change of linear momentum of a particle is proportional to the impressed force and is effective in the direction of the force.

Law 3: Action = reaction; or, the mutual forces that two particles exert on each other are equal in magnitude and opposite in direction.

A.2 Newton's first law

It should be fully appreciated that Newton's first law holds only with respect to a frame of reference which is in a state of absolute rest. For instance, we may think on a coordinate system rigidly associated with the "fixed stars" in our solar system. Such a hypothetical coordinate system is called an inertial frame of reference.

However, Newton's first law also holds with respect to reference frames which translate uniformly relative to our inertial frame of reference at rest.

To prove this, let $X_0Y_0Z_0$ be the inertial frame, and assume a frame $X_1Y_1Z_1$ to be translating uniformly with velocity \vec{V}_{10} relative to $X_0Y_0Z_0$ (Figure A.1).

The instantaneous position of a particle in point P with respect to $X_0Y_0Z_0$ and $X_1Y_1Z_1$ is given by the vectors \vec{r}_0 and \vec{r}_1 , respectively. The vector \vec{R} in Figure A.1 indicates at a given point of time the position of the origin of $X_1Y_1Z_1$ relative to $X_0Y_0Z_0$. The three vectors are related by

$$\vec{r}_0 = \vec{R} + \vec{r}_1. \quad (\text{A.1})$$

Differentiating Equation (A.1) gives

$$\frac{d_0\vec{r}_0}{dt} = \frac{d_0\vec{R}}{dt} + \frac{d_0\vec{r}_1}{dt}, \quad (\text{A.2})$$

where the subscript "0" denotes that the time derivative is taken with respect to the inertial frame $X_0Y_0Z_0$.

Since there is a constant difference between the time coordinates, Equation (A.2) can be written as

$$\frac{d_0\vec{r}_0}{dt} = \frac{d_0\vec{R}}{dt} + \frac{d_1\vec{r}_1}{dt}, \quad (\text{A.3})$$

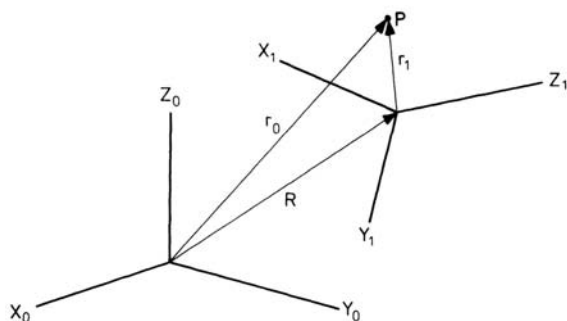


Figure A.1 Transformation of coordinates

in which the subscript "1" indicates that the derivative of \vec{r}_1 is taken with respect to the frame $X_1Y_1Z_1$.

If the particle is free of force, then its velocity relative to the inertial frame $X_0Y_0Z_0$ must be constant.

Hence, $\frac{d_0\vec{r}_0}{dt} = \vec{V}$ is a constant. Since also $\frac{d_0\vec{R}}{dt} = \vec{V}_{10}$ is a constant, it follows from Equation (A.3) that $\frac{d_1\vec{r}_1}{dt} = \vec{V}$, being the velocity of the particle relative to the frame $X_1Y_1Z_1$, is a constant too. Thus Newton's first law of motion is valid in any reference frame that moves uniformly with respect to the frame at rest.

Therefore, all nonaccelerating and nonrotating frames can be used as inertial frames of reference.

A.3 Newton's second law of motion

The mathematical formulation of the second law is

$$\vec{F} = \frac{d}{dt}(M_i\vec{V}), \quad (\text{A.4})$$

where \vec{F} is the vector force acting, and $M_i\vec{V}$ is the linear momentum of a particle with mass M_i and velocity \vec{V} .

Since the mass of a particle is constant, Equation (A.4) can be expressed as

$$\vec{F} = M_i \frac{d\vec{V}}{dt} = M_i\vec{a}, \quad (\text{A.5})$$

where $\frac{d\vec{V}}{dt} = \vec{a}$ is the acceleration of the particle.

It is important to realize that also Equation (A.5) holds only when applied with respect to an inertial frame of reference. From the preceding discussion of Newton's first law we know that coordinate systems translating uniformly to our frame at rest somewhere in the universe, also are inertial frames of reference.

To use this statement, the invariance of the second law under the coordinate transformation must be proved. Therefore, consider the particle in point P in Figure

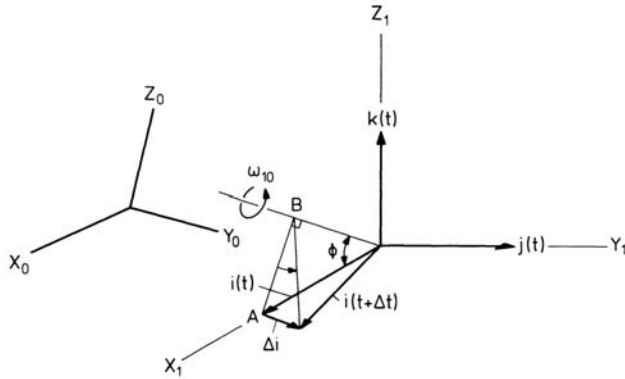


Figure A.2 Frame $X_1Y_1Z_1$ rotating with respect to the frame $X_0Y_0Z_0$

A.1. Since the force acting on the particle is invariant ($\vec{F} = \vec{F}_0 = \vec{F}_1$), from Equation (A.3), it follows that the time rates of change of momentum of the particle with respect to the reference frames $X_0Y_0Z_0$ and $X_1Y_1Z_1$ are related by

$$\frac{d_0}{dt} \left[M_i \frac{d_0 \vec{r}_0}{dt} \right] = \frac{d_1}{dt} \left[M_i \left[\frac{d_0 \vec{R}}{dt} + \frac{d_1 \vec{r}_1}{dt} \right] \right]. \quad (\text{A.6})$$

Using $\frac{d_0 \vec{R}}{dt} = \vec{V}_{10}$ is a constant, we have

$$\frac{d_0}{dt} \left[M_i \frac{d_0 \vec{r}_0}{dt} \right] = \vec{V}_{10} \frac{d_1 M_i}{dt} + \frac{d_1}{dt} \left[M_i \frac{d_1 \vec{r}_1}{dt} \right]. \quad (\text{A.7})$$

Since the mass M_i is a constant, the latter relation reduces to

$$\frac{d_0}{dt} (M_i \vec{v}) = \frac{d_1}{dt} (M_i \vec{v}_r). \quad (\text{A.8})$$

This equality indicates that Equation (A.5) indeed can be applied to both axis systems.

A.4 Effect of rotation

In order to examine the effect of rotation, consider again the reference frames $X_0Y_0Z_0$ and $X_1Y_1Z_1$. Now suppose that $X_1Y_1Z_1$ is in a rotational motion relative to $X_0Y_0Z_0$. As shown in Figure A.2 the rotational motion is about an axis through the origin and denoted by $\vec{\omega}_{10}$.

In the frame $X_1Y_1Z_1$ the triad of unit vectors in the respective coordinate directions at time t are \vec{i} , \vec{j} and \vec{k} . Figure A.2 shows what happens to the unit vector \vec{i} , when the frame $X_1Y_1Z_1$ rotates about the $\vec{\omega}_{10}$ -axis in the time Δt .

If the line AB is the perpendicular from the tip of \vec{i} to the $\vec{\omega}_{10}$ -axis, then the length of AB is equal to $\sin \phi$. Hence, the indicated change in \vec{i} in the time Δt is

$$|\Delta \vec{i}| = |\vec{\omega}_{10}| \sin \phi \Delta t. \quad (\text{A.9})$$

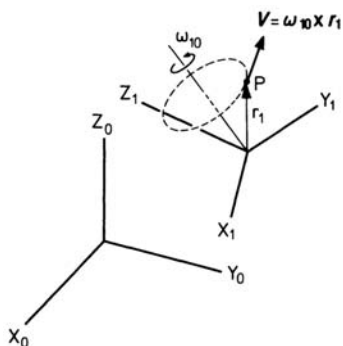


Figure A.3 Rotating coordinate system

By applying the cross or vector product of two vectors we can write

$$|\vec{\omega}_{10} \times \vec{i}| = |\vec{\omega}_{10}| \times |\vec{i}| \sin \phi = |\vec{\omega}_{10}| \sin \phi. \quad (\text{A.10})$$

Combining Equations (A.9) and (A.10) yields

$$|\Delta \vec{i}| = |\vec{\omega}_{10} \times \vec{i}| \Delta t. \quad (\text{A.11})$$

By passing to the limit

$$\lim_{\Delta t \rightarrow 0} \frac{\Delta \vec{i}}{\Delta t} = \frac{d\vec{i}}{dt} = \vec{\omega}_{10} \times \vec{i}. \quad (\text{A.12})$$

Since \vec{i} , \vec{j} and \vec{k} are similar unit vectors, we have

$$\left. \begin{aligned} \frac{d_0 \vec{i}}{dt} &= \vec{\omega}_{10} \times \vec{i} \\ \frac{d_0 \vec{j}}{dt} &= \vec{\omega}_{10} \times \vec{j} \\ \frac{d_0 \vec{k}}{dt} &= \vec{\omega}_{10} \times \vec{k} \end{aligned} \right\}. \quad (\text{A.13})$$

From this result we may establish that for a point P fixed in $X_1Y_1Z_1$ and having a position vector \vec{r}_1 , relative to the origin of $X_1Y_1Z_1$, the velocity due to the rotation is given by (Figure A.3)

$$\vec{V} = \vec{\omega}_{10} \times \vec{r}_1. \quad (\text{A.14})$$

With Equation (A.14) we can derive a relation between the time derivative of the vector \vec{V} in the rotating frame $X_1Y_1Z_1$ to the time derivative of that vector in the nonrotating frame $X_0Y_0Z_0$. Therefore we proceed to consider the fact that the vector \vec{V} can be expressed as

$$\vec{V} = V_x \vec{i} + V_y \vec{j} + V_z \vec{k}, \quad (\text{A.15})$$

where V_x , V_y and V_z are the components of \vec{V} in the frame $X_1Y_1Z_1$. By differentiating \vec{V} with respect to $X_1Y_1Z_1$ we obtain

$$\frac{d_1 \vec{V}}{dt} = \frac{dV_x}{dt} \vec{i} + \frac{dV_y}{dt} \vec{j} + \frac{dV_z}{dt} \vec{k}. \quad (\text{A.16})$$

The subscript "1" is omitted in the derivatives of the three scalar quantities as the derivative of a scalar quantity is the same in all reference frames.

The derivative of the vector \vec{V} with respect to $X_0Y_0Z_0$ is

$$\frac{d_0\vec{V}}{dt} = \frac{dV_x}{dt}\vec{i} + \frac{dV_y}{dt}\vec{j} + \frac{dV_z}{dt}\vec{k} + V_x\frac{d_0\vec{i}}{dt} + V_y\frac{d_0\vec{j}}{dt} + V_z\frac{d_0\vec{k}}{dt}. \quad (\text{A.17})$$

If Equations (A.16) and (A.13) are substituted into Equation (A.17), it follows that

$$\frac{d_0\vec{V}}{dt} = \frac{d_1\vec{V}}{dt} + \vec{\omega}_{10} \times (V_x\vec{i} + V_y\vec{j} + V_z\vec{k}). \quad (\text{A.18})$$

Using Equation (A.15), the latter result can be written as

$$\frac{d_0\vec{V}}{dt} = \frac{d_1\vec{V}}{dt} + \vec{\omega}_{10} \times \vec{V}. \quad (\text{A.19})$$

It must be emphasized that Equation (A.19) is a general relation which applies to any vector whatever. Thus for a vector \vec{P} :

$$\frac{d_0\vec{P}}{dt} = \frac{d_1\vec{P}}{dt} + \vec{\omega}_{10} \times \vec{P}. \quad (\text{A.20})$$

It is also important to note that Equation (A.20) holds for any pair of systems rotating relative to each other.

A.5 Noninertial reference frames

Now the case is considered that a frame $X_1Y_1Z_1$ is translating and rotating in a general manner relative to the inertial frame $X_0Y_0Z_0$.

Using Equation (A.20), we can express Equation (A.2) as follows

$$\frac{d_0\vec{r}_0}{dt} = \frac{d_0\vec{R}}{dr} + \frac{d_1\vec{r}_1}{dt} + \vec{\omega}_{10} \times \vec{r}_1. \quad (\text{A.21})$$

Differentiating Equation (A.21) with respect to $X_0Y_0Z_0$ gives

$$\frac{d_0^2\vec{r}_0}{dt^2} = \frac{d_0^2\vec{R}}{dt^2} + \frac{d_0}{dt} \left[\frac{d_1\vec{r}_1}{dt} \right] + \vec{\omega}_{10} \times \frac{d_0\vec{r}_1}{dt} + \frac{d_0\vec{\omega}_{10}}{dt} \times \vec{r}_1. \quad (\text{A.22})$$

The left-hand term of this equation is the acceleration of P with respect to $X_0Y_0Z_0$ and is called the *absolute acceleration*, \vec{a} . Equation (A.20) enables us to develop from Equation (A.22) the following expression for the absolute acceleration

$$\vec{a} = \frac{d_0^2\vec{R}}{dt^2} + \frac{d_0\vec{\omega}_{10}}{dt} \times \vec{r}_1 + \vec{\omega}_{10} \times (\vec{\omega}_{10} \times \vec{r}_1) + \frac{d_1^2\vec{r}_1}{dt^2} + 2\vec{\omega}_{10} \times \frac{d_1\vec{r}_1}{dt}. \quad (\text{A.23})$$

The term $\frac{d_0^2\vec{R}}{dt^2}$ is the acceleration of the origin of the moving frame $X_1Y_1Z_1$ with respect to $X_0Y_0Z_0$. The term $\frac{d_0\vec{\omega}_{10}}{dt} \times \vec{r}_1$ is called the *tangential acceleration* owing

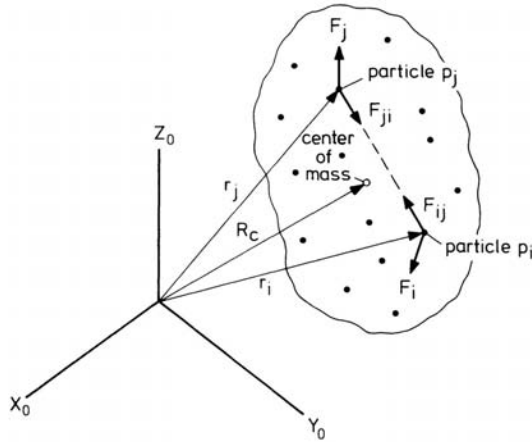


Figure A.4 System of particles in an inertial frame

to the rotational acceleration of $X_1Y_1Z_1$ relative to $X_0Y_0Z_0$. The term $\vec{\omega}_{10} \times (\vec{\omega}_{10} \times \vec{r}_1)$ is caused by the rotation of $X_1Y_1Z_1$ with respect to $X_0Y_0Z_0$ and represents the *centripetal acceleration*.

The sum of these three terms is the acceleration of the point P fixed to $X_1Y_1Z_1$ as seen by an observer in the frame $X_0Y_0Z_0$, and is named the *transport acceleration*, \vec{a}_t .

The term $\frac{d^2\vec{r}_1}{dt^2}$ is the acceleration of P with respect to the frame $X_1Y_1Z_1$ and is called the *relative acceleration* \vec{a}_r . The term $2\vec{\omega}_{10} \times \frac{d\vec{r}_1}{dt}$, finally, is the so-called *Coriolis acceleration*, \vec{a}_c . The sum of the last two terms of the right-hand side of Equation (A.23) is the acceleration of the particle relative to $X_1Y_1Z_1$ for an observer in the frame $X_0Y_0Z_0$.

If \vec{F} is the total force acting on a particle, then according to Equations (A.5) and (A.23) we can write the following vector equation:

$$\vec{F} = M_i\vec{a} = M_i\vec{a}_t + M_i\vec{a}_r + M_i\vec{a}_c \quad \text{or} \quad (\text{A.24})$$

$$\vec{F} - M_i\vec{a}_t - M_i\vec{a}_c = M_i\vec{a}_r. \quad (\text{A.25})$$

Apparently, Newton's second law of motion can be used to determine the motion of a particle relative to noninertial frames by modifying the actual force according to the left-hand side of Equation (A.25).

A.6 Systems of particles

We now consider a mass system, which consists of n particles with masses M_1, M_2, \dots, M_n and with position vectors $\vec{r}_1, \vec{r}_2, \dots, \vec{r}_n$ relative to the origin of an inertial frame $X_0Y_0Z_0$ (Figure A.4).

The forces acting on particle p_i may be formed by an external force \vec{F}_i and internal forces due to the interactions among the particles.

According to Newton's third law of motion we can write for the internal forces acting along a straight line between two particles:

$$\vec{F}_{ij} = -\vec{F}_{ji}, \quad (\text{A.26})$$

where \vec{F}_{ij} is the internal force acting on particle p_i due to particle p_j , and \vec{F}_{ji} is the internal force acting on particle p_j due to particle p_i .

Applying Newton's second law of motion on particle p_i , we obtain

$$\vec{F}_i + \sum_{j=1}^n \vec{F}_{ij} = \frac{d}{dt} \left[M_i \frac{d\vec{r}_i}{dt} \right], \quad (\text{A.27})$$

where the quantity $M_i \frac{d\vec{r}_i}{dt}$ is the linear momentum of particle p_i relative to $X_0Y_0Z_0$. Note that the subscript "0" is not appended to the vector symbols since only the inertial frame $X_0Y_0Z_0$ is used in the present analysis.

Summing of all particles of the system gives

$$\sum_{i=1}^n \vec{F}_i + \sum_{i=1}^n \sum_{j=1}^n \vec{F}_{ij} = \sum_{i=1}^n \frac{d}{dt} \left[M_i \frac{d\vec{r}_i}{dt} \right]. \quad (\text{A.28})$$

Since Equation (A.26) indicates that the internal forces occur in equal and opposite pairs, we have $\sum_{i=1}^n \sum_{j=1}^n \vec{F}_{ij} = 0$, and Equation (A.28) reduces to

$$\sum_{i=1}^n \vec{F}_i = \sum_{i=1}^n \frac{d}{dt} \left[M_i \frac{d\vec{r}_i}{dt} \right] = \sum_{i=1}^n M_i \frac{d^2\vec{r}_i}{dt^2}. \quad (\text{A.29})$$

If we consider an invariable mass system (n is a constant), in Equation (A.29) summation and differentiation can be interchanged, yielding

$$\vec{F} = \sum_{i=1}^n \vec{F}_i = \frac{d^2}{dt^2} \left[\sum_{i=1}^n M_i \vec{r}_i \right], \quad (\text{A.30})$$

where \vec{F} is the entire external force applied to the system.

Now let $\sum_{i=1}^n M_i = M$ be the total mass of the system. Further we introduce the position vector of the center of mass of the system, defined by

$$\vec{R}_c = \frac{1}{M} \sum_{i=1}^n M_i \vec{r}_i. \quad (\text{A.31})$$

Substituting the latter quantities in Equation (A.30) yields

$$\vec{F} = M \frac{d^2\vec{R}_c}{dt^2}. \quad (\text{A.32})$$

This equation indicates that the translational motion of the center of mass of the system is the same as if the total mass is located at the center of mass and subjected to the entire external force.

Equation (A.32) also has an equivalent form regarding angular motion, which is obtained by vectorial multiplication of Equation (A.27) with \vec{r}_i ,

$$\vec{r}_i \times \vec{F}_i + \sum_{j=1}^n (\vec{r}_i \times \vec{F}_{ij}) = \vec{r}_i \times \frac{d}{dt} \left[M_i \frac{d\vec{r}_i}{dt} \right]. \quad (\text{A.33})$$

The moment of \vec{F}_i with respect to the origin of $X_0Y_0Z_0$ is expressed by the vector product of \vec{F}_i and \vec{r}_i : $\vec{M}_i = \vec{r}_i \times \vec{F}_i$.

Note that besides the mass also a moment is given the symbol \vec{M} .

The angular momentum of a particle p_i is given by

$$\vec{B}_i = \vec{r}_i \times \vec{M}_i \frac{d\vec{r}_i}{dt} \quad \text{and hence} \quad (\text{A.34})$$

$$\frac{d\vec{B}_i}{dt} = \frac{d}{dt} \left[\vec{r}_i \times \vec{M}_i \frac{d\vec{r}_i}{dt} \right] = \vec{r}_i \times \frac{d}{dt} \left[\vec{M}_i \frac{d\vec{r}_i}{dt} \right]. \quad (\text{A.35})$$

Thus, Equation (A.33) can be written as

$$\vec{M}_i + \sum_{j=1}^n (\vec{r}_i \times \vec{F}_{ij}) = \frac{d\vec{B}_i}{dt}. \quad (\text{A.36})$$

For the complete system we obtain

$$\sum_{j=1}^n \vec{M}_i + \sum_{i=1}^n \sum_{j=1}^n (\vec{r}_i \times \vec{F}_{ij}) = \sum_{i=1}^n \frac{d\vec{B}_i}{dt}. \quad (\text{A.37})$$

It easily may be seen from Equation (A.26) that the second term of the left-hand side of Equation (A.37) is equal to zero. If we denote $\sum_{i=1}^n \vec{M}_i = \vec{M}$ as the entire moment with respect to the origin of the reference frame $X_0Y_0Z_0$, then, from Equations (A.37) and (A.35), we find

$$\vec{M} = \sum_{i=1}^n \frac{d\vec{B}_i}{dt} = \sum_{i=1}^n \frac{d}{dt} \left[\vec{r}_i \times \vec{M}_i \frac{d\vec{r}_i}{dt} \right] = \sum_{i=1}^n \left[\vec{r}_i \times \vec{M}_i \frac{d^2\vec{r}_i}{dt^2} \right]. \quad (\text{A.38})$$

Putting again summation and differentiation in the other's place produces the expression:

$$\vec{M} = \frac{d}{dt} \left[\sum_{i=1}^n \vec{r}_i \times \vec{M}_i \frac{d\vec{r}_i}{dt} \right] = \frac{d\vec{B}}{dt}. \quad (\text{A.39})$$

Equation (A.39) says that the external moment applied to a system of particles is equal to the time derivative of its total angular momentum.

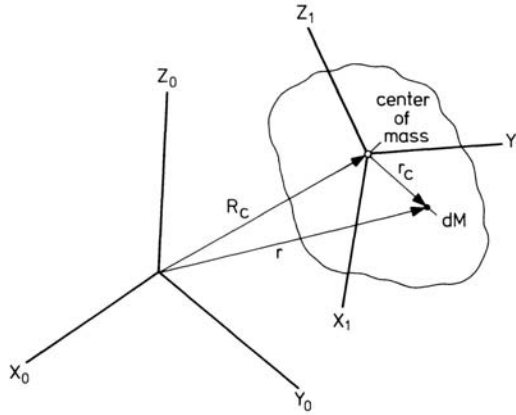


Figure A.5 Position vectors of an element of mass of a body

A.7 General bodies

A body may be considered as being made up of an infinite number of elements of which the mass is infinitesimally small. Consequently, the summations in the Equations (A.30) and (A.38) must be altered into integrations. This yields (Figure A.5)

$$\vec{F} = \int_M \frac{d^2\vec{r}}{dt^2} dM \quad \text{and} \quad (\text{A.40})$$

$$\vec{M} = \int_M \vec{r} \times \frac{d^2\vec{r}}{dt^2} dM. \quad (\text{A.41})$$

If \vec{R}_c is the position vector of the center of mass of the body and \vec{r}_c is the position vector of an element of mass dM of the body relative to the mass center, then

$$\vec{r} = \vec{R}_c + \vec{r}_c. \quad (\text{A.42})$$

The vector \vec{R}_c now is defined by

$$\vec{R}_c = \frac{1}{M} \int_M \vec{r} dM, \quad (\text{A.43})$$

where $M = \int_M dM$ is the mass of the body.

By using Equation (A.42) in Equation (A.23), the absolute acceleration of the element dM can be written as

$$\frac{d^2\vec{r}}{dt^2} = \frac{d^2\vec{R}_c}{dt^2} + \frac{d\vec{\omega}}{dt} \times \vec{r}_c + \vec{\omega} \times (\vec{\omega} \times \vec{r}_c) + \frac{\delta^2\vec{r}_c}{\delta t^2} + 2\vec{\omega} \times \frac{\delta\vec{r}_c}{\delta t}, \quad (\text{A.44})$$

where $\vec{\omega}$ is the angular velocity relative to the inertial frame $X_0Y_0Z_0$, and $\frac{\delta\vec{r}_c}{\delta t}$ and $\frac{\delta^2\vec{r}_c}{\delta t^2}$ are derivatives of the vector \vec{r}_c with respect to the center of mass of the body.

Insertion of Equation (A.42) into Equation (A.43) yields

$$\int_M \vec{r}_c dM = 0. \quad (\text{A.45})$$

Combining Equations (A.40), (A.44) and (A.45) furnishes

$$\vec{F} = \int_M \frac{d^2 \vec{R}_c}{dt^2} dM + \int_M \frac{\delta^2 \vec{r}_c}{\delta t^2} dM + 2\vec{\omega} \times \int_M \frac{\delta \vec{r}_c}{\delta t} dM. \quad (\text{A.46})$$

This is the general equation for the translational motion of an arbitrary deformable body of mass M .

Similarly, Equation (A.41) for the rotational motion can be expanded to the same variables by taking the center of mass of the body as the reference point for the calculations.

The moment due to the entire external force with respect to the center of mass of the body can be expressed as

$$\vec{M}_c = \vec{M} - \vec{R}_c \times \vec{F}, \quad (\text{A.47})$$

where \vec{M} is the moment relative to the origin of the frame $X_0 Y_0 Z_0$.

By substituting Equations (A.40) to (A.42) into Equation (A.47), we find

$$\vec{M}_c = \int_M \vec{r}_c \times \frac{d^2 \vec{r}}{dt^2} dM. \quad (\text{A.48})$$

Insertion of Equation (A.44) into Equation (A.48) yields the equation for rotational motion of a general deformable body,

$$\begin{aligned} \vec{M}_c = & \int_M \vec{r}_c \times \left(\frac{d\vec{\omega}}{dt} \times \vec{r}_c \right) dM + \int_M \vec{r}_c \times (\vec{\omega} \times (\vec{\omega} \times \vec{r}_c)) dM + \\ & + \int_M \vec{r}_c \times \frac{\delta^2 \vec{r}_c}{\delta t^2} dM + \int_M \vec{r}_c \times (2\vec{\omega} \times \frac{\delta \vec{r}_c}{\delta t}) dM. \end{aligned} \quad (\text{A.49})$$

In deriving this equation, we used the facts that $\frac{d^2 \vec{R}_c}{dt^2}$ bears no relation to dM and $\int_M \vec{r}_c dM = 0$, so that

$$\int_M \vec{r}_c \times \frac{d^2 \vec{R}_c}{dt^2} dM = \int_M \vec{r}_c dM \times \frac{d^2 \vec{R}_c}{dt^2} = 0. \quad (\text{A.50})$$

A.8 Rigid bodies

The rigid body approximation requires that $\frac{\delta \vec{r}_c}{\delta t}$ and $\frac{\delta^2 \vec{r}_c}{\delta t^2}$ are equal to zero so that the Equations (A.46) and (A.49) reduce to

$$\vec{F} = \int_M \frac{d^2 \vec{R}_c}{dt^2} dM \quad \text{and} \quad (\text{A.51})$$

$$\vec{M}_c = \int_M \vec{r}_c \times \left(\frac{d\vec{\omega}}{dt} \times \vec{r}_c \right) dM + \int_M \vec{r}_c \times (\vec{\omega} \times (\vec{\omega} \times \vec{r}_c)) dM. \quad (\text{A.52})$$

In order to recast Equation (A.52) in a more familiar form, we introduce, from Equation (A.48), the relationship

$$\vec{B}_c = \int_M \vec{r}_c \times \frac{d\vec{r}}{dt} dM. \quad (\text{A.53})$$

Inserting Equation (A.42) into (A.53) furnishes

$$\vec{B}_c = \int_M \vec{r}_c \times \frac{d\vec{R}_c}{dt} dM + \int_M \vec{r}_c \times \frac{d\vec{r}_c}{dt} dM. \quad (\text{A.54})$$

Analogous to Equation (A.50), we find that the first integral of Equation (A.54) vanishes,

$$\int_M \vec{r}_c \times \frac{d\vec{R}_c}{dt} dM = \int_M \vec{r}_c dM \times \frac{d\vec{R}_c}{dt} = 0. \quad (\text{A.55})$$

Applying Equation (A.20) for the rate of change of the vector \vec{r}_c we obtain

$$\frac{d\vec{r}_c}{dt} = \frac{\delta \vec{r}_c}{\delta t} + (\vec{\omega} \times \vec{r}_c) = \vec{\omega} \times \vec{r}_c. \quad (\text{A.56})$$

Thus by substituting Equation (A.56) into Equation (A.54) we find that for a rigid body the total angular momentum relative to the center of mass is given by

$$\vec{B}_c = \int_M \vec{r}_c \times (\vec{\omega} \times \vec{r}_c) dM. \quad (\text{A.57})$$

By combining Equation (A.52) and (A.57) we, finally, get

$$\vec{M}_c = \int_M \vec{r}_c \times \left(\frac{d\vec{\omega}}{dt} \times \vec{r}_c \right) dM + \vec{\omega} \times \vec{B}_c. \quad (\text{A.58})$$

This equation is often used in solving for the rotational motion of rigid bodies.

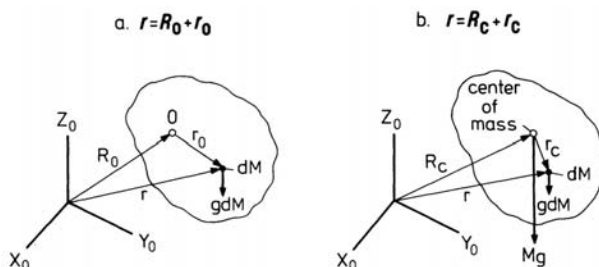


Figure A.6 Force and moment due to the gravity forces

A.9 Center of gravity

The center of gravity, being the point through which the gravity force or weight of the body acts, is identical with the center of mass.

To show this, we consider a body as in Figure A.6a. The moment due to the forces of gravity about the origin of the frame $X_0Y_0Z_0$ is given by

$$\vec{M} = \int_M \vec{r} \times \vec{g} dM, \quad (\text{A.59})$$

where \vec{g} is the acceleration of gravity, the gravity force per unit mass.

With $\vec{r} = \vec{R}_0 + \vec{r}_0$, we obtain

$$\vec{M} = \int_M (\vec{R}_0 + \vec{r}_0) \times \vec{g} dM = \vec{R}_0 \times \int_M \vec{g} dM + \int_M \vec{r}_0 \times \vec{g} dM. \quad (\text{A.60})$$

If we assume that \vec{g} is constant over the body, we can rewrite Equation (A.60) as

$$\vec{M} = \vec{R}_0 \times M\vec{g} + \int_M \vec{r}_0 dM \times \vec{g}. \quad (\text{A.61})$$

When we choose the point O in Figure A.6a at the center of mass of the body, the last term vanishes according to Equation (A.45), giving,

$$\vec{M} = \vec{R}_c \times M\vec{g}, \quad (\text{A.62})$$

where \vec{R}_c is the position vector of the center of mass of the body (Figure A.6b).

Thus we see that the entire effect of the gravity forces can be replaced by a single force $M\vec{g}$ acting on the center of mass, which point, therefore, also may be called the center of gravity.

General references for appendix

- N.C. Barford, *Mechanics*, John Wiley, New York, 1973.
- J.W. Cornelisse, H.F.R. Schöyer and K.F. Wakker, *Rocket Propulsion and Space-flight Dynamics*, Pitman, London, 1979.
- B. Etkin, *Dynamics of Atmospheric flight*, John Wiley, New York, 1972.

Appendix B

CONVERSION FACTORS

| QUANTITY | UNIT | SI-EQUIVALENT |
|---------------------|------------------------------|-------------------------------|
| Length | 1 foot (ft) | = 0.3048 m |
| | 1 mile (statute) | = 1.60934 km |
| | 1 n mile (nautical) | = 1.85200 km |
| | 1 inch (in) | = 0.0254 m |
| Area | 1 ft ² | = 0.092903 m ² |
| Volume | 1 imperial gallon | = 4.54609 dm ³ |
| | 1 U.S. gallon | = 3.78541 dm ³ |
| | 1 pint (pt) | = 0.568261 dm ³ |
| | 1 quart (qt) | = 1.13652 dm ³ |
| Velocity | 1 ft/min | = 0.00508 m/s |
| | 1 ft/s | = 0.3048 m/s |
| | 1 mile/h (m.p.h.) | = 1.60934 km/h |
| | 1 n mile/h (knot) | = 1.852 km/h |
| Acceleration | 1 ft/s ² | = 0.3048 m/s ² |
| Mass | 1 pound (lb) | = 0.453592 kg |
| | 1 slug | = 14.5939 kg |
| Mass rate of flow | 1 lb/s | = 0.453592 kg/s |
| Volume rate of flow | 1 gal/h | = 4.54609 dm ³ /h |
| | 1 ft ³ /s | = 0.0283168 m ³ /s |
| Density | 1 lb/ft ³ | = 16.0185 kg/m ³ |
| | 1 slug/ft ³ | = 515.379 kg/m ³ |
| Force | 1 kgf | = 9.80665 N |
| | 1 lbf | = 4.44822 N |
| Moment of force | 1 lbf ft | = 1.35582 Nm |
| Moment of inertia | 1 lb ft ² | = 0.0421401 kg m ² |
| Pressure and stress | 1 lbf/in ² (psi) | = 6.89476 kPa |
| | 1 lbf/ft ² | = 47.8803 Pa |
| | 1 inch mercury (in Hg) | = 3.38639 kPa |
| | 1 atmosphere (atm) | = 101325 N/m ² |
| Dynamic viscosity | 1 lb/ft s | = 1.48816 kg/m s |
| Kinematic viscosity | 1 ft ² /s | = 0.092903 m ² /s |
| Energy and work | 1 ft lbf | = 1.35582 J |
| | 1 Btu | = 1.05506 kJ |
| | 1 kgf m | = 9.80665 J |
| Power | 1 hp (550 ft lbf/s) | = 745.700 W |
| | 1 hp (metric; 75 kgf m/s) | = 735.499 W |
| | 1 ft lbf/s | = 1.35582 W |
| | 1 kgf m/s | = 9.80665 W |
| Heat flow rate | 1 Btu/h | = 0.293071 W |
| Temperature | T °C (celsius; centigrade) | = (T °C + 273.15)K |
| | T °F (fahrenheit) | = 5/9 (T °F + 459.67) K |
| | T °R (rankine) | = 5/9 (T °R) K |

Appendix C

INTERNATIONAL STANDARD ATMOSPHERE

| H , m | T , K | p , N/m ² | ρ , kg/m ³ | c , m/s | $\mu \times 10^5$ kg/m s |
|------------|------------|---------------------------|-------------------------------|--------------|-----------------------------|
| -1000 | 294.65 | 113929 | 1.3470 | 344.11 | 1.8206 |
| -900 | 294.00 | 112614 | 1.3344 | 343.73 | 1.8175 |
| -800 | 293.35 | 111312 | 1.3219 | 343.35 | 1.8144 |
| -700 | 292.70 | 110022 | 1.3095 | 342.97 | 1.8113 |
| -600 | 292.05 | 108744 | 1.2971 | 342.59 | 1.8081 |
| -500 | 291.40 | 107478 | 1.2849 | 342.21 | 1.8050 |
| -400 | 290.75 | 106223 | 1.2728 | 341.82 | 1.8019 |
| -300 | 290.10 | 104981 | 1.2607 | 341.44 | 1.7988 |
| -200 | 289.45 | 103751 | 1.2487 | 341.06 | 1.7956 |
| -100 | 288.80 | 102532 | 1.2368 | 340.68 | 1.7925 |
| 0 | 288.15 | 101325 | 1.2250 | 340.29 | 1.7894 |
| 100 | 287.50 | 100129 | 1.2133 | 339.91 | 1.7862 |
| 200 | 286.85 | 98945 | 1.2017 | 339.52 | 1.7831 |
| 300 | 286.20 | 97773 | 1.1901 | 339.14 | 1.7800 |
| 400 | 285.55 | 96611 | 1.1787 | 338.75 | 1.7768 |
| 500 | 284.90 | 95461 | 1.1673 | 338.37 | 1.7737 |
| 600 | 284.25 | 94322 | 1.1560 | 337.98 | 1.7705 |
| 700 | 283.60 | 93193 | 1.1448 | 337.59 | 1.7673 |
| 800 | 282.95 | 92076 | 1.1337 | 337.21 | 1.7642 |
| 900 | 282.30 | 90970 | 1.1226 | 336.82 | 1.7610 |
| 1000 | 281.65 | 89874 | 1.1117 | 336.43 | 1.7578 |
| 1100 | 281.00 | 88790 | 1.1008 | 336.04 | 1.7547 |
| 1200 | 280.35 | 87715 | 1.0900 | 335.65 | 1.7515 |
| 1300 | 279.70 | 86652 | 1.0793 | 335.27 | 1.7483 |
| 1400 | 279.05 | 85599 | 1.0686 | 334.88 | 1.7451 |
| 1500 | 278.40 | 84556 | 1.0581 | 334.49 | 1.7419 |
| 1600 | 277.75 | 83523 | 1.0476 | 334.09 | 1.7388 |
| 1700 | 277.10 | 82501 | 1.0372 | 333.70 | 1.7356 |
| 1800 | 276.45 | 81489 | 1.0269 | 333.31 | 1.7324 |
| 1900 | 275.80 | 80487 | 1.0167 | 332.92 | 1.7292 |
| 2000 | 275.15 | 79495 | 1.0065 | 332.53 | 1.7260 |
| 2100 | 274.50 | 78513 | 0.9964 | 332.13 | 1.7228 |
| 2200 | 273.85 | 77541 | 0.9864 | 331.74 | 1.7195 |
| 2300 | 273.20 | 76578 | 0.9765 | 331.35 | 1.7163 |
| 2400 | 272.55 | 75625 | 0.9666 | 330.95 | 1.7131 |
| 2500 | 271.90 | 74682 | 0.9569 | 330.56 | 1.7099 |
| 2600 | 271.25 | 73749 | 0.9472 | 330.16 | 1.7067 |

| H , m | T , K | p , N/m ² | ρ , kg/m ³ | c , m/s | $\mu \times 10^5$ kg/m s |
|------------|------------|---------------------------|-------------------------------|--------------|-----------------------------|
| 2700 | 270.60 | 72825 | 0.9375 | 329.77 | 1.7034 |
| 2800 | 269.95 | 71910 | 0.9280 | 329.37 | 1.7002 |
| 2900 | 269.30 | 71004 | 0.9185 | 328.97 | 1.697 |
| 3000 | 268.65 | 70108 | 0.9091 | 328.58 | 1.6937 |
| 3100 | 268.00 | 69221 | 0.8998 | 328.18 | 1.6905 |
| 3200 | 267.35 | 68343 | 0.8906 | 327.78 | 1.6872 |
| 3300 | 266.70 | 67475 | 0.8814 | 327.38 | 1.6840 |
| 3400 | 266.05 | 66615 | 0.8723 | 326.98 | 1.6807 |
| 3500 | 265.40 | 65764 | 0.8632 | 326.58 | 1.6775 |
| 3600 | 264.75 | 64922 | 0.8543 | 326.18 | 1.6742 |
| 3700 | 264.10 | 64088 | 0.8454 | 325.78 | 1.6709 |
| 3800 | 263.45 | 63264 | 0.8366 | 325.38 | 1.6677 |
| 3900 | 262.80 | 62447 | 0.8278 | 324.98 | 1.6644 |
| 4000 | 262.15 | 61640 | 0.8191 | 324.58 | 1.6611 |
| 4100 | 261.50 | 60841 | 0.8105 | 324.17 | 1.6578 |
| 4200 | 260.85 | 60050 | 0.8020 | 323.77 | 1.6545 |
| 4300 | 260.20 | 59268 | 0.7935 | 323.37 | 1.6513 |
| 4400 | 259.55 | 58494 | 0.7851 | 322.96 | 1.6480 |
| 4500 | 258.90 | 57728 | 0.7768 | 322.56 | 1.6447 |
| 4600 | 258.25 | 56970 | 0.7685 | 322.15 | 1.6414 |
| 4700 | 257.60 | 56221 | 0.7603 | 321.75 | 1.6381 |
| 4800 | 256.95 | 55479 | 0.7522 | 321.34 | 1.6347 |
| 4900 | 256.30 | 54745 | 0.7441 | 320.93 | 1.6314 |
| 5000 | 255.65 | 54020 | 0.7361 | 320.53 | 1.6281 |
| 5100 | 255.00 | 53302 | 0.7282 | 320.12 | 1.6248 |
| 5200 | 254.35 | 52591 | 0.7203 | 319.71 | 1.6215 |
| 5300 | 253.70 | 51889 | 0.7125 | 319.30 | 1.6181 |
| 5400 | 253.05 | 51194 | 0.7048 | 318.89 | 1.6148 |
| 5500 | 252.40 | 50506 | 0.6971 | 318.48 | 1.6115 |
| 5600 | 251.75 | 49827 | 0.6895 | 318.07 | 1.6081 |
| 5700 | 251.10 | 49154 | 0.6820 | 317.66 | 1.6048 |
| 5800 | 250.45 | 48489 | 0.6745 | 317.25 | 1.6014 |
| 5900 | 249.80 | 47831 | 0.6671 | 316.84 | 1.5981 |
| 6000 | 249.15 | 47181 | 0.6597 | 316.43 | 1.5947 |
| 6100 | 248.50 | 46537 | 0.6524 | 316.01 | 1.5914 |
| 6200 | 247.85 | 45901 | 0.6452 | 315.60 | 1.5880 |
| 6300 | 247.20 | 45272 | 0.6380 | 315.19 | 1.5846 |
| 6400 | 246.55 | 44650 | 0.6309 | 314.77 | 1.5813 |
| 6500 | 245.90 | 44034 | 0.6238 | 314.36 | 1.5779 |
| 6600 | 245.25 | 43426 | 0.6169 | 313.94 | 1.5745 |
| 6700 | 244.60 | 42825 | 0.6099 | 313.52 | 1.5711 |
| 6800 | 243.95 | 42230 | 0.6031 | 313.11 | 1.5677 |
| 6900 | 243.30 | 41642 | 0.5963 | 312.69 | 1.5644 |

| H , m | T , K | p , N/m ² | ρ , kg/m ³ | c , m/s | $\mu \times 10^5$ kg/m s |
|------------|------------|---------------------------|-------------------------------|--------------|-----------------------------|
| 7000 | 242.65 | 41060 | 0.5895 | 312.27 | 1.5610 |
| 7100 | 242.00 | 40486 | 0.5828 | 311.85 | 1.5576 |
| 7200 | 241.35 | 39917 | 0.5762 | 311.43 | 1.5542 |
| 7300 | 240.70 | 39355 | 0.5696 | 311.01 | 1.5507 |
| 7400 | 240.05 | 38800 | 0.5631 | 310.59 | 1.5473 |
| 7500 | 239.40 | 38251 | 0.5566 | 310.17 | 1.5439 |
| 7600 | 238.75 | 37708 | 0.5502 | 309.75 | 1.5405 |
| 7700 | 238.10 | 37172 | 0.5439 | 309.33 | 1.5371 |
| 7800 | 237.45 | 36642 | 0.5376 | 308.91 | 1.5336 |
| 7900 | 236.80 | 36117 | 0.5313 | 308.48 | 1.5302 |
| 8000 | 236.15 | 35599 | 0.5252 | 308.06 | 1.5268 |
| 8100 | 235.50 | 35087 | 0.5190 | 307.64 | 1.5233 |
| 8200 | 234.85 | 34581 | 0.5130 | 307.21 | 1.5199 |
| 8300 | 234.20 | 34081 | 0.5070 | 306.79 | 1.5164 |
| 8400 | 233.55 | 33587 | 0.5010 | 306.36 | 1.5130 |
| 8500 | 232.90 | 33099 | 0.4951 | 305.93 | 1.5095 |
| 8600 | 232.25 | 32616 | 0.4892 | 305.51 | 1.5061 |
| 8700 | 231.60 | 32139 | 0.4834 | 305.08 | 1.5026 |
| 8800 | 230.95 | 31668 | 0.4777 | 304.65 | 1.4991 |
| 8900 | 230.30 | 31202 | 0.4720 | 304.22 | 1.4956 |
| 9000 | 229.65 | 30742 | 0.4663 | 303.79 | 1.4922 |
| 9100 | 229.00 | 30287 | 0.4608 | 303.36 | 1.4887 |
| 9200 | 228.35 | 29838 | 0.4552 | 302.93 | 1.4852 |
| 9300 | 227.70 | 29395 | 0.4497 | 302.50 | 1.4817 |
| 9400 | 227.05 | 28956 | 0.4443 | 302.07 | 1.4782 |
| 9500 | 226.40 | 28523 | 0.4389 | 301.63 | 1.4747 |
| 9600 | 225.75 | 28095 | 0.4336 | 301.20 | 1.4712 |
| 9700 | 225.10 | 27673 | 0.4283 | 300.77 | 1.4677 |
| 9800 | 224.45 | 27255 | 0.4230 | 300.33 | 1.4642 |
| 9900 | 223.80 | 26843 | 0.4178 | 299.90 | 1.4606 |
| 10000 | 223.15 | 26436 | 0.4127 | 299.46 | 1.4671 |
| 10100 | 222.50 | 26034 | 0.4076 | 299.03 | 1.4536 |
| 10200 | 221.85 | 25636 | 0.4026 | 298.59 | 1.4500 |
| 10300 | 221.20 | 25244 | 0.3976 | 298.15 | 1.4465 |
| 10400 | 220.55 | 24857 | 0.3926 | 297.71 | 1.4430 |
| 10500 | 219.90 | 24474 | 0.3877 | 297.27 | 1.4394 |
| 10600 | 219.25 | 24096 | 0.3829 | 296.83 | 1.4359 |
| 10700 | 218.60 | 23723 | 0.3781 | 296.39 | 1.4323 |
| 10800 | 217.95 | 23355 | 0.3733 | 295.95 | 1.4287 |
| 10900 | 217.30 | 22991 | 0.3686 | 295.51 | 1.4252 |
| 11000 | 216.65 | 22632 | 0.3639 | 295.07 | 1.4216 |
| 11100 | 216.65 | 22278 | 0.3582 | 295.07 | 1.4216 |
| 11200 | 216.65 | 21929 | 0.3526 | 295.07 | 1.4216 |

| H , m | T , K | p , N/m ² | ρ , kg/m ³ | c , m/s | $\mu \times 10^5$ kg/m s |
|------------|------------|---------------------------|-------------------------------|--------------|-----------------------------|
| 11300 | 216.65 | 21586 | 0.3471 | 295.07 | 1.4216 |
| 11400 | 216.65 | 21248 | 0.3417 | 295.07 | 1.4216 |
| 11500 | 216.65 | 20916 | 0.3363 | 295.07 | 1.4216 |
| 11600 | 216.65 | 20589 | 0.3311 | 295.07 | 1.4216 |
| 11700 | 216.65 | 20266 | 0.3259 | 295.07 | 1.4216 |
| 11800 | 216.65 | 19949 | 0.3208 | 295.07 | 1.4216 |
| 11900 | 216.65 | 19637 | 0.3158 | 295.07 | 1.4216 |
| 12000 | 216.65 | 19330 | 0.3108 | 295.07 | 1.4216 |
| 12100 | 216.65 | 19028 | 0.3060 | 295.07 | 1.4216 |
| 12200 | 216.65 | 18730 | 0.3012 | 295.07 | 1.4216 |
| 12300 | 216.65 | 18437 | 0.2965 | 295.07 | 1.4216 |
| 12400 | 216.65 | 18148 | 0.2918 | 295.07 | 1.4216 |
| 12500 | 216.65 | 17865 | 0.2873 | 295.07 | 1.4216 |
| 12600 | 216.65 | 17585 | 0.2828 | 295.07 | 1.4216 |
| 12700 | 216.65 | 17310 | 0.2783 | 295.07 | 1.4216 |
| 12800 | 216.65 | 17039 | 0.2740 | 295.07 | 1.4216 |
| 12900 | 216.65 | 16772 | 0.2697 | 295.07 | 1.4216 |
| 13000 | 216.65 | 16510 | 0.2655 | 295.07 | 1.4216 |
| 13100 | 216.65 | 16252 | 0.2613 | 295.07 | 1.4216 |
| 13200 | 216.65 | 15998 | 0.2572 | 295.07 | 1.4216 |
| 13300 | 216.65 | 15747 | 0.2532 | 295.07 | 1.4216 |
| 13400 | 216.65 | 15501 | 0.2493 | 295.07 | 1.4216 |
| 13500 | 216.65 | 15258 | 0.2454 | 295.07 | 1.4216 |
| 13600 | 216.65 | 15020 | 0.2415 | 295.07 | 1.4216 |
| 13700 | 216.65 | 14785 | 0.2377 | 295.07 | 1.4216 |
| 13800 | 216.65 | 14553 | 0.2340 | 295.07 | 1.4216 |
| 13900 | 216.65 | 14326 | 0.2304 | 295.07 | 1.4216 |
| 14000 | 216.65 | 14101 | 0.2268 | 295.07 | 1.4216 |
| 14100 | 216.65 | 13881 | 0.2232 | 295.07 | 1.4216 |
| 14200 | 216.65 | 13664 | 0.2197 | 295.07 | 1.4216 |
| 14300 | 216.65 | 13450 | 0.2163 | 295.07 | 1.4216 |
| 14400 | 216.65 | 13240 | 0.2129 | 295.07 | 1.4216 |
| 14500 | 216.65 | 13032 | 0.2096 | 295.07 | 1.4216 |
| 14600 | 216.65 | 12828 | 0.2063 | 295.07 | 1.4216 |
| 14700 | 216.65 | 12628 | 0.2031 | 295.07 | 1.4216 |
| 14800 | 216.65 | 12430 | 0.1999 | 295.07 | 1.4216 |
| 14900 | 216.65 | 12236 | 0.1967 | 295.07 | 1.4216 |
| 15000 | 216.65 | 12044 | 0.1937 | 295.07 | 1.4216 |
| 15100 | 216.65 | 11856 | 0.1906 | 295.07 | 1.4216 |
| 15200 | 216.65 | 11670 | 0.1877 | 295.07 | 1.4216 |
| 15300 | 216.65 | 11488 | 0.1847 | 295.07 | 1.4216 |
| 15400 | 216.65 | 11308 | 0.1818 | 295.07 | 1.4216 |
| 15500 | 216.65 | 11131 | 0.1790 | 295.07 | 1.4216 |

| H , m | T , K | p , N/m ² | ρ , kg/m ³ | c , m/s | $\mu \times 10^5$ kg/m s |
|------------|------------|---------------------------|-------------------------------|--------------|-----------------------------|
| 15600 | 216.65 | 10957 | 0.1762 | 295.07 | 1.4216 |
| 15700 | 216.65 | 10786 | 0.1734 | 295.07 | 1.4216 |
| 15800 | 216.65 | 10617 | 0.1707 | 295.07 | 1.4216 |
| 15900 | 216.65 | 10451 | 0.1680 | 295.07 | 1.4216 |
| 16000 | 216.65 | 10287 | 0.1654 | 295.07 | 1.4216 |
| 16100 | 216.65 | 10126 | 0.1628 | 295.07 | 1.4216 |
| 16200 | 216.65 | 9968 | 0.1603 | 295.07 | 1.4216 |
| 16300 | 216.65 | 9812 | 0.1578 | 295.07 | 1.4216 |
| 16400 | 216.65 | 9658 | 0.1553 | 295.07 | 1.4216 |
| 16500 | 216.65 | 9507 | 0.1529 | 295.07 | 1.4216 |
| 16600 | 216.65 | 9359 | 0.1505 | 295.07 | 1.4216 |
| 16700 | 216.65 | 9212 | 0.1481 | 295.07 | 1.4216 |
| 16800 | 216.65 | 9068 | 0.1458 | 295.07 | 1.4216 |
| 16900 | 216.65 | 8926 | 0.1435 | 295.07 | 1.4216 |
| 17000 | 216.65 | 8786 | 0.1413 | 295.07 | 1.4216 |
| 17100 | 216.65 | 8649 | 0.1391 | 295.07 | 1.4216 |
| 17200 | 216.65 | 8514 | 0.1369 | 295.07 | 1.4216 |
| 17300 | 216.65 | 8380 | 0.1348 | 295.07 | 1.4216 |
| 17400 | 216.65 | 8249 | 0.1326 | 295.07 | 1.4216 |
| 17500 | 216.65 | 8120 | 0.1306 | 295.07 | 1.4216 |
| 17600 | 216.65 | 7993 | 0.1285 | 295.07 | 1.4216 |
| 17700 | 216.65 | 7868 | 0.1265 | 295.07 | 1.4216 |
| 17800 | 216.65 | 7745 | 0.1245 | 295.07 | 1.4216 |
| 17900 | 216.65 | 7624 | 0.1226 | 295.07 | 1.4216 |
| 18000 | 216.65 | 7505 | 0.1207 | 295.07 | 1.4216 |
| 18100 | 216.65 | 7387 | 0.1188 | 295.07 | 1.4216 |
| 18200 | 216.65 | 7272 | 0.1169 | 295.07 | 1.4216 |
| 18300 | 216.65 | 7158 | 0.1151 | 295.07 | 1.4216 |
| 18400 | 216.65 | 7046 | 0.1133 | 295.07 | 1.4216 |
| 18500 | 216.65 | 6936 | 0.1115 | 295.07 | 1.4216 |
| 18600 | 216.65 | 6827 | 0.1098 | 295.07 | 1.4216 |
| 18700 | 216.65 | 6720 | 0.1081 | 295.07 | 1.4216 |
| 18800 | 216.65 | 6615 | 0.1064 | 295.07 | 1.4216 |
| 18900 | 216.65 | 6512 | 0.1047 | 295.07 | 1.4216 |
| 19000 | 216.65 | 6410 | 0.1031 | 295.07 | 1.4216 |
| 19100 | 216.65 | 6310 | 0.1015 | 295.07 | 1.4216 |
| 19200 | 216.65 | 6211 | 0.0999 | 295.07 | 1.4216 |
| 19300 | 216.65 | 6114 | 0.0983 | 295.07 | 1.4216 |
| 19400 | 216.65 | 6018 | 0.0968 | 295.07 | 1.4216 |
| 19500 | 216.65 | 5924 | 0.0953 | 295.07 | 1.4216 |
| 19600 | 216.65 | 5831 | 0.0938 | 295.07 | 1.4216 |
| 19700 | 216.65 | 5740 | 0.0923 | 295.07 | 1.4216 |
| 19800 | 216.65 | 5650 | 0.0909 | 295.07 | 1.4216 |

| H , m | T , K | p , N/m ² | ρ , kg/m ³ | c , m/s | $\mu \times 10^5$ kg/m s |
|------------|------------|---------------------------|-------------------------------|--------------|-----------------------------|
| 19900 | 216.65 | 5562 | 0.0894 | 295.07 | 1.4216 |
| 20000 | 216.65 | 5475 | 0.0880 | 295.07 | 1.4216 |
| 20100 | 216.75 | 5389 | 0.0866 | 295.14 | 1.4222 |
| 20200 | 216.85 | 5305 | 0.0852 | 295.20 | 1.4227 |
| 20300 | 216.95 | 5222 | 0.0839 | 295.27 | 1.4233 |
| 20400 | 217.05 | 5140 | 0.0825 | 295.34 | 1.4238 |
| 20500 | 217.15 | 5060 | 0.0812 | 295.41 | 1.4244 |
| 20600 | 217.25 | 4981 | 0.0799 | 295.48 | 1.4249 |
| 20700 | 217.35 | 4903 | 0.0786 | 295.54 | 1.4255 |
| 20800 | 217.45 | 4827 | 0.0773 | 295.61 | 1.4260 |
| 20900 | 217.55 | 4752 | 0.0761 | 295.68 | 1.4266 |
| 21000 | 217.65 | 4678 | 0.0749 | 295.75 | 1.4271 |
| 21100 | 217.75 | 4605 | 0.0737 | 295.82 | 1.4277 |
| 21200 | 217.85 | 4533 | 0.0725 | 295.88 | 1.4282 |
| 21300 | 217.95 | 4463 | 0.0713 | 295.95 | 1.4287 |
| 21400 | 218.05 | 4393 | 0.0702 | 296.02 | 1.4293 |
| 21500 | 218.15 | 4325 | 0.0691 | 296.09 | 1.4298 |
| 21600 | 218.25 | 4258 | 0.0680 | 296.16 | 1.4304 |
| 21700 | 218.35 | 4192 | 0.0669 | 296.22 | 1.4309 |
| 21800 | 218.45 | 4127 | 0.0658 | 296.29 | 1.4315 |
| 21900 | 218.55 | 4063 | 0.0648 | 296.36 | 1.4320 |
| 22000 | 218.65 | 4000 | 0.0637 | 296.43 | 1.4326 |
| 22100 | 218.75 | 3938 | 0.0627 | 296.49 | 1.4331 |
| 22200 | 218.85 | 3877 | 0.0617 | 296.56 | 1.4337 |
| 22300 | 218.95 | 3817 | 0.0607 | 296.63 | 1.4342 |
| 22400 | 219.05 | 3758 | 0.0598 | 296.70 | 1.4348 |
| 22500 | 219.15 | 3699 | 0.0588 | 296.77 | 1.4353 |
| 22600 | 219.25 | 3642 | 0.0579 | 296.83 | 1.4359 |
| 22700 | 219.35 | 3586 | 0.0570 | 296.90 | 1.4364 |
| 22800 | 219.45 | 3530 | 0.0560 | 296.97 | 1.4370 |
| 22900 | 219.55 | 3476 | 0.0552 | 297.04 | 1.4375 |
| 23000 | 219.65 | 3422 | 0.0543 | 297.10 | 1.4381 |
| 23100 | 219.75 | 3370 | 0.0534 | 297.17 | 1.4386 |
| 23200 | 219.85 | 3318 | 0.0526 | 297.24 | 1.4391 |
| 23300 | 219.95 | 3266 | 0.0517 | 297.31 | 1.4397 |
| 23400 | 220.05 | 3216 | 0.0509 | 297.37 | 1.4402 |
| 23500 | 220.15 | 3167 | 0.0501 | 297.44 | 1.4408 |
| 23600 | 220.25 | 3118 | 0.0493 | 297.51 | 1.4413 |
| 23700 | 220.35 | 3070 | 0.0485 | 297.58 | 1.4419 |
| 23800 | 220.45 | 3023 | 0.0478 | 297.64 | 1.4424 |
| 23900 | 220.55 | 2976 | 0.0470 | 297.71 | 1.4430 |
| 24000 | 220.65 | 2930 | 0.0463 | 297.78 | 1.4435 |
| 24100 | 220.75 | 2885 | 0.0455 | 297.85 | 1.4441 |

| H , m | T , K | p , N/m ² | ρ , kg/m ³ | c , m/s | $\mu \times 10^5$ kg/m s |
|------------|------------|---------------------------|-------------------------------|--------------|-----------------------------|
| 24200 | 220.85 | 2841 | 0.0448 | 297.91 | 1.4446 |
| 24300 | 220.95 | 2797 | 0.0441 | 297.98 | 1.4451 |
| 24400 | 221.05 | 2755 | 0.0434 | 298.05 | 1.4457 |
| 24500 | 221.15 | 2712 | 0.0427 | 298.12 | 1.4462 |
| 24600 | 221.25 | 2671 | 0.0421 | 298.18 | 1.4468 |
| 24700 | 221.35 | 2630 | 0.0414 | 298.25 | 1.4473 |
| 24800 | 221.45 | 2590 | 0.0407 | 298.32 | 1.4479 |
| 24900 | 221.55 | 2550 | 0.0401 | 298.39 | 1.4484 |
| 25000 | 221.65 | 2511 | 0.0395 | 298.45 | 1.4490 |
| 25100 | 221.75 | 2473 | 0.0388 | 298.52 | 1.4495 |
| 25200 | 221.85 | 2435 | 0.0382 | 298.59 | 1.4500 |
| 25300 | 221.95 | 2398 | 0.0376 | 298.66 | 1.4506 |
| 25400 | 222.05 | 2361 | 0.0370 | 298.72 | 1.4511 |
| 25500 | 222.15 | 2325 | 0.0365 | 298.79 | 1.4517 |
| 25600 | 222.25 | 2289 | 0.0359 | 298.86 | 1.4522 |
| 25700 | 222.35 | 2254 | 0.0353 | 298.92 | 1.4528 |
| 25800 | 222.45 | 2220 | 0.0348 | 298.99 | 1.4533 |
| 25900 | 222.55 | 2186 | 0.0342 | 299.06 | 1.4539 |
| 26000 | 222.65 | 2153 | 0.0337 | 299.13 | 1.4544 |
| 26100 | 222.75 | 2120 | 0.0332 | 299.19 | 1.4549 |
| 26200 | 222.85 | 2088 | 0.0326 | 299.26 | 1.4555 |
| 26300 | 222.95 | 2056 | 0.0321 | 299.33 | 1.4560 |
| 26400 | 223.05 | 2025 | 0.0316 | 299.39 | 1.4566 |
| 26500 | 223.15 | 1994 | 0.0311 | 299.46 | 1.4571 |
| 26600 | 223.25 | 1964 | 0.0306 | 299.53 | 1.4577 |
| 26700 | 223.35 | 1934 | 0.0302 | 299.60 | 1.4582 |
| 26800 | 223.45 | 1905 | 0.0297 | 299.66 | 1.4587 |
| 26900 | 223.55 | 1876 | 0.0292 | 299.73 | 1.4593 |
| 27000 | 223.65 | 1847 | 0.0288 | 299.80 | 1.4598 |
| 27100 | 223.75 | 1819 | 0.0283 | 299.86 | 1.4604 |
| 27200 | 223.85 | 1792 | 0.0279 | 299.93 | 1.4609 |
| 27300 | 223.95 | 1765 | 0.0275 | 300.00 | 1.4614 |
| 27400 | 224.05 | 1738 | 0.0270 | 300.06 | 1.4620 |
| 27500 | 224.15 | 1712 | 0.0266 | 300.13 | 1.4625 |
| 27600 | 224.25 | 1686 | 0.0262 | 300.20 | 1.4631 |
| 27700 | 224.35 | 1660 | 0.0258 | 300.27 | 1.4636 |
| 27800 | 224.45 | 1635 | 0.0254 | 300.33 | 1.4642 |
| 27900 | 224.55 | 1611 | 0.0250 | 300.40 | 1.4647 |
| 28000 | 224.65 | 1586 | 0.0246 | 300.47 | 1.4652 |
| 28100 | 224.75 | 1562 | 0.0242 | 300.53 | 1.4658 |
| 28200 | 224.85 | 1539 | 0.0238 | 300.60 | 1.4663 |
| 28300 | 224.95 | 1516 | 0.0235 | 300.67 | 1.4669 |
| 28400 | 225.05 | 1493 | 0.0231 | 300.73 | 1.4674 |

| H , m | T , K | p , N/m ² | ρ , kg/m ³ | c , m/s | $\mu \times 10^5$ kg/m s |
|------------|------------|---------------------------|-------------------------------|--------------|-----------------------------|
| 28500 | 225.15 | 1470 | 0.0227 | 300.80 | 1.4679 |
| 28600 | 225.25 | 1448 | 0.0224 | 300.87 | 1.4685 |
| 28700 | 225.35 | 1426 | 0.0220 | 300.93 | 1.4690 |
| 28800 | 225.45 | 1405 | 0.0217 | 301.00 | 1.4696 |
| 28900 | 225.55 | 1384 | 0.0214 | 301.07 | 1.4701 |
| 29000 | 225.65 | 1363 | 0.0210 | 301.13 | 1.4706 |
| 29100 | 225.75 | 1342 | 0.0207 | 301.20 | 1.4712 |
| 29200 | 225.85 | 1322 | 0.0204 | 301.27 | 1.4717 |
| 29300 | 225.95 | 1302 | 0.0201 | 301.33 | 1.4723 |
| 29400 | 226.05 | 1283 | 0.0198 | 301.40 | 1.4728 |
| 29500 | 226.15 | 1264 | 0.0195 | 301.47 | 1.4733 |
| 29600 | 226.25 | 1245 | 0.0192 | 301.53 | 1.4739 |
| 29700 | 226.35 | 1226 | 0.0189 | 301.60 | 1.4744 |
| 29800 | 226.45 | 1208 | 0.0186 | 301.67 | 1.4750 |
| 29900 | 226.55 | 1190 | 0.0183 | 301.73 | 1.4755 |
| 30000 | 226.65 | 1172 | 0.0180 | 301.80 | 1.4760 |
| 30100 | 226.75 | 1154 | 0.0177 | 301.87 | 1.4766 |
| 30200 | 226.85 | 1137 | 0.0175 | 301.93 | 1.4771 |
| 30300 | 226.95 | 1120 | 0.0172 | 302.00 | 1.4777 |
| 30400 | 227.05 | 1103 | 0.0169 | 302.07 | 1.4782 |
| 30500 | 227.15 | 1087 | 0.0167 | 302.13 | 1.4787 |
| 30600 | 227.25 | 1071 | 0.0164 | 302.20 | 1.4793 |
| 30700 | 227.35 | 1055 | 0.0162 | 302.27 | 1.4798 |
| 30800 | 227.45 | 1039 | 0.0159 | 302.33 | 1.4803 |
| 30900 | 227.55 | 1023 | 0.0157 | 302.40 | 1.4809 |
| 31000 | 227.65 | 1008 | 0.0154 | 302.47 | 1.4814 |
| 31100 | 227.75 | 993 | 0.0152 | 302.53 | 1.4820 |
| 31200 | 227.85 | 978 | 0.0150 | 302.60 | 1.4825 |
| 31300 | 227.95 | 964 | 0.0147 | 302.67 | 1.4830 |
| 31400 | 228.05 | 949 | 0.0145 | 302.73 | 1.4836 |
| 31500 | 228.15 | 935 | 0.0143 | 302.80 | 1.4841 |
| 31600 | 228.25 | 921 | 0.0141 | 302.86 | 1.4846 |
| 31700 | 228.35 | 908 | 0.0138 | 302.93 | 1.4852 |
| 31800 | 228.45 | 894 | 0.0136 | 303.00 | 1.4857 |
| 31900 | 228.55 | 881 | 0.0134 | 303.06 | 1.4863 |
| 32000 | 228.65 | 868 | 0.0132 | 303.13 | 1.4868 |

Appendix D

ONE-DIMENSIONAL STEADY FLOW EQUATIONS

D.1 Continuity equation

The continuity equation expresses the physical principle that mass can be neither created nor destroyed. Consider a gas flowing through a channel (Figure D.1). When the flow is steady, there will be no variation with time of the mass of the gas confined inside the channel between the cross-sections 1 and 2. Consequently, the same rate of mass flow will cross each section of the channel. Thus, the condition for continuity is

$$m = \rho V A = \text{constant}, \quad (\text{D.1})$$

where m is the mass flow per unit time, V is the flow velocity and A is the cross-sectional area.

Equation (D.1) is the continuity equation. In the logarithmic differential form this equation reads

$$\frac{d\rho}{\rho} + \frac{dV}{V} + \frac{dA}{A} = 0. \quad (\text{D.2})$$

Emphasis is made that Equation (D.1) is derived by using the simplifying conditions of one-dimensional steady flow. This implies that all gas properties are uniform over any cross-section of the channel and independent of time.

In steady flow, the gas particles move along streamlines, which represent the local flow direction. Thus, by definition, particles cannot cross a streamline. All the streamlines that go through the circumference of a surface directed perpendicular to the flow direction form a streamtube (Figure D.2). Since no particle can enter or leave the streamtube through its walls, it follows that when dealing with steady flow, the continuity equation holds also along a streamtube.

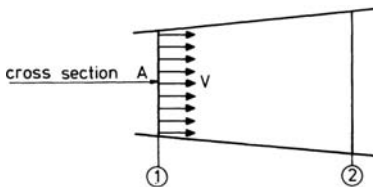


Figure D.1 Channel flow

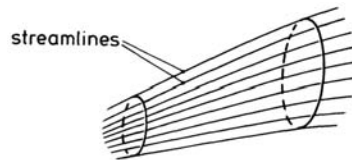


Figure D.2 Streamtube

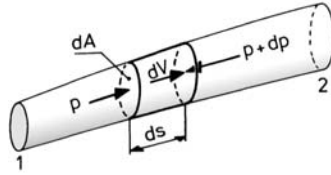


Figure D.3 Elemental streamtube

D.2 Bernoulli's equation

Bernoulli's equation expresses the relationship between pressure and velocity along a streamline for a frictionless steady flow.

To derive this equation, we may consider an element of an elemental streamtube with mass $\rho ds dA$, where ds is the length and dA is the cross-sectional area of the element (Figure D.3).

If the effect of altitude on pressure is neglected, we obtain from Newton's second law of motion:

$$-dp dA = \rho ds dA \frac{dV}{dt}, \quad (\text{D.3})$$

where dp is the difference in pressure across the two cross-sections of the element of the streamtube. The acceleration of the element is given by

$$\frac{dV}{dt} = \frac{\partial V}{\partial s} \frac{ds}{dt} + \frac{\partial V}{\partial t}.$$

Since in steady flow the derivative with respect to time is zero, the acceleration reduces to

$$\frac{dV}{dt} = V \frac{dV}{ds}. \quad (\text{D.4})$$

Insertion of the latter expression into Equation (D.3) furnishes Euler's equation:

$$\frac{dp}{\rho} = -V dV. \quad (\text{D.5})$$

When the flow is continuous, Equation (D.5) can be integrated between the stations 1 and 2 of the streamtube in Figure D.2. This yields

$$\int_{p_1}^{p_2} \frac{dp}{\rho} + \frac{1}{2}(V_2^2 - V_1^2) = 0. \quad (\text{D.6})$$

If we use the assumption that ρ is constant, we obtain Bernoulli's equation:

$$p_1 + \frac{1}{2}\rho V_1^2 = p_2 + \frac{1}{2}\rho V_2^2 \quad \text{or} \quad (\text{D.7})$$

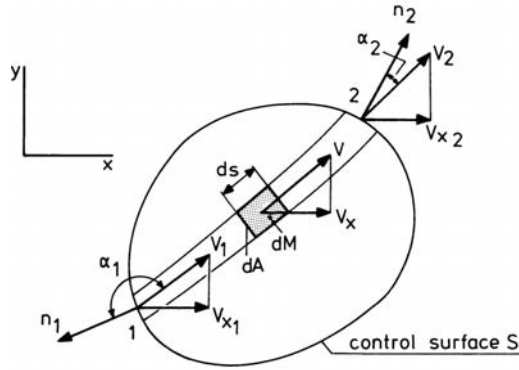


Figure D.4 The flow in a control surface

$$p_t = p + \frac{1}{2}\rho V^2 = \text{constant}, \quad (\text{D.8})$$

where p_t is the *total pressure* and $\frac{1}{2}\rho V^2$ is the *dynamic pressure*.

A flow can only be assumed to be incompressible if the velocity is low, that is, low when compared with its speed of sound.

For the case of compressible flow, the integral in Equation (D.6) can only be solved if we have additional information on the variation of density with pressure, which will be discussed in Section D.7.

D.3 The momentum equation

To derive the momentum equation we consider a gas flowing steadily through a fixed control volume bounded by a control surface S (Figure D.4).

In order to apply Newton's second law of motion to the gas, the control volume is divided into elemental streamtubes of cross-section dA (see Figure D.3).

As the flow is steady, the x -component of the acceleration of a streamtube element is given by

$$a_x = \frac{dV_x}{dt} = V \frac{dV_x}{ds}, \quad (\text{D.9})$$

where V_x is the x -component of the velocity V . The mass of the gas enclosed by the element is

$$dM = \rho ds dA. \quad (\text{D.10})$$

The x -component of the force acting on the element is therefore

$$dF_x = \rho ds dA V \frac{dV_x}{ds}. \quad (\text{D.11})$$

To determine the integral of Equation (D.11) extended over the complete control volume, it is appropriate to first consider the contributions of the individual streamtubes.

The contribution of the streamtube 1-2 to the force F_x becomes

$$\int_1^2 \rho ds dA V \frac{dV_x}{ds} = \int_1^2 (\rho V dA) dV_x, \quad (\text{D.12})$$

where the product $\rho V dA$ represents the mass flow rate, which has a constant value along the streamtube. Hence

$$\int_1^2 (\rho V dA) dV_x = \rho V dA (V_{x_2} - V_{x_1}). \quad (\text{D.13})$$

Then for the entire system, we can write

$$F_x + W_x = \int_S \rho V (V_{x_2} - V_{x_1}) dA. \quad (\text{D.14})$$

The term on the left-hand side of Equation (D.14) is the sum of the x-components of the resultant force F acting on the gas within the control surface S and the weight W of the gas confined in the control volume.

Evidently, we can write Equation (D.14) as

$$F_x + W_x = \int_S \rho V V_x \cos \alpha dS, \quad (\text{D.15})$$

where dS represents the area of the surface element that an elemental streamtube cuts out of the control surface. The angle α is the angle between the direction of the velocity V at the place where the streamtube pierces through the control surface and the outward normal at the same point. The product $V \cos \alpha$ in Equation (D.15) is the projection of the velocity V on the outward normal of S . Let V_n denote $V \cos \alpha$. Then, Equation (D.15) becomes

$$F_x + W_x = \int_S \rho V_n V_x dS. \quad (\text{D.16})$$

Note that the normal velocity V_n is positive at points where the gas leaves the control volume and negative at points where the gas goes into the control volume. Equation (D.16) is the momentum equation, written in a general form. Since the product $\rho V_n dS$ is the mass flow rate that passes a surface element dS , Equation (D.16) says that the sum of the components of the external forces in a given direction acting on a gas contained in a control volume equals the rate of change of momentum of the gas in the same direction.

In the application of the momentum equation, it is normally found convenient to employ special forms. As a typical example, we will consider here the steady one-dimensional flow through a channel (Figure D.5).

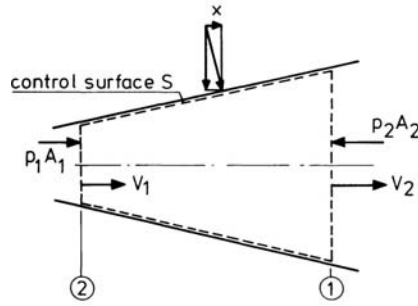


Figure D.5 Flow through a channel

Let the control surface consist of the interior surface of the channel and the cross-sections 1 and 2. Neglecting the weight of the gas, the momentum equation then furnishes for the component in the direction of flow of the force exerted by the walls of the channel on the fluid:

$$X = m(V_2 - V_1) + p_2A_2 - p_1A_1. \quad (\text{D.17})$$

In this equation p_1A_1 and p_2A_2 are the forces that the gas outside the portion of the channel between stations 1 and 2 exerts on the flow within the control volume.

D.4 The energy equation

The energy equation is based on the first law of thermodynamics that states that energy is conserved in a thermodynamic system. Thus, for a system of gas, the energy supplied must equal the sum of the increase in the internal energy of the system and the energy which leaves the system as work. The first law of thermodynamics may be written as

$$dQ = dE + dW, \quad (\text{D.18})$$

where dQ is the amount of energy added to the system, dW is the amount of work done by the system and dE is the corresponding change in internal energy.

It is convenient to employ lower case letters to denote the values of extensive variables per unit mass of fluid. Then, Equation (D.18) becomes

$$dq = de + dw. \quad (\text{D.19})$$

For any system we can break the work dw into two parts:

$$dw = dw_m + p d\left(\frac{1}{\rho}\right), \quad (\text{D.20})$$

in which $p d(1/\rho)$ is the increment of work done by the gas on the surrounding control surfaces and dw_m includes all other forms of work.

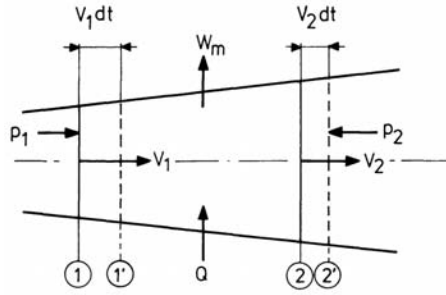


Figure D.6 Channel flow with addition and extraction of energy

The internal energy is all the energy internal to the system boundaries. Neglecting the potential energy,

$$e = u + \frac{V^2}{2}, \quad (\text{D.21})$$

in which u denotes the internal molecular energy, and $V^2/2$ is the kinetic energy of the system per unit mass.

For our analysis, we consider a flow through a channel, and we define the system as the gas in the channel between the cross-sections 1 and 2 (Figure D.6). After a time dt , the system will have moved to the position $1'-2'$. Then, from the principle of the conservation of energy, the net energy transferred to the system is the energy in volume $1'-2'$ at time $t + dt$ minus the energy in volume 1-2 at time t .

For steady flow, the internal energy in region $1'-2$ remains unchanged so that the net energy transferred to the system is also given by the energy in region $2-2'$ at time $t + dt$ minus the energy in region $1-1'$ at time t .

Assuming that the properties of the gas masses in the regions $2-2'$ and $1-1'$ can be considered to be the same as the properties of the gases when they pass their respective entry-sections 1 and 2, we obtain the energy balance for a flowing gas as

$$\left[m(q - w_m) - (p_2 V_2 A_2 - p_1 V_1 A_1) \right] dt = m \left[(u_2 - u_1) + \left[\frac{V_2^2}{2} - \frac{V_1^2}{2} \right] \right] dt, \quad (\text{D.22})$$

where m is the mass flow rate and pVA represents the work done by the system on the surroundings.

Equation (D.22) expresses that in time dt , heat is added and energy in the form of work is extracted at the rates q and w_m units of energy per unit mass.

Noting that from Equation (D.1),

$$m = \rho_1 V_1 A_1 = \rho_2 V_2 A_2.$$

we get the following form of the energy equation,

$$q - w_m = \left[\frac{p_2}{\rho_2} - \frac{p_1}{\rho_1} \right] + (u_2 - u_1) + \left[\frac{V_2^2}{2} - \frac{V_1^2}{2} \right], \quad (\text{D.23})$$

or in differential form,

$$dq - dw_m = d\left(\frac{p}{\rho}\right) + du + VdV \quad (\text{D.24})$$

Again, it should be noted that Equations (D.23) and (D.24) refer to a steady one-dimensional flow of unit mass.

D.5 Isentropic relations

The first law of thermodynamics for an incremental change of state of a system of gas may be written as

$$dq = du + pd\left(\frac{1}{\rho}\right). \quad (\text{D.25})$$

When we use the concept of enthalpy, h , defined as

$$h = u + \frac{p}{\rho} \quad (\text{D.26})$$

then, for an infinitesimal process,

$$dh = du + pd\left(\frac{1}{\rho}\right) + \frac{1}{\rho}dp. \quad (\text{D.27})$$

Combination of Equations (D.25) and (D.27) yields

$$dq = dh - \frac{1}{\rho}dp. \quad (\text{D.28})$$

The specific heat at constant pressure is therefore

$$c_p = \left(\frac{\partial q}{\partial T}\right)_p = \frac{\partial h}{\partial T}. \quad (\text{D.29})$$

The specific heat at constant volume is

$$c_v = \left(\frac{\partial q}{\partial T}\right)_v = \frac{\partial u}{\partial T}. \quad (\text{D.30})$$

Assuming that we are dealing with a perfect gas we have the equation of state, i.e.,

$$\frac{p}{\rho} = RT, \quad (\text{D.31})$$

where R is the specific gas constant.

For a perfect gas the specific heats are related by

$$c_p = \frac{\partial}{\partial T}\left(u + \frac{p}{\rho}\right) = \frac{\partial}{\partial T}(u + RT) = c_v + R. \quad (\text{D.32})$$

insertion of Equations (D.30) to (D.32) into Equation (D.23) leads to the following form of the energy equation per unit mass flow rate of a perfect gas:

$$q - w_m = c_p(T_2 - T_1) + \frac{V_2^2}{2} - \frac{V_1^2}{2}. \quad (\text{D.33})$$

For adiabatic flow ($q = w_m = 0$) we have

$$c_p T + \frac{V^2}{2} = \text{constant}, \quad (\text{D.34})$$

or in differential form

$$c_p dT + V dV = 0. \quad (\text{D.35})$$

For inviscid flow, Equation (D.35) can be combined with Euler's equation, Equation (D.5). The resulting form is:

$$c_p dT - \frac{dp}{\rho} = 0. \quad (\text{D.36})$$

Substituting Equations (D.31) and (D.32) into (D.36), we obtain

$$\frac{dp}{\rho} = \frac{\gamma}{\gamma - 1} \frac{dT}{T}, \quad (\text{D.37})$$

where γ is the ratio of the specific heats, $\gamma = c_p/c_v$.

For the case of constant specific heats, Equation (D.37) may be integrated, with the result that

$$\frac{p}{T^{(\gamma/(\gamma-1))}} = \text{constant}. \quad (\text{D.38})$$

Using the perfect gas law, Equation (D.31), the latter equation can be transformed to

$$\frac{p}{\rho^\gamma} = \text{constant}. \quad (\text{D.39})$$

Equations (D.38) and (D.39) are called the Poisson relations, and provide information on the variations of p , T , and ρ along a streamline in an isentropic (adiabatic and reversible) flow.

D.6 The speed of sound

The speed of sound is the rate at which a weak disturbance or sound wave propagates through a medium. In order to derive an expression for the speed of sound, we consider a sound wave moving with speed c through a perfect gas at rest in a constant area duct (Figure D.7).

Suppose that we are traveling with the sound wave. We then see at both sides of the sound wave a steady flow to the right. Across the sound wave, the velocity,

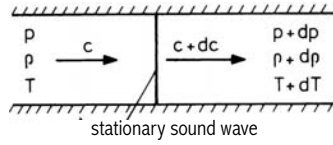


Figure D.7 Derivation of a formula for the speed of sound

pressure, density and temperature of the gas are changed by the amounts dc , dp , $d\rho$ and dT , respectively.

Applying the continuity equation, Equation (D.1), we get

$$\rho c = (\rho + d\rho)(c + dc). \quad (\text{D.40})$$

When neglecting the product of two small quantities, we obtain from Equation (D.40)

$$c = -\rho \frac{dc}{d\rho}. \quad (\text{D.41})$$

From Euler's equation, Equation (D.5), we have

$$dc = -\frac{dp}{\rho c}. \quad (\text{D.42})$$

Substitution of Equation (D.42) into (D.41) yields

$$c^2 = \frac{dp}{d\rho}. \quad (\text{D.43})$$

Assuming that the flow through the sound wave is isentropic, the relationship between pressure and density is given by Equation (D.39),

$$\frac{p}{\rho^\gamma} = \text{constant} = C. \quad (\text{D.44})$$

Hence

$$\frac{dp}{d\rho} = \frac{d(C\rho^\gamma)}{d\rho} = \gamma C \rho^{\gamma-1} = \gamma \frac{p}{\rho}. \quad (\text{D.45})$$

Combining Equations (D.43) and (D.45) results in the following expression for the speed of sound,

$$c = \sqrt{\gamma \frac{p}{\rho}}. \quad (\text{D.46})$$

Substituting the perfect gas law, Equation (D.31), into Equation (D.46) yields

$$c = \sqrt{\gamma RT}. \quad (\text{D.47})$$

This equation shows that the speed of sound in a perfect gas depends only on the (absolute) temperature of the gas.

D.7 Bernoulli's equation for compressible flow

According to the energy equation for adiabatic flow, Equation (D.34), we may write

$$c_p T + \frac{V^2}{2} = \text{constant} = c_p T_t, \quad (\text{D.48})$$

where T_t is the value of the temperature that would occur if the velocity was slowed down adiabatically to zero velocity and is called the stagnation or *total temperature*.

Calculations are often facilitated if the flow velocities are taken into account implicitly by introducing the concept of total temperature and by expressing the flow velocities in terms of Mach number. The Mach number M is defined as

$$M = V/c, \quad (\text{D.49})$$

where c is the speed of sound.

For a perfect gas the speed of sound can be expressed diversely as

$$c = \sqrt{\gamma \frac{p}{\rho}} = \sqrt{\gamma R T} = \sqrt{(\gamma - 1) c_p T}. \quad (\text{D.50})$$

Combining Equations (D.48) and (D.50) yields the relationships

$$\frac{T_t}{T} = 1 + \frac{V^2}{2c_p T} = 1 + \frac{\gamma - 1}{2} M^2. \quad (\text{D.51})$$

From Equation (D.51), and the Equations (D.38) and (D.39) we get for the corresponding pressure and density ratios for isentropic flow:

$$\frac{p_t}{p} = \left[\frac{T_t}{T} \right]^{\frac{\gamma}{\gamma-1}} = \left[1 + \frac{\gamma - 1}{2} M^2 \right]^{\frac{\gamma}{\gamma-1}} \quad (\text{D.52})$$

$$\frac{\rho_t}{\rho} = \left[\frac{p_t}{p} \right]^{\frac{1}{\gamma}} = \left[1 + \frac{\gamma - 1}{2} M^2 \right]^{\frac{1}{\gamma-1}}. \quad (\text{D.53})$$

Equations (D.51) to (D.53) show that the static temperature, pressure and density and the velocity of a moving gas are equivalent in terms of energy to a total temperature, total pressure, and total density. This may be useful, for example, in studying the gas flow through a jet engine.

With the substitution of Equations (D.49) and (D.50), Equation (D.52) can be written as

$$\frac{p_t}{p} = \left[1 + \frac{\gamma - 1}{2\gamma} \frac{\rho}{p} V^2 \right]^{\frac{\gamma}{\gamma-1}}. \quad (\text{D.54})$$

The latter form is often called *Bernoulli's equation for compressible flow*, where p_t is the total pressure that would occur if the flow was decelerated isentropically to zero velocity.

D.8 Isentropic flow of a perfect gas through a channel of varying cross-section

For steady flow the mass flow rate crossing a section of the flow passage follows from the continuity equation. Equation (D.1)

$$m = \rho VA. \quad (\text{D.55})$$

For a perfect gas, Equation (D.55) can be transformed to

$$m = \frac{p}{RT} M \sqrt{\gamma RT} A = \frac{p}{\sqrt{T}} \sqrt{\frac{\gamma}{R}} M A. \quad (\text{D.56})$$

By insertion of Equations (D.51) and (D.52) into Equation (D.56) the mass flow rate can be expressed in terms of stagnation conditions,

$$m = \frac{p_t}{\sqrt{T_t}} \sqrt{\frac{\gamma}{R}} M \left[1 + \frac{\gamma-1}{2} M^2 \right]^{-\frac{\gamma+1}{2(\gamma-1)}} A. \quad (\text{D.57})$$

Since for steady isentropic flow the quantities m , T_t and p_t are constants, we find by differentiating Equation (D.57) that

$$\frac{dA}{A} + \frac{dM}{M} - \frac{\frac{\gamma+1}{2} M^2}{1 + \frac{\gamma-1}{2} M^2} \frac{dM}{M} = 0. \quad (\text{D.58})$$

Rearranging, we get for the variation of the Mach number with cross-sectional area

$$\frac{dM}{M} = -\frac{1 + \frac{\gamma-1}{2} M^2}{1 - M^2} \frac{dA}{A}. \quad (\text{D.59})$$

The related variations of velocity, temperature, pressure and density with area change follow from Equation (D.59) in combination with the Equations (D.51), (D.52) and (D.53). These are repeated below for easy reference in the following analysis and made visible in Figure D.8,

$$\frac{T_t}{T} = 1 + \frac{\gamma-1}{2} M^2 = 1 + \frac{V^2}{2c_p T} \quad (\text{D.51})$$

$$\frac{p_t}{p} = \left[1 + \frac{\gamma-1}{2} M^2 \right]^{\frac{\gamma}{\gamma-1}} \quad (\text{D.52})$$

$$\frac{\rho_t}{\rho} = \left[1 + \frac{\gamma-1}{2} M^2 \right]^{\frac{1}{\gamma-1}}. \quad (\text{D.53})$$

From Figure D.8 we see that the effects of area change are opposite for subsonic and supersonic flow.

In the case of a converging-diverging channel, the minimum cross-sectional area is called the throat ($dA = 0$). There, according to Equation (D.59), the flow must

| type of flow | converging channel ($dA < 0$) | diverging channel ($dA > 0$) |
|-----------------------------|---|---|
| subsonic flow ($M < 1$) |  $M < 1$ → $M < 1$ M increases V increases T decreases p decreases ρ decreases |  $M < 1$ → $M < 1$ M decreases V decreases T increases p increases ρ increases |
| supersonic flow ($M > 1$) |  $M > 1$ → $M > 1$ M decreases V decreases T increases p increases ρ increases |  $M > 1$ → $M > 1$ M increases V increases T decreases p decreases ρ decreases |

Figure D.8 Effects of area change in isentropic flow through a duct

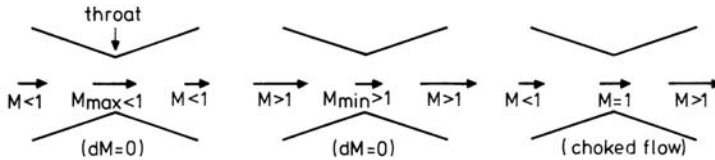


Figure D.9 Isentropic flow through a converging-diverging channel

satisfy the condition that the Mach number either shows an extreme ($dM = 0$) or is equal to unity (Figure D.9).

Under the first-mentioned condition, in the channel subsonic expansion takes place followed by subsonic diffusion or for supersonic flow a decreasing Mach number in the converging section but not reaching a Mach number of unity, and in the diverging section an increasing Mach number.

When $M = 1$ we have the condition where the flow velocity at the throat equals the local speed of sound.

Under this condition the flow is said to be choked because the mass flow is the maximum which the throat can cross with the given stagnation temperature and pressure. The mass flow rate in a choked flow, from Equation (D.57), is given by

$$m^* = \frac{p_t}{\sqrt{T_t}} \sqrt{\frac{\gamma}{R} \left[\frac{\gamma + 1}{2} \right]^{-\frac{\gamma+1}{2(\gamma-1)}}} A^*, \tag{D.60}$$

where an asterisk is used to mark the properties of the flow at the throat. Equating Equations (D.60) and (D.57) yields

$$\frac{A}{A^*} = \frac{1}{M} \left[\frac{2}{\gamma + 1} \left[1 + \frac{\gamma - 1}{2} M^2 \right] \right]^{-\frac{\gamma+1}{2(\gamma-1)}}. \tag{D.61}$$

In Figure D.10 are plotted the ratios T/T_t , p/p_t , ρ/ρ_t and A/A^* for a perfect gas of $\gamma = 1.4$, as expressed by the Equations (D.51), (D.52), (D.53) and (D.61).

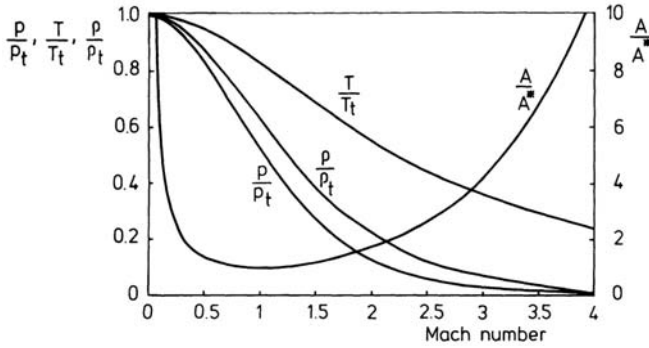


Figure D.10 Characteristic ratios for isentropic flow ($\gamma = 1.4$)

To find the conditions at a particular section of a channel with a given shape, the local Mach number follows directly from the ratio A/A^* in Figure D.10. Then, with known stagnation conditions, the curves also give the corresponding values of T , p and ρ .

The conditions at the throat are found by setting $M = 1$ in Equations (D.51) to (D.53):

$$\frac{T_t}{T^*} = \frac{\gamma + 1}{2} = 1.2 \quad (\gamma = 1.4) \quad (\text{D.62})$$

$$\frac{p_t}{p^*} = \left[\frac{\gamma + 1}{2} \right]^{\frac{\gamma}{\gamma - 1}} = 1.893 \quad (\gamma = 1.4) \quad (\text{D.63})$$

$$\frac{\rho_t}{\rho^*} = \left[\frac{\gamma + 1}{2} \right]^{\frac{1}{\gamma - 1}} = 1.577 \quad (\gamma = 1.4). \quad (\text{D.64})$$

In order to establish in a convergent-divergent channel a subsonic expansion in the convergent part with a Mach number of unity at the throat section, followed by a supersonic expansion in the divergent part of the channel, the pressure at the throat must be greater than the ambient pressure at the outlet p_0 . Thus, the pressure ratio required for obtaining the condition $M^* = 1$ is

$$\frac{p_t}{p^*} \geq \left[\frac{\gamma + 1}{2} \right]^{\frac{\gamma}{\gamma - 1}} = 1.893 \quad (\gamma = 1.4) \quad (\text{D.65})$$

Again, in the case of a converging-diverging channel, the presence of a throat does not necessarily imply $M^* = 1$ because for values of p_t/p_0 lower than given by Equation (D.63) subsonic flow is found throughout (unchoked flow).

D.9 Normal shock waves

Consider an adiabatic flow through a constant area duct, where the gas properties change between the cross-sections 1 and 2 (Figure D.11). With the assumption of

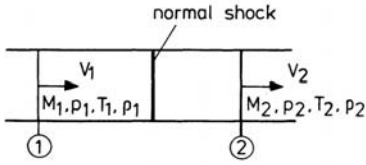


Figure D.11 Adiabatic flow in a constant area duct

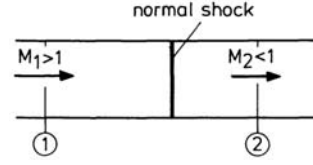


Figure D.12 Shock wave formation in a supersonic flow

a perfect gas, the governing equations are:

1. The equation of state $p = \rho RT$. (D.66)

2. The continuity equation $m = \rho_1 V_1 A = \rho_2 V_2 A$. (D.67)

3. The momentum equation $(p_1 - p_2)A = m(V_2 - V_1)$. (D.68)

4. The energy equation $c_p T_1 + \frac{V_1^2}{2} = c_p T_2 + \frac{V_2^2}{2}$. (D.69)

The above four equations contain the four variables, p , ρ , T and V . Therefore, the gas properties at section 2 can be expressed in terms of the properties at section 1. Substitution of Equation (D.67) into (D.68) yields

$$p_1 + \rho_1 V_1^2 = p_2 + \rho_2 V_2^2. \quad (\text{D.70})$$

Using the perfect gas law, Equation (D.66), and with $R\gamma/(\gamma - 1)$ substituted for the specific heat at constant pressure in Equation (D.69), we obtain

$$\frac{\gamma}{\gamma - 1} \frac{p_1}{\rho_1} + \frac{V_1^2}{2} = \frac{\gamma}{\gamma - 1} \frac{p_2}{\rho_2} + \frac{V_2^2}{2}. \quad (\text{D.71})$$

Combining Equations (D.67), (D.70) and (D.71) results in the following single equation,

$$\frac{V_1^2}{2} \left[1 + \frac{V_2}{V_1} \right] \left[1 - \frac{V_2}{V_1} \right] = \frac{\gamma}{\gamma - 1} V_1 V_2 \left[1 - \frac{V_2}{V_1} \right] - \frac{\gamma}{\gamma - 1} \frac{p_1}{\rho_1} \left[1 - \frac{V_2}{V_1} \right]. \quad (\text{D.72})$$

In addition to the trivial solution that V_2 is equal to V_1 , a second solution is valid mathematically, namely,

$$\frac{V_1^2}{2} \left[1 + \frac{V_2}{V_1} \right] = \frac{\gamma}{\gamma - 1} \left[V_1 V_2 - \frac{p_1}{\rho_1} \right]. \quad (\text{D.73})$$

We can manipulate Equation (D.73) to produce explicitly the velocity ratio,

$$\frac{V_2}{V_1} = \frac{\gamma - 1}{\gamma + 1} \left[1 + \frac{2\gamma}{\gamma - 1} \frac{p_1}{\rho_1} \frac{1}{V_1^2} \right]. \quad (\text{D.74})$$

A velocity variation may be experienced in a supersonic flow in the form of a discontinuity which is called a *shock wave* (Figure D.12).

With $V = M\sqrt{\gamma p/\rho}$ and the continuity equation, we can express the relationship between the velocities before and after the shock in terms of the initial Mach number M_1 :

$$\frac{V_2}{V_1} = \frac{\rho_1}{\rho_2} = \frac{2}{\gamma+1} \frac{1}{M_1^2} + \frac{\gamma-1}{\gamma+1}. \quad (\text{D.75})$$

The relationship between the pressures p_2 and p_1 is found from Equations (D.70) and (D.75) as

$$\begin{aligned} \frac{p_2}{p_1} &= 1 + \frac{\rho_1 V_1^2}{p_1} - \frac{\rho_2 V_2^2}{p_1} = 1 + \gamma M_1^2 - \gamma M_1^2 \left[\frac{2}{\gamma+1} \frac{1}{M_1^2} + \frac{\gamma-1}{\gamma+1} \right] \quad \text{or} \\ \frac{p_2}{p_1} &= \frac{2\gamma}{\gamma+1} M_1^2 - \frac{\gamma-1}{\gamma+1}. \end{aligned} \quad (\text{D.76})$$

Using Equations (D.66), (D.75) and (D.76), the temperature ratio is found to be

$$\frac{T_2}{T_1} = \frac{p_2}{p_1} \frac{\rho_1}{\rho_2} = \left[\frac{2\gamma}{\gamma+1} M_1^2 - \frac{\gamma-1}{\gamma+1} \right] \left[\frac{2}{\gamma+1} \frac{1}{M_1^2} + \frac{\gamma-1}{\gamma+1} \right]. \quad (\text{D.77})$$

The corresponding equation for the ratio of the Mach numbers is found, from Equations (D.75) and (D.77), to be

$$\left[\frac{M_2}{M_1} \right]^2 = \left[\frac{V_2}{V_1} \right]^2 \frac{T_1}{T_2} = \frac{\frac{2}{\gamma+1} \frac{1}{M_1^2} + \frac{\gamma-1}{\gamma+1}}{\frac{2\gamma}{\gamma+1} M_1^2 - \frac{\gamma-1}{\gamma+1}} \quad \text{or} \quad M_2 = \left[\frac{1 + \frac{\gamma-1}{2} M_1^2}{\gamma M_1^2 - \frac{\gamma-1}{2}} \right]^{1/2}. \quad (\text{D.78})$$

Apparently, for a given value of γ , the ratios p_2/p_1 , T_2/T_1 , ρ_2/ρ_1 , V_2/V_1 and the Mach number M_2 are unique functions of the initial Mach number M_1 . For $M_1 \geq 1$, we have:

$$\frac{p_2}{p_1} \geq 1, \quad \frac{T_2}{T_1} \geq 1, \quad \frac{\rho_2}{\rho_1} \geq 1, \quad \frac{V_2}{V_1} \leq 1, \quad M_2 \leq 1.$$

Thus, at supersonic velocities, all changes are accompanied by shock waves, through which the pressure, temperature and density are increased, and the flow velocity and Mach number are reduced.

The relationship between the initial and final Mach number is plotted in Figure D.13, which shows that the flow velocity behind a normal shock is always subsonic ($M_2 < 1$). The loss in kinetic energy is converted into heat so that the occurrence of a shock wave is an irreversible adiabatic (nonisentropic) process.

Though mathematically possible, the case of $M_1 < 1$ with the resulting M_2 being greater than unity, is physically impossible, since this solution to the equations is in defiance of the second law of thermodynamics.

The relationship between the total pressures on the two sides of the normal shock is given by

$$\frac{p_{t2}}{p_{t1}} = \frac{p_2}{p_1} \left[\frac{1 + \frac{\gamma-1}{2} M_2^2}{1 + \frac{\gamma-1}{2} M_1^2} \right]^{\frac{\gamma}{\gamma-1}}.$$

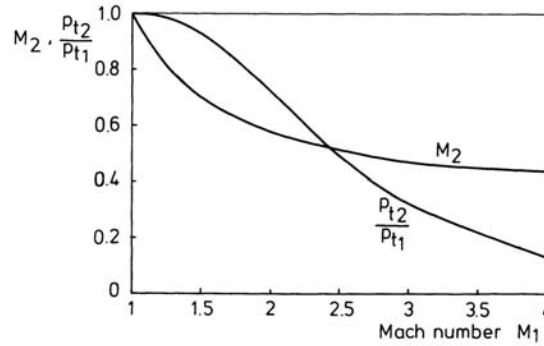


Figure D.13 Final Mach number and total pressure ratio versus initial Mach number for a normal shock ($\gamma = 1.4$)

Using Equations (D.76) and (D.78), this ratio can be written

$$\frac{p_{t2}}{p_{t1}} = \left[\frac{\gamma + 1}{2\gamma M_1^2 - (\gamma - 1)} \right]^{\frac{1}{\gamma-1}} \left[\frac{(\gamma + 1)M_1^2}{2 + (\gamma - 1)M_1^2} \right]^{\frac{\gamma}{\gamma-1}}. \quad (\text{D.79})$$

Figure D.13 shows that, for $M_1 > 1$, the total pressure always decreases when the flow passes a shock wave. Finally, it is worthwhile to derive a similar expression for the ratio of the total pressure behind the normal shock to the initial static pressure,

$$\frac{p_{t2}}{p_1} = \frac{p_{t2}}{p_{t1}} \frac{p_{t1}}{p_1} = \left[\frac{\gamma + 1}{2} M_1^2 \right]^{\frac{\gamma}{\gamma-1}} \left[\frac{2\gamma M_1^2}{\gamma + 1} - \frac{\gamma - 1}{\gamma + 1} \right]^{\frac{1}{1-\gamma}}. \quad (\text{D.80})$$

This relationship is called the Rayleigh formula, and is of importance to the measurement of airspeed.

D.10 Oblique shock waves

If, in a direction parallel to the shock wave, a uniform velocity V_i is superimposed on the flow field of the normal shock, the resultant upstream velocity is (Figure D.14a)

$$V_1 = \sqrt{V_{n1}^2 + V_i^2}. \quad (\text{D.81})$$

where V_{n1} is the normal component of the velocity V_1 . The inclination of the velocity V_1 relative to the shock is given by

$$\beta = \tan^{-1}(V_{ni}/V_i). \quad (\text{D.82})$$

Since $V_{n2} < V_{n1}$, the resultant velocity V_2 behind the shock makes a smaller angle with the shock than the upstream velocity. That is, the flow is deflected over an angle θ toward the shock.

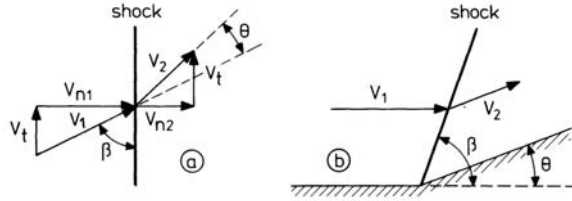


Figure D.14 Flow through oblique shock

Since in a frictionless steady flow any streamline can be replaced by a boundary, the oblique shock wave represents the behavior of a supersonic flow when turning suddenly through a deflection angle θ (Figure D.14b).

The equations relating the gas properties before and after the oblique shock can be obtained readily, if we recognize that these properties are not affected by the superposition of a velocity parallel to the shock wave. Thus, all the relations derived in Section D.9 for the normal shock are applicable if the Mach number M_1 in the normal shock equations is replaced by $M_1 \sin \beta$, where now $M_1 = V_1/c_1$ refers to the upstream Mach number before the oblique shock. Then, from Equations (D.75) to (D.77), we have the following ratios across the shock:

$$\frac{\rho_1}{\rho_2} = \frac{V_{n2}}{V_{n1}} = \frac{2}{\gamma+1} \frac{1}{M_1^2 \sin^2 \beta} + \frac{\gamma-1}{\gamma+1} \quad (\text{D.83})$$

$$\frac{p_2}{p_1} = \frac{2\gamma}{\gamma+1} M_1^2 \sin^2 \beta - \frac{\gamma-1}{\gamma+1} \quad (\text{D.84})$$

$$\frac{T_2}{T_1} = \left[\frac{2\gamma}{\gamma+1} M_1^2 \sin^2 \beta - \frac{\gamma-1}{\gamma+1} \right] \left[\frac{2}{\gamma+1} \frac{1}{M_1^2 \sin^2 \beta} + \frac{\gamma-1}{\gamma+1} \right]. \quad (\text{D.85})$$

Similarly, from Equation (D.79), the total pressure ratio becomes

$$\frac{p_{t2}}{p_{t1}} = \left[\frac{\gamma+1}{2\gamma M_1^2 \sin^2 \beta - (\gamma-1)} \right]^{\frac{1}{\gamma-1}} \left[\frac{(\gamma+1) M_1^2 \sin^2 \beta}{2 + (\gamma-1) M_1^2 \sin^2 \beta} \right]^{\frac{\gamma}{\gamma-1}}. \quad (\text{D.86})$$

From Figure D.14a and Equation (D.83) we obtain

$$\frac{\tan(\beta - \theta)}{\tan \beta} = \frac{V_{n2}}{V_{n1}} = \frac{2}{\gamma+1} \frac{1}{M_1^2 \sin^2 \beta} + \frac{\gamma-1}{\gamma+1}. \quad (\text{D.87})$$

Solving Equation (D.87) for the deflection angle θ produces the following expression

$$\theta = \tan^{-1} \left[\frac{M_1^2 \sin 2\beta - 2 \cot \beta}{2 + M_1^2 (\gamma + \cos 2\beta)} \right]. \quad (\text{D.88})$$

Finally, the Mach number M_2 after the shock may be obtained by writing

$$\frac{M_2}{M_1} = \frac{V_2 c_1}{c_2 V_1} = \frac{\sin \beta}{\sin(\beta - \theta)} \frac{V_{n2}}{V_{n1}} \frac{c_1}{c_2}. \quad (\text{D.89})$$

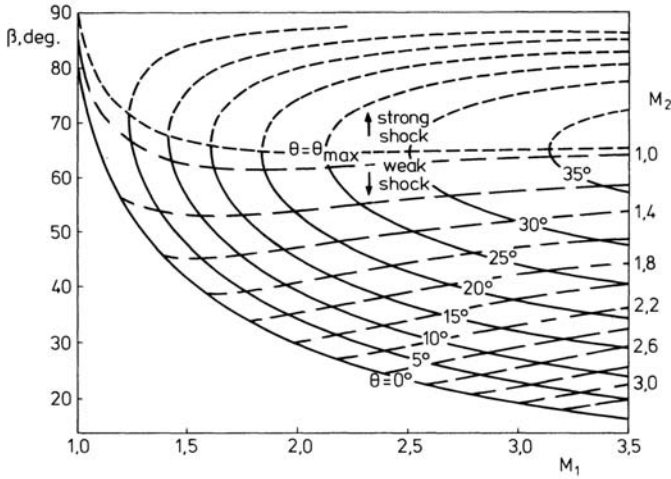


Figure D.15 Oblique shock properties



Figure D.16 Supersonic flow in a corner

Noting that $c_1/c_2 = \sqrt{T_1/T_2}$ and using Equations (D.83) and (D.85) yields

$$M_2^2 = \frac{1}{\sin^2(\beta - \theta)} \frac{1 + \frac{\gamma-1}{2} M_1^2 \sin^2 \beta}{\gamma M_1^2 \sin^2 \beta - \frac{\gamma-1}{2}} \quad (\text{D.90})$$

Combining Equations (D.90) and (D.88) furnishes

$$M_2^2 = \frac{1 + \frac{\gamma-1}{2} M_1^2}{\gamma M_1^2 \sin^2 \beta - \frac{\gamma-1}{2}} + \frac{M_1^2 \cos^2 \beta}{1 + \frac{\gamma-1}{2} M_1^2 \sin^2 \beta} \quad (\text{D.91})$$

In Figure D.15 is plotted β versus M_1 for constant values of θ . The points on the curves that correspond to the same value of M_2 are joined by dashed lines. The graph shows that for each value of M_1 there exists a maximum value of θ . If the deflection angle is greater than θ_{\max} , the gas properties are no longer described by the preceding equations since a detached shock will occur (Figure D.16).

Examining the curves in Figure D.15, we also see that there are two possible inclination angles for each value of M_1 and θ . The shock with the larger β results in a subsonic M_2 and is a stronger shock than that with the smaller inclination angle. Experience indicates, however, that a weak shock with the smaller β usually is found in actual flow. This means that the Mach number behind an oblique shock remains supersonic, except for a small range of values of θ near θ_{\max} .

Clearly, the occurrence of an attached oblique-shock requires that $\theta < \theta_{\max}$ and an inclination angle such that

$$\frac{\pi}{2} \geq \beta \geq \sin^{-1} \left[\frac{1}{M_1} \right]. \quad (\text{D.92})$$

The upper limit, $\beta = \pi/2$, leads to the presence of a normal shock, whilst at the lower limit of β we have the condition for an infinitely weak shock or *Mach wave* ($M_{n1} = 1$). The associated minimum shock inclination is called the *Mach angle*, usually given the symbol μ :

$$\beta_{\min} = \mu = \sin^{-1} \left[\frac{1}{M_1} \right]. \quad (\text{D.93})$$

When the condition (D.93) is applied to the preceding equations, we find that the value of θ is zero and that there is no change whatever in the gas properties across the Mach wave.

GENERAL REFERENCES FOR APPENDIX D

- L. Prandtl and O.G. Tietjens, *Applied Hydro- and Aeromechanics*, McGraw-Hill, New York, 1934.
- H.W. Liepmann and A. Roshko, *Elements of Gasdynamics*, John Wiley, New York, 1957.
- A.M. Kuethe and J.D. Schetzer, *Foundations of Aerodynamics*, John Wiley, New York, 1959.
- R.M. Rotty, *Introduction to Gas Dynamics*, John Wiley, New York, 1962.
- A.M. Kuethe and C. -Y. Chow, *Foundations of Aerodynamics*, John Wiley, New York, 1976.
- J.J. Bertin and M.L. Smith, *Aerodynamics for Engineers*, Prentice-Hall, Inc., Englewood-Cliffs, New Jersey, 1979.
- M.A. Saad, *Compressible Fluid Flow*, Prentice-Hall, Inc., Englewood-Ciffes, New Jersey, 1985.

References

1. J.R. von Mises, *Theory of Flight*, McGraw-Hill, New York, 1945.
2. F.J. Hale, *Aircraft Performance, Selection, and Design*, John Wiley, New York, 1984.
3. J.D. Anderson, Jr., *Introduction to Flight*, McGraw-Hill, New York, third edition, 1989.
4. A.C. Kermode, *Mechanics of Flight*, Pitman, London, 1962.
5. A. Miele, *Flight Mechanics*, Vol 1, Theory of Flight Paths, Addison-Wesley, Reading, Massachusetts, 1962.
6. D.O. Dommasch, S.S. Sherby and T.F. Connolly, *Airplane Aerodynamics*, Pitman, London, 1961.
7. H. Ashley, *Engineering Analysis of Flight Vehicles*, Addison-Wesley, Reading, Massachusetts, 1974.
8. Anon., *Handbook of Geophysics*, Macmillan, New York, 1960.
9. Anon., *International Standard Atmosphere (ISA)*, International Organization for Standardization, ISO 2533, 1975.
10. J.V. Iribarne and H.-R. Cho, *Atmospheric Physics*, D. Reidel Publishing Company, Dordrecht, Holland, 1980.
11. Anon., U.S. *Standard Atmosphere, 1976*, National Oceanic and Atmospheric Administration, National Aeronautics and Space Administration, United States Air Force, U.S. Government Printing Office, Washington, D.C., 1976.
12. F.W. Cole, *Introduction to Meteorology*, John Wiley, New York, 1980.
13. I.H. Abbot and A.E. von Doenhoff, *Theory of Wing Sections*, McGraw-Hill, New York, 1949.
14. E. Torenbeek, *Synthesis of Subsonic Airplane Design*, Delft University Press, 1976.
15. W. Gracey, *Measurement of Aircraft Speed and Altitude*, John Wiley, New York, 1981.
16. E.H.J. Pallett, *Aircraft Instruments*, Pitman, London, 1981.
17. J. Andresen, *Fundamentals of Aircraft Flight and Engine Instruments*, Hayden Book Company, New York, 1970.
18. H. Cohen, G.F.C. Rogers and H.I.H. Saravanamuttoo, *Gas Turbine Theory*, Longman, London, 2001.
19. P.J. McMahon, *Aircraft Propulsion*, Pitman, London, 1971.
20. J.L. Kerrebrock, *Aircraft Engines and Gas Turbines*, The MIT Press, Massachusetts, 1977.
21. P.G. Hill and C.R. Peterson, *Mechanics and Thermodynamics of Propulsion*, Addison-Wesley, Reading, Massachusetts, 1965.

22. M.J. Zucrow, *Gas Turbines and Jet Propulsion*, Volume II of Aircraft and Missile Propulsion, John Wiley, New York, 1958.
23. D. Fielding and J.E.C. Topps, *Thermodynamics Data for the Calculation of Gas Turbine Performance*, Aeronautical Research Council, R.&M. No. 3099, HMSO, London, 1959.
24. J.C. Samuels and B.M. Gale, *Effect of Humidity on Performance of Turbo-jet Engines*, National Advisory Committee for Aeronautics, Technical Note 2119, Washington, June 1950.
25. G. Jackon, *The Effect of Atmospheric Humidity and Temperature on the Engine Power and Takeoff Performance of a Hastings I*, Aeronautical Research Council, C.P. No. 77, HMSO, London, 1952.
26. H. Roxbee Cox (Consulting Editor), *Gas Turbine Principles and Practice*, George Newnes Limited, London, 1955.
27. N.D. Van Sickle (Editor), *Modern Airmanship*, Van Nostrand Reinhold Company, New York, 1971.
28. R.D. Hager and D. Vrabel, *Advanced Turboprop Project*, NASA SP-495, NASA Scientific and Technical Information Division, Washington, D.C., 1988.
29. H. Glauert, *Airplane Propellers*, Aerodynamic Theory, Vol. IV (William F. Durand, ed.). Dover Publications Inc., New York, 1963.
30. T. Theodorsen, *Theory of Propellers*, McGraw-Hill, New York, 1948.
31. E.P. Hartman and D. Biermann, *The Aerodynamic Characteristics of Full-Scale Propellers Having 2, 3, and 4 Blades of Clark Y and R.A.F. 6 Airfoil Sections*, NACA Report 640, 1937.
32. B.W. McCormick, *Aerodynamics, Aeronautics, and Flight Mechanics*, John Wiley, New York, 1979.
33. B.W. McCormick, *Aerodynamics of V/STOL Flight*, Academic Press, New York, 1967.
34. Hamilton Standard Division, United Aircraft Corp., *Generalized Method of Propeller Performance Estimation*, Hamilton Standard Publication PDB 6101 A, 1963.
35. Anon., *SBAC Standard Method of Propeller Performance Estimation*, Society of British Aircraft Constructors Ltd., 1950.
36. A.J. Bocci, *A New Series of Aerofoil Sections Suitable for Aircraft Propellers*, Aeronautical Quarterly, February, 1977.
37. C. Rohrbach and H.S. Wainauski, *Aerodynamic Characteristics of an Advanced Technology Propeller for Commuter Aircraft*, American Institute of Aeronautics and Astronautics, AIAA Paper No. 81-1565, 1981.
38. Anon., *U.S. Standard Atmosphere, 1962*, U.S. Government Printing Office, Washington, D.C., 1962.
39. Anon., *Engineering Sciences Data*, Aeronautical Series, Performance Vol. 1-6, Engineering Sciences Data Unit (ESDU) International Ltd., London.
40. D.P. Davies, *Handling the Big Jets*, Air Registration Board, Brabazon House, Redhill, Surrey, England, 1967.

41. R.S. Shevell, *Fundamentals of Flight*, Prentice-Hall, Inc., Englewood Cliffs, New Jersey, 1983.
42. D. Stinton, *The Anatomy of the Airplane*, G.T. Foulis & Co Ltd., London, 1966.
43. C.D. Perkins and R.E. Hage, *Airplane Performance Stability and Control*, John Wiley, New York, 1949.
44. F.H. Hawkins, *Human Factors in Flight*, Gower Technical Press Ltd., England, 1987.
45. A. and L. Welch and F. Irving, *Now Soaring Pilot*, John Murray, England, 1970.
46. A.E. Bryson, Jr. and Y.-C. Ho, *Applied Optimal Control*, Hemisphere Publishing Corporation, Washington, D.C., 1975.
47. N.X. Vinh, *Optimal Trajectories in Atmospheric Flight*, Elsevier, Amsterdam, 1981.
48. E.S. Rutowski, *Energy Approach to the General Aircraft Performance Problem*, Journal of the Aeronautical Sciences, Vol. 21, No. 3, March 1954.
49. A.E. Bryson, Jr., M.N. Desai and W.C. Hoffman, *Energy-State Approximation in Performance Optimization of Supersonic Aircraft*, Journal of Aircraft, Vol. 6, No. 6, Nov./Dec. 1969.
50. A.D. Edwards, *Performance Estimation of Civil jet Aircraft*, Aircraft Engineering, Vol. 22, No. 254, April 1950.
51. A.H. Stratford, *Air Transport Economics in the Supersonic Era*, MacMillan, London, 1973.
52. Anon., *Standard Method for the Estimation of Direct Operating Costs of Aircraft*, Society of British Aircraft Constructors, Issue No. 4, 1959.
53. Anon., *Standard Method of Estimating Comparative Direct Operating Costs of Turbine Powered Transport Airplanes*, Air Transport Association of America, 1967.
54. D.V. Maddalon, *Estimating Airline Operating Costs*, NASA Technical Memorandum 78694, May 1978.
55. Anon., *Short-Medium Range Aircraft - AEA Requirements*, Association of European Airlines, Brussels, Nov. 1986.
56. E. Ower, R. Warden and W.S. Brown, *An Investigation of Ground Effect with a Model of a Mid-Wing Monoplane*, Aeronautical Research Council, R.&M. No. 1847, HMSO, London, 1938.
57. D.H. Perry, *The Airborne Path During Take-off for Constant Rate-of-Pitch Manoeuvres*, Aeronautical Research Council, C.P. No. 1042, HMSO, London, 1969.
58. F.E. Douwes Dekker and D. Lean, *Take-off and Landing Performance*, AGARD Flight Test Manual, Volume 1, Chapter 8, Pergamon Press, 1962.
59. C.E. Padilla, *Optimizing Jet Transport Efficiency, Performance, Operations & Economics*. McGraw-Hill, New York, 1996.
60. J.D. Anderson, *Aircraft Performance and Design*, McGraw-Hill, New York, 1999.

61. M.E. Eshelby, *Aircraft Performance - Theory and Practice*, Arnold, London, 2000.
62. P. Clark, *Buying the Big Jets: Fleet planning for airlines*, Ashgate Publishing Ltd. Aldershot, UK, 2001.
63. M. Saarlal, *Aircraft Performance*, John Wiley, New York, 2007.

Index

- absolute acceleration, 326
- absolute ceiling, 202
- accelerate stop distance, 302
- accelerate-climb distance, 302
- advance angle, 146
- advance ratio, 147
- aerodynamic advance angle, 149
- aerodynamic ceiling, 211
- afterburner, 103
- air data instruments, 87
- air-path axis system, 10
- airfoil or wing section, 67
- airplane condition, 19
- airplane configuration, 19
- asymmetric pressure distribution, 63
- avionics systems, 87

- balanced field lengths, 302
- banked turn, 59
- Beaufort scale of wind force, 43
- Bernoulli's equation for compressible flow, 352
- blade angle, 147
- Blind flying instruments, 87
- block distance, 283
- block speed, 298
- block time, 298
- body axis system, 10
- braking slip ratio, 317
- Brayton-cycle, 112
- Breguet formula, 287
- Breguet range equations, 291
- Buys-Ballot, 46
- bypass ratio, 134

- calibrated airspeed, 93, 97
- centrifugal force, 8
- centripetal acceleration, 327

- choked flow, 123
- clear-air turbulence, 47
- cold front occlusion, 49
- combustion efficiency, 137
- condensation, 38
- conditional instability, 41
- control laws, 164
- control variables, 164
- convection, 42
- coordinated turn, 60
- Coriolis acceleration, 327
- critical pressure ratio, 134
- cruise chart, 285
- cruise-climb flight, 287

- dew point, 38
- dimensional analysis, 65
- drag-divergence Mach number, 80
- dry adiabatic rate, 40, 41
- dynamic pressure, 345

- effective pitch, 147
- effective velocity, 149
- endurance, 284
- energy conversion, 101
- energy height, 275
- energy-state approximation, 275
- Engine instruments, 87
- engineless glider, 249
- equivalent airspeed, 94, 97
- equivalent shaft power, 131
- Euler's equations of rotational motion, 54
- Eustachian tube, 280
- exosphere, 25
- exospheric temperature, 26
- external (aerodynamic) moment on the airplane, 54

- fan pressure ratio, 134
- fast-moving cold fronts, 49
- Federal Aviation Regulations, 173
- first law of thermodynamics, 39
- fixed-pitch propeller, 156
- flat turn, 59, 60
- flight condition, 19
- flight dynamics, 55
- flight level, 89
- flight program, 165
- flight technique, 165
- freeair thrust, 140
- freestream Mach number, 66
- frost point, 38
- full power, 125

- gas generator, 101
- geopotential density altitude, 34
- geopotential pressure height, 88
- gustiness, 47

- heterosphere, 24
- holding off bank, 247
- homosphere, 24
- hypersonic flow, 78

- ice crystals, 43
- ideal turbojet cycle, 112
- ILS, 314
- impact pressure, 93
- indicated airspeed, 97
- induced drag factor, 84
- Instrument Landing System, 314
- intake adiabatic efficiency, 118
- integral performance, 166
- ionosphere, 26

- jet streams, 46
- Joint Airworthiness Requirements, 173

- kinetic energy correction factor, 273

- limit load factors, 171
- load factor, 168
- lower stratosphere, 25

- Mach angle, 78, 361

- Mach number, 65
- Mach wave, 78, 361
- Machmeter, 97
- maximum cruise, 125
- maximum except takeoff (METO-)power, 125
- mesopause, 25
- mesosphere, 25
- minimum comfortable airspeed, 226
- minimum control speed, 224
- minimum stalling speed, 169
- momentum blade element theory, 151
- momentum theory, 141

- off-design performance, 124
- one-g stalling speed, 170
- Oswald's efficiency factor, 83
- Otto-cycle, 105
- ozonepause, 25

- parasite drag coefficient, 82
- path performance, 166
- Penaud diagram, 177
- performance diagram, 177
- planetary boundary layer, 45
- point performance, 166
- power available, 101
- power conversion process, 101
- power output, 39
- pressure recovery factor, 118
- products of inertia, 54
- profile drag coefficient, 72
- propeller slip, 148
- propfans, 144

- QFE, 89
- QNE, 89
- QNH, 89

- range factor, 291
- region of reversed command, 192
- relative acceleration, 327
- relative humidity, 38
- resultant aerodynamic force, 52
- revenue-earning capacity, 300

- Reynolds number, 66
- sailplane, 249
- saturation, 38
- saturation adiabatic rate, 40, 41
- service ceiling, 203
- shock induced boundary layer separation, 79
- shock wave, 356
- slat, 73
- slow-moving cold fronts, 49
- soaring, 259
- specific compressor power, 130
- specific excess power, 272
- specific fuel consumption, 117
- specific thrust, 112
- speed stability, 226
- spin, 240
- spiral climb, 56
- stability and control, 2
- stage length, 283
- stagnation temperature, 352
- stalling speed, 170
- standard power diagram, 107
- standard rate turn, 234
- static performance, 166
- static thrust, 141
- stratopause, 25
- stratosphere, 25
- tangential acceleration, 326
- taper ratio, 70
- temperature inversion, 41
- tensor of inertia, 54
- theoretical ceiling, 202
- thermodynamic cycle of the flow, 138
- thermosphere, 25
- thrust, 39
- total activity factor, 154
- total compressor pressure ratio, 134
- total pressure, 345
- total range, 283
- total temperature, 352
- transport acceleration, 327
- transport product, 299
- transport productivity, 299
- tropopause, 25
- troposphere, 25
- true airspeed, 94, 97
- true banked turn, 60
- turbine entry temperature, 134
- turbine isentropic efficiency, 120
- turbofan, 103
- turboprop, 103
- turbulence, 47
- two-spool engine, 102
- unchoked flow, 122
- upper stratosphere, 25
- variable-pitch propeller, 157
- variation of temperature with altitude, 40
- virtual temperature, 39
- warm front, 48
- wind correction angle, 260
- wind shear, 278
- wing area, 67